eman ta zabal zazu

Universidad del País Vasco
Euskal Herriko Unibertsitatea

Critical behavior and magnetocaloric effect in rare-earth based intermetallic materials

Aritz Herrero Hernandez

Supervisor:
Prof. Alberto Oleaga Páramo

- 2021 -

Contents

Acknowledgments I

Introduction III

I Theoretical background 1

1 Thermal Properties 3
- 1.1 Heat transfer mechanisms in solids . . . 4
- 1.2 Description of thermal properties . . . 6
- 1.3 Diffusion equation and thermal waves . . . 11
  - 1.3.1 Diffusion equation . . . 11
  - 1.3.2 Thermal waves . . . 11
- 1.4 Photopyroelectric calorimetry, PPE . . . 15
  - 1.4.1 Solution to a multilayer system . . . 17
  - 1.4.2 Frequency dependent measurements . . . 20
  - 1.4.3 Temperature dependent measurements . . . 21
  - 1.4.4 Experimental devices . . . 22

2 Magnetic and Magnetocaloric Properties 27
- 2.1 Introduction to magnetism in materials . . . 28
  - 2.1.1 Magnetic ordering . . . 28
  - 2.1.2 Magnetic exchange interactions . . . 30
  - 2.1.3 Relevant magnetic concepts . . . 32
- 2.2 Magnetocaloric effect . . . 36
  - 2.2.1 Historical context and recent trends . . . 36
  - 2.2.2 Interest and applications of magnetocaloric materials . . . 37
  - 2.2.3 Physical origin of MCE . . . 39
  - 2.2.4 Direct and indirect methods . . . 42
  - 2.2.5 Correct evaluation of the MCE . . . 46
  - 2.2.6 What are we looking for? . . . 48

3 Phase Transitions and Critical Behavior 53
- 3.1 Introduction to phase transitions . . . 54
  - 3.1.1 The critical point . . . 56
- 3.2 Critical behavior theory . . . 57
  - 3.2.1 Critical point exponents . . . 58
  - 3.2.2 Universality and scaling laws . . . 59

3.3 Critical behavior of thermal properties 64
3.3.1 Fitting procedure of thermal critical behavior 66
3.4 Critical behavior of magnetic properties 68
3.4.1 Fitting procedure of magnetic critical behavior 71
3.5 Scaling of magnetocaloric properties 72
3.6 Critical exponents table 76

II Experimental results 79

4 RTX intermetallics 81
4.1 Introduction 82
4.2 Preparation of samples and experimental techniques 83
4.3 Experimental results and discussion 84
4.3.1 Thermal diffusivity in RTX family 85
4.3.2 Critical behavior in RTX family 87
4.3.3 Magnetocaloric effect in RTX family 97
4.4 Conclusions 105

5 R_3CoNi intermetallics 107
5.1 Introduction 108
5.2 Preparation of samples, characterization, and experimental techniques 108
5.3 Experimental results and discussion 110
5.3.1 Crystal structure of R_3CoNi family 110
5.3.2 Magnetic characterization of R_3CoNi family 111
5.3.3 Critical behavior in R_3CoNi family 114
5.3.4 Magnetocaloric effect in R_3CoNi family 123
5.4 Conclusions 129

6 R_3T intermetallics 131
6.1 Introduction 132
6.2 Samples and experimental techniques 134
6.3 Dy_3Co 136
6.3.1 Thermal properties of Dy_3Co compound 136
6.3.2 Thermal critical behavior in Dy_3Co 137
6.4 Tb_3Co 141
6.4.1 Thermal and magnetic evolution of Tb_3Co 142
6.4.2 Thermal critical behavior in Tb_3Co 144
6.4.3 Character of the AFM-FM transition in Tb_3Co 146
6.4.4 Single crystal neutron diffraction and magnetic phase diagram for Tb_3Co 147
6.4.5 Magnetocaloric effect in Tb_3Co 150
6.5 Tb_3Ni 154
6.5.1 Thermal and magnetic evolution of Tb_3Ni 155
6.5.2 Thermal critical behavior in Tb_3Ni 156
6.5.3 Magnetocaloric effect in Tb_3Ni 158
6.5.4 Magnetic anisotropy and RMCE in Tb_3Ni 164

6.6 Conclusions 171

7 R_6TX_2 intermetallics 173
7.1 Introduction 174
7.2 Samples and experimental techniques 175
7.3 $Ho_6(Fe, Mn)Bi_2$ family 176
7.3.1 Structural data and magnetic characterization of $Ho_6(Fe, Mn)Bi_2$ family 176
7.3.2 Critical behavior in $Ho_6(Fe, Mn)Bi_2$ family 179
7.3.3 Magnetocaloric effect in $Ho_6(Fe, Mn)Bi_2$ family 185
7.4 $(Gd, Tb)_6(Fe, Mn)Bi_2$ family 190
7.4.1 Structural data and magnetic characterization of $(Gd, Tb)_6(Fe, Mn)Bi_2$ family 191
7.4.2 Critical behavior in $(Gd, Tb)_6(Fe, Mn)Bi_2$ family 195
7.4.3 Magnetocaloric effect in $(Gd, Tb)_6(Fe, Mn)Bi_2$ family . . . 203
7.5 $Dy_6(Fe, Mn)X_2$ (X = Sb, Te, Bi) family 209
7.5.1 Structural data, magnetic and thermal characterization of $Dy_6(Fe, Mn)X_2$ family 210
7.5.2 Critical behavior in $Dy_6(Fe, Mn)X_2$ family 216
7.5.3 Magnetocaloric effect in $Dy_6(Fe, Mn)X_2$ family 219
7.6 Conclusions 225

8 $Y_{0.9}Pr_{0.1}Fe_2D_{3.5}$ Laves phase intermetallic 227
8.1 Introduction 228
8.2 Sample and experimental techniques 228
8.3 Experimental results and discussion 229
8.3.1 Crystal structure and its temperature evolution 229
8.3.2 Critical behavior in $Y_{0.9}Pr_{0.1}Fe_2D_{3.5}$ 232
8.3.3 Magnetocaloric effect in $Y_{0.9}Pr_{0.1}Fe_2D_{3.5}$ 236
8.4 Conclusions 239

9 Conclusions and future work 241

Resumen 247

Publications 253

Bibliography 257

Acknowledgments

I believe we are all born with an intrinsic curiosity towards the world surrounding us, unfortunately, in many cases the spark is extinguished at an early age. I'm aware of how lucky I have been for always being encouraged and supported by my teachers, to whom I am enormously thankful for not letting the spark of my curiosity vanish.

A Ph.D thesis is an inflexion point in every researcher's career. I must thank the Department of Education of the Basque Government for granting me with an scolarship from the programme *"Programa Predoctoral de Formación de Personal Investigador No Doctor"* which made possible these four years, and also for providing me the opportunity of performing a research stay supported by the *"Estancia Predoctoral"* programme.

As many other things, my research stay at the *Institut de Chimie et des Matériaux Paris Est* in Thiais (France) was affected by the 2020 Covid-19 global pandemic. I am very thankful to every one in Thiais who, even in the given situation, made my stay a very nice experience. I have to specially acknowledge the help and care provided by Prof. Paul-Boncour before, during and after my stay. Working with her and being able to learn from her has been a privilege. Merci beaucoup Valérie pour votre humanité, vos soins et votre dévouement.

I feel extremely lucky for spending my last four years (and a little bit more) at the Department of Applied Physics in the Faculty of Engineering in Bilbao, where the hard work has been more bearable thanks to the great working environment and amazing people. Of course I need to make a special mention to the group *Mandarinas*, for all the good moments during lunch times (before Covid-19), for our whiteboard discussions, and for putting up with me. Eskerrik asko Hao, Iñaki, Itxaso, Asier, Jorge, Macarena, Peio, Itziar, Mateu, Arrate eta Naiara urte hauengatik, ez zaituztet ahaztuko eta laister gure arbela berriz txorakeriz bete dezagun espero dut.

Even before starting my thesis, when I was a master student, I knew I had made the right decision by joining the *Photothermal Thecniques Laboratory* (PTL) research group, where I have always felt valued and challenged to extend my knowledge scope. Thank you Agustín, Arantza, Esti, Javier, Ivan and Angel. Needless to say that I wouldn't have reached here without the unconditional support and help of my supervisor Alberto Oleaga. All the fears I could have before starting this thesis fade away thanks to his guidance and all the trust he placed in me. He made me gain confidence and shaped me as the researcher I have become. It's hard to express the gratitude I feel for all the care I have received and all the opportunities this group has granted me.

Muchas gracias por todos estos años, me siento muy afortunado de haberos tenido como compañeros.

A wise man once said: *"It is our choices that show what we truly are, far more than our abilities"*. My friends are my choices, and I couldn't be prouder of every single one of them. Agurne, Garoa, Iratxe, Izei, Kepa, Klartje, Maialen, Mateu y Naiara, espero poder crear muchos más recuerdos junto a vosotras. Mila esker nire historiaren parte izateagatik.

To my *Army*, Uxue and Ru. You always tell me I'm very good at using words to express my ideas, but now I'm not even able to connect the words so that I can write down how grateful I am for having you. You saved me, you know that. Me hacéis muy feliz, y eso es algo que no cambiaría por nada. Gracias por haber sido mucho más que mi apoyo emocional durante estos años. But, let me show you 'cause talk is cheap ;).

Si he crecido con estos valores y he llegado hasta aquí se lo debo en gran medida a mi familia: mi aita, Raul, mi ama, Isabel, y mi hermano, Endika. Quienes siempre han sabido valorar mi esfuerzo y han creido en mí incluso cuando yo no lo hacía. Siempre seréis corresponsables de mis logros.

A long and beautiful journey comes to an end with this manuscript, and, although future perspective might look scary sometimes, I am lucky to know I will have the best companions by my side.

Un largo y hermoso viaje llega a su fin con esta tesis y, aunque el futuro puede dar miedo a veces, tengo la suerte de saber que tendré a los mejores compañeros a mi lado.

Tesi honekin bidaia luze eta eder bat bukatzen da, eta etorkizunak batzuetan beldurra eman badezake ere, zorionez badakit lagun hoberenak izango ditudala nire alboan.

Introduction

Magnetic refrigeration has recently emerged as a promising technological ally on the mitigation of climate change effects. This thesis manuscript is devoted to the study of compounds which could potentially play an important role in the transition to a more efficient and environmentally friendly refrigeration based on magnetic solid materials.

My intention with this manuscript, other than showing our work, is to provide the reader with a guide to the theoretical background and experimental techniques which can be used to explore magnetocaloric materials and the critical behavior of their magnetic transitions. With this idea in mind, I have divided the manuscript in two major parts. The first one is devoted to the presentation of the general theoretical framework, which is valid for any kind of magnetic material. The second part is oriented to the application of this theory to specific materials; the rare-earth based intermetallic compounds, on which we have focused our work.

The theoretical part is intended to contain all the topics which will later be applied in the experimental results part. Given its importance, I have tried to make it as easy reading as possible without loosing any piece of accuracy. This part is divided in three chapters, one for each pillar of our work. The first one presents the basic concepts of thermal properties, from their physical meaning and the heat propagation mechanisms to the description of the *ac* photopyroelectric calorimetry and its application. We will show how this photothermal technique, based on generating heat waves on a sample with an amplitude modulated laser beam, allows performing high resolution measurements and retrieving thermal properties such as the thermal diffusivity, thermal effusivity, thermal conductivity and specific heat. The second chapter focuses on magnetic phenomena. A brief introduction to magnetism in matter will be given prior to the presentation of the magnetocaloric effect. Topics such as magnetic arrangements, exchange interactions, the history of the magnetocaloric effect since its discovery to recent years, the interest of this phenomena and its applications, its physical origin, and how to correctly measure it will be addressed. The theoretical background will conclude with an introduction to the critical behavior theory, which will show up as a very useful tool to gain some insight on the underlying physics of the systems under study. We will finish by showing how this theory is connected to the beforehand discussed thermal, magnetic and magnetocaloric properties.

The experimental results are focused on the particular case of rare-earth based intermetallic compounds. Our interest on these materials comes from their magnetic complexity, which causes behaviors not observed in other kind

of compounds. Magnetism in rare-earth elements is governed by indirect exchange interactions between the inner *4f* shells, mediated by the polarization of the conduction electrons. The particular mechanism is described by the long-range oscillatory Ruderman-Kittel-Kasuya-Yosida exchange interaction (RKKY). Without going into further details, this gives rise to the complex helix, cone and longitudinal-wave magnetic structures found in rare-earths [1–3]. When this peculiar behavior is mixed with other metals to form intermetallic compounds, the complexity of the system increases and new magnetic phenomena appear. This will be explored through the study of different intermetallic families.

This thesis covers five big families of intermetallic materials, each one is collected in an independent chapter presenting its interest, the experimental techniques, the analysis performed and, obviously, the corresponding discussion on the obtained results. Though additional studies have been performed in some of the compounds, all of the experimental chapters will have specific sections focused on the critical behavior of their magnetic phase transitions and the evaluation of their magnetocaloric effect, exploring the potential of both analysis. One of our goals through this study is to observe the effect that the substitution of different elements in the composition (rare-earths specially but not exclusively) has on the properties of the compounds, and more concretely, how this affects the critical behavior or how these substitutions can be used to enhance and tune the magnetocaloric effect within the intermetallic family.

We start presenting our experimental work in Chapter 4 by addressing some seldom studied issues in the well-known ternary RTX family (R = rare-earth, T = transition metal, X = *p*-block element), leading to a better understanding of this promising family. Moving to Chapter 5 we will study the newly discovered R_3CoNi family, for which several members have been synthesized for the first time for this work, and explore its potential application and general properties. The magnetic complexity of the rare-earth based intermetallic compounds will fully glow up in Chapter 6, with a careful analysis concerning the order of several magnetic transitions and with Tb_3Ni coming up as an intriguing and promising material. The tailoring of the critical temperatures and magnetocaloric effect will be a central topic in Chapter 7, covering three *"sub-families"* of the parent R_6TX_2 family, which, as will be shown, is rich in complexity and variety. The experimental results will conclude in Chapter 8 presenting part of the work I performed during my scientific stay at the *Institut de Chimie et des Matériaux Paris Est* in Thiais (France), where, among other things, we studied the critical behavior and magnetocaloric effect of $Y_{0.9}Pr_{0.1}Fe_2D_{3.5}$ *Laves phase* intermetallic deuteride, as well as the temperature evolution of its crystal structure. Finally, the conclusions of our work and the possible future research plans are collected in Chapter 9.

Part I
Theoretical background

Every scientific work must be constructed over solid and well established foundations. This first part of the thesis is devoted to the presentation and development of the theoretical and technical background as well as to the methodology used for the later analysis of the experimental results. Thermal, magnetic, magnetocaloric and critical behavior concepts will be presented to be used as the shoulders from where to see further. Experimental devices, and procedures will also be described, and a historical overview, as well as a state of the art situation, of the magnetocaloric refrigeration will be presented.

1 | Thermal Properties

"The more I study, the more insatiable do I feel my genius for it to be."

– Ada Lovelace

An important part of this thesis is devoted to the acquisition, study and analysis of different thermal properties. This chapter aims to *"satiate"* the *"genius"* of the reader with a rigorous presentation of the heat conduction mechanisms in solids, relevant thermal concepts, a description of the physical meaning of the thermal properties, and the basis of the *ac* photopyroelectric calorimetry technique (PPE) used to obtain the thermal properties of the samples under study.

Thermal characterization and study have always been of great interest in many scientific areas. This is so because different mechanisms (at both macroscopic and microscopic scales) let a print on the thermal properties. In solid state physics heat transport is mainly mediated by phonons and electrons (in the case of metals), and affected by the magnetic ordering and other effects. In particular we will see that different kind of phase transitions are signalled on specific heat (c), thermal diffusivity (D), thermal effusivity (e), and thermal conductivity (K). An accurate acquisition of these properties and the later application of the renormalization group theory will allow the comprehension of the underlying physics in the systems.

1.1 Heat transfer mechanisms in solids

Whenever there is a temperature difference energy is transferred from the hotter side to the colder one, this energy is what we referred to when we talk about heat. In this section I will focus on the main mechanisms by which heat is transferred in solids: conduction, convection and radiation. All these processes are expressed by equations relating either the temperature of the body, T, or its gradient, $\vec{\nabla}T$, to the heat flux, $\vec{q}$. It will be shown that, although in almost every real situation the three mechanisms take part to some extent, in our case it will be enough to only consider heat conduction. In order to understand the reasons for this, let's have an insight into the mentioned mechanisms.

Conduction

When referring to thermal conduction in solids, the heat transfer happens within the body itself. In solid materials this transport is generally mediated by the lattice vibrations, the well known phonons. However, when dealing with metals, the greatest contribution to the heat propagation comes from the electrons in the conduction band, and therefore they must be taken into account for an accurate description.

If we consider a metal bar with its extremes at different temperatures, so that $T_1 < T_2$, without any heat source or sink, the hot end would gradually cool as the cold side warms, with heat flowing in the opposite sense to the temperature gradient, $\vec{\nabla}T$, until eventually they reach an equilibrium temperature, T_3. If, instead of isolating the system, we now apply heat to the hot end as fast as it flows away and we remove the heat at the cold side, we get a steady state with constant temperature gradient and heat flow ($\vec{q}$). In 1822 Joseph Fourier stated that under these conditions, and for homogeneous and isotropic materials, the heat flow through the material is proportional to the negative temperature gradient. This is known as *Fourier's law* [4]:

$$\vec{q}_{con} = -K\vec{\nabla}T \,, \tag{1.1}$$

where the proportionality factor K is the well known thermal conductivity, which is a positive parameter dependent on temperature and pressure; however, over a moderate range K can be consider constant in solids. In the following sections a more detailed description of thermal conductivity will be given; however, it is worth mentioning that K is used to express the capacity of a given material to conduct heat; furthermore, although in Eq. (1.1) K is expressed as a scalar, this will not be the general case.

Convection

Convection is usually the dominant heat transfer mechanism in fluids; however, in opposition to conduction, convection can not occur in a solid without a fluid taking part in the heat transmission because it involves fluid movements.

If we have a solid with temperature T_S surrounded by a colder fluid at temperature T_∞, the fluid will extract heat from the solid and get warmer. As a warm fluid is less dense than a cold fluid an upwards movement will appear generating convective cells. This is the basic mechanism behind air circulation on Earth or oceanic currents. If we consider heat sinks in order to maintain T_S and T_∞ constant, we get a steady state heat flow which is proportional to the temperature difference between the solid material and its surrounding. This relation is expressed by *Newton's cooling law* [5]:

$$q_{conv} = hA(T_S - T_\infty)\,. \tag{1.2}$$

In this expression A is the area of thermal contact and h is the heat transfer coefficient which depends not only on the properties of the fluid, but also on its velocity, geometry and flux. Although h depends on several variables, its values in gases usually lie between $2-25 W/m^2K$ in free-convection (where the only driving force is gravity and there is no external influence). We should keep in mind that this is a simplistic version of reality, where we have considered an steady state case with the heat transfer coefficient being independent of the temperature difference between the solid and the fluid. This is not always the case in heat convection and h certainly depends on the temperature difference; however, *Newton's cooling law* is still reliable to describe the process as long as the temperature difference is kept relatively small.

Thermal radiation

Above absolute zero every object or element emits energy as radiation. Temperature is directly related to the motion and oscillations of particles, and it is well know from electromagnetism that acceleration of charged particles implies the emission of electromagnetic radiation. In order for the radiation to take place there is no need of any medium, this is, for example, the mechanism by which the heat from the Sun reaches the Earth. In the case of a perfect Black Body (an ideal body which absorbs all the incident electromagnetic radiation) this energy emission is distributed along a bunch of different frequencies or wavelengths (λ) according to *Plank's law*:

$$B_\lambda(\lambda, T) = \frac{2hc^2}{\lambda^5} \frac{1}{e^{\frac{hc}{\lambda K_B T}} - 1}\,. \tag{1.3}$$

By integrating this energy distribution over all the wavelength spectra it can be proved that the maximum heat flux (which corresponds to a Black Body) is given by *Stefan-Boltzmann law*:

$$q_{rad} = \sigma T_S^4\,. \tag{1.4}$$

Here $\sigma = 5.67 \cdot 10^8 W m^{-2} K^{-4}$ is the Stefan-Boltzmann constant. However, real bodies are not perfect emitters (Black Bodies) and, therefore, in order to account for the heat flux radiated by real bodies the previous expression must be

modified into the following one:

$$q_{rad} = \epsilon \sigma T_S^4 \,, \tag{1.5}$$

where ϵ is the emissivity of the body, i.e., the effectiveness of the material in emitting energy as electromagnetic radiation. ϵ takes positive values ranging from 0 to 1, where the latter would be the case of a Black Body. Whenever we have two bodies or elements there will be a net balance between the radiation emitted and absorbed by each one of them. In general, studying this exchange is not an easy task; however, this can be done in the case where we have a material surrounded by a gas, which will be our case. If T_S and T_g are the temperatures of the sample and the surrounding gas respectively, the equilibrium net heat exchange can be expressed as follows:

$$q_{rad} = \epsilon \sigma A (T_S^4 - T_g^4) \,, \tag{1.6}$$

where A is the area of the body. If T_S is only slightly higher than T_g the heat losses due to radiation can be express as:

$$q_{rad} = h \Delta T \,, \tag{1.7}$$

with $\Delta T = T_S - T_g$ and h the heat loss factor.

Taking a look at equations (1.1), (1.2), and (1.6), we can see that as long as the temperature changes induced in our experiments are small, the only significant process is heat conduction. It will be latter shown that the temperature change in our samples, when the measurements are performed, will be of the order of few mK and, therefore, we can safely neglect the effects of both thermal convection and radiation.

1.2 Description of thermal properties

When dealing with heat conduction several properties are needed to describe our systems; while some of them are well known and understood, the role of others is usually misunderstood as they are conceptually more challenging. Consequently, it is the aim of this section to present the main thermal properties which will come up continuously along this work in order to clear up their meaning and relevance.

We will need one or another thermal property according to whether the system we are dealing with is static (independent of time and position), steady (time independent but with spatial dependency) or transitory (time dependent). In the first case specific heat, c, itself it's enough to describe the system, while the only required property in steady systems is thermal conductivity, K. Lastly, for completely describing a time dependent system we need to consider two new properties: thermal diffusivity (D) and thermal effusivity (e) [6]. We will now describe the aforementioned properties in the case of homogeneous materials.

Specific heat, c

Among all the thermal properties specific heat is probably the most recognizable one. It measures the amount of energy (heat) per unit of mass that must be introduced into a system in order to increase its temperature one kelvin. If we consider a thermally isolated body with mass m, the relation between the temperature difference generated and the amount of energy introduced (or extracted) from the system is given by the following thermodynamic relation:

$$\Delta Q = mc\Delta T \, . \tag{1.8}$$

Moreover, specific heat also quantifies the ability of a material to store internal thermal energy. However, we must keep in mind that this relation is not always valid. For instance, as we will see, c is temperature dependent, thus the previous expression is only valid for small temperature changes where c is practically constant. It should also be noticed that Eq. (1.8) can not be applied during a first order phase transition, where the heat added or removed is used for the transition to take place and it is not translated into a change of temperature.

Thermal conductivity, K

Thermal conductivity describes the capacity of a material to allow the heat flow in the same way as electrical conductivity measures the ability of a material to allow the electrical current through it. This resemblance makes the meaning of thermal conductivity very well understood compared with other thermal properties. We have already seen that, in the case of homogeneous and isotropic materials, *Fourier's law* describes heat conduction.

Expression (1.1) tells us that whenever we stablish a temperature gradient on a material, a heat flux will appear from the hottest place to the coldest one; in other words, *Fourier's law* tells us how much heat is being extracted from the hot spot. Therefore, K relates a temperature difference of 1 K with the heat flow per unit of time through a unit area of a sample of unit thickness. This means that, in the case of thermal conductors (high thermal conductivity), heat transfer, i.e., the heat extracted from the source per second, occurs at a higher rate across the material than in thermal insulators (low thermal conductivity).

It is worth mentioning that the reciprocal of thermal conductivity is called thermal resistivity, this property expresses the ability of any material to resist a heat flux. Furthermore, thermal resistivity is added when several materials are placed in series, in clear analogy to electrical resistivity.

Finally, Eq. (1.1) is not valid in the case of anisotropic materials because thermal conductivity is not a scalar but a tensor, that is, it has, in general, different values along different propagation directions. In this case *Fourier's law* takes this form [7]:

$$q_i = -\sum_{j=1}^{3} K_{ij} \frac{\partial T}{\partial x_j} \quad i = 1,2,3 \ , \tag{1.9}$$

where K_{ij} is expressed by a second order tensor:

$$K_{ij} = \begin{pmatrix} K_{11} & K_{12} & K_{13} \\ K_{21} & K_{22} & K_{23} \\ K_{31} & K_{32} & K_{33} \end{pmatrix} . \tag{1.10}$$

According to the reciprocity relation K_{ij} tensor is symmetrical ($K_{ij} = K_{ji}$) [8], moreover, all of the values are real. Under these conditions it is possible to find a new reference system (X, Y, Z) under which the tensor in Eq. (1.10) is diagonal:

$$K_{ij} = \begin{pmatrix} K_x & 0 & 0 \\ 0 & K_y & 0 \\ 0 & 0 & K_z \end{pmatrix} . \tag{1.11}$$

K_x, K_y and K_z are known as principal thermal conductivities and they represent the thermal conductivity along the principal axes (the ones for which K_{ij} is diagonal). Taking Eqs. (1.9) and (1.11) into account, *Fourier's law* is recovered for each principal axis:

$$q_i = -K_i \frac{dT}{di} \quad i = x,y,z \ . \tag{1.12}$$

Along these principal axis the sample behaves as an isotropic material.

Thermal diffusivity, *D*

Thermal diffusivity is usually defined as an abstract parameter related to specific heat, thermal conductivity and density, ρ [5]:

$$D = \frac{K}{\rho c} , \tag{1.13}$$

but little attention has been played to its physical meaning. Thermal diffusivity measures the speed at which heat propagates across a material during temperature changes over time, hence, the time needed by a material (in contact with a constant temperature source) to reach thermal equilibrium. It has been generally stated that a material gets warm or cold quickly (slowly) if it is a good (bad) thermal conductor, but, actually, the reason for this is given by thermal diffusivity. It is true that, in general, and particularly in condensed matter, it is a good guess to say that a good thermal diffuser is also a good thermal conductor, and this could be the explanation for the common confusion between thermal conductivity and diffusivity. This can clearly be seen in the "condensed matter" region of Fig. 1.1, where different materials have been plotted considering their thermal conductivity and diffusivity. However, if we look at the region occupied by gases we notice that while they are great diffusers they are very bad thermal conductors (good thermal insulators), i.e.,

due to small K values a gas in contact with a heat source extracts few heat from it, but the absorbed energy is transmitted rapidly through the gas due to high D values.

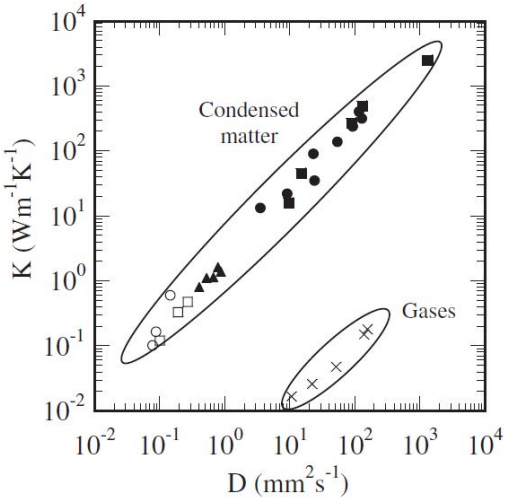


Figure 1.1: Relation between thermal conductivity and diffusivity for different materials [6].

The reason for the materials to lie along a straight line in Fig. 1.1 and the difference between gases and condensed matter can be found in Eq. (1.13). This equation establishes the thermodynamic relation among several thermal properties. Due to *Dulong-Petit's law*, $K/D = \rho c$ remains almost constant in condensed matter, with values in the range of $1{\cdot}10^6\ Jm^{-3}K^{-1}$ and $4{\cdot}10^6\ Jm^{-3}K^{-1}$. On the other hand, ρc value in gases is three orders of magnitude lower, falling between $0,7 \cdot 10^3\ Jm^{-3}K^{-1}$ and $2 \cdot 10^3\ Jm^{-3}K^{-1}$.

Just as in the case of K, when dealing with anisotropic materials D is described by a second order tensor which, following the same arguments as in the case of thermal conductivity, it can be reduced into a diagonal form with the principal thermal diffusivities D_x, D_y and D_z along the principal axes:

$$D_{ij} = \begin{pmatrix} D_x & 0 & 0 \\ 0 & D_y & 0 \\ 0 & 0 & D_z \end{pmatrix}. \tag{1.14}$$

Thermal effusivity, *e*

Thermal effusivity is probably the most unknown thermal property; however, it must completely be taken into account in transitory problems where the system changes over time. We have already seen that in time-varying situations thermal diffusivity controls the temperature evolution and the speed at which heat is transferred, but it is thermal effusivity which controls the heat flux through a surface in this situations. For instance, this magnitude measures the ability of a material to exchange heat with the environment or with another material in contact. It is usually defined as a combination of the thermodynamic variables that we have already discussed [4]:

$$e = \frac{K}{\sqrt{D}} = \sqrt{\rho c K} = \rho c \sqrt{D}\,. \tag{1.15}$$

In order to better understand the role of thermal effusivity lets imagine a simple situation in which we put into contact a semi-infinite material, at temperature T_0, with a perfect heat source at $T_1 > T_0$. Under these conditions the heat flux established across the interface of both materials is given by [5]:

$$q = \frac{e(T_1 - T_0)}{\sqrt{\pi t}}\,, \tag{1.16}$$

where t is the time since both materials were put into contact. From Eqs. (1.16) and (1.1) we can see the similarity between thermal conductivity and effusivity. They are both equivalent in their proper regimes. While in the steady case heat flux was proportional to K, in time dependent conditions it is proportional to e.

Thermal effusivity plays a big role when describing non-stationary phenomena, and it is the responsible for many daily life experiences. However, these experiences have mistakenly been attributed to thermal conductivity [9]. For example, the reason why a piece of metal at 20 ºC "feels" colder than a piece of wood at the same temperature when we touch it with our hands comes from the difference of their respective thermal effusivities. To check this lets study the case in which we put into perfect thermal contact two half infinite materials with temperatures T_1 and T_2 where $T_1 > T_2$, and e_1 and e_2 thermal effusivities for the hottest and colder material respectively. The temperature at both contact surfaces will suddenly reach a temperature T_3 which is somewhere between T_1 and T_2. Using Eq. (1.16) and equating the heat flux out of the hottest material and the one into the coldest one:

$$\frac{e_1(T_1 - T_3)}{\sqrt{\pi t}} = \frac{e_2(T_3 - T_2)}{\sqrt{\pi t}}\,, \tag{1.17}$$

we can get the following expression for T_3:

$$T_3 = \frac{e_1 T_1 + e_2 T_2}{e_1 + e_2}\,. \tag{1.18}$$

Back to our "feeling" of temperature, from Eq. (1.18) we can see that if we touch a piece of Cu ($e_{Cu} = 37140\ Jm^{-2}K^{-1}s^{-1/2}$) at T_2 =20 ºC with our hand ($e_{skin} = 1120\ Jm^{-2}K^{-1}s^{-1/2}$) at T_1 =37 ºC, the surface temperature of the hand, will inmediatelly drop to $T_3 \sim 20,5$ ºC. However, if we touch a piece of hard wood ($e_{wood} = 380\ Jm^{-2}K^{-1}s^{-1/2}$) at the same T_2 =20 ºC temperature, our hand's temperature will only drop to $T_3 \sim 32,7$ ºC [9].

The conclusion is that thermal effusivity and diffusivity must not be undervalued or misunderstood because they are the main properties to be considered when dealing with non-stationary thermal phenomena. It must be noticed, from Eqs. (1.13) and (1.15), that only two of the thermal parameters discussed are independent.

1.3 Diffusion equation and thermal waves

Until now we have seen how heat can be transferred in solid materials and we have concluded that the main mechanism in our case is conduction. The main thermal properties to which we will constantly refer have also been described so far. It is now time to present two of the most important concepts needed for the understanding of *ac* photopyroelectric technique: the diffusion equation and thermal waves.

1.3.1 Diffusion equation

When we consider a solid material with a temperature gradient, we know that heat will flow from the hottest part to the coldest one, warming the latter and cooling the former. We are now interested on how the temperature will change across the material. Applying both Eq. (1.1) and energy conservation principle it is possible to determine the temperature field, i.e., the spatial and temporal distribution of temperature, $T(\vec{r},t)$, in the sample. In the simplest case, with an isotropic and homogeneous material, and in the absence of any heat source, the temperature field is obtained by solving the heat diffusion equation [5]:

$$\nabla^2 T(\vec{r},t) - \frac{1}{D}\frac{\partial T(\vec{r},t)}{\partial t} = 0\,, \tag{1.19}$$

with D being the thermal diffusivity previously discussed. This previous expression is often called parabolic heat equation or *Fourier's second law* [9].

We will see that under our working conditions in the *ac* photopyroelectric technique, Eq. (1.19) is the basic tool for the analysis of heat propagation in the system. However, in general, Eq. (1.19) needs to be rewritten in order to take into account heat sources ($Q > 0$) or heat losses ($Q < 0$). In that case the heat diffusion equation looks like this:

$$\nabla^2 T(\vec{r},t) - \frac{1}{D}\frac{\partial T(\vec{r},t)}{\partial t} = -\frac{Q}{K}\,, \tag{1.20}$$

where thermal conductivity, K, appears.

1.3.2 Thermal waves

Thermal wave is the widely used term to describe the temperature field solution to the diffusion equation (Eq. (1.20)) as a consequence of a periodical heating [5, 9–11]. However, this is a rather confusing term which could lead to misinterpretations because, as we will see, thermal waves do not transport energy and, therefore, are not real waves, at least not in the way we are used to [12]. They were given this name due to their mathematical resemblance to real waves; furthermore, their interpretation as waves makes it easier to study and understand certain photothermal experiments in terms of wave theories [9].

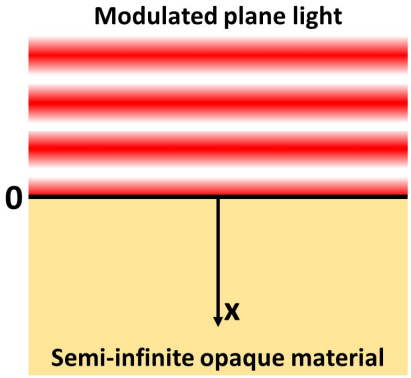


Figure 1.2: Semi-infinite, homogeneous, isotropic, and opaque material exposed to a modulated plane light.

In what follows we will see how thermal waves are generated in a simple, yet representative, situation. Lets start considering a semi-infinite, homogeneous, isotropic, and opaque material. The surface is located at $X = 0$ plane and the material extends downwards along positive X axis as can be seen in Fig. 1.2. In order to generate thermal waves on the material a periodic heat source must be used. In our case the surface will be uniformly excited by a light beam with a periodically modulated intensity:

$$I(t) = \frac{I_0}{2}(1 + \cos(\omega t)) \,. \tag{1.21}$$

Here $\omega = 2\pi f$ is the common angular frequency, with f as the modulation frequency of the light beam, and I_0 is the intensity of the light source. When the stationary state has been reached in the system, the temperature field at any point and time can be decomposed in the following way:

$$T(x,t) = T_{\text{room}} + T_{dc}(x) + T_{ac}(x,t) \,. \tag{1.22}$$

T_{room} represents room temperature and the initial temperature of the material before exciting it, $T_{dc}(x)$ is a time-independent increase of temperature above room temperature caused by the lightening of the sample, this value is equal to the temperature that would be obtained if the sample was lightened up with a beam at a constant intensity $I_0/2$. Finally, as we will show, $T_{ac}(x,t)$ is the most relevant term for our study, it is a periodic oscillation of temperature with the same frequency as the modulation of the light beam. A schematic representation of these components is presented in Fig. 1.3.

Our modulated homogeneous heat source can be expressed in the following way:

$$Q = Q_0[1 + e^{i\omega t}] \tag{1.23}$$

And introducing both Eqs. (1.22) and (1.23) into Eq. (1.20), we get:

$$\nabla^2 T_{dc} = -\frac{Q_0}{K} \,, \tag{1.24}$$

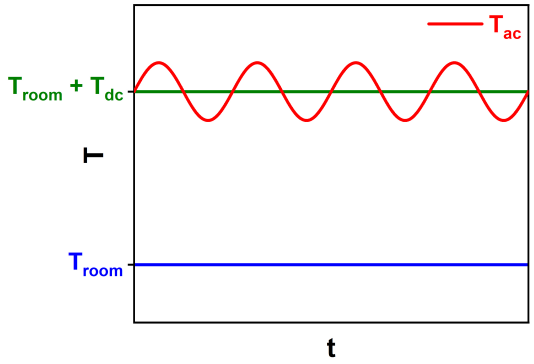


Figure 1.3: Temperature components on the surface of a semi-infinite opaque material exposed to a modulated light beam in stationary state.

$$\nabla^2 T_{ac} - \frac{1}{D}\frac{\partial T_{ac}}{\partial t} = -\frac{Q_0 e^{i\omega t}}{K} \,. \tag{1.25}$$

The *dc* component will not carry any valuable information and do not generate thermal waves into the material, thus, we shall focus on solutions to Eq. (1.25). There are two ways to deal with this expression, one could try to directly solve the inhomogeneous equation as it is, or solve the homogeneous equation and later account for the inhomogeneous term with the corresponding boundary conditions. Here the second way will be taken. It can be easily seen that solutions to the homogeneous equation will have the following form:

$$T_{ac}(x,t) = T_{ac}(x)e^{i\omega t} \,, \tag{1.26}$$

where the spatial, $T_{ac}(x)$, and the time dependent components have been separated. Introducing this solution into Eq. (1.19) it can be proven that $T_{ac}(x)$ obeys the *Helmholtz's equation*:

$$\nabla^2 T_{ac}(x) - \sigma^2 T_{ac}(x) = 0 \,. \tag{1.27}$$

In order to simplify the notation σ has been defined as follows:

$$\sigma = \sqrt{\frac{i\omega}{D}} \,, \tag{1.28}$$

and, thus, the solutions to Eq. (1.27) can be expressed as:

$$T_{ac}(x) = Ae^{-\sigma x} + Be^{\sigma x} \,. \tag{1.29}$$

Here A and B are constants which can be determined using the correct boundary conditions. The first boundary condition comes from considering that as x tends to infinity, i.e., when we go deeper into our material, the temperature must have a finite value. This condition demands $B = 0$. The second boundary condition is related to the flux continuity on the surface of the sample ($x = 0$), where according to *Fourier's law* (Eq. (1.1)):

$$-K\frac{dT_{ac}}{dx}\bigg|_{x=0} = K\sigma A e^{-\sigma x}\bigg|_{x=0} = \frac{I_0}{2} \,, \tag{1.30}$$

must be satisfied. From the latter condition we directly get $A = I_0/2K\sigma$. This, together with Eq. (1.26) gives us:

$$T_{ac}(x,t) = \frac{I_0}{2K\sigma} e^{-\sigma x} e^{i\omega t}\,, \tag{1.31}$$

where substituting the definition of σ in Eq. (1.28) (with $\omega = 2\pi f$) we get:

$$T_{ac}(x,t) = \frac{I_0}{2\sqrt{2\pi f}} \frac{\sqrt{D}}{K} e^{-\frac{x}{\mu}} e^{i\left(\omega t - \frac{1}{\mu}x - \frac{\pi}{4}\right)}\,. \tag{1.32}$$

Let me point out that, although thermal effusivity is not explicitly shown here, in order to avoid confusion with Euler's number e, it is actually present and plays an important role on this temperature field expression. To check this one just need to remember that $\sqrt{D}/K = 1/e$ according to expression (1.15).

The other important parameter in Eq. (1.32) is the so called thermal diffusion length, $\mu = (D/\pi f)^{1/2}$. Thermal diffusion length can be interpreted as the distance penetrated by the thermal wave where the amplitude decays by a factor of e (Fig. 1.4, left), or when the phase is reduced by one radian (Fig. 1.4, right). This is why μ is usually used to define the depth at which the thermal wave penetrates; for instance, if the sample is thicker than μ ($l_S > \mu$) it is considered as thermally thick (for a given modulation frequency), this means that the thermal wave hardly reaches the back face of the sample. As can be seen from its definition, the thermal diffusion length depends on both the thermal diffusivity of the sample and the modulation frequency of the laser beam. The first one is fixed by the material and can't be modified; however, depending on our interests, the modulation frequency can be properly changed. The penetration of thermal waves decreases with increasing modulation frequency, and at a fixed frequency the penetration is greater in high diffusive materials.

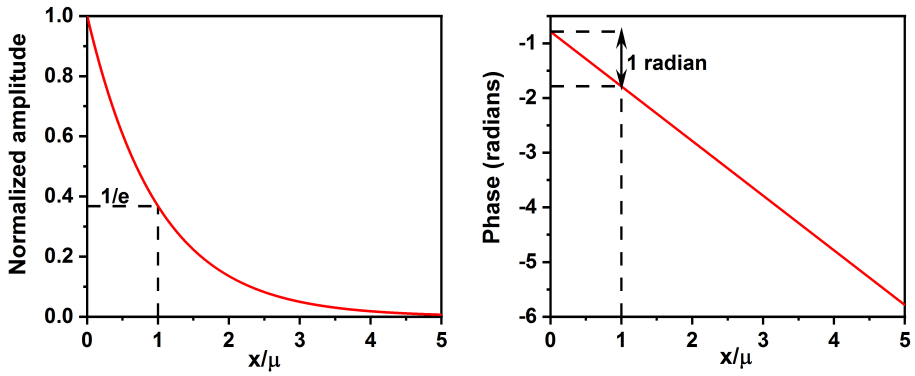


Figure 1.4: Normalized amplitude of T_{ac} (left), and its phase (right) as a function of the relative penetration x/μ.

Coming back to the expression for the *ac* component of the temperature (Eq. (1.32)), we can see that it has the same mathematical form as a plane, harmonic wave propagating along x direction, and that is why we referred to it as "thermal wave". The frequency of this wave is the same as the one corresponding to the modulation of the laser beam, f. The amplitude exponentially

decays as it penetrates the material, i.e., the wave is attenuated. On the other hand, the phase decreases linearly with x/μ. Furthermore, at the surface ($x = 0$) there is a 45° ($\pi/4$) phase shift with respect to the excitation. This can all be seen in Fig. 1.4.

It has been mentioned that thermal waves are really just oscillations on the temperature field but not actual waves because they do not transport energy unlike electromagnetic, acoustic or mechanical waves. This can be easily proven by calculating the heat flux associated to T_{ac} using Eq. (1.1) [12]:

$$\vec{q}_{ac} = Re\left[-K\vec{\nabla}T_{ac}\right] = \frac{I_0}{2}e^{-x/\mu}\cos\left(x/\mu - \omega t\right)\hat{i}\,. \tag{1.33}$$

It is trivial to check that the time average of this heat flux is $<\vec{q}_{ac}> = 0$. This does not mean that energy is not transmitted on this experiment, energy (as heat) is in fact transmitted, but the responsible for this is the *dc* component, T_{dc}, and not the thermal wave.

1.4 Photopyroelectric calorimetry, PPE

Photothermal techniques (PT) cover a large variety of experimental methods which have been proven to be very efficient and reliable on the study of different thermal and optical properties of gases, liquids and solids [4, 13, 14]. Our main goal is to study the critical behavior of second order phase transitions on thermal properties. In order to do that we need to have a very good temperature resolution around the phase transition. The widely used differential scanning calorimetry (DSC) is not a good solution for our purpose as it has poor temperature resolution and low accuracy. As we will see, the best candidate for this work is the *ac* Photopyroelectric calorimetry (PPE), which has been successfully used to this end both with solid materials (in magnetic and ferroelectric transitions) [15–22] and liquid crystals [23–25].

The aim of this section is to present the working principles of PPE technique applied to solid materials, as well as its advantages when dealing with the study of phase transitions. The solution of the thermal diffusion equation for a multilayer system and the approximation to the linear regime will be discussed in order to obtain the temperature evolution of the relevant thermal properties.

The *ac* photopyroelectric calorimetry is called this way because a modulated laser beam (*ac* photo-) is used to generate a thermal gradient on the sample which will be later converted into an electrical signal by a pyroelectric detector. Pyroelectricity is the ability of some materials to change their spontaneous polarization when a temperature gradient is applied, or to change their temperature under a variation of their polarization [26]. Furthermore, due to their crystal structure, pyroelectric materials are also piezoelectric and, therefore, special attention must be paid to avoid mechanical variations on our measurements. In our experiments $LiTaO_3$ pyroelectric crystals are used as detectors due to their sensitive *ac* temperature detection over a wide temperature range.

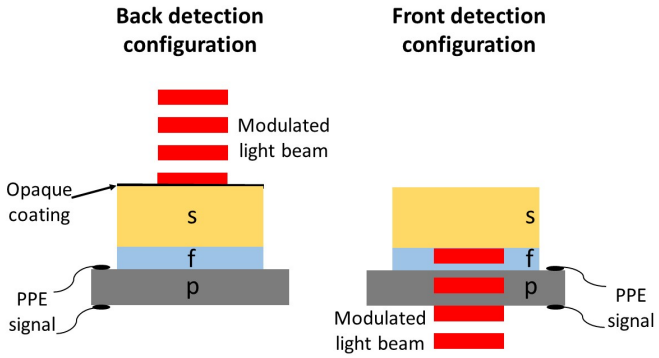


Figure 1.5: Diagram of both PPE detection configurations: back configuration (left) and front configuration (right). The figure shows the sample (s), thermal coupling fluid (f), and the pyroelectric detector (p).

Although the actual experimental set-up will be presented later, it is convenient at this point to describe the two main basic configurations (back and front) generally used in PPE calorimetry for the study of solids (which is our field of interest), these are shown in Figure 1.5. From the configuration point of view the main difference is that in the back detection configuration (BPPE) the sample is directly illuminated with an amplitude modulated laser beam and the pyroelectric detector is placed behind, while, in the front configuration (FPPE) the pyroelectric sensor is the one being illuminated. The obtained results are also different, the BPPE configuration enables the simultaneous determination of several thermal properties, which FPPE does not allow. On the other hand, FPPE experiments can be performed at a wider frequency range than those at BPPE configuration [27]. In both cases a thin layer of thermal grease is used in order to assure a good thermal contact between the pyroelectric detector and the sample. In the case of the back detection configuration a thin (few μm) graphite coating covers the face of the sample which is being illuminated to assure the opacity of the sample and the maximum absorption of the incident light, which are requirements for this technique.

Due to the possibility of simultaneously obtaining several thermal parameters, we use the back detection configuration for our experimental set-up. The *ac* photopyroelectric calorimeter, and particularly in its back detection configuration, is a very well known technique for the study of the critical behavior of phase transitions due to several advantages over other techniques [27]:

- **High sensitivity:** Inducing small temperature variations is crucial in the vicinity of phase transitions to assure a good temperature homogeneity on the sample and avoid a wrong temperature attribution. The main advantage of PPE technique is its sensitivity. By placing a very small amount of energy (<5 mW) and generating in the sample temperature gradients as small as few mK/mm, we can get a very good signal to noise ratio.

- **High resolution:** The system allows us to perform the experiments at very low temperature rates, down to 10 mK/min. Although this makes

the experiment longer it gives a very high resolution around phase transitions. This also allows a very precise measurement of thermal hysteresis and, therefore, can help to determine the order of the transition.

- **Thermal equilibrium:** Given the small amount of sample required, the small temperature oscillations induced and the slow temperature rates, thermal equilibrium is easily achieved even in close proximity of the transition.

- **Simultaneous determination of several thermal parameters:** It will be shown that this technique, in the back detection configuration, allows the direct determination of both thermal diffusivity and effusivity, from where (by using thermodynamic relations) we can obtain the specific heat and thermal conductivity. The critical behaviour of these parameters around phase transitions will shed some light on the magnetic structure and interactions of the materials under study.

From now on, unless it is said otherwise, when talking about PPE we will refer to the back detection configuration, which is the one that we actually use.

1.4.1 Solution to a multilayer system

The final purpose of the PPE technique is to analyse the electrical signal generated by the pyroelectric detector due to the thermal gradients induced on the sample. In order to do this we need to know how the expected signal is going to be and, therefore, the temperature field across the whole system must be obtained. In this section the thermal diffusion equation will be applied to the multilayer system used on the experimental set-up of the back detection configuration.

The multilayer system on BPPE can be represented as shown in Fig. 1.6, where the sample (s) of thickness l_s is directly illuminated by an amplitude modulated laser beam with frequency f. A thin layer of thermal fluid (f) of width l_f is used to assure a good thermal contact between the sample and the pyroelectric sensor (p) of thickness l_p. It must also be considered that the whole system will be surrounded by a gas, both on its front (g) and on its back (b). The system is composed of 5 different layers, the incident light in Fig. 1.6 comes from right to left and illuminates the sample's face placed at $z = 0$. We can limit ourselves to the analysis of the one-dimensional heat diffusion regime along the z direction.

The electrical signal on the pyroelectric detector (V) is directly proportional to the spatial average of the temperature field of the detector, $\langle T_p \rangle$ [28]:

$$V = ab\langle T_p \rangle \,, \tag{1.34}$$

where a is a factor related to the physical properties of the detector and b takes into account the influence of the electronics. We will not worry about these components here because they will vanish after the normalization of the signal which will be discussed later. Considering Fig. 1.6 the spatially averaged temperature is expressed as follows:

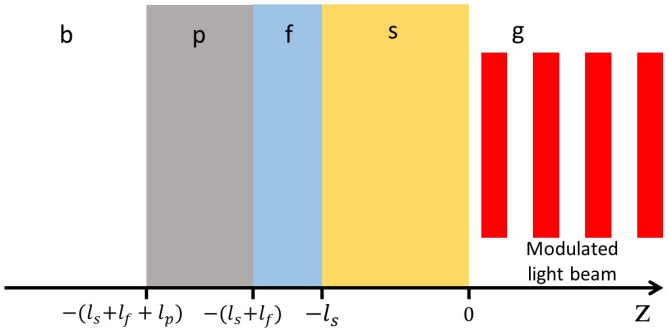


Figure 1.6: Scheme of the multilayer system used on the back detection configuration. From right to left the sample (s), thermal grease (f) and pyroelectric detector (p) with widths l_s, l_f and l_p respectively. The system is completed with the surrounding front (g) and the back (b) layers of gas.

$$\langle T_p \rangle = \frac{1}{l_p} \int_{-(l_s+l_f)}^{-(l_s+l_f+l_p)} T_p(z) dz \,. \tag{1.35}$$

The next step is to obtain the temperature field at the pyroelectric detector (T_z) by solving the thermal diffusion Eq. (1.19) for each layer of the system:

$$\frac{\partial^2 T_i}{\partial z^2} - \frac{1}{D_i} \frac{\partial T_i}{\partial t} = 0 \,. \tag{1.36}$$

Here the subindex i represent the different layers (i =g (gas), s (sample), f (coupling fluid), p (pyroelectric detector), and b (back medium)), T_i is the *ac* component of the temperature for each layer and D_i the diffusivity of the corresponding medium. Following the analysis carried out in Section 1.3.2 it can be seen that the solutions can be written as:

$$\begin{aligned}
T_g &= Ae^{-\sigma_g z} && z \geq 0 \\
T_s &= Be^{\sigma_s z} + Ce^{-\sigma_s z} && -l_s \leq z \leq 0 \\
T_f &= De^{\sigma_f (z+l_s)} + Ee^{-\sigma_f (z+l_s)} && -(l_s+l_f) \leq z \leq -l_s \\
T_p &= Fe^{\sigma_p (z+l_s+l_f)} + Ge^{-\sigma_p (z+l_s+l_f)} && -(l_s+l_f+l_p) \leq z \leq -(l_s+l_f) \\
T_b &= He^{\sigma_b (z+l_p+l_f+l_s)} && z \leq -(l_s+l_f+l_p)
\end{aligned} \,, \tag{1.37}$$

where σ_i is defined in the same way as in Eq. (1.28) for each layer, and constants A to H are determined by the appropriate boundary conditions at the interfaces, such as the temperature continuity:

$$\begin{aligned}
T_g\big|_{z=0} &= T_s\big|_{z=0} \,, & T_s\big|_{z=-l_s} &= T_f\big|_{z=-l_s} \,, \\
T_p\big|_{z=-(l_s+l_f+l_p)} &= T_b\big|_{z=-(l_s+l_f+l_p)} \,, & T_f\big|_{z=-(l_s+l_f)} &= T_p\big|_{z=-(l_s+l_f)} \,,
\end{aligned} \tag{1.38}$$

and the heat flux continuity, as well as the light absorption ($I_0/2$) at $z = 0$:

$$\frac{I_0}{2} + K_g \left.\frac{\partial T_g}{\partial z}\right|_{z=0} = K_s \left.\frac{\partial T_s}{\partial z}\right|_{z=0} , \qquad K_s \left.\frac{\partial T_s}{\partial z}\right|_{z=-l_s} = K_f \left.\frac{\partial T_f}{\partial z}\right|_{z=-l_s} ,$$
$$K_p \left.\frac{\partial T_p}{\partial z}\right|_{z=-(l_s+l_f+l_p)} = K_b \left.\frac{\partial T_b}{\partial z}\right|_{z=-(l_s+l_f+l_p)} , \quad K_f \left.\frac{\partial T_f}{\partial z}\right|_{z=-(l_s+l_f)} = K_p \left.\frac{\partial T_p}{\partial z}\right|_{z=-(l_s+l_f)} . \tag{1.39}$$

This process gives a huge and complex expression which can be found elsewhere [28,29]; however, this expression can be considerably simplified assuming several reasonable experimental conditions. In particular, the system will be surrounded by the same gas on the front and back ($b = g$), the effusivity of this gas will be negligible in comparison to the effusivity of the other layers, the coupling fluid layer will be really thin (few microns), $l_f \sim 0$, the sample must be opaque or covered by a thin opaque coating, and we will always work at modulation frequencies for which both the pyroelectric detector and the sample are thermally thick ($l_s, l_p > \mu$). Furthermore, as seen in Eq. (1.34) the resulting expression depends on both the electronics of the system and the physical properties of the detector; however, if this signal is normalized by the signal of the bare detector illuminated under the same conditions, those components are eliminated. With this normalization and under the mentioned experimental conditions the normalized signal can be expressed in the following way:

$$V_n = 2\frac{e_p}{e_p + e_s} e^{-\sigma_s l_s} \tag{1.40}$$

From this expression, and considering Eq. (1.28), one can easily obtain the natural logarithm of the normalized amplitude ($\ln V_n$) and its phase (Ψ_n):

$$\ln(V_n) = \ln\left(\frac{2e_p}{e_s + e_p}\right) - \sqrt{\frac{\pi f}{D_s}} l_s , \tag{1.41}$$

$$\Psi_n = -\sqrt{\frac{\pi f}{D_s}} l_s , \tag{1.42}$$

where $\omega = 2\pi f$ relation has been used to explicitly show the linear dependence with the square root of the modulation frequency, $\sqrt{f}$. It is immediately seen in Eqs. (1.41) and (1.42) that when represented as a function of $\sqrt{f}$ they have the same slope, m:

$$m = -\sqrt{\frac{\pi l_s^2}{D_s}} . \tag{1.43}$$

Furthermore, the distance (d) between both straight lines is given by:

$$d = \ln\left(\frac{2e_p}{e_s + e_p}\right) . \tag{1.44}$$

The last two expressions give us the key to obtain both the thermal diffusivity of the sample and its thermal effusivity [30]:

$$D_s = \frac{\pi l_s^2}{m^2}\,, \tag{1.45}$$

$$e_s = e_p\left(\frac{2}{\exp(d)} - 1\right), \tag{1.46}$$

with l_s as the thickness of the sample and e_p as the thermal effusivity of the pyroelectric material.

Two kind of measurements are always done in order to properly obtain the thermal parameters, as a function of the modulation frequency and as a function of temperature.

1.4.2 Frequency dependent measurements

The general expression of the natural logarithm of the normalized amplitude of the signal and the normalized phase versus $\sqrt{f}$, without the considerations taken into account in order to obtain Eq. (1.40), is shown in figure 1.7. When plotted like this we can distinguish three different regions. In region I, at low frequencies, the penetration length is big and the sample is thermally thin ($l_s < \mu$), this causes a lost of linearity and parallelism which takes this region out of our approximation. Region II is a transition region at which the parallelism is still not perfect and errors higher than 1% can be obtained. Finally Region III, at higher modulation frequencies, is the so called "linear region" where the sample is thermally thick ($l_s > \mu$) and all the expressions from Eq. (1.40) to Eq. (1.46) are valid.

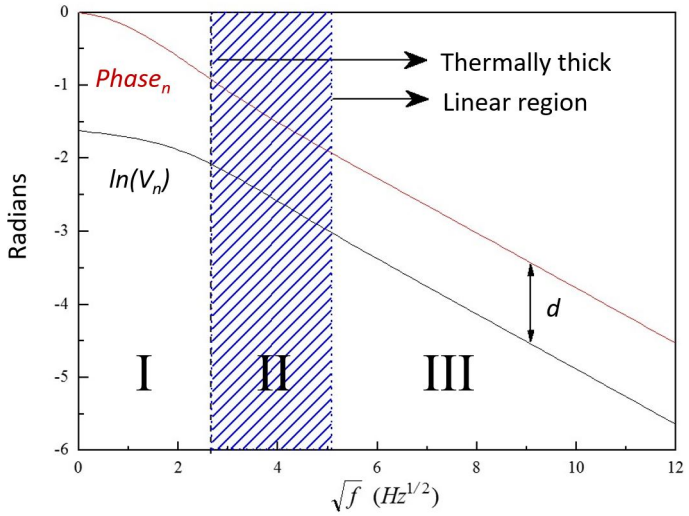


Figure 1.7: General expression of the normalized phase and natural logarithm of the amplitude plotted as a function of the square root of the modulation frequency.

The linear region is the one from which we will extract information about our thermal parameters. Out of this region the general approach is not valid and we have to deal with more complex expressions if we want to extract any

information. In order to keep our expressions simple and useful it is very important to study the dependency of $\ln(V_n)$ and Ψ_n with the modulation frequency. It must be considered that, although the signal sensitivity can be improved at higher frequencies (or increasing the sample thickness), this is accompanied by a decrease of the signal, eventually reaching noise level.

Apart from the low frequency regime where the sample is thermally thin (Region I in Fig. 1.7), there are several other factors that can alter the results and linearity. The coupling fluid between the sample and the detector, for example, has some influence on the results, underestimating the value of the thermal diffusivity [31]; however there are normalization techniques which allow to overcome this problem [32, 33]. Another effect related to the thermal grease appears when measuring below its freezing temperature. When the fluid freezes, the contact between the sample and the detector is rigid and this induces a piezoelectric effect on the detector because the thermal expansions of the sample are more efficiently transmitted. This effect can be considerably relevant, but, usually, the region affected by the piezoelectric effect (high frequencies) can be neglected or avoided; however, when this is not possible a more complex multiparametric fitting can be used to retrieve the thermal parameters [34]. Other minor effects, which have also been studied and experimentally minimized, are the ones related to the surrounding gas, the back medium, the electronic noise, and parasitic light. The possible influence of heat losses due to thermal radiation and convection has also been studied. This is done by adding a linear term in the boundary conditions, and it has been proven that those losses do not affect the signal at frequencies in the thermally thick regime.

To sum up, experiments as a function of the modulation frequency are performed at a fixed temperature (T_{ref}) in order to locate the linear region (where our approximations are valid) and to obtain reference values of thermal diffusivity (D_{ref}) and thermal effusivity (e_{ref}), which will be needed to obtain the temperature evolution of those parameters.

1.4.3 Temperature dependent measurements

In the previous section we have seen that through frequency dependent measurements we can obtain reference values of the thermal properties; however, our main interest is the temperature evolution of those parameters. Temperature dependent measurements are done at a fixed modulation frequency which must be in the linear region. Once this frequency is chosen the temperature is changed while the amplitude and the phase of the signal are recorded. This process is done with the sample and then repeated (at the same frequency) with the pyroelectric detector on its own in order to normalize the signal. When this is done the temperature evolution of the thermal diffusivity and thermal effusivity can be obtained from the following expressions [30, 31]:

$$D(T) = \left[\frac{1}{\sqrt{D_{\text{ref}}}} - \frac{\Delta(T)}{l_s \sqrt{\pi f}} \right]^{-2}, \tag{1.47}$$

$$e(T) = e_p(T)\left[\frac{1+\dfrac{e_{\text{ref}}}{e_p(T_{\text{ref}})}}{\exp(\Delta'(T))} - 1\right], \tag{1.48}$$

where $\Delta(T) = \Psi_n(T) - \Psi_n(T_{\text{ref}})$ is the phase difference between the measured normalized phase and the value at the reference temperature at which D_{ref} and e_{ref} were obtained. In a similar way $\Delta'(T) = (\ln V_n(T) - \Psi_n(T)) - (\ln V_n(T_{ref}) - \Psi_n(T_{ref}))$ is defined. $e_p(T)$ is the temperature evolution of the thermal effusivity of the pyroelectric detector, which is known.

As mentioned before, one of the main advantages of PPE technique on its back detection configuration is the possibility to obtain several thermal properties simultaneously. From the previous results and using well known thermodynamic relations, the temperature evolution of the specific heat and thermal conductivity can be obtained [27]:

$$c(T) = \frac{e(T)}{\rho\sqrt{D(T)}} \tag{1.49}$$

$$K(T) = e(T)\sqrt{D(T)} \tag{1.50}$$

It is important to notice that while thermal diffusivity depends only on the phase of the signal, the thermal effusivity, and consequently, the specific heat and thermal conductivity depend on both the phase and the amplitude of the signal, and this, in practice, is going to be translated into cleaner measurements of the thermal diffusivity over the rest of the parameters. This is due to the fact that the amplitude is always noisier than the phase because it is more sensitive to the laser instability and electronic noise.

We have already mentioned that, due to the effect of the coupling fluid, when measuring a reference value of thermal diffusivity at a given temperature there is an underestimation of its value, this and other minor effects can make the value of D differ around a 2% of its real value. However, the coupling fluid does not affect the temperature evolution of the thermal parameters [31], and the relative error between the experimental points in this case is minimum (around 0.5%). This precision is another important reason to choose this technique in order to study the behaviour of the thermal properties around their phase transitions. Lastly, it is important to mention that through this technique the thermal parameters are measured in the direction of the incident light; thus, changing the orientation of the sample allows the extraction of the parameters at different directions, which can be interesting in order to study anisotropic materials. However, the critical behavior does not depend on the orientation at which the thermal or magnetic properties are measured and, therefore, do not affect our analysis.

1.4.4 Experimental devices

The different experimental devices developed by our research group at the *Photothermal Techniques Laboratory* (PTL) for the PPE technique, the basic procedure, and set-up for the back detection configuration will be presented here. The devices can be divided into two main groups: those which only measure

as a function of frequency at room temperature, and those who can measure both as a function of temperature (at different regions) and as a function of the modulation frequency at a fixed temperature. As will be seen, since we are working with very low signals, especial care has been taken to minimize any kind of noise that could be introduced into the system.

Room temperature measurements

We have seen that frequency dependent measurements are always done in order to locate the linear region and to obtain reference values of the thermal parameters. In this sense a simple and precise room temperature device is very useful. Although this device can be used for both front and back detection configurations we will focus on the description of the latter. In the set-up presented in Fig. 1.8, where only frequency dependent measurements at room temperature can be performed, the sample, the pyroelectric detector and the electrical contacts are placed inside a *Faraday's cage* in order to isolate the system and minimize the noise associated with induced currents by external electromagnetic signals.

Regarding the sample, it has to be carefully prepared so that its faces are perfectly plane and parallel. Normally the thickness of the sample is in a range between 500 μm and 2 mm, depending on its thermal diffusivity, a trade-off between the signal level and the appropriate thermal thickness must be reached. It must also be taken into account that the material could be a bad absorber or even transparent to the laser wavelength (λ = 632 nm). If this is the case, the surface of the sample which is illuminated is coated with a graphite paint in order to make it opaque; in this way the absorption of light is increased resulting on a higher signal.

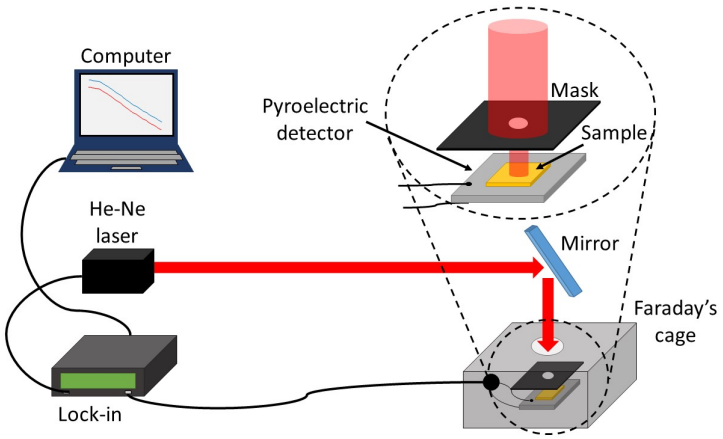


Figure 1.8: Device for room temperature measurements as a function of modulation frequency.

A mask with a hole is placed over the sample in order to assure that only the material is being illuminated and that the detector does not receive any parasitic light (see Fig. 1.8), which would result on an additional signal affecting specially high frequencies and distorting the linear region. When the

sample and the mask are correctly placed inside the *Faraday's cage*, the amplitude modulated laser beam enters vertically through a small hole on the cage. A low power (<5 mW) He-Ne laser (λ = 632 nm) is used. In this way the amount of energy deposited on the sample is small, and so are the induced temperature gradients. Indeed, this small power is required to assure that the sample remains at the same constant temperature at which we want to obtain the reference values. It also enables a quick thermal equilibrium, which in the case of phase transitions is crucial to guarantee that all the regions in the sample suffer the transition simultaneously. With this low power laser we manage to generate small T_{ac} variations as well as an insignificant T_{dc} increase.

The temperature oscillations are transmitted to the pyroelectric detector, but in the case of solid samples a coupling fluid, such as a thermal grease, is needed in order to assure a good thermal contact between the sample and the detector. The layer of the thermal grease should be as thin as possible (few μm) as long as a good coupling is achieved. We use a $LiTaO_3$ pyroelectric sensor due to its sensitivity, and high working range, both in frequency and temperature. Each face of the detector is covered by a conductive layer and isolated from the other face. Electrical contacts are placed on both faces and connected to a lock-in amplifier.

The lock-in amplifier has two functions. On the one hand, the system controls the modulation frequency of the laser beam and, on the other hand, it is also the responsible for receiving, amplifying and processing the signal from the pyroelectric detector. The signal at the detector has the same frequency as the modulation of the laser, this fact is used by the lock-in in order to get a cleaner resulting signal. The working system of the amplifier is based on a bandpass filter synchronized in frequency with the incoming signal; in this simple way, the frequencies outside the bandwidth will be filtered, significantly reducing the noise. Furthermore, the signal integration time of the lock-in can be adjusted to eliminate the random electronic noise at the same frequency as the modulation. Finally the lock-in transmits independently the amplitude and phase of the signal to a computer where it is then collected and analysed. All the connections and cables are specifically designed and connected to the same ground to minimize as much as possible the electronic noise.

When working, the system sweeps over a wide range of frequencies allowing us to locate the linear region. However, although theoretically there are no limitations to this frequency range, in real experimental conditions we must take into account that we deal with very low signals and that increasing the modulation frequency reduces the signal, eventually reaching noise level, where any kind of information is lost in a random background.

Temperature dependent measurements (14-500 K)

We shall not forget that our aim is to obtain the thermal properties around the phase transitions in order to study their critical behavior. To do that, we first need to reach the temperature at which these transitions take place and then be able to slowly vary the temperature around the region. This is managed by placing the sample and the detector inside a cryostat. In particular we

have two systems to work at different temperature ranges. Apart from their respective working regions, the main difference between them is the way in which the temperature is controlled. The system which can reach the lower temperature uses a closed helium gas cycle and can work from around 14 K up to a little bit higher than room temperature, around 320 K. The second system uses liquid nitrogen and, therefore, can work down to 77 K. This latter system allows the study of higher temperature transitions as it can reach up to 500 K.

Although both systems differ in their refrigeration system, the general characteristics are very similar. To avoid unnecessary repetitions we are going to focus our description on the system working at lower temperature (14-320 K) (see Fig. 1.9). This cryostat was specifically designed and modified by the PTL group for our working requirements. The higher temperature system is the Optistat^{DN} model designed by *Oxford Instruments*.

As shown in Fig. 1.9, the whole system has several subsystems, each one with a specific function. The main component, which enables to cover the corresponding temperature range, is a conventional closed cycle He cryostat in vertical configuration which was modified by *Janis Research Company* following all the requirements to work as an *ac* phrotopyroelectric calorimeter. The refrigerator uses helium gas in a closed loop working under a Gifford-McMahon thermodynamic cycle based on the expansion and compression of the gas. The temperature is decreased by a cooling head at the bottom of the cryostat which is connected to the temperature controller and refrigerator.

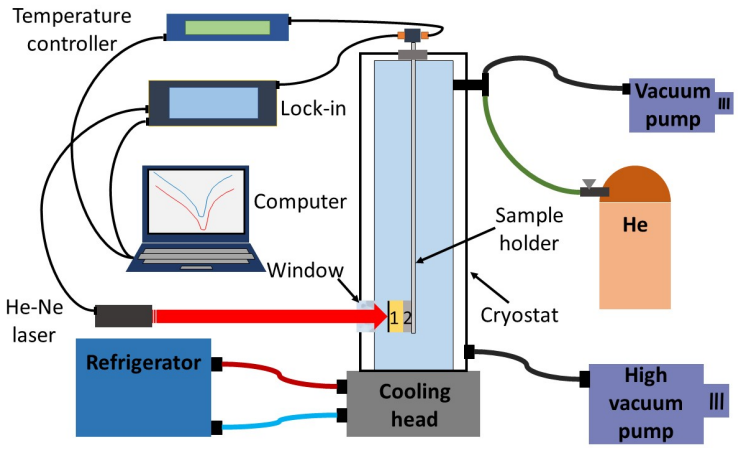


Figure 1.9: Device for temperature dependent measurements, where 1 is the sample and 2 the pyroelectric detector.

The sample and the detector (1 and 2 in Fig. 1.9 respectively) are introduced inside the cryostat by a sample holder placed in vertical position. In this set-up the coupling fluid also works as a glue, preventing the sample from falling. There are two chambers surrounding the sample holder. In the space between both chambers, a high vacuum pump assures the best permanent vacuum possible in order to avoid heat transfers and condensation on the external part when reaching cold temperatures. The inner chamber is filled with helium gas to act as a heat exchanger, extracting heat from the sample to the cooling head (or the other way around). Not only that, when the sample is in

the chamber, it assures some pressure on it allowing a better contact with the detector while maintaining an inert atmosphere. Prior to every new measurement all the gas inside the inner chamber must be removed before introducing again He gas, this is done with another vacuum pump.

The temperature controller monitors the temperature inside the cryostat and nearby the sample and takes care of changing the temperature according to the pre-established parameters. The system is able to work at very low temperature rates, down to 10 mK/min, both when increasing and decreasing temperature, resulting in high resolution data. As in the case of the room temperature device, the signal is extracted through connections on the sample holder and received on the lock-in amplifier before being sent to the computer, where the phase and the amplitude of the signal are independently recorded.

The excitation on the sample is again produced by an amplitude modulated light beam from a low power He-Ne laser. The laser is placed outside and the incident beam enters the system through a specially designed window located at the same height as the sample. This window is wedged to avoid interferences related to its thermal dilatation. The sample is again covered by a mask to avoid parasitic light to fall on the detector. When working at room or lower temperatures this mask can be made out of cardboard; however, when going to higher temperatures polyimide is used to prevent spontaneous combustion.

Another important part of the system is the antidumping mechanism (not shown in Fig. 1.9). The functioning of the cooling head, as well as normal human activity, induces vibrations into the system. It has already been discussed that pyroelectric materials are also piezoelectric and, therefore, this mechanical vibrations are also detected by the sensor, increasing the noise on the measurement. The antidumping system is crucial to prevent this. It consists on four pressurized air cells, one on every leg of a table, controlled by a pressure pump. The table has several functions, one of them is to separate the sample holder and the rest of the system, in this way we avoid the effects due to the vibrations from the cryostat. The table is also used to place the laser and optical path along which the incident laser beam will travel before reaching the sample.

Temperature dependent measurements are always done after frequency dependent measurements. For the temperature varying measurement the correct modulation frequency must be chosen within the linear region. The linear region depends on the diffusivity of the sample and, therefore, on its temperature. Consequently, reference values and frequency must be selected at a temperature close to the region of interest, to assure that the selected frequency remains inside the linear region along the measurement. Finally, I want to stress out that every process is repeated, at least, two times: for the sample with the thermal grease and the pyroelectric detector, and then, again, for the detector on its own in order to later normalize the signal.

2 | Magnetic and Magnetocaloric Properties

"We have this very clean picture of science, you know, these well-established rules with which we make predictions. But when you're really doing science, when you're doing research, you're at the edge of what we know."

– Lisa Randall

Magnetism has attracted the curiosity of many along the history since it was first discovered in the magnetite mineral back in the ancient world. There are several levels in which one could deepen on the mysterious nature of this phenomena. Each "why" question takes us to a deeper and more intriguing layer of its nature. However, I must advise the reader that it is not the purpose of this work to reveal the microscopic quantum *"clean picture"* of magnetism. We settle for a more modest presentation of the necessary *"well-established rules"* that allow us to push *"the edge of what we know."*

This chapter will start with a small introduction on magnetic orderings, magnetic exchange interactions, and basic, yet important, relevant magnetic properties of matter. We will then focus our attention on the central magnetic topic of this thesis, the magnetocaloric effect. A background on the history of this effect and its applications will be presented, together with a mathematical and physical description of the magnetocaloric phenomena. The main figures of merit, differences in first and second order phase transitions, and the general working procedure will also be discussed.

2.1 Introduction to magnetism in materials

Creation of magnetic moments can be explained on the basis of quantum physics and orbital occupations. However, this is out of the scope of this work and we will start this section assuming that those magnetic moments exist. We will describe different magnetic exchange interactions and the magnetic orderings to which they can give rise, and present the magnetic properties which will be relevant for our work.

2.1.1 Magnetic ordering

We must consider that not all materials are magnetically ordered, in fact, the opposite is more general. In the absence of exchange interactions between individual magnetic moments each moment acts independently and no magnetic ordering arises. This is the case of diamagnetic (DM) and paramagnetic (PM) materials. The vast majority of materials are diamagnetic, their electronic orbitals are filled and opposite spin electrons are paired. This pairing contributes to the slight repulsion of external magnetic fields typical of diamagnetic materials. On the contrary, paramagnetic materials do not have all the orbitals filled and some electrons are unpaired. Ions in paramagnetic materials do have magnetic moments, but thermal agitation is higher than magnetic interactions and all the magnetic moments are randomly distributed without generating any net magnetization on the material. However, when cooling PM materials below a certain critical temperature magnetic interactions dominate over thermal agitation and magnetically ordered structures may arise.

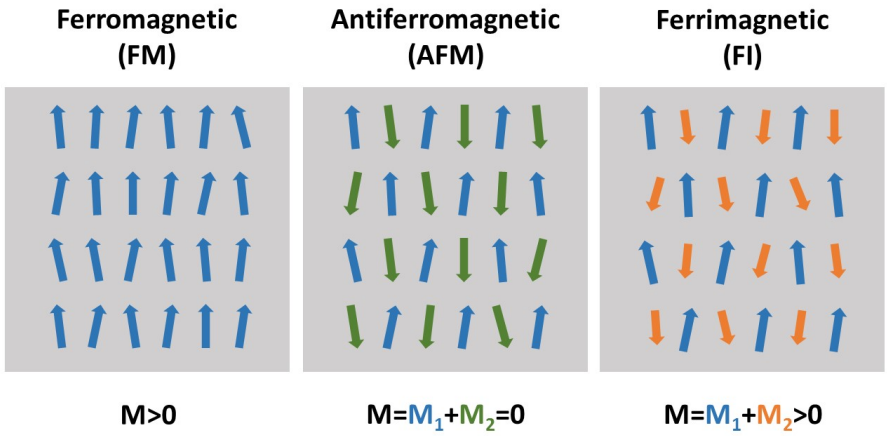


Figure 2.1: Examples of common magnetic orders, where the atomic or molecular moments are represented by arrows. From left to right: ferromagnetic, antiferromagnetic and ferrimagnetic ordering. Upwards magnetization is taken as positive.

Some materials are magnetically ordered below a given critical temperature. These materials may, or may not, sum up their magnetic moments to generate a non zero net magnetization for the whole solid. This is known

as "spontaneous magnetization", it decreases with increasing temperature and vanishes at the critical temperature. Therefore, when referring to different magnetic ordered states we are always referring to the state below that critical temperature, above which it is no longer ordered in the absence of an applied magnetic field.

When the atomic (or molecular) magnetic moments on a solid are aligned almost in the same direction we have a ferromagnetic (FM) arrangement (see left picture in Fig. 2.1). In 1906 Pierre Weiss proposed the molecular field theory to explain this phenomena and, although it has some limitations, it remains useful nowadays. According to this theory, there is an internal effective molecular field ($\vec{H}_m$) affecting the magnetic moments, which is proportional to the magnetization ($\vec{M}$) and is responsible of the ferromagnetic alignment [35]:

$$\vec{H}_m = w\vec{M} + \vec{H}_a \,, \tag{2.1}$$

where w is the proportionality constant (sometimes called Weiss constant) and the external applied magnetic field ($\vec{H}_a$) is added. The magnetization is given by the *Brillouin function*, $B_J(x)$:

$$\vec{M} = \vec{M}_0 B_J(x) \,. \tag{2.2}$$

Here M_0 is the spontaneous magnetization at 0 K, and x depends on several factors including temperature, M and H_a. This complex function vanishes at the critical temperature (or Curie temperature), T_C. In the absence of external magnetic fields, M is the spontaneous magnetization or zero-field magnetization.

In other solids, there is no net magnetization even though there is a magnetic order below a certain temperature. These are called antiferromagnets (AFM), and the temperature below which this alignment takes place is known as *Neel's* temperature, T_N. AFM materials are composed of two or more hidden magnetically ordered sublattices, each of which have a net macroscopic magnetization but when combined with the others the total magnetization disappears (central figure in Fig. 2.1). In the simplest case, with only two lattices, 1 and 2, the magnetizations are equal but in opposite directions [36]:

$$\vec{M}_1 = -\vec{M}_2 \,. \tag{2.3}$$

Therefore, the total magnetization $\vec{M}$ vanishes when $\vec{H}_a = 0$:

$$\vec{M} = \vec{M}_1 + \vec{M}_2 = 0 \,. \tag{2.4}$$

If the atoms giving rise to the magnetization in the different sublattices are not the same, both magnetizations can point in opposite directions without completely cancelling each other:

$$\vec{M} = \vec{M}_1 + \vec{M}_2 \neq 0 \,. \tag{2.5}$$

This is the case of ferrimagnets (FI), where, although antiferromagnetic arrangement is favoured, the lack of complete cancellation produces a net no-zero macroscopic magnetization on the material (see right picture in Fig. 2.1).

Some other curious magnetic orderings are also possible. Helimagnetism, for example, is the result of the competition between FM and AFM exchange interactions. In helimagnets neighbouring magnetic moments arrange in complex helical patterns [37, 38]. Interestingly for us, pure rare-earths order in these kind of peculiar arrangements. Tb, Dy and Ho form a helix structure at room temperature, while Er and Tm prefer a longitudinal-wave structure. These structures are even more complex at lower temperatures, where cone or square-wave type structures appear (just to mention some examples). We redirect the reader to Refs. [1,2,39] for a more detailed discussion of this topic.

Although it is common to speak about magnetic materials as having a specific magnetic ordering, it must be taken into account that, strictly speaking, a material is not ferromagentic, or antiferromagnetic, or of other kind. Materials can have different magnetic orderings at different temperatures, and very complex magnetic phases may coexist. As has been mentioned all the magnetically ordered materials turn to paramagnetic state above a certain temperature (T_C for FM and FI or T_N for AFM). Moreover, there can also be transitions between FM and AFM states, between different FM or AFM phases, and so on. Metamagnetic transitions, where the application of an external magnetic field above a certain critical field, H_C, drives a transition from one state into another can also take place. Along this work we are going to witness and study the rich variety of magnetic phase transitions in a number of interesting materials.

2.1.2 Magnetic exchange interactions

Magnetically ordered states are formed when magnetic moments couple, in one way or another, between them. The overlap between electron wavefunctions together with *Pauli's exclusion principle* are responsible for these exchange interactions, which are purely quantum mechanical. Although the coupling is between magnetic moments, the source of this interaction is mainly electrostatic, due to electron-electron interaction. We can differentiate three main exchange interactions: direct exchange, superexchange, and indirect exchange [40].

Direct exchange

When magnetic moments are close enough to each other so that electrons from two neighbouring atoms interact, i.e., their corresponding wave-functions overlap, direct Coulomb interaction takes place, causing a strong coupling. A schematic representation can be seen in the left side of Fig. 2.2, page 32. The resulting magnetic ordering from this interaction depends on two factors: the band occupation and inter-atomic distance [36].

Direct exchange describes very well *3d* metals. In these metals, when *d*-orbitals are half-filled, *Pauli's exclusion principle* only allows anti-parallel moments to couple and, therefore, antiferromagentic ordering arises. If the bands are only roughly half-filled, energy balance also favours antiferromagnetic ordering. However, when *3d* orbitals are either nearly filled or nearly empty, electrons can jump to neighbouring states with the same spin, allowing ferro-

magnetic ordering.

The distance between the ions also affects the resulting magnetic ordering. When the atoms are very close *Pauli's exclusion principle* gives rise to antiparallel alignment (antiferromagnetic), while greater distance favours parallel (ferromagnetic) alignment.

Superexchange

Another common case appears when two atoms are too far apart to overlap and be directly connected. It is then possible to have a magnetic interaction between two magnetic atoms mediated by the electrons of a nonmagnetic atom between them, as shown in the central part of Fig. 2.2. This is called superexchange interaction. Although the intermediate atom does not have any net magnetic moment, its electrons are disturbed by the surrounding magnetic atoms enabling and enlarging the magnetic exchange interactions over long distances, which would be impossible through a direct exchange.

Indirect exchange

Indirect exchange is better known as RKKY interaction after Ruderman, Kittel, Kasuya and Yosida, who described the mechanism [41–43]. This is the main exchange interaction in rare-earths, where the core spins are not in a d-shell but in an inner f-shell. The overlapping of f-shells is generally very small and, therefore, direct exchange is not very relevant. In this case f-shell electrons couple one another through hyperfine interactions with electrons in the conduction band (in this context also named itinerant electrons). The conduction *5d* or *6s* electrons can be polarized by the magnetic moment of an ion and then interact with other magnetic ion giving rise to this indirect coupling between two magnetic ions far apart each other. A schematic representation can be seen in the right hand side of Fig. 2.2.

RKKY interaction between conduction electrons and unfilled inner shell electrons can induce ferromagnetic or antiferromagnetic alignment depending on the nature of the rare-earth and the separation between atoms.

Fig. 2.2 is an schematic representation of the previous exchange interactions. On the direct exchange interacion (left) we can se how the orbital overlapping of magnetic ions (or molecules) produces the ordering of the magnetic moments. In the central part we see that the magnetic ions (blue) do not overlap; however, an interaction between them is possible thanks to the mediation with a non-magnetic atom (yellow) between them (superexchange). Finally, in the right panel, indirect exchange (or RKKY interaction) is represented, where magnetic atoms, which do not overlap, interact through the conduction electrons.

In general, several of these exchange interactions take place simultaneously. However, as it has been mentioned, the most relevant one in the case of rare-earths is generally the RKKY interaction. This will be discussed in more detail in the particular case of each intermetallic family presented in the results.

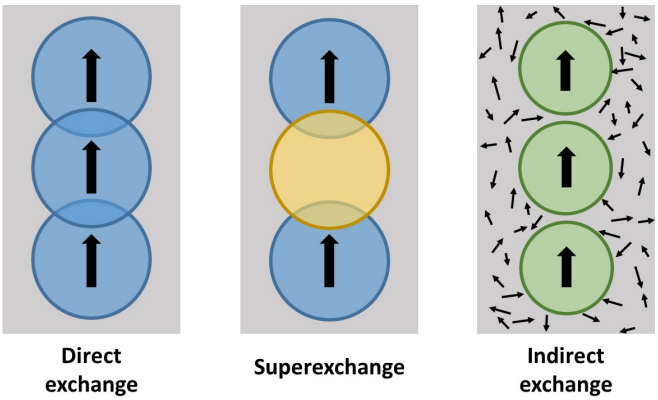


Figure 2.2: Scquematic representation of the main exchange interaction mechanisms: Direct exchange (left), superexchange (center), and indirect exchange or RKKY interaction (right). Arrows represent magnetic moments, while the diameter of the circles indicates the extent of the orbitals. Conduction electrons are also represented as small arrows in the indirect exchange panel.

2.1.3 Relevant magnetic concepts

There are a lot of interesting concepts in the magnetism of matter. It is not the aim of this section to discuss all of them, only the most relevant ones for our work will be compiled here.

Probably the most striking fact about magnetic materials is that some of them present a natural net magnetization below a certain temperature, even in the absence of externally applied magnetic fields. This property is called **spontaneous magnetization** (or zero-field magnetization), M_S, and it is characteristic of ferromagnetic materials. Spontaneous magnetization depends on temperature; it is maximum when all the spins are exactly aligned in the same direction without thermal fluctuations, i.e, when $T = 0$ K (in the absence of other effects), and it vanishes at $T = T_C$ due to the thermal fluctuations of the magnetic moments. When discussing the critical behavior theory we will see that the behavior of M_S just below T_C (in second order phase transitions) will be characterized by a critical exponent, β, which will be used in our analysis.

However, in our daily live, magnetic materials do not show spontaneous magnetization, not even those ferromagnetic materials with critical temperatures well above room temperature. Take iron as an example. Iron's Curie's temperature is around 1043 K ($\sim$ 770 ºC); however, in general, we do not observe iron's magnetization unless an external magnetic field is applied. Does this mean that magnetic moments in iron at room temperature are not ferromagnetically ordered? No. This is not a failure of the magnetic theory but a proof of the existence of **magnetic domains**.

Dipolar interactions are responsible for the formation of magnetic domains [40]. Magnetic moments are magnetically ordered inside those domains, but each domain points into a different direction, and that is why the magnetic material as a whole is demagnetized in zero field (see left side of Figure 2.3). Bellow T_C, when an external magnetic field is applied, the domain in the direction of H_a gets bigger, resulting in a total magnetization of the sample (right

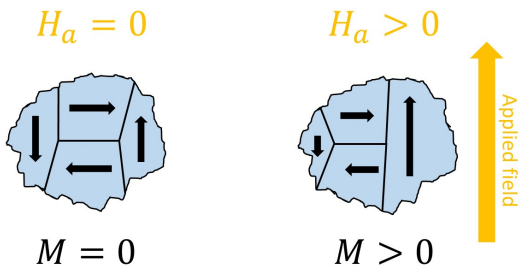


Figure 2.3: Magnetic domains in a ferromagnetic material at zero applied field (left) and upwards applied field (right). In the latter case a net magnetization ($M > 0$) is measured.

picture in Figure 2.3). If the applied field is small this change is reversible when the field is removed. However, if the field is high enough the change is irreversible and a remanent magnetization (M_r) can be measured when the field is removed. The sample can then be demagnetized again applying a coercive field in the opposite direction. This generates the famous **magnetic hysteresis** cycle.

With the existence of magnetic domains, which, in the absence of applied fields hide the magnetization of the sample, the legit question about how to obtain the spontaneous magnetization may arise. It turns out that, when measuring isothermal magnetization as a function of applied fields, at high enough fields, the behaviour of the magnetization is linear and obeys the following relation [44]:

$$M(H) = M_S(T) + \chi(T)H_a\,, \tag{2.6}$$

from where M_S at different temperatures can be obtained extrapolating the previous expression to zero fields, $H_a = 0$. χ in Eq. (2.6) is the magnetic susceptibility.

Magnetic susceptibility indicates the response of a magnetic material under the application of a magnetic field. In paramagnetic and diamagnetic materials the relation between magnetization and the applied field is linear according to $M = \chi H_a$; however, in ferromagnetic regions this is not the case and, therefore, a more suitable definition of the magnetic susceptibility is used:

$$\chi = \frac{\partial M}{\partial H_a}\,. \tag{2.7}$$

In most magnetic materials the magnetization does not only occur in the direction of the applied field. In those cases magnetic susceptibility is not a scalar but a tensor:

$$\chi_{ij} = \frac{\partial M_i}{\partial H_{aj}}\,, \tag{2.8}$$

However, we are going to be interested only in the magnetization along the direction of the applied field, thus, it will be enough to consider expression

(2.7).

In the paramagnetic region the temperature evolution of magnetic susceptibility follows the *Curie-Weiss law* [36]:

$$\chi(T) = \frac{C}{T + \theta_p} \,. \tag{2.9}$$

Here C is the Curie constant, which includes information about effective magnetic moments, and θ_p is the paramagnetic Curie temperature. In the case of a material with a PM-FM transition $\theta_p \approx T_C$, while in materials with a PM-AFM transition θ_p can be higher or lower (even negative) than the actual Néel temperature, T_N, where the transition takes place.

When magnetic susceptibility is measured at zero applied fields the resulting quantity is called initial susceptibility or zero-field isothermal susceptibility [40]:

$$\chi_0 = \left(\frac{\partial M}{\partial H_a}\right)_{H_a=0} \,. \tag{2.10}$$

In following chapters it will be shown that this parameter diverges at the transition temperature, and its critical behavior in that region will be useful for our study.

The magnetic susceptibility discussed so far is the so called *dc* magnetic susceptibility, that is, the one describing how a magnet responds to a *dc* constant magnetic field. A more interesting case takes place when the applied magnetic field is not *dc* but *ac* (oscillatory). In this case, a small *ac* component is superimposed on the *dc* field, and magnets respond according to the ***ac* susceptibility** or **dynamic susceptibility**.

The applied field now oscillates with frequency f and causes a phase shift, φ, in the magnetization. This phenomena can be understood as a complex susceptibility with a real (χ'_{ac}) and an imaginary (χ''_{ac}) part [45]:

$$\chi'_{ac} = \chi_{ac} \cos(\varphi) \,, \tag{2.11}$$

$$\chi''_{ac} = \chi_{ac} \sin(\varphi) \,, \tag{2.12}$$

with,

$$\chi_{ac} = \sqrt{\chi'^2_{ac} + \chi''^2_{ac}} \,, \tag{2.13}$$

$$\varphi = \arctan(\chi''_{ac}/\chi'_{ac}) \,. \tag{2.14}$$

Both the real and imaginary parts of the *ac* susceptibility are very sensitive to magnetic phase transitions. Whether it is a FM, FI or AFM transition, χ'_{ac} has a maximum at the transition temperature. This maximum is taken as the most accurate position of the transition temperature (T_C or T_N). χ''_{ac} also has a peak at FM or FI phase transitions but its value is almost zero in AFM phase transitions [45].

The imaginary part is sensitive to dissipative processes such as irreversible domain wall movements, energy losses from irreversible magnetization, or energy absorption from the magnetic field among others [46].

Ac susceptibility can have a frequency dependence due to magnetic domain processes, glassy magnetic behavior, Hopkinson effect (specially in FI), metamagnetic transitions, or incommensurate magnetic states [45, 46]. This dependency on the frequency of the applied *ac* field generally appears at the phase transition and at temperatures below it, and it can even displace the position of the peak.

Another interesting fact is that the peak value of the real part, χ'^{pk}_{ac}, also known as Hopkinson or principal maximum, measured at zero-field, gives the value of the **demagnetization factor** [47–49]:

$$N_D = \frac{1}{\chi'^{pk}_{ac}} \,. \tag{2.15}$$

The demagnetization factor, is the proportionality factor between the magnetization and the **demagnetization field** and it depends in a complex way on the physical shape of the sample. Dipolar interactions in magnets generate a demagnetization field (H_D) opposed to the external applied field (H_a) and proportional to the magnetization, so that the real internal magnetic field (H_i) inside the magnet is given by:

$$\vec{H}_i = \vec{H}_a - N_D \vec{M} \,, \tag{2.16}$$

where,

$$\vec{H}_D = -N_D \vec{M} \,, \tag{2.17}$$

is the demagnetization field. Figure 2.4 gives a schematic representation of internal and demagnetization fields on a magnet when an external field is applied. In ferromagnetic materials this field can be very important, and that is why in our studies it is crucial to correct the applied field and consider only the true internal field, both for the magnetic critical behavior study and for the correct evaluation of the magnetocaloric effect. Unless it is said otherwise, from now on it must be understand that all the magnetic fields are corrected from demagnetization effects and, therefore, for simplicity, H will be used referring to the corrected magnetic field.

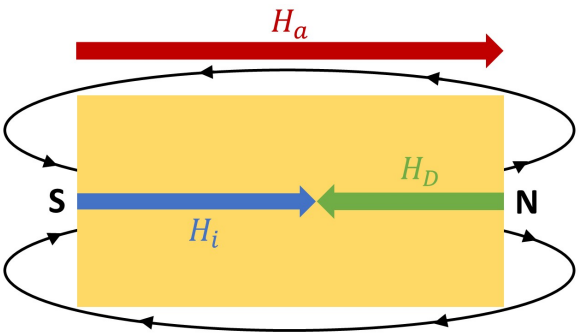


Figure 2.4: Internal (H_i) and demagnetization (H_D) fields on a magnet under an applied (H_a) magnetic field.

2.2 Magnetocaloric effect

The magnetocaloric effect (MCE) is an intrinsic property of all the magnetic materials. It is defined as an adiabatic (no heat exchange) change of the temperature (ΔT_{ad}) when a magnetic field is applied to the material, i.e., the material heats up or cools down with the application or removal of an externally applied field. Alternatively it can also be characterized by an isothermal (constant temperature) change of the magnetic entropy (ΔS_M).

Both concepts will be discussed later and this general definition will be properly completed with the physical origin of MCE, but before that lets see how this effect has gained popularity since its discovery.

2.2.1 Historical context and recent trends

The attribution of the discovery of the magnetocaloric effect has not been straightforward. Thomson, in 1878, was the first one to propose the theoretical concept of what is now known as MCE. Thomson realized that, according to thermodynamic relations, a piece of iron or nickel at very high temperatures and cobalt at room temperature, would experience a temperature change when exposed to a magnetic field or when this field was removed adiabatically [50].

The first experimental discovery of this phenomena has been more controversial. In 1999 very influential papers on this topic were published [51–53], attributing the experimental discovery of MCE to Warburg in 1881. It is now accepted that this attribution was wrong, because, although Warbug was aware of Thomsom's paper and carried out experiments on the heating of iron at small applied fields, he was only able to demonstrate heating due to irreversible hysteresis phenomena, but he was not able to measure MCE in iron [54]. Nowadays, the scientific community agrees that the first ever experimental measurement of the magnetocaloric effect was achieved in 1917 by Weiss and Piccard [55], when they managed to measure a 0.7 K temperature change on nickel under the application of 1.5 T.

Years later, Debye (1926) and Giauque (1927) independently proposed the possibility of cooling through adiabatic demagnetization in order to achieve temperatures below 1 K [56, 57]. It was not until 6 years later, in 1933, when Giauque and MacDougall demonstrated experimentally the utility of adiabatic demagnetization for cryogenic purposes, reaching 0.25 K by demagnetizing gadolinium sulfate [58]. Thanks to this and other studies, in 1949 Giauque was awarded the Nobel price in Chemistry for his studies in the properties of matter at temperatures close to absolute zero.

The discovery of important magnetocaloric properties in Gd, at near room temperature (294 K), by Brown in 1976 was another important milestone in the history of MCE [59]. The path of magnetic refrigeration was slow until the end of 20^{th} century and beginning of 21^{st}, when two major breakthroughs took place. In 1997 Pecharsky and Gschneider discovered the "giant" magnetocaloric effect and developed the first near room temperature proof of concept of magnetic refrigeration [60]. The second breakthrough came in 2002 when Tegus et al. published in *Nature* the discovery of a giant magnetocaloric effect

near room temperature in MnFe(P,As) alloys, which are based on abundant materials [61]. Since then, the interest on the search for optimum magnetocaloric materials has drastically increased.

In recent years an overwhelming amount of effort is being put in the research of different families of promising magnetocaloric materials, including: manganites [62–66], Heusler alloys [66–69], several Fe and Mn based materials [70], perovskites, glass composites and alloys, oxide based composites, spinel ferrites [63], and others [65, 71–74].

Due to their interesting magnetic properties, rare-earth (R) containing intermetallic compounds are being exhaustively studied in the search for more interesting magnetocaloric properties. Pure rare-earths on their own have been studied [75], among which Gd has shown very interesting magnetocaloric properties around room temperature [59], and that is why Gd based alloys have also been on the focal point of many researches [60,76,77]. New and interesting families of intermetallic compounds are being continuously synthesized every year, with an incredible amount of different properties. To mention some of them we can find the RTX family (R = Rare-earth; T = Transition metal; X = *p*-block element) [76, 78], R_3(Co,Ni) family [77, 79–81], R_2T_2X family (R = Gd–Tm; T = Cu, Ni, Co; X = Cd, In, Ga, Sn, Al) [82], and several other binary, ternary, or even quaternary families [83, 84]. There are also innovative trends in the production of multi-component compounds which might give a wider temperature range with a constant value of the magnetic entropy change, mixing intermetallic materials [82, 85]. Finally, for their simplicity and interest in many areas *Laves phase* materials (AB_2 composition) containing rare-earth elements are being also actively studied [65, 66, 86–90].

2.2.2 Interest and applications of magnetocaloric materials

Global warming (GW) is the major climate, environmental, social, and economic crisis we have ever faced. The scientific consent on the human origin of GW is overwhelming. The efforts of the different nations to fight together against this threat are collected in the *Paris Climate Change Agreement*, which urges every country to take actions in order to keep the global temperature increase due to GW below 1.5 ºC. The emission (due to human activity) of CO_2 and other greenhouse effect gases is the main cause of GW. The aim is to reach zero CO_2 emissions in 2050. According to the IPCC (Intergovernmental Panel on Climate Change) this will only be possible if the per capita CO_2 emissions are reduced by half before 2030. The solution to this crisis will come from the combined efforts of politics, industries, individuals and science.

Energy production based on fossil fuels is one of the main responsibles of GW; however, we must consider that every energy production process, and its transformations, have an environmental impact. Therefore, the reduction of the energy consumption is crucial. A great part of the energy produced is used for temperature control; in particular this accounts for the 25-50% of the energy consumption in households and a 57% in commercial buildings [66, 69]. Improving the efficiency of energy conversion is also a great concern as it has been calculated that around 61% of he energy in USA, and 63% in UK

or Spain is wasted energy [69, 91].

In western countries domestic refrigeration has been part of our daily life since its introduction into the market, with more fridges than households nowadays. The amount of these devices is incredibly increasing each year, specially due to the huge demand coming from eastern developing countries such as China and India. Those countries are experiencing what has been already called a "refrigeration revolution" [92]. Obviously the downwards of this demand is the amount of harmful fluids and gases used in refrigeration systems, such as chlorofluorocarbons (CFCs), hydrochlorofluorocarbons (HCFCs), and hydrofluorocarbons (HFCs). Due to their damage to the environment, contributing to greenhouse effect and affecting the ozone layer, the first two have already been forbidden by the *Montreal protocol*. However, this has only increased the use of HFC gases which contribute to greenhouse effect even more than CO_2 [64].

In this context, magnetocaloric materials play an important role. The main technological application of these materials is their use as magnetic refrigerators. Their ability to change their temperature under the application or removal of a magnetic field has brought the opportunity to replace the environmentally harmful conventional refrigeration technology (based on gas compression devices) with the more environmentally friendly magnetic refrigeration [65, 66, 69, 91–98]. Besides domestic refrigeration or air-conditioning, magnetic cooling has other interesting applications at near room temperature region: in the food industry, in electronic devices, for data servers cooling, solar cell panels, vehicle passenger cooling, IR detectors, high speed computers, SQUIDs, or even space industry among others [70, 99].

In addition to the no use of ozone depleting or greenhouse effect related gases, magnetic refrigeration is also energetically more efficient than conventional refrigerators. The latter can, in the best case, reach a 40% ideal efficiency of a *Carnot* cycle, whereas magnetic refrigeration prototypes have proven to reach at least 60% efficiency [64, 66, 69, 100, 101]. Overall, magnetic refrigerators are expected to save up to 30% more energy than the vapor cycle refrigerators [69, 102]. Magnetic refrigeration also has the advantage of being less noisy and exhibiting fewer vibrations.

The development of magnetic refrigerators is a very active research field. The first prototypes were tested by Collins and Zimmer in 1953 [103], and by Heer et al. a year later [104]. Those prototypes worked in the range of 1 to 0.73 K in the first case and between 1 and 0.2 K in the second case. The magnetic refrigerant used in both cases was iron ammonium alum. However, it was only after the development of a near room temperature working magnetic refrigeration by Brown in 1976 [59], and the subsequent introduction of the active magnetic regenerator concept by Steyert [105] and Barclay [106], that the efforts on building a commercial refrigerator incredibly grew. A good review of the recent trends on this area can be found in Ref. [107].

Although there is a huge interest in developing room temperature domestic magnetic refrigerators, the interest on magnetocaloric materials is beyond that. The application of magnetic refrigeration at different temperature regions, such as nitrogen and hydrogen liquefactions regions, with cryogenic purposes,

is also very promising [65, 82–85, 91, 108]. Moreover, the application of magnetocaloric materials is not limited to refrigeration; their potential use in medicine, for targeted drug delivery and release, or hyperthermia methods for the destruction of cancer cells, is also being studied [96, 99, 109]. However, this is still an emerging field.

It is worth mentioning that magnetocaloric materials are on their own very interesting from the point of view of solid state physics and magnetism. MCE gives us a complementary method to study several interesting phenomena in magnetic materials. Furthermore, the study and understanding of the physics behind this phenomena is the only way to develop future novel applications.

2.2.3 Physical origin of MCE

Up to now we have discussed the historical path of magnetocaloric effect and its possible applications. We have also stated that the MCE is characterized by either an isothermal change of the magnetic entropy (ΔS_M), or by an adiabatic change of the temperature (ΔT_{ad}) when a magnetic field is applied. However, the physical origin of this phenomena has not been presented yet. It is the aim of this section to address this issue.

Cooling through adiabatic demagnetization can be easily understood by analysing what happens with the entropy (S) of a given system experiencing this process. In a thermodynamic system entropy is an extensive property, i.e, it is proportional to the size of the system. It is common to refer to entropy as the amount of (dis)order on a system, according to which a more disordered system would have higher entropy than an ordered one. However, although this can certainly give an intuitive idea of the entropy of a system, it can lead to misconceptions. The entropy, as used in statistical mechanics, quantifies the amount of microstates (microscopic configurations) which are allowed by the macroscopic quantities, such as: temperature, pressure, volume, and so on.

In the particular case in which all the possible microscopic configurations are equally probable to happen, the entropy is proportional to the natural logarithmic of the number of microestates, Ω:

$$S = \kappa_B \ln \Omega \,, \tag{2.18}$$

where $\kappa_B = 1.380649 \cdot 10^{-23}$ J/K is the *Boltzmann's constant*.

Real systems are not so simple and in general entropy is defined as a temperature derivative of the Gibbs free energy (G):

$$S = -\left(\frac{\partial G}{\partial T}\right)_{p,H} . \tag{2.19}$$

Gibbs free energy is a thermochemical potential from which all the macroscopic thermodynamic properties can be derived. In its differential form it can be expressed as:

$$dG = V dp - S dT - \mu_0 M dH \,, \tag{2.20}$$

where $\mu_0 = 4\pi \cdot 10^{-7}$ H/m is the magnetic permeability in vacuum. G can be obtained from:

$$G = -\kappa_B T \ln Z \,, \tag{2.21}$$

where Z is the well known *partition function*:

$$Z(T,H) = \sum_i e^{-E_i/\kappa_B T} \,. \tag{2.22}$$

This function weights the probability of a system to be in different microstates (i) with energy E_i.

In the case of a magnetic material the total entropy of the system (S) is a function of temperature and magnetic field, and it is a combination of the magnetic (S_M), lattice (S_{lat}) and electronic (S_{el}) entropies [64]:

$$S(T,H) = S_M(T,H) + S_{lat}(T) + S_{el}(T) \,. \tag{2.23}$$

The effect of the magnetic field on the lattice and electronic entropies can be neglected while the magnetic entropy has a big dependence on the magnetic field. The electron contribution to the total entropy of the system is also usually neglected because the effect is small, specially in systems with a very localized magnetism, as it is the case of rare-earth based materials. On this basis, cooling through adiabatic demagnetization can now be easily understood following a refrigeration cycle as an example, which, in this case, will be analogous to the *Carnot* refrigeration cycle in classical gas compression refrigeration. The main difference is that instead of increasing and decreasing the pressure of the system, the strength of the applied magnetic field will be changed.

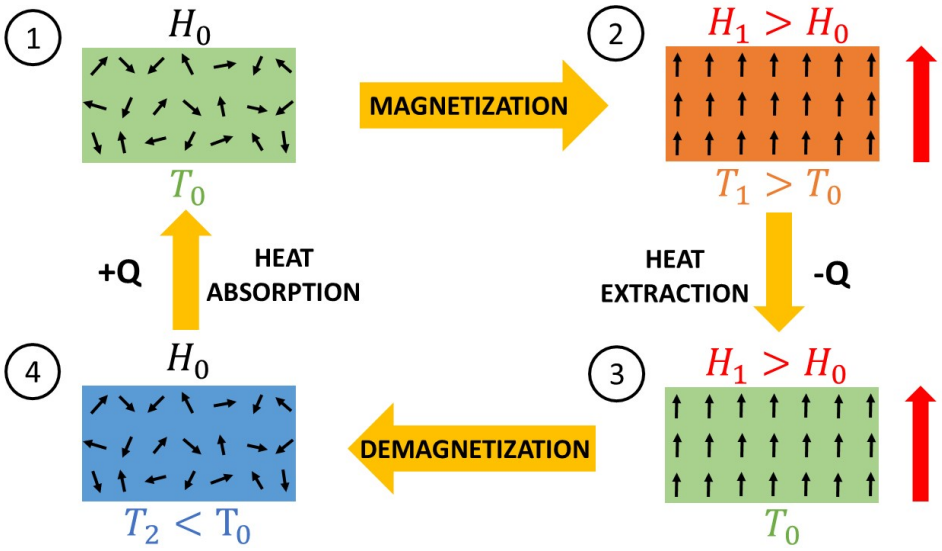


Figure 2.5: Squematic representation of the four stages of a magnetic refrigeration cycle.

The refrigeration cycle starts with a ferromagnetic material (we will later discuss what happens in the case of an antiferromagnetic material) at temper-

ature T_0. This is the temperature at which the material is in thermal equilibrium with the environment we want to refrigerate. We will name the initial magnetic field H_0, which, for instance, can be zero. With this field and at this temperature the magnetic moments of the material are disordered, or at least not completely ordered (see (1) in Fig. 2.5).

The first step of the cycle is to adiabatically apply a higher magnetic field, H_1. This increase of the applied magnetic field, $\Delta H = H_1 - H_0$, orders the magnetic moments in the FM material. More ordered FM moments decrease the allowed microstates of the system, thus, decreasing the magnetic entropy:

$$S_M(H_0) > S_M(H_1)\,, \tag{2.24}$$

$$\Delta S_M < 0\,. \tag{2.25}$$

However, since this process is adiabatic, the total entropy of the system does not change:

$$S(H_0) = S(H_1)\,. \tag{2.26}$$

This means that the magnetic entropy loss is compensated by an increase of the lattice vibration, i.e, an increase of the lattice entropy, which is translated into an adiabatic temperature increase, $\Delta T_{ad} > 0$, on the material, as is represented in the second stage of Fig. 2.5.

With the material at $T_1 = T_0 + \Delta T_{ad}$, the added heat is removed in an isomagnetic enthalpic transfer. A fluid can be used to do this job, while the applied magnetic field is kept constant to avoid a disordering of the magnetic moments. This fluid can be air or water at room temperature, to which some antifreeze can be added if the working temperature is lower, while for much colder temperatures helium can be used. In any of the previous cases no environmentally harmful fluids are needed [69]. Once the heat is removed and the initial temperature (T_0) is again reached, the heat absorbing fluid is removed. At this point the magnetic refrigerant is at the initial temperature but with the magnetic moments aligned ((3) in Fig. 2.5).

The material is again isolated and adiabatically demagnetized. The total entropy is again kept constant but the magnetic field is decreased. This allows the lattice entropy to decrease by increasing the magnetic entropy. Hence, as shown in picture (4) of Fig. 2.5, in this process magnetic moments are disordered and the temperature is reduced, reaching a lower temperature than at the beginning of the cycle, $T_2 = T_0 - \Delta T_{ad}$. The colder material is now placed into thermal contact with the environment so that the magnetic refrigerant extracts heat from it cooling it down. During this isomagnetic entropic transfer the magnetic field is held constant and the material heats up to T_0.

With these four steps represented in Fig. 2.5, the refrigerant reaches again its initial state (1). This cycle is repeated in order to refrigerate the environment.

We have seen that a FM material heats up when the applied magnetic field is applied and cools downs when it is decreased, due to a decrease of the magnetic entropy in the first case and an increased in the second case. This behavior is called a direct magnetocaloric effect (DMCE). However, this is not

always the case for other magnetic orderings, it depends on the initial and final magnetic states when the field is applied. For instance, when a material moves from a stable AFM state to a less ordered FM or PM state, under the aplication of an external magnetic field, the magnetic entropy increases ($\Delta S_M > 0$) and the temperature decreases ($\Delta T_{ad} < 0$). This is considered an inverse magnetocaloric effect (IMCE), where cooling is obtained by adiabatic magnetization instead of adiabatic demagnetization. This effect was first reported for antiferromagnets in 1963 [110]. The IMCE can also take place in paramagnetic compounds [111–113], AFM-ferrimagnetic transitions [114], or AFM-collinear/AFM-non-collinear transitions [108, 115].

Materials with an IMCE can be used, not only for cooling, but as heat-sinks as well, for heat generated when a conventional magnetocaloric material is magnetized before cooling by adiabatic demagnetization [115, 116]. Along this line, materials which present, in a row, inverse and direct magnetocaloric effect are specially interesting for this kind of applications, as they can increase refrigeration efficiency [117–120]. Therefore, IMCE is also very interesting from the point of view of its technological application.

2.2.4 Direct and indirect methods

Methods for characterizing the MCE parameters can be classified as direct or indirect depending on how those parameters are obtained. We will see that, although conceptually direct methods are more straightforward, indirect methods, where different thermodynamic relations are used in order to finally obtain the MCE parameters, are easier to obtain experimentally.

Direct methods

It has been already shown that when a magnetic field is adiabatically applied to a magnetocaloric material, an adiabatic temperature change takes place. This is represented in the squematic S-T plot in Fig. 2.6 by the orange horizontal arrow, where under the adiabatic increase of the applied magnetic field, $\Delta H = H_1 - H_0$, the system is moved from $S(T_0, H_0)$ to $S(T_1, H_1)$, generating a temperature increase of $\Delta T_{ad} = T_1 - T_0$. Therefore, the most intuitive way of measuring this effect would be to directly measure the temperature of the isolated sample while applying a magnetic field. The temperature measurement can be done either by direct contact with the sample through a thermocouple detector or by non-contact methods such as thermoacoustic technique and others [93, 121–129].

However, although devices for this kind of direct measurements exist, they are generally custom-built for specific procedures, and they are not readily available for the majority of research groups [66]. Furthermore, this technique requires a quick change of the magnetic field which is not always easy to get. In the best cases between a 5% and a 10% error is induced; however, this error can even reach 20-25% [130]. Moreover, if the thermal mass of the sample is not large enough compared to the thermal mass of the sample holder, additional recalibration procedures are needed [131].

Indirect methods

A limitation of direct methods is that they can only be used to measure the adiabatic temperature change, ΔT_{ad}, as the entropy change can not be directly measured. Indirect methods, on the other hand, allow the study of both properties. Theses methods are called indirect because the properties we are interested on are obtained from other properties to which they are thermodynamically related. Indirect methods have been proven to be useful, reliable and comparable to the direct ones in order to obtain the MCE [132, 133].

From the second law of thermodynamics and Eq. (1.8) the entropy of the system at a given state can be expressed as a function of the heat capacity:

$$C_p(H) = \left(\frac{dQ}{dT}\right)_{H,p} = T\left(\frac{dS}{dT}\right)_{H,p}, \tag{2.27}$$

$$S(T,H) = \int_0^T \frac{C_p(H)}{T} dT\,. \tag{2.28}$$

Here $C_p(H)$ is the heat capacity at constant pressure and at a given magnetic field. Therefore, using this expression, the total entropy curves for different applied fields can be constructed as shown in Fig. 2.6, and from there the isothermal magnetic entropy change can be calculated as:

$$\Delta S_M(T_0) = [S(T_0,H_1) - S(T_0,H_0)] = \int_0^{T_0} \frac{C_p(H_1) - C_p(H_0)}{T} dT\,. \tag{2.29}$$

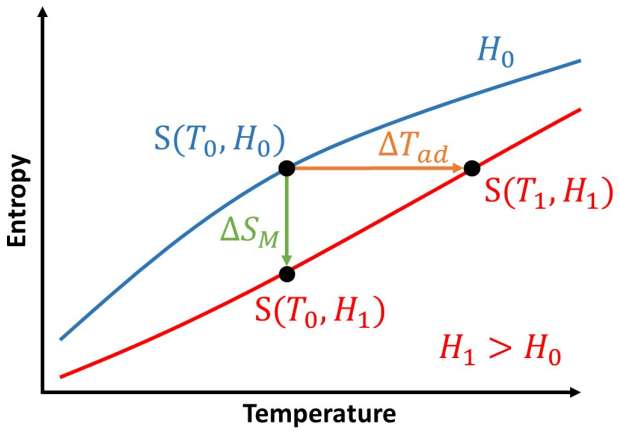


Figure 2.6: Schematic total entropy vs. temperature plot for a FM material. The lines represent the total entropy with an applied magnetic field of H_0 (blue), and a higher field H_1 (red). Horizontal arrow represents the adiabatic temperature change, ΔT_{ad}, and vertical arrow the isothermal magnetic entropy change, ΔS_M.

Once the entropy at different fields is obtained, ΔT_{ad} can directly be calculated from the corresponding S-T plot as represented in Fig. 2.6:

$$\Delta T_{ad} = [T(S(H_1)) - T(S(H_0))]\,. \tag{2.30}$$

The problem with this method is the difficulty of measuring heat capacities at different fields, but even if that can be experimentally obtained, the measurements must be performed down to 0 K in order to correctly integrate Eq. (2.28) [134]. This greatly complicates the availability of the necessary experimental set-up. However, thermodynamics gives us another solution to this problem.

The Gibbs free energy presented in Eq. (2.20) is a state function of any thermodynamic system and, hence, can also be expressed as:

$$dG = \left(\frac{\partial G}{\partial P}\right)_{H,T} dP + \left(\frac{\partial G}{\partial T}\right)_{H,p} dT + \left(\frac{\partial G}{\partial H}\right)_{p,T} dH \,. \tag{2.31}$$

Comparing Eq. (2.20) with Eq. (2.31) the extensive properties of the system can be easily obtained:

$$V = \left(\frac{\partial G}{\partial P}\right)_{H,T} , \tag{2.32}$$

$$S = -\left(\frac{\partial G}{\partial T}\right)_{H,p} , \tag{2.33}$$

$$M = -\frac{1}{\mu_0}\left(\frac{\partial G}{\partial H}\right)_{p,T} . \tag{2.34}$$

From now on we will always assume that pressure is kept constant and the subindex p (indicating constant pressure conditions) will be removed in order to simplify the notation.

If the partial derivative with respect to temperature is taken in expression (2.34), we get:

$$\left(\frac{\partial M}{\partial T}\right)_H = -\frac{1}{\mu_0}\frac{\partial}{\partial T}\left(\left(\frac{\partial G}{\partial H}\right)_T\right)_H . \tag{2.35}$$

Considering that second order derivatives can be exchanged the previous expression can be rewritten as:

$$\left(\frac{\partial M}{\partial T}\right)_H = -\frac{1}{\mu_0}\frac{\partial}{\partial T}\left(\left(\frac{\partial G}{\partial H}\right)_T\right)_H = -\frac{1}{\mu_0}\frac{\partial}{\partial H}\left(\left(\frac{\partial G}{\partial T}\right)_H\right)_T , \tag{2.36}$$

where, inside the bigger brackets of the right hand side, expression (2.33) can be identified to finally obtain the following *Maxwell relation*:

$$\mu_0\left(\frac{\partial M}{\partial T}\right)_H = \left(\frac{\partial S}{\partial H}\right)_T . \tag{2.37}$$

On the other hand, the entropy of the system depends on both the temperature and the magnetic field, and it can be expressed in a differential way as:

$$dS = \left(\frac{\partial S}{\partial T}\right)_H dT + \left(\frac{\partial S}{\partial H}\right)_T dH \,. \tag{2.38}$$

It has already been mentioned that MCE can be expressed by either an adiabatic temperature change or by an isothermal magnetic entropy change. Considering the first case, an adiabatic process where $dS = 0$, Eq. (2.38) can be rearranged so that it looks like this:

$$dT = -\left(\frac{\partial S}{\partial T}\right)_H^{-1}\left(\frac{\partial S}{\partial H}\right)_T dH\,, \tag{2.39}$$

which, using Eq. (2.27) and the previously obtained *Maxwell relation*, Eq. (2.37), can be rewritten in an integral way as:

$$\Delta T_{ad} = -\mu_0 \int_{H_0}^{H_1} \frac{T}{C_p(H)}\left(\frac{\partial M}{\partial T}\right)_H dH\,. \tag{2.40}$$

The problem with this expression comes again from the difficulty to obtain C_p values as a function of the magnetic field. That is why the most common way in literature to evaluate the MCE comes from the consideration of an isothermal process ($dT = 0$). In this case Eq. (2.38) takes the following form:

$$dS = \left(\frac{\partial S}{\partial H}\right)_T dH\,, \tag{2.41}$$

where, applying the *Maxwell relation* (2.37), the integral form is expressed as:

$$\Delta S_M(T, \Delta H) = \mu_0 \int_{H_0}^{H_1} \left(\frac{\partial M}{\partial T}\right)_H dH\,. \tag{2.42}$$

This is the main equation used to evaluate the MCE. $\Delta H = H_1 - H_0$ indicates the magnetic field change, where H_0 is the initial magnetic field and H_1 the final one. The M sub-index has been used to expressed that the entropy change under the isothermal application of a magnetic field is produced on the magnetic component of the entropy (see Eq. (2.23)).

Expression (2.42) allows us to obtain the magnetic entropy change from standard magnetic measurements, which can be performed in a much simpler way with commercial and widely available magnetometers. This is by far the easiest and most commonly used indirect method to study the MCE. In our case magnetic measurements are performed using a VSM (Vibrating Sample Magnetometer) by Cryogenic Limited. On this kind of measurements magnetization is obtained as a function of temperature and magnetic field, $M(T, H)$. Magnetization data is collected isothermally, at a fixed temperature, under the application of the magnetic field, and then Eq. (2.42) is numerically integrated:

$$\Delta S_M(T_i, \Delta H = H_k - H_0) = \mu_0 \sum_{k'=0}^{k} \frac{M_{i+1,k'} - M_{i-1,k'}}{T_{i+1} - T_{i-1}}(H_{i,k'+1} - H_{i,k'})\,. \tag{2.43}$$

Here i is the temperature index and k the magnetic field index.

2.2.5 Correct evaluation of the MCE

In order to correctly evaluate the magnetocaloric effect there are several factors that must be taken into account.

First of all, it must be considered that the purity of the sample affects the value of the MCE, increasing or lowering the effect [75]. This could have a great impact on practical applications.

When evaluating MCE on a single crystal it is also important, in order to obtain comparable results, to consider the axis along which the magnetization is being measured, because, in general, the magnetocaloric effect will be different along each axis; in fact, MCE is maximized when the magnetic field is applied in the direction of the easy-axis, i.e., the axis for which the magnetization is higher. This phenomena is used in rotating magnetocaloric effect (RMCE), where MCE is generated not by changing the applied magnetic field but by rotating the material from its easy-axis to its hard-axis [64, 135]. Obviously this does not apply to polycrystalline samples, where the MCE is an average value of the one corresponding to the different directions due to the arbitrary grain orientation.

If the magnetocaloric effect is indirectly evaluated using Eq. (2.40) or (2.42), where magnetizations curves are used, the effect of the demagnetization field must be considered. For a long time this effect has been neglected; however, recent studies suggest that this effect is in fact relevant for the correct evaluation of the MCE, specially if one wants to compare magnetic and magnetocaloric properties of different materials, or wants to obtain reproducible results using different geometries [64, 99, 136–139]. An increase of the demagnetization factor (N_D) produces a decrease of the magnetic entropy change, specially below the critical temperature [140, 141]. Correctly considering the demagnetization field increases the peak values of the magnetic entropy change and avoids the shift of the temperature at which this peak value takes place [142]. This is why all our magnetic and magnetocaloric results are corrected from this effect and presented as a function of the internal field.

Although the order of phase transitions will be discussed on the following chapter, it is an important factor to take into account when evaluating the magnetocaloric effect from *Maxwell relations*. Expression (2.37), and therefore Eq. (2.42), are only valid if both the entropy and magnetization are continuous functions of the temperature and magnetic field, and this is only true in second order magnetic phase transitions (SOMPT). First order magnetic phase transitions (FOMPT) are characterized by a discontinuity in the first derivative of the Gibbs potential, which, as can be seen in Eq. (2.33) and Eq. (2.34), directly affects the entropy and the magnetization.

The incorrect application of *Maxwell relations* to first order magnetic phase transitions (FOMPT) has been responsible for wrongly attributed "colossal" MCE in several materials [143–148].

Taking a look at expression (2.43) one can see that ΔS_M is obtained by adding up the areas between different magnetization isotherms as a function of the magnetic field. In the case of a metamagnetic (field induced) FOMPT from a PM to a FM phase or from an AFM to a FM phase, in the proximity of the phase transition, both phases, the initial and the final one, coexist. This

coexistence is shown in the isothermal magnetization curves as a transition region [149, 150] or a step-like behavior with a plateau region [151, 152], and it is responsible for the spurious values when the *Maxwell relation* (Eq. (2.42)) is applied. This overestimation comes from considering not only the contribution to the change in magnetization as a result of the orientation of the magnetic moments in an applied field, but also the result of the relative change in the fractions of the two coexisting phases. This distorts the integration process and adds an extra area (which should not be considered) to the sum in Eq. (2.43), which is presented as an anomalous peak in the final result [150–153].

Two different solutions have been proposed to deal with magnetocaloric effect in materials with a FOMPT:

Clausius-Clapeyron equation

In order to avoid the spurious results and the overestimation of the magnetic entropy change when applying indirect methods in FOMPT (where two magnetic phases coexist), it has been suggested that the proper calculation must be done not by Eq. (2.42) but by using the so called *Clausius-Clapeyron* (CC) equation within the transition region, instead:

$$\Delta S_M^{CC}(T, H_C) = -\mu_0 \Delta M \frac{dH_C}{dT} \,. \tag{2.44}$$

Here, $\Delta S_M^{CC} = S_M^B - S_M^A$, $\Delta M = M^B - M^A$ are the gaps of the magnetic entropy change and magnetization of the coexisting phases A and B, while H_C is the critical field calculated from the inflexion point of the magnetization isotherms. This expression can also be interpreted as the calculation of an area on a M vs. H plot, and can be derived from thermodynamic relations if the singular nature of the first order phase transition is correctly considered [150, 154, 155]. This method has been successfully applied in different systems leading to the correct entropy change values [149, 156, 157]. Furthermore, it has been shown that the *Clausius-Clapeyron* equation is equivalent to the *Maxwell relation* provided that the latter is evaluated only within the transition region and that the applied field is high enough to complete the transition, otherwise, the temperature and field dependence of the magnetization outside the transition region causes the overestimation of the magnetic entropy change [152, 158]. This method has also been proven to be in excellent agreement with results obtained by direct methods [144].

If magnetization curves are not saturated after the transition because the applied field is not high enough, or the transition does not sharply occur at H_C but in a small region (δH) around the critical field ($H_C \pm \delta H$), which is the case in real materials, the use of Eq. (2.44) alone underestimates the real entropy change, since the contributions to the entropy change bellow and above the discontinuity in the region $H_C \pm \delta H$ are not considered. Therefore, following references [155] and [157], the correct way of evaluating the magnetic entropy change of FOMPTs using the *Clausius-Clapeyron* equation is to combine it with the *Maxwell relation* (MR) outside the transition region, where the sample is in a single equilibrium state and Eq. (2.42) can be applied. Thus, the proper

expression for the whole range in the case of FOMPTs looks like this:

$$\Delta S_M(T,\Delta H) = \overbrace{\mu_0 \int_{H_0}^{H_C-\delta H} \left(\frac{\partial M}{\partial T}\right)_H dH}^{\text{MR in magnetic phase A}} \underbrace{-\mu_0 \Delta M \frac{dH_C}{dT}}_{\Delta S_M^{CC}} + \overbrace{\mu_0 \int_{H_C+\delta H}^{H_1} \left(\frac{\partial M}{\partial T}\right)_H dH}^{\text{MR in magnetic phase B}} . \tag{2.45}$$

Measuring protocol

The second solution to the spurious results caused by Eq. (2.42) is related to the method used in order to measure the magnetization curves. The simplest and most used experimental method consists on measuring the magnetization of several isotherms starting from the lower temperature. The temperature is fixed and the magnetic field, starting at 0 T, is gradually increased until the desired maximum field is reached. Once the measurement at a given temperature is done, the magnetic field is removed and the temperature is increased one step. The procedure continues until the higher temperature is reached.

Following the previous method, the non-equilibrium nature of FOMPTs and their characteristic hysteresis affect the magnetization measurements generating artefacts when the magnetic entropy change is calculated from Eq. (2.42). However, Caron et al. proposed a measuring method which highly reduces these effects and allows us to directly use *Maxwell relation* in the whole range even in FOMPTs [159].

This protocol, which is also very well described by Franco [160], consists on eliminating the residual ferromagnetic volume by warming up the sample well above its critical temperature, i.e., into the paramagnetic phase, before the measurement of each isotherm. In this way magnetic memory is erased. This method is being widely used, proving its suitability for both DMCE [161–164] and IMCE [117, 165, 166]. The main advantage of this method is that, if the protocol is correctly applied, Eq. (2.42) can be directly used in order to calculate the magnetic entropy change. The drawback of this technique is that it takes more experimental time, since the sample has to be heated up before each new isothermal measurement.

2.2.6 What are we looking for?

When measuring MCE we will need some reference parameters which at the same time give us some valuable information about the performance of the corresponding material as a refrigerant, and allow us to compare this performance with other materials. This section will present the main figures of merit that will be used to characterize our materials and discuss the desirable characteristics of an ideal magnetocaloric material for its technological application.

Lets start by having a look at expressions (2.40) and (2.42). These equations, which are obtained from thermodynamic *Maxwell relations*, hide some

hints about the general shape of the expected curves. The first thing to notice is that both expressions depend on the change of magnetization with respect to temperature, $(\partial M/\partial T)_H$, and, as this change is maximum around the critical temperature, the absolute value of the adiabatic temperature change, $|\Delta T_{ad}|$, and isothermal magnetic entropy change, $|\Delta S_M|$, will peak near the corresponding ordering temperature. In general, in the case of ferromagnetic materials, this peak takes place at T_C when no field is applied [51]; however, depending on the order of the transition, the peak can be displaced to higher temperatures as the field is increased. In the case of AFM materials (which show an IMCE) the peak appears at a slightly lower temperature than their Néel temperature, T_N, which in this case is marked by a sharp change from negative (DMCE) to positive (IMCE) magnetic entropy change [93, 114, 167, 168].

The dependency of ΔT_{ad} and ΔS_M on $(\partial M/\partial T)_H$ also show us where DMCE and IMCE come from:

- **DMCE:** When $(\partial M/\partial T)_H < 0$ resulting in $\Delta S_M < 0$ and $\Delta T_{ad} > 0$.
- **IMCE:** When $(\partial M/\partial T)_H > 0$ resulting in $\Delta S_M > 0$ and $\Delta T_{ad} < 0$.

From Eq. (2.40) it can be also seen that, for the same value of magnetization change, $|\Delta T_{ad}|$ will be larger at higher temperature. On the contrary, a higher heat capacity lowers $|\Delta T_{ad}|$ value.

The general behavior for both ΔT_{ad} and ΔS_M is similar: a peak around the phase transition (which increases with higher applied magnetic fields) and a gradual reduction on both sides of the transition. As MCE is mostly significant around the transition temperature, magnetocaloric materials are selected according to their transition temperature for applications at different temperature regions, i.e., for room temperature devices we would look for materials with a transition close to room temperature, while for cryogenic purposes this transition must be located at much lower temperature, in the region of interest.

From now on we will let the adiabatic temperature change, ΔT_{ad}, aside, since we will not be measuring it. Our attention will be focused on the isothermal magnetic entropy change, ΔS_M, and more specifically on its value at the peak, $|\Delta S_M^{pk}|$, which will be one of the main parameters used to evaluate the MCE and compare it to other materials. This is the most commonly used parameter in literature to characterize MCE.

In 1985, Wood and Potter stated that in order to compare the performance of magnetocaloric refrigerant a compromise between magnetic entropy change and the width of the peak should be introduced [169]. This gave rise to a relevant parameter which is now widely used; the **refrigerant capacity**, (RC):

$$RC(H) = \int_{T_{cold}}^{T_{hot}} \Delta S_M(T, \Delta H) dT \,. \tag{2.46}$$

This magnitude tells us how much heat can be transferred between the hot and cold sources on a magnetic refrigeration cycle [170]. Depending on the approximations to this integral one can find several definitions for RC used in literature, among which the most common ones are: RC_{FWHM} and RC_{Area}.

The first one is known as the refrigerant capacity at *full width half maxima* (FWHM), and it is calculated as the product of the peak value of the entropy change times the width of ΔS_M between the points at half the value of the peak:

$$RC_{\mathrm{FWHM}} = |\Delta S_M^{pk}| \delta T_{\mathrm{FWHM}} \,. \tag{2.47}$$

Here δT_{FWHM} is the temperature span which acording to Fig. 2.7 would be $\delta T_{\mathrm{FWHM}} = T_2 - T_1$. In literature RC_{FWHM} can also be found as relative cooling power (RCP). In the left hand side of Fig. 2.7 the shaded area in blue gives an schematic representation of RC_{FWHM}.

On the other hand, RC_{Area} is the area enclosed by the ΔS_M vs. temperature curves in the temperature range enclosed by the full width at half maximum of the peak.

$$RC_{\mathrm{Area}} = \int_{T_1}^{T_2} |\Delta S_M(T, \Delta H)| dT \,. \tag{2.48}$$

This is represented by the area shaded in yellow on the right hand side of Fig. 2.7. As it is clear from the figure, by definition, RC_{FWHM} is always greater than RC_{Area}. In both cases the value increases with increasing magnetic field change, and a RC value as high as possible is desirable. A higher value of RC depends on $|\Delta S_M^{pk}|$ value and the temperature span for which the MCE is relevant, which is usually considered as the the width of ΔS_M at half maximum.

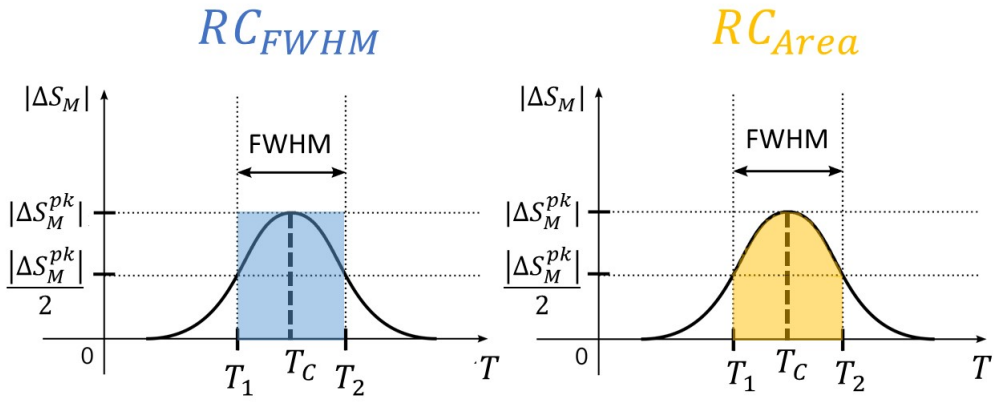


Figure 2.7: Representation of RC_{FWHM} (left) and RC_{Area} (right) on a $|\Delta S_M|$ vs. T schematic plot.

The order of the magnetic phase transition also plays an important role on the performance of the magnetocaloric materials. At first the attention was focused on materials with a FOMPT because these materials usually have a bigger MCE that materials with SOMPT. However, it was later seen that materials experiencing FOMPTs have several drawbacks. Although, it is true that

the MCE is usually larger, the temperature span for which this effect is relevant is smaller, and even with lower $|\Delta S_M^{pk}|$ values, materials with a SOMPT can have higher RC values due to the bigger temperature span. Furthermore, the main disadvantage of first order phase transitions is their thermal and magnetic hysteresis (linked to the existence of latent heat), which highly limits their application [93, 171]. That is why in recent years the attention has moved towards materials presenting a second order phase transition (which does not present hysteresis) [91], or, alternatively, to the search of materials with FOMPTs but negligible hysteresis [172].

Considering the technological application of magnetocaloric materials it is important to ensure that their effect is considerably large over a wide range of temperatures. Usually the FWHM of the magnetic entropy change is considered as the optimal working region. A considerable MCE over a broad temperature range around the operating temperature can be achieved by, for example, making a composite material containing materials with magnetic transitions all over the temperature span on which we are interested to work [82,173–178]. Another less explored way of obtaining the same effect would be to find a material with several close-by magnetic phase transitions. Whichever the case, the goal is to achieve a "table-like" (flat) behavior of the MCE for the largest possible temperature span [74, 168, 179].

Finally, when designing new magnetocaloric materials, special attention must also be paid to the thermal properties of magnetic refrigerators, since their application depends on being efficient and quick when exchanging heat with the fluid in the refrigerator in order to allow high working frequencies [98, 180–183]. While working as a magnetic refrigerator the temperature in the material will change as it follows the cycles in the refrigerator, therefore, as was shown in Section 1.3.1, the equation which reflects heat transfer in that non-steady situation is:

$$\nabla^2 T(\vec{r},t) + \frac{Q(\vec{r},t)}{K} = \frac{1}{D}\frac{\partial T(\vec{r},t)}{\partial t}\,, \tag{2.49}$$

where $T(\vec{r},t)$ is the temperature field as a function of the position vector and time, $Q(\vec{r},t)$ is the heat generated in the medium per unit time and unit volume, K is the thermal conductivity and D is the thermal diffusivity of the material, which, as was already explained in Section 1.2, characterizes how fast heat is transferred in the material [6]. D is related to specific heat and thermal conductivity by the following expression:

$$D = \frac{K}{\rho c_p}\,, \tag{2.50}$$

where ρ is the density. Thus, low specific heat and high thermal conductivities (high D) are required in order to increase ΔT_{ad} value and facilitate the heat transfer process.

Summing up, the desirable physical properties of an ideal magnetocaloric material would be:

- Critical temperature near working temperature.

- Large $|\Delta S_M^{pk}|$ and RC values.
- No thermal or magnetic hysteresis.
- Wide working temperature range (table-like behavior).
- High thermal diffusivity values, i.e., low specific heat and high thermal conductivity.

3 | Phase Transitions and Critical Behavior

"Treasure your curiosity and nurture your imagination. Have confidence in yourself. Do not let others put limits on you. Dare to imagine the unimaginable."

– Shirley Ann Jackson

Following Shirley's advice, it is now time to approach, with *"confidence"*, the critical behavior theory in order to understand how it is applied to the previously introduced thermal, magnetic and magnetocaloric properties in the vicinity of second order phase transitions.

The theory of phase transitions and their critical behavior is a huge field about which we can find very detailed books to which we redirect the reader for a deeper comprehension of the phenomena [184–187]. This topic remains open nowadays, and it has taken the interest of both theoretical and experimental scientists all around the world since its first steps. Although a complete development of this theory is far from the scope of this thesis, the aim of this chapter is to present the principal ideas and tools that have been used in our study of the critical phenomena of phase transitions. The concepts presented here will be of great importance when discussing the results and their interpretation.

3.1 Introduction to phase transitions

This thesis is basically focused on physical phenomena happening in the proximity of phase transitions, and on the effects that those transitions have on magnetic materials. In one way or another everyone is familiar with the concept of phase. Probably, when mentioning equilibrium phases, the first example that comes to our mind are the solid, liquid and gaseous states of water. A phase transition is nothing else than the evolution of a thermodynamic system from one phase to another. We have already seen that phase transitions are not limited to the evolution of matter from solid to liquid or to gas, magnetic materials also evolve from one magnetic state to another. The evolution between different chemical states of a substance or different ferroelectric phases on a ferroelectric material are other examples of phase transitions.

Overall, phase transitions, regardless the nature of the thermodynamic system, share certain properties, for instance, at a certain point there is a huge change of one or more physical properties when a small change on a thermodynamic variable (temperature, pressure, magnetic field, concentration, etc.) takes place. For example, iced water can melt when temperature is increased or, in the particular case of water, when pressure is applied. In the case of a magnetic material it can, for example, change from a ferromagnetic state to a paramagnetic phase when temperature is increased, or it can also change its magnetic state under the application of a external magnetic field (metamagnetic transition). Although this work mainly deals with phase transitions where the varying parameter is the temperature, we will also observe and discuss metamagnetic transitions, where the magnetic field drives the phase transition.

Another common feature of any phase transition is the existence of a parameter (or parameters) which is null on one phase and not null on the other. We refer to this parameter as the **order parameter**. In the case of a liquid-gas transition the order parameter is the density difference between phases, on a ferroelectric system the polarization acts as order parameter, and on a magnetic system it is usually the magnetization which takes this role.

It is known from thermodynamics and statistical mechanics that by using an appropriate thermodynamic potential all of the thermodynamic properties can be deduced from it. We have already seen that this is the case of the Gibbs free energy (G) presented in Eq. (2.20), from where the volume (V), entropy (S), and magnetization (M) of the system can be obtained from its first derivatives as shown by expressions (2.32), (2.33) and (2.34) respectively. By using Eqs. (2.27) and (2.33) it can also be easily seen that the heat capacity (C_p) is related to the second derivative of the Gibbs free energy:

$$C_p = -T\left(\frac{\partial^2 G}{\partial T^2}\right)_H . \tag{3.1}$$

An optimistic reader may think that at this point the problem is completely solved; we only need the Gibbs free energy (or any other valid potential) in order to describe the system. However, although this is theoretically right, nature tends to be tricky. The exact expression of the Gibbs free energy is only

known for a few simple systems, which, in general, are only of phenomenological interest. Finding this expression for complex systems is often an impossible task. This should not discourage anyone, the thermodynamic relations still hold and give us a valuable tool to study our systems.

Mathematically speaking, a phase transition is defined as a point (or points) in the parameter space where the thermodynamic potential becomes non analytic. A function is considered non-analytic when there is a point inside that function for which at least one of the derivatives of the function is not defined, i.e., it has a singularity. In conclusion, a phase transition takes place when the potential, and, thus, the behavior of the thermodynamic system is singular with respect to a certain variable (or variables) in the parameter space, such as: temperature, pressure, magnetic field...

If we want to be strict we must point out that these mathematical singularities only arise when the system is infinite or when it can be considered as such, above the so called thermodynamic limit, under which the system is always analytical. Although sharp phase transitions are a mathematical idealization, because there are no infinite systems in real life, they describe reality really well.

Phase transitions can be classified according to the order of the thermodynamic potential derivative at which the singularity arises. P. Ehrenfest was the first one to classify phase transitions as first order (or discontinuous) when the first derivative of the thermodynamic potential ($\partial G/\partial T$) exhibits a discontinuity, or as second order (or continuous) phase transitions when singularities appear at higher order derivatives ($\partial^2 G/\partial T^2$, $\partial^3 G/\partial T^3$, ...).

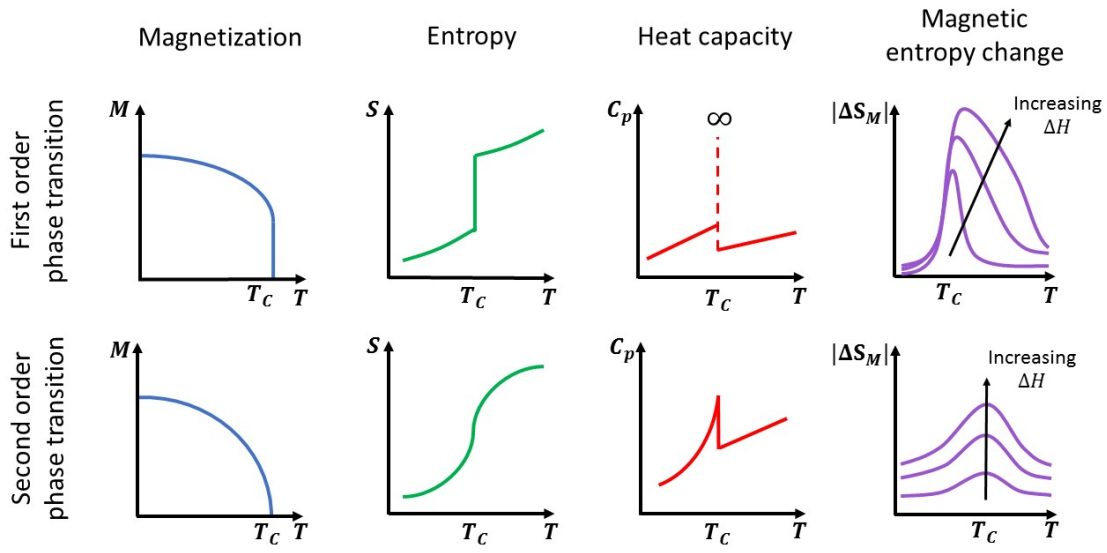


Figure 3.1: Schematic representation of magnetization (M), entropy (S), heat capacity (C_p) and absolute value of magnetic entropy change ($|\Delta S_M|$) in the case of first (upper line) and second order (bottom line) phase transitions.

Fig. 3.1 shows the difference between first and second order phase transitions for different properties. In first order transitions, since the discontinuity

appears in the magnetization and entropy (which are first derivatives of G) their corresponding derivatives $\partial M/\partial T$ and $\partial S/\partial T$ are infinite, which is the case of C_p (see Eq. (2.27)). Fig. 3.1 also shows that in the case of second order phase transitions magnetization and entropy vary smoothly at T_C, and the discontinuity in this case appears in C_p (which is a second derivative of G). The different behavior of $|\Delta S_M|$ in first and second order transitions is also represented in that figure. It can be observed that in both cases the magnetic entropy change increases with increasing applied field. In first order transitions this entropy change is higher but narrower than in second order transitions, and the maximum value is usually displaced to higher temperatures, breaking the symmetry [188]. The behavior of $|\Delta T_{ad}|$ is similar to the one of $|\Delta S_M|$.

It must be clarified that Fig. 3.1 is only a schematic representation in order to represent the order classification of phase transitions based on the singularities in different order derivatives of the Gibbs free energy potential, and some basic characteristics. In real systems discontinuities are never so sharp, the main reason for this is that sharp transitions are a mathematical idealization, and the real nature of systems together with existing impurities make the peaks to get softened or rounded. Some measuring techniques, or too quick measurements, can also contribute to this rounding.

A simpler modern classification for phase transitions has also been established [186]. On the modern approach, the phase transitions are also divided into two groups and are named similarly to the Ehrenfest classes, but a different criterion is taken. A discontinuous (first order) phase transition is characterized by the coexistence of two phases (as has already been discussed for magnetic materials) and is linked to the presence of latent heat (the amount of absorbed or emitted energy during the phase transition), which often (but not always) induces hysteresis [189]. On a continuous (second order) phase transition the system evolves continuously from one phase to another without their coexistence and it is not accompanied by latent heat, therefore, there is no hysteresis in the process [188].

3.1.1 The critical point

The critical point is usually defined as the point at which a phase equilibrium curve finishes, above which one phase can be converted into another continuously. Probably the best known example of this is the case of the vapour-liquid system, where the equilibrium curve between both phases do not extent infinitely in the *P-T* diagram but terminates in the critical point. In the case of magnetic systems the situation is analogous [184, 185].

In order to picture the critical point of a magnetic system lets consider the simplest possible phase diagram of a ferromagnetic material, represented in the left graph of Fig. 3.2. The critical point is indicated by a dot at T_C (the critical temperature) located at the end of the thicker line in $H = 0$, which represents the phase equilibrium line in the FM region. Following $H = 0$ line from low temperatures to higher ones the system would be FM until the critical point is reached, where the magnetization drops to 0 and PM phase starts. Under this condition, with 0 applied field, is how our thermal experiments are

performed, and also how *ac* susceptibility and zero-field magnetization (both as a function of temperature) are measured (in real experimental conditions $M(T, H = 0)$ and $\chi_{ac}(T, H = 0)$ measurements are carried out under the application of a negligible, almost 0, magnetic field).

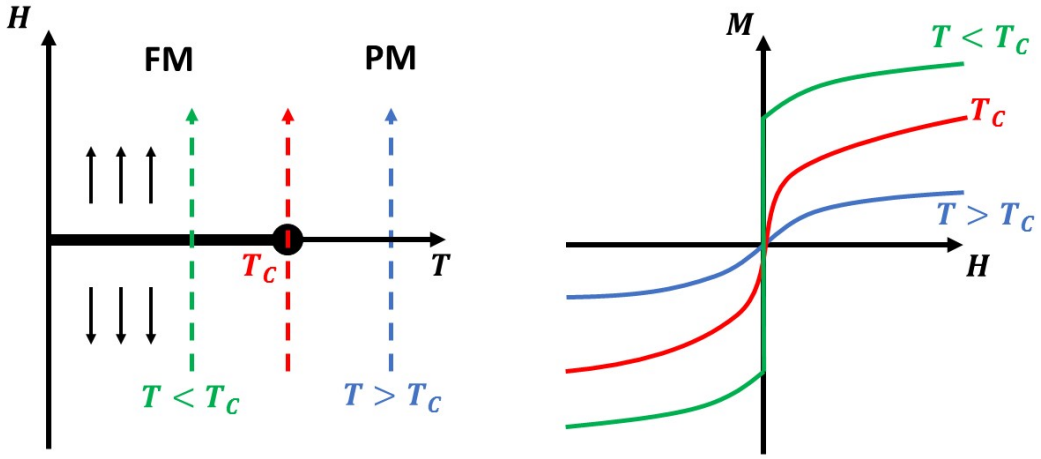


Figure 3.2: Projection of the HMT phase diagram for a simple ferromagnet in H-T plane (left) and isothermal field dependence of the magnetization without hysteresis (right).

Magnetization as a function of magnetic field is obtained from isothermal measurements. These measurements follow the perpendicular dashed lines in the H-T phase diagram of Fig. 3.2, and the corresponding isotherms are represented in the M-H plot on the right side of the figure (for simplification purposes hysteresis is not taken into account here). At $T < T_C$, when the applied field increases crossing $H = 0$ transition line, an abrupt jump on magnetization takes place, which is indicative of a first order transition, in fact, the thicker line at $H = 0$ and below T_C is a first order transition line which flips the direction of the magnetic moment (represented by the small arrows in Fig. 3.2). However, for isotherms above the critical point ($T > T_C$) the magnetization change is smooth and continuous at M=H=0. Both behaviors are divided by the isotherm which crosses the critical point at T_C.

Along this chapter we will see how the behavior of several physical properties near the critical point of second order phase transitions gives us valuable information about our systems.

3.2 Critical behavior theory

Magnetic theories attempting to explain magnetic ordering near the critical temperature, where magnetism disappears, have always been very hard to construct. This is not related to the general nature of magnetism but to the

singularity of the critical point; this same problem appears, for example, in liquid to vapour transitions. Although this behavior is still not fully understood, modern quantum approaches, such as the renormalization group theory, are obtaining promising results which allow the comprehension of part of this phenomena.

In particular, scaling hypothesis within the framework of renormalization group theory assesses that the Gibbs free energy thermodynamic potential is a generalized homogeneous function such that [184, 185, 190]:

$$G(a^{\lambda_1} t, a^{\lambda_2} H) = aG(t, H)\,. \tag{3.2}$$

Here λ_1 and λ_2 are called scaling parameters and a is a number.

From this starting point it can be proven that the critical behavior of **second order phase transitions** in the near vicinity of the critical temperature (T_C) is characterized by a set of **critical exponents** associated with different thermal and magnetic properties [184, 185]. Let me stress out that this whole theory and the conclusions that will follow from it do not apply to first order (discontinuous) phase transitions.

3.2.1 Critical point exponents

The critical point exponents, also called critical exponents, have become the main tool to study the behavior of physical properties near the critical point. In order to justify their central role we shall start by defining what we understand as a critical point exponent.

If we consider a general thermodynamic function such as $F(t)$, where t is the reduced temperature, i.e, the deviation from the critical temperature:

$$t = \frac{T - T_C}{T_C}\,, \tag{3.3}$$

then, the critical exponent related to $F(t)$ is defined as:

$$\lambda = \lim_{t \longrightarrow 0} \frac{\ln |F(t)|}{\ln |t|}\,. \tag{3.4}$$

Assuming that the previous limit exists, the fact that λ is the critical exponent of $F(t)$ is more commonly denoted by the following shorthand notation:

$$F(t) \sim |t|^{\lambda}\,. \tag{3.5}$$

In this expression $\sim$ sign represents the asymptotic behaviour of the function $F(t)$ as $t \longrightarrow 0$, and it must not be confused with an equality. The general form of a thermodynamic function in the vicinity of the critical point is expressed by:

$$F(t) = A|t|^{\lambda}(1 + bt^{\lambda_1} + \ldots)\,, \tag{3.6}$$

with $\lambda_1 > 0$. A and b are system depending parameters while the terms inside parentheses are correction terms [184].

Those critical exponents are linked to different physical properties such as the specific heat (c_p), spontaneous magnetization (M_S), inverse of the initial susceptibility (χ_0^{-1}), and critical isotherm ($M(H)$ at $T = T_C$) in the vicinity of second order phase transitions:

$$c_p(T) \sim A^{\pm}|t|^{-\alpha}\,, \tag{3.7}$$

$$M_S(T) \sim |t|^{\beta} \quad (T < T_C)\,, \tag{3.8}$$

$$\chi_0^{-1}(T) \sim |t|^{\gamma} \quad (T > T_C)\,, \tag{3.9}$$

$$M(H) \sim H^{1/\delta} \quad (T = T_C)\,. \tag{3.10}$$

In the case of specific heat A^- and A^+ stand for $T < T_C$ and $T > T_C$ regions respectively. Furthermore the ratio A^+/A^- is also a critical parameter which, as will be shown, can be related to a certain universality class. In expressions (3.7) to (3.10) α, β, γ and δ are the critical point exponents attributed to each physical property. It can be seen that while α is linked to thermal properties the rest are linked to magnetic ones. The critical behavior of spontaneous magnetization arises as it vanishes, when the magnetic ordering temperature is reached from below. On the contrary, the critical behavior of χ_0^{-1} is observed in the paramagnetic region just above T_C. Moreover, the evolution of magnetization with magnetic field is related to the critical exponent δ only at the critical isotherm ($T = T_C$).

3.2.2 Universality and scaling laws

The critical exponents have already been presented but their importance has not been justified yet. A bunch of critical exponents with some particular values would not have any interest on their own; however, it turns out that the critical behavior near the critical point among systems which are very different in nature, such as a magnetic and a liquid-vapour system, is strikingly similar. Therefore, what makes critical exponents interesting is the fact that they are universal within certain classes. Universality means that no matter how different two systems may seem, they will behave the same way in the vicinity of the critical point as long as they share some properties.

Critical exponents, α, β, γ and δ, take different values for different models or universality classes and, therefore, obtaining a set of values of those critical exponents for a given material allows us to attribute a certain second order phase transition to a certain universality class, which gives an insight of the underlying physics on the system, as well as the role that other mechanisms can play if the obtained critical parameters do not exactly match one of the classes (effect of spin-orbit interactions, disorder, dipolar long-range order interactions, and so on).

Materials belonging to the same universality class share some common properties [191]:

- **Dimension of the system:** Physical systems can be described as one, two or three dimensional. Models and critical exponents change according to the dimension of the system.

- **Interaction extent:** In a magnetic system, for example, the interaction between magnetic moments can be either short-range order, if magnetic moments only interact with neighbouring magnetic moments, or long-range order, when magnetic moments interact even at large distances.
- **Symmetry group of the Hamiltonian:** Universality classes are developed from different Hamiltonians which describe the system; belonging to a certain model means that the system can be described by a certain Hamiltonian and this is why materials belonging to the same class share the same symmetry.
- **Symmetry of the order parameter:** In the case we are concerned with, the order parameter is the magnetization, and we will see that its symmetry is determined by the universality class.

In other words, the critical exponents depend only on those properties which are invariant under a scale transformation.

It turns out that most physical systems can be described by a relatively small amount of universality classes. The history of critical behavior started with Landau in 1937. He was the first one to successfully propose a model describing second order phase transitions based on a Mean Field approximation [192–194]. However, it was soon clear that this Mean Field model was not able to correctly explain all the observed phenomena. The major breakthrough on the study of critical phenomena came from scaling relations in the framework of renormalization group theory [184–186, 195–197].

The development of the models describing the physics which underlies this phenomena is far from our scope on this work. Some of the models are only analytically solvable for low dimensions ($d = 1, 2$) and, more usually, impossible to solve exactly. The most successful attempts are the so called *Q-state Potts* model [185, 198, 199] and the better known *n-vector* model [200, 201], which provide useful and satisfactory representations of real systems. We shall constrain ourselves to a general description of the most common universality classes in the case of magnetic systems.

Mean Field model

The Mean Field model is equivalent to the classical Landau model [192–194]. This model is based on **long-range** order interactions where instead of considering a n-body problem all the interactions are replaced by an effective Mean Field interaction. This theory assumes that the thermodynamic potentials, such as the Gibbs free energy, can be expressed as a power series of the order parameter, which in the case of magnetic systems is magnetization. In the case of a simple ferromagnetic material without applied field [185]:

$$G = G_0 + atM^2 + bM^4 + ... \tag{3.11}$$

Here a and b are material related parameters. Higher powers can be neglected for our interest and only even powers of M are considered because they are the only invariant terms under a reversal of the magnetization sign [184,185]. This

simple power series expansion allows the comprehension of several magnetic phenomena and gives a first description of second order phase transitions. Furthermore, critical exponents can be easily deduced from Eq. (3.11). Spontaneous magnetization, for example, is given by the minimum value of the free energy, which can be calculated from its first derivative:

$$\frac{dG}{dM} = 2atM_S + 4bM_S^3 = 0\,, \tag{3.12}$$

$$M_S = -\left(\frac{a}{2b}\right)^{1/2} t^{1/2}\,, \tag{3.13}$$

or,

$$M_S \sim -t^{1/2}\,, \tag{3.14}$$

which, since $t < 0$ at $T < T_C$, can be compared to Eq. (3.8) to get $\beta = 1/2$ in Mean Field model. If we now consider an applied magnetic field the Gibbs potential is modified as:

$$G = G_0 + atM^2 + bM^4 - \mu_0 HM\,, \tag{3.15}$$

which at equilibrium (energy minimization) now looks like:

$$\frac{dG}{dM} = 2atM + 4bM^3 - \mu_0 H = 0\,. \tag{3.16}$$

From here it can be easily seen that at the critical isotherm ($t = 0$):

$$M \sim H^{1/3} \tag{3.17}$$

and, therefore, comparing this expression to Eq. (3.10) we get that $\delta = 3$. On the other hand, taking into account the definition of magnetic susceptibility given by Eq. (2.10), χ_0^{-1} can be written as:

$$\chi_0^{-1} = \frac{dH}{dM} = \frac{2a}{\mu_0}t + \frac{12b}{\mu_0}M^2 \tag{3.18}$$

Considering that for $t \longrightarrow 0^-$ we have $M \sim t^{1/2}$ and that for $t \longrightarrow 0^+$ the magnetization is 0 ($M = 0$), we get that in both cases the behavior of χ_0^{-1} can be expressed as:

$$\chi_0^{-1} \sim t\,, \tag{3.19}$$

which comparing to Eq. (3.9) gives $\gamma = 1$. Following a similar analysis it can also been proven that the specific heat critical exponent in the Mean Field model is zero, $\alpha = 0$ [185].

Ising model

Although Landau's Mean Field model is a very useful tool to describe several material it does not take into account several factors such as the fluctuations of the order parameter near the critical point. That is why modern approaches come from renormalization group theory, where models are developed from

Hamiltonians which consider n-body interactions. In the case of *n-vector* models, the Hamiltonian in the absence of a magnetic field is given by:

$$\mathscr{H}(d,N) = -\sum_{\langle ij\rangle} J_{ij}\vec{S}_i \cdot \vec{S}_j \,. \tag{3.20}$$

Here d is the dimensionality of the system and N the dimension of the order parameter. $\vec{S}_i$ is the spin vector, which has dimension N. J_{ij} represents the coupling energy between neighbouring spins i and j. In order to consider an applied field an additional term is added:

$$\mathscr{H}(d,N) = -\sum_{\langle ij\rangle} J_{ij}\vec{S}_i \cdot \vec{S}_j - H\sum_i \vec{S}_i \,. \tag{3.21}$$

The Ising model is the simplest possible model arising from this Hamiltonian. In this case $N = 1$ and Eq. (3.21) can be written as:

$$\mathscr{H}(d,1) = -J\sum_{\langle ij\rangle} \vec{S}_i \cdot \vec{S}_j - H\sum_i \vec{S}_i \,. \tag{3.22}$$

This model allows spins to take only two positions, $S = \pm 1$, as represented in the left hand side of Fig. 3.3. J is equal in all the cases because only neighbouring spins are considered. The Ising model gives a simplified description of uniaxial magnetic materials, i.e, materials with **uniaxial anisotropy** where magnetic moments are only aligned along a single easy axis. It is worth mentioning that, despite the simplicity of this model, it describes any interacting two-state system (not only magnetic systems).

The Ising model has been a remarkably successful model of a **short-range** interacting system. It was first proposed by Lenz [202], but it was first solved for $d = 1$ by Ising [203]. Solutions to $d = 2$ models (with and without applied magnetic field) came later [204, 205]. Although the three-dimensional model, even in zero field, remains not exactly solved, its properties and critical exponents have been obtained from numerical works [206, 207]: $\alpha = 0.11$, $\beta = 0.3265$, $\gamma = 1.237$, and $\delta = 4.79$.

XY model

The XY model, also called plane-rotator model, adds an extra degree of freedom to the spins and it is described by the Hamiltonian in Eq. (3.21) with two spin components $N = 2$, $\mathscr{H}(d,2)$.

This model also considers **short-range** order interactions, but, unlike in the Ising model, spins are allowed to orient themselves at any direction within a plane. In the central part of Fig. 3.3 the spin represented by the yellow arrow can rotate along the doted circumference on the horizontal plane. Therefore, XY model is very useful for describing magnets with an **easy plane anisotropy**. This model has been numerically solved for $3D$ systems [208]: $\alpha = -0.014$, $\beta = 0.348$, $\gamma = 1.317$, and $\delta = 4.78$.

Heisenberg model

The most general case is described by the Hamiltonian in Eq. (3.21) with $N = 3$, $\mathscr{H}(d,3)$. This is the well known classical Heisenberg model. In fact the previous Ising and XY models can be understood as a particular case of Heisenberg model.

The Heisenberg model has been successfully used to describe **isotropic systems**, i.e., systems in which spins can point at any direction in space. This is represented in the right hand side of Fig. 3.3 by the yellow arrow which can point at any place within the surface of the sphere. This model is also a **short-range** interaction model and the critical exponents for the three dimensional system have been obtained numerically from Monte-Carlo and other numerical methods [209]: $\alpha = -0.134$, $\beta = 0.369$, $\gamma = 1.396$, and $\delta = 4.78$.

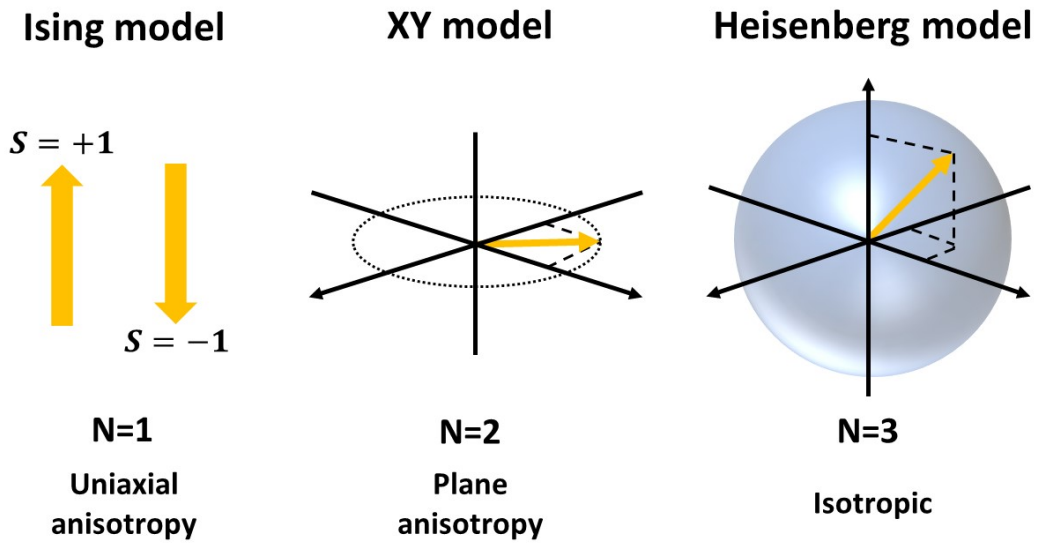


Figure 3.3: Representation of the three main short-range order interaction universality classes according to the *n-vector* model.

Roughly speaking we can group the most common models into two big categories according to their interaction range: long-range order interactions (Mean Field model) and short-range order interactions (Ising, XY and Heisenberg models). Their critical exponent values as well as their critical A^+/A^- coefficient for the previously described systems in 3 dimensional space are summarized in Table 3.1. The first thing to notice is that the critical exponent and coefficient corresponding to thermal properties (α and A^+/A^-) are much more different among models than magnetic critical exponents, with even a sign change in α. This is the reason why thermal critical exponents are usually better for distinguishing different universality classes.

As a remark we should point out that, although the models presented are really good at capturing the physics of the more general cases, several materials belong to different universality classes, some of which have been listed in

Universality class	Thermal		Magnetic		
	α	A^+/A^-	β	γ	δ
Mean Field	0	-	0.5	1.0	3.00
3D Ising	0.11	0.536	0.3265	1.237	4.79
3D XY	-0.014	1.06	0.348	1.317	4.78
3D Heisenberg	-0.134	1.52	0.369	1.396	4.78

Table 3.1: Main universality classes for magnetic materials and their corresponding critical exponents and coefficient.

Table 3.2 in Section 3.6, page 76. However, as mentioned before, solving these systems is a hard theoretical work and some materials do not agree with any of the known universality classes. Even in those cases the experimental study of their critical parameters can point out the reason of their deviation, allowing the study of disorder effects or different kind of perturbations in the system. This can also help theorists to address perturbations of model Hamiltonians in order to capture the nature of more complex systems, enlarging the actual theoretical framework [210].

While renormalization group theory leads to the description of different universality models and to the numerical value of the main critical exponents, scaling accounts for the relations among those critical exponents. It turns out that the exponents are not completely independent, they are related by the **scaling laws** [184, 185, 211]:

$$\alpha + 2\beta + \gamma = 2 \qquad \textbf{(Rushbrook equality)}\,, \tag{3.23}$$

$$\gamma = \beta(\delta - 1) \qquad \textbf{(Widom equality)}\,. \tag{3.24}$$

From the previous relations it can be seen that only two of those critical exponents are really independent, and obtaining any two the rest could, in principle, be determined. Furthermore, substituting Eq. (3.24) into Eq. (3.23) we can easily get the well known *Griffiths equality*:

$$\alpha + \beta(\delta + 1) = 2 \qquad \textbf{(Griffiths equality)}\,. \tag{3.25}$$

3.3 Critical behavior of thermal properties

We have already seen that in order to obtain the thermal properties an *ac* photopyroelectric calorimeter is used in this work. As has been discussed, due to its high resolution and sensitivity, this is a very suitable technique for the study of phase transitions and, in particular, for the study of their critical behavior. Since the thermal critical exponents and amplitude ratio values are very different among models, the critical analysis of thermal parameters is a very reliable tool for classifying materials into universality classes.

Expression (3.7) gives us the critical asymptotic behavior of specific heat in the vicinity of a second order phase transition. However, that is only a

simplified version of the general expression which includes additional terms [16, 212]:

$$c_p = B + Ct + A^{\pm}|t|^{-\alpha}(1 + E^{\pm}|t|^{0.5}) . \tag{3.26}$$

Here $A^{\pm}$, B, C, $E^{\pm}$, together with the critical exponent α are fitting parameters. Superscripts + and - stand for $T > T_C$ and $T < T_C$, respectively. The linear term $(B + Ct)$ represents the background contribution to the specific heat due to phonons and electrons. The rest is the anomalous contribution due to the phase transition itself. The factor inside the parentheses is a correction to scaling term which has been found to be needed, from both theoretical and experimental works, in order to extend the range over which the expression can be fitted [213–216].

Critical behavior theory involving thermal properties is mainly constructed around specific heat; however, this is not the only thermal property which can be analysed. From Eq. (1.13) it can be seen that the inverse of the thermal diffusivity is proportional to c_p, thus, near a second order phase transition it can also be expressed as [217, 218]:

$$1/D = G + Jt + L^{\pm}|t|^{-\alpha}(1 + I^{\pm}|t|^{0.5}) . \tag{3.27}$$

It follows from Eq. (1.13) and Eq. (3.26) that both c_p and $1/D$ have the same critical exponent α and the same critical ratio, $A^+/A^- = L^+/L^-$. However, it must be considered that expression (3.27) can only be used if thermal conductivity (K) does not present any singularity, which is not always the case. Fortunately, it can be proven that thermal diffusivity on its own can also be expressed in a similar way to the specific heat; with a regular term plus a singular one including the correction to scale [16, 212, 219–221]:

$$D = V + Wt + U^{\pm}|t|^{-b}(1 + F^{\pm}|t|^{0.5}) . \tag{3.28}$$

In this case the critical exponent is b. The terms in Eqs. (3.27) and (3.28) have a similar meaning to those in Eq. (3.26). As mentioned, thermal conductivity can also show a singularity around the critical point. In this case the fitting is done over the inverse of the thermal conductivity, i.e., over the thermal resistivity. The reason for this is that contributions to thermal resistance are added in series, therefore, by fitting $1/K$ the regular term, coming from non magnetic sources, and the singular term, due to the magnetic phase transition, can be easily distinguished [212, 221]:

$$1/K = 1/K_{\text{nonmag}} + 1/K_{\text{mag}} = L + Mt + N^{\pm}|t|^{-g}(1 + H^{\pm}|t|^{0.5}) . \tag{3.29}$$

Here K_{nonmag} is the part related to phonon-phonon scattering, umklapp, scattering with impurities, etc., while K_{mag} refers to the spin-phonon scattering mechanisms and phonon scattering by critical fluctuations of the order parameter close to the critical region. The exponent g in Eq. (3.29) is the critical exponent associated to $1/K$.

There is no theoretical support coming from renormalization group theory on the critical behavior of thermal diffusivity or thermal conductivity. Critical

exponents have been theoretically developed only for the singular behavior of specific heat; however, recent theoretical and experimental studies have shown that in some cases, when there is no singularity in thermal conductivity (which is normally the case), or when the singularity is small, some relations between the critical exponents of specific heat (α and A^+/A^-), thermal diffusivity (b and U^+/U^-), and thermal conductivity (g and N^+/N^-) can be established for some universality classes such as the 3D Ising, 3D XY and 3D Heisenberg models [212, 220–223].

In the particular case of the 3D Ising model [222]:

$$\alpha \approx -b\,, \tag{3.30}$$

$$A^+/A^- \approx U^-/U^+\,. \tag{3.31}$$

For the 3D XY model the relations are written as [223]:

$$\alpha \approx b\,, \tag{3.32}$$

$$A^+/A^- \approx U^+/U^-\,. \tag{3.33}$$

And finally for the isotropic 3D Heisenberg model the following relations can be obtained [212]:

$$\alpha \approx b \approx g\,, \tag{3.34}$$

$$A^+/A^- \approx U^+/U^- \approx N^+/N^-\,. \tag{3.35}$$

3.3.1 Fitting procedure of thermal critical behavior

When it comes to fitting the corresponding expressions to the experimental data, the procedure for all the thermal properties is the same, so we will focus our attention on c_p as an example. In the case of specific heat the fitting is accomplished following Eq. (3.26). Fitting regions are splitted into two branches, one for $T < T_C$ and the other one for $T > T_C$. The multi-variable fitting is done simultaneously in both branches under strict conditions in order to assure a rigorous application of scaling and renormalization group theories. According to these theories, the critical exponent α as well as the constants B and C must be the same for both branches [184, 224]. That is why those parameters are imposed to be equal at both sides of the critical temperature during the simultaneous fitting procedure. On the other hand, A^- and E^- in the $T < T_C$ region and A^+ and E^+ in the $T > T_C$ region are fitted independently.

It has already been discussed that real second order phase transitions are not as sharp as can be seen in Fig. 3.1 for heat capacity, or specific heat, thermal diffusivity and thermal conductivity in our case. In general the peak is rounded as shown in Fig. 3.4. It must be clear that in our case this rounding is not caused by the measuring technique, but by the inherent physical nature of the sample [213]. In general this rounding is bigger when the impurities or defects levels are higher, and it is smaller in high purity single crystals than in polycrystals.

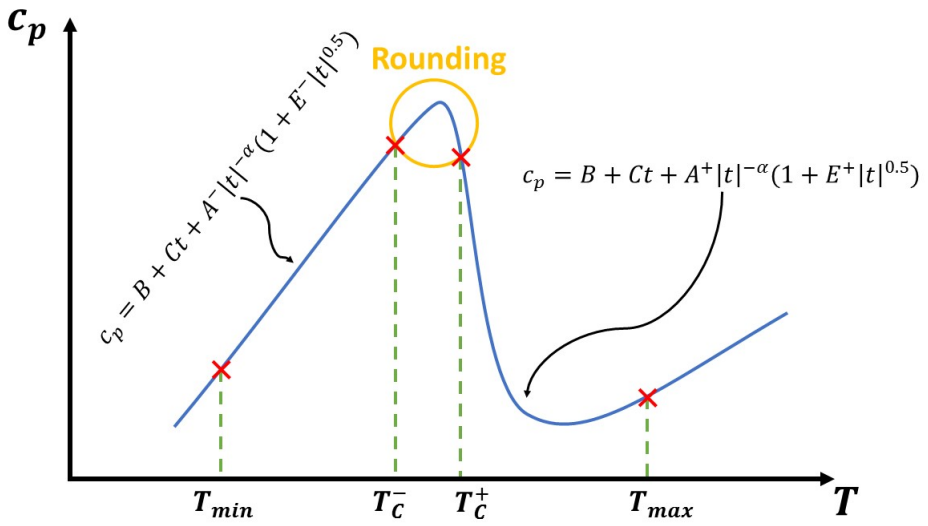


Figure 3.4: Schematic representation of the specific heat fitting regions: From $T_{\min}$ to T_C^- and from T_C^+ to $T_{\max}$.

The experimental data at both branches is simultaneously fitted using the Lavenberg-Marquardt method with a non-linear least square routine. The first fitting step is to adequately choose the fitting range close to the phase transition while avoiding the rounding in the region between T_C^- and T_C^+, which are the highest fitting limit for the lower temperature branch and the lowest limit for the higher temperature one respectively (see Fig. 3.4). The first fitting is done fixing the value of the critical temperature and neglecting the correction to scaling term ($E^\pm = 0$), which should be small in any case. From this first step a set of adjusted initial parameters is obtained. The following step consists on increasing the number of experimental points considered in the fitting. This is done in small steps, first increasing $T_{\max}$ while keeping $T_{\min}$ fixed, and then the other way around; decreasing $T_{\min}$ while keeping $T_{\max}$ fixed (these points are represented in Fig. 3.4). After this step finishes, and the fitting converges, the correction to scaling term is introduced and the process is repeated improving the fitting. The final fitting is performed by allowing the critical temperature to be a free parameter but with the same value for both branches.

A special mention must be done in the particular case in which the Mean Field model is of application, where $\alpha = 0$. In this case the equation (3.26) takes an asymptotical logarithmic form for the region just above the transition, $T > T_C$ (paramagnetic phase) [225, 226]:

$$c_p = A \ln t + B + Ct\,, \tag{3.36}$$

while in the region just below the critical temperature ($T < T_C$) c_p is described by a Landau classical formulation [225, 226]:

$$c_p = A_1 \frac{T}{\sqrt{1 - 4A_2(T - T_C)}} + B' + C'(T - T_C)\,. \tag{3.37}$$

Along the whole fitting process the root mean square values and the devi-

ation plots, which represent the difference between the experimental data and the fitted values as a function of the reduced temperature (t), are constantly checked to evaluate the quality of the fitting [19]. This strict procedure assures very good quality fittings as will be observed in the results.

3.4 Critical behavior of magnetic properties

Unlike thermal critical exponents, the values of magnetic critical exponents are quite similar for different universality classes (see Table 3.1 in page 64), this usually makes it harder to discriminate among models. However, since several critical exponents can be retrieved from simple magnetic measurements, with the correct analysis, robust results can be obtained.

Our magnetic measurements are performed in a Vibrating Sample Magnetometer (VSM) by Cryogenic Limited. The measuring procedure is standard and magnetization isotherms as a function of the magnetic field are obtained from it. Since we are particularly interested in what happens around the second order phase transition, isotherms in a reasonable region around the critical temperature are measured at a smaller temperature interval, $\Delta T = 1$ K, so that we have more experimental points for our analysis.

Magnetic critical exponents (β, γ and δ) can be independently obtained from multiple techniques, which add reliability to the final results.

Arrott Plot and Modified Arrot Plot

The Arrott Plot (AP) method is a well established conventional way of studying magnetic phase transitions. This method is based on the series expansion of the free energy carried out by Landau for the Mean Field model. Considering the energy minimization at the equilibrium point of the Gibbs free energy, shown in Eq. (3.16), and rearranging the terms, the following expression can be obtained:

$$H/M = A + BM^2 \,, \tag{3.38}$$

where the constants have been renamed to simplify the notation and A and B are now temperature dependent parameters. Arrott Plot method consists on plotting M^2 vs H/M according to Eq. (3.38) in order to obtain a set of parallel lines around T_C [227]. However, since this plot originates from the Mean Field model, it does not generate straight lines whenever it is applied to materials belonging to other universality classes. This problem was solved by generalizing the AP to the so called Modified Arrott Plot (MAP), also known as Arrott-Noakes Plot [228]:

$$(H/M)^{1/\gamma} = A + BM^{1/\beta} \,. \tag{3.39}$$

Here β and γ are the critical exponents corresponding to spontaneous magnetization (Eq. (3.8)) and inverse of the initial susceptibility (Eq. (3.9)) respectively. It can now be easily seen that Eq. (3.38) is a particular case of Eq. (3.39)

when the critical exponents of the Mean Field model are used ($\beta_{MF} = 0.5$ and $\gamma_{MF} = 1.0$).

When magnetic data is plotted following the MAP with the critical exponents corresponding to the universality class to which the material belongs, the plot should yield parallel straight lines for high fields. Moreover, the critical isotherm ($T = T_C$) will exactly pass through the origin. Isotherms at $T < T_C$ will intersect the $M^{1/\beta}$ axis at positive values, while for isotherms above critical temperature the intercept with $M^{1/\beta}$ axis will occur at negative values. This has all been schematically represented in Fig. 3.5.

This method allows to obtain the critical exponents β and γ by testing different values of the parameters until the isotherms in the MAP are straight and parallel. On its own this process can be tedious; however, in Section 3.4.1 we will see that, combined with other methods, this process can be optimized and give very robust and reliable results.

Arrott Plots are also widely used to determine the order of phase transitions. It turns out that according to the *Banerjee criterion* a negative slope on the AP is indicative of a first order phase transition, while an always positive slope is characteristic of second order phase transitions [229].

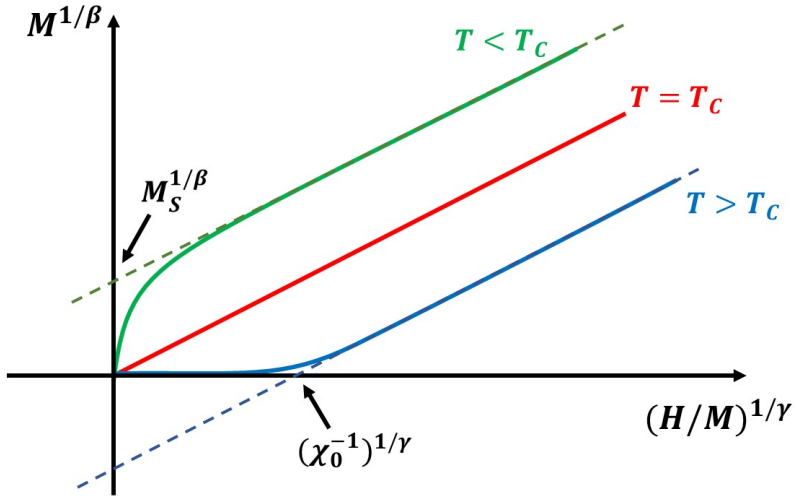


Figure 3.5: Modified Arrott Plot (MAP) with the correct values of β and γ for which the isotherms are linear and parallel at high enough magnetic fields. The critical isotherm crosses the origin and positive slopes indicate the second order nature of the transition. Extrapolations from the linear parts and their intersection points with vertical and horizontal axes give $(M_S)^{1/\beta}$ and $(\chi_0^{-1})^{1/\gamma}$ respectively.

Spontaneous magnetizations and initial susceptibility fitting

Spontaneous magnetization and initial susceptibility are both defined at zero applied field and show a singular behaviour around the critical temperature according to Eqs. (3.8) and (3.9) respectively. Although we do not directly measure these properties they can be directly obtained from the Modified Arrott Plot. A linear extrapolation of the isotherms below T_C from the high field values gives $(M_S)^{1/\beta}$ as an intercept on $M^{1/\beta}$ axis ($H = 0$) (see Fig. 3.5). On

the other hand, the intercept of the linear extrapolation for isotherms above critical temperature with $(H/M)^{1/\gamma}$ gives the value of $(\chi_0^{-1})^{1/\gamma}$, as it is shown in Fig. 3.5.

By repeating the previous process for all the isotherms around T_C the temperature evolution of spontaneous magnetization ($M_S(T)$) and the inverse of the initial susceptibility ($\chi_0^{-1}(T)$) can be obtained. As has been previously stated, the critical behavior of those parameters in the vicinity of a second order phase transition can be fitted to the following expressions [184, 230–232]:

$$M_S(T) = A'|t|^{\beta} \qquad (T < T_C)\,, \tag{3.40}$$

$$\chi_0^{-1}(T) = B'|t|^{\gamma} \qquad (T > T_C)\,, \tag{3.41}$$

where A' and B' are critical amplitudes. From the fitting of the experimental data to these expressions not only the critical exponents β and γ can be obtained, but also the critical temperature, T_C.

Kouvel Fisher method

The Kouvel Fisher method (KF) is another very well known technique in order to extract the values of the critical exponents β and γ, as well as the critical temperature. This method assesses that the behavior of $M_S(dM_S/dT)^{-1}$ and $\chi_0^{-1}(d\chi_0^{-1}/dT)^{-1}$ is linear when represented with respect to T, with slopes $1/\beta$ and $1/\gamma$ respectively [233]:

$$\frac{M_S(T)}{(dM_S(T)/dT)} = \frac{(T - T_C)}{\beta}\,, \tag{3.42}$$

$$\frac{\chi_0^{-1}(T)}{(d\chi_0^{-1}(T)/dT)} = \frac{(T - T_C)}{\gamma}\,. \tag{3.43}$$

Therefore, a simple linear fit to the KF plots gives a straightforward way of obtaining the critical exponents. T_C arises from the intercept of the straight fitted lines on the temperature axis.

Critical isotherm fitting

The behavior of magnetization with respect to the magnetic field at the critical isotherm ($T = T_C$) depends on the critical exponent δ, as shown by Eq. (3.10). The complete expression is given by [184, 230–232]:

$$M = D'H^{1/\delta} \qquad (T = T_C)\,, \tag{3.44}$$

with D' representing the critical amplitude. According to Eq. (3.44), a $\log(M)$ vs. $\log(H)$ plot yields a straight line where the slope is given by $1/\delta$. Therefore, δ can be easily obtained from the linear fit of the critical isotherm's log-log plot.

Magnetic equation of state

According to the scaling hypothesis, the magnetic equation of state, which relates magnetization (M), magnetic field (H) and temperature (T), in the neighbourhood of the critical point can be written as [184, 190, 232]:

$$M(H,t) = |t|^{\beta} f_{\pm}(H/|t|^{\beta+\gamma}) , \tag{3.45}$$

Here f_- and f_+ are regular analytic functions for $T < T_C$ and $T > T_C$ respectively. It can also be observed that Eq. (3.45) involves the critical exponents. The magnetic equation of state can be rewritten in a simplified way as a function of the renormalized magnetization, $m = M|t|^{-\beta}$, and renormalized field, $h = H|t|^{-(\beta+\gamma)}$:

$$m = f_{\pm}(h) . \tag{3.46}$$

This expression implies that if m is plotted as a function of h for the correct values of β and γ the isotherms will fall into two universal curves: one for isotherms below critical temperature and the other one for temperatures above it. The collapse of the curves into these two branches is taken as a strong evidence of correct critical exponents.

3.4.1 Fitting procedure of magnetic critical behavior

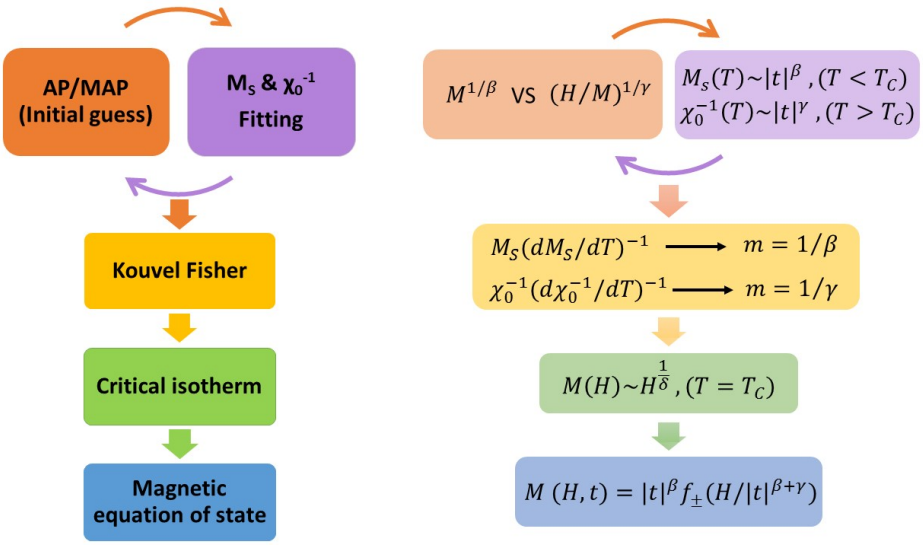


Figure 3.6: Summary of the fitting procedure for the correct acquisition of the magnetic critical exponent (left), and expressions used at each step (right).

The fitting procedure followed in order to obtain reliable magnetic critical exponents is summarized in Fig. 3.6. The first step is to start with an initial guess of the critical parameters to plot a MAP. The common procedure consists on drawing several MAPs with the critical exponents of the common universality classes. The initial parameters are chosen as those corresponding to the universality class for which the isotherms in the MAP are more parallel and

straighter. The next step is to extract the $M_S(T)$ and χ_0^{-1} values from the initial MAP in order to fit them according to Eqs. (3.40) and (3.41). This will give slightly different values of β and γ as well as for T_C. Then, an iterative process begin in which a new MAP is represented with the critical exponents values obtained from the $M_S(T)$ and χ_0^{-1} fits. The linearity and slopes are again checked and the whole process is repeated until β and γ values converge for both methods.

After this, in order to determine the critical exponents and temperature with more accuracy, the Kouvel Fisher method is applied. A linear fit of Eqs. (3.42) and (3.43) gives new values of β, γ and T_C. These values are compared with the previously obtained ones in order to check the agreement.

The following step consists on obtaining the critical exponent δ from the critical isotherm, Eq. (3.44). This value of δ is then compared to the one obtained from *Widom scaling law*, Eq. (3.24), which can be rewritten as:

$$\delta = 1 + \gamma/\beta \,, \tag{3.47}$$

where γ and β values are the ones obtained from the KF method and from the $M_S(T)$ and χ_0^{-1} fit.

Finally, the fulfilment of the magnetic equation of state Eq. (3.45), with the critical temperature and exponents β and γ previously obtained, is checked. A correct fulfilment, with the isotherms collapsing into two well distinguished branches, is considered as the most severe confirmation of a good scaling.

This systematic procedure, where the critical exponents obtained from different methods are compared, assures highly reliable values of the critical exponents. This method works really well for FM ordering states, but, unfortunately, it is not that good for AFM orderings, where the magnetization is low.

3.5 Scaling of magnetocaloric properties

Since magnetocaloric properties are deduced from magnetic ones, it is legit to search for scaling relations on magnetocaloric figures of merit. In fact, in this section we will see that those relations between magnetocaloric magnitudes and critical exponents exist, and their utility will be discussed.

In 1984, Oesterreicher and Parker proposed the first scaling relation for a magnetocaloric property. They established that, in the case of a second order phase transition described by the Mean Field model, the peak value of the magnetic entropy change varies with the magnetic field change according to [234]:

$$|\Delta S_M^{pk}| \propto H^{2/3} \,, \tag{3.48}$$

However, it has been experimentally seen that the scaling exponent of 2/3 is not useful to describe any other model apart from the Mean Field one. In 2006 Franco et al. generalized the previous scaling law and showed that the magnetic field dependence of the MCE in second order phase transition could be expressed as [235]:

$$\Delta S_M(T) \propto H^{n(T)} . \tag{3.49}$$

Here, the exponent $n(T)$ is temperature dependent. Furthermore, the behavior of $n(T)$ at temperatures well below and well above T_C is common for all materials. The *Curie-Weiss law* imposes the value of n to be $n = 2$ at $T >> T_C$, on the other hand, n usually tends to 1 for $T << T_C$ [235–238]; however high magnetic fields and models departing a lot from Mean Field may decrease the $n = 1$ value at low temperatures [237, 238], while the presence of other phases in the material may increase its value [239]. In spite of that, the most relevant value of n is given at $T = T_C$, i.e, at the peak of the magnetic entropy change, where the minimum value of n is located. As shown in Ref. [235], $|\Delta S_M^{pk}|$ scales with the magnetic field according to:

$$|\Delta S_M^{pk}| \propto H^{n(T_C)} , \tag{3.50}$$

where $n(T_C)$ is related to the magnetic critical exponents:

$$n(T_C) = 1 + \frac{\beta - 1}{\beta + \gamma} , \tag{3.51}$$

which using Eq. (3.24) can also be expressed as:

$$n(T_C) = 1 + \frac{1}{\delta}\left(1 - \frac{1}{\beta}\right). \tag{3.52}$$

Therefore, the evolution of the maximum value of the magnetic entropy change when a magnetic field is applied depends on the universality class to which the material belongs. It can be seen that using the critical exponents corresponding to the Mean Field model ($\beta = 0.5$, $\gamma = 1.0$ and $\delta = 3.0$), the $n(T_C) = 2/3$ value from Eq. (3.48) is recovered.

It has also been proven that both definitions of the refrigerant capacity; RC_{FWHM} and RC_{Area}, depend on the magnetic field as [236, 240]:

$$RC_{FWHM} \propto H^{1+1/\delta} , \tag{3.53}$$

$$RC_{\text{Area}} \propto H^{1+1/\delta} . \tag{3.54}$$

We should keep in mind that these relations are only valid for second order phase transitions.

Since only two of the three magnetic critical exponents are independent, from the fitting of Eqs. (3.50) and (3.53) or (3.54) one can in principle obtain the critical exponents from $n(T_C)$ and δ [241]:

$$\beta = \frac{1}{\delta(1-n)+1} , \tag{3.55}$$

$$\gamma = \frac{\delta - 1}{\delta(1-n)+1} . \tag{3.56}$$

The values obtained from this method are usually less reliable than the ones obtained from magnetic properties; however, when Eqs. (3.50), (3.53) and (3.54) are plotted in a log-log scale, the experimental data must lie on a straight

line for the correct values of the critical exponents. This fulfilment of the scaling relations for the magnetocaloric properties is used as an additional test for the critical values obtained from the critical behavior analysis performed over the magnetic properties.

The fact that the main magnetocaloric properties are related to magnetic critical exponents through Eqs. (3.50), (3.53) and (3.54), allows the extrapolation of $|\Delta S_M^{pk}|$ and RC to magnetic field values which otherwise may not be experimentally reachable. Therefore, the knowledge of the correct critical exponents can enhance the limits of experimental set-ups and permit the study of the magnetocaloric performance at in other ways unreachable experimental conditions.

Another relevant concept is the so called **universal curve** for the field dependence of ΔS_M in materials with a second order phase transition. This curve was first phenomenologically described in 2006 [235], and theoretically grounded few years later, in 2008 [240]. The universal curve is constructed with the ΔS_M data as a function of temperature for several magnetic fields in two steps [240]:

- **Normalization:** The first step consists on normalizing each isofield with respect to their corresponding maximum value ΔS_M^{pk}, in order to obtain $\Delta S_M(T)/\Delta S_M^{pk}$ for the different fields.
- **Temperature rescaling:** The second step is to rescale the temperature axis according to:

$$\theta_1 = \frac{T - T_C}{T_r - T_C}\,, \tag{3.57}$$

where T_r is selected for each isofield as a reference temperature above T_C corresponding to a certain fraction, η, of ΔS_M^{pk}:

$$\Delta S_M(T_r) = \eta \Delta S_M^{pk}\,. \tag{3.58}$$

This fraction η can be chosen to take any value between 0 and 1, but it is always better to consider an intermediate value. According to this rescaling T_r will always lie on $\theta_1 = 1$.

This universal curve is not a curious artefact, but rather a very useful tool related to the universal nature of second order phase transitions. Universal curves can also be used in order to discriminate the order of the phase transition. In the case of second order phase transitions the experimental data collapse into the universal curve, while in the case of first order phase transition, even after normalizing and rescaling, the curves do not collapse [242, 243]. Therefore, the construction of universal curves gives an easy alternative way of checking the order of the transition.

In fact, since the existence of universal curves is linked to the universality of the SOMPTs, $\Delta S_M(T)/\Delta S_M^{pk}$ curves as a function of the rescaled temperature of different materials also collapse into a single universal curve as long as

they belong to the same universality class [236, 243–246]. This allows to check whether two different materials belong or not to the same universality model without any prior information about their critical exponents.

In addition, the reference temperature, T_r, defined in Eq. (3.58) is also related to the magnetic field through a scaling relation involving the critical exponents [240, 247]:

$$T_r \propto H^{1/(\beta+\gamma)} . \tag{3.59}$$

This directly takes us to one of the main applications of the universal curve. Considering Eq. (3.59) and using the correct critical exponents β and γ (which we have seen how to obtain from magnetic measurements), we can obtain T_r values for magnetic fields which where experimentally not reachable. We have already seen that this can also be done for ΔS_M^{pk} by using the scaling relation in Eq. (3.50). Since the universal curves collapse is reached only by using the corresponding reference temperature and ΔS_M^{pk} value for a given magnetic field, and since we can get those values for any H from Eqs. (3.59) and (3.50), it is possible to obtain a whole new $\Delta S_M(T)$ curve for missing magnetic fields by correctly undoing the temperature rescaling and normalization. Moreover, due to the temperature axis rescaling, larger field isofields are constrained to a narrower θ_1 range than lower field ones; this fact can be used in higher field curves to extrapolate data to temperatures not measured [236].

The collapse of the curves with a single reference temperature is usually very good, collapsing not only the nearest points to the critical temperature but also considerably far ones. However, the existence of minority magnetic phases or a high demagnetizing field avoids a good collapse, specially at temperatures below T_C. The former case gives lower $\Delta S_M(T)/\Delta S_M^{pk}$ values for higher magnetic fields [248], while the latter has the opposite effect [249]. Fortunately, this problem can be solved by rescaling the temperature axis with two reference temperatures instead of using a single one like in Eq. (3.57) [66, 82, 235, 236, 241, 243, 246, 248–250]:

$$\theta_2 = \begin{cases} -(T - T_C)/(T_{r1} - T_C) , & T \leqslant T_C \\ (T - T_C)/(T_{r2} - T_C) , & T > T_C \end{cases} , \tag{3.60}$$

where T_{r1} and T_{r2} are defined similarly to T_r in Eq. (3.58) for $T \leqslant T_C$ and $T > T_C$ respectively. With this rescaling T_{r1} lies on $\theta_2 = -1$ and T_{r2} on $\theta_2 = 1$. When two reference temperatures are used to rescale the temperature axis, the overlapping is even greater.

It must be mentioned that the rescaling of the temperature axis is needed to construct the universal curve only in the direct magnetocaloric effect (DMCE). In the case of a second order IMCE, in an AFM-PM phase transition for example, it has been shown that there is no need to rescale the temperature, the normalization of ΔS_M to its peak value being enough to construct the universal curve in this case [251–253]. This behavior is attributed to the fact that IMCE shows a constant value (temperature and field independent) of the exponent n ($n \sim 2$) [253].

Finally, lets discuss some properties about the parameter n which relates the magnetic entropy change with the magnetic field. According to Eq. (3.49) $n(T)$ can be obtained from:

$$n(T,H) = \frac{d\ln|\Delta S_M(T,H)|}{d\ln H}\,. \tag{3.61}$$

We have already seen that $n(T)$ generally tends to 1 for temperatures well below T_C while it is 2 for temperatures much higher than the transition temperature. The minimum value is reached at $T = T_C$ where n is related to the magnetic critical exponents according to Eqs. (3.51) and (3.52). However, one should be careful when extracting critical exponents from n following Eq. (3.61), since it depends on the magnetic field and it usually has lower values for higher magnetic fields [237, 254]. Furthermore, the peak of the magnetic entropy change in second order phase transitions can also be slightly displaced in temperature under the application of magnetic fields, which makes it harder to extract a correct $n(T_C)$ value [255–257]. Apart from these considerations, $n(T)$ still hides other interesting properties. Similarly to the universal curve for ΔS_M, $n(T,H)$ curves also collapse for second order phase transitions when plotted against the same rescaled temperature as the one used for the universal curves [236, 238, 240, 248].

Nevertheless, the most relevant fact about $n(T,H)$ is that its evolution is sensitive to the order of the transition. A first order phase transition can be identified by a big shoot on the n value well above $n = 2$ [258–260], which is not present on second order phase transitions. Furthermore, it has also been observed that at the critical temperature the value of n is lower than 0.4 ($n(T_C) < 0.4$) in the case of first order phase transitions, while $n(T_C) > 0.4$ in second order phase transitions [161, 260, 261]. This adds the representation of $n(T)$ to the list of methods that can be used to determine the order of a phase transition.

3.6 Critical exponents table

This chapter is closed with Table 3.2, where the values of the critical exponents, critical ratio and n (which has been calculated using Eq. (3.52)) for several universality classes are collected in order to be used as reference for a later discussion of the experimental results.

In each case, several references containing different methods from where the critical exponents are obtained are given for the interested reader. The differences among the methods used to calculate the critical exponents are small, and the values shown here are the most recent ones in literature. In the case of the 3D Heisenberg universality class it is worth mentioning that although $\alpha = -0.134$ and $\gamma = 1.396$ are the most recently obtained values from numerical calculations [209], previous slightly different values of those parameters have been (and still are) widely used in literature [262]: $\alpha = -0.115$ and $\gamma = 1.336$.

Universality class	d	N	α	A^+/A^-	β	γ	δ	n	Ref.
Mean Field			0	-	0.5	1.00	3.00	0.6666	[185]
2D Ising	2	1	0	1	0.125	1.75	15.00	0.533	[185, 262]
3D Ising	3	1	0.11	0.536	0.3265	1.237	4.79	0.569	[185, 201, 206, 262, 263]
3D XY	3	2	-0.014	1.06	0.348	1.317	4.78	0.608	[185, 201, 208, 262, 263]
3D Heisenberg	3	3	-0.134	1.52	0.369	1.396	4.78	0.642	[185, 201, 209, 262, 263]
Chiral XY	3	2	0.34	0.36	0.253	1.13	5.47	0.460	[264]
Chiral Heisenberg	3	3	0.24	0.54	0.30	1.17	4.90	0.524	[264]
Tricritical Mean Field			0.5		0.25	1.00	5.00	0.400	[265]
2D Long range	2	1			0.298	1.393	5.67	0.585	[266]
3D Ising spin glass	3	1	-1.9		0.5	2.9	6.80	0.853	[267]

Table 3.2: Main universality classes for different magnetic systems. d dimension, N number of spin components, α and A^+/A^- are for specific heat, β for spontaneous magnetization, γ for initial susceptibility, δ for critical isotherm, and n for the peak value of the magnetic entropy change.

Part II
Experimental results

Once the theoretical fundamentals are properly grounded, it is now time to present the experimental results obtained from our work. Though the previous part was general and valid for every magnetic compound, our studies have been focused on rare-earth containing intermetallic families. Their magnetic, thermal and magnetocaloric properties make them unique. These families cover a wide range of possible working temperatures, from almost 0 to 400 K. The special particularities and interest of each family will be discussed and the great amount of phenomena in these compounds will be shown, ending with some general conclusions and future work perspectives. The complexity and variety of the rare-earth containing intermetallics is what makes them so interesting from the point of view of their technological application, but, also, from the point of view of a more basic physical understanding of their nature.

4 | RTX intermetallics

"Life need not be easy, provided only that it is not empty."

– Lise Meitner

In this chapter I am going to present our results concerning the critical behavior and magnetocaloric effect of several members of the promising RTX (R = rare-earth, T = transition metal, X = *p*-block element) intermetallic family. In this work we can distinguish 3 *"sub-families"* according to the rare-earth they are based on: Pr, Nd, or Gd. In the three cases T = Sc, except in one member of the Gd-based compounds where Ti is also included. In the case of the *p*-block element (X), Si, Ge and an admixture of them, have been used. The main difference among these *"sub-families"* is that Pr-based compounds order antiferromagnetically below their critical temperature, while Nd and Gd compounds order ferromagnetically. This, together with the peculiar shape of the thermal diffusivity in Pr containing samples, prevented us from performing a complete study over the latter. Fortunately, the study could be successfully completed for the Nd- and Gd-based materials, obtaining very interesting results.

The following materials will be studied in this chapter:

- **GdScSi**
- **GdScGe**
- **GdSc($Si_{0.5}Ge_{0.5}$)**
- **Gd($Sc_{0.5}Ti_{0.5}$)Ge**
- **NdScSi**
- **NdScGe**
- **PrScSi**
- **PrScGe**
- **PrSc($Si_{0.5}Ge_{0.5}$)**

4.1 Introduction

Ternary intermetallic systems RTX (R = rare-earth, T = transition metal, X = *p*-block element) have been known for several years, but it was not until few years ago that they attracted again the attention of researchers. This family is being extensively studied as promising magnetic systems for technological applications, specially due to the high temperature of their magnetic transitions. This makes them suitable candidates to look into the possibility of presenting strong magnetocaloric effects. Furthermore, these compounds show interesting magnetic and pressure related properties, and their spin ordering temperatures cover a wide range of temperatures, from liquid He temperatures to well above room temperature. In order to study their viability as magnetic refrigerators, a knowledge as broad as possible of their properties (crystallographic as well as magnetic) is desirable. In particular, some extensive studies have already been undertaken on RScSi, RScGe, RTiSi, RTiGe (R = Ce, Pr, Nd, Sm, Gd, Tb, Dy, Ho, Er, Y) [268–279], and a thorough review on this family can be found in Ref. [78], where it can be seen that there is still a lot of research to be done in order to fully understand their poperties. We have focused our attention on two important aspects, the magnetocaloric effect and the critical behavior of the magnetic transitions, which has been seldom studied up to now. The study of critical behavior gives valuable information about the range and dimensionality of the magnetic exchange interactions, together with the role that other mechanisms can play if the critical parameters obtained do not match a particular universality class. The knowledge of the variations of the universality class (which is tantamount to the physical mechanisms involved) with R, with T or with X (even with admixtures of T, X) will have to be taken into account when designing compositions in search of a strong magnetocaloric material.

Our work on RTX family has been oriented to R(Sc,Ti)(Si,Ge) (with R = Nd, Pr, Gd) compounds, all of which crystallize in CeScSi-type structure (*I4/mmm* space group). We will see later that, although according to the literature and our measurements all of our compounds have second order magnetic phase transitions [76, 269, 271, 272, 274, 278], the critical behavior could not be studied in the case of Pr-based compounds (PrScSi, PrScGe and PrSc($Si_{0.5}Ge_{0.5}$)), due to the shape of their transition in thermal measurements and the AFM ordering below their Neel temperature, therefore, only their thermal diffusivity (D) evolution as a function of temperature could be studied. The critical behavior of Nd containing samples (NdScSi and NdScGe) had been already studied by our group [225], though their MCE has been obtained for the first time in this work. Therefore, we will be focusing our attention on the critical behavior of Gd members of this family: GdScSi, GdScGe, GdSc($Si_{0.5}Ge_{0.5}$) and Gd($Sc_{0.5}Ti_{0.5}$)Ge. It turns out that the latter have the highest Curie temperature, slightly above room temperature, which make them good candidates for technological applications. We are presenting a complete study of the critical exponents (α, β, γ and δ) for these compounds, in order to acknowledge whether, and how, a change in either the *p*-block element or the transition metal can alter their critical behavior. These results will also be compared to

the ones obtained for Nd-based compounds.

On the other hand we will also be interested in evaluating the magnetocaloric variables ΔS_M and RC for both the Nd and Gd containing samples, taking well into account possible misleading effects (such as demagnetization or the existence of other phases), and establishing their potential as magnetocaloric materials. We will then extend the study to the evolution of the magnetocaloric variables with the applied magnetic field in order to obtain a complete information and, finally, check whether they follow the scaling relations with the critical parameters obtained in the previous critical behavior analysis.

4.2 Preparation of samples and experimental techniques

All the samples we have studied within the ternary and pseudo-ternary RTX compounds were prepared in form of polycrystalline alloys by our collaborators P. Manfrinetti and A. Provino from the University of Genova in Italy.

Concerning the Gd(Sc,Ti)(Si,Ge) family, the starting materials were high purity elements supplied by commercial vendors: 99.9 wt.% for both Gd and Sc (R metals from Koch-Light, England), 99.99 + wt.% Ti (from Aldrich Chem. USA), and 99.9999 wt.% for Si and Ge (from Alfa-Aesar, Germany). The alloys were prepared by arc melting stoichiometric amounts of the elements under a pure argon atmosphere on a watercooled copper hearth; after a first melting and reaction of elements, the buttons were re-melted four times (turning them upside-down each time) to ensure homogenization (total weight of about 2 g; weight loss lower than 0.2 wt.%). The final alloys were placed inside an outgassed Ta tube, sealed under vacuum in silica tubes and annealed at 1000 °C for 10 days. Phase analysis, to check for quality of the samples, was performed by X-ray powder diffraction using a Guinier camera [Cu Kα1 radiation; Si as internal standard (a=5.4308(1) Å] and optical microscopy. Indexing of the powder diffraction patterns was carried out by comparison with the pattern calculated by the help of the Lazy-Pulverix program [280]; then, the lattice parameters calculated by least-squares fit. The alloys, prepared as above, resulted to be practically single phase: in the two samples containing Si only a 2–3 vol% of $Gd_{5-x}Sc_xSi_3$ (Mn_5Si_3-type) was present as secondary phase, while in the other two containing Ge the homologous phase $Gd_{5-x}Sc_xGe_3$ [281] was not even detectable (from Guinier pattern and as grain separation in the micrographic specimens).

The NdSc(Si,Ge) samples were also prepared by arc-melting the constituents under a pure TiZr-gettered Ar atmosphere on a water-cooled Cu-hearth. Samples were re-melted two times to ensure homogeneity. High purity metals were used: 99.9 wt% purity Nd, 99.95 wt% purity Sc and 99.999 wt% purity Ge. Total weight of the buttons was about 3.0 g, with negligible weight loss (less than 0.1 wt%). The small ingots were wrapped in an outgassed Ta foil, sealed under vacuum in a quartz tube and annealed at 900 °C for 9 days. They were slowly cooled down to 680 °C, inside the furnace, and then air cooled. As in the previous case, phase analysis to check for the quality of

the samples was performed by optical microscopy and X-ray powder diffraction. Powder patterns were also recorded by Guinier method, and the alloys prepared were single phase, with less than 1–2% of secondary phase barely evident as grain separation. Lattice parameters, calculated by least-squares fit, are a = 4.2921(2) Å and c = 15.715(2) Å for NdScSi and a = 4.3166(3) Å and c = 15.835(2) Å for NdScGe, well in agreement with the values given in Ref. [271]. Pr-based samples were synthesized in a similar procedure to the previous ones.

Magnetization (M) measurements have been carried out in a VSM (Vibrating Sample Magnetometer) by Cryogenic Limited under external applied magnetic fields H_a ranging from 0 to 8 T for the critical behaviour study and from 0 to 2 T for the magnetocaloric effect study. The temperature region covered has been 30-300 K for Nd-based compounds and 100-400 K for the samples containing Gd. In order to completely cover the critical region, isotherms have been collected over a range of about 30 K around T_C ($\Delta T = 1K$). As has been emphasised through Chapters 2 and 3, the applied magnetic field H_a has to be corrected for demagnetization effects in order to correctly evaluate both the critical behaviour and the magnetocaloric effect. The correct internal field is calculated using the relation $H_i = H_a - N_D M$, where M is the measured magnetization and N_D the demagnetization factor. This demagnetization factor has been obtained using the method described in Chapter 2 Section 2.1.3 and given in Refs. [47–49]; measuring the zero-field *ac* susceptibility, extracting the maximum value of this magnitude (often referred as the Hopkinson/principal maximum) and using the relation $N_D = 1/\chi_{ac}^{'pk}$. This magnetic susceptibility was measured with AC Measurement System Option in PPMS (Physical Properties Measurement System) by Quantum Design. The so obtained H_i has been the one used for the scaling analysis. For simplicity in what follows we will refer to H_i as simply H.

A high resolution *ac* photopyroelectric calorimeter in the back detection configuration as described in Chapter 1 Section 1.4.4 has been used for the thermal measurements. Following the process described in Sections 1.4.2 and 1.4.3 the thermal diffusivity for a wide temperature range (including the transition region) was obtain for all of the samples, and specific heat as a function of temperature in the region around the Curie temperature was also retrieved for the four Gd containing samples.

4.3 Experimental results and discussion

This section will be divided in three subsections; the first one devoted to the characterization and discussion of thermal diffusivity evolution, a second section on the analysis of the thermal and magnetic critical behavior in Gd-based materials, together with a thorough discussion of the obtained results, and a third subsection focused on a complete magnetocaloric effect study for Gd-based and Nd-based samples.

4.3.1 Thermal diffusivity in RTX family

The thermal diffusivity as a function of temperature for the Nd and Pr-based samples is represented in Fig. 4.1, from low temperatures up to room temperature. Here we can already observe some general features of intermetallic materials. First of all the PM to FM phase transition in Nd containing samples and the PM to AFM transition in Pr containing samples are marked as a dip which alters the monotonic decrease from high temperatures to lower ones, which is a characteristic of intermetallic materials when there is no phase transition [282–284]. This behavior is due to the added contribution of the electronic and phononic part of the thermal diffusivity; at high temperatures, the electronic contribution dominates and it decreases as temperature decreases, whereas at lower temperatures (in the case of this family once the transition takes place) the phonon contribution starts to dominate, making the thermal diffusivity increase with decreasing temperature. This increase is slow at first, but, at even lower temperatures, the phonon mean free path is severely increased and the thermal diffusivity background quickly increases. Generally, the dips indicating the transition are superimposed at some point of this evolution. The dips can appear when the diffusivity is still decreasing with decreasing temperature, when we have the opposite effect, or even trigger the change in the thermal diffusivity trend, as appears to be the case in RTX family.

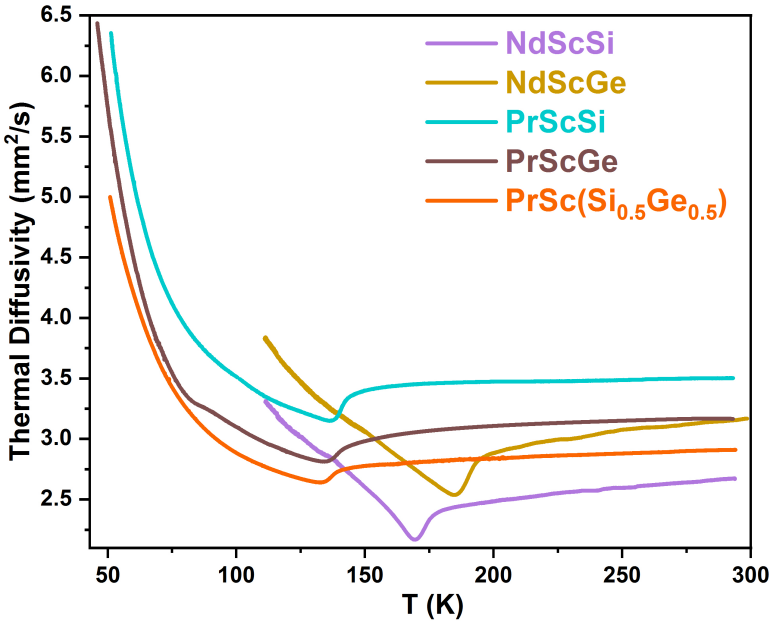


Figure 4.1: Thermal diffusivity as a function of temperature for Nd-based and Pr-based materials.

These kind of dips in thermal diffusivity can signal different types of phase transitions. Dips in ferromagnetic to paramagnetic transitions are common in many other magnetic materials, such as manganites [285,286] but with the difference that in the latter, as thermal insulators, the thermal diffusivity monotonically increases while temperature is reduced in the whole range. These

dips can also be found in antiferromagnetic to paramagnetic phase transitions, as has been seen in other materials [16, 17, 22].

In the Nd containing samples the dip is displaced to lower temperatures when Ge is substituted by Si, from $T_C \approx 189$ K in NdScGe to $T_C \approx 171$ K in NdScSi, in good agreement with those found in literature [271, 272]. The substitution of Nd by Pr further decreases the transition temperature and transforms the FM state into an AFM one. The effect of Si or Ge amount doesn't affect significantly the T_N of Pr compounds (≈ 139 K for PrScSi, ≈ 137 K for PrScGe and ≈ 136 K for PrSc($Si_{0.5}Ge_{0.5}$)). However, PrScGe shows multiple spin reorientations: apart from the previously mentioned one at ≈ 137 K it has another antiferromagnetic transition at ≈ 88 K and a ferromagnetic transition at ≈ 80 K [271]. These lower temperature spin reorientations can be seen in Fig. 4.1 as inflections around 88 K and 81 K in the thermal diffusivity corresponding to PrScGe.

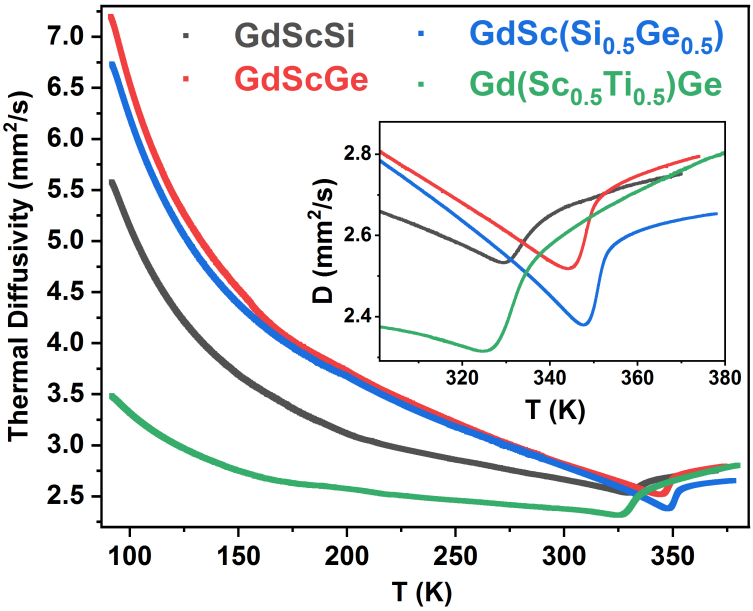


Figure 4.2: Thermal diffusivity as a function of temperature for Gd-based materials. Inset shows the transition region in detail.

Fig. 4.2 shows the temperature evolution of thermal diffusivity for the Gd-based family, with an inset where the FM-PM transition region is shown in greater detail. It is worth mentioning that, even though the measurements were performed both increasing and decreasing the temperature at very slow temperature rates (few mK/min), no thermal hysteresis was observe around the phase transition for any of the samples, which agrees with their second order nature reported in literature. The behavior of thermal diffusivity is completely equivalent to Nd or Pr-based materials, the only difference is that now the T_C is increased above room temperature, in a range between 325 and 343 K. Starting from GdScGe, which has the higher values of thermal diffusivity, the substitution of Ge by 50% Si reduces somewhat the thermal diffusivity and slightly shifts the critical temperature up while the shape of the dip remains

similar. The total substitution of Ge by Si, on the other hand, shifts down the critical temperature about 15 K and makes the dip shallower, with a thermal diffusivity in general smaller than the one for GdScGe. Finally, the substitution of 50% Sc by Ti does introduce a big change in the general shape of the curve, reducing even more the thermal diffusivity values while shifting down the Curie temperature about 15 K.

In Section 2.2.6 we already pointed out the importance of good thermal diffusivity values in order to enhance the heat flux on magnetic refrigerators, thus increasing their efficiency and allowing a high frequency refrigeration cycle. The samples analysed here posses D values between 2.3 and 3.7 mm^2/s in their applicability regions (close to the phase transitions), and these values drastically increase at lower temperatures. Thermall diffusivity has been rarely studied in magnetocaloric materials, but the values here obtained are comparable to the ones given by good magnetocaloric materials in literature, such as $Gd_5Si_2Ge_2$, $La(Fe_{0.88}Si_{0.12})_{13}$ and one order of magnitude higher than the case of MnAs [180] or $Ni_{50}Mn_{35}Al_2Sn_{13}$ [287].

4.3.2 Critical behavior in RTX family

Following with the thermal analysis, I will now present the critical behavior analysis of the specific heat in Gd(Sc,Ti)(Si,Ge) family. As mentioned before, the analogous critical behavior study of $1/D$ for NdSc(Si,Ge) samples had already been performed by our group in Ref. [225]. The thermal critical behavior of Pr-based compounds could not be studied due to the shape of the dips where the transition takes place. If we observe these dips in Fig. 4.1 we can see that the thermal diffusivity curve just below the transition temperature is convex instead of concave, as it should be in order to fit the data to the theoretical expressions.

The value of the critical exponent α has been evaluated through high resolution measurements of the specific heat in the near vicinity of the Curie temperature using an *ac* photopyroelectric calorimeter following the procedure explained in Section 3.3.1. Therefore, experimental data in the vicinity of the phase transition is fitted to the well known equation:

$$c_p = B + Ct + A^{\pm}|t|^{-\alpha}(1 + E^{\pm}|t|^{0.5}) , \tag{4.1}$$

where $t = (T - T_C)/T_C$ is the reduced temperature and α, $A^{\pm}$, B, C and $E^{\pm}$ are adjustable parameters. Superscripts + and - stand for $T > T_C$ and $T < T_C$ respectively. Expression (4.1) is the sum of the background contribution to the specific heat (linear term), and the anomalous contribution rising from the phase transition itself. Both branches of the specific heat, above and below the T_C, are simultaneously fitted following a non-linear least square routine using a *Levenberg-Marquardt* method.

Figs. 4.3 and 4.4 show the experimental specific heat curves in the near vicinity of the critical temperature as a function of the reduced temperature, together with the fittings, for the four compositions. In each case, a deviation plot is also included, showing the difference between the experimental and fitted curves, as a percentage. In all of the cases the deviation is within ±1%,

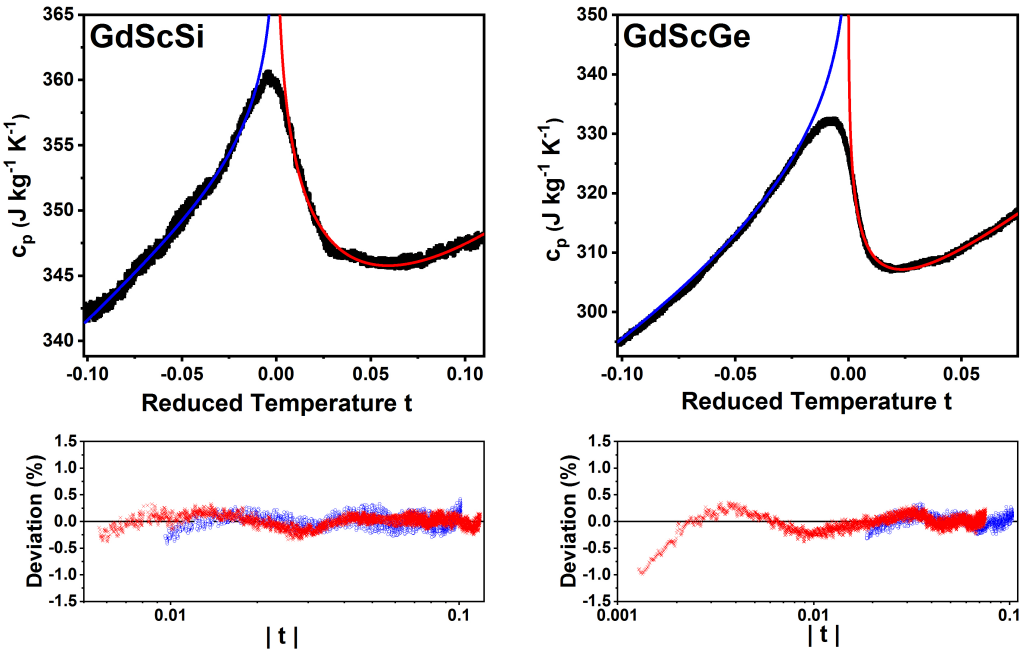


Figure 4.3: Experimental (dots) and fitted curves (continuous lines) of the specific heat as a function of the reduced temperature for GdScSi (left), GdScGe (right) in the near vicinity of T_C (top); deviation plots for the fittings (bottom). Open circles are for $T < T_C$, crosses for $T > T_C$.

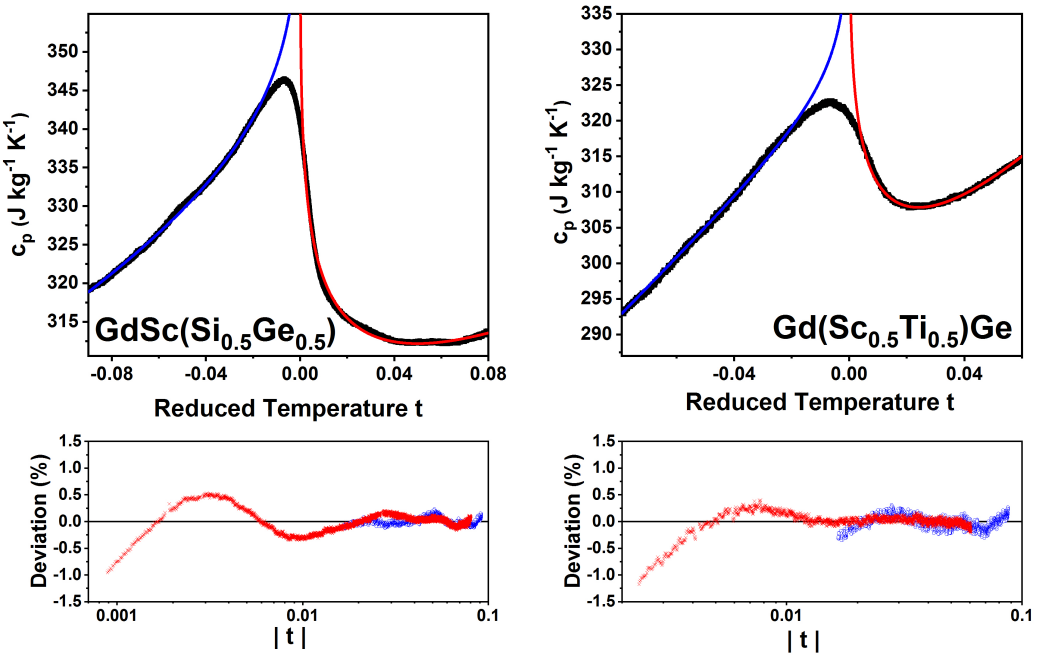


Figure 4.4: Experimental (dots) and fitted curves (continuous lines) of the specific heat as a function of the reduced temperature for GdSc(Si$_{0.5}$Ge$_{0.5}$) (left), Gd(Sc$_{0.5}$Ti$_{0.5}$)Ge (right) in the near vicinity of T_C (top); deviation plots for the fittings (bottom). Open circles are for $T < T_C$, crosses for $T > T_C$.

and, except in the closest region to T_C, i.e., close to $|t| \approx 0$, the deviation remains within ±0.5%. This shows that the fitting is very good in all cases and the obtained parameters α and A^+/A^- have been included in Table 4.1 page 95. The sign and value of α (-0.120 ± 0.020 for GdScSi, -0.134 ± 0.005 for GdScGe, -0.135 ± 0.007 for GdSc($Si_{0.5}Ge_{0.5}$), and -0.122 ± 0.010 for Gd($Sc_{0.5}Ti_{0.5}$)Ge) agrees in all cases very well with the 3D Heisenberg model (for which the theoretical value is -0.134, see Table 3.2 in page 77), while the ratio A^+/A^- (1.52 for the 3D Heisenberg model) agrees well for GdScGe (1.63 ± 0.07) and GdSc($Si_{0.5}Ge_{0.5}$) (1.56 ± 0.07) but shows some deviation in the case of GdScSi (1.02 ± 0.13), and Gd($Sc_{0.5}Ti_{0.5}$)Ge (1.16 ± 0.08).

Once α is obtained from thermal measurements, the following step is to complete the study with the acquisition of the critical exponents associated to the magnetic properties: β, γ and δ. As has already been mentioned, these exponents were obtained for Gd(Sc,Ti)(Si,Ge) family, since Pr containing samples are AFM and the study had already been performed for Nd-based samples [225]. The magnetization per unit mass as a function of temperature for the four samples containing Gd can be seen in Fig. 4.5. All of them are very similar in shape, with the non-codoped samples GdScSi and GdScGe giving the highest values.

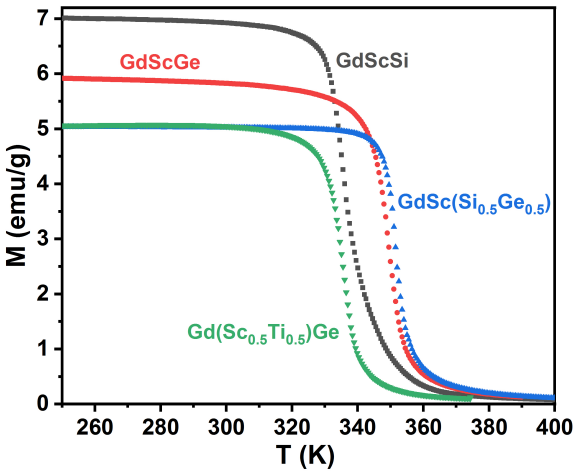


Figure 4.5: Magnetization as a function of temperature for GdScSi, GdScGe, GdSc($Si_{0.5}Ge_{0.5}$), and Gd($Sc_{0.5}Ti_{0.5}$)Ge using a magnetic field of 100 Oe.

The usual procedure in order to obtain the magnetic critical exponents is described in detail in Section 3.4. The first step is to represent the standard Arrott Plot (M^2 as a function of H/M) for isotherms in an appropriate temperature range around the Curie temperature in each case (301-356 K for GdScSi, 316-375 K for GdScGe, 318-372 K for GdSc($Si_{0.5}Ge_{0.5}$) and 301-360 K for Gd($Sc_{0.5}Ti_{0.5}$)Ge). If long-range interactions were responsible for the ferromagnetic transition, there would be a linear behavior at high fields on that plot. Fig. 4.6 contains the experimental points obtained for the four samples, in which it is clearly seen that this is not the case for any case: the curves are not linear and all of them have a positive slope, the latter confirming the second order character of the transition after the Banerjee criterion [229], while the former discards a Mean Field behavior.

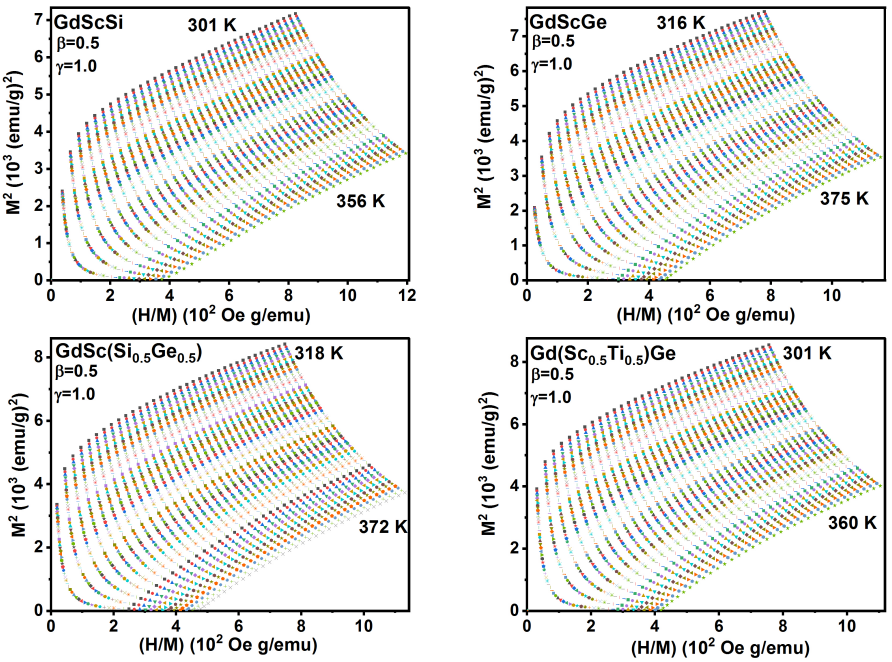


Figure 4.6: Arrot Plot of the isotherms collected around the corresponding T_C for each Gd-based compound.

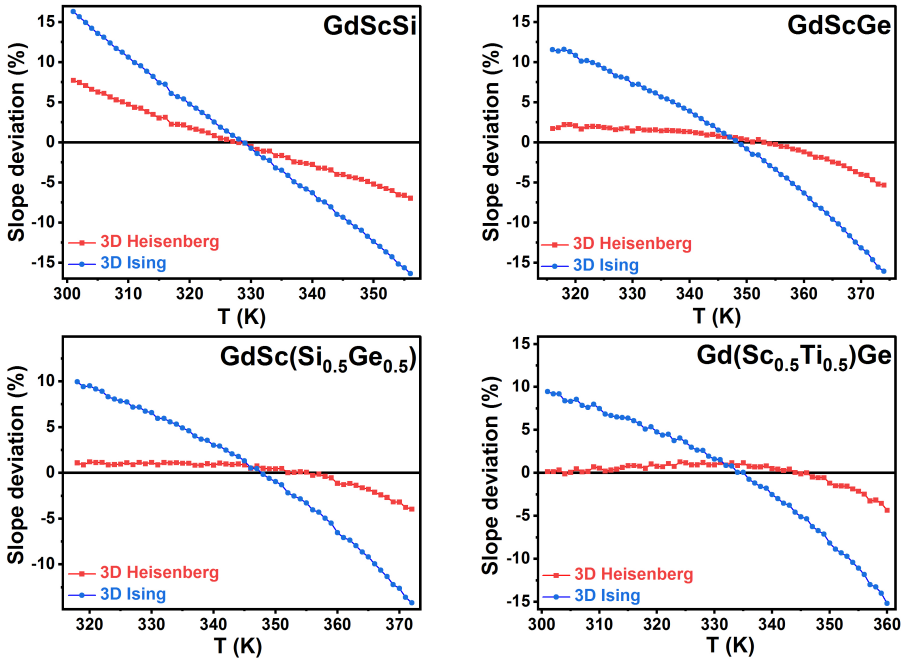


Figure 4.7: Slope deviations of the MAP for the 3D Heisenberg and 3D Ising models for the Gd-based compounds.

Our attention is then turned to the so-called Modified Arrott Plots (MAP) as the next step, representing $M^{1/\beta}$ versus $(H/M)^{1/\gamma}$ for certain relevant universality classes, such as 3D Heisenberg ($\beta = 0.369$, $\gamma = 1.396$) and 3D Ising ($\beta = 0.3265$, $\gamma = 1.237$). Linear fittings of the experimental points at high

fields have been performed with the result that in both cases straight lines are obtained but much more parallel among them for the Heisenberg case than for the Ising one. In order to quantify the parallelism and make a decision about the best one, we have calculated the deviation of the slopes from the mean value for the Heisenberg and Ising cases for the four samples: $\approx \pm 7\%$ against $\approx \pm 16\%$ for GdScSi, $\approx \pm 5\%$ against $\approx \pm 16\%$ for GdScGe, $\approx \pm 4\%$ against $\approx \pm 14\%$ for $GdSc(Si_{0.5}Ge_{0.5})$, $\approx \pm 4\%$ against $\approx \pm 15\%$ for $Gd(Sc_{0.5}Ti_{0.5})Ge$. Fig. 4.7 shows the slope deviation for both models, where it can be clearly seen than the Heisenberg class is a better starting point, specially for the Ge containing compounds. On the other hand, Fig. 4.8 shows the particular case of the MAP with the Heisenberg values for all the compounds, where it is clear that the fitting to straight lines is good and that they present a good parallelism. It can be seen that, in every case, the MAP built using the 3D Heisenberg critical exponents (Fig. 4.8) is much better that the AP represented in Fig. 4.6.

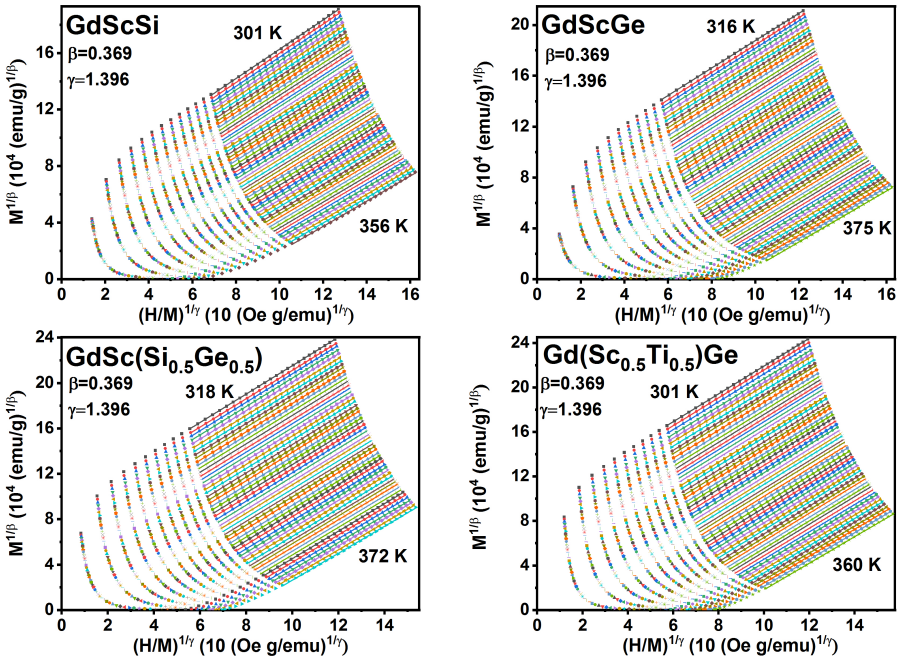


Figure 4.8: Modified Arrott Plot of the isotherms collected around T_C for Gd-based samples, with the Heisenberg trial exponents showing the parallelism of the linear fittings at high fields.

Thus, in the four cases, the Heisenberg critical exponents have been taken as the first trial to refine them using the well known iteration procedure presented in Section 3.4.1.

A linear extrapolation of the isotherms in Fig. 4.8 has been taken from the high field values to extract $(M_S)^{(1/\beta)}$ and $(\chi_0^{-1})^{1/\gamma}$ as an intercept on Y and X axes, respectively. The so obtained values of $M_S(T)$ and $\chi_0^{-1}(T)$ are then independently fitted to the following expressions:

$$M_S(T) \sim |t|^{\beta} \qquad (T < T_C)\,, \tag{4.2}$$

$$\chi_0^{-1}(T) \sim |t|^{\gamma} \qquad (T > T_C)\,, \tag{4.3}$$

where once again t is the reduced temperature ($t = (T - T_C)/T_C$). From this fitting new β and γ values are extracted. The process is repeated till convergence is reached and the best values of β, γ and T_C are obtained. The final values of $M_S(T)$ and $\chi_0^{-1}(T)$ are plotted as a function of temperature in Fig. 4.9 for the four compositions, while Table 4.1 in page 95 contains all the critical exponents and temperatures obtained from the fittings. In the four cases, β takes values within $0.3617 - 0.370$ and therefore agrees with the Heisenberg case ($\beta = 0.369$), while γ exactly agrees for GdScSi ($\gamma = 1.384$) and in the other three cases is slightly smaller, though in no case it takes a value as low as the one for the Ising case.

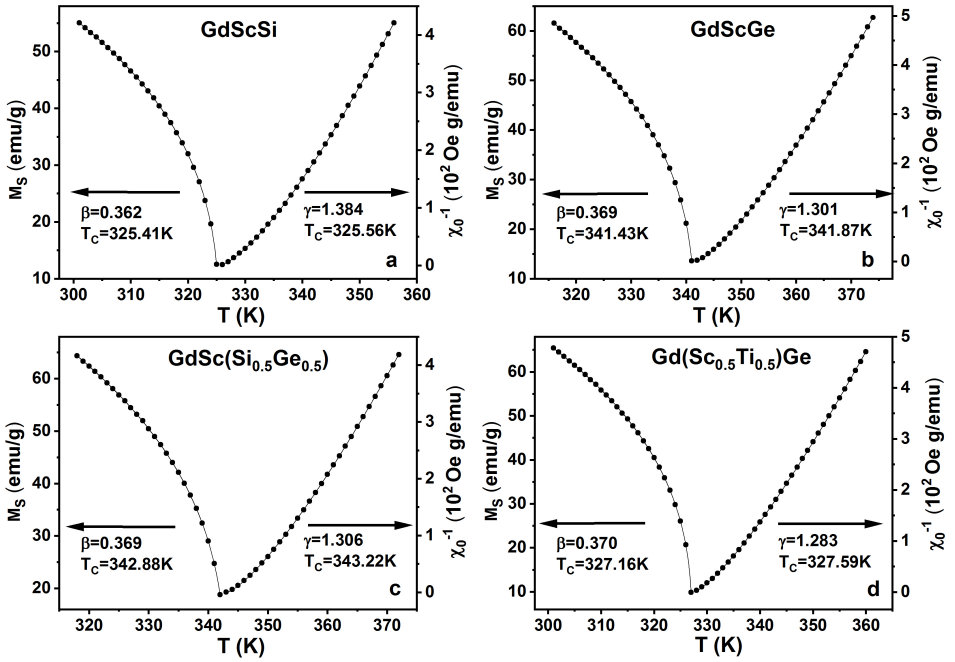


Figure 4.9: Spontaneous magnetization (left) and inverse of initial susceptibility (right) vs. temperature for GdScSi (a), GdScGe (b), $GdSc(Si_{0.5}Ge_{0.5})$ (c), $Gd(Sc_{0.5}Ti_{0.5})Ge$ (d), as obtained from the optimized Modified Arrot Plot. The solid curves correspond to the fits to Eqs. (4.2) and (4.3).

Our next step consists on applying the Kouvel Fisher (KF) method in order to determine β, γ and T_C with more accuracy. As explained in Section 3.4, this method assesses that $M_S(dM_S/dT)^{-1}$ and $\chi_0^{-1}(d\chi_0^{-1}/dT)^{-1}$ have a linear behavior with respect to T, with slopes $1/\beta$ and $1/\gamma$, respectively. The Curie temperature is obtained from the intercept of the straight fitted lines on the temperature axis. The four Kouvel Fisher plots for Gd(Sc,Ti)(Si,Ge) samples are shown in Fig. 4.10 and the critical exponents obtained are grouped in Table 4.1 (page 95). For each sample, both methods (MAP and Kouvel Fisher) give very similar values, confirming the reliability of the results.

The last magnetic critical exponent is δ, which is related to the critical isotherm by the following expression:

$$M \sim H^{1/\delta} \qquad (T = T_C)\,. \tag{4.4}$$

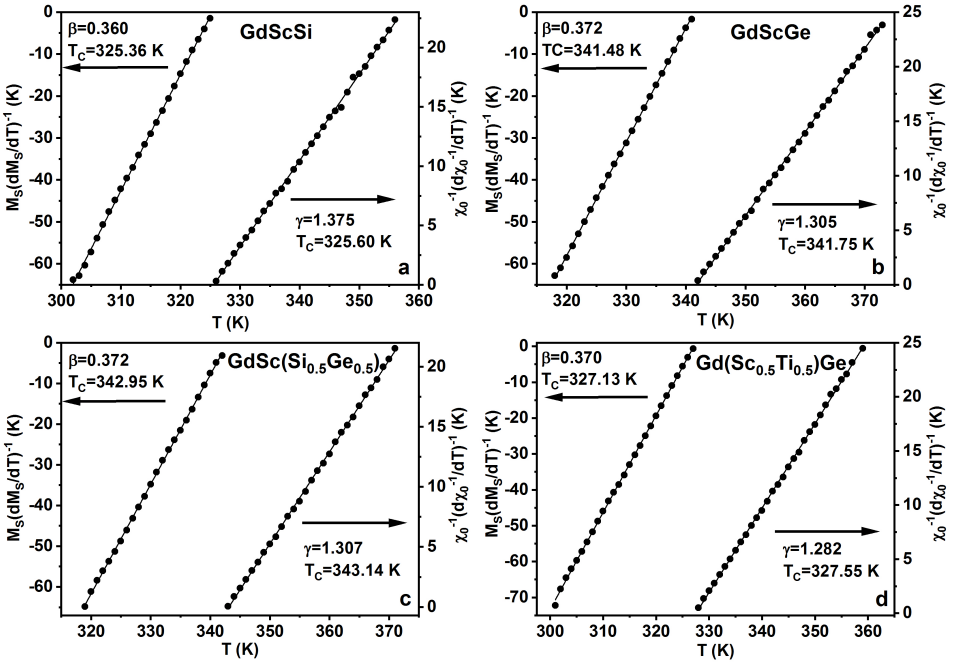


Figure 4.10: Kouvel Fisher plot of spontaneous magnetization (left) and inverse of initial susceptibility (right) for GdScSi (a), GdScGe (b), $GdSc(Si_{0.5}Ge_{0.5})$ (c), $Gd(Sc_{0.5}Ti_{0.5})Ge$ (d). The straight lines are linear fits, from which T_C and the critical exponents are obtained.

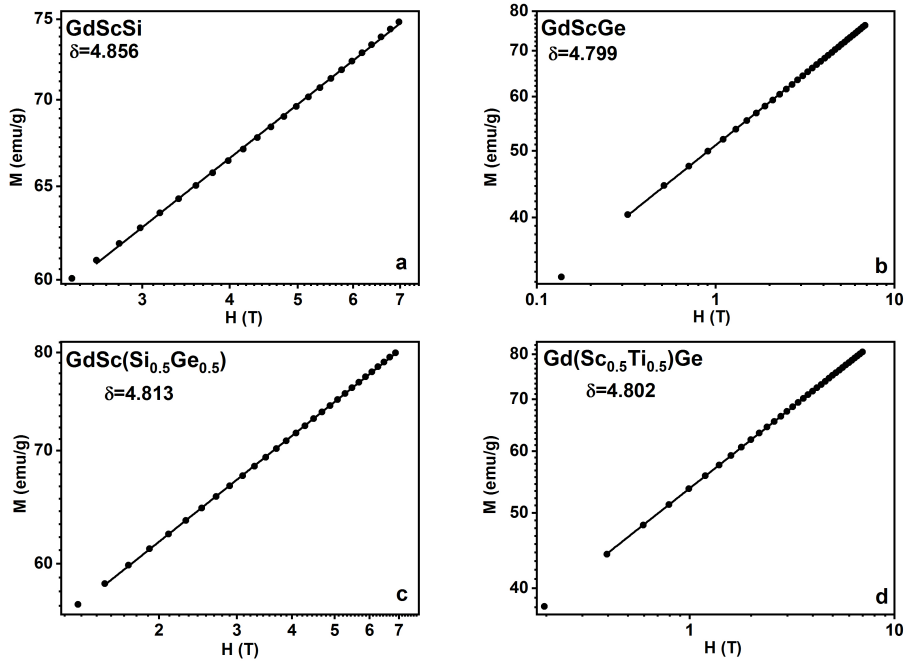


Figure 4.11: M vs. H plot in a log-log scale collected at critical isotherms for GdScSi (a), GdScGe (b), $GdSc(Si_{0.5}Ge_{0.5})$ (c), $Gd(Sc_{0.5}Ti_{0.5})Ge$ (d). The straight line is the linear fit from which the exponent δ is obtained.

Fig. 4.11 contains the critical isotherms at 325 K for GdScSi, 342 K for GdScGe, 343 K for GdSc($Si_{0.5}Ge_{0.5}$) and 327 K for Gd($Sc_{0.5}Ti_{0.5}$)Ge, all of them in log-log scale, showing that they are good straight lines whose slopes give the values for δ. The experimental values obtained from this method ($\delta = 4.86 \pm 0.02$ for GdScSi, $\delta = 4.799 \pm 0.006$ for GdScGe, $\delta = 4.813 \pm 0.006$ for GdSc($Si_{0.5}Ge_{0.5}$), and $\delta = 4.802 \pm 0.002$ for Gd($Sc_{0.5}Ti_{0.5}$)Ge) are also listed in Table 4.1 and agree very well with the theoretical one for 3D Heisenberg ($\delta = 4.78$). Furthermore, δ can be mathematically derived from the previously obtained β and γ values through *Widom's scaling law*, which was presented in Section 3.2.2:

$$\delta = 1 + \gamma/\beta \,. \tag{4.5}$$

The values obtained from this scaling law are very close to the ones obtained from the linear fit of the critical isotherms, further supporting our results. These values are also contained in Table 4.1.

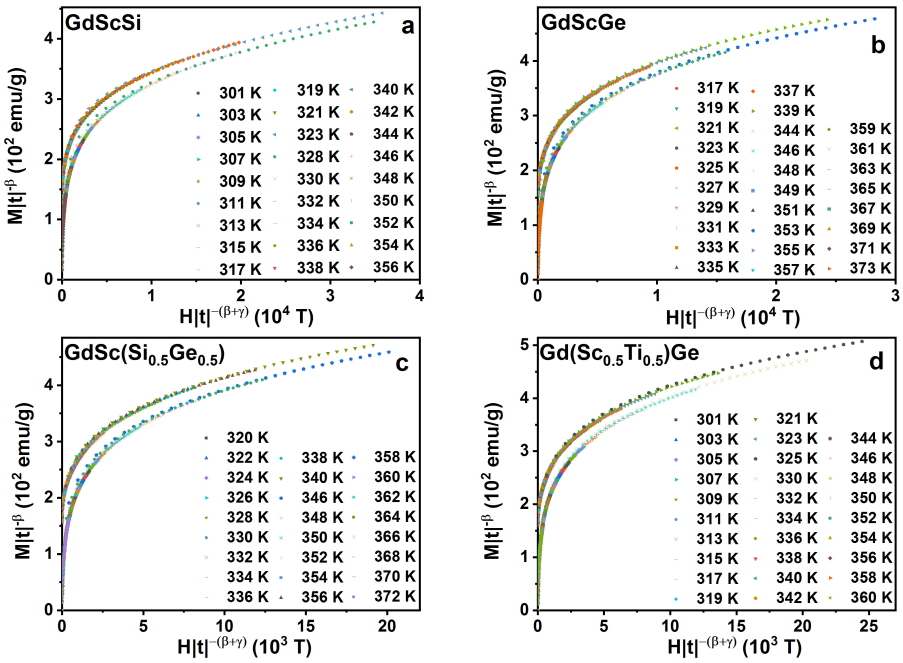


Figure 4.12: The renormalized magnetization plotted as a function of the renormalized field following Eq. (4.6) for GdScSi (a), GdScGe (b), GdSc($Si_{0.5}Ge_{0.5}$) (c), Gd($Sc_{0.5}Ti_{0.5}$)Ge (d). In each case, all data collapse in two separate branches, one above and one below T_C. The graphs contain curves with $\Delta T = 1$ K, though the legends do not show all temperatures.

Finally, the fulfilment of the magnetic equation of state presented in Section 3.4 as:

$$M(H,t) = |t|^{\beta} f_{\pm}(H/|t|^{\beta+\gamma}) \,, \tag{4.6}$$

with the critical exponents β and γ just obtained, is considered as the most severe confirmation of a good scaling. Fig. 4.12 shows that, in the four cases,

the results collapse extremely well into two independent branches, above and below T_C, as a good scaling requires.

Material	Technique	β	γ	δ	α	A^+/A^-
GdScSi	MAP	0.3617 ± 0.0005 $T_C = 325.41 \pm 0.01$ K	1.384 ± 0.004 $T_C = 325.56 \pm 0.05$ K	4.83 ± 0.02^a		
	KF Method	0.360 ± 0.004 $T_C = 325.36 \pm 0.03$ K	1.375 ± 0.007 $T_C = 325.60 \pm 0.06$ K	4.82 ± 0.06^a		
	Critical Isotherm			4.86 ± 0.02		
	PPE calorimetry				-0.120 ± 0.020	1.02 ± 0.13
GdScGe	MAP	0.3688 ± 0.0004 $T_C = 341.43 \pm 0.01$ K	1.301 ± 0.004 $T_C = 341.87 \pm 0.05$ K	4.53 ± 0.02^a		
	KF Method	0.372 ± 0.003 $T_C = 341.48 \pm 0.03$ K	1.305 ± 0.005 $T_C = 341.75 \pm 0.06$ K	4.51 ± 0.04^a		
	Critical Isotherm			4.799 ± 0.006		
	PPE calorimetry				-0.134 ± 0.005	1.63 ± 0.07
$GdSc(Si_{0.5}Ge_{0.5})$	MAP	0.369 ± 0.001 $T_C = 342.88 \pm 0.01$ K	1.306 ± 0.004 $T_C = 343.22 \pm 0.04$ K	4.54 ± 0.02^a		
	KF Method	0.372 ± 0.002 $T_C = 342.95 \pm 0.03$ K	1.307 ± 0.005 $T_C = 343.14 \pm 0.05$ K	4.52 ± 0.03^a		
	Critical Isotherm			4.813 ± 0.006		
	PPE calorimetry				-0.135 ± 0.007	1.56 ± 0.07
$Gd(Sc_{0.5}Ti_{0.5})Ge$	MAP	0.370 ± 0.001 $T_C = 327.16 \pm 0.01$ K	1.283 ± 0.004 $T_C = 327.59 \pm 0.06$ K	4.47 ± 0.02^a		
	KF Method	0.370 ± 0.004 $T_C = 327.13 \pm 0.03$ K	1.282 ± 0.005 $T_C = 327.55 \pm 0.07$ K	4.47 ± 0.05^a		
	Critical Isotherm			4.802 ± 0.002		
	PPE calorimetry				-0.122 ± 0.010	1.16 ± 0.08
NdScSi [225]	MAP	0.343 ± 0.001 $T_C = 170.72 \pm 0.02$ K	1.304 ± 0.008 $T_C = 171 \pm 0.05$ K	4.80 ± 0.03^a		
	KF Method	0.339 ± 0.003 $T_C = 170.65 \pm 0.02$ K	1.297 ± 0.009 $T_C = 171.08 \pm 0.04$ K	4.82 ± 0.06^a		
	Critical Isotherm			4.939 ± 0.001		
	PPE calorimetry				-0.015 ± 0.003	1.02 ± 0.43
NdScGe [225]	MAP	0.473 ± 0.008 $T_C = 188.74 \pm 0.08$ K	1.162 ± 0.009 $T_C = 188.69 \pm 0.06$ K	3.46 ± 0.06^a		
	KF Method	0.446 ± 0.007 $T_C = 188.45 \pm 0.08$ K	1.146 ± 0.012 $T_C = 188.77 \pm 0.09$ K	3.57 ± 0.07^a		
	Critical Isotherm			3.44 ± 0.03		
	PPE calorimetry				$\to 0$	Non applicable

[a] Calculated from Eq. (4.5): $\delta = 1 + \gamma/\beta$.

Table 4.1: Values of the obtained critical exponents and parameters β, γ, δ, α, and A^+/A^-.

A discussion on the critical behavior of NdSc(Si,Ge) samples can be found in Ref. [225]. The critical exponents obtained in that work have also been listed in Table 4.1 for comparison and later use in the scaling of magnetocaloric effect. It was observed that NdScSi belongs to 3D XY universality class (characterized by short-range interactions and plane anisotropy), while NdScGe is closed to the Mean Field model (long-range ordering). This difference was discussed in terms of the different orbitals hybridization when changing Si by Ge. With the study of the Gd-based family we deepen on this idea in order to better understand the magnetic mechanisms of this intermetallic family.

It is considered that the magnetism in this family arises mainly from the RKKY (Ruderman-Kittel-Kasuya-Yosida) interaction between the magnetic moments of the rare-earth atoms, with no magnetic contribution coming from the transition metals (Sc and Ti in our case). This is explained by the hybrid-

ization of the *3d* band in the transition metals with the *p* band of Si or Ge, leading to a filling of the *3d* band [269]. However, rare-earth atoms are quite distant apart [270] and the interaction between them on its own can not explain the relatively high spin-ordering temperatures of this compounds compared to that of the rare-earth alone, which in the case of Gd takes place at 294 K [274] (almost 50 K lower than our Gd-based compound). Furthermore, the interaction between *f*-electrons decreases with increasing distance; therefore, a lower transition temperature would be expected when the Gd ions are within the tetragonal CeScSi structure, as there is a larger separation between rare-earths [76, 275, 288].

In an effort to account for the high ordering temperature of the Gd spins, a common mechanism has been suggested for GdScSi and some Ti containing members (GdTiGe and GdTiSi). A significant spin polarization of the *3d* electrons of the transition metals Sc and Ti has been found in both cases, with a strong hybridization between these electrons and the also spin polarized *5d* band electrons of the rare-earth, which would enable an enhancement of the indirect exchange interaction between the *4f*-subshells of rare-earth ions through a RKKY mechanism, leading to an increase of the critical temperature [274, 276, 277, 289].

The Curie temperatures that we obtained for GdScSi and GdScGe are in general agreement with those found in literature [76, 269, 274, 278] though there are some discrepancies about which one has a higher Curie temperature (GdScGe in our case, with nearly the same value than the one given by Manfrinetti [278] and Couillaud [76]). $GdSc(Si_{0.5}Ge_{0.5})$ has nearly the same Curie temperature as GdScGe while $Gd(Sc_{0.5}Ti_{0.5})Ge$ has a lower one, which is interesting because GdTiGe (in the same CeScSi structure) was reported with a Curie temperature higher than that of GdScGe, of about 25 K [276]. These differences have to do with the effective hybridization between the Gd-*5d* states and the transition metal-*3d* states. In particular, in the case of GdTiSi and GdTiGe it was proved that the substitution of Si by Ge made the *5d*-*3d* hybridization stronger, resulting in a higher Curie temperature [276]. Therefore, we can interpret that the effective hybridization between the *d*-states must be weaker in $Gd(Sc_{0.5}Ti_{0.5})Ge$ than in GdTiGe and GdScGe. Besides, a similar situation arises when comparing GdScSi and GdScGe: the higher critical temperature in the latter is surely due to a stronger *5d*-*3d* hybridization as a consequence of the change in the *X*-block element.

The results of the critical behavior study (summarized in Table 4.1) allow us to conclude that all four ferromagnetic transitions in Gd-based compounds belong to the 3D Heisenberg class, presenting isotropic and short-range order magnetic interactions. This is in stark discrepancy with previous results on NdScSi and NdScGe, where it was proved that the first one belongs to the 3D XY universality class while the second one presented critical exponents close to the Mean Field model [225]. A further proof that the magnetic properties of Nd and Gd compounds are extremely different. In the first place, the Curie temperature has been raised about 150 K between the compounds with Nd and Gd; secondly, the crystalline electric field anisotropies from localized *4f* states which appear in other rare-earth ions, such as Pr and Nd, are not present

in Gd [274, 277], thus favoring the non appearance of magnetocrystalline anisotropies which could make the critical behavior deviate from isotropic to planar (3D XY) or uniaxial (3D Ising) universality models. Nevertheless, there are small deviations in some of the critical parameters from the perfect 3D Heisenberg universality class. In GdScSi, the ratio of the critical coefficients A^+/A^- is smaller than the theoretical one (1.02 against 1.52); in GdScGe, γ is slightly smaller (1.305 against 1.396), as well as in $GdSc(Si_{0.5}Ge_{0.5})$ (1.307 versus 1.396). These are indications that there is not a perfect magnetic isotropy; a result which can be attributed to the fact that there is a non-negligible spin-orbit coupling of the itinerant electrons which could introduce a subtle magnetocrystalline anisotropy, as it happens in pure Gd [290] and has been suggested for $GdScGe_{1-x}Sb_x$ [274]. In the analysis of critical behavior in manganites, for instance, these small deviations from perfect 3D Heisenberg exponents arise often [291–294]. What is clear is that the fact that the X-block element in GdScX be Si, Ge or a combination of both does not make much difference in the magnetic properties, even if it must have some influence in the orbitals hybridization; it simply places the transition slightly lower or higher, without however having more than a slight effect on the critical behavior of the transition. After the publication of our work, this behavior was confirmed by García et al. through *ab*-initio calculations, where they found that the replacement of Si by Ge does not lead to a significant change in the exchange couplings of GdScX [295]. Guillou et al. [274] also found that in $Gd_{1.02}Sc_{0.98}Ge_{1-x}Sb_x$ the magnetic exchange interactions were not directly affected by the substitution of Ge by Sb.

The composition which more evidently deviates from the perfect 3D Heisenberg is $Gd(Sc_{0.5}Ti_{0.5})Ge$, for which γ is 1.283 and $A^+/A^- = 1.16$ (instead of 1.396 and 1.52), though α and β are in agreement with the Heisenberg model and these last two exponents are always taken as the leading parameters in the attribution of universality classes. As the mechanism of *d*-states hybridization is at the core of the magnetic properties of this intermetallic family, the fact that we have two different transition metals with different state of polarization of their *3d*-spins must surely be responsible for this slight deviations in γ and A^+/A^-.

4.3.3 Magnetocaloric effect in RTX family

The magnetocaloric effect has been studied for the four Gd-based samples and the two Nd-based ones. This MCE was evaluated through the isothermal magnetic entropy change, ΔS_M, which is obtained by an indirect method based on the acquisition of isothermal magnetization measurements as described in Section 4.2. Since all of the phase transitions under study are second order phase transitions, the magnetic entropy change is easily obtained from the direct application of the *Maxwell relation*:

$$\Delta S_M(T, \Delta H) = \mu_0 \int_{H_0}^{H_1} \left(\frac{\partial M}{\partial T} \right)_H dH \,. \tag{4.7}$$

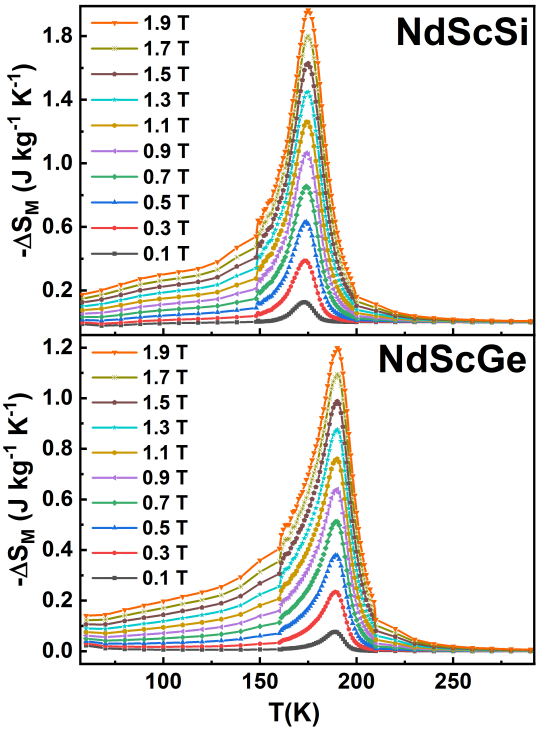


Figure 4.13: Magnetic entropy change as a function of temperature for different applied fields, for NdScSi and NdScGe.

The magnetization measurements were performed up to 2 T and the demagnetization field was considered in the MCE calculation. N_D factors obtained are: 2.82 g Oe/emu for GdScSi, 19.14 g Oe/emu for GdScGe, 15.77 g Oe/emu for GdSc($Si_{0.5}Ge_{0.5}$), 1.09 g Oe/emu for Gd($Sc_{0.5}Ti_{0.5}$)Ge, 78.6 g Oe/emu for NdScSi, and 48.22 g Oe/emu for NdScGe. The negative magnetic entropy change ($-\Delta S_M$) is shown as a function of temperature in Fig. 4.13 for the Nd- samples and in Fig. 4.14 for Gd- samples. The positions of the Curie temperatures (where the peak of the magnetic entropy change takes place) are well in agreement with our previous results (171 K for NdScSi, 189 K for NdScGe, 325 K for GdScSi, 342 K for GdScGe, 343 K for GdSc($Si_{0.5}Ge_{0.5}$) and 327 K for Gd($Sc_{0.5}Ti_{0.5}$)Ge) as well as with studies performed by other groups. Table 4.2 contains the value of the maximum magnetic entropy change, $|\Delta S_M^{pk}|$, for the highest applied fields used $\mu_0 H_a \approx 2$ T, together with the refrigerant capacity, calculated in two ways, as it is found in different papers in literature: RC_{Area} is the area enclosed by the ΔS_M vs. temperature curves in the temperature range enclosed by the full width at half maximum of the peak, $\delta T_{\text{FWHM}} = T_2 - T_1$:

$$RC_{\text{Area}} = \int_{T_1}^{T_2} |\Delta S_M(T, \Delta H)| dT \,, \tag{4.8}$$

while RC_{FWHM} is the product of $|\Delta S_M^{pk}|$ times the width of ΔS_M at half maximum:

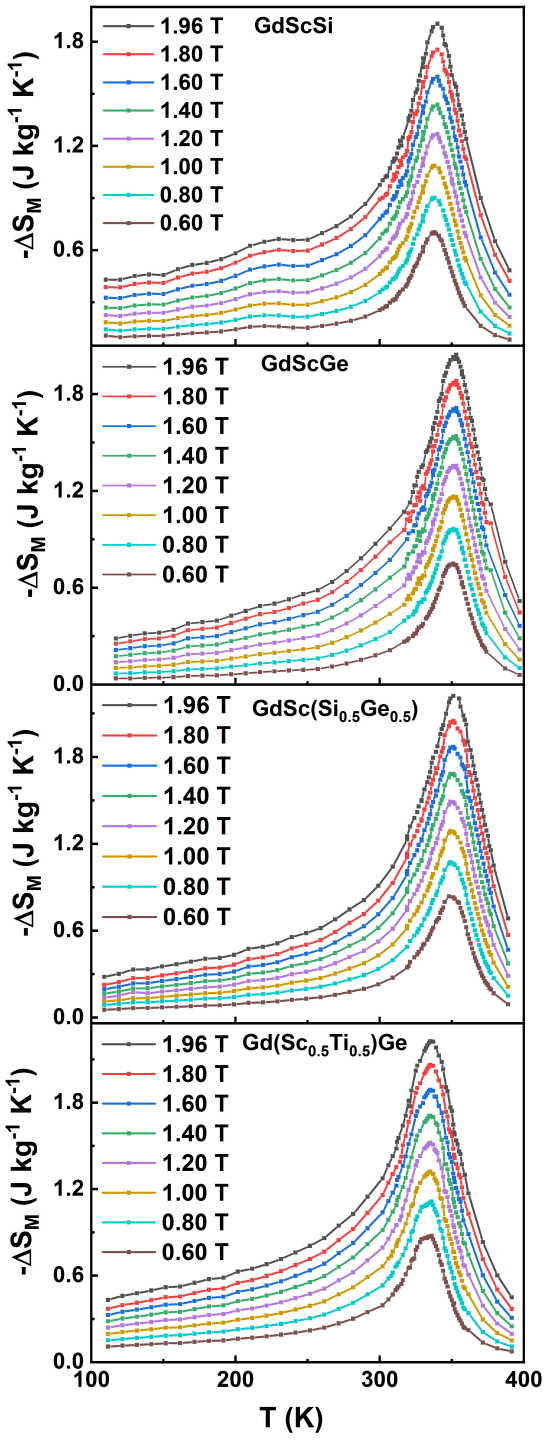


Figure 4.14: Magnetic entropy change as a function of temperature for different applied fields, for GdScSi and GdScGe, $GdSc(Si_{0.5}Ge_{0.5})$ and $Gd(Sc_{0.5}Ti_{0.5})Ge$.

$$RC_{\mathrm{FWHM}} = |\Delta S_M^{pk}| \delta T_{\mathrm{FWHM}} \,. \tag{4.9}$$

The results in Table 4.2 indicate that the Gd-based family has good magnetocaloric properties, comparable to other compounds based on Gd [296–299] and to the results obtained for two of the same compositions (GdScSi,

Compound	$-\Delta S_M^{pk}(Jkg^{-1}K^{-1})$ [$\approx$ 2 T]	$RC_{\mathrm{FWHM}}(Jkg^{-1})$ [$\approx$ 2 T]	$RC_{\mathrm{Area}}(Jkg^{-1})$ [$\approx$ 2 T]
GdScSi	1.90	133	100
GdScGe	2.04	135	100
$GdSc(Si_{0.5}Ge_{0.5})$	2.22	145	110
$Gd(Sc_{0.5}Ti_{0.5})Ge$	2.23	166	123
NdScSi	1.96	47	36
NdScGe	1.20	35	26

Table 4.2: Experimental values obtained for the peak entropy change $-\Delta S_M^{pk}$ and refrigerant capacities RC_{FWHM}, RC_{Area} obtained with an applied field of 1.96 T for the Gd-based compounds and 1.9 T for the Nd-based ones.

GdScGe) found in Ref. [76], though the values presented here for RC_{Area} are slightly higher. The small discrepancy may arise from the fact that the demagnetization field is considered in our calculation for a correct evaluation of the MCE. It is worth noting that $GdSc(Si_{0.5}Ge_{0.5})$ and $Gd(Sc_{0.5}Ti_{0.5})Ge$ (especially the latter) give a significantly higher refrigerant capacity showing that tuning the composition in this family improves their magnetocaloric properties. On the other hand, Nd-based compounds have lower RC values, this is mainly due to a narrower width of the magnetic entropy change peak.

In order to make a general comparison with data published in literature for other compounds, we need to be able to extrapolate these values to higher fields. As explained in Section 3.5, the scaling of magetocaloric properties with the magnetic field allows us to make these extrapolations (in second order magnetic transitions) following equations [235, 237, 240]:

$$|\Delta S_M^{pk}| \propto H^{1+\frac{1}{\delta}(1-\frac{1}{\beta})}\,, \tag{4.10}$$

and

$$RC \propto H^{1+1/\delta}\,. \tag{4.11}$$

Where Eq. (4.11) is valid for both RC_{Area} and RC_{FWHM}. The critical exponents β and δ in Eqs. (4.10) and (4.11) are the ones previously obtained through the magnetic critical behavior study and gathered in Table 4.1 (page 95) for each compound. We have checked that, in all cases, $|\Delta S_M^{pk}|$ and RC scale with those parameters, which is shown in Fig. 4.15 for all the compounds. Left column (a) in Fig. 4.15 shows the scaling of $|\Delta S_M^{pk}|$ and central column (b) the scaling of RC_{FWHM}. In all of the cases the experimental points lie along a straight line when the proper critical exponents are used. This behavior confirms the attribution of the different universality classes (short-range 3D Heisenberg for the Gd-based compounds, short-range 3D XY for NdScSi, and close to the long-range Mean Field for NdScGe). This allows us to extrapolate $|\Delta S_M^{pk}|$ and RC values to an applied field of 5 T (see Table 4.3 in page 102) in order to compare the magnetocaloric performance of these compounds with that of other rare-earth containing compounds presented by Franco et al. in Fig. 25 of his extensive review in Ref. [91]. In that way we see that the Gd family gives values similar to the ones presented there in the same temperature range (above room

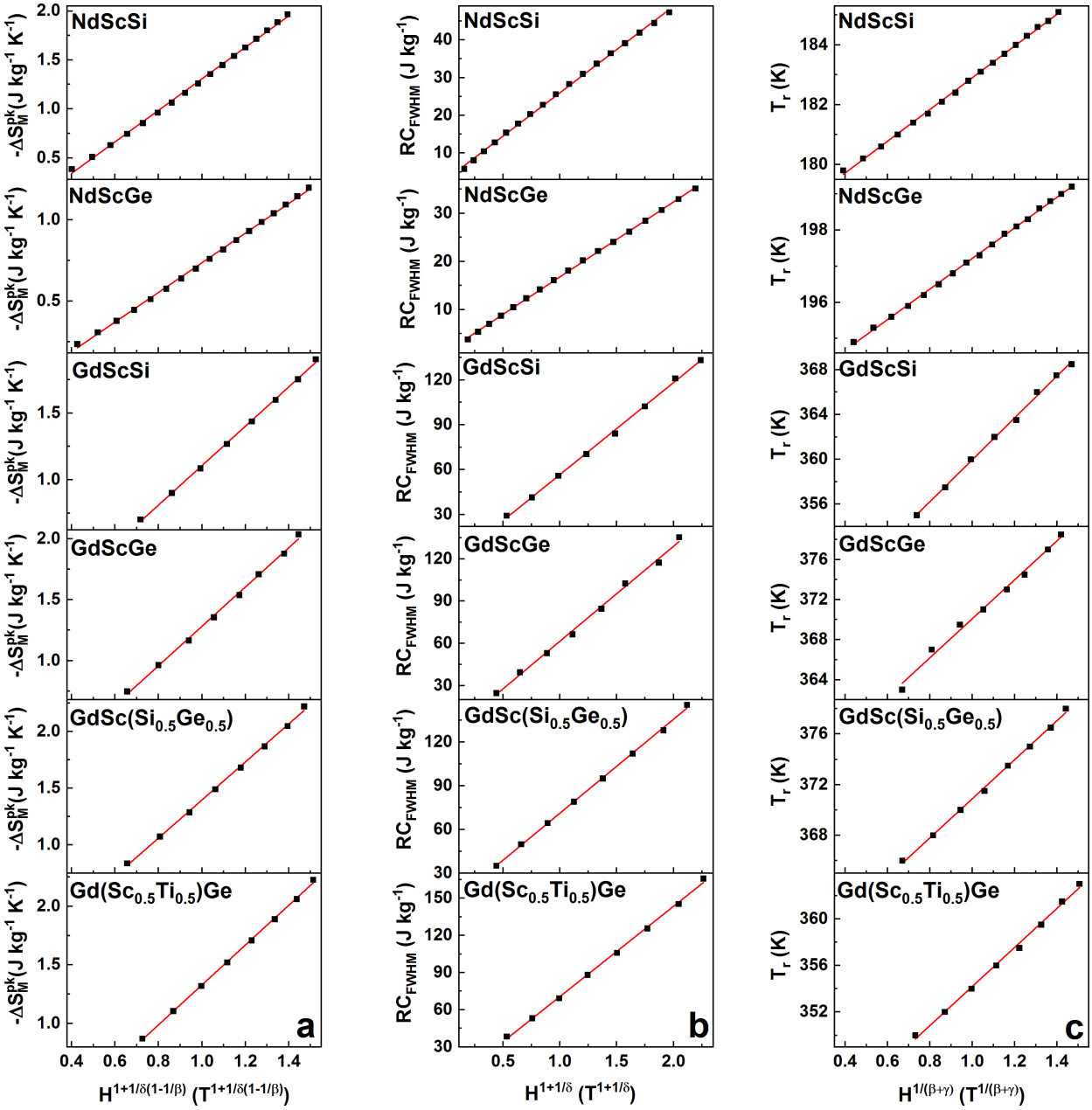


Figure 4.15: Field dependences of the peak magnetic entropy change (column a), refrigerant capacity (column b), and reference temperature T_r (column c) for Nd- and Gd- based compounds. The values of β, γ, and δ for each compound are the ones presented in Table 4.1. The red straight lines are linear fits to visually show the good scaling.

temperature) while the Nd family has values in the average of those presented in that review for the range 170-190 K. This implies that they could be competitive magnetocaloric materials within their respective Curie temperature ranges.

Compound	$-\Delta S_M^{pk}(Jkg^{-1}K^{-1})$ [5 T]	$RC_{\mathrm{FWHM}}(Jkg^{-1})$ [5 T]	$RC_{\mathrm{Area}}(Jkg^{-1})$ [5 T]
GdScSi	3.70	422	315
GdScGe	4.00	439	320
$GdSc(Si_{0.5}Ge_{0.5})$	4.26	447	337
$Gd(Sc_{0.5}Ti_{0.5})Ge$	4.23	517	380
NdScSi	3.84	146	113
NdScGe	2.42	118	88

Table 4.3: Extrapolated values for an applied field of 5 T obtained for the peak entropy change $-\Delta S_M^{pk}$ and refrigerant capacities RC_{FWHM}, RC_{Area} using scaling laws in Eqs. (4.10) and (4.11).

The next step in this magnetocaloric analysis is to build up the master curves for the different compounds calculating, for each one of them, the normalized curve for the magnetic entropy change by dividing it by the corresponding maximum for the different values of the applied field and rescaling the temperature axis. As was shown in Section 3.5, it has been demonstrated that, in an ideal case, it should be enough to use one reference point in order to rescale the temperature axis above and below the Curie temperature [240]:

$$\theta_1 = \frac{T - T_C}{T_r - T_C}\,, \tag{4.12}$$

(the reference temperature T_r being selected as that corresponding to a certain fraction of $|\Delta_M^{pk}|$; in this case 0.5 has been used). Nevertheless, it has also been shown that in some experimental cases, where the material departs from the ideal behavior given by the magnetic equation of state, the use of two reference temperatures (T_{r1} and T_{r2}) becomes necessary to construct the universal curves [235]:

$$\theta_2 = \begin{cases} -(T - T_C)/(T_{r1} - T_C)\,, & T \leqslant T_C \\ (T - T_C)/(T_{r2} - T_C)\,, & T > T_C \end{cases}\,. \tag{4.13}$$

As was explained in Section 3.5 in greater detail, this last situation arises when, for instance, there is a non-negligible demagnetizing field or there is no single magnetic phase.

Fig. 4.16 shows the normalized curves for NdScSi on the top, using one (left box, a) and two (right bob, b) reference temperatures; the bottom part shows the same for NdScGe, where the left hand side box (c) is rescaled with a single reference temperature and the right hand side box (d) uses two. We can see that there is a good collapse around the Curie temperature with only one reference T_r but that there are some deviations in the low temperature part, which are subdued when using two references T_{r1}, T_{r2}. We can see the analogous for the Gd containing compounds in Fig. 4.17 (page 104). We have already seen in Section 3.5 that deviations from a perfect collapse of the curves can have two main origins: if increasing the applied field gives as a consequence an increase in the normalized magnetic entropy change (for a given value of the rescaled temperature), then the deviation is due to the presence of a demagnetization

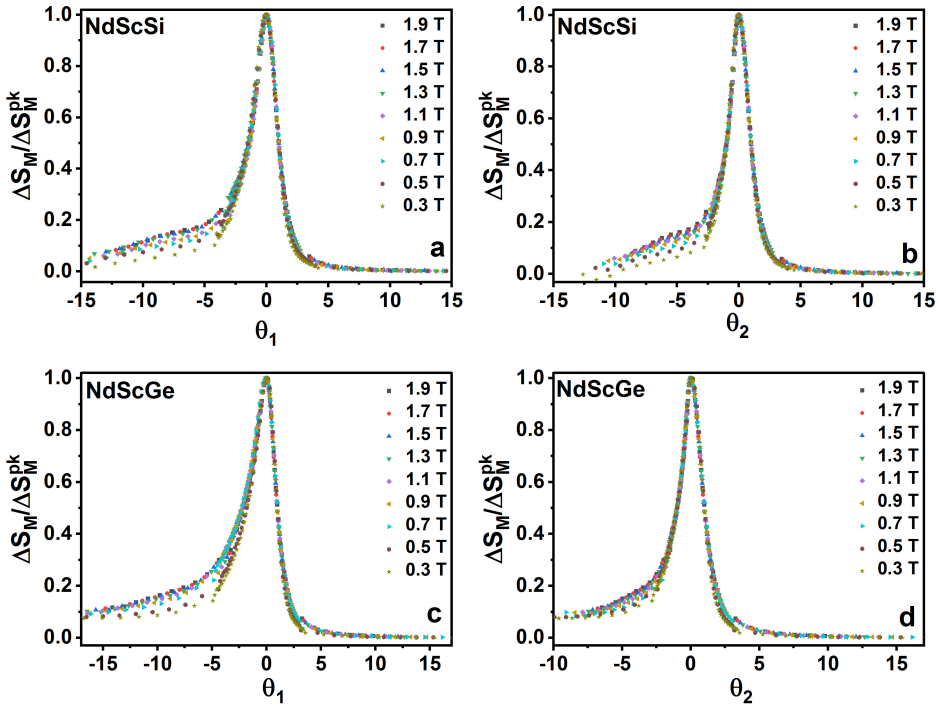


Figure 4.16: Universal curve with the rescaled magnetic entropy changes for NdScSi on the top (a, b) and NdScGe on the bottom (c, d), using one (a, c) or two (b, d) reference temperatures.

field [249]; on the contrary, if the consequence is a decrease in the normalized entropy, then the physical origin of the deviation is the presence of other magnetic phases [246, 248]. In all the compounds of this family we find that the entropy increases with the applied field, implying that the demagnetization field in these samples is important enough to be taken into account, confirming our strategy to calculate the refrigerant capacity from internal field data instead of directly using the applied field. The fact that even with two reference temperatures the collapse is not complete at low temperature values well below the peak is due to the fact that the magnetic equation of state is only valid in the near vicinity of the critical temperature [246]. Interestingly, even if in two samples (GdScSi and GdSc($Si_{0.5}Ge_{0.5}$)) there is a small amount of secondary phase, the results imply that only the main phase is responsible for the ferromagnetic transition, as no effect linked to the presence of other phases has been found.

In order to complete the magnetocaloric study the scaling of reference temperature (T_r) with the magnetic field has also been checked. It has also been theoretically shown that the reference temperature T_r scales following relation [240]:

$$T_r \propto H^{1/(\beta+\gamma)} . \tag{4.14}$$

The right hand side column (c) in Fig. 4.15 (page 101) shows how this scaling is fulfilled using the critical exponents collected in Table 4.1 (page 95). Using the scaling relations in Eqs. (4.10) and (4.14) together with universal curves

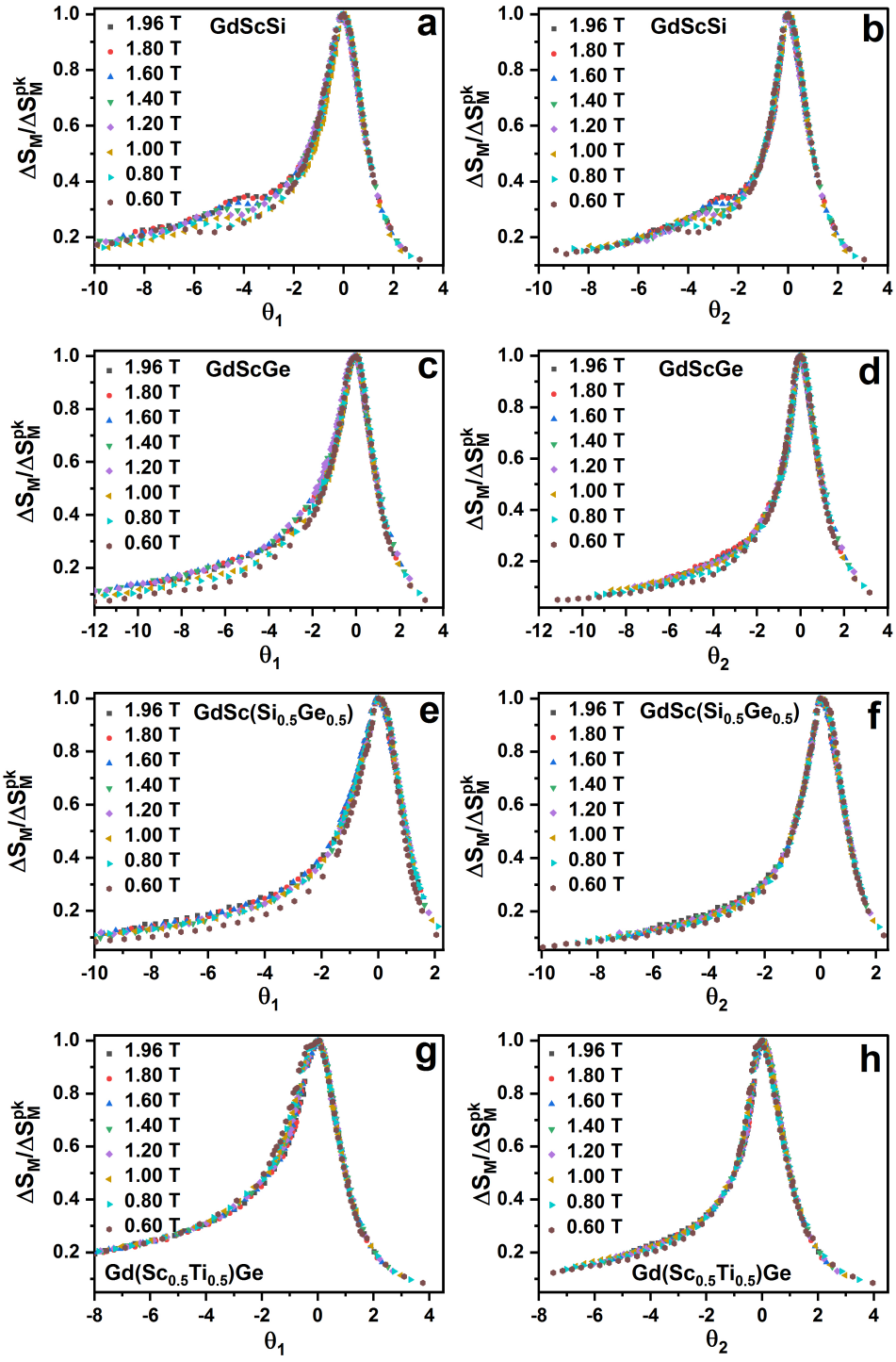


Figure 4.17: Universal curve with the rescaled magnetic entropy changes for Gd-based compounds. From top to bottom: GdScSi (a, b), GdScGe (c, d), $GdSc(Si_{0.5}Ge_{0.5})$ (e, f), and $Gd(Sc_{0.5}Ti_{0.5})Ge$ (g, h). In every case, the left hand side shows the rescaling with one reference temperature (θ_1) while the right hand side presents the rescaling with two reference temperatures (θ_2).

allows the extrapolation of $\Delta S_M(T)$ curves to fields and temperatures which otherwise might not be experimentally reachable [236].

Finally, the normalized magnetic entropy curves for different materials which share the same universality class should also collapse on one universal curve in the close vicinity of the critical temperature, as they share the critical exponents [237, 244]. Fig. 4.18 shows the result with the four samples of the Gd-based compounds (which comply with the 3D Heisenberg class), confirming this theoretical universality. In the same figure, the Nd-based samples curves have also been superimposed, showing that NdScGe clearly deviates from this universality (which is logical as the difference in β and δ are important from the Heisenberg class to the nearly Mean Field one to which NdScGe belongs), while NdScSi nearly collapses on the rest, which is understandable as the critical exponents for 3D Heisenberg and 3D XY are very similar: $\beta_{\text{Heis}} = 0.369$, $\beta_{\text{XY}} = 0.348$, and $\delta_{\text{Heis}} = 4.78$, $\delta_{\text{XY}} = 4.78$ (see Table 3.2 in page 77).

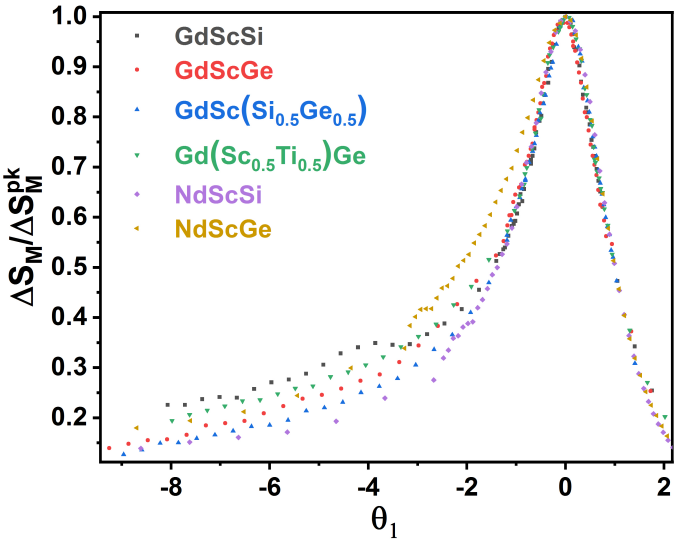


Figure 4.18: Construction of the rescaled magnetic entropy changes for all compounds using a single reference temperature at $\mu_0 \Delta H_a \approx 2$ T.

4.4 Conclusions

We have performed a complete study of both the critical behavior and magnetocaloric effect of several members of the intermetallic family RTX. A high resolution *ac* photopyroelectric calorimeter was used in order to obtain the temperature evolution of thermal diffusivity for Pr-, Nd-, and Gd- based compounds.

Then, the critical behavior of the second order ferromagnetic transition in GdScSi, GdScGe, GdSc($Si_{0.5}Ge_{0.5}$) and Gd($Sc_{0.5}Ti_{0.5}$)Ge was studied by means of calorimetric as well as magnetic techniques. The critical parameters α, β, γ, δ, and A^+/A^- were independently obtained and they agree with the 3D Heisenberg universality class, stating that the magnetic interactions are short-range and that the spins are ordered isotropically, in contrast with the results previously obtained by our group for NdScSi (which belongs to a 3D XY universality

class) and NdScGe (Mean Field model). The differences in the T_C among the compositions and certain deviations of the critical parameters from the theoretical values are explained on the basis of the variation of the *d*-states hybridization between the rare-earth and the transition metal, as well as the presence of small magnetocrystalline anisotropies arising from spin-orbit coupling effects.

Finally we have shown that the intermetallic family RTX (R = Nd, Gd; T = Sc, Ti; X = Si, Ge) presents competitive magnetocaloric properties, signalled by the magnetic entropy change at the Curie temperature as well as by the refrigerant capacity. It has been demonstrated that they fulfill the scaling equations with the critical parameters corresponding to the universality classes to which they respectively belong (3D XY, 3D Heisenberg, Mean Field) and that universal curves can indeed be built up: on the one hand, for a given material as a function of the magnetic field and, on the other hand, for materials which share the same universality class.

5 | R_3CoNi intermetallics

"Science and everyday life cannot and should not be separated."

– Rosalind E. Franklin

This chapter presents our results concerning the magnetic properties, critical behavior and magnetocaloric effect of the novel R_3CoNi intermetallic family (R = Tb, Dy, Ho, Er, and Tm). Synthesized for the first time, this family shows high magnetocaloric properties around their second order paramagnetic to ferromagnetic phase transitions in the range 6-96 K. Our study suggests that the members of this family could be promising candidates for magnetic refrigeration in the gas liquefaction region. Magnetic properties will be discussed for all the members of the family, and the thermal and magnetic critical behavior of the first three members (R = Tb, Dy, Ho) will be presented. Due to the low ordering temperatures and the proximity of a lower temperature spin reorientation transition, the critical behavior analysis could not be performed for Er_3CoNi and Tm_3CoNi compounds. Magnetocaloric scaling laws have been checked and universal curves were obtained.

The following materials will be studied in this chapter:

- **Tb_3CoNi**
- **Dy_3CoNi**
- **Ho_3CoNi**
- **Er_3CoNi**
- **Tm_3CoNi**

5.1 Introduction

We have already seen that intermetallic materials are in the focus of many scientific works due to their great variety and interesting properties. For this reason, novel intermetallic materials are being synthetized by many research groups in the world in search of relevant magnetic properties for technological applications. One of the main application fields for these materials is magnetic refrigeration making use of the magnetocaloric effect. In spite of the fact that, nowadays, room temperature devices are the ones most looked for, there is also a need for materials operating in other temperature regions, such as the gas liquefaction ranges.

The focus of this work is placed on the latter region, for which we have synthetized and studied the intermetallic family R_3CoNi where R is a heavy rare-earth atom R = Tb, Dy, Ho, Er, and Tm. So far, only the structure and some magnetic properties of Gd_3CoNi [300,301] and Tb_3CoNi [302] have been investigated, the rest of the series being a complete novelty.

As it happens in many other families of rare-earth intermetallics, such as RTX (R = rare-earth, T = transition metal, X = *p*-block element) [78, 269], R_6TX_2 [303–305], or R_3Co [306], in Tb_3CoNi no magnetic contribution coming from the transition metals (Co, Ni) was found [302]; therefore, the magnetism only arises due to the spin ordering of the R atoms. The aim of this work is to study in detail the magnetic properties of this ordering in the five members of the aforementioned series, paying special attention to the magnetocaloric properties (maximum entropy change, refrigerant capacity, and universal curves) and get a deeper insight into the magnetism of the paramagnetic to ferromagnetic phase transitions by means of the study of their critical behavior, when possible. We will look for the set of critical exponents (α, β, γ, δ, n) which describes the critical behavior of the standard physical variables specific heat, spontaneous magnetization, inverse of the initial susceptibility, critical isotherm, and maximum of the magnetic entropy change, respectively. The correspondence of those sets with a particular universality class will provide information about the spin ordering and dimensionality of the transition.

5.2 Preparation of samples, characterization, and experimental techniques

Samples with nominal composition R_3CoNi were synthesized by our collaborators P. Manfrinetti and A. Provino from the University of Genova in Italy, for R = Tb, Dy, Ho, Er, and Tm. The alloys, in the form of a polycrystalline material, were prepared by arc melting, with the elements taken in stoichiometric proportions under a TiZr-gettered Ar atmosphere (total weight of 3-4 g). The starting constituents were commercial high purity metals: 99.9 wt. % purity for the R metals (Koch-Light Laboratories Ltd. England), 99.99 wt. % purity for both Co and Ni (REacton Alfa, Johnson Matthey GmbH. Germany). After first melting for reaction, the buttons were remelted other three times, turning them upside down each time, to ensure homogeneity. Weight losses after the

melting procedure were less than 0.4 % (except for Tm; in this case losses were within 1.0 %). The small ingots were wrapped in an outgassed Ta foil, sealed under vacuum in quartz tubes and annealed in a resistance furnace. Due to the formation of these phases, likely occurring by a peritectic reaction (solid phase + liquid phase forming a second solid phase), the thermal annealing was generally performed in two steps: 680 ºC + 700 ºC for Tb_3CoNi (for which a formation through a peritectic reaction occurring at 720 ºC is reported) [302], and 700 ºC + 730 ºC for the other R_3CoNi samples (3-4 days each step, for a total of 7-8 days).

The homogeneity of the alloys was checked, and phase analysis performed by optical microscopy (LOM) on micrographic specimens prepared with standard methods and powder X-ray diffraction (XRD). The XRD patterns were recorded on a Guinier camera (Cu Kα1 radiation), using pure Si as an internal standard [a = 5.4308(1) $\AA$]; they were indexed by comparison with the ones calculated by the Lazy PULVERIX program [280]; then, the lattice parameters were determined by means of a least-squares method. The refinement of the crystal structure was performed for Ho_3CoNi, Er_3CoNi and Tm_3CoNi by the Rietveld refinement program FULLPROF [307]. In this case powder XRD data were recorded on a Philips diffractometer (Cu Kα radiation), in the 2θ range of 10º-100º, with steps of 0.02º and counting time of 26-28 sec/step.

Magnetic measurements have been performed using a Vibrating Sample Magnetometer by Cryogenic Limited, obtaining first the magnetization curves from 2 K to room temperature. The magnetization was measured in a standard procedure. First the sample is cooled from room temperature to 2 K with out any applied magnetic field, at this temperature a small field (100 Oe in our case) is applied in order to make the measurement, and the magnetization is measured while increasing the temperature well above the T_C. This is the so called Zero-Field Cooled (ZFC) measurement. After that, and maintaining the small applied field, the magnetization is again measured while decreasing temperature down to 2 K, this procedure is known as Field-Cooled (FC). Once the magnetic transitions have been located, the magnetization (M) of the samples under external applied magnetic fields H_a in the range of 0 to 7 T has been measured. For all samples, isotherms have been collected from 2 K to temperatures well above the corresponding Curie temperature (T_C), using different steps, depending on the temperature range. In order to study in detail the critical behavior of the paramagnetic to ferromagnetic transition, a step of $\Delta T = 1$ K has been taken between consecutive isotherms around T_C; moreover, as has been already explained in Section 3.5, in order to perform a correct evaluation of the magnetocaloric effect and the scaling analysis, demagnetization effects have been taken into account [109, 136]. For this purpose, the demagnetization factor N_D has been obtained by means of *ac* susceptibility measurements, and the internal magnetic field (H_i) has afterwards been calculated using the well known relation: $H_i = H_a - N_D M$, as shown in detail in Section 2.1.3. For simplicity, from now on H will be used to indicate H_i. The magnetic susceptibility has been measured with the AC Measurement System Option in a Physical Properties Measurement System (PPMS) by Quantum Design. The values of N_D for the samples are gathered in Table 5.2, page 111.

The specific heat c_p has been retrieved using a high resolution *ac* photopyroelectric calorimeter in the back detection configuration, which allows to perform extremely slow temperature ramps in order to extract the detailed shape of c_p, the precise way in which this measurement is done and c_p is extracted can be found in detail in Section 1.4. Unfortunately, the lowest temperature that this system can achieve is 14 K, so it has not been possible to obtain this data for all samples, as it will be shown later on.

5.3 Experimental results and discussion

This section will be divided in four subsections. Since this is a novel family, a brief crystallographic description will be presented in the first subsection. The second subsection will be devoted to the discussion of some general magnetic properties, such as their magnetization, critical temperature, and low temperature magnetic behavior. Following this, a complete study of the critical behavior of the thermal as well as the magnetic properties will be presented for Tb_3CoNi, Dy_3CoNi and Ho_3CoNi. Finally, the fourth subsection will be focused on the magnetocaloric effect; from the evaluation of the main figures of merits (ΔS_M, RC), to the testing of the magnetocaloric scaling laws and the construction of the "master curves".

5.3.1 Crystal structure of R_3CoNi family

Compound	a [Å]	c [Å]	V_{obs} [Å^3]	ΔV %
Tb_3CoNi	8.6062(3)	15.679(1)	1005.72	-5.62
Dy_3CoNi	8.5638(7)	15.618(2)	991.96	-5.45
Ho_3CoNi	8.5268(5)	15.563(2)	979.95	-5.62
Er_3CoNi	8.4840(5)	15.561(2)	969.99	-5.40
Tm_3CoNi	8.4500(3)	15.453(1)	955.55	-5.47

Table 5.1: Lattice parameters (a and c), observed unit cell volume (V_{obs}) and volume contraction in formation of the phase (ΔV %) for the R_3CoNi compounds (R = Tb-Tm); all crystallizing in the rhombohedral Er_3Ni_2-type (Pearson's symbol $hR45$, space group $R\bar{3}h$; Z = 9). Data are from Guinier patterns.

The series of ternary phases R_3CoNi have been prepared and a complete crystallographic analysis was performed by our collaborators in Genova. The room temperature X-ray data reveal that besides Gd [300] and Tb [302] all the heavy R down to Tm also form a ternary R_3CoNi compound. While Gd_3CoNi adopts the monoclinic Dy_3Ni_2-type (mS20; space group $C2/m$, N. 12) [308], all compounds formed by the other heavy R (Tb to Tm) crystallize with the rhombohedral Er_3Ni_2-type structure (Pearson symbol $hR45$; space group $R\bar{3}h$, N. 148) [309]. This means that not only for Tb_3Ni_2 but in Dy_3Ni_2 and Ho_3Ni_2 as well, the structure changes from the Dy_3Ni_2-type to the Er_3Ni_2-type when partially replacing Ni by Co (to the equiatomic ratio). The lattice parameters

(a and c), unit cell volume (V_{obs}) and volume contraction in the formation of compounds ΔV % (where $\Delta V = [((V_{obs} - V_{calc})/V_{calc}) \times 100]$; V_{calc} is the volume of the compound calculated from the atomic volumes of the individual atoms [310]) are collected in Table 5.1. Both the lattice parameters and unit cell volume linearly decrease from Tb down to Tm, well following the lanthanide contraction trend.

5.3.2 Magnetic characterization of R_3CoNi family

Being this a novel family, it is important to localize the magnetic phase transitions (if any) in the materials, as well as to study their magnetic behavior. In order to do this, magnetization in Zero-Field Cooled (ZFC) and Field-Cooled (FC) (with an applied field of 100 Oe) was obtained for the five magnetic samples (R = Tb, Dy, Ho, Er, and Tm). In all cases (except for Tm_3CoNi) there is a clear divergence between the ZFC and FC curves, showing thermomagnetic irreversibility, typical of many ferro/ferrimagnetic transitions. This is shown in the upper part (a) of Fig. 5.1, while the lower box (b) shows the real part of the *ac* susceptibility, which is a very helpful tool to precisely locate the critical temperatures and to obtain N_D factor. Both T_C and N_D for each sample are presented in Table 5.2. As can be clearly seen in Fig. 5.1, T_C decreases as the rare-earth gets heavier. With the combination of magnetization and susceptibility measurements we see that there is a paramagnetic to ferromagnetic (PM-FM) transition at 96 K in the case of Tb_3CoNi, with a nearly identical shape of the magnetization to the one published in [302]. The small peak at about 75 K in the FC curve is surely due to a spin reorientation transition. In fact, in Ref. [302] it was observed by neutron diffraction data that, while below T_C the arrangement of the three Tb sublattices is ferromagnetic with components of the magnetic moments in the directions of the a and c vectors (though not completely collinear), at 3.5 K the magnetic moments were on the ab-plane for the now 5 different Tb sublattices, with a canted contribution along the c-direction for 3 of them.

Compound	T_C (K)	N_D (gOe/emu)
Tb_3CoNi	96	41.57
Dy_3CoNi	53	43.95
Ho_3CoNi	26	48.99
Er_3CoNi	15	47.89
Tm_3CoNi	6	51.13

Table 5.2: Critical temperatures (T_C) of the PM-FM transitions and demagnetization factors (N_D) obtained from *ac* susceptibility measurements for R_3CoNi compounds.

Dy_3CoNi and Ho_3CoNi present similar features with T_C at 53 K and 26 K, respectively. In both cases, at lower temperatures, there is also a hint of a spin reorientation transition, signalled by the small maximum in the former and a change in slope in the latter in the FC curves (top graph in Fig. 5.1). Er_3CoNi

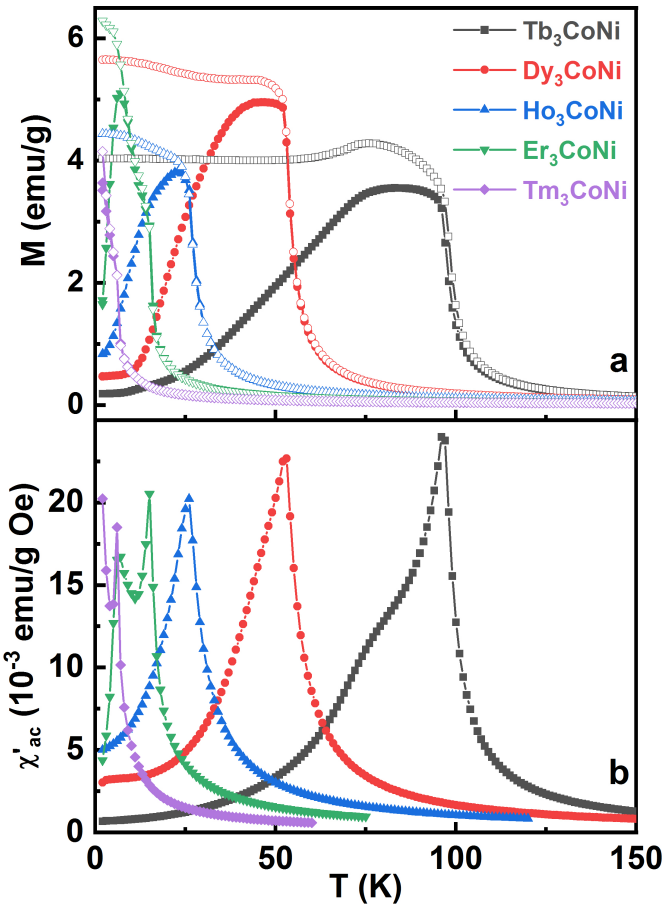


Figure 5.1: (a) Magnetization as a function of temperature in Zero-Field Cooled (filled-in symbols) and Field-Cooled (empty symbols) mode with applied field $\mu_0 H$= 100 Oe; (b) Real part of the *ac* susceptibility at f = 100 Hz.

also presents thermomagnetic irreversibility but there are two clear maxima in the *ac* susceptibility (bottom graph in Fig. 5.1), at 15 K and 7 K, indicating two different transitions, the first one being the PM-FM while the second one is probably a spin reorientation transition. Finally, Tm_3CoNi has a very small magnetic irreversibility and T_C is located at 6 K but there is the trace of another maximum at a temperature lower than 2 K in the susceptibility.

The thermomagnetic irreversibility and its evolution with the change in rare-earth is confirmed by the hysteresis cycles at 2 K, which are shown in Fig. 5.2, where the coercive field is reduced as the atomic number is increased. In the particular case of Tb_3CoNi the cycle clearly shows step-like jumps which indicate the presence of metamagnetic transitions (not seen in the cycles for the other four samples), pointing to the presence of strong antiferromagnetic components at very low temperature. Nevertheless, a small antiferromagnetic behavior at low temperature and field is also present in Dy_3CoNi and Er_3CoNi. This can be seen in the low temperature isotherms presented for the three samples in Fig. 5.3, where magnetization increases with increasing temperature, a characteristic of AFM ordering. The effect is bigger and takes place for a larger temperature region on the Tb containing sample, while there are less

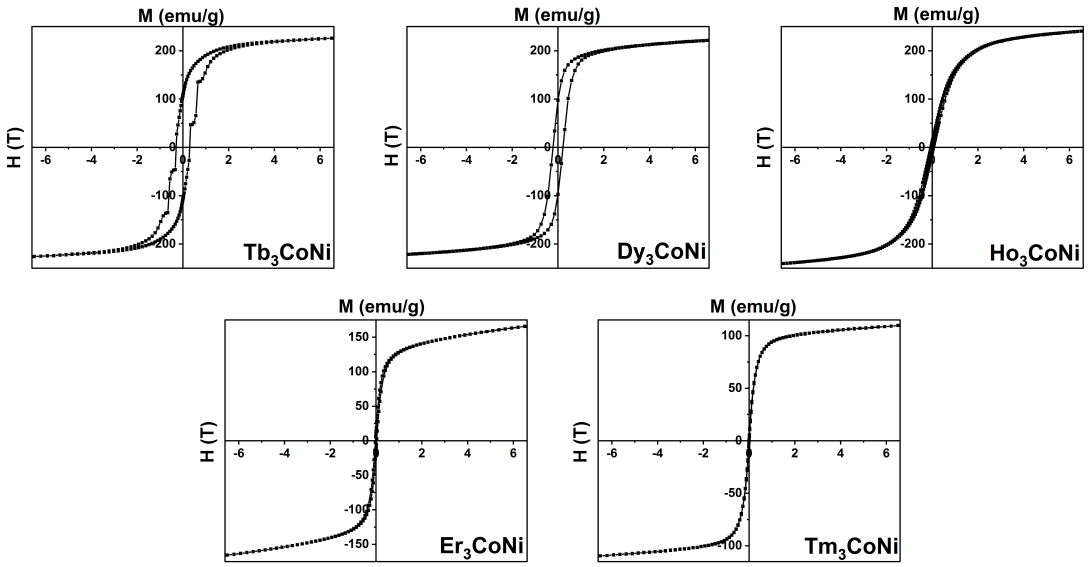


Figure 5.2: Hysteresis loops at 2 K for the five R_3CoNi samples.

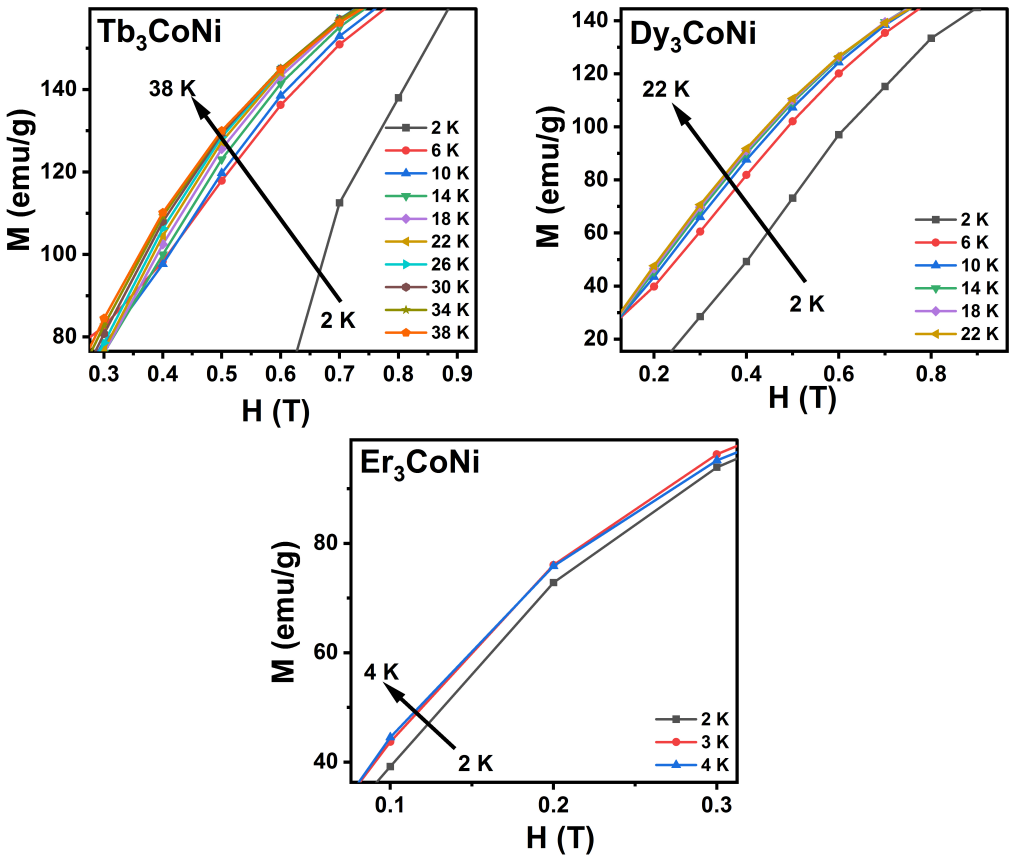


Figure 5.3: Details of the magnetization isotherms for the cases in which an antiferromagnetic behavior is found at low temperature.

isotherms at which this effect is visible in Dy and Er samples. This behavior will show up again when discussing the magnetocaloric properties.

Thermomagnetic irreversibility is a phenomenon which can be found in spin glasses, ferromagnetic materials with magnetocrystalline anisotropies, and materials with competing magnetic interactions [311–313]. The features shown in the hysteresis cycles at 2 K in Fig. 5.2 (coercive fields, metamagnetic transitions in Tb_3CoNi) support the possibility of magnetocrystalline anisotropies at low temperature, which would induce a strong narrow-domain-wall pinning [313], as it happens in many other materials [313–316].

5.3.3 Critical behavior in R_3CoNi family

This section is devoted to the obtention of the critical exponents (α, β, γ, δ) associated to the thermal and magnetic properties (see Section 3.2) for the PM-FM transitions in Tb_3CoNi, Dy_3CoNi, and Ho_3CoNi (all of them being second order transitions). In the case of Er_3CoNi, the presence of a second transition very close to it (7 K versus 15 K) makes it impossible to isolate the critical behavior of the PM-FM one. A similar situation is found for Tm_3CoNi. Furthermore, Er_3CoNi has its PM-FM transition (15 K) just in the lower working limit of the *ac* photopyroelectric calorimeter ($\sim$ 14 K), while the PM-FM transition in Tm_3CoNi is well below this limit (6 K).

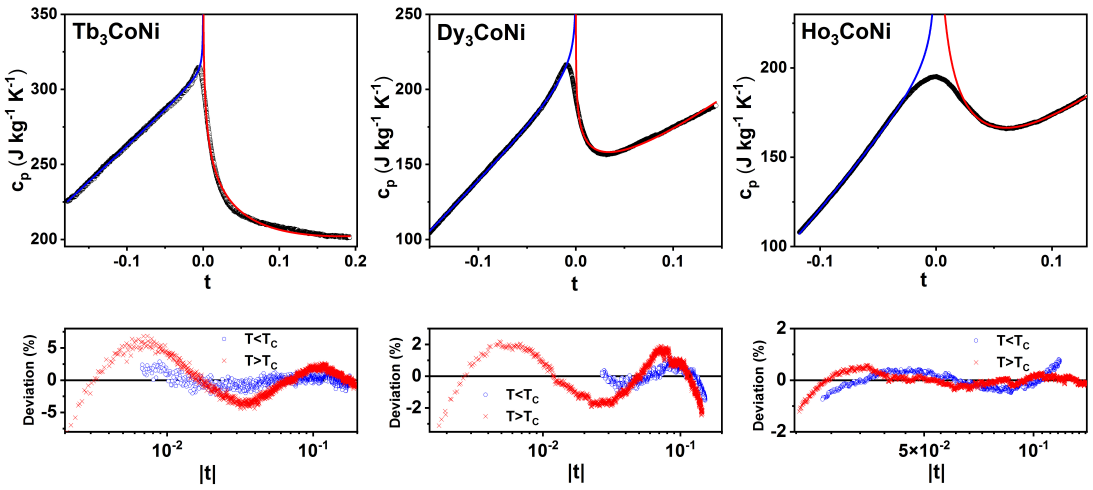


Figure 5.4: Top line: Experimental (black open circles) and fitted curves (continuous lines) of the specific heat as a function of the reduced temperature for the three compounds in the near vicinity of T_C. Bottom line: deviation plots for the fittings (difference between the experimental points and the fittings, in percentage) where blue circles correspond to $T < T_C$, red stars for $T > T_C$.

Let's start by analysing the critical behavior of the the specific heat in the samples where it was possible to obtain. Recalling what has already been seen in Section 3.3, the function customarily used to fit the experimental curves of this magnitude is:

$$c_p = B + Ct + A^{\pm}|t|^{-\alpha}(1 + E^{\pm}|t|^{0.5}) \,. \tag{5.1}$$

where t is the reduced temperature and α (the critical exponent), $A^{\pm}$, B, C, $E^{\pm}$ are adjustable parameters. Superscripts + and − stand for $T > T_C$ and $T < T_C$

respectively. The particulars on how this standard fitting procedure is carried out are described in Section 3.3.1, page 66.

Fig. 5.4 shows the experimental specific heats, the fittings and the deviation plots (the latter are shown below each c_p and contain the difference between the experimental and the fitted points, in percentage). The resulting values of α for the best fittings of Dy_3CoNi and Ho_3CoNi are $\alpha = +0.33 \pm 0.04$ and $\alpha = +0.30 \pm 0.01$, respectively. A^+/A^- is also a critical parameter predicted from renormalization group theory for universality classes, the values from the fittings for this parameter are $A^+/A^- = 0.62$ for Dy_3CoNi and $A^+/A^- = 2.5$ for Ho_3CoNi (though, as the rounding is quite severe, it is not too reliable). The same procedure was tried for Tb_3CoNi, but fitting the experimental data to Eq. (5.1) didn't lead to good enough results and α tended to 0. This suggested that the Mean Field model could be of application in this case. As it has already been discussed in Section 3.3.1, if a compound belongs to the Mean Field universality class, the critical equation would take an asymptotical logarithmic form at the paramagnetic phase, while the ferromagnetic phase may be described by a Landau classical formulation [225, 226]. As a consequence, the paramagnetic region is fitted to:

$$c_p = A \ln t + B + Ct \,, \tag{5.2}$$

whereas the ferromagnetic one is fitted to:

$$c_p = A_1 \frac{T}{\sqrt{1 - 4A_2(T - T_C)}} + B' + C'(T - T_C) \,. \tag{5.3}$$

The best fitting of Tb_3CoNi is obtained precisely when Eqs. (5.2) and (5.3) are used, instead of Eq. (5.1), implying that the critical exponent α is close or equal to 0, which corresponds to the Mean Field model. From the deviation plots in Fig. 5.4 it is clear that the quality of the fittings is very good. The highest deviation is found for the $T > T_C$ branch of Tb_3CoNi in the closest part to T_C; this deviation is within ±6%. For the other cases the deviation is within ±2% or even ±1% in the case of Ho_3CoNi.

Now, let's turn our attention to the magnetic critical behavior in order to obtain the missing critical exponents (β, γ, δ). The procedure followed is the one previously explained in Section 3.4.1. As a starting point for the analysis, the standard Arrott Plot (M^2 isotherms as a function of H/M in the near vicinity of T_C) has been drawn, as well as the Modified Arrott Plots (MAP), plotting $M^{1/\beta}$ versus $(H/M)^{1/\gamma}$ for the 3D Heisenberg ($\beta = 0.369$, $\gamma = 1.396$) and 3D Ising universality classes ($\beta = 0.3265$, $\gamma = 1.237$) (check Table 3.2 in page 77). The standard Arrott Plot shown for Tb_3CoNi, Dy_3CoNi, and Ho_3CoNi in Fig. 5.5 corresponds to the case of the Mean Field universality class ($\beta = 0.5$, $\gamma = 1$), and the slope of the isotherms in this plot indicates the order of the transition, which in all cases on this family turns out to be second order according to the Banerjee criterion (positive slopes) [229].

Regarding the fitting procedure, the case which presents, as a whole, a better bunch of straight and parallel lines is taken as the starting point for the analysis. For this end the deviation of the slopes with respect to the mean value and the R^2 value of the linear fits are considered. In the case of Dy_3CoNi

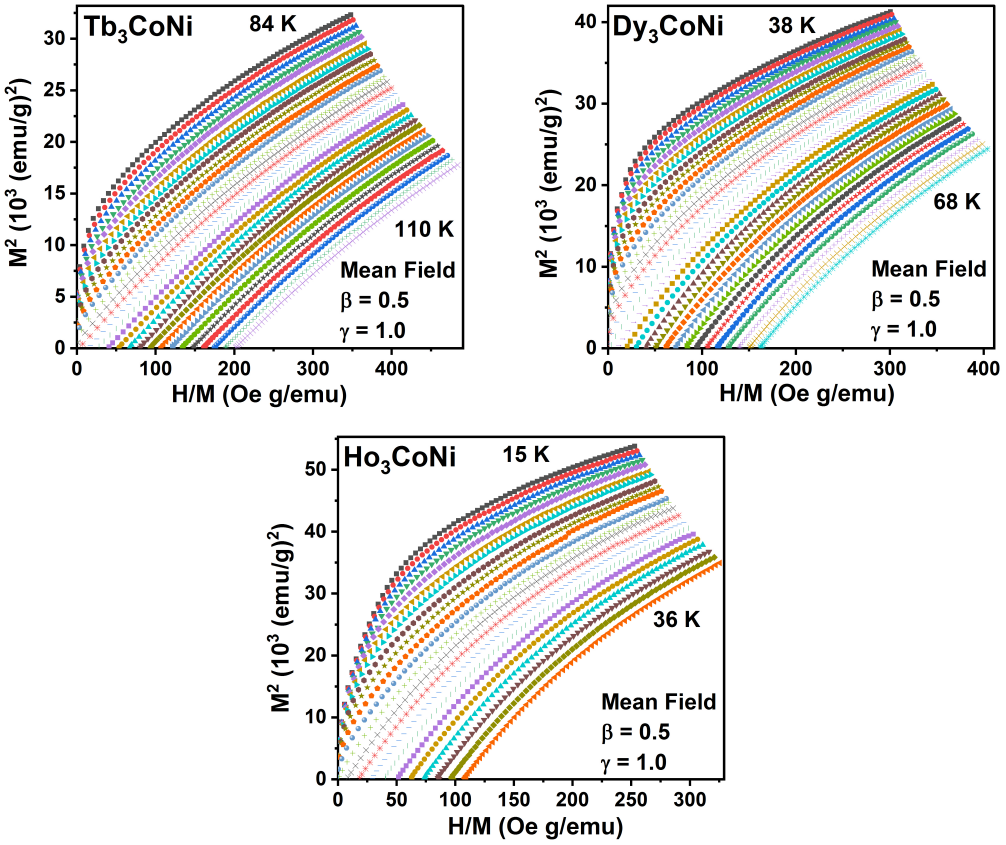


Figure 5.5: Arrot Plots for Tb_3CoNi, Dy_3CoNi, and Ho_3CoNi. Positives slopes indicate the second order nature of the PM-FM phase transition.

and Ho_3CoNi the Ising model has been the starting point while in Tb_3CoNi additional pairs for β and γ have been checked (since the linearity in the general (Modified) Arrott Plots was not good enough with the three previous models), with the result that the best one as starting point has been $\beta = 0.38$, $\gamma = 1.1$. Starting from the one in which the curves at high fields are straighter and more parallel among them, the usual iterative process to find the best values for β and γ has been followed: a linear extrapolation of these isotherms has been taken from the high field values to extract $(M_S)^{1/\beta}$ and $(\chi_0^{-1})^{1/\gamma}$ as an intercept on $M^{1/\beta}$ and $(H/M)^{1/\gamma}$ axis, respectively. As we have already seen, the values of $M_S(T)$ and $\chi_0^{-1}(T)$ obtained this way can be independently fitted to:

$$M_S(T) \sim |t|^{\beta} \qquad (T < T_C)\,, \tag{5.4}$$

$$\chi_0^{-1}(T) \sim |t|^{\gamma} \qquad (T > T_C)\,, \tag{5.5}$$

respectively, in order to extract the critical exponents β and γ. With these values new MAPs are drawn, new extrapolations are done, new fittings to Eqs. (5.4) and (5.5) are performed and so forth till the values of the critical exponents converge and the best parallelism is obtained in the MAPs. Fig. 5.6 shows the result of this iterative process for the three samples (3 rounds were enough for Ho_3CoNi, 2 rounds for Tb_3CoNi and Dy_3CoNi) and Table 5.3 in

page 120 contains the critical exponents obtained through this process with their corresponding uncertainties. As it is clear from the optimized MAPs in the right hand side of Fig. 5.6, the corresponding values of β and γ give straight parallel lines at high fields.

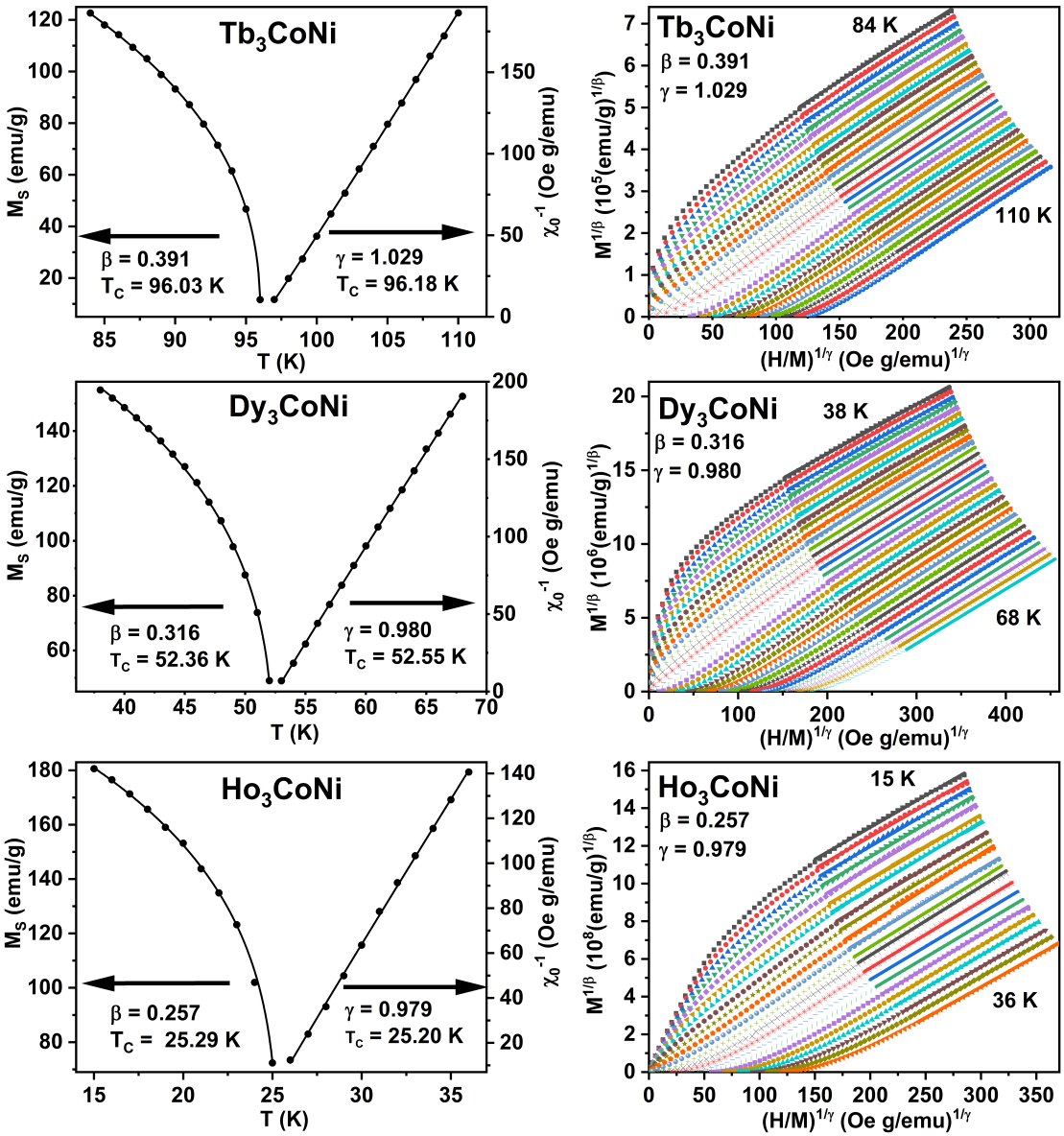


Figure 5.6: Left column: Spontaneous magnetization (left) and inverse of initial susceptibility (right) vs. temperature for Tb_3CoNi, Dy_3CoNi, and Ho_3CoNi. The solid curves correspond to the fits to Eq. (5.4) and (5.5). Right column: optimized Modified Arrot Plots.

As a second step, the Kouvel Fisher (KF) analysis has been undertaken, which assesses that $M_S(dM_S/dT)^{-1}$ and $\chi_0^{-1}(d\chi_0^{-1}/dT)^{-1}$ have a linear behavior with respect to T, with slopes $1/\beta$ and $1/\gamma$, respectively. Fig. 5.7 shows these data and the corresponding fittings, from which new β and γ are obtained. As can be checked in Table 5.3 (page 120), the KF methods gives values very close to the previous ones for each material. In this analysis, the Curie temperature

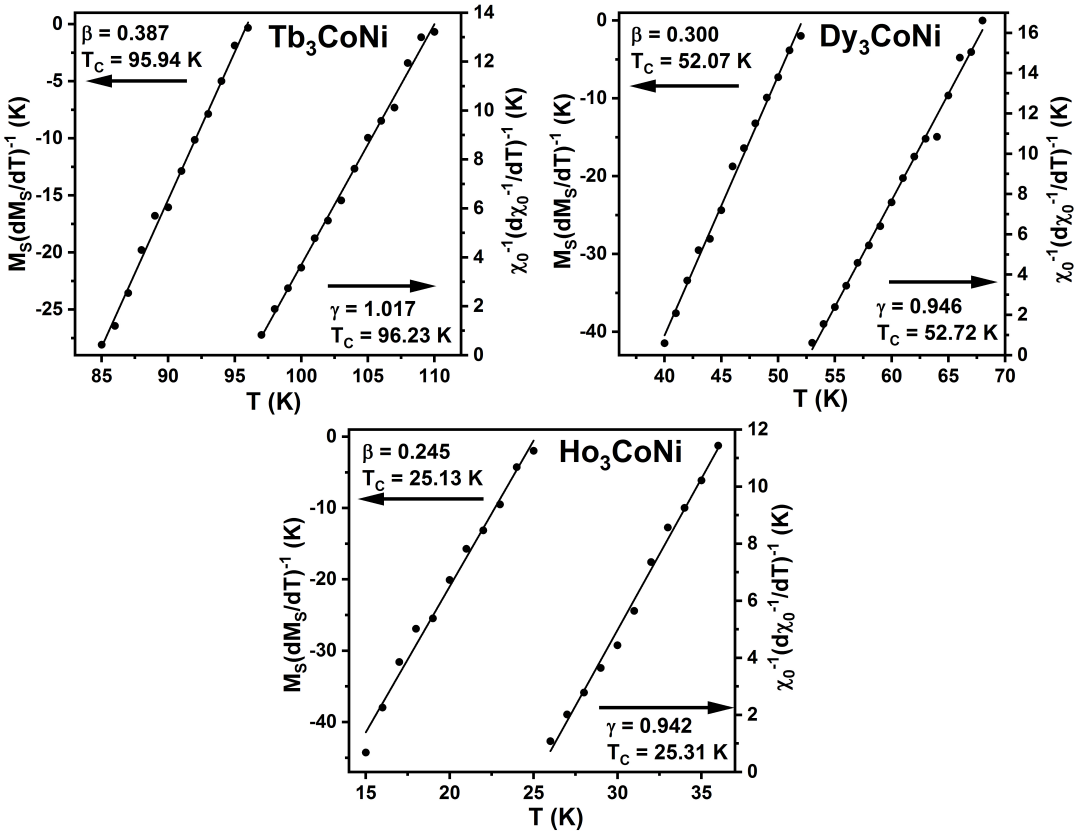


Figure 5.7: Kouvel Fisher plot of spontaneous magnetization (left) and inverse of initial susceptibility (right) for each compound: Tb_3CoNi, Dy_3CoNi, and Ho_3CoNi. The straight lines are linear fits, from which T_C and the critical exponents are obtained.

is found from the intercept of the straight fitted lines on the temperature axis, which has also been gathered in Table 5.3.

Then, the last magnetic critical exponent, δ, is obtained from the critical isotherm, which, according to the theory, obeys the following relation:

$$M \sim H^{1/\delta} \qquad (T = T_C)\,. \tag{5.6}$$

Fig. 5.8 shows the critical isotherm for the three samples in a log-log scale. In this form, a fit to a linear function easily gives the value of δ as the inverse of the slope. The δ values obtained through this method can be compared with the one calculated using the experimentally found β and γ and the *Widom scaling law*:

$$\delta = 1 + \gamma/\beta\,. \tag{5.7}$$

All δ values are collected in Table 5.3, and it can be seen that in all cases the agreement among the experimental ones and the ones calculated using relation (5.7) is very good, further confirming the correct critical exponent values.

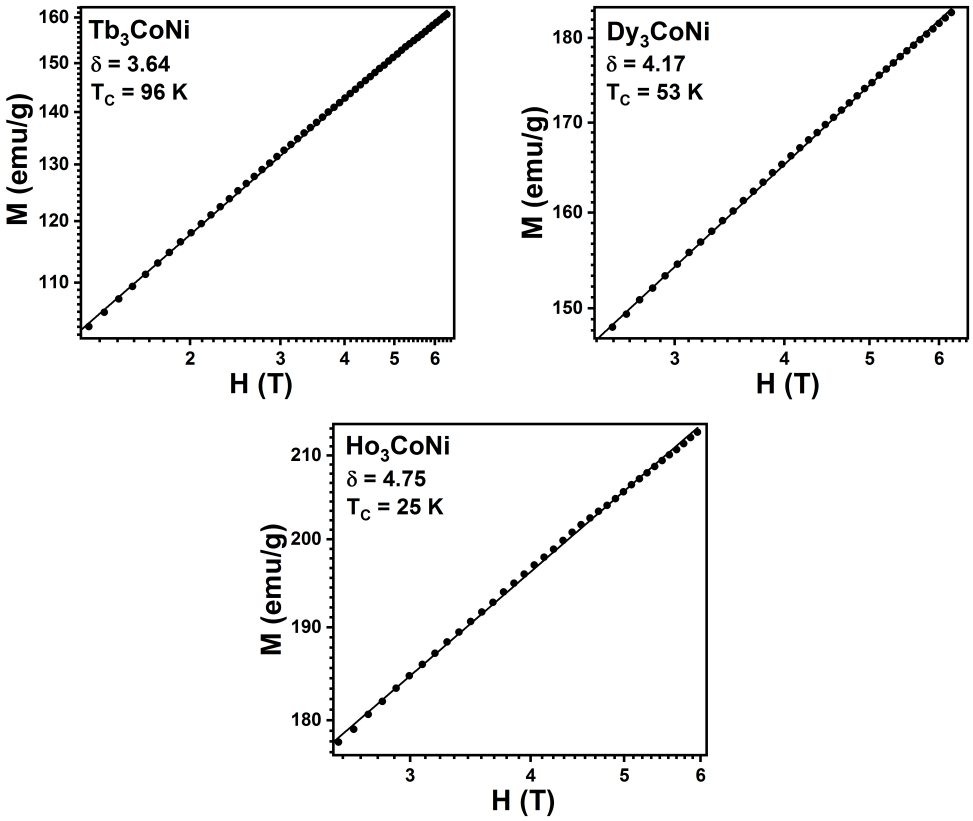


Figure 5.8: M vs. H plot in a log-log scale collected at critical isotherms for Tb_3CoNi, Dy_3CoNi, and Ho_3CoNi (from left to right).The straight line, in each case, is the linear fit from which the exponent δ is obtained.

The last step consists on checking the fulfillment of the magnetic equation of state:

$$M(H,t) = |t|^{\beta} f_{\pm}(H/|t|^{\beta+\gamma}) \,, \tag{5.8}$$

which, with the correct β and γ values, should make all the isotherms collapse into two independent branches, one for those above T_C, and another one for those below it. Fig. 5.9 shows that a very good collapse of the isotherms is obtained in the three cases when the corresponding critical exponents are used. This collapse is generally accepted as a severe confirmation of the validity of the critical exponents to describe the magnetic transition.

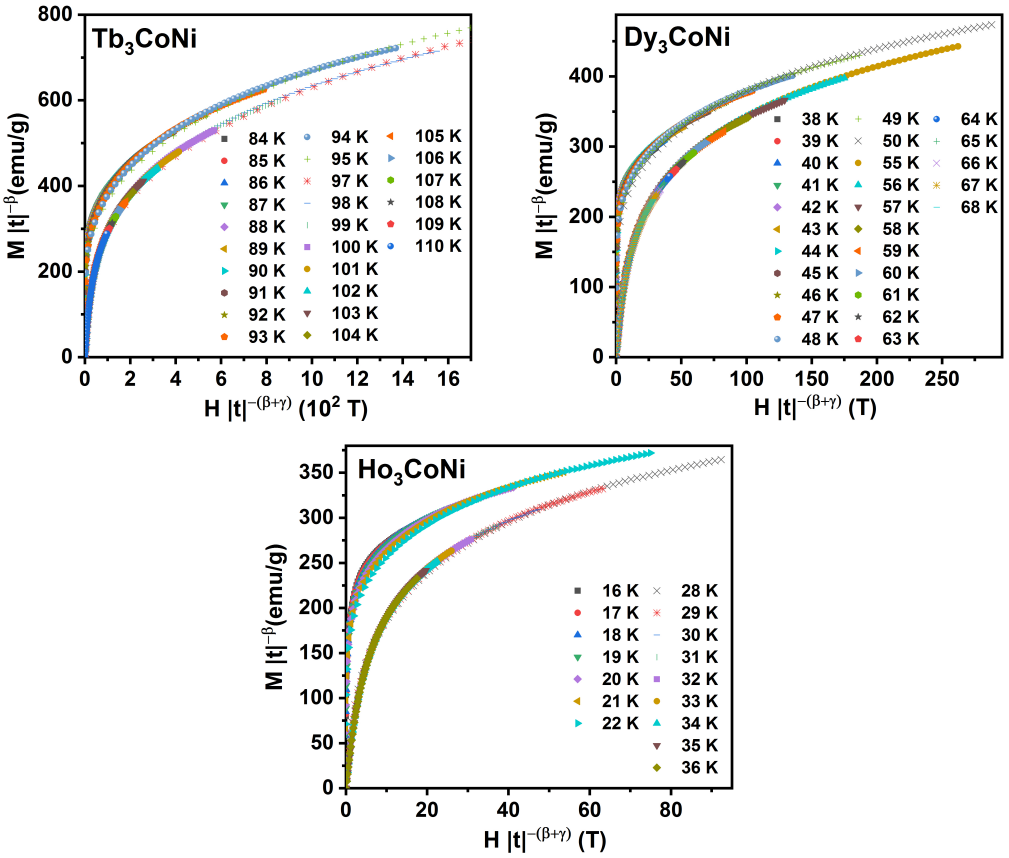


Figure 5.9: The renormalized magnetization plotted as a function of the renormalized field following Eq. (5.8) for Tb_3CoNi, Dy_3CoNi, and Ho_3CoNi. In the three cases, the data collapse onto two separate branches, one above and one below the respective T_C.

Material	Technique	β	γ	δ	α	A^+/A^-
Tb_3CoNi	MAP	0.391 ± 0.002	1.03 ± 0.01	3.63 ± 0.04^a		
		$T_C = 96.03 \pm 0.01$ K	$T_C = 96.18 \pm 0.06$ K			
	KF Method	0.387 ± 0.007	1.02 ± 0.02	3.6 ± 0.1^a		
		$T_C = 95.94 \pm 0.02$ K	$T_C = 96.23 \pm 0.09$ K			
	Critical Isotherm			3.64 ± 0.01		
	PPE calorimetry				$\to 0$	Non applicable
Dy_3CoNi	MAP	0.316 ± 0.003	0.98 ± 0.08	4.11 ± 0.05^a		
		$T_C = 52.36 \pm 0.03$ K	$T_C = 52.55 \pm 0.05$ K			
	KF Method	0.300 ± 0.006	0.95 ± 0.02	4.2 ± 0.1^a		
		$T_C = 52.07 \pm 0.04$ K	$T_C = 52.72 \pm 0.09$ K			
	Critical Isotherm			4.17 ± 0.01		
	PPE calorimetry				$+0.33 \pm 0.04$	0.62
Ho_3CoNi	MAP	0.257 ± 0.003	0.98 ± 0.03	4.8 ± 0.2^a		
		$T_C = 25.29 \pm 0.02$ K	$T_C = 25.2 \pm 0.1$ K			
	KF Method	0.245 ± 0.009	0.94 ± 0.03	4.8 ± 0.3^a		
		$T_C = 25.13 \pm 0.04$ K	$T_C = 25.3 \pm 0.1$ K			
	Critical Isotherm			4.75 ± 0.02		
	PPE calorimetry				$+0.30 \pm 0.01$	2.5

[a] Calculated from Eq. (5.7): $\delta = 1 + \gamma/\beta$.

Table 5.3: Critical exponents obtained for Tb_3CoNi, Dy_3CoNi, and Ho_3CoNi.

In order to discuss our results and facilitate the reading, Table 5.4 contains the principal university classes which are of interest for our analysis.

Universality class	d	N	α	A^+/A^-	β	γ	δ
Mean Field			0	-	0.5	1.00	3.00
3D Ising	3	1	0.11	0.536	0.3265	1.237	4.79
3D XY	3	2	-0.014	1.06	0.348	1.317	4.78
3D Heisenberg	3	3	-0.134	1.52	0.369	1.396	4.78
Chiral XY	3	2	0.34	0.36	0.253	1.13	5.47
Chiral Heisenberg	3	3	0.24	0.54	0.30	1.17	4.90
Tricritical Mean Field			0.5		0.25	1.00	5.00

Table 5.4: Critical exponents for several universality classes. d dimension of the system, N number of spin components.

In the particular case of Tb_3CoNi, the value of γ (1.03 ± 0.01) and the fitting of the specific heat ($\alpha \to 0$) agree quite well with the Mean Field model ($\gamma_{MF} = 1.0$, $\alpha_{MF} = 0$) while β (0.391 ± 0.002) and δ (3.64 ± 0.01) are in between the 3D Heisenberg ($\beta_{Heis} = 0.369$, $\delta_{Heis} = 4.78$) and the Mean Field model ($\beta_{MF} = 0.5$, $\delta_{MF} = 3.0$) (see Table 5.4). This would suggest that the PM-FM transition in this case would belong to the Mean Field model, indicating that long range order interactions are responsible for this transition but with a certain deviation from it. In fact, renormalization group analysis maintains that the range of the exchange interaction $J(r)$ is determined by the critical parameter γ by means of the following dependence [317]:

$$J(r) \sim r^{-(d+\sigma)}\,, \tag{5.9}$$

where d is the dimension of the system, r the distance and σ the range of the exchange interaction. The relation between the latter and γ is given by:

$$\gamma = 1 + \frac{4}{d}\left(\frac{N+2}{N+8}\right)\Delta\sigma + \frac{8(N+2)(N-4)}{d^2(N+8)^2}\left[1 + \frac{2G\left(\frac{d}{2}\right)(7N+20)}{(N-4)(N+8)}\right]\Delta\sigma^2\,, \tag{5.10}$$

where $\Delta\sigma = \sigma - d/2$ and $G\left(\frac{d}{2}\right) = 3 - \frac{1}{4}\left(\frac{d}{2}\right)^2$, being N the spin dimensionality. For 3 dimensional systems, with $N = 3$, expression (5.10) is reduced to:

$$\gamma \approx 1 + 0.606\Delta\sigma + 0.630687\Delta\sigma^2\,, \tag{5.11}$$

with $\sigma = \Delta\sigma + \frac{3}{2}$. Therefore, in the case of Tb_3CoNi, with $\gamma = 1.03$, the resulting value is $\sigma = 1.55$. For three dimensional materials where the spin is also three dimensional ($d = 3$, $N = 3$), long-range interaction corresponds to $\sigma = 1.5$, while, for instance, for the short-range 3D Heisenberg universality class, $\sigma = 2$ [317–320]. This result further confirms that the magnetic interactions are closer to a long-range interaction than to short-range ones.

In the case of Dy_3CoNi, β (0.316±0.003) and γ (0.98±0.08) agree quite well with the Chiral Heisenberg universality class ($\beta_{C.Heis}$ = 0.30, $\gamma_{C.Heis}$ = 1.17); the sign of α and the ratio A^+/A^- (0.62) also agree with it ($A^+/A^-_{C.Heis}$ = 0.54), though the value of α (+0.33 ± 0.04) agrees better with the Chiral XY ($\alpha_{C.XY}$ = 0.34); as a whole, the complete set of exponents is between the two Chiral models. Finally, as can be seen from Tables 5.3 and 5.4, in the case of Ho_3CoNi, there are three exponents (α, β and γ) whose values are quite close to the Chiral XY model.

These critical exponents imply that Dy_3CoNi and Ho_3CoNi are not common collinear ferromagnets but a certain kind of frustrated non-collinear magnets. Renormalization group theories and Monte-Carlo approaches have been used to study the symmetry and the corresponding critical exponents of frustrated non-collinear magnets, among which are the stacked triangular antiferromagnets (such as the vanadium dihalides VCl_2, VBr_2 or $CsMnBr_3$, $CsVCl_3$) or the helical magnets (such as pure Dy and Ho), developing what is known as the Chiral XY class, whose critical exponents can be found in Table 5.4 and references [39, 264, 321–323]. Experimental measurements on all these materials have shown that they belong to the Chiral XY universality class [324–326].

The low ordering temperature from the paramagnetic phase indicates the degree of magnetic frustration which takes place in R_3CoNi. The magnetic properties in this system mainly arise from the rare-earth (it has been established in Tb_3CoNi that neither Co nor Ni present magnetic moment [302]) though the ordering temperatures are much lower than in the case of the pure systems where the spins take an helical arrangement (179 K in Dy, 132 K in Ho [1]), in opposition to the behaviour found in other intermetallic families where the magnetism also arises solely from the rare-earth element and it is found that the transition temperature is increased with respect to that of the rare-earth, such as in the RTX family presented in Chapter 4. Without neutron diffraction measurements, it is not possible to ascertain which the spins arrangement is in Dy_3CoNi or Ho_3CoNi; however, the critical exponents here obtained suggest some kind of non-collinearity as it happens in pure Dy and Ho [1, 2]. Canted ferromagnetic or helical arrangements have also been found in other intermetallic systems where only the rare-earth presents magnetic moment, such as Dy_6MnBi_2, Ho_6MnTe_2, Ho_6CoTe_2 [327].

In the case of pure Dy and Ho it has been also suggested that the magnetic transition might be weakly first order, as the critical exponents of the Chiral XY class are very close to the Tricritical Mean Field model (see Table 5.4). In the study presented in this work, the experimental values of the critical exponents for Ho_3CoNi, are indeed very close to this class, save for α. Nevertheless, we discard this option since in the thermal measurements (which have been done at a very low pace, 20 mK/min) there is no hysteresis at all in heating or cooling runs and the shape of the transition is exactly the same one. Furthermore, as has been already mentioned, the slopes in the Arrot Plots are positive, which, according to the Banerjee criterion, is the case in second order phase transition [229].

5.3.4 Magnetocaloric effect in R_3CoNi family

In order to study the magnetocaloric properties of the five magnetic compounds of the series, magnetization isotherms have been measured from 2 K to temperatures well above their corresponding T_C, as described in Section 5.2. Since all the PM-FM transitions are second order, the *Maxwell relation* has been used to calculate the magnetic entropy change as a function of temperature and magnetic field in the usual way:

$$\Delta S_M(T, \Delta H) = \mu_0 \int_{H_0}^{H_1} \left(\frac{\partial M}{\partial T} \right)_H dH \,. \tag{5.12}$$

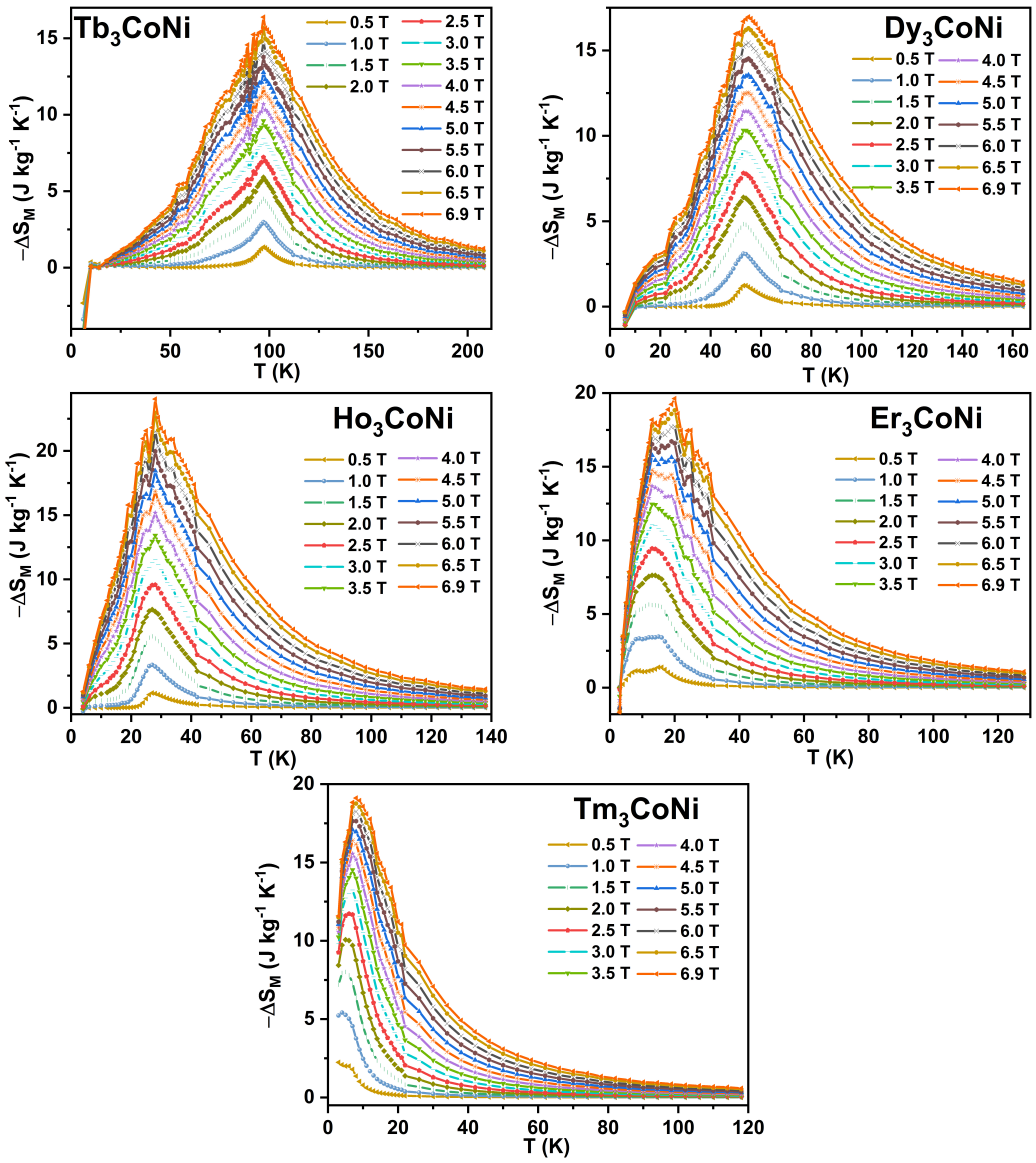


Figure 5.10: Magnetic entropy change $-\Delta S_M$ for $\mu_0 \Delta H$ from 0.5 T to 6.9 T for Tb_3CoNi, Dy_3CoNi, Ho_3CoNi, Er_3CoNi, and Tm_3CoNi.

The results are shown in Fig. 5.10 where it is seen that there is an important direct magnetocaloric effect for all of them. Table 5.5 presents the maximum

values of the curves $|\Delta S_M^{pk}|$ for $\mu_0\Delta H$ = 2, 5 and 6.9 T, together with the refrigerant capacities, calculated using the two standard definitions:

$$RC_{\text{FWHM}} = |\Delta S_M^{pk}|\delta T_{\text{FWHM}} \,, \tag{5.13}$$

where δT_{FWHM} is the temperature width of the magnetic entropy change at half maximum (FWHM) and:

$$RC_{\text{Area}} = \int_{T_1}^{T_2} |\Delta S_M(T, \Delta H)| dT \,, \tag{5.14}$$

which is the area enclosed by the magnetic entropy change vs. temperature curve in the range enclosed by the full width at half maximum. The results at $\mu_0\Delta H$ = 5 T are the ones which are more comparable with literature. We can see in Table 5.5 that the maximum entropy changes at $\mu_0\Delta H$ = 5 T are 12.8, 13.6, 18.5, 15.8 and 17.1 J/kgK for Tb_3CoNi, Dy_3CoNi, Ho_3CoNi, Er_3CoNi and Tm_3CoNi, respectively, while their RC_{FWHM} are 699, 597, 582, 449, and 412 J/kg (as the magnetic entropy change peak for Tm_3CoNi is not complete on the lower temperature side, the common arrangement of considering it symmetric with respect to the maximum has been adopted to evaluate RC_{FWHM}). Although the highest $|\Delta S_M(T, \Delta H)|$ value at $\mu_0\Delta H$ = 5 T is given by Ho_3CoNi, the highest RC_{FWHM} and RC_{Area} values are given by Tb_3CoNi. This is due to a broader peak in the latter case, as can be easily observed in Fig. 5.10. If the values collected in Table 5.5 are compared with results shown in literature for other rare-earth based materials in their respective temperature ranges [82, 84, 91, 108], they are among the highest ones, making this intermetallic family specially promising for future applications and showing that the working temperature range can be efficiently tuned by exchanging the rare-earth, while maintaining good magnetocaloric properties. To complete the analysis of the magnetocaloric properties in this family, we can also consider the figures of merit presented in Ref. [300] for Gd_3CoNi (T_C = 176 K) at $\mu_0\Delta H$ = 5 T: $|\Delta S_M^{pk}|$ = 8.3 $\text{Jkg}^{-1}\text{K}^{-1}$, and RC_{FWHM} = 546 J/kg. These values are in agreement with the values we have obtained for the compounds with heavier rare-earth elements. The absolute value of the magnetic entropy change peak ($|\Delta S_M^{pk}|$) slightly decreases-for Gd-based sample, following the tendency we observe in our compounds. On the other hand, the RC_{FWHM} value is greater than the one in Er_3CoNi and Tm_3CoNi, but without reaching the values found for the other three compounds. It would become very interesting now to investigate the possibility of mixing the rare-earths to see if this working range can be efficiently displaced or extended while maintaining a high value of the maximum of the magnetic entropy change and of the refrigerant capacity, as it happens with other rare-earth intermetallic families [82, 85].

It is worth mentioning that, paying attention to Fig. 5.10, it can be seen that there is a small inverse magnetocaloric effect (IMCE) at very low temperature, very clear for Tb_3CoNi, small for Dy_3CoNi and Er_3CoNi and nearly negligible for Ho_3CoNi. This is related, in all cases, to a certain antiferromagnetic behavior at those temperatures which was already discussed before, when we saw that in the magnetization isotherms at low temperature the magnetization in-

$\mu_0\Delta H$	Magnitude	Tb_3CoNi $T_C = 97$ K	Dy_3CoNi $T_C = 53$ K	Ho_3CoNi $T_C = 27$ K	Er_3CoNi $T_C = 13$ K	Tm_3CoNi $T_C = 7$ K
2 T	$\lvert\Delta S_M^{pk}\rvert$ (J kg^{-1} K^{-1})	5.9	6.4	7.6	7.6	10.0
	RC_{FWHM} (J kg^{-1})	217	166	146	152	142[a]
	RC_{Area} (J kg^{-1})	152	128	113	124	-
5 T	$\lvert\Delta S_M^{pk}\rvert$ (J kg^{-1} K^{-1})	12.8	13.6	18.5	15.8	17.1
	RC_{FWHM} (J kg^{-1})	699	597	582	449	412[a]
	RC_{Area} (J kg^{-1})	516	454	433	356	-
6.9 T	$\lvert\Delta S_M^{pk}\rvert$ (J kg^{-1} K^{-1})	16.4	17.0	24.0	19.6	19.1
	RC_{FWHM} (J kg^{-1})	1008	887	876	681	560[a]
	RC_{Area} (J kg^{-1})	745	675	644	521	-

[a] Calculated considering the symmetry of the peak.

Table 5.5: Maximum of the magnetic entropy change $|\Delta S_M^{pk}|$ and refrigerant capacities RC_{FWHM}, RC_{Area} at applied fields $\mu_0\Delta H = 2$, 5 and 6.9 T for the five compounds. The indicated T_C corresponds to the positiom of the maximum of $-\Delta S_M$.

creases (for a given field) with temperature, typical of an antiferromagnetic state (see Fig. 5.3). This is specially marked in the case of Tb_3CoNi, where the presence of metamagnetic transitions was already confirmed in Fig. 5.2. Nevertheless, the magnitude of the magnetic entropy change as well as the temperature span of these phenomena rules out any practical application.

The assignation of a particular universality class to the PM-FM transition can be further checked by means of the magnetocaloric variables, as there are several scaling equations that they also fulfil. In particular, the maximum of the magnetic entropy change scales with a critical exponent n which, as already discussed in Section 3.5, is a combination of the magnetic critical exponents β and δ:

$$|\Delta S_M^{pk}| \propto H^{1+\frac{1}{\delta}(1-\frac{1}{\beta})} = H^n \,, \tag{5.15}$$

while both defined refrigerant capacities (RC_{FWHM} and RC_{Area}) scale as:

$$RC \propto H^{1+1/\delta} \,. \tag{5.16}$$

When representing the previous expressions with the values of β and γ obtained for each compound, the experimental points should lie on a straight line which would allow the extrapolation of their values at magnetic fields at which they where not measured. This is precisely what we see in Fig. 5.11. In al cases the experimental points lie extremely well along straight lines (a red line has been added for visual help), showing the correct fulfilment of the scalings in Eqs. (5.15) and (5.16), thus, confirming the validity of the critical exponents contained in Table 5.5.

It was also shown in Section 3.5 that, in the case of second order phase transitions, it is possible to build universal curves for the magnetic entropy

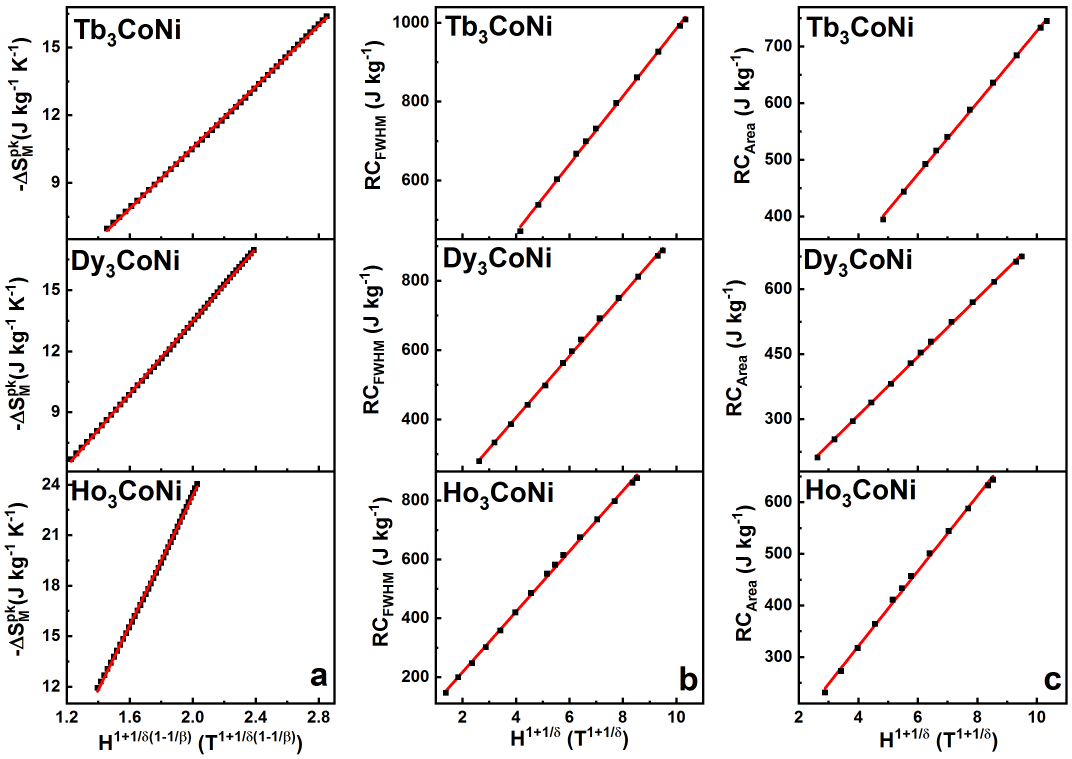


Figure 5.11: Field dependence of the peak magnetic entropy change, column (a), scaling laws for RC_{FWHM}, column (b), and RC_{Area}, column (c), for Tb_3CoNi, Dy_3CoNi and Ho_3CoNi from top to bottom respectively. The values of β and δ used are the ones presented in Table 5.3. Straight lines are linear fits acting as visual guides.

change in the close vicinity of the critical temperature. This method implies that there is no other phase transition close enough to meddle with the first one. Therefore, this method has been applied to the case of the paramagnetic to ferromagnetic transition in Tb_3CoNi, Dy_3CoNi, and Ho_3CoNi. The magnetic entropy change is normalized with its peak value and the temperature axis is rescaled. As a first step, one reference temperature T_r is used in order to obtain a universal curve, scaling the temperature axis as follows:

$$\theta_1 = \frac{T - T_C}{T_r - T_C}\,, \tag{5.17}$$

where T_r is selected to be above T_C, corresponding to a particular fraction of $|\Delta S_M^{pk}|$, which has been chosen in these cases as 0.5. Nevertheless, it has also been shown in Section 3.5 that, in many cases, two reference temperatures T_{r1}, T_{r2} (where $T_{r1} < T_C < T_{r2}$) are necessary to build up the universal curves [235]. The scaling of the temperature axis in this case is as follows:

$$\theta_2 = \begin{cases} -(T - T_C)/(T_{r1} - T_C)\,, & T \leqslant T_C \\ (T - T_C)/(T_{r2} - T_C)\,, & T > T_C \end{cases}. \tag{5.18}$$

The universal curves using one and two reference temperatures are shown in Fig. 5.12, for the three samples: Tb_3CoNi, Dy_3CoNi, and Ho_3CoNi. The

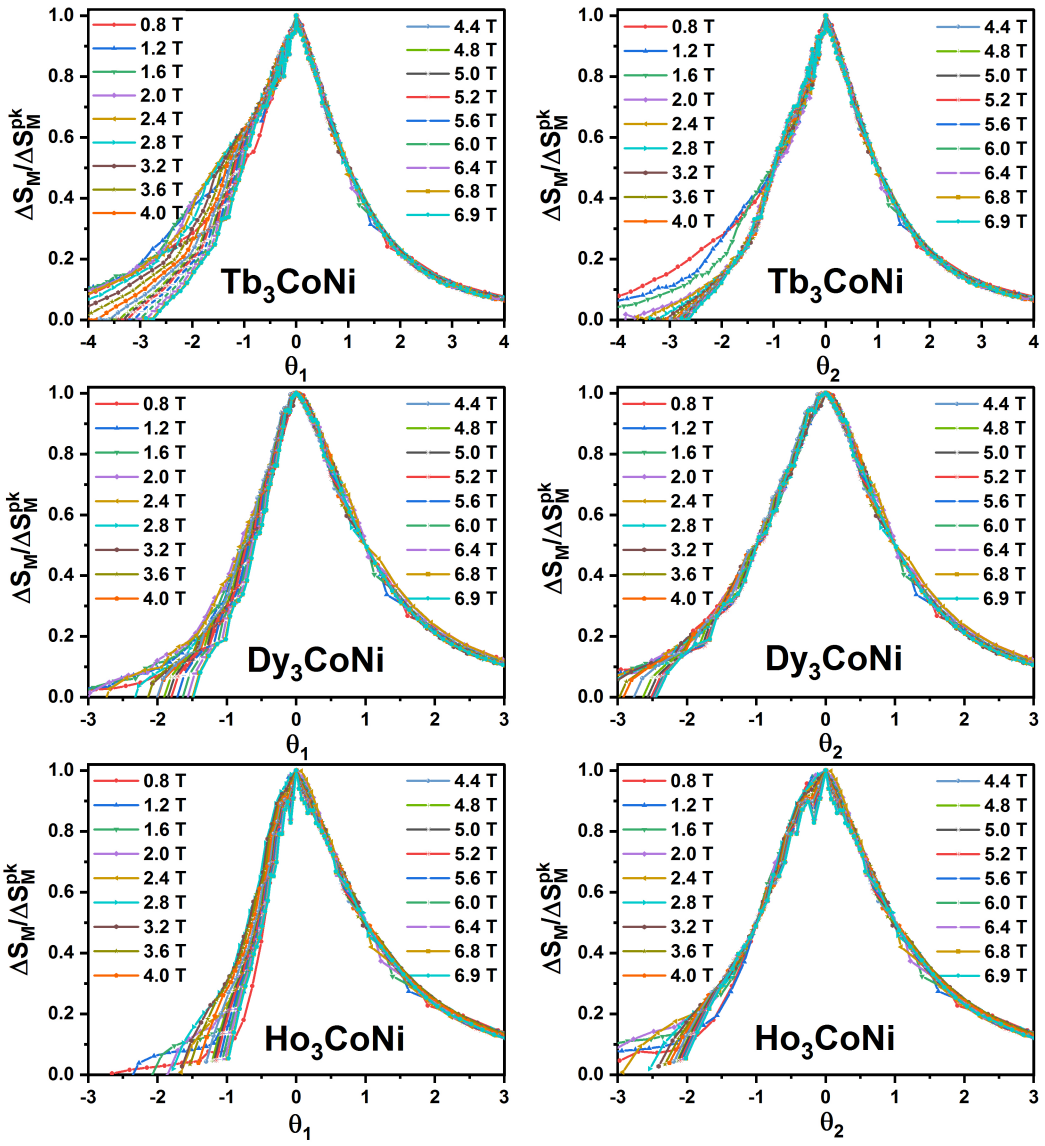


Figure 5.12: Universal curve with the rescaled magnetic entropy changes using one (left) or two (right) reference temperatures, for Tb_3CoNi, Dy_3CoNi and Ho_3CoNi from top to bottom respectively.

overlapping must take place in the near vicinity of the second order phase transition (the critical region) [236,237], where critical theory is fulfilled, which happens both with one or two reference temperatures but better in the last case. It is generally accepted that there are two causes for the deviations when using only one reference temperature: either demagnetization effects (where the effect is that the curves below T_C move to higher values of $\Delta S_M/\Delta S_M^{pk}$ as the magnetic field increases [140]) or the presence of another magnetic phase with a much higher T_C than the one of the transition under study and, in this case, the curves would move to smaller values of $\Delta S_M/\Delta S_M^{pk}$ as the magnetic field increases [248]. In Fig. 5.12 it is clearly seen that the evolution of the curves at low fields is the one due to demagnetization effects, as expected, but that at

fields higher than 1.6 T for Tb_3CoNi, 2 T for Dy_3CoNi and 2.8 T for Ho_3CoNi, the tendency is reversed and it is now the one described in the second case. Nevertheless, there is no trace of any other magnetic phase, neither in the X-ray nor in all the magnetic measurements performed up to room temperature. It has lately been discovered that the presence of additional magnetic phase transitions is not the only cause of the lack of universal scaling at low temperatures with that particular behavior with the field, as it has been shown that, in several single-phase Gd-alloys, the lower the critical temperature, the stronger this effect [237]. It is suggested that it might also have to do with the universality class not being a perfect Mean Field. This behavior has also been observed in other heavy rare-earths compounds such as $RTiO_3$ (R = Dy, Ho, Er, Tm, Yb) [328] or HoZn [329]. If we focus our attention on the regions far below T_C, there is a deployment of non-overlapping curves, which corresponds to temperatures well beyond the critical region, where the spin reorientation transitions have already taken place. The fact that these universal curves have been obtained is further proof of the second order character of the PM-FM transition in these materials.

Finally, the scaling relation of the reference temperature T_r, which was already presented in Section 3.5, has also been checked:

$$T_r \propto H^{1/(\beta+\gamma)} . \tag{5.19}$$

Were β and γ are the critical exponents already obtained for each material and presented in Table 5.3, page 120. Fig. 5.13 shows the results. The red straight line is a linear fit in order to show that the experimental points lie very well on it. In the case of Ho_3CoNi, the experimental points are noisier. However, the fulfilment of the scaling relation in Eq. (5.19) is very good.

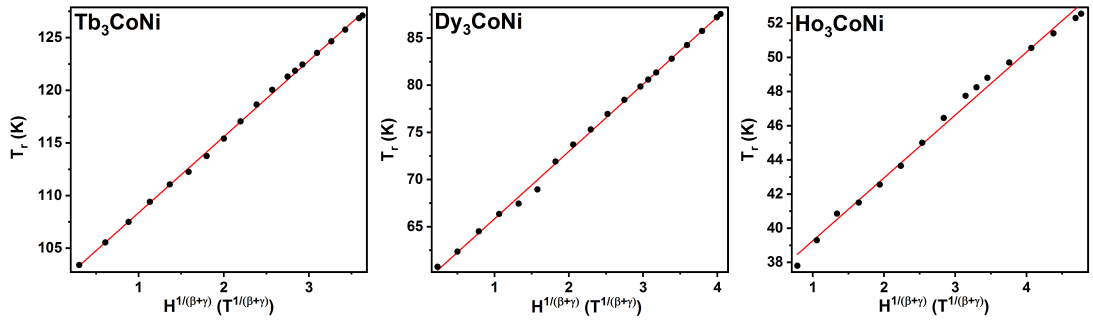


Figure 5.13: Field dependence of the reference temperature T_r for Tb_3CoNi, Dy_3CoNi and Ho_3CoNi from left to right respectively. The values of β and γ used are the ones presented in Table 5.3. Straight lines are linear fits acting as visual guides.

It is worth emphasizing the usefulness of the scaling of the magnetocaloric variables, as it allows their extrapolation to different fields, which might not be experimentally accessible. Moreover, using the scaling laws together with the universal curves, also called "master curves", allows the extrapolation of the whole magnetic entropy change curve to non-accessible magnetic fields and temperature ranges [236].

5.4 Conclusions

The formation and properties of ternary rare-earth intermetallics with stoichiometry R_3CoNi have been studied. Besides the recently reported Gd_3CoNi and Tb_3CoNi, the new compounds with R = Dy, Ho, Er, and Tm have been identified; they are isomorphous, all crystallizing in the rhombohedral Er_3Ni_2-type structure. The magnetic and magnetocaloric properties of this novel intermetallic family R_3CoNi (R = Tb, Dy, Ho, Er, Tm) have been studied in detail showing that they all present a second order paramagnetic to ferromagnetic transition at temperatures in the range 96-6 K, with different reorientation transitions below the respective T_C. The set of critical exponents (α, β, γ, δ) for this second order phase transition has been experimentally found for three cases: Tb_3CoNi, which was found to be close to the Mean Field model, implying that long range ordering interactions rule the transition; Dy_3CoNi, between the Chiral XY and Chiral Heisenberg; Ho_3CoNi, close to the Chiral XY model. These two last cases suggest that they are some kind of frustrated non-collinear ferromagnets. The whole family presents very competitive magnetocaloric properties in their respective temperature ranges, with high magnetic entropy changes (from 12.8 to 18.5 J/kgK at $\mu_0\Delta H = 5$ T) and refrigerant capacities (from 412 to 699 J/kg at $\mu_0\Delta H = 5$ T); these results indicate the possibility of tuning the application range by a proper mixing of the rare-earth ions. The scaling of the magnetocaloric variables (magnetic entropy change, refrigerant capacity, and reference temperature) for Tb_3CoNi, Dy_3CoNi, and Ho_3CoNi confirms the validity of the universality classes. Finally, universal curves for the magnetocaloric properties have also been found in these three cases.

6 | R_3T intermetallics

"Science progresses best when observations force us to alter our preconceptions."

– Vera Rubin

The intermetallic family R_3T (R = Gd, Tb, Dy, Ho, Er; T = Co, Ni) is specially interesting because of its promising technological applications: in the first place, these compounds are potential cryocoolers in the range of helium, hydrogen and nitrogen liquefaction, due to the presence of magnetocaloric effect; besides, they also present giant magnetoresistance as well as relatively high spin-ordering temperatures for the rare-earths [330]. Their complex magnetic structures and variety also make them interesting from the point of view of basic research.

In this chapter an extensive presentation of three single crystals belonging to the R_3T family will be done. Different thermal properties, such as the thermal diffusivity, specific heat or thermal conductivity, will be used to discuss the critical behavior of Dy_3Co, Tb_3Co and Tb_3Ni. The magnetic and magnetocaloric properties of the latter two will also be presented. Finally, the rotating magnetocaloric effect (RMCE) will be explored for the anisotropic Tb_3Ni compound.

The following materials will be studied in this chapter:

- **Dy_3Co**
- **Tb_3Co**
- **Tb_3Ni**

6.1 Introduction

R_3T family has attracted a big interest from the scientific community. In fact, different studies have been undertaken to study the particulars of the magnetic ordering and other properties of the rare-earth spins in R_3(Co; Ni) with R = La [331], Pr [331], Nd [332], Gd [77, 331–337], Tb [81, 331, 332, 338, 339], Dy [80, 332, 340–342], Ho [331, 332, 343], and Er [79, 331, 332, 344]. A shared feature among all of them is that there is an antiferromagnetic ordering from the paramagnetic phase, with T_N decreasing as the atomic number increases.

This family has the particularity of being the one with higher rare-earth contents within the larger and more general R_nT_m family. This is relevant because the magnetic moment of the *3d* transition metal (T) depends on the n : m ratio. If this ratio is small, the transition metal ions can have a net moment regardless of the magnetic state of the rare-earth sublattice. As the n : m ratio increases there is a decrease in the magnetic moment of the transition metals ions due to the filling of the *3d* band of T atoms by outer-shell electrons of R atoms [345, 346]. The latter is the case in R_3T family, where it has been found that the magnetic moment of the transition metal is lost.

All the members of this family have an orthorhombic crystal structure of the Fe_3C type (space group *Pnma*) where the rare-earth occupies two non-equivalent positions: *4c* (site symmetry *m*) and *8d* (site symmetry *I*) [306, 347]. This arrangement forms rare-earth layers parallel to the *bc* plane which are separated by T ions. Since the latter ions do not have a net magnetic moment, all the magnetism is expected to arise from the rare-earth. The spin ordering in rare-earths has traditionally been explained by means of the RKKY (Ruderman–Kittel–Kasuya–Yosida) interaction, which consists of an indirect exchange interaction between *4f-4f* electron spins by means of conduction electron spins. But this description has been found not to be adequate for rare-earth in metals, where it presents significant shortcomings. In the model introduced by Campbell [348] (which is valid for pure R compounds), the *4f-4f* coupling consists of two steps: an intra-atomic *4f-5d* exchange followed by an inter-atomic *5d-5d* spin interaction between neighbouring R atoms, leading to a *4f-5d-5d-4f* interaction. This mechanism has been found to be the exchange interaction taking part within the R layers. However, the interaction between the layers is mediated by the *3d* electrons of T elements, despite the complete absence of their magnetic moment. Therefore, the process between the layers would be described by a *4f-5d-3d-5d-4f* interaction [306]. Furthermore, as it is well known, the increase of the rare-earth atomic number contracts the *4f* shell reducing the overlap between this and the *5d* shell. This fact implies a decrease on the *4f-5d* exchange energy for increasing atomic numbers of R.

Neutron diffraction studies have suggested a survival of short-range order magnetic interactions well above the Néel temperature of these compounds, up to 5-6 times T_N. The stronger intra-layer R-R interactions in comparison with the inter-layer ones, together with the geometrical frustration caused by the low symmetry positions occupied by the R elements has been proposed as an explanation to the presence of short-range order interaction at temperatures

far beyond the critical one [306]. Further studies have found that the magnetic structure of Tb_3Ni is non-coplanar owing to the competition between the influence of the low symmetry crystal electric field and the RKKY-exchange interaction described above [349]. This complicated arrangement has been confirmed for Gd_3Co [333], Tb_3Co [339], Dy_3Co [340], Ho_3Co [343], and Er_3Co [344] with particularities depending on the rare-earth atom.

In order to explore the possible capabilities and applications, a knowledge as deep as possible of the physical properties of the system is necessary, including the details of the phase transitions, such as the ordering of the spins, the extent of the interaction (short or long range order), etc. Some of the members of the family have already been found to present magnetocaloric properties (Gd_3Co, Dy_3Co, Tb_3Co, Gd_3Ni) through a direct magnetocaloric effect, with values of the variation of the magnetic entropy and refrigeration capacity competitive in their respective temperature ranges [77, 80, 81, 364].

We have studied three samples among the R_3T family: Dy_3Co, Tb_3Co and Tb_3Ni. Without applying any external magnetic field Dy_3Co and Tb_3Ni have an AFM ordering below their Néel temperature (with a reordering to a second AFM state at lower temperatures in the former case), while the ground state of Tb_3Co at low temperatures is ferromagnetic. The difference in the ground state of Tb_3Co and Tb_3Ni has been explained on the basis of the modification of the conduction band caused by the substitution of Co by Ni, which introduces negative interactions causing the stabilization of the AFM state. This is related to the different occupation of the *d*-band in Co and Ni and its effect on the polarization of the conduction band [349].

Due to the particularity of each sample, a profound and extensive study has been done for each one. The critical behavior of the higher temperature transition in each sample has been analysed through different thermal properties. Apart from that, the critical behavior of the lower temperature transition was also analysed for the case Dy_3Co, the study of which started during my master thesis. Furthermore an exhaustive magnetic study was performed in Tb_3Co and Tb_3Ni, concluding with the correct MCE evaluation. The order of the lower temperature transition in Tb_3Co, which was unclear, has been established and its neutron diffraction patterns were studied.

In the case of Tb_3Ni two studies have been performed; a first one completed two years before the writing of this manuscript, and an ongoing collaboration with the aim of studying the magnetic anisotropy on this system and its magnetocaloric behavior at high magnetic fields. For the latter, the adiabatic temperature change of the sample will be measured at the European Magnetic Field Laboratoy in Dresden (Germany) with applied fields up to 50 T along the three crystallographic axes. As this is an ongoing work, and at the moment of writing this text it is in its initial stage, just some preliminary results will be presented here, including the study of the rotating magnetocaloric effect (RMCE), also known as "anisotropic magnetocaloric effect", for the highly anisotropic Tb_3Ni.

Given the different analysis performed for each sample, the results are presented separately for the sake of clarity.

6.2 Samples and experimental techniques

All the samples presented in this chapter have been grown as single crystals by our collaborators A.F. Gubkin and N.V. Baranov from the Ural Branch of the Russian Academy of Sciences and Ural Federal University in Ekaterinburg, Russia.

Dy_3Co, Tb_3Co and Tb_3Ni polycrystalline ingots were prepared by arc-melting in a He atmosphere using Dy and Tb of 99.9% purity, and Co and Ni of 99.99% purity (Tb_3Ni sample is the same one as used in Ref. [347]). The single crystal samples with dimensions of approximately 4×4×5 mm^3 for Dy_3Co, 3×3×4 mm^3 for Tb_3Co, and 4×5×6 mm^3 for Tb_3Ni were grown by remelting the ingots at temperatures just above the peritectic point in a resistance furnace. The quality of the as-grown single crystal samples was characterized by the back reflection Laue method measuring X-ray diffraction patterns from different surfaces of the samples. No extra reflections from other grains were detected. In the case of Tb_3Co sample, the absence of additional grains and good quality of the single crystal was confirmed on the neutron diffraction experiment as well. Then, Dy_3Co and Tb_3Co single crystal samples were cut into plane-parallel slabs that are parallel to the (010) crystallographic plane, while Tb_3Ni final sample was prepared as a parallelepiped with its surfaces perpendicular to the three axis a, b, and c. Finally all those surfaces had been well polished and additionally checked by the back Laue method. The thicknesses of the slabs was about 600 μm.

The usual high-resolution *ac* photopyroelectric calorimeter in the back detection configuration described in Section 1.4 has been used in this work to extract thermal diffusivity D, specific heat c_p and thermal conductivity K. For Tb_3Co and Tb_3Ni single crystals, thermal diffusivity has been measured from room temperature down to 30 K, paying special attention to the region around the magnetic transitions, where also specific heat has been retrieved (except for Tb_3Co), using slow temperature rates (down to 10-20 mK/min) in order to acquire the shape of the transitions in detail, checking possible thermal hysteresis at the same time. As said, the details of the theory on how to extract the thermal variables from the photopyroelectric signal and the experimental set-up can be found in Section 1.4. With this technique, thermal diffusivity is measured in a direction perpendicular to the surface; the crystallographic plane (010) in the case of Dy_3Co and Tb_3Co single crystals, and the direction a for Tb_3Ni.

Magnetization (M) measurements have been carried out for Tb_3Co and Tb_3Ni samples in a VSM (Vibrating Sample Magnetometer) by Cryogenic Limited. The isotherms for Tb_3Co were measured under external applied magnetic fields $\mu_0 H_a$ ranging from 0 to 8 T, and they were collected over a range of 50-145 K with ΔT = 1 K between 50 and 100 K, ΔT = 2 K in the range 100-120 K and ΔT = 5 K from 120 to 145 K. As mentioned in the previous section, two independent studies have been performed over Tb_3Ni. For the first one the magnetic isotherms were measured under a magnetic field ranging from 0 to 6 T, with the field being applied along the c crystallographic direction, which is the easy axis of magnetization for this sample. These isotherms were collected

over a range of 3-130 K with ΔT = 1 K between 35 and 76 K, ΔT = 2 K between 3-35 K and 76-100 K and ΔT = 5 K between 100 and 130 K.

The difference between both Tb_3Ni measurements comes from the acquisition protocol of the magnetic isotherms. In the first Tb_3Ni measurement, as well as in the Tb_3Co measurements, the isotherms have been collected starting at the lowest temperature, applying the magnetic field up to the highest field in each case, then removing it, and moving to the next temperature, repeating the procedure till the last isotherm is acquired. This is the quickest acquisition procedure and it gives good results in second order magnetic phase transitions when obtaining the MCE from *Maxwell relation*. However, in first order magnetic transitions with stair-like behavior and/or field-induced metastable states, the correct evaluation of the magnetocaloric effect should be done by either considering the *Clausius-Clapeyron* equation, or by applying the discontinuous measuring protocol. This was discussed in detail in Section 2.2.5. The former method was used for the first study on Tb_3Ni and the latter for the second, more recent, study. The discontinuous measuring protocol, with which we can directly use the *Maxwell relation* to obtain the MCE, takes more measuring time since after the measurement of each isotherm the magnetic field must be removed and the sample heated above the critical temperature to eliminate the magnetic memory. In the case of the second study for Tb_3Ni, the isotherms were collected from 2 K to 136 K, with an applied field up to 7 T. Isotherms were collected each 2 K in the range 2-100 K and each 4 K above 100 K. As mentioned, the field was removed and the sample heated above 130 K before being cooled again and moved to the following isotherm. This procedure was performed along the three crystallographic axes, *a*, *b*, and *c*.

Then, as in all our magnetic measurements, the applied magnetic field has been corrected for demagnetization effects and the internal field calculated. The precise procedure was explained in Section 2.1.3, and for RTX and R_3CoNi intermetallics in Sections 4.2 and 5.2, respectively. The magnetic susceptibility was measured with AC Measurement System Option in PPMS (Physical Properties Measurement System) by Quantum Design.

Finally, Tb_3Co single crystal was also analysed by neutron diffraction on a diffractometer equipped with a position sensitive detector (PSD) which covers a wide angle and is known to be a powerful tool to acquire a map in the reciprocal space. These maps are a very good tool to investigate magnetic structures or crystallographic superstructures from a qualitative point. Inherent to this technique is the restriction to a 2-dimensional map when a 1-D PSD is used and the data from one map is in most cases insufficient to refine a structure model. In this experiment the cold neutron powder diffractometer DMC (Double axis MultiCounter) at the Swiss Spallation Neutron Source SINQ equipped with a 6 T vertical field cryomagnet was used. The wavelength used was 2.41 $\AA$ with additional pyrolytic graphite filters in the beam to suppress $\lambda/2$ contamination. The detector was set at a starting angle of 5° with the resulting coverage in **Q** from 0.23 $\AA^{-1}$ to 3.52 $\AA^{-1}$. The Tb_3Co single crystal was oriented on a custom Al-holder in the *HK0* scattering plane with the vertical magnetic field parallel to the crystallographic *c*-direction. The crystal was then rotated around the vertical axis in 0.2° steps to cover a

total of 180º. Using the software TvTueb the measured maps were transformed to *HK0* reciprocal maps. The experimental protocol was to measure maps first in zero magnetic field at 90 K, 75 K, 60 K and 1.5 K and then applying a magnetic field of 2 T and measure at 1.5 K, 75 K and 90 K.

6.3 Dy_3Co

It is known that Dy_3Co has two magnetic phase transitions, the first one taking place at around 42 K from the PM state to an AFM state. Further lowering the temperature (at about 32 K) there is a reorientation of the antiferromagnetic structure into another antiferromagnetic state whose period has been suggested to be doubled along the *a*- and *c*-axes [340]. Another interesting feature in Dy_3Co is that it is suggested that there might exist a survival of short-range magnetic correlations in the paramagnetic state [80], as well as it happens in some other R_3(Co; Ni) compounds [306].

The magnetocaloric effect of this sample has already been discussed in other works [80, 365], and due to its AFM nature a critical behavior analysis of the magnetic properties is not possible. That is why we will focus our work on the study of the critical behavior of the magnetic transitions in Dy_3Co using thermal variables: specific heat, thermal diffusivity and thermal conductivity. The main advantage of the thermal variables is that the critical exponents for the different universality classes are much more different among them (with even changes in sign) than what happens in the case of the magnetic exponents, where the differences are smaller (see Table 3.2 in page 77).

6.3.1 Thermal properties of Dy_3Co compound

Fig. 6.1(a) presents the thermal diffusivity as a function of temperature in the region of interest. The value here is similar or even higher to the ones found in literature for magnetocaloric materials [180, 287]. It is worth mentioning that at room temperature, the thermal diffusivity is 2.65 mm^2/s and it decreases with temperature till it reaches the value of 1.16 mm^2/s at 100 K, a behavior quite typical of intermetallic materials due to the added contribution of the electronic and phononic part of the thermal diffusivity; below 100 K the phonon contribution starts to dominate, making the thermal diffusivity increase till 1.21 mm^2/s at 50 K. From then on, the thermal diffusivity background quickly increases as the phonon mean free path is severely increased and the magnetic transitions are superimposed on this background as two dips. This is the same behaviour found in RTX intermetallics presented in Chapter 4 and in many other materials in literature [15–17, 20, 22]. In this particular case, the dips are located at 32.07 K and 41.57 K.

Fig. 6.1(b) shows the specific heat in the same temperature range as Fig. 6.1(a) while Fig. 6.1(c) shows the thermal conductivity. Specific heat and thermal conductivity are always noisier than thermal diffusivity using this technique, as the latter is obtained only using the phase of the photopyroelectric signal while for the former two both amplitude and phase are needed. The position of the specific heat peaks (32.26 K and 41.82 K) are similar to those

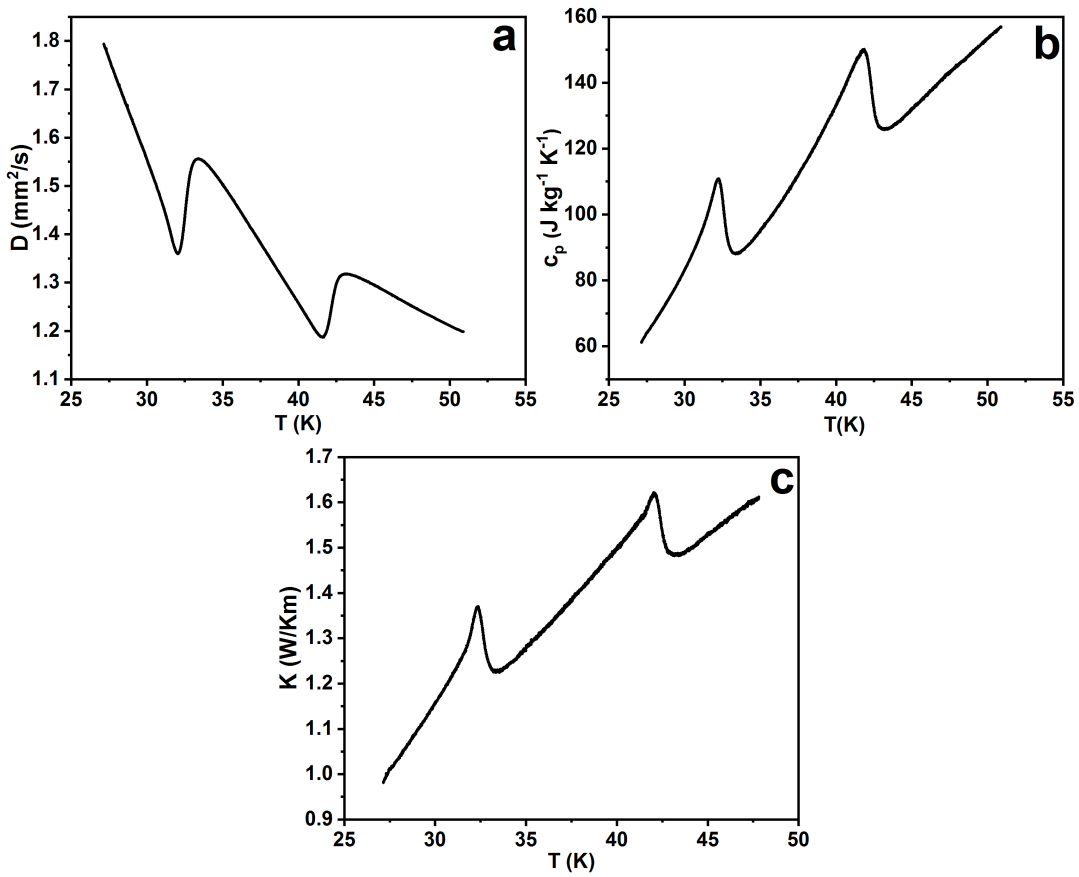


Figure 6.1: (a) Thermal diffusivity (D), (b) specific heat (c_p) and (c) thermal conductivity (K) as a function of temperature for Dy_3Co.

found in literature [340], where it is firmly established that the transition at higher temperature corresponds to an antiferromagnetic ordering of the rare-earth spins from a paramagnetic state while the one at lower temperature is due to a reordering of those spins into another antiferromagnetic distribution. The thermal conductivity also presents singularities at both transitions; this physical quantity has not been measured before in this intermetallic family. It is not usual to find anomalies in the form of peaks at magnetic transitions but it has been found for several magnetic transitions in materials such as Gd [15], FeF_2 [16], $RbMnF_3$ [17], and $KMnF_3$ [366]. The decreasing background in thermal conductivity with decreasing temperature is also another feature common to many intermetallic families [283, 367, 368].

6.3.2 Thermal critical behavior in Dy_3Co

It was already shown in Section 3.3 that the three thermal properties (c_p, D, K) can be expressed by well known equations in the vicinity of a second order phase transition. In the case of specific heat (c_p), and thermal diffusivity (D) these expressions are given by:

$$c_p = B + Ct + A^{\pm}|t|^{-\alpha}(1 + E^{\pm}|t|^{0.5}) , \tag{6.1}$$

and

$$D = V + Wt + U^{\pm}|t|^{-b}(1 + F^{\pm}|t|^{0.5}) , \tag{6.2}$$

respectively. As explained in Section 3.3, the fitting of thermal conductivity (K) is performed using its inverse ($1/K$), because all the thermal resistances associated to the various heat conduction mechanisms in the sample are in series [17, 366]:

$$1/K = L + Mt + N^{\pm}|t|^{-g}(1 + H^{\pm}|t|^{0.5}) . \tag{6.3}$$

In the previous expressions $t = (T - T_N)/T_N$ is the reduced temperature, T_N the Néel Temperature, α, $A^{\pm}$, B, C, and $E^{\pm}$ are adjustable parameters for c_p, while b, $U^{\pm}$, V, W, and $F^{\pm}$ are the corresponding ones for thermal diffusivity, and g, $N^{\pm}$, L, M, and $H^{\pm}$ for thermal resistivity ($1/K$). Superscripts + and − stand for $T > T_N$ and $T < T_N$ respectively. In all the cases the linear term represents the background contribution to the corresponding magnitude, while the last term accounts for the anomalous contribution arising due to the transition itself. Finally, the factor under parenthesis is the correction to scaling that represents a singular contribution to the leading power as known from experiments and theory [219].

In section 3.3, some relations between the critical parameters of the specific heat (α and A^+/A^-), thermal diffusivity (b and U^+/U^-), and inverse of the thermal conductivity (g and N^+/N^-) were given for the most common magnetic universality classes. Advancing the results, let us recover the relations among the critical parameters in the particular case of the 3D Heisenberg class:

$$\alpha \approx b \approx g , \tag{6.4}$$

$$A^+/A^- \approx U^+/U^- \approx N^+/N^- . \tag{6.5}$$

The three thermal properties were fitted to Eqs. (6.1), (6.2) and (6.3) in the proximity of both phase transitions. Fig. 6.2 shows the fittings for the three magnitudes: specific heat (a), thermal diffusivity (c) and the inverse of the thermal conductivity (e), for the paramagnetic to antiferromagnetic phase transition in the near vicinity of the Néel temperature as a function of the reduced temperature $t = (T - T_N)/T_N$, where the dots correspond to the experimental and the continuous lines to the best fitting to Eqs. (6.1), (6.2) and (6.3). The figure also contains the deviation plots of each fitting with respect to the experimental curves, assessing the quality of the fittings. The deviation is in all cases within ±2%; not only that, it can be seen that for most of the region these deviations are within ±0.5%. Table 6.1 contains the values of the critical parameters. If attention is focused on the results for specific heat, the critical parameters ($\alpha = -0.13 \pm 0.01$, $A^+/A^- = 1.64$) agree quite well with the isotropic 3D Heisenberg model ($\alpha_{\text{Heis}} = -0.134$, $A^+/A^-_{\text{Heis}} = 1.52$), see Table 3.2 in page 77. The slight deviation between the experimental and the theoretical value of the critical ratio A^+/A^- might be attributed to a lack of complete isotropy, as manifested in the *ac* susceptibility measurements along the three axes [340], which shows some differences.

Our results confirm that both the critical exponent and the ratio of the critical coefficients for the thermal diffusivity nearly match those for specific heat,

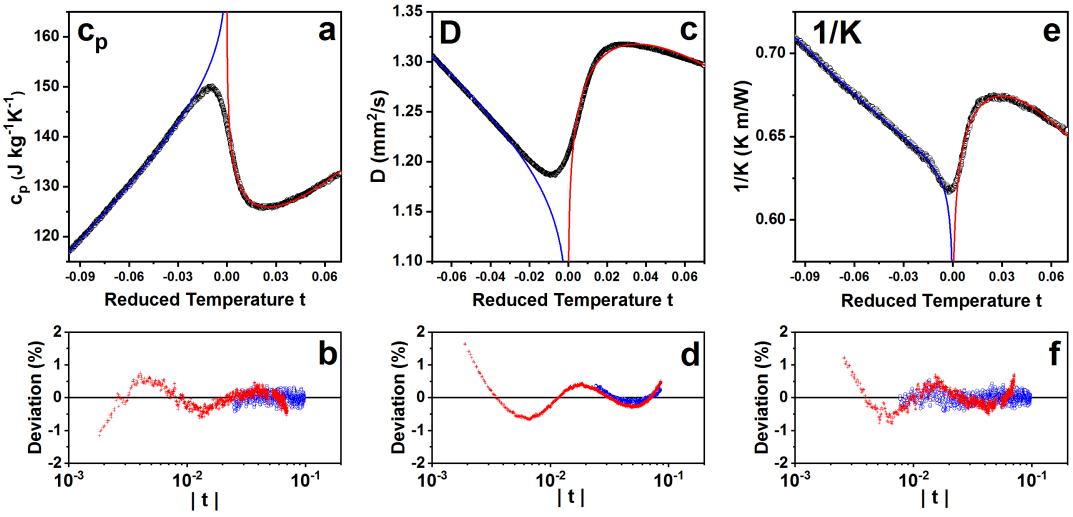


Figure 6.2: Experimental (dots) and fitted curves (continuous lines) of the specific heat (a), thermal diffusivity (c) and inverse of thermal conductivity (e) as a function of the reduced temperature for the antiferromagnetic to paramagnetic transition in Dy_3Co. (b), (d), and (f) present the corresponding deviation plots. Open circles are for $T < T_N$ and crosses for $T > T_N$.

where $b = -0.15 \pm 0.02$, $U^+/U^- = 1.41$. Both parameters can be considered to fulfill the approximate Eqs. (6.4), (6.5), confirming that the transition belongs to the Heisenberg class. Finally, the inverse of the thermal conductivity also gives a close value of its critical exponent g to the Heisenberg model ($g = -0.10 \pm 0.01$) (therefore confirming Eq. (6.4)) while the ratio of the critical coefficients $N^+/N^- = 0.94$ gets away from the theoretical value. This behavior for the inverse of thermal conductivity is very similar to the one found for other isotropic magnets such as $RbMnF_3$ ($g = -0.08$, $N^+/N^- = 1.1$) [17] and $KMnF_3$ ($g = -0.10$, $N^+/N^- = 1.15$) [212], although further studies are necessary in order to fully understand its meaning.

Another interesting conclusion is that, indeed, our results declare that short-range order interactions are responsible for this magnetic transition and not long-range ones (for which the proper universality class would have been the Mean Field model). This is in agreement with the studies which have pointed out that even in the paramagnetic phase there is a survival of short range order interactions [80], as it also happens in some other R_3(Co,Ni) [306].

Now we will turn our attention to the lower temperature transition, where the ordering changes from one antiferromagnetic structure to another one. Fig. 6.3 shows the equivalent to Fig. 6.2 for this transition and the relevant critical parameters are gathered in Table 6.1 together with the ones corresponding to the PM-AFM transition. The critical exponent for specific heat does not really comply with any universality class ($\alpha = -0.17 \pm 0.01$, $A^+/A^- = 1.18$); there is a stronger deviation from the 3D Heisenberg class but without reaching neither the 3D XY ($\alpha_{XY} = -0.014$, $A^+/A^-_{XY} = 1.06$) nor the 3D Ising ($\alpha_{Ising} = +0.11$, $A^+/A^-_{Ising} = 0.536$). Our interpretation is that the isotropy is being smoothed

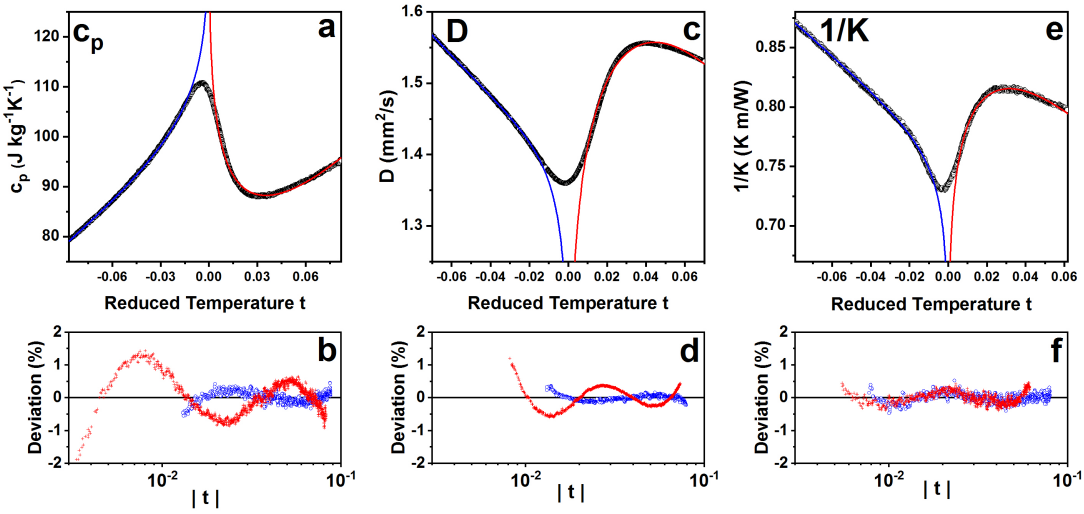


Figure 6.3: Experimental (dots) and fitted curves (continuous lines) of the specific heat (a), thermal diffusivity (c) and inverse of thermal conductivity (e) as a function of the reduced temperature for the antiferromagnetic to antiferromagnetic transition in Dy_3Co. (b), (d), and (f) present the corresponding deviation plots. Open circles are for $T < T_N$ and crosses for $T > T_N$.

somehow, in agreement with Baranov *et al.* [341] who showed that there is a smaller projection of the magnetic moment along the *b*-axis than along the *a*- and *c*-axes (4.5 μ_B, 6.0 μ_B, and 6.3 μ_B, respectively) [340, 341], giving rise to what is labeled as *"a highly anisotropic non-collinear magnetic structure"* [341] but without the presence of an easy plane or an easy axis. Magnetic susceptibility measurements have also assessed an important difference in the spin ordering in the two transitions: In the higher temperature one there is an anomaly in χ when applying magnetic field along the three axes *a*, *b* and *c* while in the lower temperature one the anomaly is only visible when applying the field along the *b*-axis [340, 342].

	c_p		D		1/K	
Transition	α	A^+/A^-	b	U^+/U^-	g	N^+/N^-
PM-AFM (42 K)	-0.13 ± 0.01	1.64	-0.15 ± 0.02	1.41	-0.10 ± 0.01	0.94
AFM-AFM (32 K)	-0.17 ± 0.01	1.18	-0.14 ± 0.03	0.85	-0.10 ± 0.02	0.98

Table 6.1: Critical parameters for the PM-AFM and AFM-AFM transitions in Dy_3Co.

This deviation from an isotropic magnet is further confirmed with the fittings for thermal diffusivity ($b = -0.14 \pm 0.03$, $U^+/U^- = 0.85$) and the inverse of the thermal conductivity ($g = -0.10 \pm 0.02$, $N^+/N^- = 0.98$). The deviations in the fulfillment of Eqs. (6.4), (6.5) are now strong, supporting that the Heisenberg class is no longer of application.

As was mentioned before, we haven't performed any magnetic measurement on this sample since the most important magnetic and magnetocaloric

analysis had already been published [80,340–342,365], and a magnetic critical behavior analysis is not possible due to the AFM ordering state and the metamagnetic field induced transition from the AFM state to a FM state reported in literature [80,340,365]. This metamagnetic transition has been reported to occur along the three crystallographic axes [340], and its nature has been confirmed to be first order [80]. The MCE has already been measured for a bulk polycrystalline alloy [80], as well as for rapidly solidified ribbons [365]. The results obtained in those works (at $\mu_0\Delta H$ = 5 T) are gathered in Table 6.2. It can be seen that the magnetic entropy change and RC_{FWHM} values are better (almost twice higher) for the bulk alloy, which, although being polycrystalline, is the most similar one to our sample.

Compound	$\lvert\Delta S_M^{pk}\rvert$ (J kg^{-1} K^{-1})	RC_{FWHM} (J kg^{-1})	Ref.
Dy_3Co bulk	13.9	614	[80]
Dy_3Co ribbons	6.5	364	[365]

Table 6.2: Peak of the magnetic entropy change $\lvert\Delta S_M^{pk}\rvert$ and RC_{FWHM} at $\mu_0\Delta H$ = 5 T for different Dy_3Co alloys in literature.

6.4 Tb_3Co

As reported, there are two magnetic phase transitions in Tb_3Co, a first one at about 82 K (T_N), from a paramagnetic to an antiferromagnetic phase and a second one at a lower temperature, about 72 K (T_2), with a change to a complex non-coplanar ferromagnetic phase, with the spins ordering along the easy c-axis, but with an AFM ordering along the a- and b-axes [339,349,369].

Tb_3Co presents quite a complex behavior and there are several issues not studied or resolved yet: the precise crystal and magnetic structures as well as their evolution, the magnetic phase diagram, establishing the character of the lower temperature AFM-FM phase transition, the critical behavior analysis of the higher temperature PM-AFM transition, and finally the study of the potentiality of Tb_3Co as a magnetocaloric material.

Concerning the crystal structure, this is a Fe_3C type structure with the orthorhombic $Pnma$ space group. However, after literature, the magnetic structure of Tb_3Co is not commensurate with the crystal one below T_N as magnetic reflections can be indexed with the propagation vector $\mathbf{k}$ = (0.155, 0, 0). Magnetic intensity on these position can be detected below the AFM-FM transition until about 66 K (several degrees below T_2). This implies that at the magnetic AFM-FM transition (72 K) the magnetic phase is still incommensurate with $\mathbf{k}$ = (0.155, 0, 0) and that only at a lower temperature the propagation vector changes. At temperatures below 66 K the neutron diffraction patterns have been reported to be explained by a mixture of both commensurate ($\mathbf{k}$ = (0, 0, 0)) and incommensurate ($\mathbf{k}$ = (0.32, 0.32, 0)) components [339].

The character of the PM-AFM transition is considered as second order but, as the two magnetic transitions are so close, there has not been much effort to study the AFM phase in detail; in particular, no critical behavior study has been performed, which is a very sensitive tool to assess if the magnetic order parameter is 3 dimensional or has lower dimensionality, as well as the range of the magnetic interactions (either short or long). This critical behavior study will be performed by the analysis of both thermal diffusivity and its inverse. We will see that the character of the lower temperature transition will make it impossible to also perform a critical behavior analysis of the magnetic properties.

On the other hand, the AFM-FM transition is believed to have a first order character, but this is based on indirect evidences. In particular, this has been interpreted from the shape of the specific heat curves, but without showing any thermal hysteresis or having calculated a latent heat [364, 370]. Besides, as mentioned before, neutron diffraction data suggest that there is a superposition of two magnetic structures [339] which may contribute differently to the specific heat.

Another interesting feature in Tb_3Co is that, as has already been mentioned, Tb occupies two non-equivalent positions: *4c* (site symmetry *m*) and *8d* (site symmetry *I*). The low symmetry orthorhombic crystalline structure in which Tb atoms occupy these two non-equivalent sites leads to an increase of the crystal field effect, which has been held responsible for the complexity of the magnetic properties revealed so far [339].

Therefore, our aim is to extend our knowledge on Tb_3Co and to clarify all the open issues stated in the previous paragraphs.

6.4.1 Thermal and magnetic evolution of Tb_3Co

Thermal diffusivity (D) of Tb_3Co as a function of temperature is presented in Fig. 6.4, showing the common behavior in intermetallic materials where heat is transferred both by electrons and phonons [225, 282, 283]. This is the same behavior as the one found for the samples presented in Chapters 4 and 5, as well as for the previously presented Dy_3Co. From room temperature down, the electronic contribution is severely reduced due to the reduction of the resistivity while the increase in phonon contribution as the phonon mean free path increases is not enough to compensate. In the case of Tb_3Co, this general decrease stops at the magnetic phase transitions, signalled by the two dips shown in detail in the inset of Fig. 6.4. As we have already discussed for the materials previously presented in this manuscript, these dips are the common signature of magnetic phase transitions on the thermal diffusivity curves. After the spin ordering, the phonon mean free path greatly increases, counteracting the lesser input by electron mobility leading to a huge increase in the thermal diffusivity. It is worth noting that, although thermal diffusivity curve in Fig. 6.4 looks like a single solid line, it is actually made up of thousands of experimental points as the temperature ramp rate is extremely low (especially in the region of the phase transitions). This allows retrieving the shape of the transitions with high resolution in order to make a quantitative

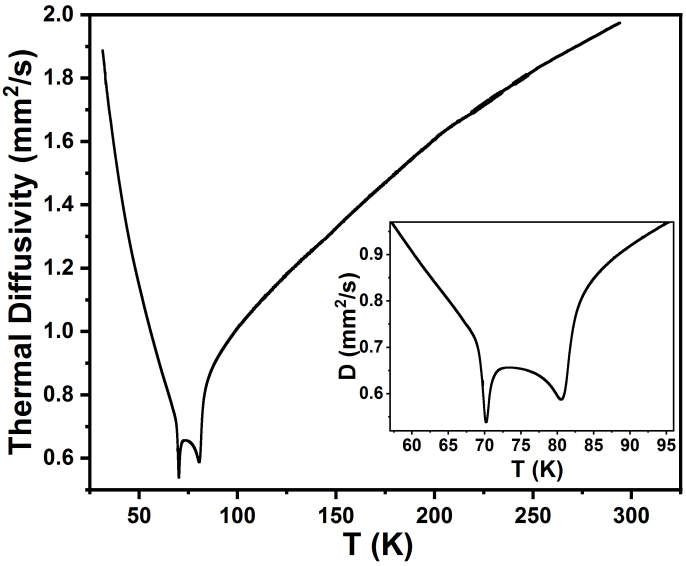


Figure 6.4: Thermal diffusivity as a function of temperature for Tb_3Co showing two transitions at ≈ 70 K and ≈ 81 K. The inset shows in detail the D vs T dependence in the vicinity of the phase transitions.

treatment later on. It is also worth mentioning that while the value of thermal diffusivity at room temperature is similar to the highest values found on literature for magnetocaloric materials [180], the D value in the working region (where the transitions take place) is lower, though similar to the one found in other materials [287].

It is clearly seen that there are two well separated phase transitions, the first one at 81 K, which corresponds to the PM-AFM transition, the second one at 70.2 K, with a change in magnetic ordering from AFM to FM. This attribution, in agreement with literature [339], has been corroborated by the measurement of the Field Cooled (FC) and Field Warmed (FW) magnetization, and the real part of the *ac* magnetic susceptibility as a function of temperature, presented in Fig. 6.5. The transition temperatures are signalled by the derivative of the magnetization (inset in the top graph of Fig. 6.5) and the peaks in the real part of the *ac* magnetic susceptibility (bottom graph in Fig. 6.5), which, as it is clear from the figure, are in agreement between them and the peaks in thermal diffusivity.

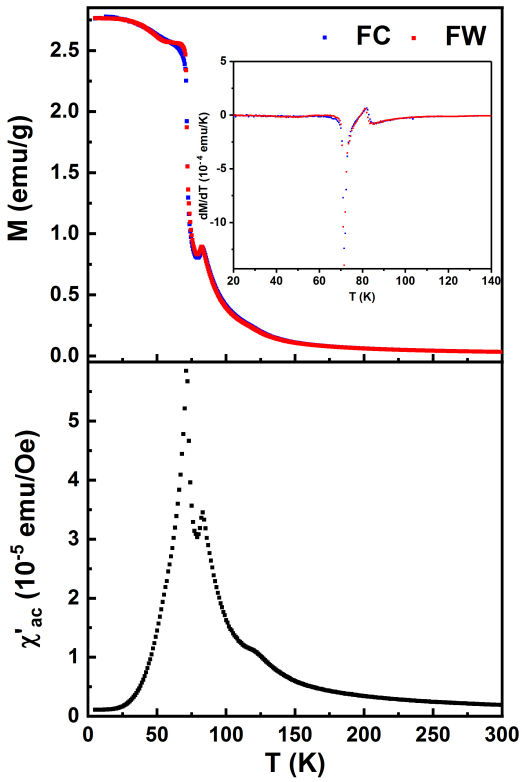


Figure 6.5: Magnetization as a function of temperature for Tb_3Co, Field Warmed (FW) and Field Cooled (FC) measured on the plane (010) with $H = 100$ Oe (top). Inset: First derivative of the magnetization. Real part of the *ac* magnetic susceptibility (bottom).

6.4.2 Thermal critical behavior in Tb_3Co

It is commonly accepted that the PM-AFM transition is second order and our results confirm this as there is no sign of thermal hysteresis in the thermal diffusivity measurements. These measurements have been performed in heating and cooling runs with ramp rates down to 20 mK/min and neither the position nor the shape of the signal at the transition changes. This allows the use of the scaling equations from critical behavior theory to get a deeper understanding of the magnetic properties of the spins when the phase transition takes place. In this case, the amplitude of the signal from the *ac* PPE calorimeter was too noisy to extract a good specific heat, that's why both, thermal diffusivity (D) and its inverse ($1/D$) have been fitted. According to what has already been explained in Section 3.3, in the critical region both D and $1/D$ can be fitted to the following expressions:

$$D = V + Wt + U^{\pm}|t|^{-b}(1 + F^{\pm}|t|^{0.5}), \tag{6.6}$$

$$1/D = G + Jt + L^{\pm}|t|^{-\alpha}(1 + I^{\pm}|t|^{0.5}), \tag{6.7}$$

where $t = (T - T_N)/T_N$ is the reduced temperature, T_N the Néel temperature, α, b are the critical exponents, while V, W, G, J, U^+, U^-, L^+, L^-, F^+, F^-, I^+, I^- are adjustable parameters (the plus sign corresponds to the branches above the

critical temperature, the minus sign to the ones below it). Following renormalization group theory, the values of the critical exponents α, b and the critical ratios L^+/L^-, U^+/U^- are the ones which indicate the universality class of this transition. The fitting procedure was explained in Section 3.3.1. The fittings, together with the deviation plots, which show the difference between the experimental points and the fitted curve, and thus, the quality of the fit, are presented in Fig. 6.6. The deviation in all cases is within ±2%, and in most of the region this deviation is as low as ±0.5%.

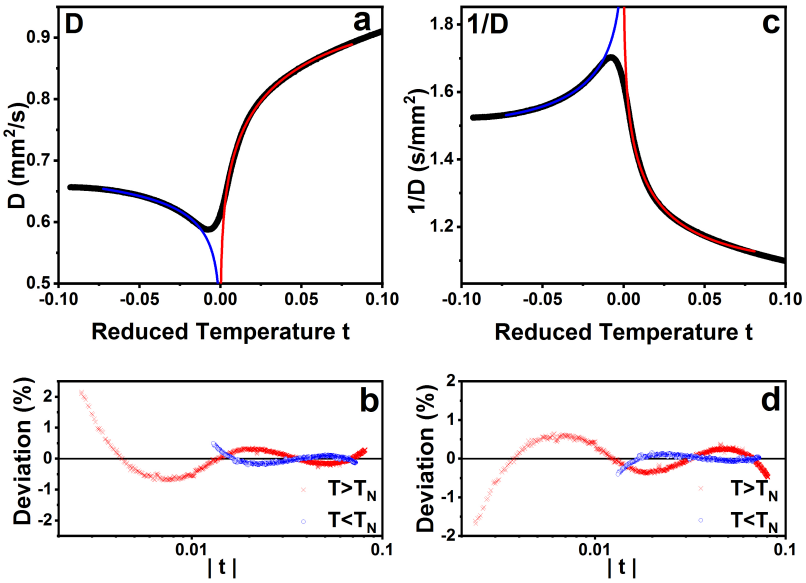


Figure 6.6: (a), (c) Experimental thermal diffusivity and its inverse (dots) together with the fitted functions (continuous curves) to Eqs. (6.6), (6.7), respectively; (b), (d) corresponding deviation plots: crosses for $T > T_N$, circles for $T < T_N$.

	D		1/D	
Transition	**b**	**U^+/U^-**	**α**	**L^+/L^-**
PM-AFM (81 K)	-0.136 ± 0.009	1.2	-0.133 ± 0.008	1.33

Table 6.3: Critical parameters for the PM-AFM transition in Tb_3Co.

The results obtained from the fittings have been collected in Table 6.3. The values of $\alpha = -0.136 \pm 0.009$ and $b = -0.133 \pm 0.008$ agree very well with the 3D Heisenberg universality class ($\alpha_{\text{Heis}} = -0.134 \approx b_{\text{Heis}}$) which implies short-range order interaction of the spins and that they would have an isotropic distribution. However, the theoretical ratio for this model is $L^+/L^-_{\text{Heis}} = 1.52 \approx U^+/U^-_{\text{Heis}}$ (see Table 3.2 in page 77), slightly higher than the ones obtained ($L^+/L^- = 1.33$ and $U^+/U^- = 1.2$). This situation (critical exponent in agreement with the theoretical value but a smaller ratio of the critical parameters) arises when the spin distribution is not completely isotropic but without reaching the situation in which there is an easy plane (3D XY model, $\alpha_{\text{XY}} = -0.014$) or an easy axis (3D Ising model, $\alpha_{\text{Ising}} = +0.11$). Among the different mechanisms

which could introduce this deviation, crystal-field effects are the most likely, due to the Tb occupancy in the orthorhombic lattice, which agrees with magnetization measurements along the principal crystallographic directions [339], where it is confirmed that, in the AFM phase, a deviation from isotropy has started to develop, which will give rise, afterwards, to the FM easy axis in the low temperature magnetic phase. The attribution of this transition to a 3D Heisenberg universality class assesses that short-range order magnetic interactions are responsible for the magnetic ordering. As it has already been mentioned, short-range order interactions have already been proven to exist in other members of the R_3(Co; Ni) family and even surviving in the paramagnetic phase [80, 306].

6.4.3 Character of the AFM-FM transition in Tb_3Co

Regarding the AFM-FM transition at lower temperature, it is worth revising again its character as, so far, diffraction studies have not given proof of any structural change indicating a first order phase transition, though there are several evidences of being a first order one [364, 370].

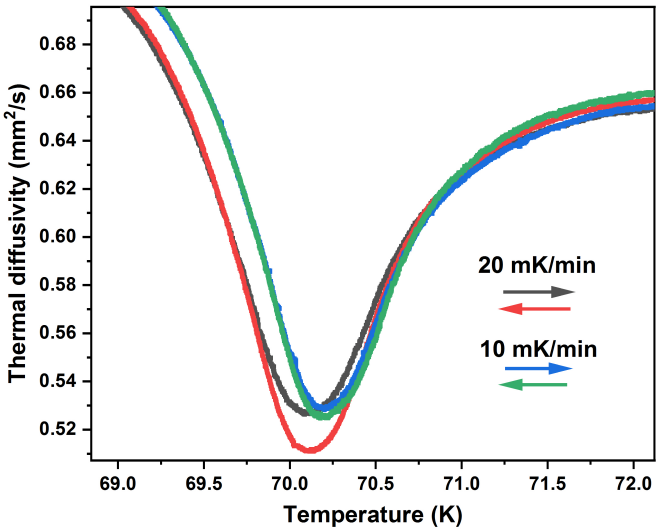


Figure 6.7: Experimental thermal diffusivity curves obtained on heating and cooling at 10 mK/min and 20 mK/min to check the presence of thermal hysteresis.

Concerning the thermal diffusivity measurements, in order to check the possibility of a thermal hysteresis, temperature rates as low as 10 mK/min have been used in heating and cooling runs looking for a difference in the position and/or the shape of the dip, with the result shown in Fig. 6.7, where a slight difference is seen at 20 mK/min which is reduced at 10 mK/min, indicating that, at most, this is a weak first order phase transition.

If we now look back to the top graph in Fig. 6.5, it can be seen that no thermal hysteresis is found in the magnetization measurements on heating (FW) and cooling (FC) under an small applied field of 100 Oe (see the inset with the first derivative which marks the same position for the critical temperature), so we have looked for other ways to assess the character of this transi-

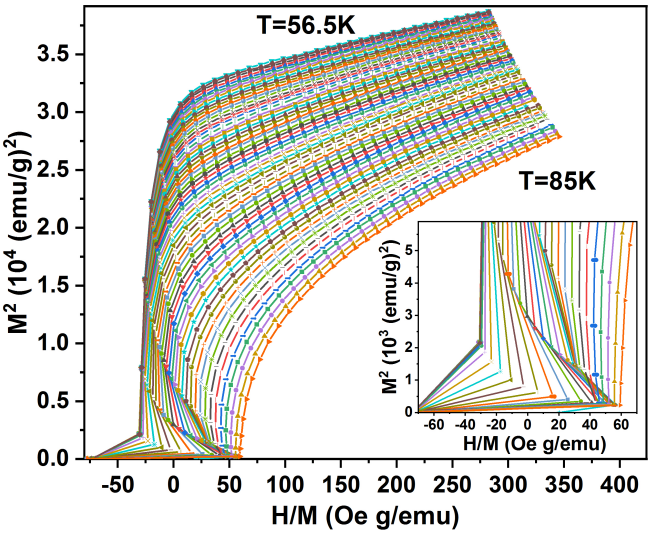


Figure 6.8: Arrott Plot for Tb_3Co measured on the plane (010). Inset: detail at low fields.

tion. In the first place, magnetization has been measured as a function of an applied magnetic field at a series of isotherms to build up the Arrott Plot (M^2 as a function of the ratio H/M), shown in Fig. 6.8, where the demagnetization factor has been taken into account, as previously explained. After the Banerjee criterion [229], if the slope of these curves is positive, the transition is second order while if it is negative it is first order. As it can be seen in the inset, at low fields the slopes are negative but only in a very short region, indicating that, indeed, the transition has a weak first order character.

6.4.4 Single crystal neutron diffraction and magnetic phase diagram for Tb_3Co

Concerning the single crystal neutron diffraction measurements, Fig. 6.9(a)-(c) show a reciprocal $HK0$ maps of Tb_3Co measured in zero magnetic field above and below Néel temperature at $T = 90$, 75 and 60 K. The intensity is color coded and the color map has been chosen to reveal also weak intensities. In the paramagnetic state at $T = 90$ K, the main structural reflections have approximately 6000 counts as peak value and if the color scale is chosen with this as maximum only the main structural peaks according to space group 62 ($Pnma$) are visible ($h = 2n$, $k = 2n$). This structure has been observed in a previous powder diffraction experiment [339]. In the chosen color scale, additional much weaker peaks (factor 100) on positions forbidden for space group 62 (h, k odd) can be found. It should be noted that a structural instability has been found in the nonmagnetic compound Y_3Co and lower symmetry space groups $P2_12_12_1$ and $P112_1$ were proposed [371]. The latter one is the highest symmetry space group which is in agreement with the observed neutron scattering pattern obtained on the Tb_3Co single crystal sample at $T = 90$ K.

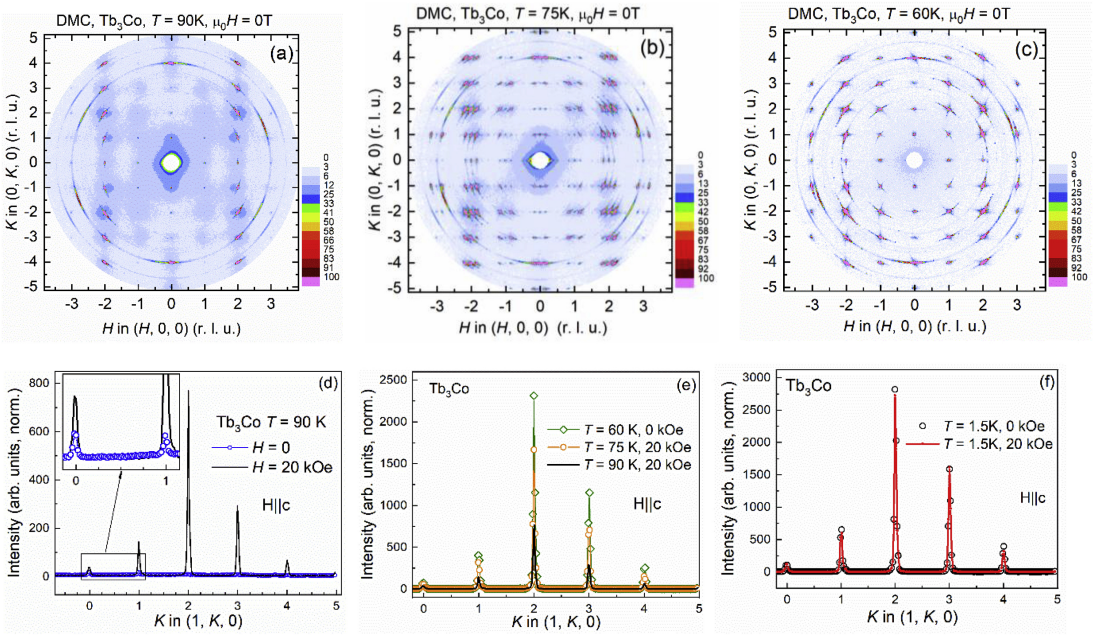


Figure 6.9: Reciprocal *HK0* map of Tb_3Co measured (a) at $T = 90$ K, (b) $T = 75$ K and (c) $T = 60$ K in $\mu_0 H = 0$ Oe. (d) Linecuts along *1K0* assessing the change of magnetic intensity in the applied magnetic field at $T = 90$ K. Comparison of linecuts along *1K0* measured at (e) $T = 60K$ in $\mu_0 H = 0$ Oe and $T = 75$ K, 90 K in $\mu_0 H = 20$ kOe and (f) at $T = 1.5$ K in $\mu_0 H = 0$ Oe and $\mu_0 H = 20$ kOe.

The magnetic scattering above T_N can be found as diffuse critical scattering around the position where magnetic Bragg peaks emerge below the ordering temperature (Fig. 6.9(d)). Interestingly, the observed diffuse intensity is isotropic around the nuclear position, indicating dominating ferromagnetic correlations. However, as previously reported [339] Tb_3Co orders antiferromagnetically below T_N in an incommensurate magnetic structure with a propagation vector $\mathbf{k} = (0.155, 0, 0)$. The reciprocal *HK0* map measured at $T = 75$ K is shown in Fig. 6.9(b). Incommensurate magnetic satellites indexed by a propagation vector $\mathbf{k} = (0.155, 0, 0)$ can be seen around integer (h, k, 0)-type Bragg nodes. Below T_2 (AFM-FM phase transition) Tb_3Co becomes a ferromagnet as shown in Fig. 6.9(c) on the reciprocal *HK0* map measured at $T = 60$ K. Intensity due to magnetic scattering is observed on all integer *HK0* positions. The lack of a clear directional dependence indicates that the magnetic moments direction must be mainly oriented perpendicular to the scattering vector, which means the magnetic moments are mostly aligned along the crystallographic c-axis. Additional reflections from a previously observed incommensurate component with the propagation vector $\mathbf{k} = (0.3, 0.3, 0)$ [339] cannot be seen. One possible explanation is that the cryomagnet had a small remanent magnetic field which affected the formation of the observed phase. Lowering the temperature increases the intensity due to magnetic scattering as the ordered magnetic moment follows the Brillouin function. The map at lowest temperature $T = 1.5$ K shows an identical pattern compared to $T = 60$ K (Fig. 6.9(f) and (e) respectively).

The one-dimensional line cuts where a section is extracted from the recip-

rocal *HK0* maps are shown in Fig. 6.9(d)-(f). The *1K0* linecuts for instance are a vertical line along K on the position $H = 1$. In Fig. 6.9(d), two linecuts measured at 90 K in zero magnetic field and in external magnetic field applied along the c crystallographic axis are plotted on top of each other. It can be seen that the ferromagnetic phase can be field induced from the paramagnetic state on application of the external magnetic along the c crystallographic axes. Fig. 6.9(e) compares *1K0* linecuts for different points of the ferromagnetic phase (60 K, 0 T; 75 K, 2 T and 90 K, 2 T). There is no change in the relative intensities between any of the observed peaks. Again, the decrease in the magnetic intensities can be explained by the reduction of the ordered magnetic moment due to thermal fluctuations. In Fig. 6.9(f), two linecuts are plotted on top of each other, both measured at 1.5 K. The black line comes from the measurement in zero field, the red line a vertical magnetic field of 2 T has been applied. Both linecuts are identical within the statistical error. Also, in the reciprocal maps no difference between zero and applied magnetic field can be detected. This indicates that the ferromagnetic state is indeed the ground state of Tb_3Co at below T_2. Comparing these different measurements, it can be concluded that the ferromagnetic phase found below T_2 and above a critical field are identical.

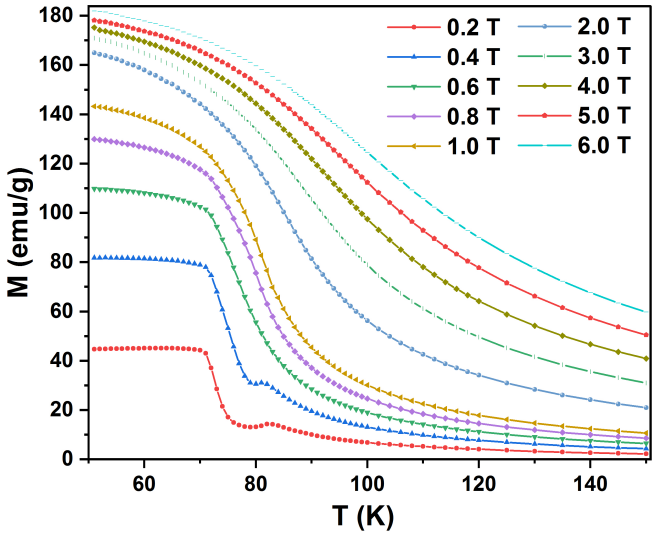


Figure 6.10: Magnetization isofields for Tb_3Co at selected fields extracted from magnetization isotherms measured on the plane (010).

Bearing in mind the magnetization data measured on the single crystal sample [369], one can conclude that the application of the external magnetic field above $\mu_0 H = 0.5$ T along the c crystallographic axis results in an AFM-FM type magnetic phase transition in the intermediate temperature range $T_2 < T < T_N$. This is in agreement with our neutron diffraction data measured at $T = 75$ K in external magnetic field $\mu_0 H = 2$ T, where we also checked that the low temperature FM phase is the same as the field induced one from AFM state. Furthermore, in our magnetization isofields presented in Fig. 6.10 (which are

obtained from the isotherms measured on the plane (010)), it is clearly seen how the PM-AFM transition peak vanishes when the applied field is somewhere between 0.4 and 0.6 T, since in the 0.4 T isofield (and lower) the peak is still visible, but no hint of it is present at 0.6 T (or higher). Therefore, the proposed behavior of Tb_3Co in an applied magnetic field along the *c*-axis can be summarized with a schematic phase diagram as depicted in Fig. 6.11.

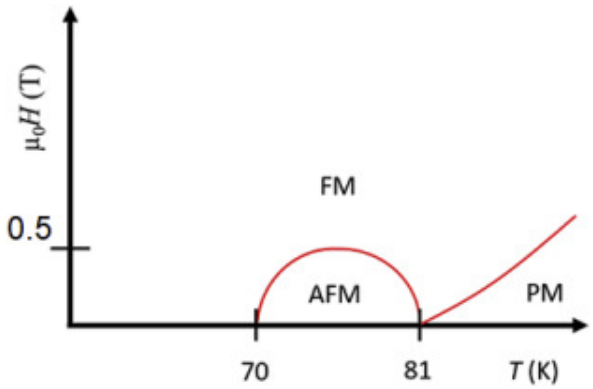


Figure 6.11: Schematic phase diagram for Tb_3Co in the magnetic field applied along the *c* crystallographic direction.

6.4.5 Magnetocaloric effect in Tb_3Co

It was shown in Section 2.2.5 that, while the magnetic entropy change of SOMPTs could be correctly evaluated through the *Maxwell relation*, a particular measurement protocol or the use of *Clausius-Clapeyron* equation is needed for FOMPTs in order to avoid overestimations. This is due to the stepwise behavior of the magnetization isotherms in the latter case. We have also seen that the highest temperature transition in Tb_3Co is a second order transition and the lower temperature one is weakly first order. However, the latter transition loses the first order character at relatively low magnetic fields and no stepwise behavior is spotted on magnetization isotherms, which means that the influence on the MCE of the week first order transition (if any) is negligible and, therefore, *Maxwell relation* can be safely used to evaluate the magnetic entropy change as usual:

$$\Delta S_M(T,\Delta H) = \mu_0 \int_{H_0}^{H_1} \left(\frac{\partial M}{\partial T}\right)_H dH\,. \tag{6.8}$$

As there are two phase transitions and with the aim of discriminating which is responsible for the magnetocaloric effect, a detailed number of isotherms have been taken, as explained in Section 6.2 with the result shown in Fig. 6.12 (a) and (b) for two different magnetic field regimes. Low fields are shown in Fig. 6.12 (a), where an IMCE (characterized by a positive magnetic entropy change) corresponding to the AFM regime can be clearly seen. An interesting thing to notice in this plot is that the dip at 73 K gets deeper from 0.2 T to 0.4 T but is reduced with higher fields. This is due to the field induced meta-

magnetic transition from the AFM state to the FM state taking place at 0.5 T.

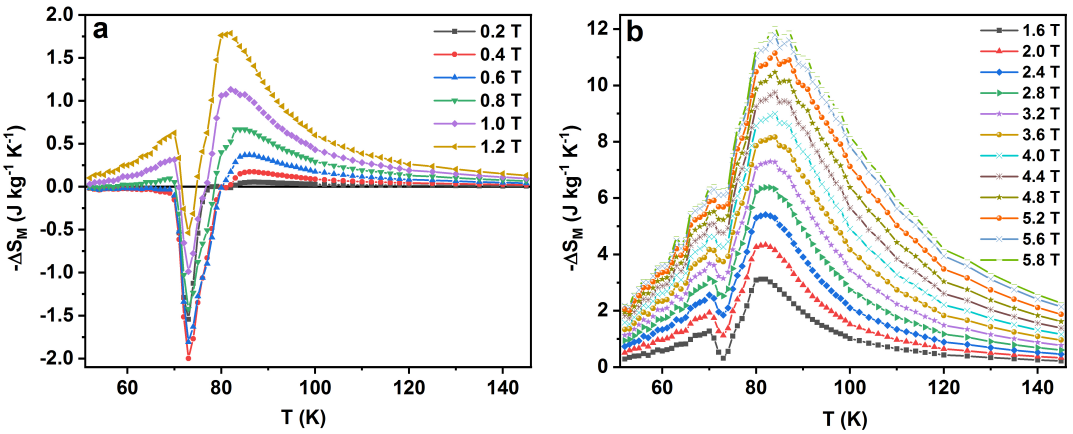


Figure 6.12: Negative magnetic entropy change ($-\Delta S_M$) as a function of temperature for Tb_3Co for different fields: $\mu_0\Delta H$: 0.2-1.2 T (a) and $\mu_0\Delta H$: 1.6-5.8 T (b).

Though for small fields in Fig. 6.12(b) there is a structure in the peak of the magnetic entropy change, it is quite clear that the maximum is located at the high temperature transition and the shape of the peak is the one commonly found for second order phase transitions. It can be seen in Fig. 6.8 that the first order character of the low temperature transition turns into second order as the magnetic field is increased. The values of the main MCE figures of merit ($|\Delta S_M^{\mathrm{pk}}|$, RC_{FWHM}, and RC_{Area}) are collected in Table 6.4. These values are given for $\mu_0\Delta H = 5$ T to allow the comparison with other published results for Tb_3Co. If we compare the values found in the current work with the ones found for other rare-earth based magnetocaloric materials in the same temperature range (see Fig. 25 in Ref. [91]) we can see that Tb_3Co is a competitive magnetocaloric material.

Compound	$\lvert\Delta S_M^{pk}\rvert$ (J kg^{-1} K^{-1})	RC_{FWHM} (J kg^{-1})	RC_{Area} (J kg^{-1})
Tb_3Co	10.73	404.5	316.8

Table 6.4: $|\Delta S_M^{pk}|$, RC_{FWHM}, and RC_{Area} at $\mu_0\Delta H = 5$ T.

The magnetocaloric properties of Tb_3Co had already been studied by at least two groups in literature before our work on Tb_3Co was published [81, 364]. The two works show strong discrepancies about the values of the maximum of the magnetic entropy change as well as of the refrigerant capacity. Using the *Maxwell relation* method Li *et al.* obtain a value of 738 J/kg for RC_{FWHM} and 18 J/kgK for $|\Delta S_M^{pk}|$ [81], which, as can be seen in Fig. 1 of Ref. [364], is too high compared to other members of this family and temperature region. It should be clarified though that this high value is obtained for a texturized sample, while the same authors report a value of $|\Delta S_M^{pk}| = 6$ J/kgK for a non-oriented powder (all the values are given for $\mu_0\Delta H = 5$ T). On the other hand,

J.C.B. Monteiro *et al.* use a heat flux technique in order to obtain the magnetic entropy change of polycrystalline samples, obtaining $|\Delta S_M^{pk}| = 12.5$ J/kgK (slightly higher than ours) and $RC_{\mathrm{FWHM}} = 360$ J/kg (lower than ours) [364]. These latter values are similar to the ones we obtain; however, it can be seen that our magnetic entropy change curves capture the structure of both phase transitions, as well as the AFM region, as no other study, confirming the quality of our measurements and analysis. Another very important issue is that, in both previous works, demagnetization effects have not been taken into account, which has been theoretically and practically demonstrated to lead to non-precise results in ΔS_M [136] or to non-universal curves [140] when the demagnetization factors are non-negligible.

In order to further check the order of the higher temperature phase transition at high magnetic fields (which turns from a PM-AFM transition at low fields to a PM-FM transition at higher ones), it is interesting to build up the normalized curve for the magnetic entropy change by dividing it by the corresponding maximum for the different values of the maximum applied field and rescaling the temperature axis according to [240]:

$$\theta_1 = \frac{T - T_C}{T_r - T_C}\,, \tag{6.9}$$

where T_C is the critical temperature and the reference temperature T_r is selected as that corresponding to a certain fraction of ΔS_M^{pk}, so that the curves should collapse on a master curve. Fig. 6.13(a) shows the result in this case. There, data collapses well in the vicinity of the critical temperature and above but not below the critical temperature due to the presence of the lower temperature weakly first order transition. We have already seen that although in theory one reference temperature should be enough to collapse the curves, this is not always the case, since the demagnetizing field and the presence of other magnetic phases deviate the curves [76, 140, 246, 248]. In the cases where the previous conditions must be taken into account (which is our case with the demagnetizing field), two reference temperatures are used for the rescaling of the temperature axis instead of one:

$$\theta_2 = \begin{cases} -(T - T_C)/(T_{r1} - T_C)\,, & T \leqslant T_C \\ (T - T_C)/(T_{r2} - T_C)\,, & T > T_C \end{cases}\,, \tag{6.10}$$

with $T_{r1} < T_C < T_{r2}$. Fig. 6.13(b) shows the universal curves with the temperature rescaling corresponding to Eq. (6.10). It can be seen that the collapse of the curves this time is slightly better than the one obtained in Fig. 6.13(a). This collapse is only obtained in second order phase transitions, further confirming the nature of the higher temperature magnetic phase transition.

Finally, the magnetocaloric effect gives us another method to check the character of the transitions, using the evolution of the exponent n of the field dependence of ΔS_M with temperature (see Section 3.5):

$$n(T,H) = \frac{d \ln |\Delta S_M(T,H)|}{d \ln H}\,. \tag{6.11}$$

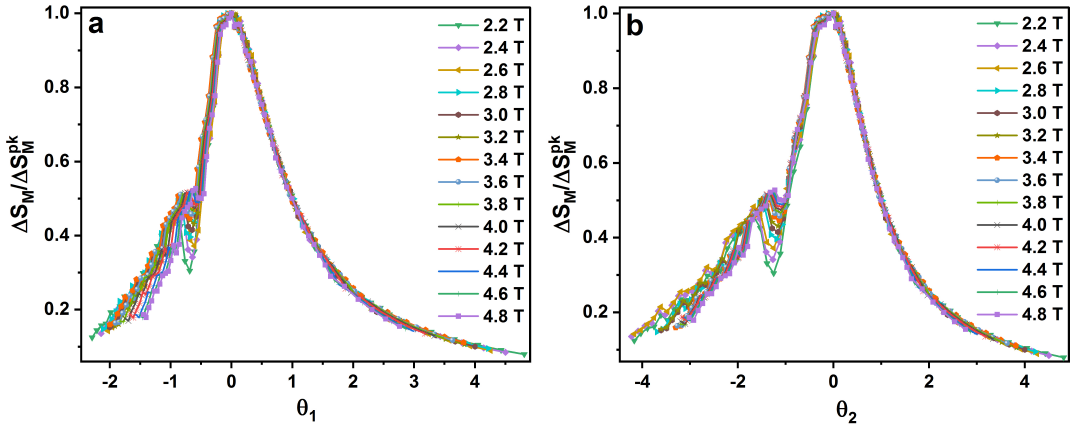


Figure 6.13: Universal curve with the rescaled magnetic entropy changes for Tb_3Co using one reference temperature θ_1 (a), and two reference temperatures θ_2 (b).

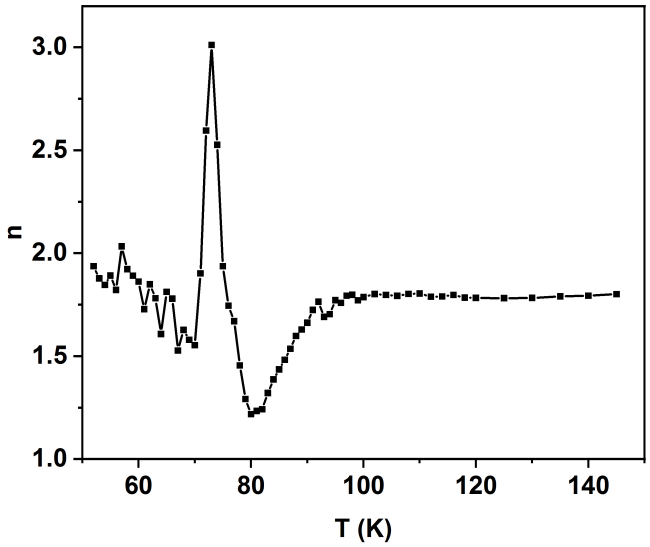


Figure 6.14: Dependence of the exponent n with temperature for $\mu_0\Delta H = 2$ T.

In the case of a second order phase transition, this should tend to 1 at temperatures well below the critical one and to 2 in the paramagnetic phase, with a minimum at the Néel/Curie temperature. It has recently been proven that, if the exponent n shows, as a function of temperature, a peak with a maximum value well above 2, a first order phase transition is present at the position of the peak [258–260]. Fig. 6.14 clearly shows that the spike indeed exists at the position of the low temperature transition, confirming its weak first order character. On the other hand, the absence of this peak in the high temperature transition confirms again its second order character.

6.5 Tb_3Ni

Concerning Tb_3Ni, only a few studies have been performed since its crystallographic structure and magnetic properties were first studied [349], where it was found that Tb_3Ni belongs to the space group *Pnma*, that there is a magnetic transition to an antiferromagnetic state at about 62 K and that it presents magnetic anisotropies, with Tb occupying two non-equivalent positions (*4c* and *8d* Wyckoff sites) which will lead to strong crystal-field effects. Electrical resistivity and specific heat have been measured as a function of temperature [372, 373] and a neutron diffraction study was performed together with magnetic measurements to prove the existence of short-range magnetic correlations in the paramagnetic state [306]. Finally, a very complete study on neutron diffraction and field-induced magnetic phase transitions in this material has been recently published, showing an extremely complex behavior: neutron diffraction data has shown that there is a transition from a paramagnetic phase at high temperature to an incommensurate magnetic phase at about 60 K, then (on lowering the temperature) to a lock-in, mixed magnetic phase with coexistence of incommensurate and lock-in components; finally, at about 46 K, there is a new transition to a commensurate antiferromagnetic phase. On applying magnetic fields, different metamagnetic transitions have been found to arise [347]. Nevertheless, the magnetocaloric properties of Tb_3Ni have not been studied yet, which is the main aim of our study. At the same time, we will shed more light on the properties of the phase transitions through the study of their behavior by combining thermal and magnetic techniques. The critical behavior of the higher temperature PM-AFM transition at 62 K will also be discussed by means of high resolution specific heat.

As mentioned before, two magnetic studies have been performed for this material. The first one was carried out 2 years before the second one. For the first study the magnetization was only measured up to 6 T along the *c* crystallographic axis, which is the easy axis of magnetization in Tb_3Ni. For the second study the magnetization was measured up to 7 T along the three crystallographic axes, in order to observe and study the anisotropy of the system, which will allow us to explore the rotating magnetocaloric effect (RMCE). Another important difference between both studies has to do with the magnetic measuring protocol and the method to obtain the MCE. Both measuring protocols have been described in Section 6.2; for the first study the magnetization isotherms were obtained one after the other, while for the second study a discontinuous protocol has been used, raising the temperature of the sample above the critical temperature before the acquisition of each isotherm, to ensure that the magnetic memory is erased. The first method, together with the *Clausius-Clapeyron* equation, has been extensively used for many years for the correct evaluation of the MCE in first order phase transitions (see Section 2.2.5 for more details). However, in recent years, the discontinuous protocol method has gained popularity after it was shown that with its application the same results could be obtained with no need of using the *Clausius-Clapeyron* equation [159, 160]. That is why the second measurement (two years after the first one) was performed using this new measuring protocol. This will also

allow us to compare both methods and check if they give equivalent results.

6.5.1 Thermal and magnetic evolution of Tb_3Ni

Fig. 6.15 shows the magnetization as a function of temperature for the Zero-Field Cooled (ZFC), Field-Warmed (FW) and Field-Cooled (FC) along the c axis, where an antiferromagnetic transition is clearly observed at $T_N = 61 \pm 0.5$ K. This curve is perfectly comparable to the results obtained in previous studies [306, 347]. At $T < T_N$ (inset in Fig. 6.15) some structure is also found with an anomaly around 48 K (T_t, found in literature to correspond to the disappearance of the lock-in transition [347]), while there is a hysteretic behavior on heating (FW) and cooling (FC).

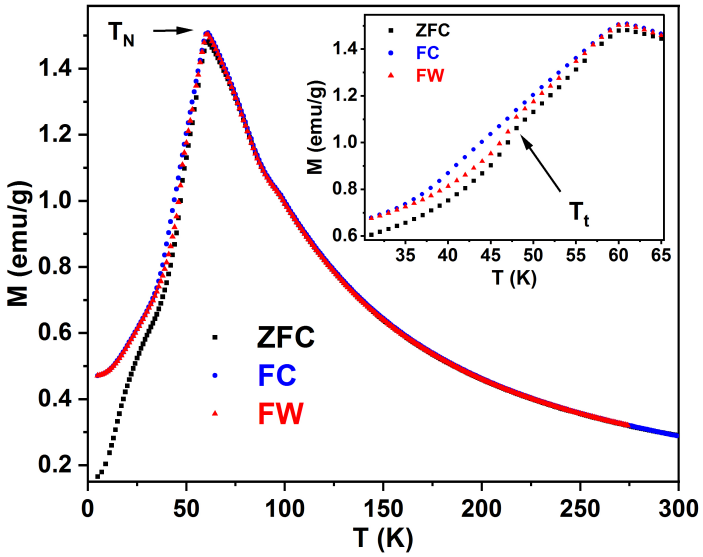


Figure 6.15: Zero-Field Cooled (ZFC), Field-Warmed (FW) and Field-Cooled (FC) magnetizations measured along the c axis with $\mu_0 H = 1$ kOe. Inset shows the region around T_t.

Fig. 6.16 contains the thermal diffusivity curve obtained as a function of temperature, without any applied magnetic field, presenting typical characteristics of intermetallic materials which we have already seen in the samples previously presented, and similar D values to the ones observed in Tb_3Co. As has been already discussed, heat is transferred both by electrons and by phonons in intermetallics. At high temperatures the electron contribution is dominant but this contribution decreases as temperature is lowered, which is why the thermal diffusivity is reduced. On the other hand, the phonon contribution becomes more important at low temperatures as the phonon mean free path increases. The competition between one mechanism which loses relevance and the other one which gains it (and both of them might be of the same order of magnitude) makes the thermal diffusivity present a well in many intermetallic materials, after which it quickly grows while temperature keeps

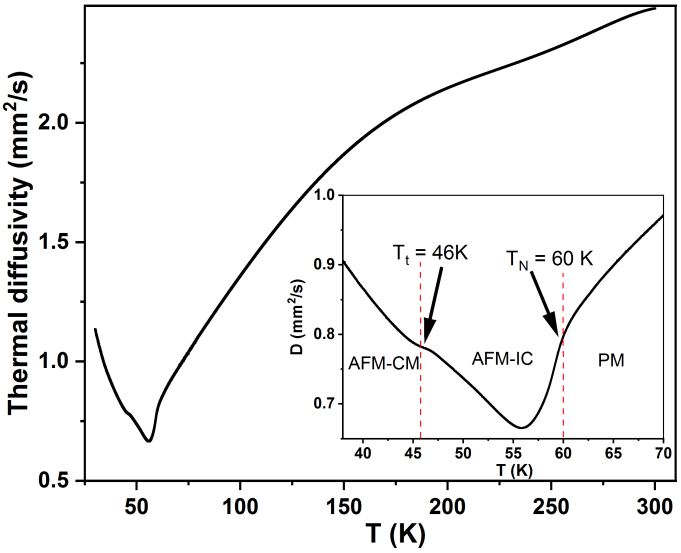


Figure 6.16: Thermal diffusivity (D) as a function of temperature. The inset indicates the temperatures at which magnetic phase transitions take place, where the phases have been labelled as indicated in literature [347]: T_t corresponds to the disappearance of the lock-in transition, T_N to the Néel temperature. AFM stands for antiferromagnetic phase, PM for paramagnetic, CM for commensurate, IC for incommensurate.

on descending. In the case of Tb_3Ni the increase in thermal diffusivity when lowering the temperature starts around 56 K. In the inset of Fig. 6.16 the found phase transitions are indicated. The paramagnetic to inconmensurate antiferromagnetic transition is signalled by the change in slope at 59.96 ± 0.01 K, in agreement with magnetic measurements shown in Fig. 6.15, while the shoulder centered around 46 K is related to the disappearance of the lock-in transition at T_t [347]. There is no hint of thermal hysteresis in any of these transitions.

6.5.2 Thermal critical behavior in Tb_3Ni

Combining the thermal diffusivity in Fig. 6.16 (which is obtained from the phase of the PPE signal) and the amplitude of the PPE signal it was possible to extract a high resolution specific heat in the region of the PM-AFM phase transition. The characteristic peak of this parameter is presented in Fig. 6.17(a). For the shape of the transition and absence of thermal hysteresis the transition at T_N is considered a second order phase transition, which allows the study of its critical behavior. As we have repeatedly seen for previous samples, the specific heat of a second order phase transition in the vicinity of its critical temperature can be fitted to:

$$c_p = B + Ct + A^{\pm}|t|^{-\alpha}(1 + E^{\pm}|t|^{0.5}), \tag{6.12}$$

where t is the reduced temperature $t = (T - T_N)/T_N$, α is the critical exponent, and the rest are adjustable parameters, with superscripts + and - standing for $T > T_N$ and $T < T_N$ respectively (see Section 3.3 for further details). We are interested in the critical exponent α and the ratio between the critical amplitudes A^+/A^-, whose values are related to different theorized universality classes.

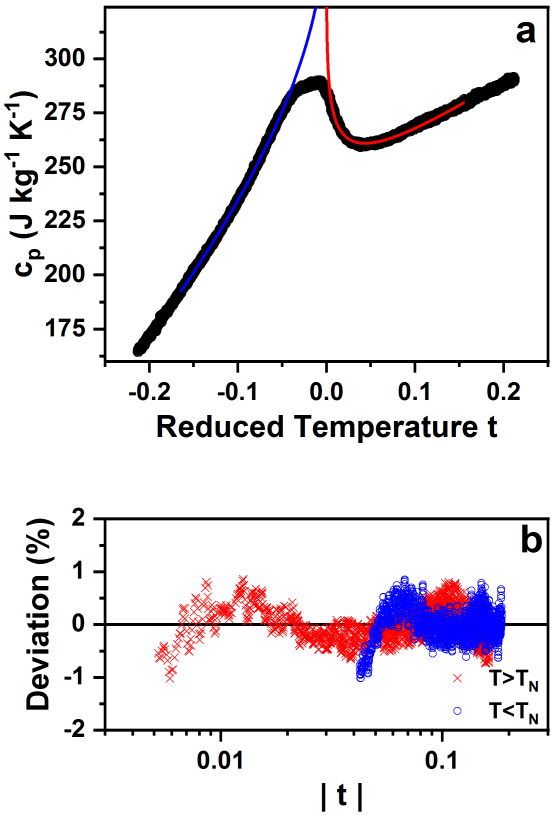


Figure 6.17: (a) Experimental c_p (dots) together with the fitted functions (continuous curves) to Eq. (6.12), as a function of the reduced temperature $t = (T - T_N)/T_N$; (b) Deviation plot: crosses for the region above T_N, circles for the region below.

Fig. 6.17(a) presents the best fitting of the experimental points to Eq. (6.12), while Fig. 6.17(b) contains the deviation plot (difference between the fitted and the experimental points, in percentage), which is within ±1% in the whole region, indicating the good quality of the fitting. The results of the fitting are collected in Table 6.5. It can be seen that the value of the critical exponent $\alpha = -0.13 \pm 0.02$ clearly points to the 3D Heisenberg, short-range, isotropic model ($\alpha_{\text{Heis}} = -0.134$), as it was also the case in Dy_3Co and Tb_3Co. However, the ratio deviates from the theoretical value for this universality class $A^+/A^-_{\text{Heis}} = 1.52$. This kind of deviations indicate that there is not a perfect isotropic distribution of spins, surely due to crystal-field effects, provoked by the Tb occupancy of low-symmetry sites in the orthorhombic lattice, which have been found to affect the magnetic properties of the whole R_3T family in general and of Tb_3Ni in particular [306, 339, 344, 374]; nevertheless, they are not important enough to reach an easy-plane or an easy-axis distribution of spins, as clearly neither the 3D XY ($\alpha_{\text{XY}} = -0.014$, $A^+/A^-_{\text{XY}} = 1.06$) nor the

3D Ising ($\alpha_{\text{Ising}} = +0.11$, $A^+/A^-_{\text{Ising}} = 0.536$) universality classes are of application. This is in agreement with the magnetic anisotropic measurements performed in Ref. [347] where it was shown that magnetization was easier along the c axis than along a or b around the Néel temperature but that only at very low temperature c became an easy axis. The fact that this transition nearly belongs to the 3D Heisenberg class also assesses that the magnetic interactions are short-range, corroborating the results previously obtained by means of neutron diffraction that sort-range order interactions were present even in the paramagnetic phase at temperatures high above T_N [306, 347].

Transition	c_p α	A^+/A^-
PM-AFM (60 K)	-0.13 ± 0.02	2.15

Table 6.5: Critical parameters for the PM-AFM transition in Tb_3Ni.

6.5.3 Magnetocaloric effect in Tb_3Ni

For this magnetocaloric effect evaluation and the analysis of the complex magnetic behavior we will stick to the magnetic measurements performed during our first study on Tb_3Ni.

Until now, in order to study the magnetocaloric properties, we have directly used the *Maxwell relation*. This is the quickest and easiest method in order to evaluate the magnetic entropy change ΔS_M from magnetization isotherms data. However, this technique can only be used for evaluating SOMPTs or weak first order transitions were no stepwise behavior is present in the magnetization isotherms, as was the case of Tb_3Co. For a FOMPT the use of *Maxwell relation* may lead to incorrect results and spurious peaks, overestimating the change in magnetic entropy, as commented in Section 2.2.5.

In the case of Tb_3Ni, the application of magnetic fields leads to a quite complex behavior, revealing different metamagnetic transitions with a critical field depending on temperature. Fig. 6.18 shows the magnetization as a function of temperature in the region of interest with applied fields up to 6 T (the data have been taken from the isotherms). At very low temperature, a field-induced metastable ferromagnetic phase appears at even zero field due to the fact that, once the field is removed after the first isotherm is collected (which takes the sample to a FM phase), the system stays in that state [347]. Increasing the temperature up to ≈ 10 K eliminates this metastable FM state and, from that temperature onwards, after having acquired each isotherm and removed the magnetic field, the sample returns to the AFM state. The magnetic field application turns this AFM state into a FM state. This development takes place at different fields, depending on the temperature regions. The first hint of the metamagnetic transition is visible in Fig. 6.18 above $\mu_0 H = 2$ T.

Fig. 6.19(a) contains isotherms measured from 3 to 130 K (not all of them have been drawn, for the sake of clarity) where it is clearly seen that the behavior is very complex, showing the presence of several metamagnetic transi-

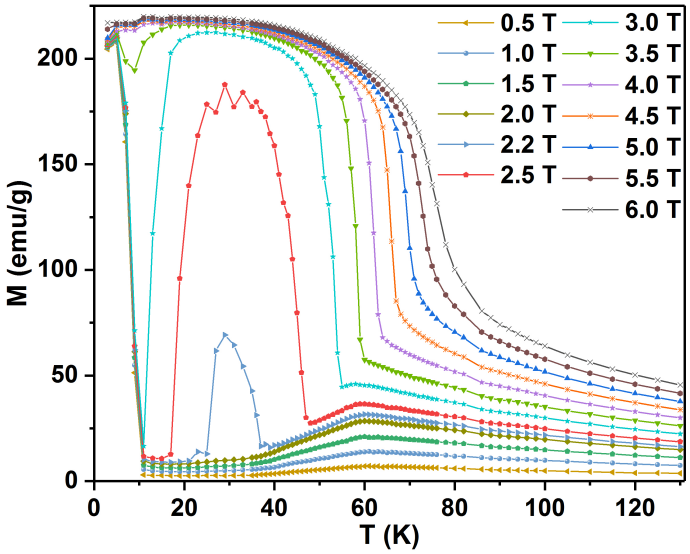


Figure 6.18: Magnetization as a function of temperature for different applied fields.

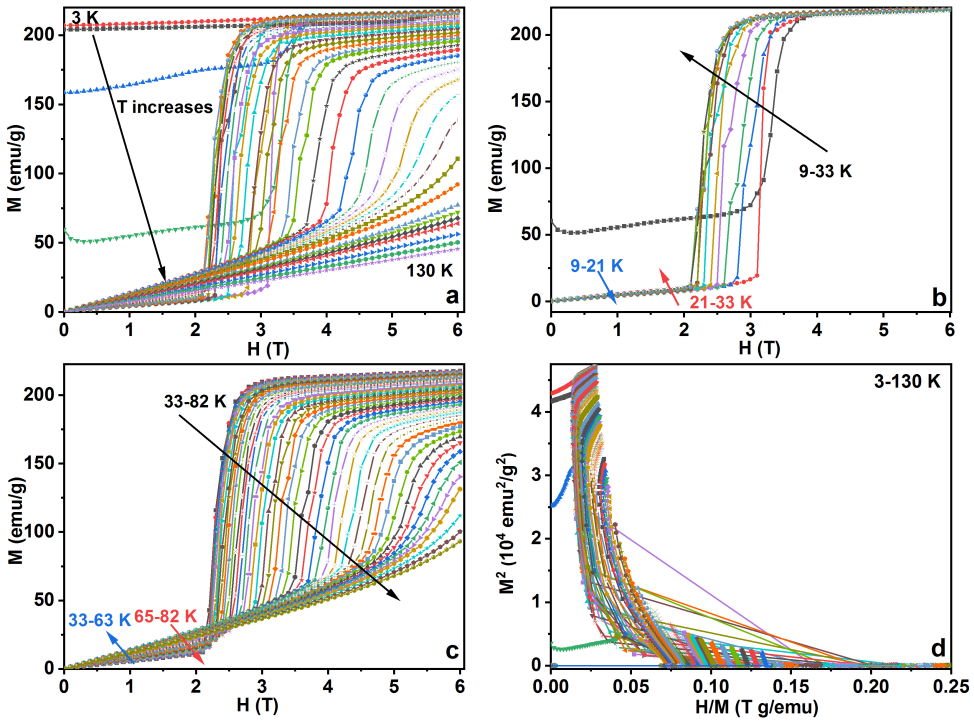


Figure 6.19: (a) M as a function of H for selected isotherms in the range 3-130 K; (b) detail from 9 to 33 K; (c) detail from 33 to 82 K; (d) Arrot plot for the range 3-130 K. The arrows indicate the direction of increasing temperatures.

tions with stepwise behavior from the lower magnetization AFM state to the higher magnetization FM state. The behavior depends on temperature regions, that is why some temperature and field regions of interest are shown in Fig. 6.19(b) and (c). From Fig. 6.19(a) and (b) it can be appreciated that, at very

low temperatures, the system is in the metastable FM state which turns into an AFM state (achieved at 11 K) as temperature is increased, at fields lower than 2 T. If the applied field is increased to values higher than roughly 2 T, then a clearly first order metamagnetic transition to a FM state appears but it is mixed with the AFM phase in the sense that as temperature increases in the region 9-21 K, for the same value of the field at high fields, magnetization increases (characteristic of AFM ordering) while, for low fields, it decreases (characteristic of FM ordering). This situation changes in the region 21-33 K (see Fig. 6.19(b)), where, at low fields, the evolution of the curves is completely in agreement with an AFM state (magnetization increases with temperature) and there is a metamagnetic transition to the FM state. Fig. 6.19(c) shows the region between 33 and 82 K. A metamagnetic transition to a pure FM state takes place at fields higher than 2 T, while, at lower fields (roughly < 2 T), there are two regions: up to 63 K the behavior is AFM (magnetization increases with temperature), while from 63 K upwards the magnetization, at a given field, decreases with temperature (PM behavior). This sequence of transitions is in agreement with the phase diagram previously found for Tb_3Ni when a magnetic field is applied along the *c*-axis [347].

Finally, Fig. 6.19(d) shows the Arrott Plot where it is clearly seen that the slopes of the curves are negative in a region which corresponds to applied fields higher than 2 T, indicating, after the Banerjee criterion [229], that the metamagnetic transitions have a first order character. From the shape of the magnetization curves (Fig. 6.19(a)-(b)) it is also clear that in the metamagnetic transitions there is a clear coexistence of the FM and AFM phases up to 33 K, as they present a marked stepwise magnetic behavior [152,375,376] (specially marked at low temperatures), while from there on this behavior is still present, though in a much lesser degree. Therefore, due to the first order character of these metamagnetic transitions, the use of the *Maxwell relation* is not adequate to calculate the magnetic entropy change as it leads to an overestimation because, whenever there is a FOMPT, *Maxwell relation* (MR) would include not only the contribution to the change in magnetization as a result of the orientation of the magnetic moments in an applied field, but also as the result of the relative change in the fractions of the two coexisting phases. As we saw in Section 2.2.5, for a proper calculation in this case, the *Clausius-Clapeyron* (CC) equation must also be used [150,152,157,375,377]. Therefore, following Caballero Flores *et al.* [157], we obtain the magnetic entropy change by independently calculating ΔS_M for the range of temperatures and magnetic fields inside the transition region using the *Clausius-Clapeyron* equation (ΔS_M^{CC}) and, outside this region, using the *Maxwell relation* (ΔS_M^{MR}):

$$\Delta S_M(T,\Delta H) = \overbrace{\mu_0 \int_{H_0}^{H_C-\delta H} \left(\frac{\partial M}{\partial T}\right)_H dH}^{\Delta S_M^{\mathrm{MR}}(\mathrm{AFM})} \underbrace{-\mu_0 \Delta M \frac{dH_C}{dT}}_{\Delta S_M^{\mathrm{CC}}} + \overbrace{\mu_0 \int_{H_C+\delta H}^{H_1} \left(\frac{\partial M}{\partial T}\right)_H dH}^{\Delta S_M^{\mathrm{MR}}(\mathrm{FM})} . \tag{6.13}$$

where $\Delta S_M^{CC} = S_M^B - S_M^A$, $\Delta M = M^B - M^A$ are the gaps of the magnetic entropy change and magnetization of the coexisting phases A and B, while H_C is the critical field. The extent of the transition region is very clear for $T < 33$ K (see Fig. 6.19(b)). For $T > 33$ K (Fig. 6.19(c)) we have taken as the beginning and end of the transition region ($H_C - \delta H$, and $H_C + \delta H$, respectively) the inflection points in the isothermal magnetizations. The critical field H_C has been taken as the value of the inflection point within the metamagnetic transitional region [375], and its variation with temperature is shown in Fig. 6.20, which is in good agreement with the phase diagram presented for Tb_3Ni in Ref. [347]. The polynomial fit (red line) from where the first derivative dH_C/dT has been retrieved is also represented in Fig. 6.20. In the low temperature region ($T < 11$ K), we have additionally followed the procedure commonly used for stepwise behavior, where only the contribution to the magnetic entropy change of the final phase is taken into account when considering the area between two particular isotherms [152, 376, 377].

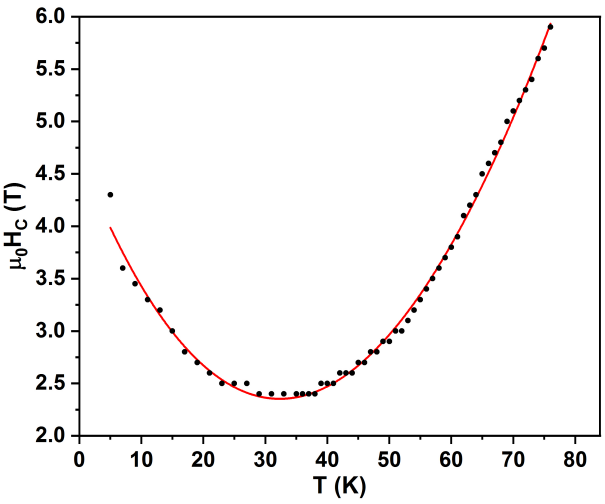


Figure 6.20: Critical field for the metamagnetic transition to take place, as a function of temperature. The dots represent the points retrieved from the measurements while the continuous line is a polynomial fit.

The total magnetic entropy change with $\mu_0 \Delta H$ from 0 to 6 T is shown in Fig. 6.21(a), where it can be seen that there are two magnetocaloric effects, an inverse one (IMCE) at low temperature and a direct one (DMCE) at a higher one. Due to the evaluation by parts of the magnetic entropy change, following Eq. (6.13), some temperatures data are missing at each isofield, these gaps correspond to the region within $H_c - \delta H$ and $H_c + \delta H$. Fig. 6.21(b) shows the detail with $\mu_0 \Delta H$ from 0.1 to 2.1 T, before the metamagnetic transitions take place. In this field region, the magnetic entropy change presents the typical behavior corresponding to an AFM-PM transition, with an inversion in the magnetic entropy change just below the Néel temperature and with a maximum developing at higher fields and moving to lower temperatures, as theoretically predicted and verified in other materials [168, 251, 378]. At higher fields (see

Fig. 6.18, Fig. 6.20) the metamagnetic transitions take place, leading to two important magnetocaloric effects, a direct one with a maximum at about 65 K, and an inverse one, with a maximum at about 11 K. The inset in Fig.6.21(a) shows $-\Delta S_M$ as a function of $\mu_0\Delta H$ at 52 K, indicating how the field induced metamagnetic transition turns what would have been a small IMEC into the relevant DMCE.

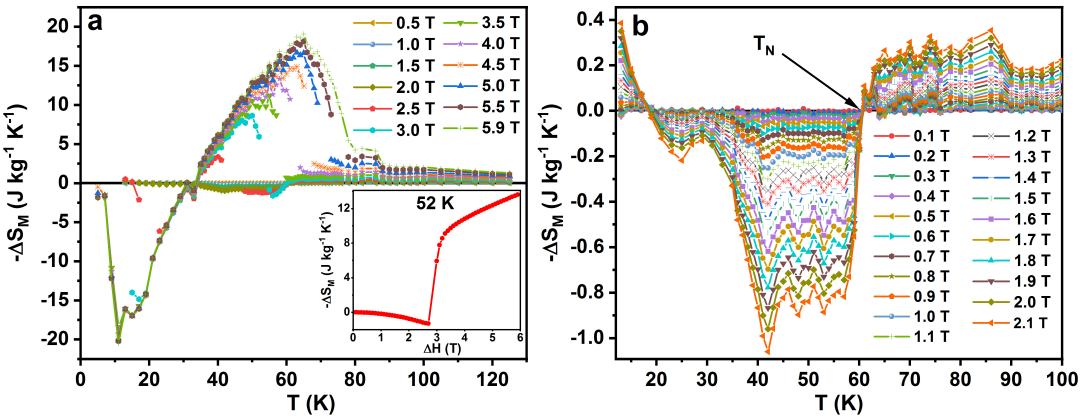


Figure 6.21: (a) Magnetic entropy change $-\Delta S_M$ for $\mu_0\Delta H$ from 0.5 T to 5.9 T in the whole temperature region. Inset: $-\Delta S_M$ as a function of $\mu_0\Delta H$ at 52 K. (b) Magnetic entropy change for $\mu_0\Delta H$ from 0.1 T to 2.1 T focused on the AFM region.

In agreement with what we already saw in Fig. 6.18, in the case of the direct effect, there is an inversion of the sign of the magnetic entropy change with an increasing applied field which starts in the region 33-40 K and grows to higher temperatures, developing a very wide magnetic entropy peak, whose maximum stabilizes at about 65 K from an applied field of 5 T upwards. In the case of the inverse effect, the magnetic entropy change peak is displaced to lower temperatures till it is fixed at 11 K for $\mu_0\Delta H > 3.5$ T.

The values of the maximum entropy and the refrigerant capacity are presented in Table 6.6 for $\mu_0\Delta H = 5$ T. These values turn out to be extremely competitive in their respective temperature ranges, especially for the DMCE, where, for $\mu_0\Delta H = 5$ T we get $|\Delta S_M^{pk}| = 16.6$ J/kgK at 65 K, which places the DMCE of Tb_3Ni in the highest region of values shown in Fig. 25 of the recent review published by Franco *et al.* [91], where a very thorough revision of materials is done. Concerning the refrigerant capacity, it is defined in the two usual ways: RC_{FWHM} is calculated as the product of $|\Delta S_M^{pk}|$ times the width of ΔS_M at half maximum, while RC_{Area} is the area enclosed by the ΔS_M vs. temperature curves in the temperature range enclosed by the full width at half maximum of the peak. For Tb_3Ni, in the DMCE, $RC_{\mathrm{FWHM}} = 432$ J/kg, $RC_{\mathrm{Area}} = 341$ J/kg which are extremely high values and with the added advantage that the width of the magnetocaloric effect is very wide. For the IMCE, the absolute value of the magnetic entropy change is slightly higher than the one for the DMCE: $|\Delta S_M^{pk}| = 19.9$ J/kgK, at 11 K, also for $\mu_0\Delta H = 5$ T. However, in this temperature region, the comparison with the materials published in the mentioned

review [91] is not as good as in the other case but its value is also quite high, as well as the refrigerant capacity values: $RC_{\mathrm{FWHM}} = 245$ J/kg and $RC_{\mathrm{Area}} = 194$ J/kg.

Peak	$\lvert\Delta S_M^{pk}\rvert$ (J kg^{-1} K^{-1})	RC_{FWHM} (J kg^{-1})	RC_{Area} (J kg^{-1})
DMCE (65 K)	16.6	432	341
IMCE (11 K)	19.9	245	194

Table 6.6: Peak of the magnetic entropy change $\lvert\Delta S_M^{pk}\rvert$, RC_{FWHM}, and RC_{Area} at $\mu_0\Delta H = 5$ T for both the DMCE and IMCE in Tb_3Ni.

Finally, the results obtained from the magnetic measurements at low fields confirm what was extracted from the thermal measurements about the character of the AFM-PM transition (before the metamagnetic transition appears), that it is second order. This is further confirmed because a universal master curve can be built up for the normalized ΔS_M curves below the critical field H_C, where all data collapse. We have already seen several times that in the case of the conventional direct magnetocaloric effect, such kind of universal curve is attained when ΔS_M is normalized to its peak value and the temperature is rescaled using one or two reference temperatures T_r [235, 240]. But it has been shown that, in the case of an IMCE in an AFM-PM second order phase transition, there is no need to rescale the temperature [251]. Fig. 6.22 shows that there is a very good collapse below 2 T without the use of any reference temperature to rescale this variable.

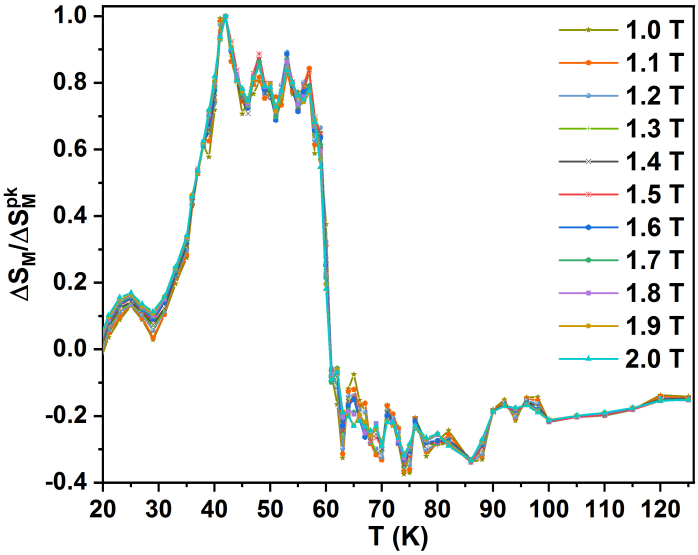


Figure 6.22: Universal master curve for $\mu_0\Delta H$ from 1 T to 2 T for the AFM region.

Concerning the metamagnetic transition which takes place on the application of higher fields, there is still another method (apart from the Banerjee criterion discussed on Fig. 6.19(d)) to check its character, using the evolution

of the exponent n related to the field dependence of ΔS_M with temperature, already used for Tb_3Co in the previous section:

$$n(T,H) = \frac{d \ln |\Delta S_M(T,H)|}{d \ln H} . \tag{6.14}$$

This exponent must have a value of 2 in the paramagnetic phase while, in the case of a first order phase transition, there should be a shoot well above this value, tending to 1 at temperatures well below the critical one [258–260]. Fig. 6.23 shows n for Tb_3Ni, at $\mu_0\Delta H = 3.5$ T. There is a clear overshoot at the metamagnetic transition at 61 K, proving that it is first order. In the region shadowed in grey there is a dip at 31 K which is due solely to the change in sign in ΔS_M [118]. At the lower phase transition, another spike starts to form due to the metamagnetic transition responsible for the IMCE but there are not enough experimental points to see it clearly developed.

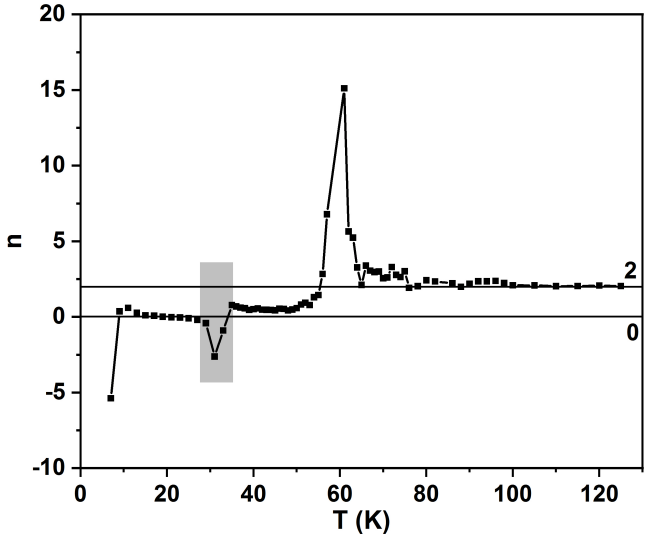


Figure 6.23: $n(T)$ for $\mu_0\Delta H = 3.5$ T. The shoot at 61 K proves the character of the transition to be first order. The dip in the shadowed region is simply due to the change in sign of the magnetic entropy change.

6.5.4 Magnetic anisotropy and RMCE in Tb_3Ni

The magnetic properties of Tb_3Ni are known to be anisotropic with the application of the magnetic field along its different crystallographic axes. Until this section we have focused our magnetic analysis on the magnetization when H is applied along the c axis, which is the easy-axis of this material. We will now extend our analysis in order to study the magnetic anisotropy of the system and how it can be used to generate a big rotating magnetocaloric effect (RMCE). The work presented in this section is a preliminary part of an ongoing collaboration aiming to explore this anisotropy at higher fields (up to 50 T)

and the adiabatic temperature change (ΔT_{ad}) of Tb_3Ni under the application of those high fields.

The magnetic phase diagrams when the field is applied parallel to the different axes have already been described in detail in Ref. [347], while the anisotropic behavior is know at least since 1982 [349]. In the latter reference it was already shown that the metamagnetic transitions in Tb_3Ni take place at different critical fields depending on the axis along which the magnetic field is applied. It was observed, for example, that at 4.2 K the critical field $\mu_0 H_C$ was 4.4 T when the magnetic field was applied along the *c* axis, 11.5 T when it was applied along the *b* axis, and two metamagnetic transitions were observed when the magnetic field was applied along the *a* axis, a lower one at 12.5 T and a higher one at 14 T. The critical field observed for the *c* axis at that time at 4.2 K completely agrees with the one we found in our compound (see Fig. 6.20). Unfortunately, our experimental device is limited to a maximum of 7 T, so only the metamagnetic transitions along the *c* axis will be observable. This is another reason for our interest on the study of Tb_3Ni at higher magnetic fields.

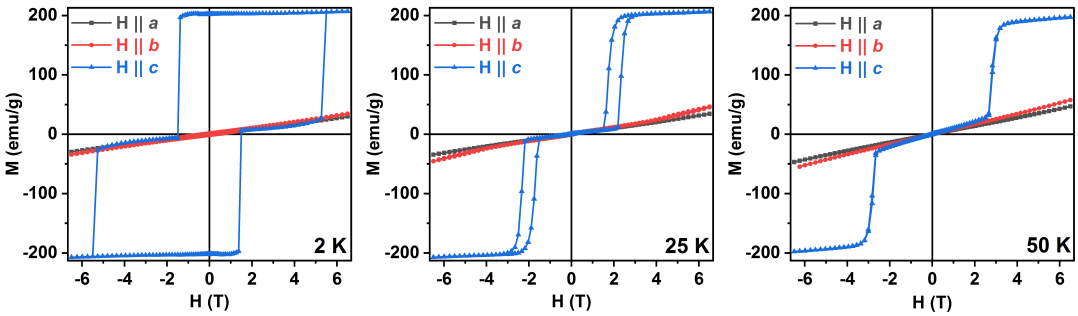


Figure 6.24: Magnetic hysteresis cycles of Tb_3Ni at 2 K, 25 K, and 50 K, when magnetic field is applied along the different axes.

The magnetic anisotropy is crystal clear from the hysteresis cycles performed at 2, 25 and 50 K along the three axes, see Fig. 6.24. The field-induced metamagnetic transition is evident at the three temperatures for the $H||c$ case in Fig. 6.24, while it is not seen when the field is applied along the other two directions, for which the transition takes place at higher fields. Fig. 6.24 also shows how the magnetic hysteresis when H is applied parallel to c decreases with increasing temperature, which was already observed in Ref. [349]. The magnetic behavior when H is applied parallel to a and b is completely AFM in this field range, but we can notice how the magnetization is slightly tilted upwards (downward for negative fields) when the field is applied parallel to the direction of b axis in comparison to when the same is done for a axis. This is due to the proximity of the metamagnetic transition on the former axis, for which $\mu_0 H_C \sim 11.5$ T. Although it is not clearly observed in Fig. 6.24, the magnetic moment when $H||b$ shows a small hysteretic effect even at these fields.

As mentioned before, the main difference between the magnetic measurements performed previously and the ones carried out for this new study is that for the latter a discontinuous measuring protocol, as described in Section 6.2, has been taken. The difference with respect to the previous measurement can

be seen in Fig. 6.25 when compared with Fig. 6.19(a). In both cases the magnetization isotherms for when $H\|c$ as a function of the field are represented, but, while the low temperature metastable field-induced ferromagnetic state is observed in Fig. 6.19(a), this completely vanishes in Fig. 6.25, since the temperature is increased above the critical temperature before the measurement of each isotherm in order to erase the magnetic memory. Furthermore, from Fig. 6.25 we can see that at low fields the compound is AFM (magnetization increases as temperature increases), while at higher fields (once the metamagnetic transition takes place) the AFM-like behaviour is only observed up to 30 K, from where magnetization starts to decrease with increasing temperature, as it is expected for a ferromagnetic state.

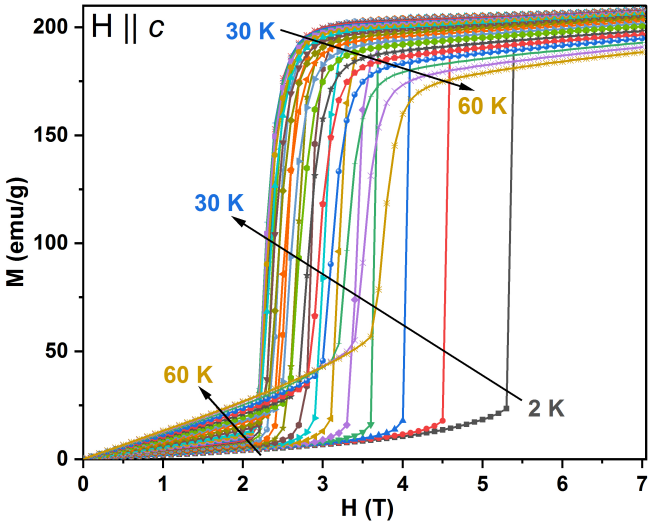


Figure 6.25: Magnetization isotherms as a function of the applied magnetic field for $H\|c$ in the range 2-60 K.

From the isotherms we can also obtain the temperature evolution of the magnetization for different applied fields along the three axes. Fig. 6.26 clearly shows the striking difference for each axes. When the magnetic field (up to 7 T) is applied parallel to a or b the transition is unequivocally PM-AFM, while if the field is applied along the c axis, metamagnetic transitions are induced above 2 T, with the exact same shape as the ones in Fig. 6.18, save at the low temperature region, where, once again, we can notice that the field-induced metastable FM state is removed due to the discontinuous measuring protocol.

As we have already mentioned, the main advantage of using a discontinuous measuring protocol for measuring the magnetization isotherms of this compound is that, by doing so, there is no longer need to use the time consuming Eq. (6.13) in order to correctly obtain the magnetic entropy change; instead ΔS_M can be calculated by directly using the *Maxwell relation*:

$$\Delta S_M(T,\Delta H) = \mu_0 \int_{H_0}^{H_1} \left(\frac{\partial M}{\partial T}\right)_H dH\,. \tag{6.15}$$

The result is shown in Fig. 6.27 where the characteristic IMCE due to the AFM phase for $H\|a$ and $H\|b$ is observed. The ΔS_M^{pk} value at $\mu_0\Delta H = 5$ T is

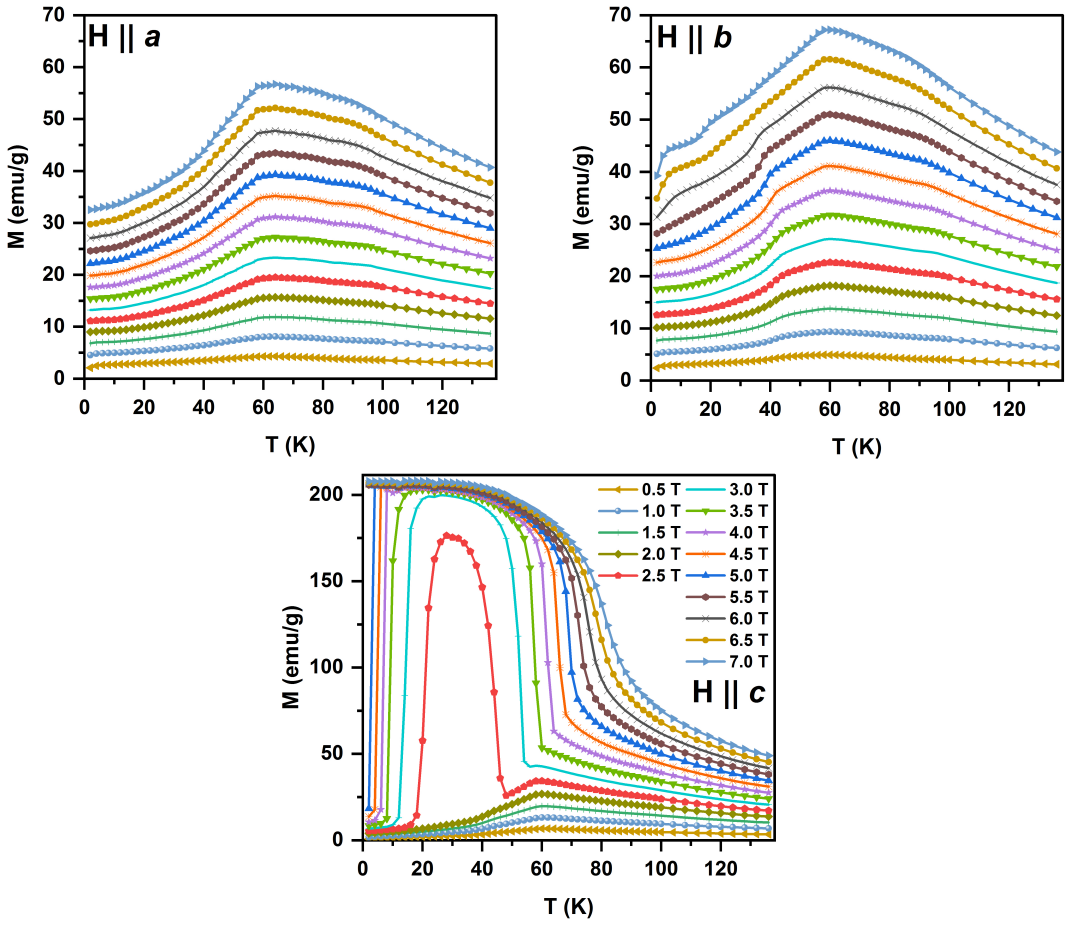


Figure 6.26: Magnetization as a function of temperature for different applied fields as obtained from isotherms. For: $H||a$, $H||b$, $H||c$. The legend is the same for every plot.

higher for $H||b$ than for $H||a$. On the contrary, the RC value is slightly higher when the magnetic field is applied along the a axis. The peak of the IMCE is displaced at lower temperature (40 K) when the field is applied in the direction of the b axis compared to when H is parallel to a (52 K). The ΔS_M^{pk} and RC values for these orientations are collected in Table 6.7, and it can be seen that the magnetocaloric effect is not relevant in any of the previous orientations at these specific magnetic fields, $\mu_0\Delta H = 5$ T. This changes when the magnetic field is applied along the c axis instead. For this particular orientation we recover the shape previously shown in the left hand side of Fig. 6.21. Given that now we can directly apply the *Maxwell relation* to obtain $-\Delta S_M(T,\Delta H)$, the curves in the $H||c$ plot of Fig. 6.27 are complete, without missing regions as it was the case in Fig. 6.21. The shape and the obtained values for the MCE are completely equivalent in both cases, with the only difference appearing at the lowest temperature points. Below 8 K, at $\mu_0\Delta H > 4T$, $-\Delta S_M(T,\Delta H)$ values are lower than the previously obtained ones (due to the correct erasing of the magnetic memory) reaching values down to -62 J/kgK. For fields below 4 T this low temperature region keeps the same shape in both cases, as it happens for every field in the region above 8 K. The inset in the $H||c$ plot of Fig. 6.27

is a zoom-in of the DMCE, where the small IMCE is visible at low magnetic fields, and the metamagnetic transition to the FM state is observed at higher fields. This shows that both methods of correctly evaluating the MCE (the use of *Clausius-Clapeyron* and the discontinuous measuring protocol) are both valid and give similar results.

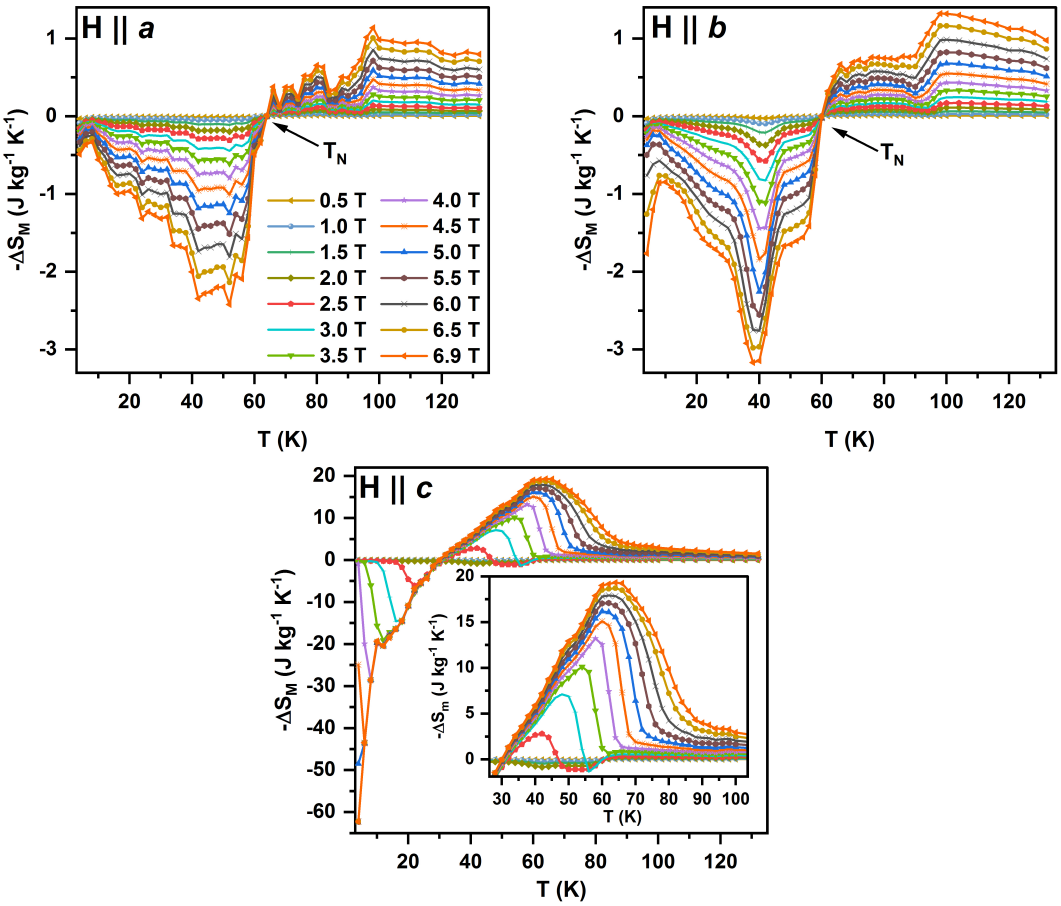


Figure 6.27: $-\Delta S_M(T, \Delta H)$ for a magnetic field change up to $\mu_0 \Delta H = 6.9$ T for $H||a$, $H||b$, and $H||c$. Inset in $H||c$ plot shows the DMCE region caused by the field-induced metamagnetic transition. The legend is the same for all of them.

Field orientation	ΔS_M^{pk} (J kg^{-1} K^{-1})	RC_{FWHM} (J kg^{-1})	RC_{Area} (J kg^{-1})
$H||a$ (52 K)	1.2	45	34
$H||b$ (40 K)	2.3	30	22

Table 6.7: Peak of the magnetic entropy change ΔS_M^{pk}, RC_{FWHM}, and RC_{Area} at $\mu_0 \Delta H = 5$ T for the IMCE when the field is applied along a or b axis in Tb_3Ni.

Up to now we have focused our interest on the most general magnetocaloric effect, where a temperature change in the material is obtained by changing an applied external magnetic field or, what would be the same, moving the mag-

netocaloric material in and out of a static magnetic field. This is the main research line concerning magnetocaloric material for refrigeration devices, yet, when designing a experimental magnetocaloric refrigerator, this approach involves some undesired drawbacks. On the one hand, a constant magnetic field variation produces energy losses due to eddy currents, and the magnetization-demagnetization process generally requires both a complex device and a great amount of mechanical energy to move the sample in and out of the magnetic field area, which decreases the efficiency of the system [64]. On the other hand, the removal of the magnetic field from a superconducting magnet in order to cool the magnetocaloric material takes some time, but this process should ideally be as fast as possible [350]. The rotating magnetocaloric effect (RMCE) solves these problems. Taking advantage of the magnetic anisotropy and geometry of the sample, more compact, simpler and efficient devices can be built, with a much faster response [64, 350]. On this kind of devices, the heating or cooling is obtained under a fixed magnetic field inside which the sample is rotated from its easy magnetization direction to its hard magnetization axis. This simple process creates a magnetic entropy change which, in adiabatic conditions, causes a temperature change. The sign of this temperature change depends on the rotation direction. If the material is oriented so that the hard magnetization axis (h) coincides with the external magnetic field ($H\|h$), it will increase its temperature when rotating to an easier magnetization axis ($H\|e$). On the contrary, the sample will cool down when the process is reversed, i.e., when moving from $H\|e$ to $H\|h$. Although it might looks like the implementation of RMCE could revolutionize magnetic refrigeration as we know it, it presents a major drawback which is responsible for the relatively small number of works on this topic compared to the ones addressing the typical magnetocaloric effect: the need of single crystals. The process to obtain a great amount of good quality single crystals is still hard and tedious, and it's not always an accessible technique. This is the reason why the RMCE is not attracting as much attention as the classical MCE.

The entropy change in a material associated to the rotation from a hard axis (h) to an easy axis (e), with the magnetic field initially in the direction of h, is given by [64, 351]:

$$\Delta S_{M,R} = \Delta S_M(H\|e) - \Delta S_M(H\|h)\,, \tag{6.16}$$

where $\Delta S_M(H\|e)$ and $\Delta S_M(H\|h)$ are the magnetic entropy changes with the application of a magnetic field along the easy and hard axis respectively. As we have already seen, the easy axis of magnetization in Tb_3Ni is c, while a and b are both hard magnetization axes. Since the magnetic entropy change under the application of a magnetic field along the three axes has already been measured (see Fig. 6.27), Eq. (6.16) will directly yield the RMCE when the compound is rotated from $H\|a$ or $H\|b$ towards $H\|c$.

Fig. 6.28(a) shows the result of applying Eq. (6.16) with $h = a$, $e = c$ while Fig. 6.28(b) is the case for $h = b$, $e = c$. Obviously, the RMCE is enhanced when the MCE has different signs along the rotation axes [352], which is our case. However, the IMCE at $T < T_N$ and the DMCE at $T > T_N$ observed in Fig. 6.27 for $H\|a$ and $H\|b$ are small in comparison to the ones obtained when $H\|c$, thus, at first sight, both $-\Delta S_{M,R}(T,H)$ graphs in Fig. 6.28 look very similar

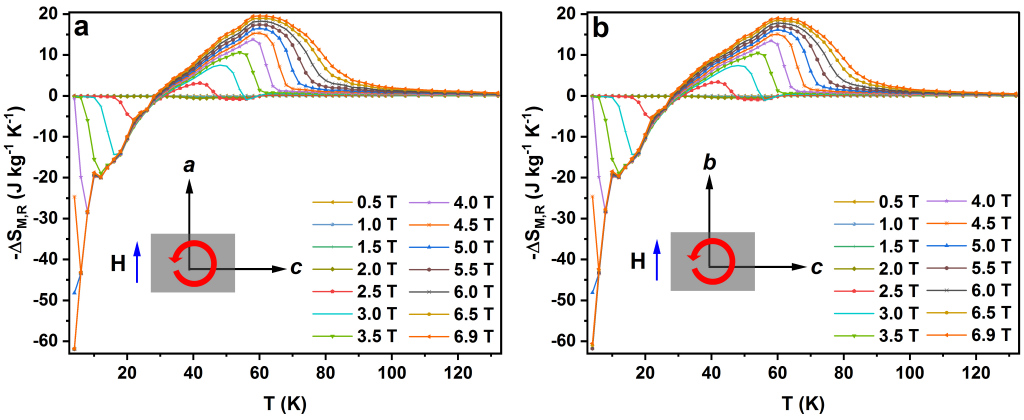


Figure 6.28: $-\Delta S_{M,R}(T,H)$ for fixed magnetic fields (up to $\mu_0 H = 6.9$ T) when rotating from $H||a$ to $H||c$ (a), and from $H||b$ to $H||c$ (b).

to the $-\Delta S_M(T,\Delta H)$ plot corresponding to $H||c$ in Fig. 6.27. The main visual difference between Fig. 6.28(a) and Fig. 6.28(b) is that the peak value in the former is slightly higher while the $-\Delta S_{M,R}(T,H)$ value in the latter is slightly increased in the region around 40 K. This is a very good result, since the high magnetocaloric properties are maintained in the rotatory configuration. The $\Delta S^{pk}_{M,R}$ and RC values in the region close to T_N for both rotation configurations are gathered in Table 6.8 for 5 and 6.9 T, the peak value is located at 60 K in every case. The minimum $-\Delta S_{M,R}$ values for an applied field of 5 T are obtained at 4 K, where the values are -48.2 J/kgK and -48.1 J/kgK for $h = a$ and $h = b$ respectively. For the highest applied field (6.9 T), these values are further enhanced to -61.8 J/kgK for $h = a$ and -60.5 J/kgK for $h = b$.

Hard axis [$\mu_0 H$]	$\lvert\Delta S^{pk}_{M,R}\rvert$ (J kg^{-1} K^{-1})	RC_{FWHM} (J kg^{-1})	RC_{Area} (J kg^{-1})
a [5 T]	16.5	429	346
b [5 T]	16.2	446	352
a [6.9 T]	19.5	726	593
b [6.9 T]	19.0	734	591

Table 6.8: Peak of the rotatory magnetic entropy change $\lvert\Delta S^{pk}_{M,R}\rvert$, RC_{FWHM}, and RC_{Area} at $\mu_0 H = 5$ and 6.9 T for the higher temperature peak when the rotation is performed from the hard axis (a or b) toward the easy axis (c).

The values in Table 6.8 at 5 T are in both cases very similar to those previously found in Table 6.6, with the difference that while the peaks are slightly smaller and displaced from 65 to 60 K, the RC values are maintained for $h = a$ or even increased for $h = b$. When comparing these RMCE results with the few cases reported in literature, we find out that they are among the highest ones. One of the most extensively studied families regarding its RMCE is the $RMnO_3$ family, whose $\lvert\Delta S^{pk}_{M,R}\rvert$ values at 5 T range from 14.6 J/kgK for R=Dy, to 5.25 J/kgK for R=Tm, with the peak taking place between 9-16

K [351, 353–356]. In that temperature range our $|\Delta S^{pk}_{M,R}|$ values at 5 T vary from ~20 to 23 J/kgK (see Fig. 6.28). When Mn in $RMnO_3$ family is substituted by Fe, $|\Delta S^{pk}_{M,R}|$ values at 5 T increase, reaching 13.5 J/kgK for $ErFeO_3$ and 19.5 J/kgK for $DyFeO_3$; however, the position of the peak is displaced to 4.1 and 4.5 K respectively [357, 358], where for Tb_3Ni we get values as high as 48 J/kgK for the same applied field. Another family showing high RMCE values is RMn_2O_5, for which the peak at 5 T in the case of R=Ho and R=Tb is located around 10 K, with $|\Delta S^{pk}_{M,R}| = 10$ J/kgK for $HoMn_2O_5$ and $|\Delta S^{pk}_{M,R}| = 12$ J/kgK for $TbMn_2O_5$ [351, 359, 360]. As mentioned before, the values we obtain for Tb_3Ni in that temperature range are twice higher. Other examples in this temperature range are: textured DyNiSi with $|\Delta S^{pk}_{M,R}| = 17.6$ J/kgK ($T_{pk} = 8.8$ K) [361], dysprosium acetate tetrahydrate with $|\Delta S^{pk}_{M,R}| = 6$ J/kgK ($T_{pk} = 10$ K) [350], or $ErAlO_3$ with $|\Delta S^{pk}_{M,R}| = 9.7$ J/kgK ($T_{pk} = 14$ K) [362], all of them measured at $\mu_0 H = 5$ T. The $|\Delta S^{pk}_{M,R}|$ value obtained at 60 K for Tb_3Ni can be compared to that of PrSi at 52 K, which is (to our knowledge) the highest one reported for the temperature region 50-70 K, with $|\Delta S^{pk}_{M,R}| = 18.6$ J/kgK for an applied field of 5 T [363]. This value is only slightly higher than the one obtained for Tb_3Ni with the same field conditions (see Table 6.8); however, the RC_{FWHM} value reported for PrSi (240 J/kg) [361] is much lower than the one for Tb_3Ni listed in Table 6.8.

The preceding discussion makes clear the potential of Tb_3Ni as a promising candidate for magnetic refrigeration in both alternating and fixed magnetic fields. Thus, it is justified the interest on further studies at higher magnetic fields in order to measure the effect of the magnetic anisotropy on the adiabatic temperature change.

6.6 Conclusions

The critical behavior of the highest temperature transition, which was observed to be a second order PM to AFM transition in every case, has been studied for the three members of this family: Dy_3Co, Tb_3Co and Tb_3Ni. Different thermal parameters, all of which were obtained from a high resolution *ac* PPE calorimeter, were used, all of them pointing to the 3D Heisenberg isotropic class, thus, confirming the short-range order interactions predicted by neutron diffraction in previous works. Some critical parameters, specially in Tb_3Co and Tb_3Ni, present small deviations from the theoretical value. These deviations from the perfect isotropy are explained by crystal field effects introduced by the Tb occupation of non-equivalent positions. In the case of Dy_3Co, the lower temperature AFM rearrangement (32 K) has also been studied within the critical behavior theory, observing a further deviation from the isotropic class, as previously observed by different measurements.

For Tb_3Co, the character of the lower temperature transition was discussed and settled, and a detailed neutron diffraction analysis was performed. We found out that in the AFM-FM transition at about 70 K there is no appreciable thermal hysteresis but the Arrott Plot as well as the behavior of the

exponent n with temperature clearly identify it as weakly first order, giving direct evidence of its character. Concerning the neutron diffraction analysis, a weak symmetry distortion from the orthorhombic *Pnma* space group to the monoclinic symmetry consistent with the $P2_1$ space group was found, for the first time, by the single crystal neutron diffraction in the paramagnetic state at $T = 90$ K. The low temperature magnetic state below $T_2 = 70$ K was confirmed to be non-coplanar ferromagnetic structure where magnetic moments of Tb ions have strong ferromagnetic components along the crystallographic c-axis. The intermediate incommensurate antiferromagnetic phase with the propagation vector $\mathbf{k} = (0.155, 0, 0)$ was confirmed to exist in the temperature range $T_2 < T < T_N$. The application of an external magnetic field $\mu_0 H = 2$ T along the c crystallographic axis was found to suppress the incommensurate antiferromagnetic phase and give rise to the ferromagnetic phase.

When the magnetic field is applied along c-axis Tb_3Ni shows a very complex magnetic structure with a metamagnetic field induced transition, whose critical field (> 2 T) is strongly temperature dependent. This metamagnetic transition has been shown to be first order, both by the Banerjee criterion applied to the Arrot Plot, and the magnetocaloric n parameter evolution.

The magnetocaloric effects of Tb_3Co and Tb_3Ni have been evaluated taking into account demagnetization effects. Due to the first order metamagnetic transitions, certain precautions have been followed in order to correctly evaluate the MCE of the latter compound. The MCE of Tb_3Ni when the magnetic field is applied along the easy axis of magnetization was evaluated in two different ways, the first of which consists on combining the *Maxwell relation* and the *Clausius-Clapeyron* equation, while for the second a discontinuous measuring protocol was used in order to evaluate the MCE using only the *Maxwell relation*. The results obtained through both methods are completely equivalent. Both materials show relevant magnetocaloric properties in their temperature ranges if compared to other materials in literature, making them extremely interesting for magnetic refrigeration applications in the gas liquefaction range. The case of Tb_3Ni is specially interesting due to the subsequent IMCE and DMCE, which could potentially increase the refrigeration efficiency [117,118]. Although the MCE for Dy_3Co was not evaluated in this study, the values observed in literature agree very well with the ones obtained for the other two members of the R_3T family.

Finally, the magnetic anisotropy in Tb_3Ni and its potential use for refrigerators based on the rotating magnetocaloric effect (RMCE) has been studied and promising preliminary results have been obtained.

7 | R_6TX_2 intermetallics

"The important thing is not to have wrinkles in the brain."

– Margarita Salas Falgueras

R_6TX_2 family, where R is a rare-earth element, T a transition metal and X a *p*-block element, is one of the richest intermetallic families concerning the amount of compounds that it includes, which is clear from the amount of samples studied in this chapter. This variety is also observed in its properties, and gives this family some competitive advantages with respect to other competitors, such as a tunable MCE over a wide temperature range. Even so, little is known about the general properties of this family.

This chapter aims to address some of the seldom studied properties of three *"sub-families"* of the parent R_6TX_2 family: $Ho_6(Fe, Mn)Bi_2$, $(Gd, Tb)_6(Fe, Mn)Bi_2$, and $Dy_6(Fe, Mn)X_2$. The attributes here presented concern their magnetic and thermal properties, critical behavior, magnetocaloric effect and scaling relations.

The following materials will be studied in this chapter:

- **Ho_6MnBi_2**
- **$Ho_6(Mn_{0.75}Fe_{0.25})Bi_2$**
- **$Ho_6(Mn_{0.5}Fe_{0.5})Bi_2$**
- **Ho_6FeBi_2**
- **Gd_6FeBi_2**
- **$Gd_3Tb_3FeBi_2$**
- **Tb_6FeBi_2**
- **$Tb_6(Fe_{0.5}Mn_{0.5})Bi_2$**
- **Dy_6FeBi_2**
- **$Dy_6(Fe_{0.5}Mn_{0.5})Bi_2$**
- **Dy_6MnBi_2**
- **Dy_6FeSb_2**
- **$Dy_6FeSbBi$**
- **$Dy_6FeSbTe$**
- **$Dy_6FeBiTe$**

7.1 Introduction

As discussed in the theoretical background, the applicability of magnetocaloric materials is huge. Obviously, most of the attention is focused on magnetic refrigeration at room temperature, or close to it. However, other temperature ranges are also of practical interest; this is the case of the gas liquefaction regions. Whatever the working temperature region of interest is, there are some characteristics that an optimal magnetocaloric material should present in order to be considered as a competitive option, such as a high magnetic entropy change at the desired temperature combined with a high refrigerant capacity. One way of obtaining large RC values is by creating composite materials with magnetic transitions close to each other in the region of interest [82, 85, 173–178]. Another line consists on searching for magnetocaloric materials presenting several spin ordering or spin reorientation transitions in order to obtain table-like magnetocaloric effects over the desired temperature range by using a single material. This latter approach is very interesting because an ideal Ericsson refrigeration cycle (consisting on two isothermal and two isofield processes) requires a constant value of the magnetic entropy change (ΔS_M) in order to obtain the maximum efficiency and optimal performance [91]. This path, which has been seldom explored, is the one we will be taking on this chapter.

Ternary intermetallic compounds of very different sort are being synthesized in this research field as the combination of rare-earths and transition metals gives interesting magnetic properties, locating the magnetic transitions at varied temperatures, depending on the particular compositions. In this chapter we are focusing our attention on three *"sub-families"* of the general R_6TX_2 family: Ho_6(Fe, Mn)Bi_2, (Gd, Tb)$_6$(Fe, Mn)Bi_2, and Dy_6(Fe, Mn)X_2. Despite having different compositions they all crystallize in the Fe_2P type structure (space group $P\bar{6}2m$, No. 189, hP9). All of the compounds which will be presented in this chapter have a paramagnetic to collinear ferromagnetic (PM-FM) transition at T_C [303, 327, 379–381], and, save for the case of Gd_6FeBi_2, a spin reorientation transition at a lower temperature T_m. The latter transition takes place when the material moves from a collinear ferromagnetic structure (at higher temperature) to a non-collinear complex magnetic arrangement (at lower temperature), including canted ferromagnets, conical or spiral or simply antiferromagnetic [303, 327, 379–382]. Another relevant characteristic of this family is that, when studied by neutron diffraction, no magnetic moment has been found for the transition metal (T) [303–305, 327, 380, 382], pointing to the rare-earth element as the sole responsible of the magnetism in this family. This is the same behavior as the one observed in the previous intermetallic families: RTX, R_3CoNi, or R_3T.

Looking for a knowledge as deep as possible of the magnetic properties in these compounds, the magnetic critical behavior for the higher temperature PM-FM transition will be discussed, in order to gain some insight on the underlying physics of this system. In the case of the (Gd, Tb)$_6$(Fe, Mn)Bi_2 family the critical behavior analysis has been extended to the thermal properties (c_p). Unfortunately, this study couldn't be carried out in the other two families due

to the noise and shape of the thermal measurements. Moreover, a complete magnetocaloric study will be performed with the expectation of analysing how changing the stoichiometry affects the general properties of the different *"sub-families"*, with special focus on the possibility of properly tuning the MCE for its desired application.

7.2 Samples and experimental techniques

All the compounds presented in this chapter have been grown by our collaborator A.V. Morozkin from the Department of Chemistry at the Moscow State University in Russia.

Alloys with a total mass of 2 g were prepared by arc-melting in an electric arc furnace (90 V, 150 A) under argon (99.992 vol %) using a non-consumable tungsten electrode and on a water-cooled copper hearth. Pieces of holmium, gadolinium, terbium, dysprosium (99.9 wt.%), iron, manganese (99.95 wt.%)) bismuth, tellurium and antimony (purity 99.99 wt.%) were used as starting components. A titanium button was used as a getter during arc-melting and the compounds were remelted three times. The arc-melted samples were encased into nickel foil and sealed in silica ampoules, evacuated and back filled with argon to 0.3 atm at room temperature. The samples were annealed at 1070 K (±2 K) for 300 h (340 h in the case of the Dy_6(Fe, Mn)X_2 (X = Sb, Te, Bi) family), then quenched in ice-water bath.

Phase analysis of the compounds was carried out using X-ray diffraction and energy dispersive X-ray spectroscopy microprobe elemental analysis (EDS). The X-ray powder data (XRD) were obtained by using a diffractometer Rigaku D/MAX-2500 (CuKα, 2θ of 10-80º, 0.02º step, $I_{max}/I_{bgr} \sim 50$). An INCA-Energy-350 X-ray EDS spectrometer (Oxford Instruments) on a Jeol JSM-6480 LV scanning electron microscope (SEM) (20 kV accelerating voltage, 0.7 nA beam current and 50 μm beam diameter, microprobe size ~ 10 nm) was employed to perform quantitative elemental analysis. Signals averaged over three points per phase gave estimated standard deviations of 0.5 at.% for holmium, gadolinium, terbium and dysprosium (measured by L-series lines), 1 at.% for Mn, Fe and Bi (0.6 at.% for Sb, Bi and Te in the case of Dy_6(Fe, Mn)X_2 compounds), measured by K-series lines.

The unit cell data were derived from powder X-ray data using the Rietan-program [383] in the isotropic approximation at room temperature.

Magnetic measurements have been performed using a VSM (Vibrating Sample Magnetometer) by Cryogenic Limited, obtaining the magnetization (M) of the samples under external applied magnetic fields H_a in the range of 0–7 T. Isotherms have been collected from very low temperatures to temperatures well above the corresponding Curie temperature (T_C) for all samples, using different steps, depending on the temperature range. A discontinuous protocol has been used in the regions where metamagnetic transitions were observed, in order to erase the magnetic memory of the samples and be able to extract the magnetic entropy change using the well known *Maxwell relation* in order to avoid spurious results. In order to study the critical behavior of the paramagnetic to ferromagnetic transition in detail, a step of $\Delta T = 1$ K has been

taken between consecutive isotherms around T_C. As usual, demagnetization effects have been taken into account in order to perform a correct evaluation of the scaling analysis and the magnetocaloric effect. The magnetic susceptibility was measured with AC Measurement System Option in PPMS (Physical Properties Measurement System) by Quantum Design.

The specific heat for (Gd, Tb)$_6$(Fe, Mn)Bi$_2$ family and thermal diffusivity for Dy$_6$(Fe, Mn)X$_2$ family has been retrieved using the high resolution *ac* photopyroelectric calorimeter described in Section 1.4.4. As we have already seen, this system allows to perform extremely slow temperature ramps in order to extract the shape of c_p and D with great accuracy.

7.3 Ho$_6$(Fe, Mn)Bi$_2$ family

In this section we are focusing our attention on the Ho-based branch of the general R$_6$TX$_2$ intermetallic family; more specifically on Ho$_6$(Mn$_{1-x}$Fe$_x$)Bi$_2$ (x = 0, 0.25, 0.5, 1) compounds. Ho, on its own, undergoes two magnetic phase transitions: a PM-AFM one at T_N = 132 K and an AFM-FM one at lower temperature, T_C = 20 K [93, 384, 385]. The magnetocaloric properties of different compounds containing Ho have already been studied (see the review work by Franco et al. [91]) and we have selected the intermetallics mentioned above as the magnetic properties already studied of Ho$_6$MnBi$_2$ and Ho$_6$FeBi$_2$ make them specially interesting [303, 327]: both of them present a paramagnetic to ferromagnetic transition (PM-FM) followed by a spin reorientation transition at a much lower temperature, and the difference between the Curie temperatures in the sample with Mn and the sample with Fe is higher than 130 K. So there is the possibility of having two magnetocaloric effects in the samples covering a wide temperature range which could be shifted varying the stoichiometry and maybe obtain a sustained value of the magnetic entropy change in the whole range. A recent magnetocaloric study on Ho$_6$TTe$_2$ (T = Fe, Co) has shown the ability of this family of ternary compounds to present this kind of properties [386], as it was already found in Gd$_6$CoTe$_2$ [380]. Therefore, the aim of this work is to carry out a thorough study on the magnetocaloric properties of Ho$_6$(Mn, Fe)Bi$_2$ intermetallics in search for a wide MCE produced by the combination of both phase transitions. The study of the critical exponents of the paramagnetic to ferromagnetic transition will also be addressed, which will give the possibility of checking the scaling equation for the maximum of the magnetic entropy change.

7.3.1 Structural data and magnetic characterization of Ho$_6$(Fe, Mn)Bi$_2$ family

The X-ray powder analysis showed that the Ho$_6$(Mn$_{1-x}$Fe$_x$)Bi$_2$ (x = 0, 0.25, 0.5, 1) family crystallizes in the Fe$_2$P type structure (space group $P\bar{6}2m$, No. 189, hP9). The refined unit cell data is given in Table 7.1. The substitution of Fe for Mn is followed via increasing of unit cell volume and anisotropic distortion of unit cell (increasing of c/a ratio) from Ho$_6$FeBi$_2$ to Ho$_6$MnBi$_2$.

Due to diffusion way of synthesis of these polycrystals, the compounds contain an admixture of Yb_5Sb_3-type $Ho_5(Fe,Mn)_{\sim 0.5}Bi_{\sim 2.5}$ phases ($\sim$ 10 wt% for Ho_6FeBi_2, $\sim$ 10% for $Ho_6(Mn_{0.5}Fe_{0.5})Bi_2$, $\sim$ 12% for $Ho_6(Mn_{0.75}Fe_{0.25})Bi_2$ and $\sim$ 14% for Ho_6MnBi_2). This admixture exhibits ferromagnetic ordering around 40 K (see e.g. Ref. [387]) and it shows a small influence for the resulting magnetic properties, as will be discussed later.

Compound	a (nm)	c (nm)	c/a	V (nm^3)
Ho_6MnBi_2	0.81822(5)	0.42609(2)	0.520752	0.247043
$Ho_6(Mn_{0.75}Fe_{0.25})Bi_2$	0.81971(5)	0.42265(2)	0.515609	0.245942
$Ho_6(Mn_{0.5}Fe_{0.5})Bi_2$	0.81983(5)	0.42096(2)	0.513472	0.245030
Ho_6FeBi_2	0.82220(6)	0.41816(3)	0.508587	0.244809

Table 7.1: Unit cell data of Fe_2P-type $Ho_6(Mn_{1-x}Fe_x)Bi_2$ compounds (space group $P\bar{6}2m$, No. 189, hP9).

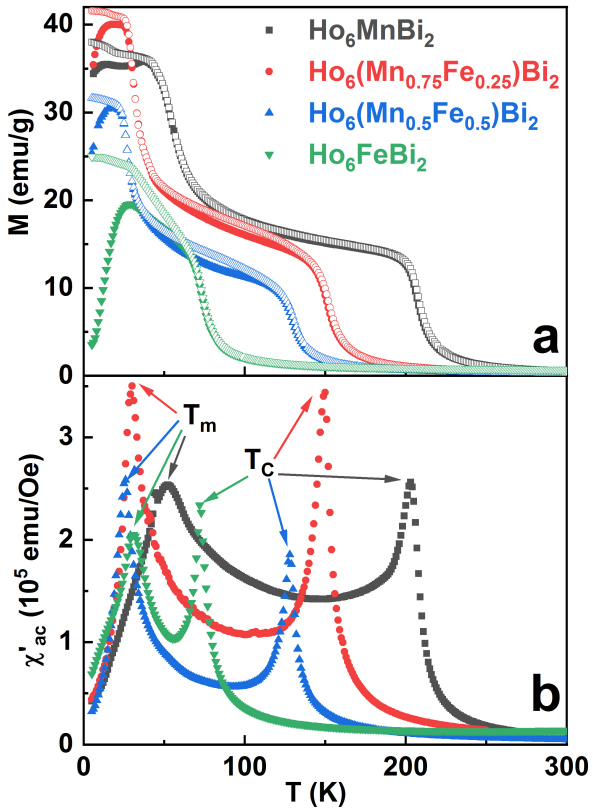


Figure 7.1: (a) Magnetic moment as a function of temperature in Zero-Field Cooled (filled symbols) and Field-Cooled (empty symbols) with applied field $\mu_0 H = 0.1$ T; (b) real part of the *ac* susceptibility at $f = 100$ Hz.

Fig. 7.1(a) shows the evolution of the magnetization per unit mass as a function of temperature for ZFC (filled symbols) and FC (empty symbols) while Fig. 7.1(b) presents the real part of the *ac* susceptibility, in order to place

the transitions with precision using the maxima. The divergence between ZFC and FC curves at low temperatures shows the thermomagnetic irreversibility on each sample, being the highest for Ho_6FeBi_2 and the lowest for Ho_6MnBi_2. They all share similar shapes: from room temperature, with decreasing temperature a first paramagnetic (PM) to ferromagnetic (FM) transition takes place at T_C (203 K, 150 K, 128 K, 72 K for Ho_6MnBi_2, $Ho_6(Mn_{0.75}Fe_{0.25})Bi_2$, $Ho_6(Mn_{0.5}Fe_{0.5})Bi_2$ and Ho_6FeBi_2, respectively); then, as temperature keeps on decreasing, the magnetization is still increasing until a second transition takes place, T_m, due to a spin reorientation [303, 327], whose value is marked by the lower temperature maxima in the susceptibility (52 K, 30 K, 26 K and 31 K, respectively). Ho_6MnBi_2 shows the highest magnetization until the lower temperature transition takes place in $Ho_6(Mn_{0.75}Fe_{0.25})Bi_2$, when the latter compound surpasses the magnetization value of the former, presenting the highest value at low temperatures. In the susceptibility measurements, a small shoulder can be traced for Ho_6MnBi_2 at 44 K and $Ho_6(Mn_{0.75}Fe_{0.25})Bi_2$ at 41 K, probably due to the ordering of the Yb_5Sb_3-type admixture phase, while it is not seen in the other two, where the amount of this phase is smaller. The demagnetization factors and Curie temperatures obtained from the real part of the *ac* susceptibility are presented in Table 7.2.

Compound	T_C (K)	N_D (gOe/emu)
Ho_6MnBi_2	203	69.29
$Ho_6(Mn_{0.75}Fe_{0.25})Bi_2$	150	78.96
$Ho_6(Mn_{0.5}Fe_{0.5})Bi_2$	128	97.59
Ho_6FeBi_2	72	84.10

Table 7.2: Experimentally obtained Curie temperature and demagnetization factors.

Comparing the results from Fig. 7.1 to those presented in Table 7.1, it can be seen that the change in the Curie temperature is related to the change in the cell parameters, which implies it is linked to the separation between rare-earth ions (see Fig. 7.2). This has already been observed in Ho-based intermetallic compounds [327] as well as in Gd-based ones [304]. The transition metals do not have a net magnetic moment in the R_6TX_2 family, in general [304, 305] and this has been proved, in particular, for Ho_6MnBi_2 and Ho_6FeBi_2 [303]. This implies that they can all be considered as rare-earth intermetallics, with magnetism only due to *4f-4f* coupling, so that the magnetism could be explained on the basis of the RKKY model. The problem arises when trying to explain the cases in which the intermetallic has a much higher T_C than the rare-earth metal, as is the case for Ho-based intermetallics (Ho presents ferromagnetic ordering at $T_C = 20$ K). It is generally considered that, apart from the distortion of the unit cell, hybridization between electronic orbitals of the rare-earth and the other ions in the compound increases the exchange interaction in intermetallics so that the Curie temperatures are raised [78, 93, 304]. In particular, Mn has a very special effect as it strongly raises the ordering temperature, much more than other transition metals [327]. The particular

mechanism through which this is obtained is still to be found.

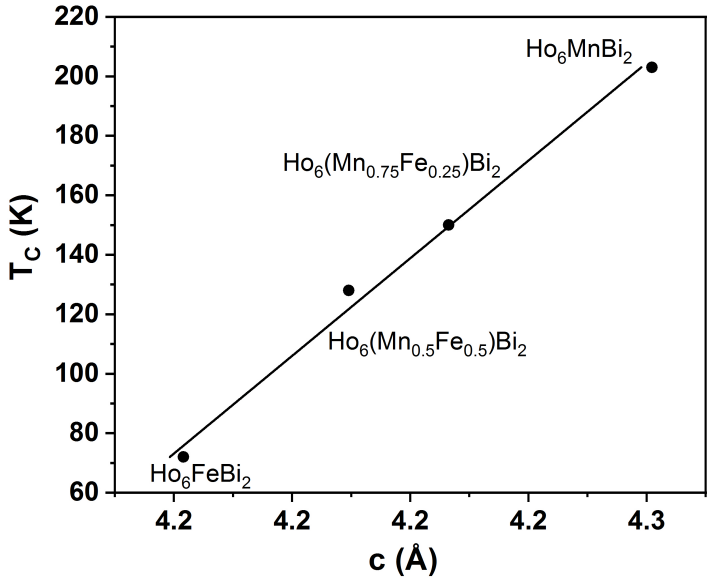


Figure 7.2: Dependence of the Curie temperature with the *c*-axis.

7.3.2 Critical behavior in $Ho_6(Fe, Mn)Bi_2$ family

As stated in the introduction, we have proceeded with the study of the universality class to which the second order PM-FM transition belongs by extracting the critical exponents from magnetic measurements, using in each case the isotherms in the region around T_C (172–232 K for Ho_6MnBi_2, 126–175 K for $Ho_6(Mn_{0.75}Fe_{0.25})Bi_2$, 106–146 K for $Ho_6(Mn_{0.5}Fe_{0.5})Bi_2$ and 50–92 K for Ho_6FeBi_2). These regions are far enough away from the low temperature transitions so that the results obtained from this study will be reliable as there is no overlapping with other critical regions.

The first step is to represent for every sample the well known Arrot Plot, where M^2 versus H/M is plotted. All the samples present the same behavior as it is illustrated by Fig. 7.3 for the four compounds. It can be seen that the slopes are positive, which according to the Banerjee criterion [229] confirms the second order character of these transitions and therefore the applicability of the critical behavior theory. Those graphs imply a particular selection of critical exponents ($\beta = 0.5$, $\gamma = 1$) which corresponds to the Mean Field universality class (see Table 3.2 in page 77). If the PM-FM transition belonged to this class, in Fig. 7.3 the isotherms at high fields should be straight lines, parallel to each other. It can be clearly seen that they are nearly straight lines but parallelism is not too good. Therefore, we have turned our attention to the so called Modified Arrot Plots (MAP), representing $M^{1/\beta}$ as a function of $(H/M)^{1/\gamma}$ for other relevant universality classes, such as 3D Heisenberg ($\beta = 0.369$, $\gamma = 1.396$) and 3D Ising ($\beta = 0.3265$, $\gamma = 1.237$). However, Mean Field critical exponents gave the most parallel and straight lines among the

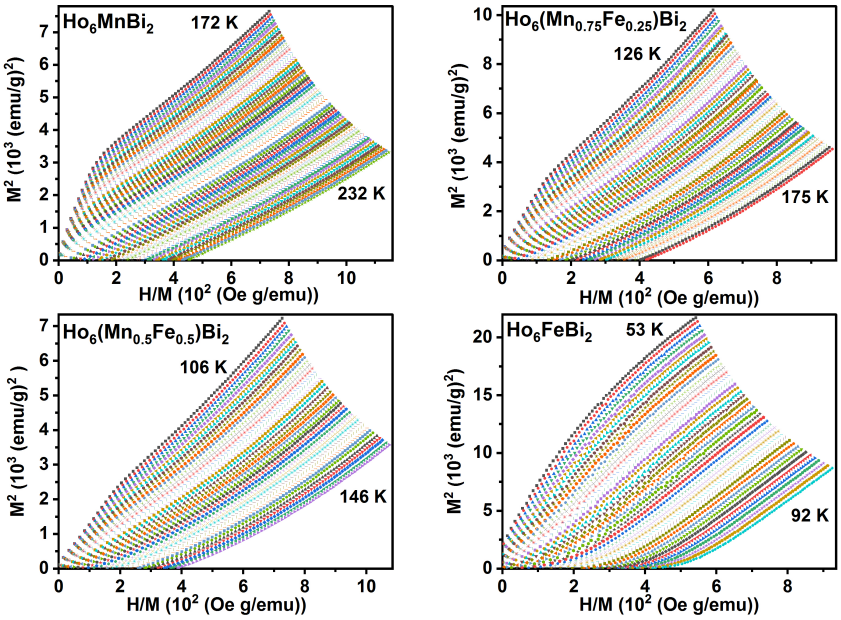


Figure 7.3: Arrot Plot, corresponding to the Mean Field universality class critical exponents, for the four compounds. Positives slopes indicate second order phase transition.

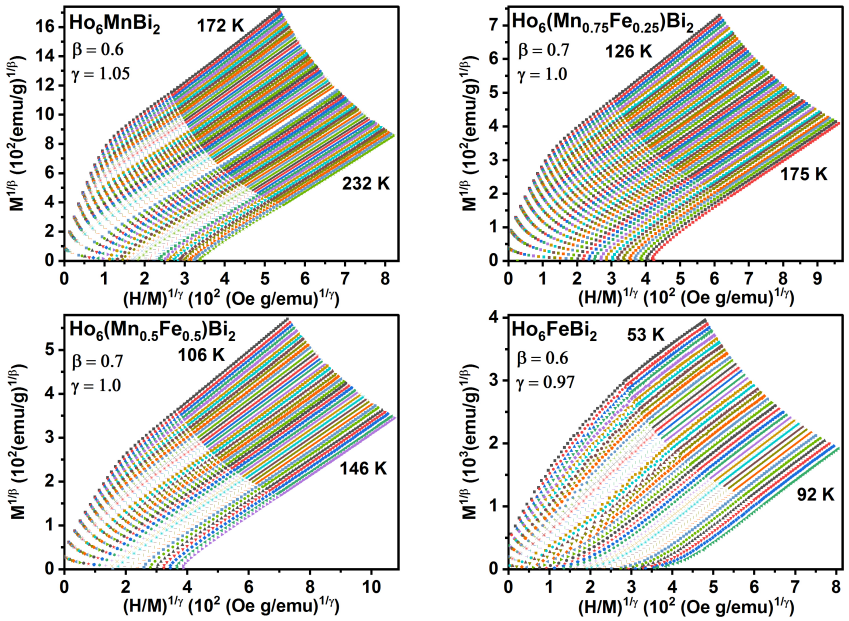


Figure 7.4: Modified Arrot Plots for selected critical parameters as starting point for their refinement. Straight lines are linear fittings from where $(M_S)^{1/\beta}$ and $(\chi_0^{-1})^{1/\gamma}$ values are obtained.

tested models for all the materials. From Fig. 7.3 it is clearly seen that the parallelism is not perfect, that is why we have tested different sets of parameters close to the Mean Field model and then followed the well known iteration procedure presented in Section 3.4.1. Fig. 7.4 contains the starting values before the iteration procedure for all the compounds, clearly showing a better

parallelism than the plots in Fig. 7.3. A linear extrapolation from high field data on the MAP has been used to extract the $(M_S)^{1/\beta}$ and $(\chi_0^{-1})^{1/\gamma}$ values as the interception with Y and X axes, respectively. Once $M_S(T)$ and $\chi_0^{-1}(T)$ have been obtained they are fitted to the well known expressions:

$$M_S(T) \sim |t|^{\beta} \qquad (T < T_C)\,, \tag{7.1}$$

$$\chi_0^{-1}(T) \sim |t|^{\gamma} \qquad (T > T_C)\,, \tag{7.2}$$

to obtain new values of β and γ, which are then used for another iteration until the values converge and good parallel, straight lines, are obtained in the MAP. Fig. 7.5 shows the final values of $M_S(T)$ and $\chi_0^{-1}(T)$ and their corresponding fittings as a function of temperature for all the samples. All the critical exponents and temperatures are collected in Table 7.3. The final obtained β values are higher than the corresponding to the MF model, where $\beta_{\mathrm{MF}} = 0.5$, in every case getting far from any other universality class, while γ is also slightly higher than 1 (the corresponding value in the MF model) except in the Ho_6FeBi_2 sample where it is slightly lower. This means that short-range magnetic interactions are not active in these compounds but long-range ones.

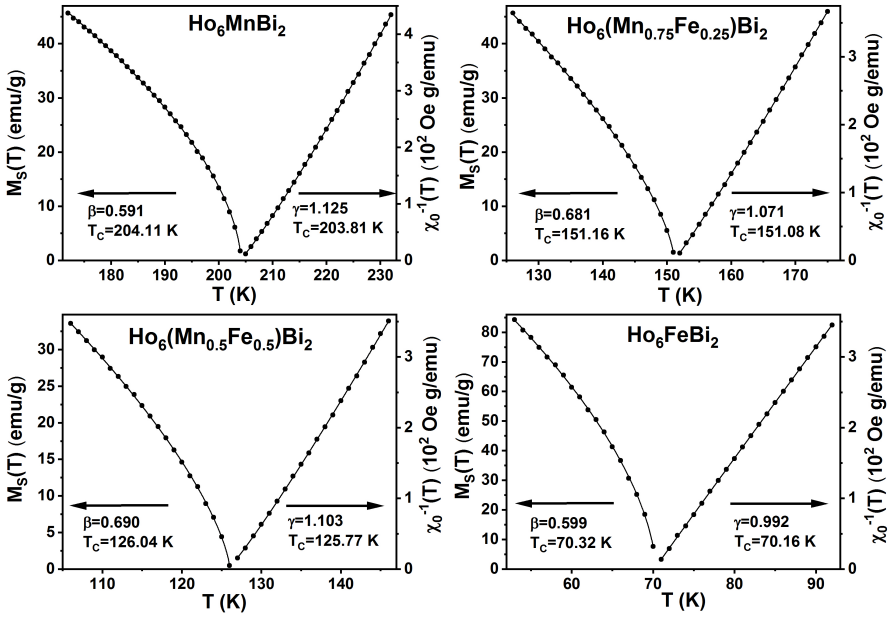


Figure 7.5: Spontaneous magnetization (left) and inverse of initial susceptibility (right) vs. temperature for the four compounds as obtained from the optimized Modified Arrot Plot. The solid curves correspond to the fits to Eqs. (7.1), (7.2).

As usual, β, γ and T_C have also been obtained by the widely used Kouvel Fisher method (KF) for the four samples. The Kouvel Fisher plots, their corresponding fittings and the retrieved parameters are shown in Fig. 7.6. As can be seen from Table 7.3 there is a good agreement between the exponents obtained by means of the Modified Arrot Plots and the Kouvel Fisher method, confirming the robustness of the results.

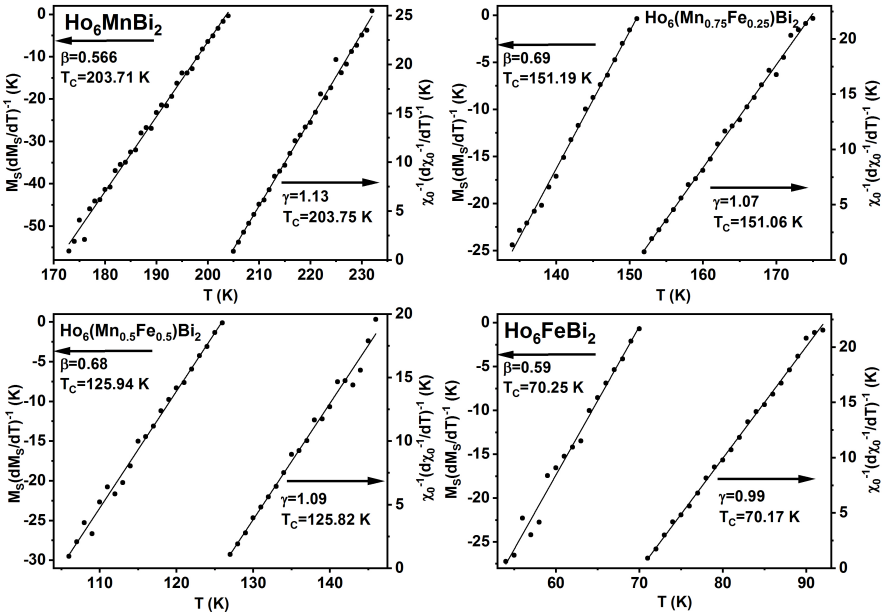


Figure 7.6: Kouvel Fisher plot of spontaneous magnetization (left) and inverse of initial susceptibility (right) for the four compounds. The straight lines are linear fits, from which TC and the critical exponents are obtained.

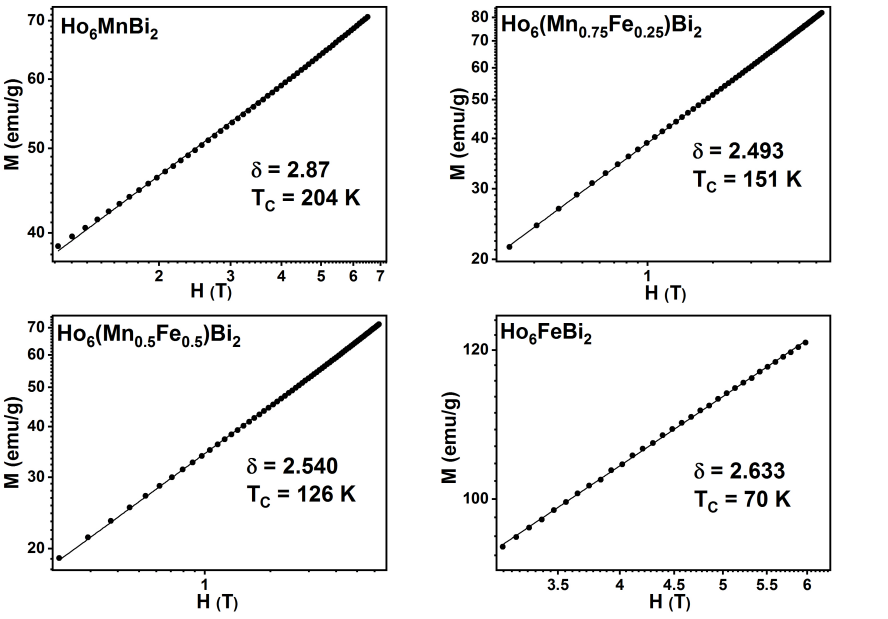


Figure 7.7: M vs. H plot in a log-log scale collected at critical isotherms for the four compounds. The straight line, in each case, is the linear fit from which the exponent δ is obtained.

The last magnetic critical exponent, δ, is associated to the critical isotherm by:

$$M \sim H^{1/\delta} \qquad (T = T_C)\,, \tag{7.3}$$

and can therefore be obtained experimentally. Fig. 7.7 shows the magnetiza-

tion as a function of the internal field for the four samples at their corresponding critical temperatures (204 K for Ho_6MnBi_2, 151 K for $Ho_6(Mn_{0.75}Fe_{0.25})Bi_2$, 126 K for $Ho_6(Mn_{0.5}Fe_{0.5})Bi_2$, and 70 K for Ho_6FeBi_2) in a log-log scale. It can be seen that the experimental data lies on good straight lines whose slopes, following Eq. (7.3), give the value of δ.

The value of δ is related to β and γ through Widom relation:

$$\delta = 1 + \gamma/\beta \,. \tag{7.4}$$

Therefore, this expression can be used to compared the value of δ obtained from the critical isotherms with the one given by the β and γ previously obtained through MAP and Kouvel Fisher methods. The values given by Eq. (7.4) are very close to those obtained directly from the critical isotherms. The results can be compared in Table 7.3.

Finally, in order to further confirm a good scaling, β and γ values have been used to check the fulfilment of the magnetic equation of state:

$$M(H,t) = |t|^{\beta} f_{\pm}(H/|t|^{\beta+\gamma}) \,, \tag{7.5}$$

and the results are shown in Fig. 7.8. The collapse of the experimental data into two independent branches, above and below T_C, is extremely good in the four cases, which is generally taken as a severe confirmation of a proper scaling.

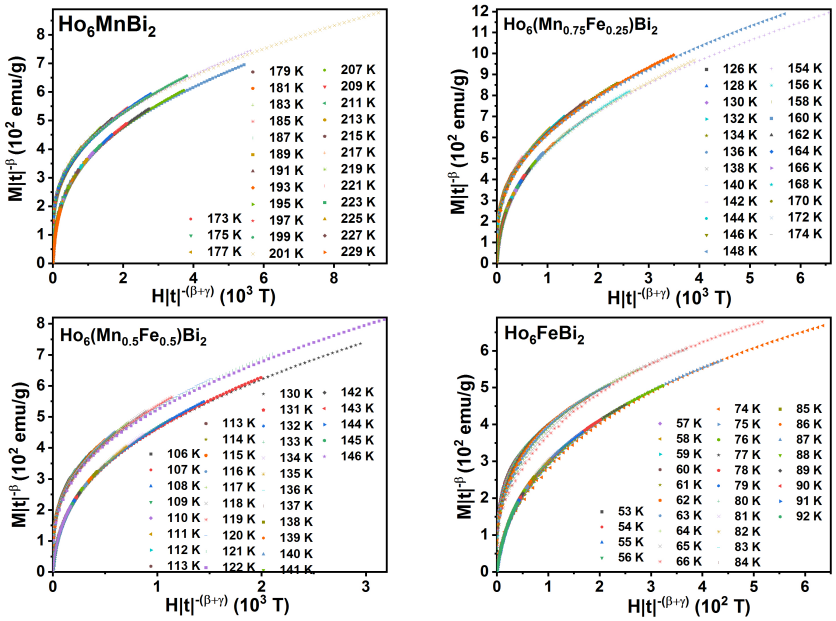


Figure 7.8: The renormalized magnetization plotted as a function of the renormalized field following Eq. (7.5) for the four compounds. In each case, all data collapse in two separate branches, one above and one below the respective T_C.

All these results indicate that the critical behavior of these transitions is close to the Mean Field universality class ($\beta_{MF} = 0.5$, $\gamma_{MF} = 1$, $\delta_{MF} = 3$) but with a deviation of the β exponent which is not too strong for Ho_6MnBi_2 and

Material	Technique	β	γ	δ
Ho_6MnBi_2	Modified Arrot Plot	0.591 ± 0.002 $T_C = 204.11 \pm 0.03$ K	1.125 ± 0.005 $T_C = 203.81 \pm 0.05$ K	2.91 ± 0.01^a
	Kouvel Fisher Method	0.566 ± 0.008 $T_C = 203.71 \pm 0.03$ K	1.13 ± 0.01 $T_C = 203.75 \pm 0.06$ K	3.00 ± 0.05^a
	Critical Isotherm			2.87 ± 0.01
$Ho_6(Mn_{0.75}Fe_{0.25})Bi_2$	Modified Arrot Plot	0.681 ± 0.003 $T_C = 151.16 \pm 0.02$ K	1.071 ± 0.004 $T_C = 151.08 \pm 0.04$ K	2.57 ± 0.01^a
	Kouvel Fisher Method	0.69 ± 0.01 $T_C = 151.19 \pm 0.03$ K	1.07 ± 0.01 $T_C = 151.06 \pm 0.06$ K	2.57 ± 0.04^a
	Critical Isotherm			2.493 ± 0.003
$Ho_6(Mn_{0.5}Fe_{0.5})Bi_2$	Modified Arrot Plot	0.690 ± 0.004 $T_C = 126.04 \pm 0.03$ K	1.103 ± 0.009 $T_C = 125.77 \pm 0.07$ K	2.59 ± 0.02^a
	Kouvel Fisher Method	0.68 ± 0.01 $T_C = 125.94 \pm 0.03$ K	1.09 ± 0.03 $T_C = 125.82 \pm 0.05$ K	2.609 ± 0.07^a
	Critical Isotherm			2.540 ± 0.005
Ho_6FeBi_2	Modified Arrot Plot	0.599 ± 0.005 $T_C = 70.32 \pm 0.03$ K	0.992 ± 0.004 $T_C = 70.16 \pm 0.04$ K	2.66 ± 0.02^a
	Kouvel Fisher Method	0.59 ± 0.02 $T_C = 70.25 \pm 0.03$ K	0.99 ± 0.01 $T_C = 70.17 \pm 0.07$ K	2.68 ± 0.07^a
	Critical Isotherm			2.633 ± 0.009

[a] Calculated from Eq. (7.4): $\delta = 1 + \gamma/\beta$.

Table 7.3: Critical exponents obtained for Ho_6MnBi_2, $Ho_6(Mn_{0.75}Fe_{0.25})Bi_2$, $Ho_6(Mn_{0.5}Fe_{0.5})Bi_2$ and Ho_6FeBi_2.

Ho_6FeBi_2 (0.57 and 0.59, respectively) but gets farther away in the samples with shared Fe and Mn (0.68-0.69); γ, on the other hand, keeps quite close to the theoretical value as it is between 0.99 and 1.13, while δ is slightly lower than the theoretical value (in the range 2.5-3).

In order to interpret these values, the possibility that the deviation from the Mean Field model is due to disorder in the system must be taken into account. There are two aspects which would indicate that disorder is present in the system and alters the critical behavior, the first one being the Harris criterion [388], i.e., the necessity for the critical exponent α to be positive. This is the critical exponent for specific heat, which can be calculated by means of the Rushbrooke's scaling law presented in Section 3.2.2:

$$\alpha + 2\beta + \gamma = 2\,. \tag{7.6}$$

It turns out that, for all the cases under study, $\alpha < 0$; therefore, these transitions do not comply with the Harris criterion.

A second way of checking the presence of disorder in the system consists on obtaining the effective critical exponent, γ_{eff}:

$$\gamma_{\text{eff}} = \frac{d(\ln \chi_0^{-1}(t))}{d(\ln t)}\,. \tag{7.7}$$

If disorder has somehow altered the critical exonents, they should have a particular asymptotic behavior visible in Eq. (7.7). In fact, it is well established that, in disordered magnets, γ_{eff} will increase with the reduced temperature t and present a well-defined maximum as we are getting farther away from the critical region, while in ordered ones it will have a monotonic behavior

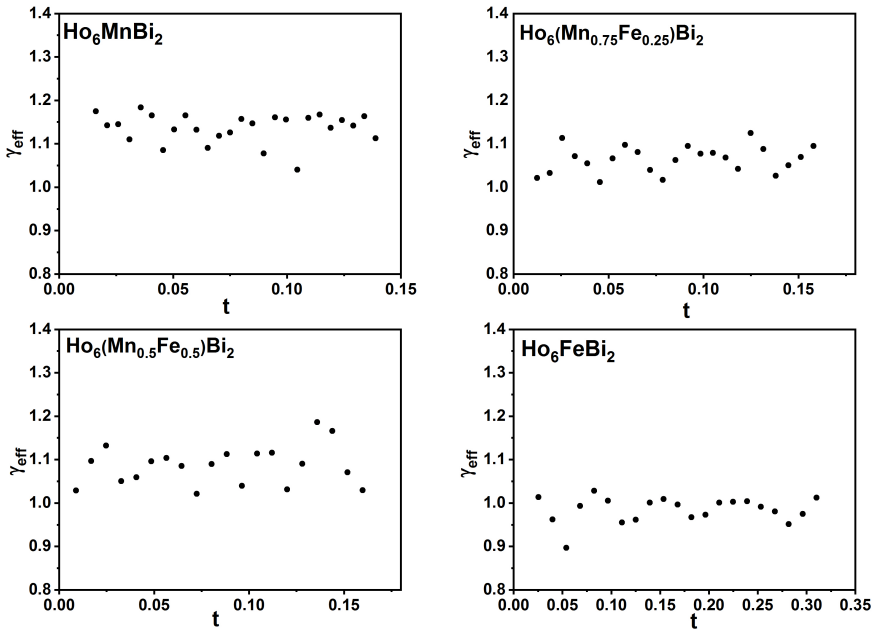


Figure 7.9: Effective critical exponent γ_{eff} for the four compounds as a function of the reduced temperature t.

[389–391]. γ_{eff} values have been calculated as a function of t and are shown in Fig. 7.9. Apart from some noise, the behavior does not match the properties related to disorder as there is no maximum as a function of t. Therefore, we can conclude that, according to the previous two criteria, disorder is not responsible for the deviation from the Mean Field model.

Universality classes are theoretically developed on the basis of a particular Hamiltonian which takes into account particular mechanisms responsible for the magnetic interactions. More theoretical development from other groups in this field would be needed in order to account for deviations of the value of the critical exponent β which will increase it, where disorder is not an issue, as it has been found for these compounds.

7.3.3 Magnetocaloric effect in $Ho_6(Fe, Mn)Bi_2$ family

As was shown in Fig. 7.3, the phase transitions in these compounds are second order and, therefore, the usual *Maxwell relation* can be safely used to evaluate the magnetocaloric effect:

$$\Delta S_M(T, \Delta H) = \mu_0 \int_{H_0}^{H_1} \left(\frac{\partial M}{\partial T}\right)_H dH \,. \tag{7.8}$$

The characterization of the magnetocaloric effect is done on the basis of the maximum value of the magnetic entropy change $|\Delta S_M^{pk}|$ for a given field and the refrigerant capacity (RC), given by the already well known RC_{FWHM} and RC_{Area}. For practical applications a magnetic entropy change peak as high as possible and a RC as large as possible over a wide range of temperatures are desirable. Fig. 7.10 shows the magnetic entropy change as a function of

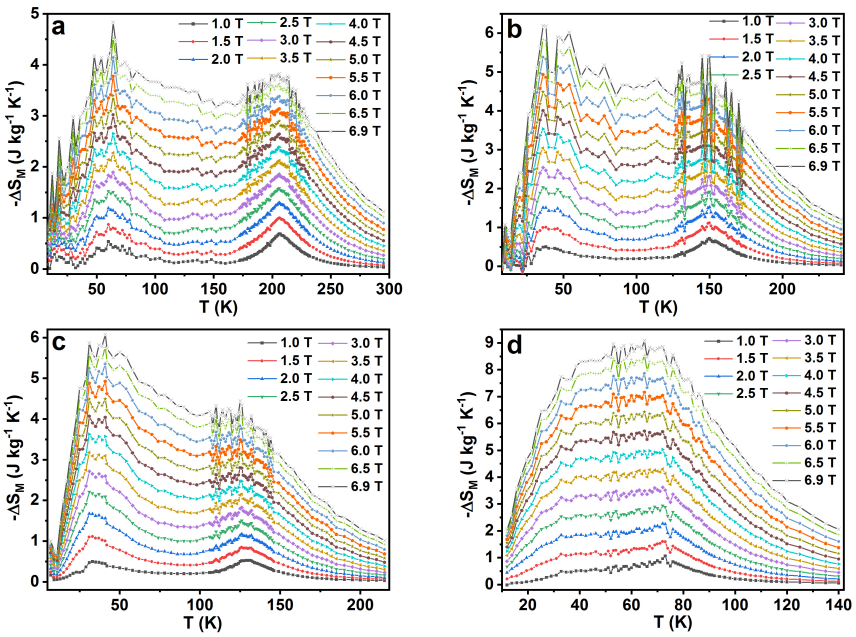


Figure 7.10: Magnetic entropy change $-\Delta S_M$ for $\mu_0\Delta H$ from 1 T to 6.9 T for: (a) Ho_6MnBi_2, (b) $Ho_6(Mn_{0.75}Fe_{0.25})Bi_2$, (c) $Ho_6(Mn_{0.5}Fe_{0.5})Bi_2$, and (d) Ho_6FeBi_2.

temperature for the four samples, and the relevant figures of merit of both phase transitions (at T_m and T_C) are collected in Table 7.4 (upper Table for T_C, lower Table for T_m) for the applied fields generally reported in literature, 2 and 5 T, also including the highest value measured, $\mu_0\Delta H = 6.9$ T. Note that the RC values at T_m are missing for Ho_6FeBi_2, this is because, as can be seen from Fig. 7.10(d), there is not a clear maximum at that temperature and any attempt to calculate RC would give incorrect results. In general the peak around T_m is displaced with increasing magnetic field, in every case the value presented is the one corresponding to the maximum of the peak close to that temperature, not precisely at T_m.

Due to the subsequent phase transitions, the span in temperature of the full width at half maximum of these compounds is large, giving rise to huge RC values at high fields. Although the temperature span for the FWHM at $\mu_0\Delta H = 5$ T decreases with Fe content, it is extremely broad: 209.0 K for Ho_6MnBi_2, 154.3 K for $Ho_6(Mn_{0.75}Fe_{0.25})Bi_2$, 126.7 K for $Ho_6(Mn_{0.5}Fe_{0.5})Bi_2$, and 80.9 K for Ho_6FeBi_2. Besides, the shapes of ΔS_M more and more tend to a plateau instead of the typical triangle, which is also interesting from the application point of view as this behavior is desired in order to increase the efficiency of an Ericsson refrigeration cycle [91].

The highest $|\Delta S_M^{pk}|$ value at a given applied field is always given by Ho_6FeBi_2 and the lowest one by Ho_6MnBi_2, though the latter shows the biggest temperature span for high applied fields and the former the lowest one, which, for the T_C peak, is translated into a higher RC value for the Mn sample over the Fe sample at 5 and 6.9 T. At lower fields, $\mu_0\Delta H = 2$ T, when the RC value is given for both T_m and T_C, Ho_6MnBi_2 shows the lowest RC values. $Ho_6(Mn_{0.75}Fe_{0.25})Bi_2$ and $Ho_6(Mn_{0.5}Fe_{0.5})Bi_2$ samples present values in the

$\mu_0\Delta H$	Magnitude	Ho_6MnBi_2 $T_C = 206$ K	$Ho_6(Mn_{0.75}Fe_{0.25})Bi_2$ $T_C = 150$ K	$Ho_6(Mn_{0.5}Fe_{0.5})Bi_2$ $T_C = 126$ K	Ho_6FeBi_2 $T_C = 72$ K
2 T	$\lvert\Delta S_M^{pk}\rvert$ (J kg^{-1} K^{-1})	1.3	1.5	1.2	2.3
	RC_{FWHM} (J kg^{-1})	80	93	161	155
	RC_{Area} (J kg^{-1})	59	63	134	122
5 T	$\lvert\Delta S_M^{pk}\rvert$ (J kg^{-1} K^{-1})	2.9	3.9	3.2	6.4
	RC_{FWHM} (J kg^{-1})	649	633	471	526
	RC_{Area} (J kg^{-1})	532	523	450	439
6.9 T	$\lvert\Delta S_M^{pk}\rvert$ (J kg^{-1} K^{-1})	3.8	5.4	4.4	8.9
	RC_{FWHM} (J kg^{-1})	899	908	678	769
	RC_{Area} (J kg^{-1})	793	770	647	639

$\mu_0\Delta H$	Magnitude	Ho_6MnBi_2 $T_m = 52$ K	$Ho_6(Mn_{0.75}Fe_{0.25})Bi_2$ $T_m = 30$ K	$Ho_6(Mn_{0.5}Fe_{0.5})Bi_2$ $T_m = 26$ K	Ho_6FeBi_2 $T_m = 31$ K
2 T	$\lvert\Delta S_M^{pk}\rvert$ (J kg^{-1} K^{-1})	1.2	1.5	1.7	1.8
	RC_{FWHM} (J kg^{-1})	73	80	81	-
	RC_{Area} (J kg^{-1})	54	61	61	-
5 T	$\lvert\Delta S_M^{pk}\rvert$ (J kg^{-1} K^{-1})	3.4	4.5	4.5	5.7
	RC_{FWHM} (J kg^{-1})	709	691	569	-
	RC_{Area} (J kg^{-1})	508	506	406	-
6.9 T	$\lvert\Delta S_M^{pk}\rvert$ (J kg^{-1} K^{-1})	4.8	6.2	6.1	7.7
	RC_{FWHM} (J kg^{-1})	1020	979	801	-
	RC_{Area} (J kg^{-1})	738	743	592	-

Table 7.4: Maximum of the magnetic entropy change $\lvert\Delta S_M^{pk}\rvert$ and refrigerant capacities RC_{FWHM}, RC_{Area} at different applied fields $\mu_0\Delta H$ (2, 5 and 6.9 T) for the four compounds at their corresponding Curie temperature T_C (upper Table), and at their corresponding spin reorientation temperature T_m (lower Table).

range between the previously mentioned materials, which suggest the possibility of tuning the magnetocaloric effect by inserting different amount of Mn and Fe in the samples in order to search for the best applications, by either improving $\lvert\Delta S_M^{pk}\rvert$ or RC. Though the values of the peak entropy change are not high when compared with other rare-earth based magnetocaloric materials (see for instance Fig. 25 in Ref. [91]), the refrigerant capacity and the temperature span are considerably better than in most of them [82,91,108]. If we make the comparison with members of the Ho_6TX_2 family of compounds, there are published results for Ho_6MnBi_2 ($\lvert\Delta S_M^{pk}\rvert = 5$ J/kgK at $\mu_0\Delta H = 5$ T and 215 K but the peak is only shown from 175 K upwards and no measurement of the refrigerant capacity is offered) [392] and Ho_6CoTe_2, but in this case the

comparison is not worthy as the maxima for the entropy change are located at 60 K and 15 K [386]. There are also some results with a different rare-earth such as Tb_6FeX_2 (X = Sb, Bi) [393] which give values of $|\Delta S_M^{pk}| = 2.25$–2.67 J/kgK at $\mu_0\Delta H = 5$ T around 250 K, but without information about *RC*; or for Gd_6FeBi_2, with $|\Delta S_M^{pk}| = 4.3$ J/kgK at $\mu_0\Delta H = 5$ T but it is displaced to a much higher temperature, around 350 K [394]. Finally, some other combinations are published, such as Gd_6CoTe_2 ($|\Delta S_M^{pk}| = 4.5$ J/kgK at 220 K and 6.5 J/kgK at 180 K, all at 5 T, no information about *RC*) [380] or Tb_6NiTe_2 ($|\Delta S_M^{pk}| = 4.86$ J/kgK at 229 K at 5 T, no information about *RC*) [381]. As a conclusion, the compounds studied in this work offer very good magnetocaloric properties within the general R_6TX_2 family over a broad temperature range.

In order to further study the magnetocaloric properties of this family, the next step is to build up the master curves of each compound for the transitions around T_C following the method already explained in Section 3.5 and applied to previously presented compounds, which consists on normalizing the variation of the magnetic entropy change for each field with respect to the corresponding maximum value and rescaling the temperature axis. In ideal cases, one reference temperature T_r is enough to obtain a good universal curve, where the scaling of the temperature axis is done in the following way:

$$\theta_1 = \frac{T - T_C}{T_r - T_C} \,. \tag{7.9}$$

T_r is selected to be above T_C, corresponding to a certain fraction of $|\Delta S_M^{pk}|$; in our case, 0.5 has been used. Nevertheless, we have already seen that when the effect of the demagnetizing field is not negligible (which is the case), it is usually needed to use not one but two reference temperatures T_{r1}, T_{r2} in order to construct the universal curves:

$$\theta_2 = \begin{cases} -(T - T_C)/(T_{r1} - T_C)\,, & T \leqslant T_C \\ (T - T_C)/(T_{r2} - T_C)\,, & T > T_C \end{cases} \,, \tag{7.10}$$

Fig. 7.11 shows the master curve for all of the compounds except for Ho_6FeBi_2, whose universal curve could not be obtained due to the flat shape of its magnetic entropy change. The curves are presented using one (left) and two (right) reference temperatures. It can be seen that, in the near vicinity of the critical temperature, different field curves overlap, confirming the second order character of the transition. When two reference temperatures are used to rescale the temperature axis the overlapping is even greater. At some point, for temperatures below T_C, the curves bend up, especially at higher fields. This is due to the presence of the lower temperature transition, and it is responsible for the huge *RC* values and the flat central region of the magnetic entropy change.

The master curves, together with the scaling of the maximum value of the magnetic entropy change with the magnetic field following:

$$|\Delta S_M^{pk}| \propto H^{1+\frac{1}{\delta}(1-\frac{1}{\beta})} = H^n \,, \tag{7.11}$$

and the scaling of the reference temperature T_r according to:

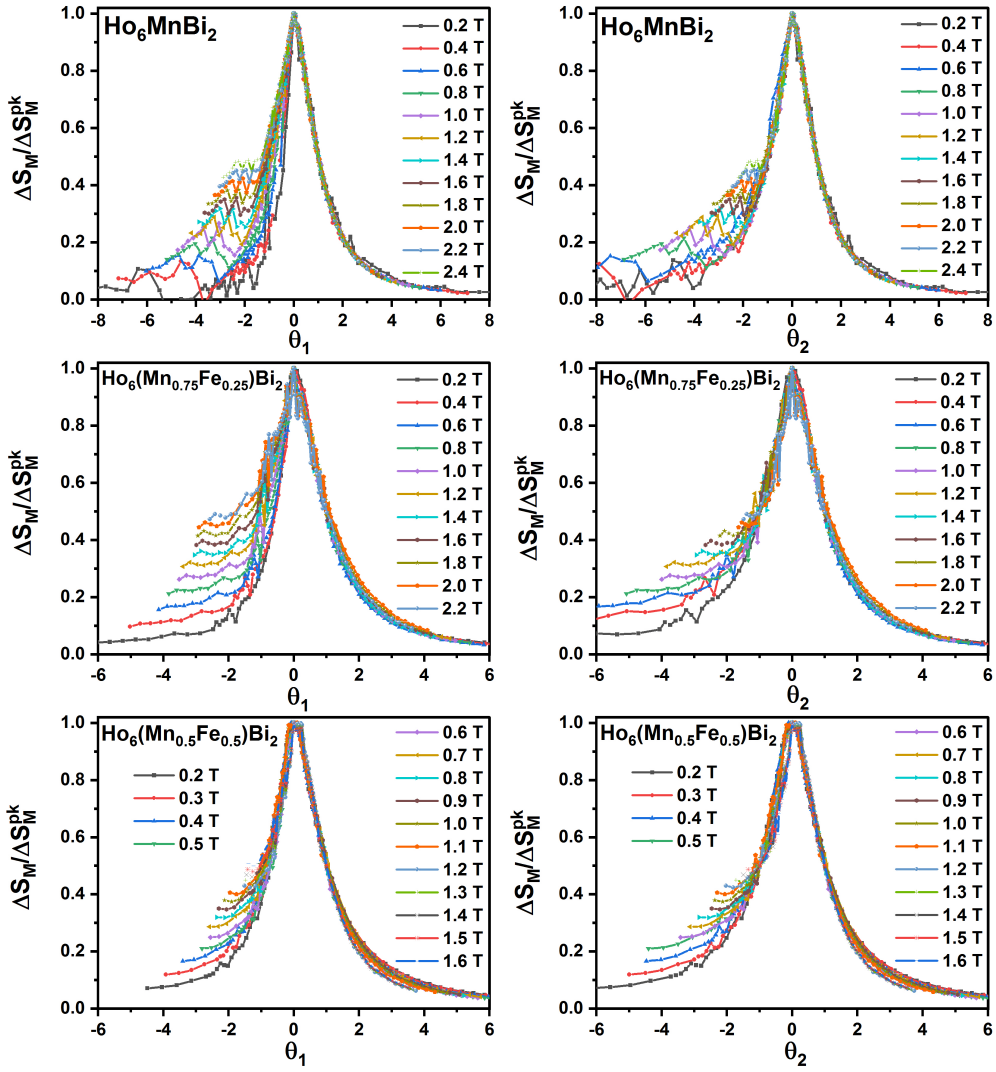


Figure 7.11: Universal curve with the rescaled magnetic entropy changes for Ho_6MnBi_2 (top), $Ho_6(Mn_{0.75}Fe_{0.25})Bi_2$ (middle), and $Ho_6(Mn_{0.5}Fe_{0.5})Bi_2$ (bottom), using one (left column) or two (right column) reference temperatures.

$$T_r \propto H^{1/(\beta+\gamma)}\,, \tag{7.12}$$

allow the extrapolation of the whole magnetic entropy change curves to no accessible magnetic fields and temperatures. The previously obtained magnetic critical exponents β, γ and δ have been used in order to check that both $|\Delta S_M^{pk}|$ and T_r scale according to Eq. (7.11) and Eq. (7.12), respectively. Fig. 7.12 shows the scaling of the maximum variation of the magnetic entropy change and the scaling of the reference temperature for every compound. The linear dependency confirms the obtained critical exponent values for the samples and, therefore, a correct scaling with the parameters previously found.

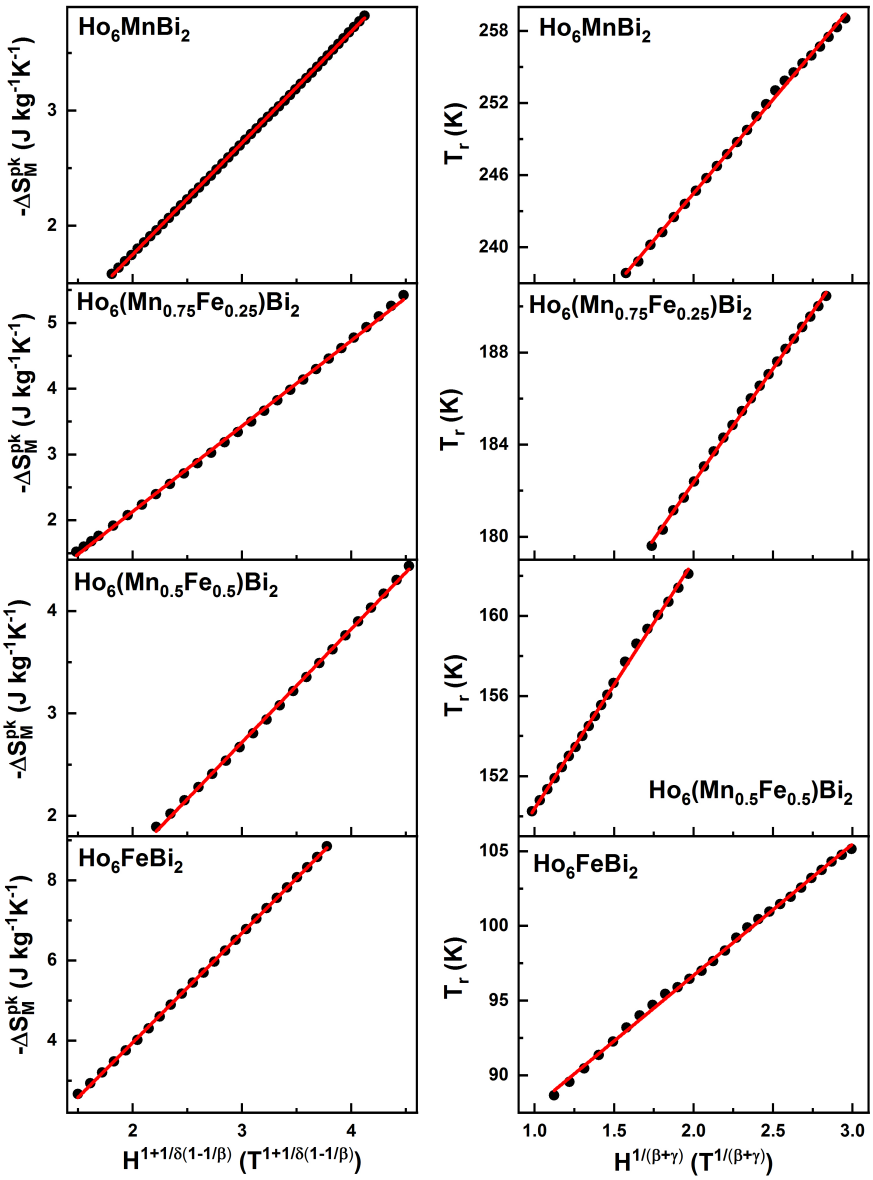


Figure 7.12: Field dependences of the peak magnetic entropy change $|\Delta S_M^{pk}|$ (left) and for the reference temperature T_r (right). The values of β, γ and δ for each compound are the ones presented in Table 7.3.

7.4 $(Gd, Tb)_6(Fe, Mn)Bi_2$ family

In the previous section we showed that changing the percentage of Fe and Mn in the $Ho_6(Mn, Fe)Bi_2$ intermetallics allows to extend the width of the operating temperature range with a nearly constant value of the magnetic entropy change, due to the presence of two magnetic transitions, as well as tuning the temperature at which the magnetic entropy change is maximum. The purpose of this section is to look for the applications of another branch of this family of R_6TBi_2 compounds; the $(Gd, Tb)_6(Fe, Mn)Bi_2$ family. The use of Gd ($T_C \approx 293$

K) and Tb ($T_C \approx 220$ K), with higher FM ordering temperatures than that of Ho ($T_C \approx 20$ K), and the tuning of the transition metal, are expected to make this family operative in the room temperature range as well as at low temperature, presenting a wide working region due to the possible presence of several magnetic transitions. In order to explore this possibility, we have focused our attention on Gd_6FeBi_2, $Gd_3Tb_3FeBi_2$, Tb_6FeBi_2 and $Tb_6(Fe_{0.5}Mn_{0.5})Bi_2$ compounds. The crystal structure and some magnetic properties have already been studied for both Gd_6FeBi_2 and Tb_6FeBi_2 [304, 379, 393–397] while a comprehensive study on the magnetic and magnetocaloric properties of the four aforementioned compositions will give a broader view of the general properties of the family and the role of the different ions, leading the path to appreciate their feasibility for practical applications.

Prior to any possible practical application a knowledge in depth of the magnetic properties is fundamental, the purpose of our work is to obtain it by means of the study of the critical behavior of the second order paramagnetic-ferromagnetic transition. The expectation is that the obtained values of the critical parameters will allow us to assign an already theorized universality class to the magnetic transition (or a nearness to one of them), so that a deeper insight in the physics of the magnetic properties will be revealed. Moreover, the complete study of the magnetocaloric properties of the four compounds presented in this study, including the refrigerant capacity, as well as the possibility to obtain universal curves from the magnetic entropy change, will fully characterize their ability to be used as magnetocaloric materials.

7.4.1 Structural data and magnetic characterization of $(Gd, Tb)_6(Fe, Mn)Bi_2$ family

The X-ray powder analysis showed that, as in the case of $Ho_6(Fe, Mn)Bi_2$ family, Gd_6FeBi_2, $Gd_3Tb_3FeBi_2$, Tb_6FeBi_2 and $Tb_6(Fe_{0.5}Mn_{0.5})Bi_2$ crystallize in the Fe_2P-type structure (space group $P\bar{6}2m$, No. 189, hP9). The refined unit cell data is given in Table 7.5. The substitution of Fe for Mn is followed via increasing of unit cell volume and anisotropic distortion of unit cell (increasing of c/a ratio) from Tb_6FeBi_2 to $Tb_6(Fe_{0.5}Mn_{0.5})Bi_2$. Meanwhile, the substitution of Tb for Gd leads to almost isotropic expansion of unit cell from Tb_6FeBi_2 to $Gd_3Tb_3FeBi_2$ and Gd_6FeBi_2 (increasing of unit cell volume, while c/a ratio is close to constant).

Compound	a (nm)	c (nm)	c/a	V (nm^3)
Gd_6FeBi_2	0.83573(8)	0.42344(3)	0.50667	0.25613
$Gd_3Tb_3FeBi_2$	0.83233(6)	0.42198(3)	0.50699	0.25317
Tb_6FeBi_2	0.82913(5)	0.42050(2)	0.50716	0.25035
$Tb_6(Fe_{0.5}Mn_{0.5})Bi_2$	0.82838(6)	0.42473(2)	0.51272	0.25241

Table 7.5: Unit cell data of Fe_2P-type $(Gd, Tb)_6(Fe, Mn)Bi_2$ compounds (space group $P\bar{6}2m$, No. 189, hP9).

Since these samples are synthesized through a diffusion process, as was explained in detail in Ref. [327], the compounds contain an admixture of Yb_5Sb_3-type $(Gd,Tb)_5(Fe,Mn)_{\sim 0.5}Bi_{\sim 2.5}$ phases (8–10 wt %). The admixture of Yb_5Sb_3-type Gd_5Bi_3 exhibits FM ordering around 110 K [398] and the Tb_5Bi_3 Yb_5Sb_3-type admixture may show ferromagnetic ordering around 70 K in accordance with de Gennes rule [399]. Meanwhile these admixtures show a small influence for the resulting magnetic properties, as will be discussed later.

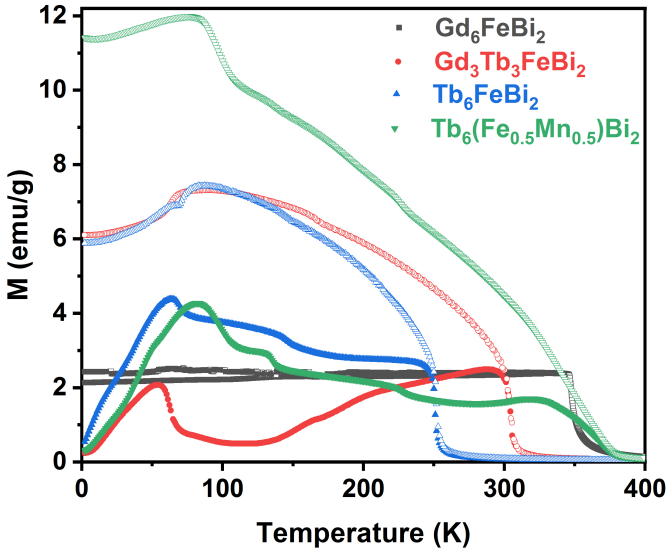


Figure 7.13: Magnetic moment as a function of temperature in Zero-Field Cooled (filled symbols) and Field-Cooled (empty symbols) mode with an applied field of $\mu_0 H = 0.01$ T.

The first step in order to understand the transitions and magnetism of our compounds is to obtain their magnetization as a function of temperature. This is shown in Fig. 7.13, both in Zero-Field Cooled (ZFC) and Field-Cooled (FC) mode for the four samples, with an applied field of 100 Oe. ZFC curves are represented by filled symbols while empty ones are used for FC. In all samples with Tb, there is a clear divergence between the ZFC and FC curves, showing thermomagnetic irreversibility, typical of many ferromagnetic (or ferrimagnetic) transitions. This thermomagnetic irreversibility is higher than the one observed for Ho-based compounds in Fig. 7.1(a). While Gd_6FeBi_2 has only a paramagnetic to ferromagnetic (PM-FM) transition at $T_C = 346$ K, there are clearly two main transitions in the other compounds, with some intermediate minor transitions due to other residual phases (see, for instance, the transition at 144 K for $Tb_5Fe_{0.4}Bi_{2.6}$, which has been detected in Tb_6FeBi_2).

The precise position of the transitions is clearly revealed in the *ac* susceptibility measurements, whose real part is represented in Fig. 7.14 for the samples with several transitions (T^* corresponds to transitions for the secondary phases). The substitution of Gd by Tb and Fe by Mn allows to tune the Curie temperature, which is placed at 302 K for $Gd_3Tb_3FeBi_2$, 250 K for Tb_6FeBi_2, and 376 K for $Tb_6(Fe_{0.5}Mn_{0.5})Bi_2$, while there are spin-reorientation transitions placed at $T_m = 60$ K, 65 K and 90 K (for $Gd_3Tb_3FeBi_2$, Tb_6FeBi_2,

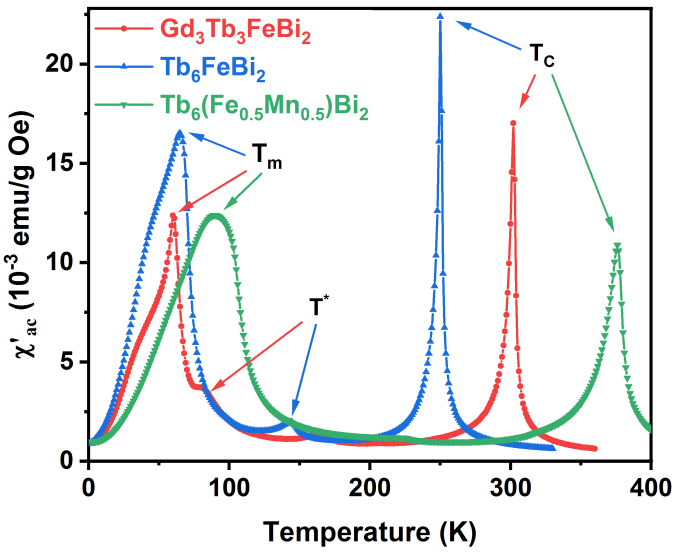


Figure 7.14: Real part of the *ac* susceptibility at $f = 100$ Hz. T_C corresponds to the paramagnetic to ferromagnetic transitions, T_m to the spin reorientation ones, T^* to ferromagnetic transitions of the secondary phases.

and $Tb_6(Fe_{0.5}Mn_{0.5})Bi_2$, respectively), which, as we already saw for the Ho containing compounds and will also be shown later, play a major role in the magnetocaloric properties of these compounds. The positions of T_C and T_m agree quite well with previous measurements in Gd_6FeBi_2 and Tb_6FeBi_2 [379, 393, 394]. According to literature, the high-temperature ferromagnetic ordering corresponds to the *c*-axis collinear ferromagnetic ordering of rare-earth sublattice, while low temperature transition of Tb_6FeBi_2, $Gd_3Tb_3FeBi_2$ and $Tb_6(Fe_{0.5}Mn_{0.5})Bi_2$ is attributed to an additional *ab*-plane ferro-antiferromagnetic component of the rare-earth sublattice [327]. The presence of low temperature phases with complex spin arrangements which include canted ferromagnets, conical or spiral structures, or simply antiferromagnetic components, is quite common in R_6TX_2 family, where no magnetic moment has been found for the transition metal [327, 380, 382]. Concerning the evolution of the magnetic properties, starting from Gd_6FeBi_2, the introduction of Tb to reach $Gd_3Tb_3FeBi_2$ and then Tb_6FeBi_2 provokes a monotonous evolution in the reduction of T_C, as well as in the general shape of the ZFC-FC curves, and it will be seen later that the magnetocaloric properties have a similar behavior. Adding Mn changes this tendency, taking the magnetic transitions to a higher temperature and separating more T_C from T_m, what it has already been observed in other compounds of the family when substituting Fe by Mn. This is the case of Ho_6FeBi_2 presented in the previous section (where we saw the same behavior), and also the case of Dy_6FeBi_2 [327], which will be studied in the following section.

Demagnetization factors (N_D) and critical temperatures (T_C) obtained from the *ac* susceptibility measurements for (Gd, Tb)$_6$(Fe, Mn)Bi$_2$ compounds are collected in Table 7.6. From Tables 7.6 and 7.5 it can also be observed an increased of T_C with increasing *c* parameter, as was already observed and discussed in Ho_6(Fe, Mn)Bi_2 family.

Compound	T_C (K)	N_D (gOe/emu)
Gd_6FeBi_2	348	43.92
$Gd_3Tb_3FeBi_2$	302	57.39
Tb_6FeBi_2	250	41.14
$Tb_6(Fe_{0.5}Mn_{0.5})Bi_2$	376	90.45

Table 7.6: Experimentally obtained Curie temperature and demagnetization factors for (Gd, Tb)$_6$(Fe, Mn)Bi$_2$ compounds.

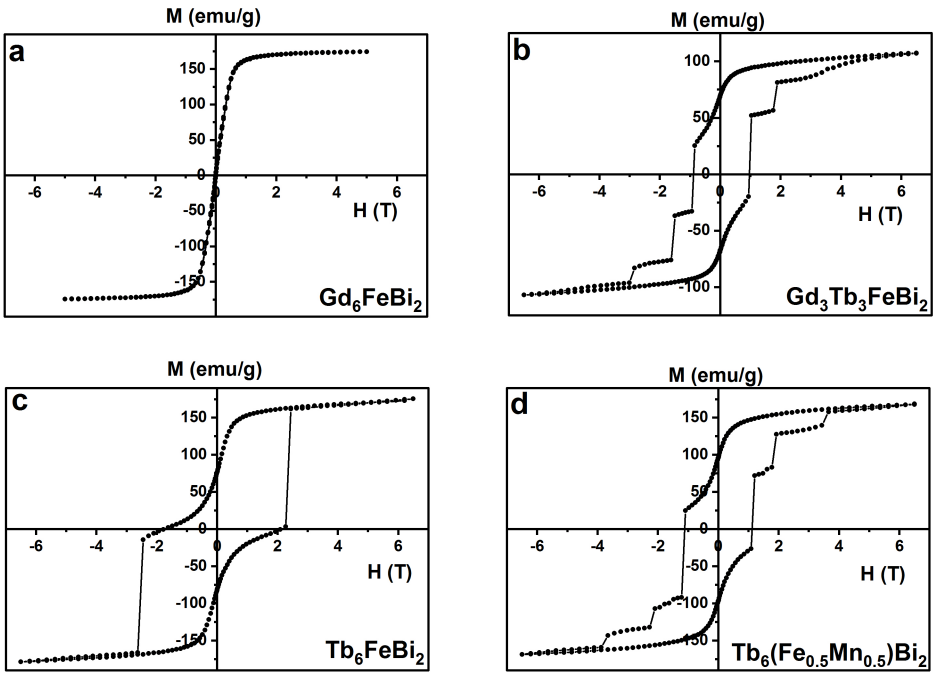


Figure 7.15: Hysteresis loops at 2 K: (a) Gd_6FeBi_2, (b) $Gd_3Tb_3FeBi_2$, (c) Tb_6FeBi_2, and (d) $Tb_6(Fe_{0.5}Mn_{0.5})Bi_2$.

The magnetism at low temperature was further studied by the isothermal magnetizations at 2 K, shown in Fig. 7.15, which help us explain the origin of the differences between ZFC and FC curves for the samples containing Tb. As it is clear from Fig. 7.15(a), in the case of Gd_6FeBi_2 there is a negligible coercive field H_C, while it is in the range 1–2.5 T for the Tb containing compounds. Moreover, there is a step-like behavior in the latter, typical of metamagnetic transitions, which points to the presence of antiferromagnetic interactions responsible for a non-collinear magnetic structure at very low temperature. The observation of several steps in two cases ($Gd_3Tb_3FeBi_2$ and $Tb_6(Fe_{0.5}Mn_{0.5})Bi_2$) indicates the existence of intermediate magnetic arrangements till the final ferromagnetic state is reached. The low temperature magnetic state quickly turns into a ferromagnetic state as the temperature is raised, as it is seen in the evolution of the magnetization isotherms as a function of the applied field presented in Fig. 7.16, where in a small tempera-

ture range (approximately 2–12 K for $Gd_3Tb_3FeBi_2$, 2–20 K for Tb_6FeBi_2, and 2–14 K for $Tb_6(Fe_{0.5}Mn_{0.5})Bi_2$) the magnetization has the general behavior of increasing from one isotherm to the following one (with increasing temperature), for the same value of the magnetic field, confirming the presence of antiferromagnetic interactions (see left column of Fig. 7.16); from then on, with increasing values of temperature, the behavior of the isotherms is the common one for a ferromagnetic state, i.e., for a given applied field, the magnetization decreases as temperature is increased (see right column in Fig. 7.16). In fact, in Fig. 7.16 an even more complicated behavior can be observed for the case of $Tb_6(Fe_{0.5}Mn_{0.5})Bi_2$, where, at very low temperature (< 3.5 K), subsequent metamagnetic transitions can be observed, changing the ground state to a ferromagnetic one from an intermediate field.

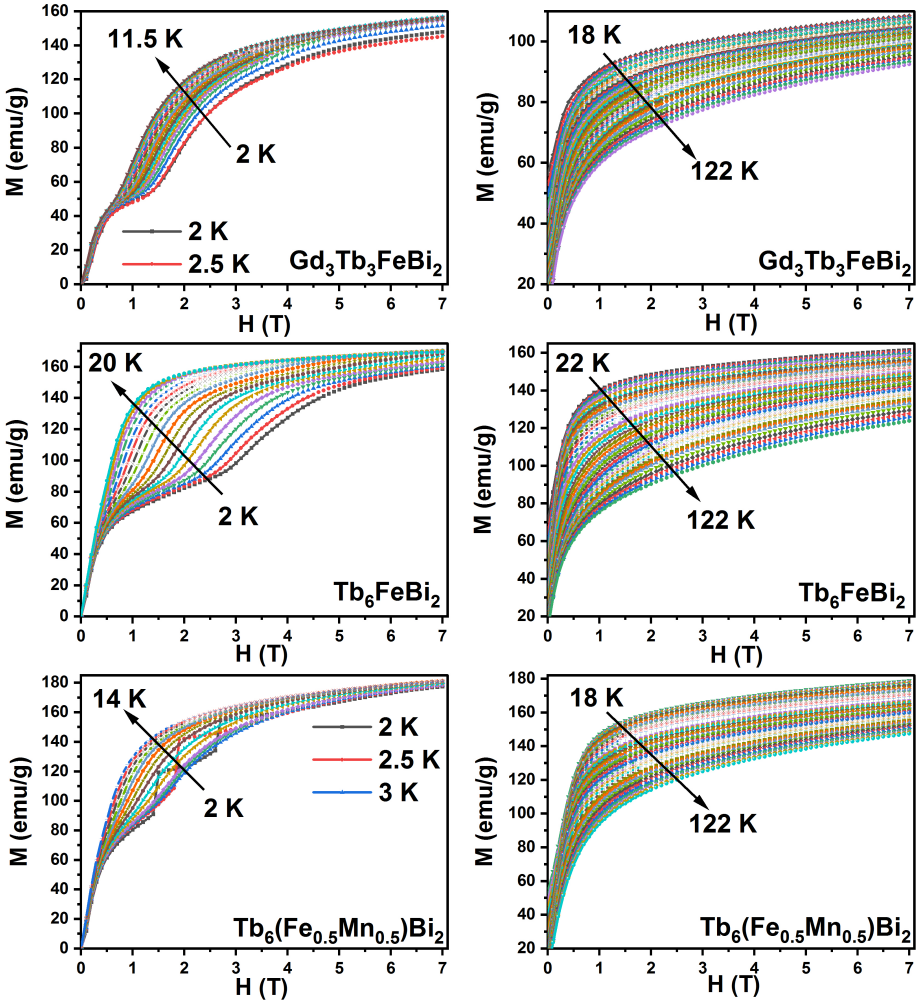


Figure 7.16: Magnetization isotherms at low (left column) and higher (right column) temperatures for $Gd_3Tb_3FeBi_2$, Tb_6FeBi_2 and $Tb_6(Fe_{0.5}Mn_{0.5})Bi_2$. The direction of the arrow indicates increasing temperature.

7.4.2 Critical behavior in $(Gd, Tb)_6(Fe, Mn)Bi_2$ family

Let us begin our critical behavior analysis with the extraction of the magnetic critical exponents (β, γ and δ) for the PM-FM transitions. In order to

do so, detailed magnetization isotherms have been measured in the vicinity of the respective Curie temperatures. In the first place we represented the Modified Arrot Plots (MAP), where $M^{1/\beta}$ is represented versus $(H/M)^{1/\gamma}$, for the most common universality classes in magnetic materials (3D Heisenberg, 3D Ising). The Arrot Plot (AP), the particular case of the MAPs corresponding to the Mean Field model, are also represented, not only to search for the applicability of this model in order to describe the critical behavior of our compounds, but also to check the order or the transition by considering the Banerjee criterion [229]. The positive slopes in the APs confirm the second order nature of the phase transitions and, therefore, the applicability of the critical behavior analysis. As we have already seen several times, the correct choice of critical exponents will be the one which gives straight parallel lines at high fields in the MAP or AP representation. This time, the analysis was very straightforward for Gd_6FeBi_2 but this was not the case for the other three samples as we will explain later.

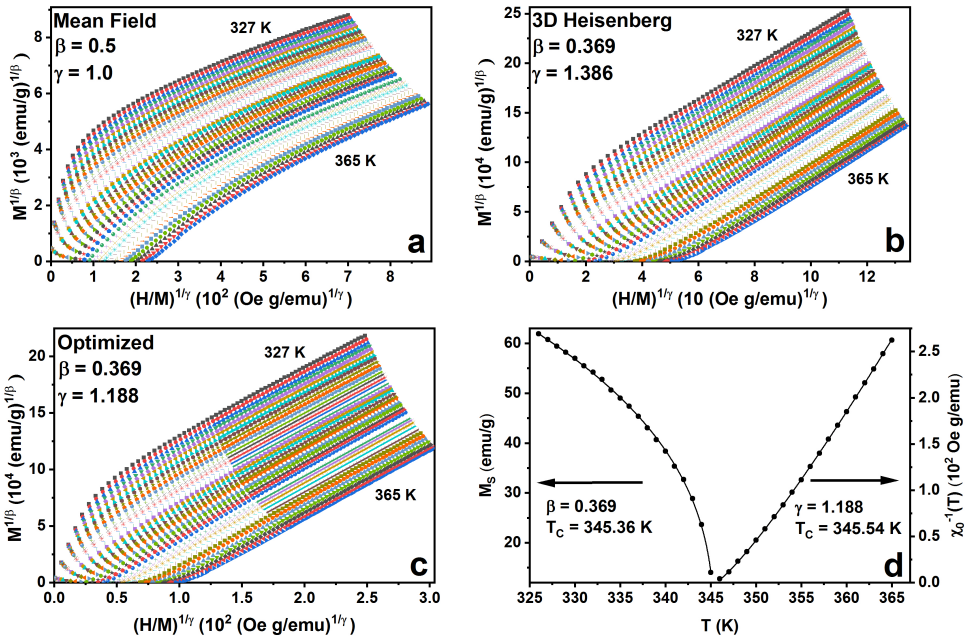


Figure 7.17: Gd_6FeBi_2: (a) Arrot Plot, corresponding to the Mean Field universality class parameters; (b) Modified Arrot Plot for the 3D Heisenberg class; (c) Optimized Modified Arrot Plot; (d) Spontaneous magnetization (left) and inverse of initial susceptibility (right) vs. temperature as obtained from the optimized MAP.

With respect to Gd_6FeBi_2, Fig. 7.17 shows the graphs for Mean Field (Fig. 7.17(a)), and Heisenberg (Fig. 7.17(b)) models for this sample. It is clearly seen that the model with best straight and parallel lines is the Heisenberg one, so this has been taken as a starting point to find the best values for β and γ (the Ising model has also been tested but the result is worse than for the Heisenberg case). The common iterative procedure presented in Section 3.4.1 has then been followed. A linear extrapolation from high field data on the MAP has been used to extract the $(M_S)^{1/\beta}$ and $(\chi_0^{-1})^{1/\gamma}$ values as the interception with

Y and X axes, respectively. Once $M_S(T)$ and $\chi_0^{-1}(T)$ have been obtained they are fitted to Eqs. (7.1) and (7.2) to obtain new values of β and γ, which are then used for another iteration until the values converge and good parallel, straight lines, are obtained in the MAP. The final result is shown in Fig. 7.17(c) and Table 7.7 contains the exponents with their errors. Fig. 7.17(d) shows the spontaneous magnetization and the inverse of the initial susceptibility vs. temperature as obtained from the optimized MAP. The obtained β value is precisely the one for the Heisenberg model ($\beta_{\text{exp}} = 0.369 \pm 0.004$, $\beta_{\text{Heis}} = 0.369$) though γ is smaller ($\gamma_{\text{exp}} = 1.188 \pm 0.007$, $\gamma_{\text{Heis}} = 1.396$).

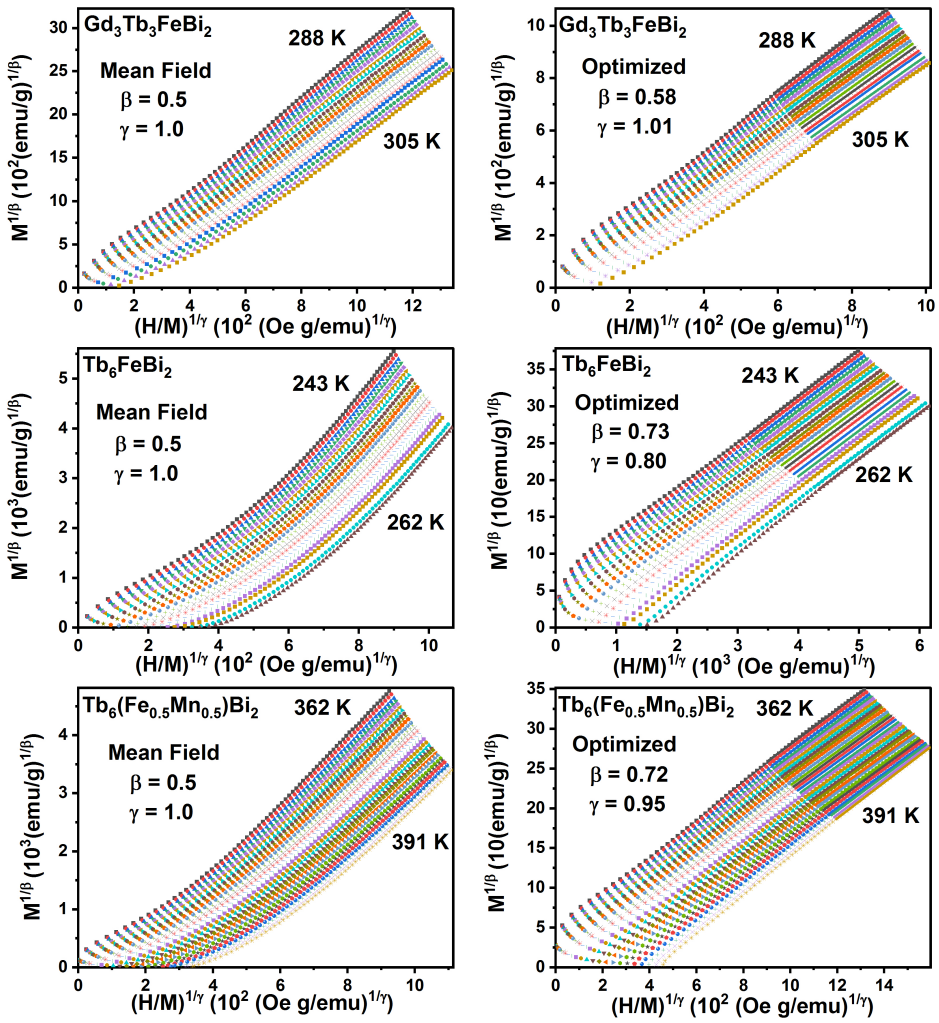


Figure 7.18: Left column: APs for $Gd_3Tb_3FeBi_2$, Tb_6FeBi_2 and $Tb_6(Fe_{0.5}Mn_{0.5})Bi_2$. Right column: Optimized MAPs for the previous compounds.

In the case of the Tb containing samples the situation is very different, while they share some common features. Left column in Fig. 7.18 presents the Arrott Plot for all of them, using the Mean Field model, which happens to be much better as a starting point than the Heisenberg or Ising models. However, it is clear at first sight that the isotherms are not straight and parallel enough at high fields, which means that the Mean Field critical exponents are not really the good ones. We have thus tested different sets of parameters close to the Mean Field model as starting points before proceeding

with the iteration procedure and the final result is shown in the right column of Fig. 7.18. On this occasion, we had to restrict the isotherms to a narrower region around the critical temperature in order to obtain a good convergence, that is why fewer isotherms than usual are shown in Fig. 7.18. In the case of $Tb_6(Fe_{0.5}Mn_{0.5})Bi_2$ γ is indeed very close to the Mean Field value ($\gamma_{exp} = 0.95 \pm 0.01$, $\gamma_{MF} = 1$) while β takes the value of 0.72 ± 0.02, higher than any proposed universality class (check Table 3.2 in page 77). Substituting half of the Gd with Tb ($Gd_3Tb_3FeBi_2$) takes the critical exponents quite close to the Mean Field model ($\beta_{exp} = 0.58 \pm 0.02$, $\gamma_{exp} = 1.01 \pm 0.02$) while completely substituting it (Tb_6FeBi_2) moves them to farther values ($\beta_{exp} = 0.73 \pm 0.09$, $\gamma_{exp} = 0.80 \pm 0.03$). The critical exponents obtained for all the samples are gathered in Table 7.7.

As the next step, the critical isotherms for the four compounds have been plotted to extract the critical exponent δ, after Eq. (7.3). Fig. 7.19 shows the result for all of them in a log-log scale, where the points should be along a straight line, as it happens in all cases. From the slope, the value of δ is easily retrieved and can be compared with the one using the Widom scaling equation: $\delta = 1 + \gamma/\beta$. These results are also gathered in Table 7.7, from where the good agreement between the calculated δ and the ones obtained from the critical isotherms can be checked.

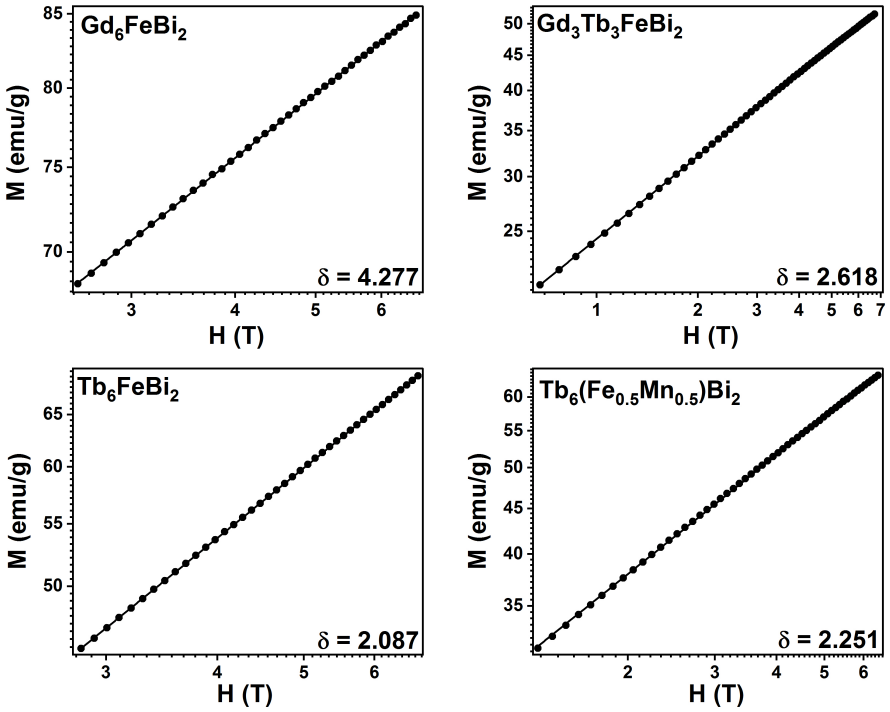


Figure 7.19: M vs. H plot in a log-log scale collected at critical isotherms for the four compounds. The straight lines are the linear fits from which δ is obtained.

A solid confirmation of the validity of these critical exponents to describe the magnetic transition is the fulfilment of the magnetic equation of state, Eq. (7.5). The latter is represented in Fig. 7.20 and has been built up with the critical exponents just obtained. As predicted from theory, it can be appreciated

that all isotherms collapse onto two independent branches, one for $T < T_C$, a second one for $T > T_C$. This happens for the four compounds and is considered a strong confirmation of the validity of the critical exponents.

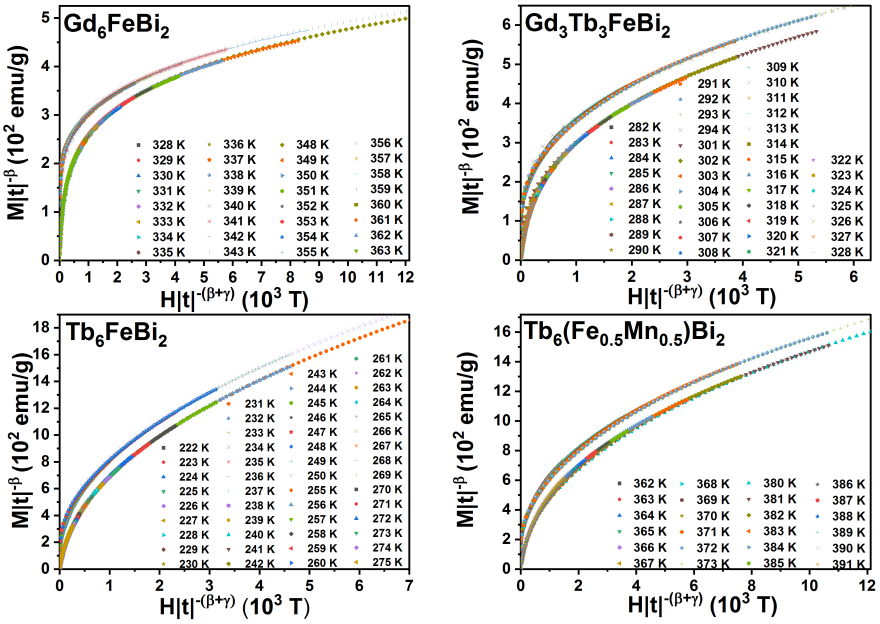


Figure 7.20: The renormalized magnetization plotted as a function of the renormalized field following Eq. (7.5) for the four compounds. In each case, all data collapse in two separate branches, one above and one below the respective T_C.

Material	Technique	β	γ	δ
Gd_6FeBi_2	Modified Arrot Plot	0.369 ± 0.004	1.188 ± 0.007	4.22 ± 0.05^a
	Critical Isotherm			4.277 ± 0.0005
$Gd_3Tb_3FeBi_2$	Modified Arrot Plot	0.58 ± 0.02	1.01 ± 0.02	2.8 ± 0.1^a
	Critical Isotherm			2.618 ± 0.004
Tb_6FeBi_2	Modified Arrot Plot	0.73 ± 0.09	0.80 ± 0.03	2.1 ± 0.2^a
	Critical Isotherm			2.087 ± 0.001
$Tb_6(Fe_{0.5}Mn_{0.5})Bi_2$	Modified Arrot Plot	0.72 ± 0.02	0.95 ± 0.01	2.31 ± 0.06^a
	Critical Isotherm			2.251 ± 0.004

[a] Calculated from Widom scaling equation: $\delta = 1 + \gamma/\beta$.

Table 7.7: Critical exponents obtained for $(Gd, Tb)_6(Fe, Mn)Bi_2$ family.

Let's examine the obtained values of the critical exponents in some detail: As we mentioned before, for the case of Gd_6FeBi_2, β completely agrees with the theoretical one for the Heisenberg case ($\beta_{exp} = 0.369 \pm 0.004$, $\beta_{Heis} = 0.369$) while γ and δ are smaller, though there is a good coherence among them, as they satisfy Eqs. (7.4), (7.5). This implies that the magnetic interactions are short-range though there is not a perfect isotropic distribution of the spins, which is the basis of this model. As was previously discussed for the Ho_6(Fe,

Mn)Bi_2 family, it is generally accepted that, in the general family R_6TBi_2, the T ions do not carry magnetic moments, as it has been proven by neutron diffraction in some of them [304, 305, 379, 382, 394] so the magnetism basically arises from the rare-earth atoms by means of an indirect *4f-4f* interaction via the Ruderman-Kittel-Kasuya-Yosida (RKKY) interaction. In a similar way to what we saw in the previous section for Ho_6(Fe, Mn)Bi_2, the Curie temperatures are higher than what corresponds to the rare-earth ion alone (for Gd T_C = 292.77 K [400] while for Gd_6FeBi_2 T_C = 345.45 K, and T_C = 220 K (T_N = 230 K) for Tb [385] while for Tb_6FeBi_2 T_C = 250 K and T_C = 376 K for $Tb_6(Fe_{0.5}Mn_{0.5})Bi_2$). This is attributed to a hybridization phenomena between electronic orbitals of the rare-earth and the other ions in the compound [78, 93, 304], though the precise mechanism is still not well understood. Gd and some Gd-based compounds present a PM-FM transition which is close to the Heisenberg universality class [15, 401] though always with some deviations. Notice that this is the same phenomena as the one already observed in Chapter 4 for the Gd(Sc,Ti)(Si,Ge) family. The deviation that we have found can not have its origin in crystal field effects, as it happens with some other rare-earths, because the orbital moment L is 0 for Gd, so it is surely due to some kind of magnetocrystalline anisotropy, such as a non-negligible spin-orbit coupling of the itinerant electrons, as it has been suggested for other Gd-based materials [274, 290].

The partial substitution of Gd by Tb and its complete substitution completely changes the scenario. $Gd_3Tb_3FeBi_2$ presents critical exponents very close to the Mean Field model ($\beta_{exp} = 0.58 \pm 0.02$, $\gamma_{exp} = 1.01 \pm 0.02$), indicating that long-range order interactions are now governing the transition; at the same time, the critical temperature is reduced around 50 K, while the complete substitution (Tb_6FeBi_2) reduces it another 40 K; in the latter, the critical exponents take values which do not comply with any universality class, with a growing β and a decreasing γ ($\beta_{exp} = 0.73 \pm 0.09$, $\gamma_{exp} = 0.80 \pm 0.03$). Besides, the introduction of Tb leads to the opening of the hysteresis loop (see Fig. 7.15), with a relevant coercive field, as well as to a spin reorientation transition at T_m and the appearance of metamagnetic transitions at low temperature, supporting the fact that the magnetism drastically changes with the presence of Tb. The reduction in T_C is due to the lower value of the total spin S for Tb compared to Gd. On the other hand, Tb (unlike Gd) has non-zero orbital moment (L = 3), which may introduce crystal field effects, together with magnetocrystalline anisotropies [402]. The substitution of Fe by Mn in $Tb_6(Fe_{0.5}Mn_{0.5})Bi_2$ only slightly modifies the values of the critical exponents ($\beta_{exp} = 0.72 \pm 0.02$, $\gamma_{exp} = 0.95 \pm 0.01$).

Since there is no universality class with β values bigger than 0.5 or γ smaller than 1.0, it is not evident to associate the values obtained here (0.72, 0.73 for β, 0.80, 0.95 for γ) to a particular distribution of spins or order of the interactions translated to a certain Hamiltonian, though the γ values suggest that it is a long-range interaction, as they are close to 1, and the values of β indicate a certain deviation from the Mean Field model, but it is difficult to understand the origin of this deviation. There are many other materials which have been also found to present an unconventional critical behavior, with critical

exponents around these values: $Sr_{1-x}A_xRuO_3$ [403,404], $La_{0.5}Ca_{0.4}Ag_{0.1}MnO_3$ [405], $La_{0.4}Ca_{0.6}MnO_3$ [406], $BaIrO_3$ [407], κ-(BEDT-TTF)$_2$X [408], Mn_3CuN [319], TDAE-C_{60} [409], just to cite some examples. This implies that, indeed, the known universality classes do not cover the whole spectrum of magnetism and, therefore, more theoretical work should be done in order to propose new universality classes. In this particular case, it is the presence of Tb which takes the critical exponents to such values, even if neutron diffraction data agree at 200 K with a collinear ferromagnetic state, with Tb occupying two non-equivalent positions; it is the low temperature transition which is ferromagnetic non-collinear [379].

In order to check the appropriateness of the values of the critical exponents found, detailed specific heat measurements in the near vicinity of the phase transition have also been undertaken, from where the critical exponent α can be extracted, by means of fitting the experimental points to the function we have already used for previous compounds presented in this work:

$$c_p = B + Ct + A^{\pm}|t|^{-\alpha}(1 + E^{\pm}|t|^{0.5}) , \tag{7.13}$$

where t is the reduced temperature and α, $A^{\pm}$, B, C and $E^{\pm}$ are adjustable parameters. Superscripts + and − stand for $T > T_C$ and $T < T_C$ respectively.

Furthermore, as already shown in Section 3.3, in the particular case in which the Mean Field model is of application, for which the critical exponent α equals to 0, the critical equation would take an asymptotical logarithmic form at the paramagnetic phase, while the ferromagnetic phase should be described by a Landau classical formulation. Therefore, the paramagnetic ($T > T_C$) region is fitted to:

$$c_p = A \ln t + B + Ct , \tag{7.14}$$

while the ferromagnetic region ($T < T_C$) is fitted to:

$$c_p = A_1 \frac{T}{\sqrt{1 - 4A_2(T - T_C)}} + B' + C'(T - T_C) . \tag{7.15}$$

The fitting procedure followed is the standard one and has already been explained in Section 3.3.1. The c_p obtained from PPE calorimetric measurements as well as their corresponding fittings are shown in Fig. 7.21. For Gd_6FeBi_2 the best fitting corresponds to Eq. (7.13) with $\alpha = -0.075 \pm 0.007$, which is close to the theoretical one for the 3D Heisenberg model ($\alpha_{\text{Heis}} = -0.134$); besides, the critical ratio $A^+/A^- = 1.32$ while $A^+/A^-_{Heis} = 1.52$. Other models have been tested but none of them has given a good fitting. This corroborates the previous magnetic results, implying that the PM-FM belongs to the Heisenberg class with a certain deviation from it.

In the Tb containing compounds, the fitting to Eq. (7.13) have not given good results, the best ones being obtained by using Eqs. (7.14) and (7.15). Starting with $Gd_3Tb_3FeBi_2$, both regions agreed quite well with this model but not exactly, as seen in the difficulty in fitting the curvature of the PM phase (see Fig. 7.21(b)). This corroborates the magnetic exponents, which are quite close to the Mean Field model but with a slight separation from it. Tb_6FeBi_2 deviates

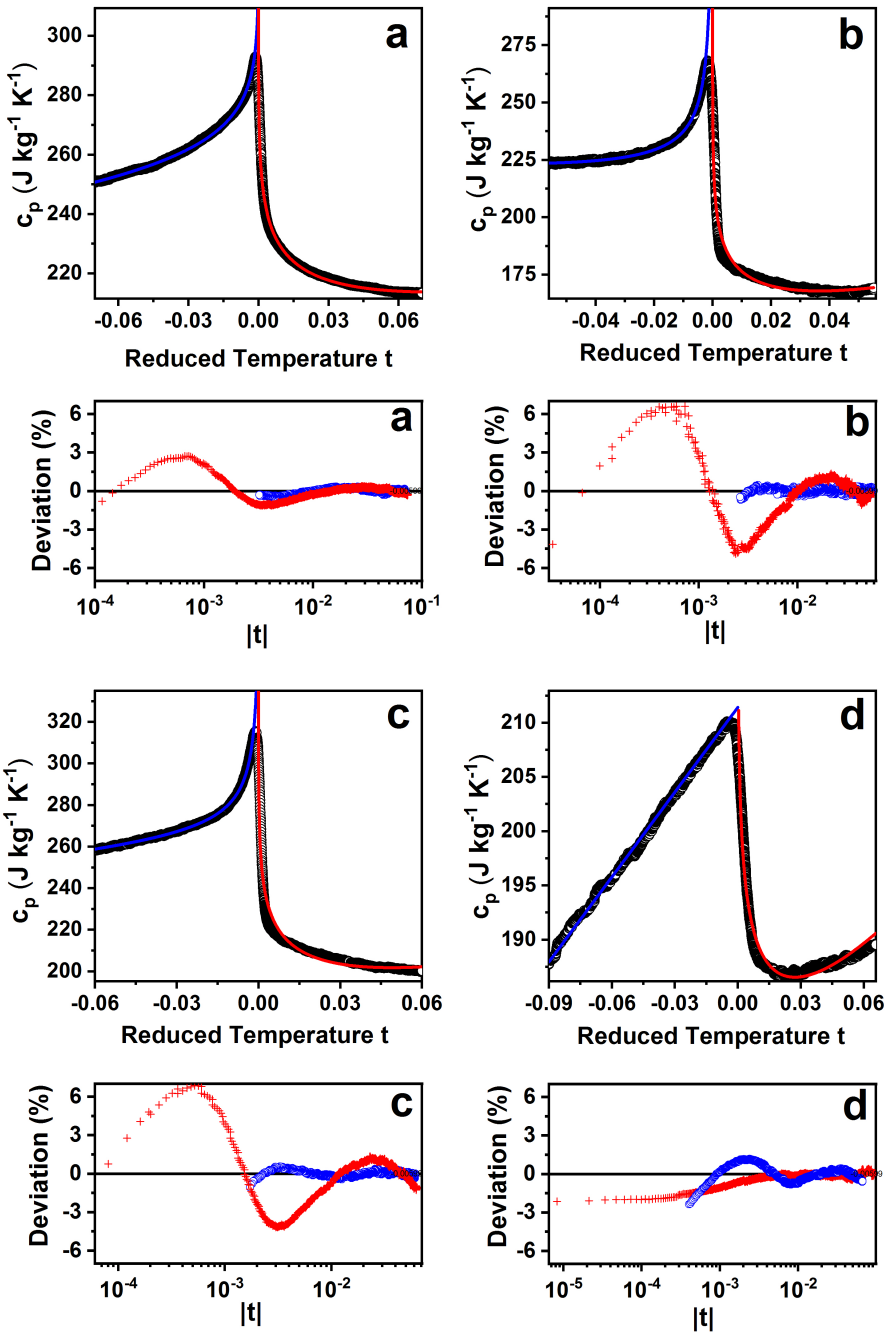


Figure 7.21: Experimental (dots) and fitted curves (continuous lines) of the c_p as a function of t for the four compounds in the vicinity of T_C (top in each case); deviation plots for the fittings (bottom in each case), where open circles are for $T < T_C$, crosses for $T > T_C$. (a) Gd_6FeBi_2, (b) $Gd_3Tb_3FeBi_2$, (c) Tb_6FeBi_2, and (d) $Tb_6(Fe_{0.5}Mn_{0.5})Bi_2$.

even more from the Mean Field model (see Fig. 7.21(c)), while the introduction of Mn in $Tb_6(Fe_{0.5}Mn_{0.5})Bi_2$ alters the shape of c_p and makes quite difficult any fitting (see Fig. 7.21(d)), the best one being obtained again with Eqs (7.14) and (7.15). These results corroborate the unconventional critical behavior of these Tb-based compounds, which will be further confirmed by the scaling of the magnetic entropy change presented in the next section.

7.4.3 Magnetocaloric effect in $(Gd, Tb)_6(Fe, Mn)Bi_2$ family

In order to evaluate possible applications of these compounds, their magnetocaloric properties have been studied by the common, indirect method, of evaluating the magnetic entropy change as a function of temperature and magnetic field through the *Maxwell relation*. This expression provides a very quick an easy way of evaluating the MCE in second order phase transitions, which as follows from the Banerjee criterion applied to the AP presented in Figs. 7.17 and 7.18, is the case of these compounds (except at low temperatures as we will discuss later).

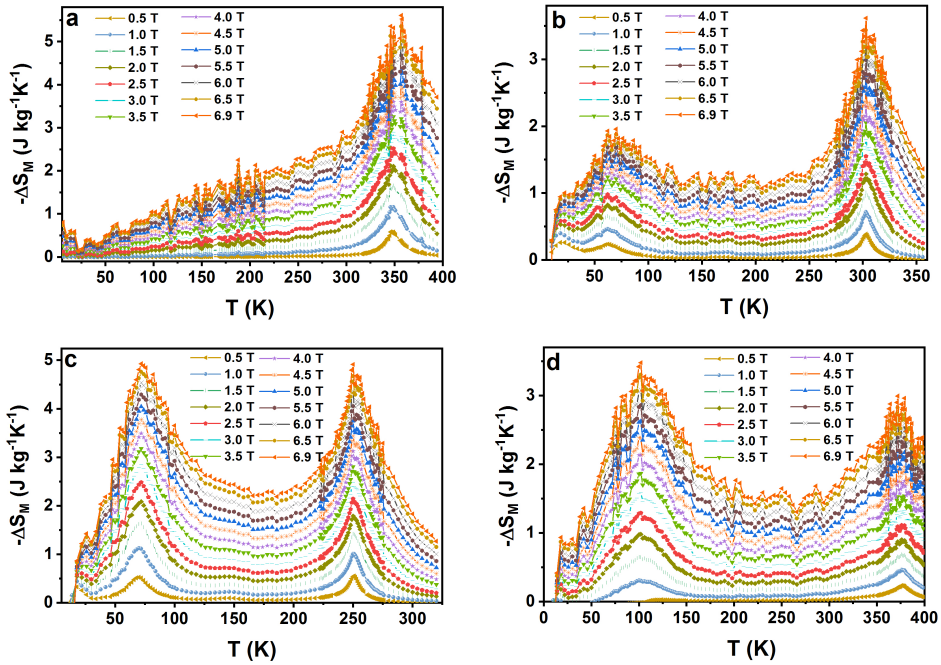


Figure 7.22: Magnetic entropy change $-\Delta S_M$ for $\mu_0\Delta H$ from 1 T to 6.9 T for: (a) Gd_6FeBi_2, (b) $Gd_3Tb_3FeBi_2$, (c) Tb_6FeBi_2, and (d) $Tb_6(Fe_{0.5}Mn_{0.5})Bi_2$.

The results are shown in Fig. 7.22 where it is seen that there is only one peak for Gd_6FeBi_2, while there are two for the other three compounds, associated to the PM-FM transitions at high temperatures and to the spin reorientation transitions at low ones. The maximum values $|\Delta S_M^{pk}|$ are similar to what is obtained in many other rare-earth based materials [82, 91, 108] including the previously presented $Ho_6(Fe, Mn)Bi_2$ family. As in the latter compounds, there are several additional features worth studying, specially the fact that the temperature span of the magnetocaloric effect is extended in the case where there are two magnetic transitions, giving relevant values of the refrigerant capacities *RC* around room temperature.

The values of the refrigerant capacities, as well as the maxima of $|\Delta S_M^{pk}|$ are tabulated in Table 7.8 (upper Table for T_C, lower Table for T_m) for $\mu_0\Delta H = 2$, 5 and 6.9 T, the first ones for the sake of comparison with literature, the third one being the highest field applied. As in Gd_6FeBi_2 and $Tb_6(Fe_{0.5}Mn_{0.5})Bi_2$ T_C is quite high and our system can not measure above 400 K, some values

$\mu_0\Delta H$	Magnitude	Gd_6FeBi_2 T_C = 346 K	$Gd_3Tb_3FeBi_2$ T_C = 303 K	Tb_6FeBi_2 T_C = 250 K	$Tb_6(Fe_{0.5}Mn_{0.5})Bi_2$ T_C = 376 K
2 T	$\lvert\Delta S_M^{pk}\rvert$ (J kg^{-1} K^{-1})	2.1	1.3	1.8	0.9
	RC_{FWHM} (J kg^{-1})	119	43	60	73[a]
	RC_{Area} (J kg^{-1})	87	31	43	-
5 T	$\lvert\Delta S_M^{pk}\rvert$ (J kg^{-1} K^{-1})	4.3	2.8	3.7	2.1
	RC_{FWHM} (J kg^{-1})	402[a]	158	231	266[a]
	RC_{Area} (J kg^{-1})	296[a]	112	162	-
6.9 T	$\lvert\Delta S_M^{pk}\rvert$ (J kg^{-1} K^{-1})	5.4	3.6	4.9	2.9
	RC_{FWHM} (J kg^{-1})	-	252	376	-
	RC_{Area} (J kg^{-1})	-	178	261	-

$\mu_0\Delta H$	Magnitude	Gd_6FeBi_2 -	$Gd_3Tb_3FeBi_2$ T_m = 62 K	Tb_6FeBi_2 T_m = 72 K	$Tb_6(Fe_{0.5}Mn_{0.5})Bi_2$ T_m = 102 K
2 T	$\lvert\Delta S_M^{pk}\rvert$ (J kg^{-1} K^{-1})	-	0.8	2.1	1.0
	RC_{FWHM} (J kg^{-1})	-	73	91	72
	RC_{Area} (J kg^{-1})	-	51	69	55
5 T	$\lvert\Delta S_M^{pk}\rvert$ (J kg^{-1} K^{-1})	-	1.6	4.0	2.6
	RC_{FWHM} (J kg^{-1})	-	210	279	279
	RC_{Area} (J kg^{-1})	-	143	208	209
6.9 T	$\lvert\Delta S_M^{pk}\rvert$ (J kg^{-1} K^{-1})	-	1.9	4.9	3.5
	RC_{FWHM} (J kg^{-1})	-	-	481	444
	RC_{Area} (J kg^{-1})	-	-	343	326

[a] Extrapolations have been needed to obtain these values.

Table 7.8: $\lvert\Delta S_M^{pk}\rvert$, RC_{FWHM} and RC_{Area} at different applied fields $\mu_0\Delta H$ (2, 5 and 6.9 T) for the four compounds at their corresponding Curie temperature T_C (upper Table), and at their corresponding spin reorientation temperature T_m (lower Table).

for RC have had to be obtained from extrapolations, while some RC_{Area} can not be obtained (these values are clearly indicated in Table 7.8). Starting from Gd_6FeBi_2, codoping it with Tb ($Gd_3Tb_3FeBi_2$) takes the maximum values from 346 to 303 K (therefore approaching room temperature) though $\lvert\Delta S_M^{pk}\rvert$ is reduced; the appearance of the spin reorientation transition at 62 K makes the values of $\lvert\Delta S_M\rvert$ increase at medium temperatures. With the complete substitution of Gd by Tb (Tb_6FeBi_2), there are nearly equivalent peaks at $\mu_0\Delta H = 5$ T, placed at 72 and 250 K, which are both interesting regions of application, with RC_{FWHM} being 279 and 231 J/kg and a very wide temperature span of the magnetocaloric effect between the peaks. Finally, there is a similar effect when partially substituting Fe by Mn ($Tb_6(Fe_{0.5}Mn_{0.5})Bi_2$) but displacing the

maxima to 102 K (T_m) and 376 K (T_C) and, though the maxima are smaller, the RC_{FWHM} is maintained at T_m while it increases at T_C due to the widening of the peak (279 and 266 J/kg, respectively).

These results show, on the one hand, the interest in mixing Gd and Tb (Fig. 7.22(a), (b), (c)) in order to tune the region of application and, on the other, to substitute Fe by Mn in the Tb-based compounds, to enhance the effect (Fig. 7.22(d)). The results here obtained are comparable to previously published results on the value of $|\Delta S_M^{pk}|$ at T_C for Gd_6FeBi_2 ($|\Delta S_M^{pk}| = 4.3$ J/kgK at $\mu_0\Delta H = 5$ T) [394] and Tb_6FeBi_2 ($|\Delta S_M^{pk}| = 2.68$ J/kgK at $\mu_0\Delta H = 2$ T) [393], though they had not been studied in the full temperature range. If we compare them with other rare-earth based compounds, the values of $|\Delta S_M^{pk}|$ are not too high (for instance, compared to the results presented in Fig. 2 of Ref. [91]) though, due to the effect of both phase transitions, the refrigerant capacity and temperature span are fully competitive [82, 91, 108], with the added advantage of the plateau region which is interesting for their application on an Ericsson cycle.

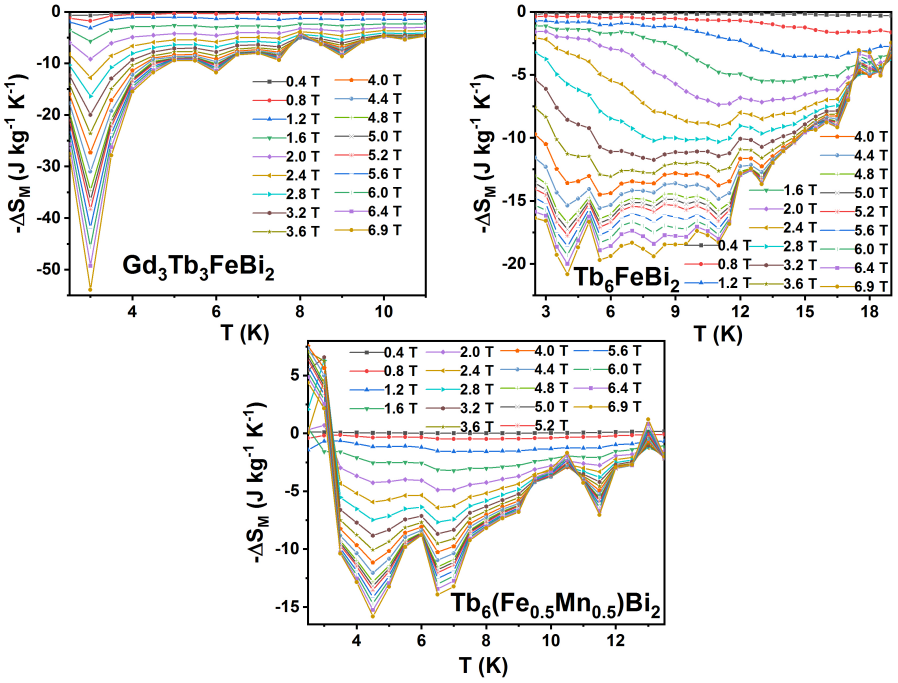


Figure 7.23: Magnetic entropy change $-\Delta S_M$ of the IMCE for $\mu_0\Delta H$ from 1 T to 6.9 T for: $Gd_3Tb_3FeBi_2$, Tb_6FeBi_2, and $Tb_6(Fe_{0.5}Mn_{0.5})Bi_2$.

Another interesting remark has to do with the magnetocaloric effect at very low temperature, which has not been shown in Fig. 7.22. Due to the magnetic behavior shown in this lower range by $Gd_3Tb_3FeBi_2$, Tb_6FeBi_2, and $Tb_6(Fe_{0.5}Mn_{0.5})Bi_2$ (see Fig. 7.16), an inverse magnetocaloric effect (IMCE) is expected. As there are metamagnetic transitions in this range, whose first order is clearly observed due to the stepwise behavior (see Fig. 7.15), the calculation of the magnetic entropy change can only be accomplished using *Maxwell relation* if the measurement of each magnetization isotherm is taken after having erased the magnetic memory of the sample, or a spurious result would be

obtained (check Section 2.2.5 in page 46). Following this procedure, previously to obtain any magnetization isotherm as a function of the applied field, the temperature is raised, without field, above T_C. Then the temperature is taken to the one corresponding to the next isotherm and the field is applied again. The procedure is repeated isotherm after isotherm. With this in mind, the IMCE of the three samples presenting AFM-like behavior at low temperatures was obtained, and the results can be observed in Fig. 7.23. A huge IMCE has been found in $Gd_3Tb_3FeBi_2$, extremely narrow, centered at $T' = 3$ K (see Fig. 7.23), with $\Delta S_M^{pk} = 36.5$ J/kgK at $\mu_0\Delta H = 5$ T and $RC_{\text{FWHM}} = 46$ J/kg, $RC_{\text{Area}} = 34$ J/kg. A relevant IMCE is also found for Tb_6FeBi_2, which becomes a wide plateau as $\mu_0\Delta H$ is increased, centered around $T' = 7$ K. The maximum value ΔS_M^{pk} is smaller than in the previous case (16.5 J/kgK at $\mu_0\Delta H = 5$ T) but the refrigerant capacity is significantly higher ($RC_{\text{FWHM}} = 137$ J/kg, $RC_{\text{Area}} = 118$ J/kg). Finally, for the case of $Tb_6(Fe_{0.5}Mn_{0.5})Bi_2$, the IMCE is less significant, with a broad peak with maximum at $T' = 4.5$ K, $\Delta S_M^{pk} = 13.1$ J/kgK, $RC_{\text{FWHM}} = 70$ J/kg, $RC_{\text{Area}} = 53$ J/kg, all at $\mu_0\Delta H = 5$ T; this compound presents another DMCE at very low temperature due to the magnetic properties already shown in Fig. 7.16. Table 7.9 contains all these results together with the ones at $\mu_0\Delta H = 2$ and 6.9 T, for the sake of comparison.

$\mu_0\Delta H$	Magnitude	$Gd_3Tb_3FeBi_2$ $T' = 3$ K	Tb_6FeBi_2	$Tb_6(Fe_{0.5}Mn_{0.5})Bi_2$
2 T	$\lvert\Delta S_M^{pk}\rvert$ (J kg^{-1} K^{-1})	9.2	7.4 ($T' = 13$ K)	4.9 ($T' = 7$ K)
	RC_{FWHM} (J kg^{-1})	20	44	40
	RC_{Area} (J kg^{-1})	14	35	31
5 T	$\lvert\Delta S_M^{pk}\rvert$ (J kg^{-1} K^{-1})	36.5	16.5 ($T' = 7$ K)	13.1 ($T' = 4.5$ K)
	RC_{FWHM} (J kg^{-1})	46	137	70
	RC_{Area} (J kg^{-1})	34	118	53
6.9 T	$\lvert\Delta S_M^{pk}\rvert$ (J kg^{-1} K^{-1})	53.9	19.4 ($T' = 7$ K)	15.8 ($T' = 4.5$ K)
	RC_{FWHM} (J kg^{-1})	56	144	75
	RC_{Area} (J kg^{-1})	42	119	55

Table 7.9: $\lvert\Delta S_M^{pk}\rvert$, RC_{FWHM} and RC_{Area} at different applied fields $\mu_0\Delta H$ (2, 5 and 6.9 T) for the IMCE in Tb_6FeBi_2 and $Tb_6(Fe_{0.5}Mn_{0.5})Bi_2$.

As was discussed for the case of Tb_3Ni in Section 6.5, materials with an IMCE can be, of course, used as coolers, but also as heat-sinks for heat generated when a conventional magnetocaloric material is magnetized before cooling by adiabatic demagnetization [67, 116]; in this particular application, materials with adjoint IMCE and DMCE, as is the case, can increase the refrigeration efficiency [117, 118].

The magnetocaloric effect also gives the possibility of studying the critical behavior of the PM-FM transition through the well known scaling relations of

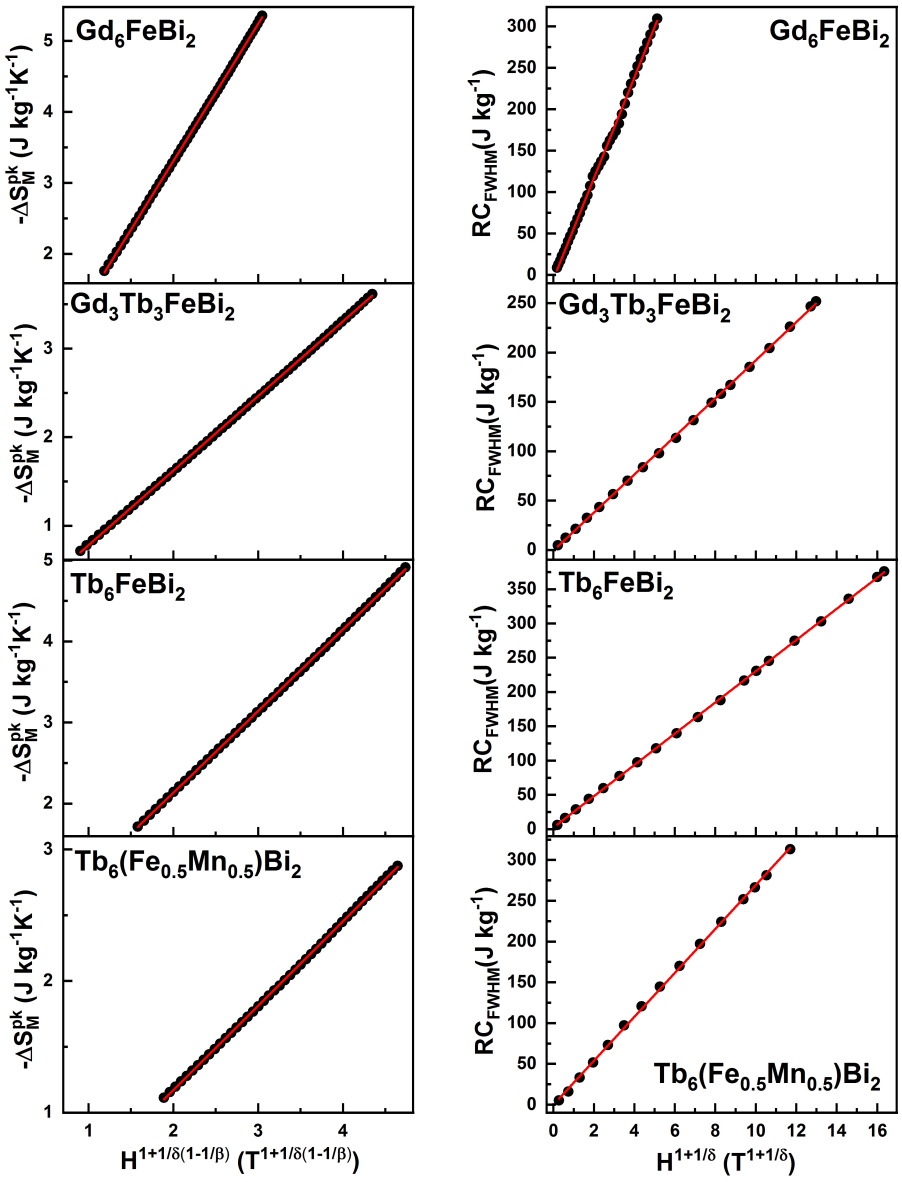


Figure 7.24: Left: Field dependence of $|\Delta S_M^{pk}|$. Right: Scaling law for RC_{FWHM}. The values of β and δ for each compound are the ones presented in Table 7.7.

$|\Delta S_M^{pk}|$ and RC with the field:

$$|\Delta S_M^{pk}| \propto H^{1+\frac{1}{\delta}(1-\frac{1}{\beta})} = H^n \,, \tag{7.16}$$

$$RC \propto H^{1+1/\delta} \,. \tag{7.17}$$

Where, as seen from Eqs. (7.16) and (7.17), the scaling power in both cases is related to the previously obtained magnetic critical exponents (β and δ). Representing the previous expressions with their corresponding critical exponents must yield straight lines for the experimental data, allowing us to check once

again the correctness of the obtained critical exponent values and extrapolating $|\Delta S_M^{pk}|$ and RC values to magnetic fields which could not be experimentally reached. Fig. 7.24 shows the scaling of $|\Delta S_M^{pk}|$ and RC_{FWHM} for all of the compounds. It can be seen that in every case the experimental data follows a straight line, represented in red for visual guide.

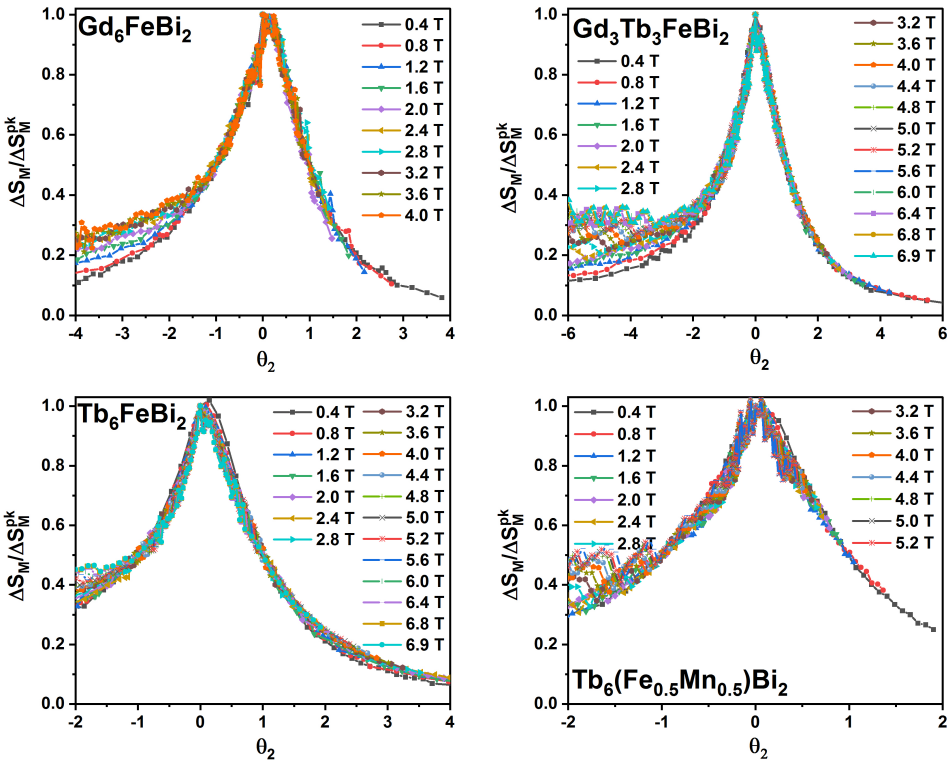


Figure 7.25: Universal curves for the four samples using two reference temperatures.

Besides, since we have already checked that the PM-FM transition is a second order transition in every case, it should be feasible to build up universal curves for each compound around T_C. Building these universal curves requires of normalizing ΔS_M for each field with respect to the corresponding maximum value and rescaling the temperature axis. The rescaling of the temperature can ideally be done by using a single reference temperature. However, we have already seen that whenever there are additional magnetic phases or when demagnetization effects are not negligible (which is our case), using a single reference temperature is not enough and two reference temperatures are needed in order to rescale the temperature axis:

$$\theta_2 = \begin{cases} -(T - T_C)/(T_{r1} - T_C)\,, & T \leqslant T_C \\ (T - T_C)/(T_{r2} - T_C)\,, & T > T_C \end{cases}\,. \tag{7.18}$$

Here T_{r1} and T_{r2} are selected as the temperature corresponding to a particular fraction of $|\Delta S_M^{pk}|$, which in our case has been 0.5, considering that $T_{r1} < T_C < T_{r2}$. The universal curves obtained following this latter method are presented in Fig. 7.25 for all the compounds. We see that the overlapping is very good

in the near vicinity of the second order phase transition, which is the region at which the collapse of the curves must take place, i.e., where critical theory is fulfilled. In the case of $Tb_6(Fe_{0.5}Mn_{0.5})Bi_2$, the overlapping is a little bit worse due to the noise in the measurements, which combined with the rescaling of the temperature axis generates this impression. At temperatures far below T_C, the curves spread out and the values quickly increase, what is specially visible in the three compounds where there is a spin reorientation transition at a low temperature. If in the region in which this methodology is applied there is another magnetic transition, no good overlapping is expected where this second transition is present, as the theory is based on the fact that the PM-FM transition belongs to a particular universality class, which is the case here. Apart from checking the order of the transition, the importance of the universal curves relies on the possibility to extrapolate the whole magnetic entropy change curves to no accessible magnetic fields.

7.5 $Dy_6(Fe, Mn)X_2$ (X = Sb, Te, Bi) family

We already showed in previous sections (7.3 and 7.4) that the combination $(Gd, Tb)_6(Fe, Mn)Bi_2$ allowed to tune a broad MCE around room temperature while $Ho_6(Mn, Fe)Bi_2$ could cover a region between 40 and 250 K. This current section focuses on Dy (which shows magnetic ordering transitions at T_N = 179 K and T_C = 89 K), trying to expand the MCE both to lower and higher temperatures while, at the same time, explores the changes that the last element (X = Sb, Te, Bi) can bring. The purpose is to study the possibility of optimizing the magnetic and magnetocaloric properties. Concerning the applications in the low temperature ranges, the fact that the samples with Tb showed in that region an inverse magnetocaloric effect foretells that Dy might have a similar effect, which could be tuned with different combination of ions to become of practical interest.

Therefore, the crystallographic, magnetic, magnetocaloric and thermal properties of seven members of the family $Dy_6(Fe, Mn)X_2$ (X = Sb, Te, Bi) will be presented in this study: Dy_6FeBi_2, $Dy_6(Fe_{0.5}Mn_{0.5})Bi_2$, Dy_6MnBi_2, Dy_6FeSb_2, $Dy_6FeSbBi$, $Dy_6FeSbTe$, and $Dy_6FeBiTe$. In the case of the second order paramagnetic to ferromagnetic transition that all of them present, a critical behavior study has been performed to extract the critical exponents (β, γ, δ, n) which will give information about the range of the magnetic interactions, the dimensionality of the system and the spins arrangement, as well as predict the magnetocaloric behavior of the system at not measured fields. This time we will also analyse and discuss the thermall diffusivity evolution of these compounds, a seldom studied parameter of great importance in order to evaluate the potential application of materials as magnetic refrigerators: The heat exchange between the magnetocaloric material and the fluid in the refrigerator must be efficient and quick, allowing high working frequencies. Furthermore, we will also introduce a recently proposed figure of merit in order to evaluate the magnetocaloric response of materials presenting a wide MCE, the Temperature Average Entropy Change (TEC).

Due to the great amount of compounds analysed for this family, the most

relevant results will be shown for all of them while in other cases just some of them will be presented as an example.

7.5.1 Structural data, magnetic and thermal characterization of $Dy_6(Fe, Mn)X_2$ family

The X-ray powder analysis showed that the already known Dy_6FeBi_2, Dy_6MnBi_2, Dy_6FeSb_2 ternary compounds [395, 410–412] and the novel $Dy_6(Fe_{0.5}Mn_{0.5})Bi_2$, Dy_6FeSb_2, $Dy_6FeSbBi$, $Dy_6FeSbTe$ and $Dy_6FeBiTe$ quasiternary solid solutions crystallize in the Fe_2P-type structure (space group $P\bar{6}2m$, No. 189, hP9), just as the other members of the general R_6TX_2 presented in this chapter. The refined unit cell data and atomic positions are given in Table 7.10.

Compound	a (nm)	c (nm)	c/a	V (nm^3)
Dy_6FeBi_2	0.82494(6)	0.41899(3)	0.50790	0.24693
$Dy_6(Fe_{0.5}Mn_{0.5})Bi_2$	0.82414(6)	0.42284(3)	0.51307	0.24872
Dy_6MnBi_2	0.82204(7)	0.42929(3)	0.52223	0.25123
Dy_6FeSb_2	0.81383(6)	0.41651(3)	0.51179	0.23890
$Dy_6FeSbBi$	0.81930(6)	0.41775(3)	0.50989	0.24285
$Dy_6FeSbTe$	0.81906(6)	0.40883(3)	0.49915	0.23752
$Dy_6FeBiTe$	0.82433(7)	0.41045(3)	0.49792	0.24154

Table 7.10: Unit cell data of Fe_2P-type $Dy_6(Fe, Mn)X_2$ (X = Sb, Te, Bi) compounds (space group $P\bar{6}2m$, No. 189, hP9).

The prepared compounds contain an admixture of Yb_5Bi_3-, Yb_5Sb_3-, NaCl- and $MgCu_2$-type phases [413] (1-9 wt %). The possible influence of these admixture phases in the magnetic properties of Fe_2P-type compounds will be considered in what follows.

In order to characterize the magnetic properties of our compounds and locate their phase transitions we will study the magnetization as a function of temperature, the *ac* susceptibility, the hysteresis cycles and the general behavior of the magnetization isotherms as a function of the applied field.

Fig. 7.26 shows the magnetization as a function of temperature, both in Zero-Field Cooled (ZFC) and Field-Cooled (FC) mode for the seven composition: at $\mu_0 H = 0.001$ T for Dy_6FeBi_2, Dy_6MnBi_2 and Dy_6FeSb_2 on the left plot and at $\mu_0 H = 0.01$ T for $Dy_6(Fe_{0.5}Mn_{0.5})Bi_2$, $Dy_6FeSbBi$, $Dy_6FeSbTe$, and $Dy_6FeBiTe$ on the right one. In all cases there is a strong difference between the FC and ZFC curves, denoting thermomagnetic irreversibility, typical of many ferromagnetic transitions. In particular, in the previously presented $(Gd, Tb)_6(Fe, Mn)Bi_2$ family, a very similar behavior was observed for $Tb_6(Fe, Mn)Bi_2$ (see Fig. 7.13 in page 192), which is no surprising, as the presence of Tb or Dy in many other families produce some common magnetic features [19]. Another example of their similarities can be observed in R_3CoNi materials presented in Chapter 5. The real part of the *ac* susceptibility represented in

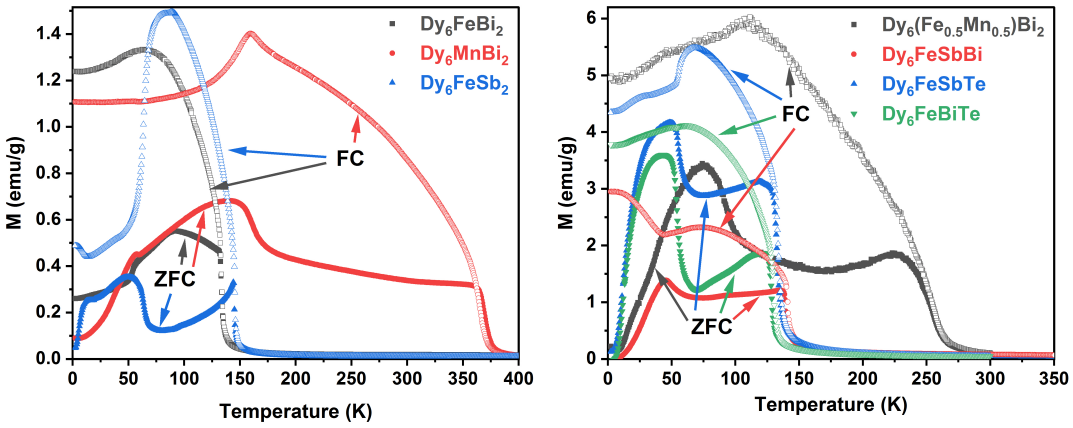


Figure 7.26: Magnetic moment as a function of temperature in Zero-Field Cooled (ZFC) and Field-Cooled (FC) mode with applied field $\mu_0 H = 0.001$ T for Dy_6FeBi_2, Dy_6MnBi_2 and Dy_6FeSb_2 on the left, and with applied field $\mu_0 H = 0.01$ T for $Dy_6(Fe_{0.5}Mn_{0.5})Bi_2$, $Dy_6FeSbBi$, $Dy_6FeSbTe$, and $Dy_6FeBiTe$ on the right.

in Fig. 7.27 for all compositions, gives a very precise location of the different transitions. In all cases there is a paramagnetic to ferromagnetic (PM-FM) transition at a certain temperature T_C which ranges from 128 K in $Dy_6FeBiTe$ to 364 K in Dy_6MnBi_2, and which commonly leads to a collinear magnetic structure of the rare-earth spins in R_6TX_2 [303, 327, 379–381]; besides, in all cases there is another transition at a lower temperature T_m (from about 56 K in Dy_6FeSb_2 to 148 K in Dy_6MnBi_2) which, in the R_6TX_2 family, is due to a reorientation of the rare-earth spins leading to complex non-collinear spin arrangements [303, 327, 379–382]. As mentioned before for $Ho_6(Fe, Mn)Bi_2$ and $(Gd, Tb)_6(Fe, Mn)Bi_2$ families, no magnetic moment has been found for the transition metal in this intermetallic family [327, 380, 382].

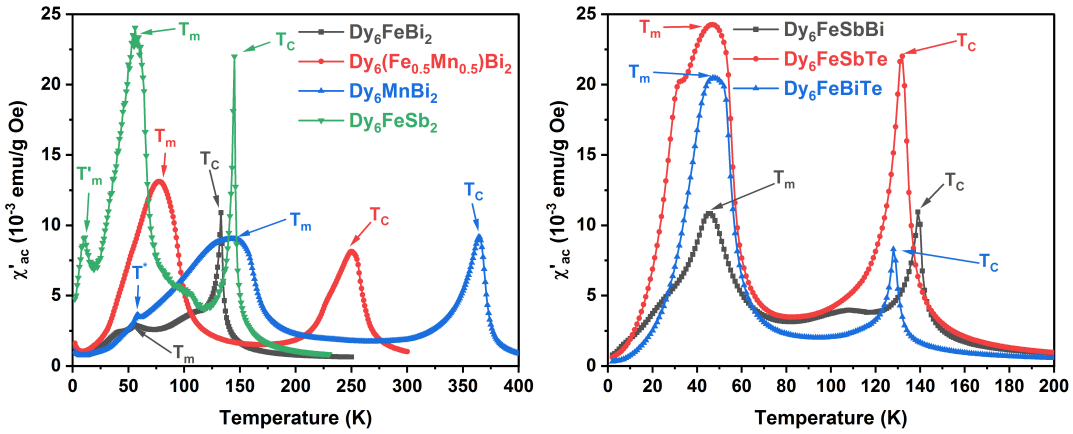


Figure 7.27: Real part of the *ac* susceptibility at $f = 100$ Hz. T_C corresponds to the paramagnetic to ferromagnetic transitions, T_m and T'_m to the spin reorientation ones, T^* to ferromagnetic transitions of the secondary phases.

The T_C of the PM-FM transitions and the demagnetization factors (N_D) ob-

tained from the peaks of χ'_{ac} can be found in Table 7.11. There is a good agreement in the position of T_C for Dy_6FeBi_2 and T_m for Dy_6MnBi_2 with literature, which are the only ones previously measured [327]. Regarding the PM-FM transition and starting from Dy_6FeBi_2, we can see in Fig. 7.27 that the substitution of Fe by 50% Mn ($Dy_6(Fe_{0.5}Mn_{0.5})Bi_2$) takes T_C about 120 K higher, while a complete substitution (Dy_6MnBi_2) increases its value more than 110 additional degrees. This further confirms the possibility of tuning the position of this transition by playing with the Mn composition, as seen before in Ho_6(Fe, Mn)Bi_2 and (Gd, Tb)$_6$(Fe, Mn)Bi_2 families (previously presented in this chapter), and other members of R_6(Fe, Mn)Bi_2 group [303, 327, 414]. On the other hand, the substitution of Bi in Dy_6FeBi_2 by Sb and Te (totally or partially) leads to a small displacement of just several degrees in T_C. Finally, it is worth noting that the effect of these substitutions is much stronger in the magnetic properties in the region of the spin reorientation transition, not only in the displacement of T_m but also in the shape of the curves with even an additional reorientation transition (T'_m) in Dy_6FeSb_2 at 11 K.

Compound	T_C (K)	N_D (gOe/emu)
Dy_6FeBi_2	133	89.31
$Dy_6(Fe_{0.5}Mn_{0.5})Bi_2$	250	119.38
Dy_6MnBi_2	364	107.52
Dy_6FeSb_2	145	45.46
$Dy_6FeSbBi$	139	89.08
$Dy_6FeSbTe$	132	45.05
$Dy_6FeBiTe$	128	116.42

Table 7.11: Experimentally obtained Curie temperature and demagnetization factors for Dy_6(Fe, Mn)X_2 compounds.

The presence of secondary phases affects very little the magnetic properties of the main phases. Dy_5Bi_3 is present in two samples: $Dy_6(Fe_{0.5}Mn_{0.5})Bi_2$ ($\sim$ 9 wt.%) and Dy_6MnBi_2 ($\sim$ 8 wt.%). This secondary phase is known to have a ferromagnetic transition at 50 K [415] but nothing can be appreciated at that temperature in $Dy_6(Fe_{0.5}Mn_{0.5})Bi_2$. In Dy_6MnBi_2, a small peak at $T^* = 58$ K can be spotted in Fig. 7.27; however, it is not evident if it belongs to that secondary phase or to the main one. Dy_5Sb_3, which presents an antiferromagnetic transition at 69 K [416], is present in Dy_6FeSb_2 ($\sim$ 5 wt.%), and, altough it's not visible, it could be superimposed on the right hand side of the peak in χ'_{ac}, which marks the strong reorientation transition which takes place at about 50 K. As we have seen, Dy_6FeSb_2 sample also presents a spin reorientation transition, at $T'_m \approx 11$ K, which can not be attributed to a secondary phase. Finally, the secondary phases in $Dy_6FeSbBi$ ($Dy_5Fe_{0.3}Sb_{1.5}Bi_{1.2}$ at $\sim$ 8 wt.%), $Dy_6FeSbTe$ ($DySb_{0.5}Te_{0.5}$ at $\sim$ 5 wt.%) and $Dy_6FeBiTe$ (Dy_2Te at $\sim$ 3 wt.% and $DyBi_{0.5}Te_{0.5}$ at $\sim$ 2 wt.%) have not been magnetically characterized yet so they could be responsible for some features such as the elbow in $Dy_6FeSbBi$ (see Fig. 7.27) on the lower temperature side of T_m but the general aspects of the

curves tell that they do not have much relevance, if any.

The order of the magnetic transitions can be evaluated by means of the Banerjee criterion [229] which states that, in the representation of M^2 versus H/M the slopes of the curves must be positive if the transition is continuous while there should be regions with negative slopes if it were a first order one. Fig. 7.28 shows, for the case of the spin reorientation transition (T_m) in $Dy_6FeSbTe$ and the PM-FM transition (T_C) in $Dy_6FeBiTe$, how all slopes are positive, confirming that they are second order transitions. This happens in the seven compounds for these transitions. This behavior will be further confirmed by the thermal diffusivity measurements.

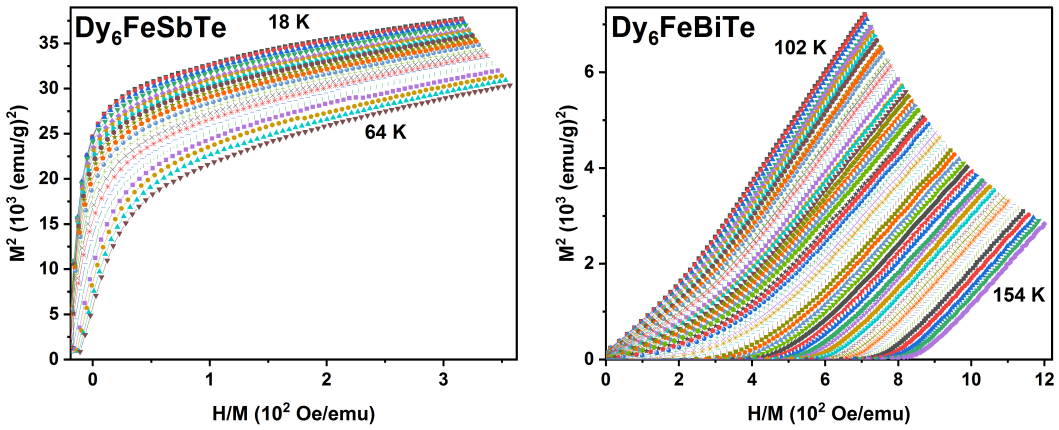


Figure 7.28: M^2 as a function of H/M around the spin reorientation transition (T_m) in $Dy_6FeSbTe$ and around the PM-FM transition (T_C) in $Dy_6FeSbTe$.

The thermomagnetic irreversibility visible in Fig. 7.26 is easily understandable when the isothermal magnetization loops at 2 K are analysed (see Fig. 7.29). In all cases there is not only a coercive field (H_C) but also step-like behaviors characteristic of metamagnetic transitions, from ground states with antiferromagnetic components responsible for non-collinear magnetic structures observed in this family, to ferromagnetic states.

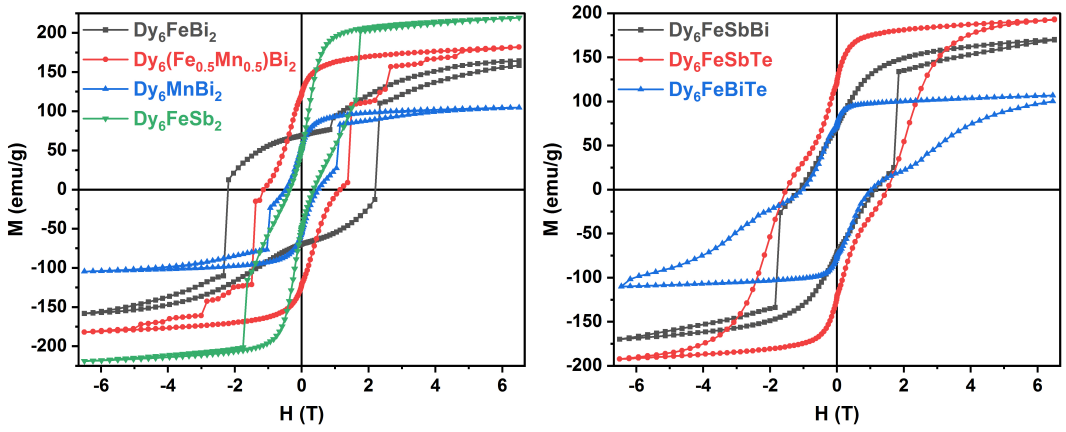


Figure 7.29: Hysteresis loops at 2 K for $Dy_6(Fe, Mn)X_2$ compounds.

Following the magnetic analysis, if the magnetization isotherms are observed, all compositions share the following properties (which are shown for some of them in Fig. 7.30): from 2 K to a certain temperature value (50 K for Dy_6FeBi_2, 36 K for $Dy_6(Fe_{0.5}Mn_{0.5})Bi_2$, 28 K for Dy_6MnBi_2, 20 K for Dy_6FeSb_2, 30 K for $Dy_6FeSbBi$, 26 K for $Dy_6FeSbTe$, and 30 K for $Dy_6FeBiTe$) the magnetization increases from one isotherm to the next one (in ascending order) for the same value of the magnetic field, assessing the existence of antiferromagnetic interactions in those temperature ranges. We will later see that this behavior will be responsible for huge IMCE at low temperatures. For higher temperatures, the ferromagnetic behavior is imposed, which means that, for a given applied field, the magnetization decreases as temperature is increased. Of course, in the low temperature ranges the metamagnetic transitions are clearly observed for all samples. In some cases it quickly disappears with the applied field at very low temperatures, reaching a ferromagnetic state.

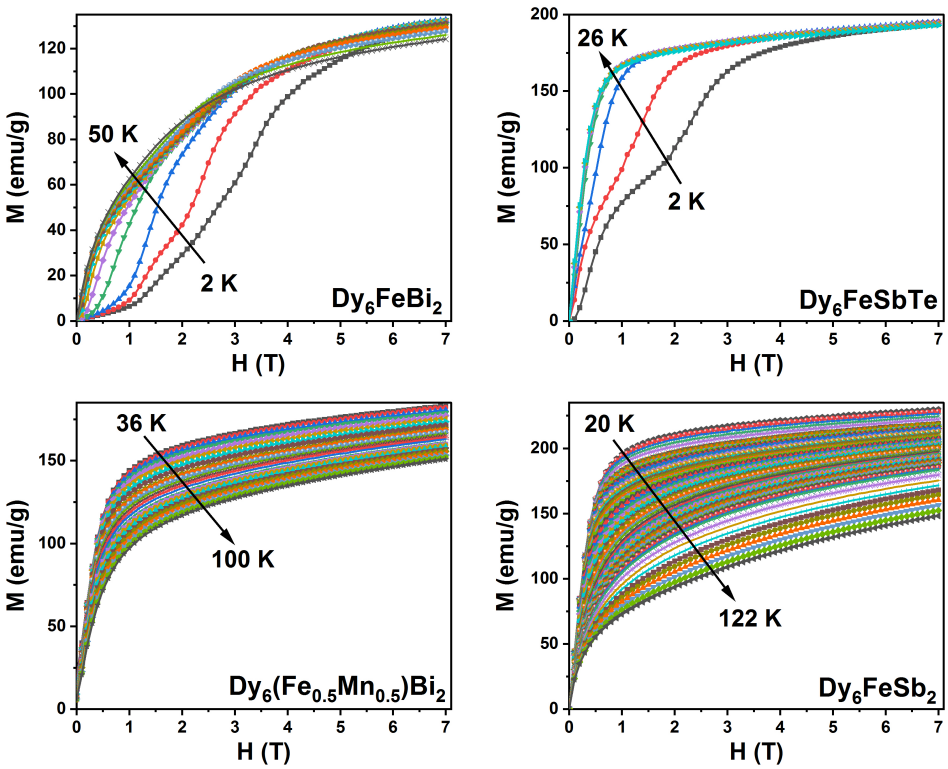


Figure 7.30: Magnetization isotherms at low temperature for Dy_6FeBi_2 and $Dy_6FeSbTe$; and at medium temperature for $Dy_6(Fe_{0.5}Mn_{0.5})Bi_2$ and Dy_6FeSb_2.

When considering the possible application of a material as a magnetic refrigerator it is crucial to characterize its thermal properties, specially thermal diffusivity, which is the parameter controlling heat exchange in non-stationary situations. Higher thermal diffusivity values allow higher working frequencies. Fig. 7.31 shows the evolution of the thermal diffusivity for all samples in the regions of interest corresponding to the DMCE. As intermetallic materials, the values are in the range 1-3 mm^2/s, which are comparable to the values exhibited by good magnetocaloric materials such as $Gd_5Si_2Ge_2$, $La(Fe_{0.88}Si_{0.12})_{13}$ and one order of magnitude higher than the case of MnAs [180].

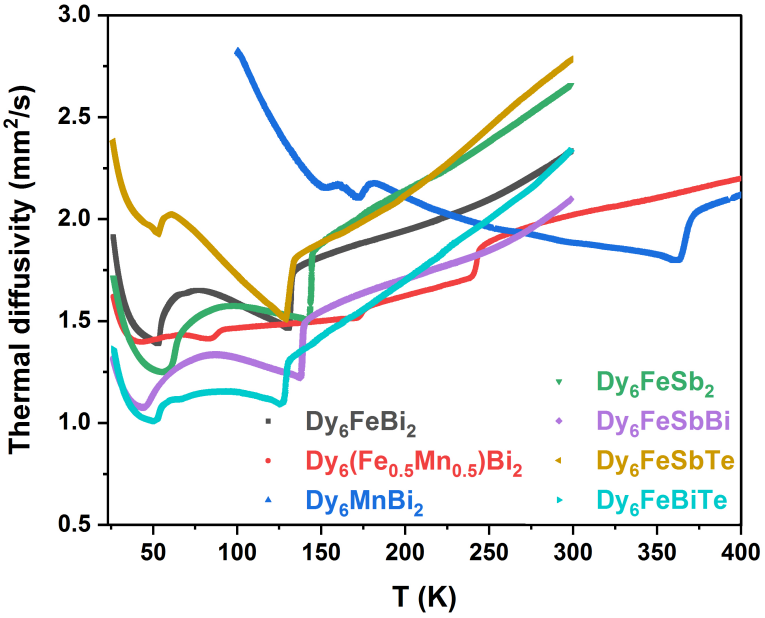


Figure 7.31: Temperature evolution of D for the seven compounds.

As we have seen several times along this manuscript, the shape of the thermal diffusivity curves in intermetallic materials share several common features, which have to do with the fact that heat is transferred both by electrons and phonons, the contribution of the latter becoming more relevant at low temperatures [282–284]. Starting from high temperature, in the paramagnetic phase, while there is no magnetic transitions as temperature is decreased, the common behavior is to have a monotonic decrease in D (see in Fig. 7.31 the cases of the five compounds without Mn) due to the reduction of the electronic contribution, after the Wiedemann-Franz law [367]. Then the PM-FM transition takes place which is signalled as a dip (this is quite common both in metallic and insulator materials [19], as well as in the other intermetallic compounds discussed in this manuscript). After this ordering, the phonon mean free path starts to increase and, depending on the leverage of the electronic and phononic contribution, different temperature dependencies arise between the PM-FM and the spin reorientation transition, which is in the region of the second dip. From then on, the phonon contribution dominates and as the phonon mean free path becomes larger and larger with the temperature decrease, a quick increase in D takes place.

In Dy_6MnBi_2, as the PM-FM transition takes place at a much higher temperature than the rest, the increase in the phononic contribution starts to compensate earlier the decrease in the electronic part. Finally, $Dy_6(Fe_{0.5}Mn_{0.5})Bi_2$, presents an intermediate behavior between Dy_6FeBi_2 and Dy_6MnBi_2.

In the PM-FM transition, in all cases, detailed measurements in heating and cooling runs at very low temperature rates have shown that there is no thermal hysteresis and that the transitions are, indeed, second order, confirming the validity of a critical behavior study in this transition.

7.5.2 Critical behavior in $Dy_6(Fe, Mn)X_2$ family

At this point of the manuscript it shouldn't be new to the reader, but it is worth stressing out that the study of the critical behavior of second order magnetic phase transitions provides information about the range of the magnetic interactions, the dimensionality of the system as well as the spins arrangement. As observed by the Banerjee criterion and the thermal diffusivity measurements just presented, all the PM-FM transitions on these samples (identically to what has already been observed in the other members of the R_6TX_2 family) are second order. This allows us, once again, to apply our knowledge on critical behavior in order to analyse those PM-FM transitions.

The usual fitting procedure of the magnetic critical behavior was attempted (check Section 3.4.1), where a first trial of different universality classes is done in order to build a good Arrot Plot (in the case of Mean Field critical exponents) or Modified Arrot Plot (when critical exponents not belonging to the MF model are used) with straight parallel lines at high fields. In this process the best starting model is selected in order to start the usual iterative procedure. But in this family, only for two of them (Dy_6MnBi_2 and $Dy_6FeSbTe$) the Mean Field was a good starting point while for the rest neither of the three most common classes (Mean Field, 3D Heisenberg, 3D Ising) was close to that situation. So different sets of β and γ values had to be taking as starting points to finally find good critical exponents which could give straight parallel lines in the Modified Arrot Plots. The final result for the MAPs is shown for each sample on the left hand side of Figs. 7.32 and 7.33, while all the critical exponents are collected in Table 7.12 in page 219.

The critical exponent δ is directly obtained from the isotherm at T_C:

$$M \sim H^{1/\delta} \qquad (T = T_C)\,, \tag{7.19}$$

which, if represented in a log-log scale should yield a straight line whose slope equals $1/\delta$. Critical isotherms for all samples are represented in the central column of Figs. 7.32 and 7.33. The value of δ thus obtained are compared to the one calculated from Widom's scaling law:

$$\delta = 1 + \gamma/\beta\,. \tag{7.20}$$

with the previously obtained β and γ values. Both values are gathered in Table 7.12 (page 219) for comparison, where a very good agreement is observed.

The final and most robust validation of the critical exponents is the fulfilment of the magnetic equation of state:

$$M(H,t) = |t|^{\beta} f_{\pm}(H/|t|^{\beta+\gamma})\,, \tag{7.21}$$

according to which, all isotherms must collapse onto two independent branches, one for $T < T_C$, a second one for $T > T_C$. This is perfectly observed for all the samples in the right column of Figs. 7.32 and 7.33.

The obtained values of β and γ give a set of straight, parallel curves in the MAPs. The value of γ obtained from the critical isotherm and the one calculated from Eq. (7.20) are very close and in the representation of the magnetic equation of state all curves collapse onto two independent branches; all

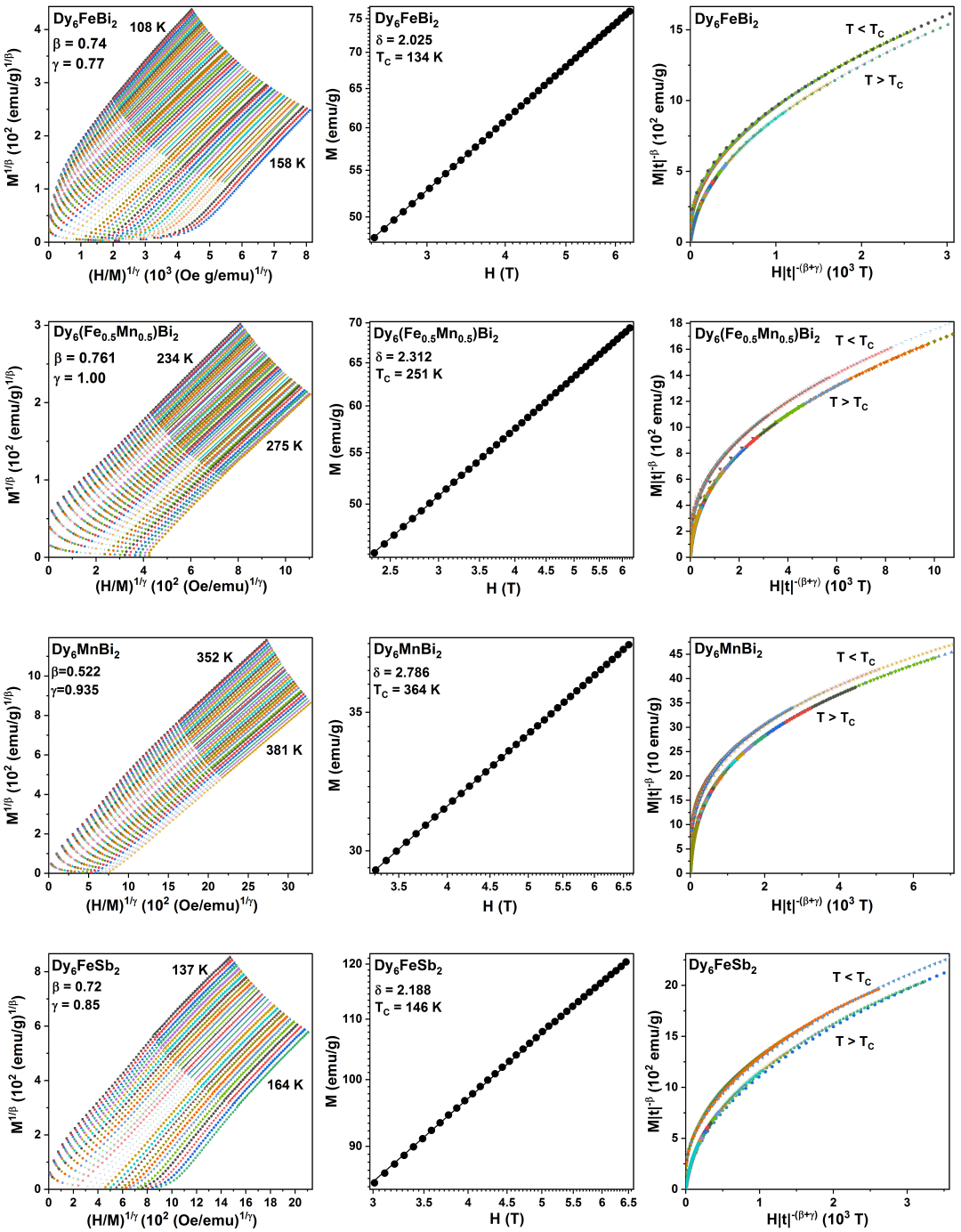


Figure 7.32: From left to right: Optimized Modified Arrot Plot, critical isotherm and renormalized magnetization plotted as a function of the renormalized field, after Eq. (7.21), for Dy_6FeBi_2, $Dy_6(Fe_{0.5}Mn_{0.5})Bi_2$, Dy_6MnBi_2 and Dy_6FeSb_2.

of these facts support the validity of the critical exponents found. As commented, in nearly all cases the fittings are very good, with the exception of $Dy_6FeBiTe$, for which the values obtained are not so good, as the region in the MAP where the curves are straight and parallel is a short one (see last row in Fig. 7.33).

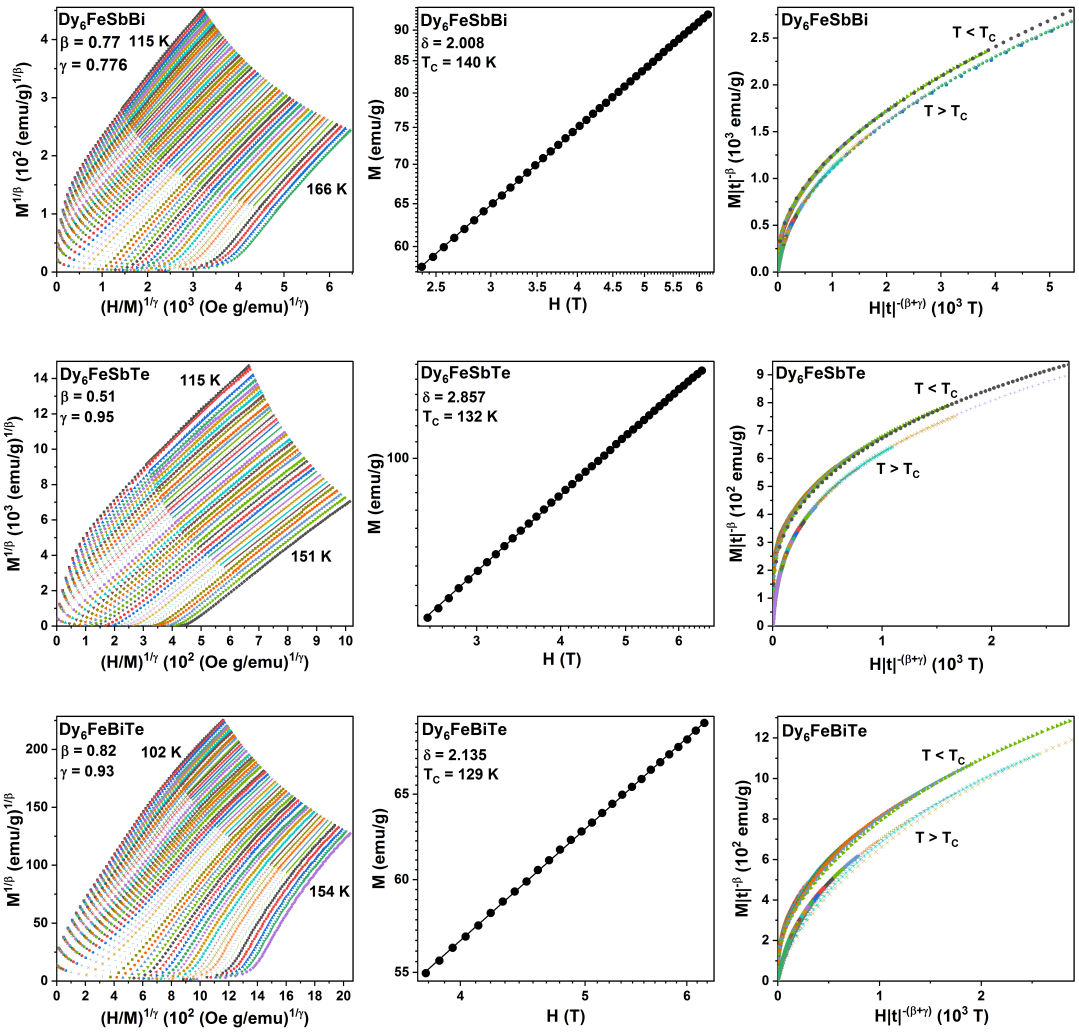


Figure 7.33: From left to right: Optimized Modified Arrot Plot, critical isotherm and renormalized magnetization plotted as a function of the renormalized field, after Eq. (7.21), for $Dy_6FeSbBi$, $Dy_6FeSbTe$, and $Dy_6FeBiTe$.

Turning our attention to the particular values of the critical exponents (Table 7.12) and the theoretical values for a number of universality classes (Table 3.2 in page 77) we can see that for Dy_6MnBi_2 ($\beta_{exp} = 0.522 \pm 0.005$, $\gamma_{exp} = 0.93 \pm 0.02$) and $Dy_6FeSbTe$ ($\beta_{exp} = 0.51 \pm 0.01$, $\gamma_{exp} = 0.95 \pm 0.02$) the results are very close to the Mean Field Model ($\beta_{MF} = 0.5$, $\gamma_{MF} = 1.0$), indicating that long-range order magnetic interactions are responsible for the transition, but in the rest the values are too high for β (from 0.72 in Dy_6FeSb_2 to 0.82 for $Dy_6FeBiTe$) to comply with any theorized universality class. On the other hand, in three cases, γ takes values far away from the Mean Field class (0.85 in Dy_6FeSb_2, 0.776 in $Dy_6FeSbBi$, and 0.774 in Dy_6FeBi_2). We have already observed this situation in other members of the R_6TX_2 family: Tb_6FeBi_2 ($\beta_{exp} = 0.73$, $\gamma_{exp} = 0.80$) and $Tb_6(Fe_{0.5}Mn_{0.5})Bi_2$ ($\beta_{exp} = 0.72$, $\gamma_{exp} = 0.95$), check Table 7.7 in page 199. Since the range of the exchange interaction $J(r)$ is mainly determined by the critical parameter γ (as shown in Section 5.3.3 for R_3CoNi family) and the theoretical values for short-range or-

der interactions in three dimensions ($d = 3$) are always above 1 (see Table 3.2 in page 77), while the values in this case are below that figure, this would suggest that in R_6TX_2 samples with R = Dy the magnetic interactions are long-range, as it happens with those with R = Tb presented previously. The values of β above 0.5 imply, for certain, a deviation from the Mean Field model, maybe associated with magnetocrystalline anisotropies due to crystal field effects and a non-zero orbital moment ($L = 5$) of the Dy ion [1]. Even if we explore the possibility of these materials behaving as layered ones ($d = 2$ in Table 7.7) we see that the critical exponents obtained agree much better with three dimensional models, as the theorized β is much smaller than 0.5 for $d = 2$ and γ much bigger than 1.

As we already discussed, there is a growing amount of materials which do not show a conventional critical behavior (κ-(BEDT-TTF)$_2$X [408], $BaIrO_3$ [407], Mn_3CuN [319], TDAE-C_{60} [409], $Sr_{1-x}A_xRuO_3$ [403,404], $La_{0.4}Ca_{0.6}MnO_3$ [406], $La_{0.5}Ca_{0.4}Ag_{0.1}MnO_3$ [405]) which points to the fact that there might be other universality classes still to be developed which could properly describe the magnetism in these materials, an issue which should be addressed by theoretical research groups.

Material	Technique	β	γ	δ
Dy_6FeBi_2	Modified Arrot Plot	0.74 ± 0.03	0.774 ± 0.004	2.04 ± 0.04^a
	Critical Isotherm			2.025 ± 0.002
$Dy_6(Fe_{0.5}Mn_{0.5})Bi_2$	Modified Arrot Plot	0.761 ± 0.008	1.00 ± 0.02	2.31 ± 0.04^a
	Critical Isotherm			2.312 ± 0.001
Dy_6MnBi_2	Modified Arrot Plot	0.522 ± 0.005	0.93 ± 0.02	2.79 ± 0.05^a
	Critical Isotherm			2.786 ± 0.001
Dy_6FeSb_2	Modified Arrot Plot	0.72 ± 0.02	0.85 ± 0.01	2.17 ± 0.04^a
	Critical Isotherm			2.188 ± 0.007
$Dy_6FeSbBi$	Modified Arrot Plot	0.77 ± 0.02	0.776 ± 0.004	2.00 ± 0.03^a
	Critical Isotherm			2.008 ± 0.003
$Dy_6FeSbTe$	Modified Arrot Plot	0.51 ± 0.01	0.95 ± 0.02	2.87 ± 0.07^a
	Critical Isotherm			2.857 ± 0.007
$Dy_6FeBiTe$	Modified Arrot Plot	0.82 ± 0.06	0.93 ± 0.04	2.1 ± 0.1^a
	Critical Isotherm			2.135 ± 0.006

[a] Calculated from Widom scaling equation: $\delta = 1 + \gamma/\beta$.

Table 7.12: Critical exponents obtained for Dy_6FeBi_2, $Dy_6(Fe_{0.5}Mn_{0.5})Bi_2$, Dy_6MnBi_2, Dy_6FeSb_2, $Dy_6FeSbBi$, $Dy_6FeSbTe$, and $Dy_6FeBiTe$.

7.5.3 Magnetocaloric effect in $Dy_6(Fe, Mn)X_2$ family

The magnetic entropy change ΔS_M and the refrigerant capacity RC have been evaluated for the seven compositions in the temperature ranges of interest, with the limit that it has not been possible to perform measurements

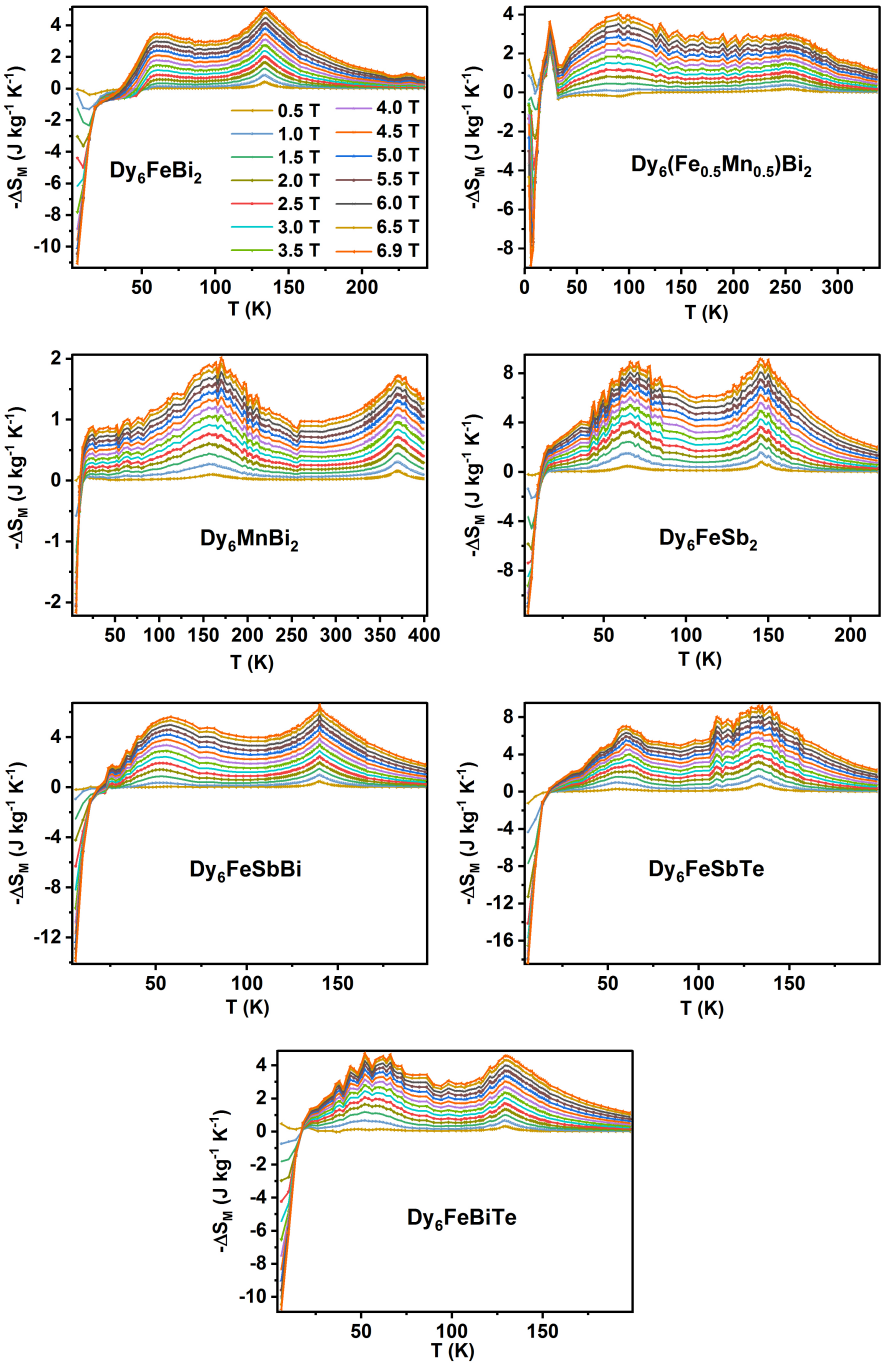


Figure 7.34: Magnetic entropy change $-\Delta S_M$ for $\mu_0 \Delta H$ from 1 T to 6.9 T for all compositions. The color code is the same for all of them.

over 400 K (due to the technical limitations of the measurement system). Since both, magnetic and thermal measurements asses that the PM-FM transitions in these samples are second order transitions, the well know *Maxwell equation* can be used to obtain the magnetic entropy change:

$$\Delta S_M(T, \Delta H) = \mu_0 \int_{H_0}^{H_1} \left(\frac{\partial M}{\partial T} \right)_H dH \,. \tag{7.22}$$

The results are shown in Fig. 7.34 for the seven compounds and the maxima at each transition are collected in Table 7.13. The magnetocaloric properties of this family are extremely rich as, in all cases, there are two direct magnetocaloric effects (DMCE) whose superposition in-between allows the maintenance of a table-like MCE effect over a wide temperature range, which is required for an ideal Ericsson refrigeration cycle; besides, there is a strong inverse magnetocaloric effect (IMCE) at very low temperatures. The highest temperature DMCE is associated with the PM-FM transition while the second DMCE is due to the spin reorientation transition. The highest values of $|\Delta S_M^{pk}|$ are, for $\mu_0\Delta H \sim 7$ T, 9 J/kgK for the two DMCE effects in Dy_6FeSb_2 and one of the DMCE for $Dy_6FeSbTe$, with the tableau in-between being 6-7 J/kgK for those compositions. It is clear from Fig. 7.34 that the role of Fe-Mn is to move the operational region for a refrigeration device in a very broad temperature range (from 40 K to more than 400 K) while the role of the X element is to improve $|\Delta S_M^{pk}|$ value. In this sense, Sb and Te give better results than Bi, specially the first one.

As already mentioned, it is commonly accepted that, in the family R_6TX_2, the rare-earth atoms are solely responsible for the magnetic properties as no hint of magnetic moment from T has been found in the cases where neutron diffraction studies have been undertaken [303–305, 327, 380, 382, 394]; rare-earth ions interact through an indirect *4f-4f* interaction via the Ruderman-Kittel-Kasuya-Yosida (RKKY) interaction mediated by the *d*-band, which is sensitive to the position of the ions in the cell and the possible orbital hybridizations among the ions in the compound. In order to formulate an interpretation on why the different ion substitutions produce such changes in the magnetic and magnetocaloric properites, *ab initio* calculations should be performed to compare theoretical predictions with the experiments, which is something our group is now working on.

It is worth mentioning that, as seen in the previous section, the presence of small secondary phases in some compounds do not have a relevant influence on the magnetic entropy change as the features appearing in Fig. 7.34 are directly linked to the magnetic transitions of the main phases.

Coming back to the experimental results, Table 7.13 collects not only the maxima of the magnetic entropy change for all MCE but also the *RC* in its two usual definitions: RC_{FWHM}, RC_{Area}. Due to the presence of both phase transitions, these *RC* values are quite high (for $\mu_0\Delta H = 5$ T at T_C, 897 J/kg for Dy_6FeSb_2, 613 J/kg for $Dy_6FeSbBi$ or 569 J/kg for $Dy_6(Fe_{0.5}Mn_{0.5})Bi_2$, for instance). The values on that table are given for $\mu_0\Delta H = 2$, 5 and 6.9 T, the first and second ones for the sake of comparison with literature, the third one being the highest field applied in this study. As pointed out in the table, in the case of Dy_6MnBi_2, *RC* values for 5 and 6.9 T are obtained from extrapolated data, as our experimental system can not reach temperatures higher than 400 K. Regarding the DMCE, the combination of good value of $|\Delta S_M^{pk}|$, high *RC* and a broad working temperature range makes this family extremely interesting for future technological applications, when compared with literature data [82, 91, 108]. Moreover, there is a good-sized IMCE at very low temperature which could be interesting on its own for refrigeration at temper-

$\mu_0\Delta H$	Magnitude	Dy_6FeBi_2 T_C = 134 K	$Dy_6(Fe_{0.5}Mn_{0.5})Bi_2$ T_C = 250 K	Dy_6MnBi_2 T_C = 370 K	Dy_6FeSb_2 T_C = 145 K	$Dy_6FeSbBi$ T_C = 140 K	$Dy_6FeSbTe$ T_C = 133 K	$Dy_6FeBiTe$ T_C = 129 K
2 T	$\lvert\Delta S_M^{pk}\rvert$ (J kg^{-1} K^{-1})	1.7	0.8	0.6	3.0	2.0	3.2	1.4
	RC_{FWHM} (J kg^{-1})	48	196	34[a]	97	56	117	36
	RC_{Area} (J kg^{-1})	35	147	-	68	40	87	27
5 T	$\lvert\Delta S_M^{pk}\rvert$ (J kg^{-1} K^{-1})	3.8	2.2	1.3	6.9	4.8	7.0	3.4
	RC_{FWHM} (J kg^{-1})	401	569	166[a]	897	613	501	420
	RC_{Area} (J kg^{-1})	259	537	-	676	422	370	324
6.9 T	$\lvert\Delta S_M^{pk}\rvert$ (J kg^{-1} K^{-1})	5.1	3.0	1.7	9.2	6.6	9.2	4.6
	RC_{FWHM} (J kg^{-1})	589	841	675[a]	1248	880	1132	596
	RC_{Area} (J kg^{-1})	404	807	-	952	626	788	457

$\mu_0\Delta H$	Magnitude	Dy_6FeBi_2 T_m = 60 K	$Dy_6(Fe_{0.5}Mn_{0.5})Bi_2$ T_m = 90 K	Dy_6MnBi_2 T_m = 170 K	Dy_6FeSb_2 T_m = 66 K	$Dy_6FeSbBi$ $T_m \approx$ 56 K	$Dy_6FeSbTe$ T_m = 60 K	$Dy_6FeBiTe$ T_m = 52 K
2 T	$\lvert\Delta S_M^{pk}\rvert$ (J kg^{-1} K^{-1})	0.6	0.8	0.6	3.3	1.4	2.2	1.7
	RC_{FWHM} (J kg^{-1})	68	190	62	130	63	97	68
	RC_{Area} (J kg^{-1})	81	148	47	99	47	74	53
5 T	$\lvert\Delta S_M^{pk}\rvert$ (J kg^{-1} K^{-1})	2.4	2.9	1.5	7.1	4.2	5.5	3.8
	RC_{FWHM} (J kg^{-1})	311	705	214	919	561	719	445
	RC_{Area} (J kg^{-1})	295	512	157	670	436	606	312
6.9 T	$\lvert\Delta S_M^{pk}\rvert$ (J kg^{-1} K^{-1})	3.47	4.1	2.0	8.9	5.7	7.0	4.7
	RC_{FWHM} (J kg^{-1})	482	1015	333	1230	814	985	605
	RC_{Area} (J kg^{-1})	452	719	238	959	659	867	451

[a] Extrapolations have been needed to obtain these values.

Table 7.13: Maximum of the magnetic entropy change $|\Delta S_M^{pk}|$ and refrigerant capacities RC_{FWHM}, RC_{Area} at different applied fields $\mu_0\Delta H$ (2, 5 and 6.9 T) for the four compounds at their corresponding Curie temperature T_C (upper Table), and at their corresponding spin reorientation temperature T_m (lower Table).

atures below 15-10 K or, as we have already discussed, to be used as heat-sinks for heat generated when a conventional magnetocaloric material is magnetized by adiabatic demagnetization before cooling. Furthermore, the refrigeration efficiency can be improved by using materials with adjoint IMCE and DMCE [117, 118].

There is a growing current in literature which disputes the suitability of RC_{FWHM} and RC_{Area} to ascertain the magnetocaloric quality of the materials when the peak is too wide or the temperature span gets enlarged by the presence of several transitions, which is our case, and, instead, proposes the use of the Temperature Average Entropy Change $TEC(10)$, which is defined as [170]:

$$TEC(10) = \frac{1}{10}\int_{T-5}^{T+5} \Delta S_M(T')dT', \tag{7.23}$$

in order to avoid the artificially large refrigerant capacity of shallow peaks [417]. Fig. 7.35 collects the result of the DMCE in the shape of circles, whose centers are placed at the value of the maxima of the magnetic entropy change and their diameters are proportional to the value of $TEC(10)$. These values are compared to the values corresponding to other rare-earth high entropy alloys, RE-HEA (grey circles), elaborated after [417, 418].

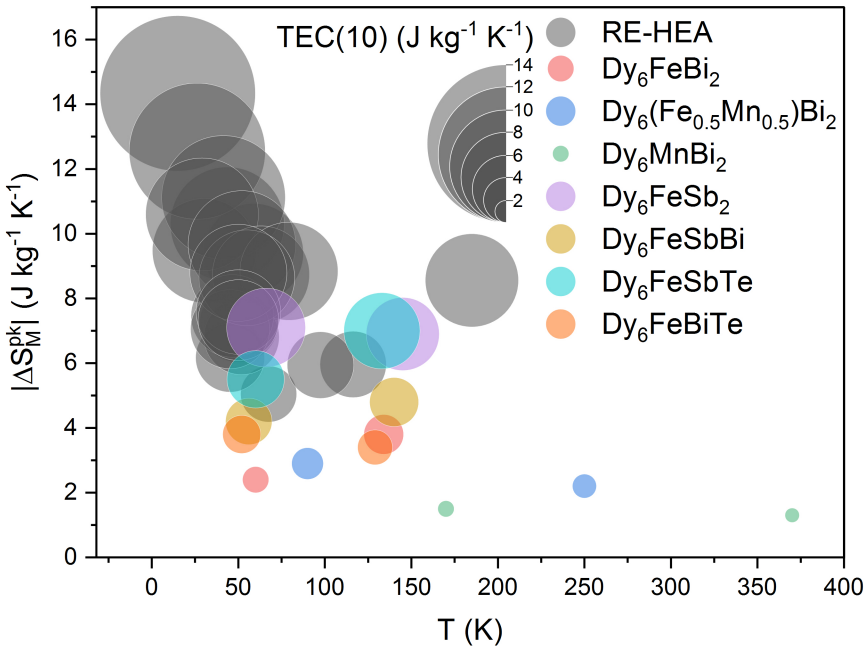


Figure 7.35: DMCE performance at $\mu_0\Delta H = 5$ T for the $Dy_6(Fe, Mn)X_2$ family and for selected rare-earth high entropy alloys (RE-HEA) found in literature [417, 418].

It is clear from Fig. 7.35 that two of the compounds containing Sb (Dy_6FeSb_2 and $Dy_6FeSbTe$) are the ones with competitive properties with respect to other rare-earth compounds. It is worth stressing that there is neither magnetic nor thermal hysteresis in the transitions, which is relevant for practical applications. Besides, the broad temperature range of application is an interesting issue, especially when considering an Ericsson cycle of refrigeration.

To further reinforce the values of the magnetic critical exponents previously obtained, the scaling relations of $|\Delta S_M^{pk}|$ and RC have also been checked for all the compounds:

$$|\Delta S_M^{pk}| \propto H^{1+\frac{1}{\delta}(1-\frac{1}{\beta})} = H^n \,, \tag{7.24}$$

$$RC \propto H^{1+1/\delta} \,. \tag{7.25}$$

The results, calculated using the values of β and δ contained in Table 7.12, are shown in Fig. 7.36 for Eq. (7.24) and in Fig. 7.37 for Eq. (7.25). In the former case, Dy_6MnBi_2 and $Dy_6FeSbBi$ have been selected as an example (it is similar with all the rest), while for the latter case (Fig. 7.37) the fulfilment of the scaling for RC_{FWHM} is presented for Dy_6FeBi_2 and $Dy_6FeSbTe$ at low fields (where the peak is well defined, as this calculation only makes sense in the critical region); it is similar in Dy_6FeBi_2, $Dy_6FeSbBi$, and $Dy_6FeBiTe$ while RC can not be calculated in Dy_6MnBi_2 (because we do not have the full curve at high temperature) and in $Dy_6(Fe_{0.5}Mn_{0.5})Bi_2$ (the shape of the curve in the low

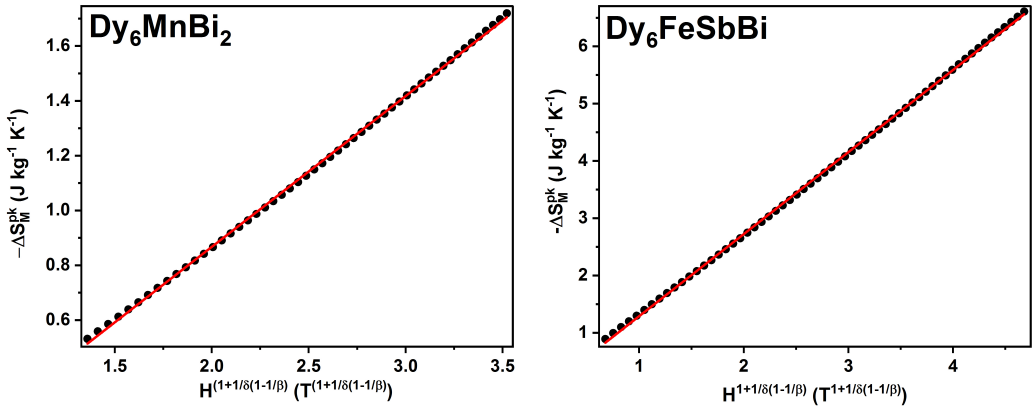


Figure 7.36: Field dependences of $-\Delta S_M^{pk}$ for Dy_6MnBi_2 (left) $Dy_6FeSbBi$ (right). The values of β and δ for each case are the ones presented in Table 7.12.

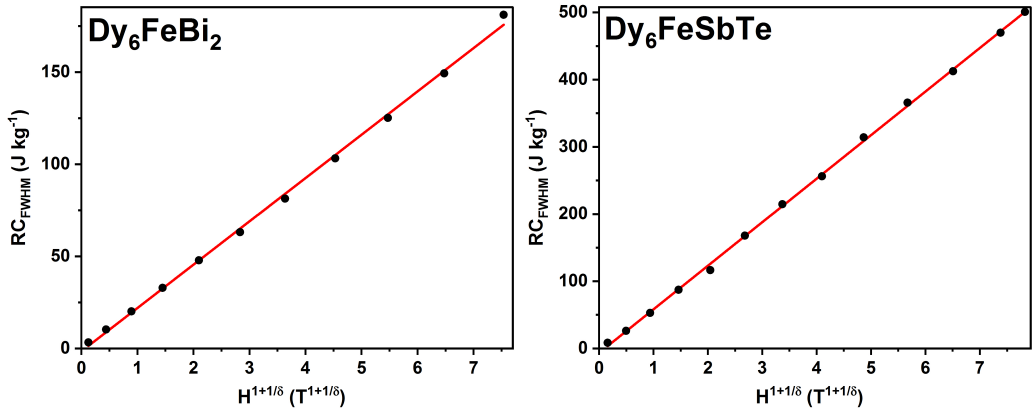


Figure 7.37: Scaling law for RC_{FWHM}; Dy_6FeBi_2 (left) and $Dy_6FeSbTe$ (right). The values of δ for each compound are the ones presented in Table 7.12.

temperature side, just below T_C, makes it impossible to separate the part which corresponds to the critical region). In both figures, the experimental points fall along a straight line, confirming the validity of the critical exponents.

Finally, let's build the so called magnetocaloric "master curves" or "universal curves" for each composition around T_C. As we have seen from previous compounds, in second order phase transitions a normalization of the magnetic entropy change for each field with respect to the corresponding maximum value, together with rescaling the temperature axis, should lead to a collapse of all points onto one single curve, in the critical region. The temperature axis rescaling can be done with one or two reference temperatures T_{r1}, T_{r2}, two being necessary when demagnetization effects are not negligible [235], as it happens in this case. Therefore, the temperature axis is rescaled according to the following expression:

$$\theta_2 = \begin{cases} -(T - T_C)/(T_{r1} - T_C)\,, & T \leqslant T_C \\ (T - T_C)/(T_{r2} - T_C)\,, & T > T_C \end{cases}\,. \tag{7.26}$$

Fig. 7.38 shows, as an example, the universal curves thus obtained for Dy_6FeBi_2 and $Dy_6FeSbBi$, where the superposition is very good, as theory ascertains for the near vicinity of the second order phase transition, where critical theory is fulfilled. On the left hand side, at temperatures well below T_C, and due to the presence of the spin-reorientation transition, the theory does not hold and, therefore, the superposition is not good. The curves are similar in all the rest, except for $Dy_6(Fe_{0.5}Mn_{0.5})Bi_2$ where, as commented before, the shape of the curve in the low temperature side makes it impossible to separate the part corresponding to the critical region.

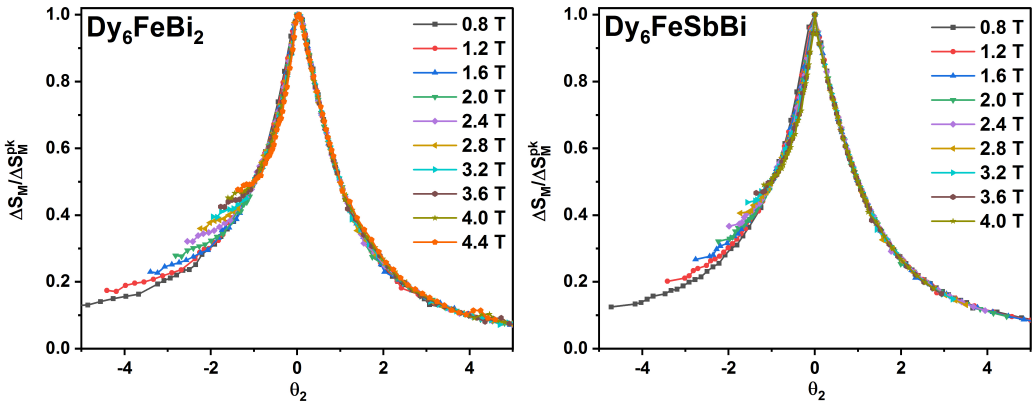


Figure 7.38: Universal curve with the rescaled magnetic entropy changes using two reference temperatures, for Dy_6FeBi_2 and $Dy_6FeSbBi$.

The fact that these master curves have been built is another strong support of the second order character of the PM-FM transition.

7.6 Conclusions

Along this chapter three *"sub-families"* of the larger R_6TX_2 family have been thoroughly studied, characterizing their crystallographic, magnetic, magnetocaloric and thermal properties.

All of the samples present a PM-FM second order phase transition at the Curie temperature, and all of them (with the exception of Gd_6FeBi_2) also show a spin reorientation transition at much lower temperature (T_m). The critical behavior of the higher temperature PM-FM transition has been studied through magnetic measurements in all cases and also through thermal ones when it was possible, the latter being the case of (Gd, Tb)$_6$(Fe, Mn)Bi_2 family. In the Ho based compounds (Ho_6(Fe, Mn)Bi_2 family), the magnetic critical exponents β, γ and δ are in near agreement with the Mean Field universality class, implying long-range order magnetic interactions. The critical behavior in (Gd, Tb)$_6$(Fe, Mn)Bi_2 family showed more variety, especially due to the difference in the rare-earth element. The transition in Gd_6FeBi_2 has been found to belong to the 3D Heisenberg universality class with deviations due to magnetocrystalline anisotropies. Substituting half of the Gd by Tb ($Gd_3Tb_3FeBi_2$) moves this behavior to the Mean Field class, implying that short-range order interactions

have given way to long-range ones. On the other hand, completely substituting Gd by Tb in Tb_6FeBi_2 and $Tb_6(Fe_{0.5}Mn_{0.5})Bi_2$ makes them present an unconventional critical behavior aligned with long-range order interactions. The analysis of the magnetic critical behavior in (Gd, Tb)$_6$(Fe, Mn)Bi$_2$ family has been further supported by the critical behavior analysis of the specific heat. Finally, due to the similarities between Tb and Dy, we observe a similar behavior for Dy$_6$(Fe, Mn)X$_2$ family, where, in all cases, the results suggest that long-range order interactions are responsible for these magnetic transitions, though only in two cases (Dy_6MnBi_2 and $Dy_6FeSbTe$) the values agree with the Mean Field universality class. The rest present an unconventional critical behavior as the values of β are too high or the values of γ too low to comply with an already theorized universality class. All these results point to the necessity of developing theoretical models which could explain the unconventional behavior here observed.

Regarding the magnetocaloric effect in R_6TX_2 family, one of the most interesting facts is that the existence of two magnetic transitions (except for Gd_6FeBi_2) generates two DMCE with a table-like effect in-between, which allows to maintain important magnetocaloric properties along a wide temperature range (more than 200 K in many cases), which is ideal for working on an Ericsson refrigeration cycle. But there's more; rare-earth as well as transition metal or X element substitutions have been proven to allow the tuning or tailoring of the magnetocaloric properties in a wide temperature range, including (but not only) room temperature. Furthermore, these materials show competitive magnetic entropy change values at 5 T for both peaks and huge values of the refrigerant capacities, the latter mainly due to the presence of the two DMCEs. Finally we have also observed big and interesting IMCEs in the low temperature region of (Gd, Tb)$_6$(Fe, Mn)Bi$_2$ and Dy$_6$(Fe, Mn)X$_2$ families. These IMCEs are linked to metamagnetic transitions from a complex non-collinear magnetic state to ferromagnetic one, and could be used on their own to act as magnetic refrigerators in those working temperatures, or as heat reservoirs in order to increase the efficiency when combined with the higher temperature DMCEs. The recently proposed Temperature Average Entropy Change (TEC) for evaluating the magnetocaloric performance of materials with wide ΔS_M peaks has also been explored for Dy$_6$(Fe, Mn)X$_2$ family.

Using the critical exponents obtained for each compound, the magnetocaloric scaling laws have been successfully tested and universal curves for the magnetic entropy change have also been obtained.

Finally, the thermal transport properties, i.e., thermal diffusivity, analysed for Dy$_6$(Fe, Mn)X$_2$ family, present high enough values for these materials to be considered as candidates for real magnetocaloric refrigeration systems.

The addition of all the characteristics presented here make this R_6TX_2 family suitable to design refrigerators able to work in extremely broad temperature ranges, from the different gas liquefaction regions to room temperature.

8 | $Y_{0.9}Pr_{0.1}Fe_2D_{3.5}$ Laves phase intermetallic

"What you do makes a difference, and you have to decide what kind of difference you want to make."

– Jane Goodall

The work presented in this chapter is a small part of what I had the opportunity to do during my stay at the *Institut de Chimie et des Matériaux Paris Est* in Thiais (France), where I had the chance to learn about *Laves phase* materials and their interest from Prof. Paul-Boncour, who has devoted her career to the study of these compounds.

My stay in Thiais was mainly focused on hydrogenation techniques and structural characterization, which is out of the scope of this manuscript. However, we were also able to perform a critical behavior and magnetocaloric effect study on $Y_{0.9}Pr_{0.1}Fe_2D_{3.5}$ *Laves phase* intermetallic, and this will be the topic of the present chapter.

The following material will be studied in this chapter:

- $\mathbf{Y_{0.9}Pr_{0.1}Fe_2D_{3.5}}$

8.1 Introduction

Laves phase compounds, named after Fritz Laves, are intermetallic compounds with AB_2 structure. Materials with A = rare-earth and B = Fe have been thoroughly investigated for their large magnetic anisotropy and magnetostriction up to room temperature [419, 420]. These RFe_2 compounds have also raised interest due to the modification of their structure and properties under hydrogen (deuterium) insertion, being able to absorb up to 5 H/f.u. (D/f.u.).

Hydrogenation usually generates structural order-disorder transitions from ordered to disordered cubic structures upon heating. The temperature at which this transition takes place, $T_{\text{O-D}}$, depends on the hydrogen (deuterium) content [421, 422]. On the other hand, H (D) insertion decreases the Curie temperature of RFe_2 compounds, allowing to tune T_C. This behavior has been particularly observed for YFe_2D_x compounds: $YFe_2D_{4.2}$ was observed to have a FM-AFM transition at 84 K [421, 422], while a decrease on D content down to 3.5 D/f.u. ($YFe_2D_{3.5}$) induces a ferromagnetic behavior with T_C = 310-360 K depending on the references (the difference is probably due to small discrepancies on D content) [423–426].

With the aim of observing a MCE near room temperature, we can further tune T_C by partially substituting Y content by a rare-earth element with larger radius. Furthermore, elements with larger radius than Y (light R elements) tend to have a ferromagnetic coupling with Fe, while heavy R elements display a ferrimagnetic ground state. That is why an improved MCE near room temperature is expected by partially substituting Y by the light rare-earth element Pr.

For these reasons, we have performed a detailed study of $Y_{0.9}Pr_{0.1}Fe_2D_{3.5}$ deuteride, determining its crystal structures, analysing both its magnetic and magnetocaloric properties, and discussing its critical behavior as has already been done for other *Laves phases* [427, 428]. For the crystal structure determination we have combined neutron powder diffraction (NPD) experiments on two different spectrometers with synchrotron radiation X-ray diffraction (SR-XRD) measurements, solving the structure at room temperature and its evolution with temperature.

8.2 Sample and experimental techniques

$Y_{0.9}Pr_{0.1}Fe_2$ intermetallic compound was prepared by induction melting of the pure elements (Y 99.9 %, Pr 99.9 %, Fe 99.99 %) followed by 3 weeks annealing treatment under vacuum at 1100 K. The chemical composition of the alloy measured by electron probe microanalysis was $Y_{0.91(1)}Pr_{0.09(1)}Fe_{1.98(2)}$. The analysis of the X-ray powder diffraction (XRD) pattern indicates that it contains 98.7 wt % of the C15 cubic phase (a = 7.36702(5) $\AA$), 0.9 wt % of Y_2O_3 and 0.4 wt % of $Y_6Fe_{16}O$. $Y_{0.9}Pr_{0.1}Fe_2D_{3.5}$ deuteride was prepared by solid-gas reaction using a Sieverts apparatus. It was activated one night under primary vacuum at 125 °C and hydrogenated at room temperature with the

final pressure of 0.2 bar D_2. The deuteride was quenched into liquid nitrogen followed by a slow heating under air to poison the surface and prevent fast gas desorption.

The alloy and the deuteride were characterized by XRD at room temperature with a Bruker D8 diffractometer operating with a Cu-Kα wavelength. Synchrotron radiation measurements (SR-XRD) were performed on the 2-circle diffractometer using the CRISTAL beam line at SOLEIL (Saint Aubin, France). The detection system was made of 9 linear Mythen modules covering a 50° 2θ circle arc at 720 mm from the sample. The wavelength refined with a LaB6 reference sample was $\lambda = 0.51302\mathring{A}$ and the 2θ range expanded from 1.2 to 52°. The powder sample was placed in a sealed glass capillary tube (0.3 mm diameter), which was rotated to ensure homogeneity. The sample was cooled or heated using a gas streamer cooler operating from 130 K up to 360 K. NPD patterns of $Y_{0.9}Pr_{0.1}Fe_2D_{3.5}$ have been recorded at the Laboratoire Léon Brillouin (LLB, CEA, Saclay, France) at 2, 300 and 345 K on the high resolution 3T2 spectrometer with a wavelength of 1.225 $\mathring{A}$, between 15° and 125° with a step of 0.05° and at selected temperatures from 1.5 to 345 K on the G4.1 spectrometer with a wavelength of 2.422 $\mathring{A}$ between 10 and 90° with a step of 0.1°. All the diffraction patterns were refined with the FULLPROF code [307].

Magnetic measurements were performed from 10 to 300 K using a conventional Physical Properties Measurement System (PPMS) from Quantum Design. Further magnetic curves were measured from 300 to 360 K with a DSM8 Manics magnetometer operating with a maximum field of 1.7 T.

8.3 Experimental results and discussion

This section will be divided in three subsection. The first one will be devoted to the determination of the crystal structure and its thermal evolution through different diffraction methods; however, since this thesis is not focused on those techniques only the most relevant conclusions of this analysis are presented. On the second section, the critical behavior of $Y_{0.9}Pr_{0.1}Fe_2D_{3.5}$ will be studied and discussed. Finally the magnetocaloric effect and its scaling laws will be presented.

8.3.1 Crystal structure and its temperature evolution

Powder diffraction patterns at 300 K were measured on CRISTAL synchrotron beam line, and on 3T2 and G4.1 neutron spectrometers in order to retrieve the crystal structure of $Y_{0.9}Pr_{0.1}Fe_2D_{3.5}$ at 300 K. G4.1 has a better resolution at low angle than 3T2 but its **Q** range is more limited (0.5-3.7 $\mathring{A}^{-1}$ for G4.1 and 0.5-9 $\mathring{A}^{-1}$ for 3T2). The three diffraction patterns at 300 K are plotted together in Fig. 8.1 for comparison.

The SR-XRD pattern at 300 K was refined with a main phase indexed in a monoclinic structure corresponding to the *C2/m* space group, No. 12, and few percent of secondary phases due to oxides (Y_2O_3 and $Y_6Fe_{16}O$), already present in the initial alloy. However, when trying to refine the NPD data in *C2/m* space group, few weak diffraction peaks in the range 3-3.6 $\mathring{A}^{-1}$ couldn't

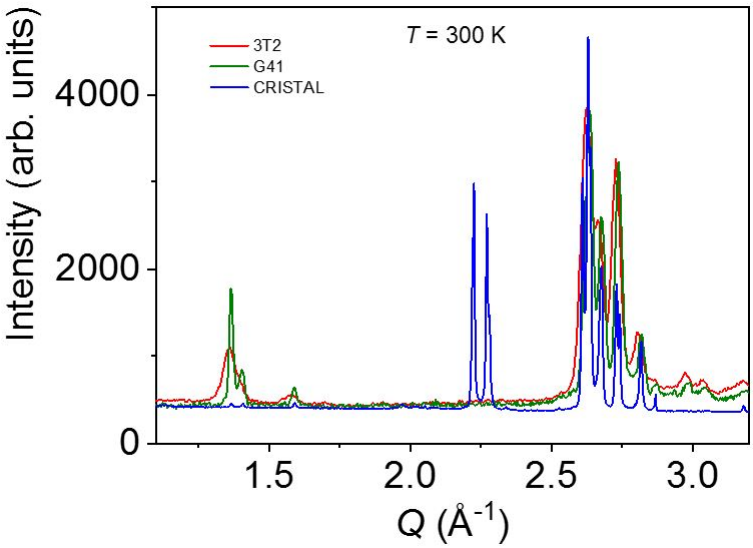


Figure 8.1: Diffraction patters measured at 300 K on CRISTAL, 3T2 and G4.1.

be indexed, suggesting a further lowering of the crystal symmetry. After checking different primitive subgroups the most appropriate primitive SG to refine the NPD pattern is found to be $P2_1/c$ (14). This was further confirmed by refining both G4.1 and 3T2 NPD patterns using FOX code, with the result that only $P2_1/c$ SG converge to a solution.

Above 300 K, a structural transformation attributed to a monoclinic pseudo-cubic transition takes place. Following the same procedure as for the diffraction patterns at 300 K, the higher temperature SX-XRD patterns are attributed to the $Fd\bar{3}m$ cubic space group, while NPD data requires a further lowering of the symmetry in order to properly index all the peaks, obtaining the rhombohedral $R\bar{3}m$ space group as the correct one for NPD patterns. As the rhombohedral cell parameters shows no elongation or contraction along the 111 axis within the instrumental synchrotron resolution, the cell is not distorted and the lowering of crystal symmetry is due to the partial ordering of the D atoms, leading to a loss of some symmetry elements as the four fold axis. It can be therefore considered as a pseudo-cubic cell.

The reduced cell volume (V/Z) and phase percentage obtained from SR-XRD refinement are plotted in Fig. 8.2 upon heating and cooling. The monoclinic cell volume shows a minimum at 274 K. A mixture of monoclinic and cubic phases is observed between 325 K (315 K upon cooling) and 350 K. Both monoclinic and cubic cell volumes decrease down to 345 K and then the cubic cell volume remains stable. The O-D transition is reversible with a small thermal hysteresis. The percentage of each phase is equal to 50 % at 342(2) K. A small D desorption after heating at 360 K, can explain the smaller cell volumes upon cooling. It can be easily observed in Figure 8.2 that the volume of the cubic cell is larger than the monoclinic one and decreases down to 345 K. This variation is opposite to the thermal expansion and cannot be related to a deuterium desorption as it is reversible upon cooling. This behavior suggests a possible magnetostrictive effect. Furthermore, a decrease of the monoclinic a and c cell parameters upon heating has also been observed, with a minimum

at 274 K, which, as we will soon see, corresponds to the FM transition temperature. This monotonic decreased is not observed on the temperature evolution of the monoclinic b cell parameter, indicating that the Pr and Fe moments should be oriented in the (a_M, c_M) plane and perpendicular to the monoclinic b_M axis.

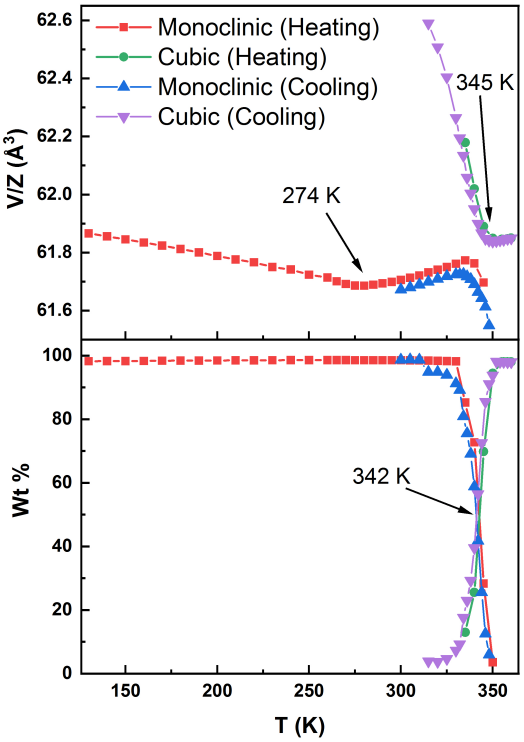


Figure 8.2: Reduced cell volumes (up) and weight percentages (down) obtained from SR-XRD data upon heating and cooling.

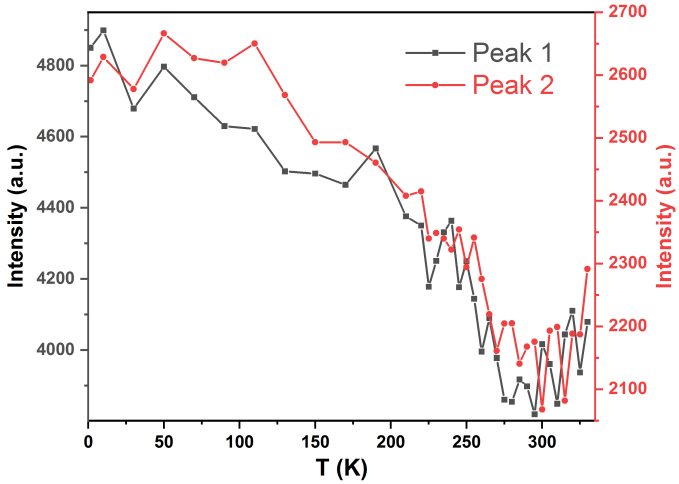


Figure 8.3: Evolution of the magnetic peak intensities in G4.1.

Finally, and connecting with the following section concerning magnetic properties, the NPD patterns below 274 K also contain information about the

magnetic structure. The integrated intensity at low **Q** peaks in G4.1 measurements decreases with increasing temperature as shown in Figure 8.3. These magnetic peaks are located at the same position as the structure peaks, probing that Fe as well as Pr sublattices are ferromagnetically aligned.

8.3.2 Critical behavior in $Y_{0.9}Pr_{0.1}Fe_2D_{3.5}$

According to the magnetic measurements shown in Fig. 8.4, ferromagnetic ordering in $Y_{0.9}Pr_{0.1}Fe_2D_{3.5}$ starts at $T_C = 274 \pm 4$ K and shows a small magnetization increase below 52 K. Above 300 K (as magnetization decreases) a weak peak can be spotted at $T = 343$ K (Fig. 8.4(b)), which occurs very close to $T_{O\text{-}D}$, suggesting a correlation between this magnetic peak and the structural transition.

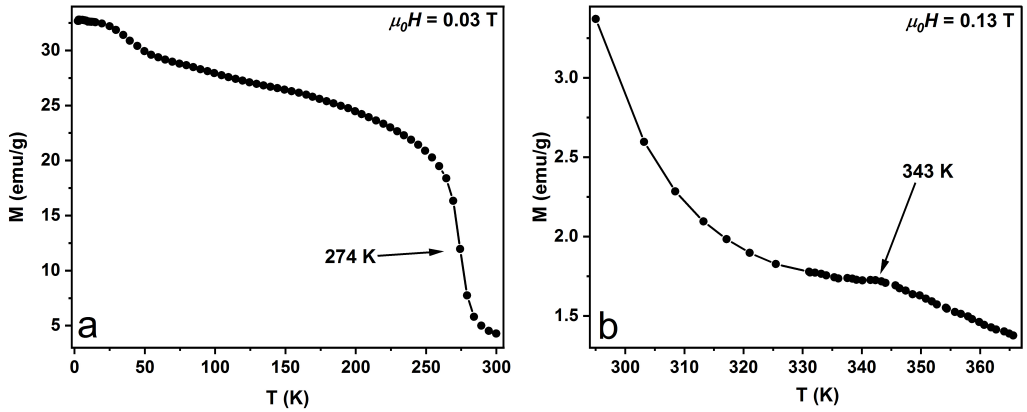


Figure 8.4: Temperature evolution of magnetization in two different regions. At 0.03 T with PPMS device below 300 K (a) and 0.13 T with MANICS DSM8 device above 300 K (b).

It is worth pointing out that T_C is found to be lower than $T_{O\text{-}D}$, meaning that the ferromagnetic order is not related to the order-disorder transition as proposed for $YFe_2D_{3.5}$ in which T_C and $T_{O\text{-}D}$ were both close to 345 K [429]. Interestingly, $T_{O\text{-}D}$ is not sensitive to the substitution of Y by Pr, whereas T_C is reduced.

The Arrot Plot in Fig. 8.5 shows positive slopes for the magnetization isotherms below 300 K, indicating a second order transition according to the Banerjee criterion [229]. This assesses that a critical behavior analysis can be performed over the ferromagnetic transition. The critical exponents are obtained through the familiar procedure already explained in detail in Section 3.4.1 and used several times along this manuscript. First the Modified Arrot Plots (MAP) are represented for the main universality classes, for which the classical AP (Fig. 8.5) is the particular case corresponding to the Mean Field model. To correctly describe the system, the MAP corresponding to that model should show good straight parallel lines at high magnetic fields in the proximity of the critical region. From Fig. 8.5 we can see that this is not the case for the Mean Field universality class. The straightness and parallelism of the different models have been checked for the most common universality classes,

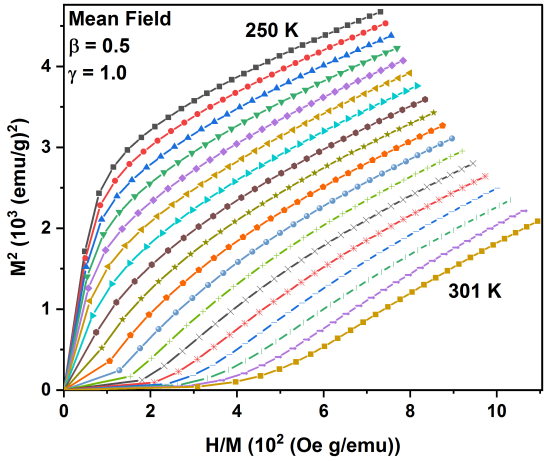


Figure 8.5: Arrot Plot for $Y_{0.9}Pr_{0.1}Fe_2D_{3.5}$, positive slopes indicate second order phase transition.

giving both the 3D Heisenberg (isotropic) and 3D XY (plane anisotropy) as the best starting points for the iterative procedure. The following step consists on obtaining the spontaneous magnetization (M_S) and inverse of the initial susceptibility (χ_0^{-1}) from the intersection of the straight lines in the MAP with the axes. These values are then fitted to:

$$M_S(T) \sim |t|^{\beta} \qquad (T < T_C)\,, \tag{8.1}$$

$$\chi_0^{-1}(T) \sim |t|^{\gamma} \qquad (T > T_C)\,, \tag{8.2}$$

in order to obtain new values of β and γ. Those new values are again used to build new MAPs to check if there is an improvement on their straightness and parallelism. If this is the case, the process is repeated till the values of β and γ converge. This iterative process was performed starting from both the 3D Heisenberg and 3D XY models, and in both cases the obtained results were equivalent. The final fittings for M_S and χ_0^{-1} and the final MAP are shown in Fig. 8.6(a) and (b), respectively, and the critical exponents and temperatures obtained from this iterative process are collected in Table 8.1, where it can be seen that the critical temperature is slightly lower than the one reported previously. This can be explain from the fact that the magnetic measurements for the critical analysis were performed several month after the diffraction measurements and the $M(T)$ curves in Fig. 8.4 were obtain. Furthermore, the measurements were performed over a different piece of the sample and small differences in D concentration may cause this small deviation in the critical temperature.

After this, the Kouvel Fisher method is used to independently obtain β and γ values. As we have already proven, this method assesses that there is a linear dependence with temperature of the spontaneous magnetization and inverse of the initial susceptibility when divided by their respective derivative with temperature, and that the slope is given by $1/\beta$ for the former case and $1/\gamma$ for the latter. The resulting fitting can be observed in Fig. 8.6(c), and the obtained critical exponents are listed in Table 8.1, with the result that the values are in

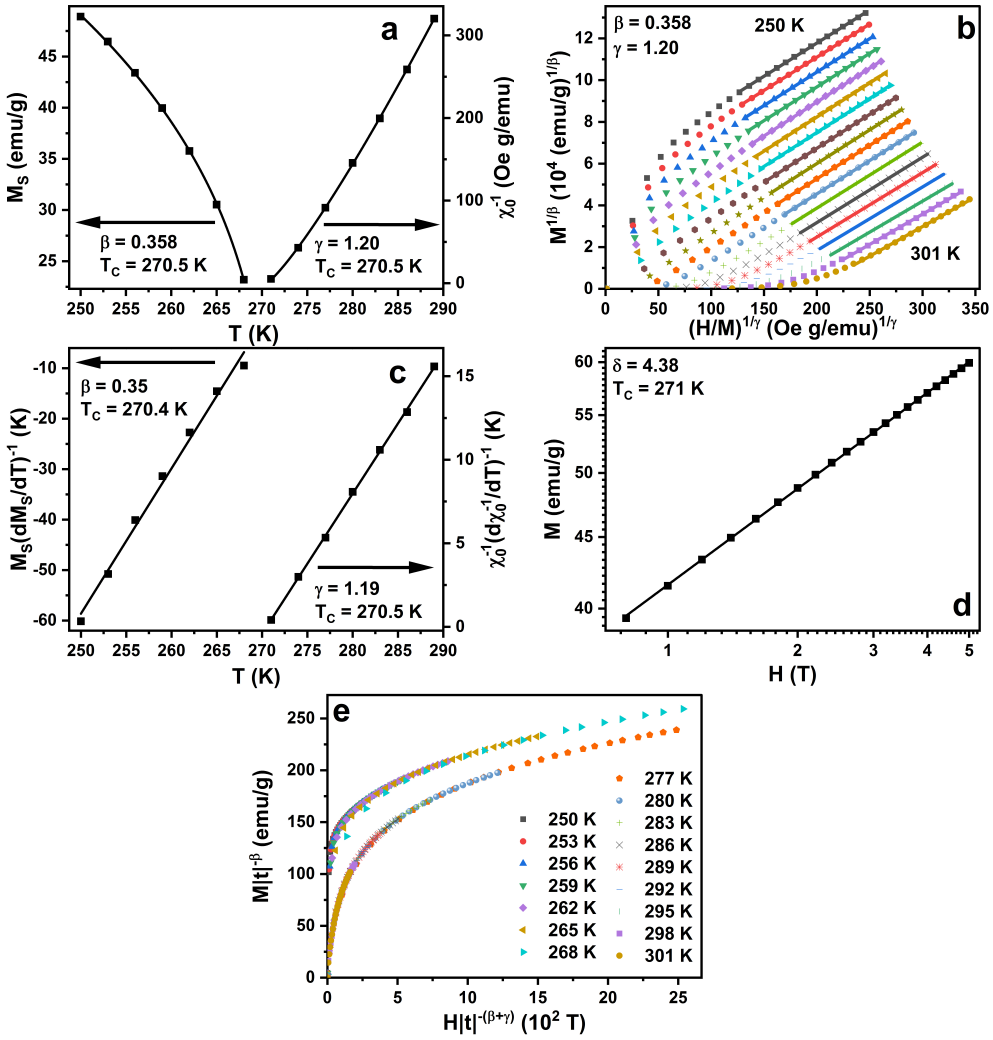


Figure 8.6: (a) Fitting of spontaneous magnetization (left) and inverse of the initial susceptibility (right). (b) Final Modified Arrot Plot. (c) Kouvel Fisher fittings. (d) Critical isotherm fitting. (e) Magnetic equation of state.

very good agreement with the ones obtained from the fitting of M_S and χ_0^{-1}.

The last critical exponent, δ, associated to the critical isotherm, can be easily obtained as the inverse of the slope in a M vs H plot at the critical temperature ($T_C = 271$ K) in logarithmic scale:

$$M \sim H^{1/\delta} \qquad (T = T_C)\,. \tag{8.3}$$

The fit is shown in Fig. 8.6(d). Furthermore, the critical exponent δ is related to β and γ through the *Widom scaling law* ($\delta = 1 + \gamma/\beta$), and, therefore, the δ obtained from the critical isotherm can be compared with the one obtained by applying *Widom scaling law* to the previously obtained β and γ values. From Table 8.1 it is easily seen that the values are in good agreement, confirming once again the correct evaluation of the critical exponents.

Finally, the most robust confirmation of the critical exponents is considered to be given by the correct fulfillment of the magnetic equation of state:

Technique	β	γ	δ
Modified Arrot Plot	0.358 ± 0.008	1.20 ± 0.02	4.3 ± 0.1^a
	$T_C = 270.5 \pm 0.2$ K	$T_C = 270.5 \pm 0.2$ K	
Kouvel Fisher Method	0.35 ± 0.01	1.19 ± 0.01	4.4 ± 0.2^a
	$T_C = 270.4 \pm 0.2$ K	$T_C = 270.5 \pm 0.4$ K	
Critical Isotherm			4.38 ± 0.01

[a] Calculated from *Widom scaling law*: $\delta = 1 + \gamma/\beta$.

Table 8.1: Values of the obtained magnetic critical exponents β, γ, δ.

$$M(H,t) = |t|^{\beta} f_{\pm}(H/|t|^{\beta+\gamma}) \,, \tag{8.4}$$

A good fulfilment for this expression would imply the collapse of all the isotherms into two distinct branches (one for $T > T_C$ and the other one for $T < T_C$) for the correct β and γ values. Fig. 8.6(e) shows that this is in fact the case when the previously obtained critical exponents in Table 8.1 are used.

Let's discuss the obtained results for the critical behavior. The β critical exponent obtained from the fitting of the spontaneous magnetization ($\beta = 0.358 \pm 0.008$) is between the values corresponding to 3D Heisenberg ($\beta_{\text{Heis}} = 0.369$) and to the 3D XY ($\beta_{\text{XY}} = 0.348$) models, while the KF analysis yields a value ($\beta = 0.35 \pm 0.01$) slightly closer to the 3D XY model. In both cases the γ values are slightly lower than the theoretical ones corresponding to any of the previous models (see Table 3.2 in page 77). Deviations of the critical parameters from theoretical models can point to strong crystal field effects, magnetocrystalline anisotropy, different kind of coupling mechanisms (such as spin-orbit coupling of the itinerant electrons) or a certain degree of disorder in the system [210]. The latter case is the most probable one in our system, since some disorder is still observed in the monoclinic phase due to D sites occupation. Overall, the critical exponents appear to deviate from the 3D Heisenberg isotropic universality class towards the 3D XY model, therefore presenting an easy plane of anisotropy. This is in agreement with our observations regarding the evolution of cell parameters, which suggest that the Pr and Fe moments should preferably lie in the (a_M, c_M) plane. However, as it is easily observed in Table 3.2 (page 77), the magnetic critical exponents for 3D Heisenberg and 3D XY universality classes are very close to each other, making it hard to discriminate the correct model by only using magnetic properties, *ac* PPE calorimetry measurements could be helpful in order to study the critical behavior of c_p which would allow us to discriminate between both models with high accuracy, since α varies from -0.134 for the 3D Heisenberg model to -0.014 in 3D XY model. In either case, the critical exponents obtained from this analysis discard long-range order interactions, for which the proper universality class would have been the Mean Field model. Therefore, we can conclude that short-range order magnetic interactions are responsible for the phase transition and magnetism in this system.

8.3.3 Magnetocaloric effect in $Y_{0.9}Pr_{0.1}Fe_2D_{3.5}$

The magnetic entropy change ΔS_M was obtained from the magnetization isotherms using the well-known *Maxwell relation*. The analysis of the magnetic entropy variation shows a DMCE peak with a maximum value of -3.3 J/kgK (at $\mu_0\Delta H$ = 4.8 T) centered at T_C (left side in Fig. 8.7), and a small IMCE with ΔS_M = 0.4 J/kgK (at $\mu_0\Delta H$ = 1.5 T) in the order-disorder structural transition region (right side in Fig. 8.7). The latter is not relevant enough for practical applications but indicates that there is a correlation between both the structural transition and magnetic properties. The origin of this IMCE can be explained by an AFM ordering, as spotted in Fig. 8.4(b).

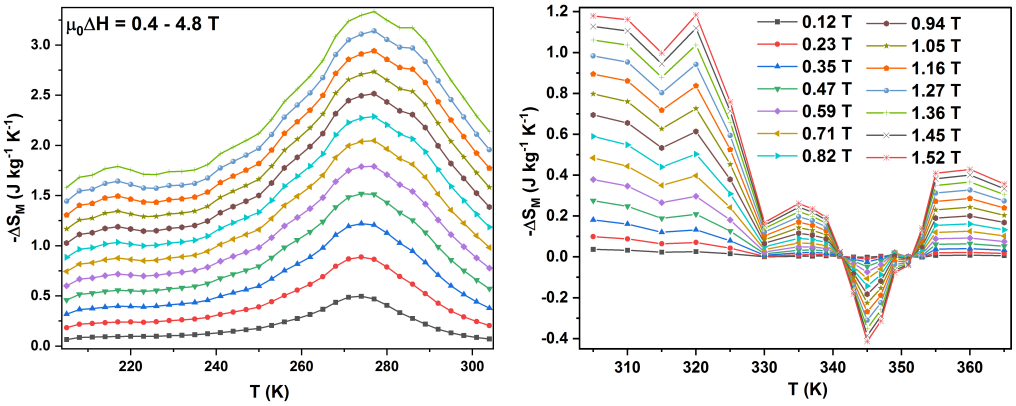


Figure 8.7: Magnetic entropy change as a function of temperature for applied fields ranging from $\mu_0\Delta H$ = 0.4 T to 4.8 T with steps of 0.4 T around T_C (left), and for $\mu_0\Delta H$ = 0.12-1.52 T around $T_{\text{O-D}}$ (righ).

If we focus on the DMCE, the magnetic entropy change analysis can be further extended by the construction of the so-called "master curves". These curves are also known as universal curves, since, for second order phase transitions, ΔS_M curves at different applied fields should collapse into a single curve in the vicinity of the critical region when ΔS_M value is normalized by the value at the peak of each isofield and the temperature axis is rescaled according to:

$$\theta_1 = \frac{T - T_C}{T_r - T_C}\,. \tag{8.5}$$

Were T_r is the usual reference temperature selected above T_C for which the value of ΔS_M is half of the one at the peak. The result is shown in Fig. 8.8(a), and a good collapse, though not completely perfect, can be observed in the critical region, confirming the second order nature of the transition. It has been shown that when using a single reference temperature the collapse could be distorted at $T < T_C$ due to demagnetizing field effects or minor magnetic phases at higher temperatures. In the former case the normalized $\Delta S_M/\Delta S_M^{pk}$ for a given temperature would increase, while in the latter case the effect would be the opposite. The inset in Fig. 8.8(a) clearly shows that we are in the second case, therefore ruling out any relevant demagnetizing field effect. Although the deviation is small, it could be due to the presence of the higher temperature AFM like transition which was spotted both in $M(T)$ and ΔS_M

measurements. In this cases a usual approach is to rescale the temperature axis using two reference temperatures ($T_{r1} < T_C < T_{r2}$) instead of a single one:

$$\theta_2 = \begin{cases} -(T - T_C)/(T_{r1} - T_C)\,, & T \leqslant T_C \\ (T - T_C)/(T_{r2} - T_C)\,, & T > T_C \end{cases} . \tag{8.6}$$

In this way the collapse of the curves below the critical temperature is even better, as can be seen in Fig. 8.8(b).

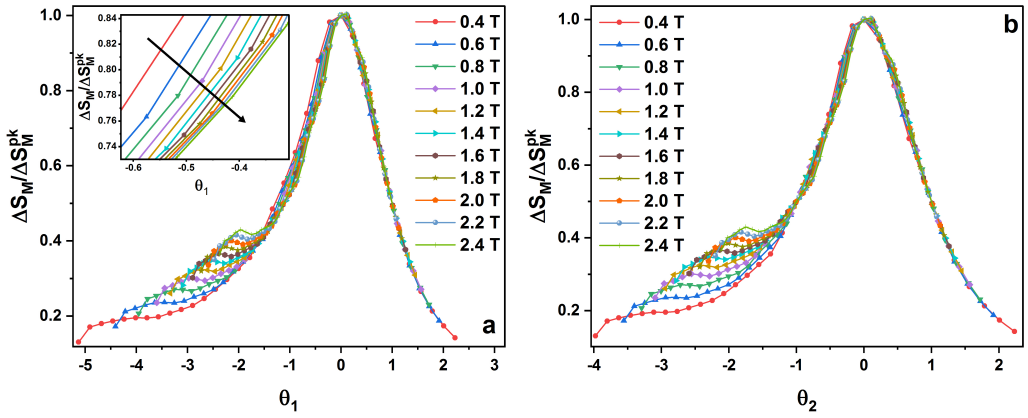


Figure 8.8: Master curves with the rescaled temperature using one θ_1 (a) and two θ_2 (b) reference temperatures. The inset in (a) shows the small deviation from a perfect collapse. The direction of the arrow represents increasing applied fields.

In order to compare the magnetocaloric effect in $Y_{0.9}Pr_{0.1}Fe_2D_{3.5}$ with the values usually given in literature and with the samples previously presented on this manuscript, we need the $|\Delta S_M^{pk}|$ and refrigerant capacity values at $\mu_0\Delta H = 2$ and 5 T. For technical reasons the maximum value of $\mu_0\Delta H$ measured this time was 4.8 T. However, we can make use of the magnetocaloric scaling relations in second order phase transitions to obtain the expected value at the desired field. As already explained in Section 3.5, the scaling relations of magnetocaloric properties yield as follows:

$$|\Delta S_M^{pk}| \propto H^{1+\frac{1}{\delta}(1-\frac{1}{\beta})}\,, \tag{8.7}$$

and

$$RC \propto H^{1+1/\delta}\,. \tag{8.8}$$

Furthermore, the reference temperature used to rescale the temperature axis in the universal curve (T_r) also scales with temperature as:

$$T_r \propto H^{1/(\beta+\gamma)}\,. \tag{8.9}$$

Thus, by using the β, γ and δ critical exponents obtained from the previous critical behavior study, we will be able to extrapolate our data to $\mu_0\Delta H = 5$ T. The scalings in Eqs. (8.7), (8.8) and (8.9) have been successfully tested using the critical exponents in Table 8.1. Fig. 8.9 shows the results for $|\Delta S_M^{pk}|$, RC_{FWHM}, RC_{Area} and T_r, where the red line is a visual guide to show that the

experimental values lie very well along the straight line, as they should for a good scaling. This further confirms the values obtained for the critical exponents and allows the extrapolation of the magnetic entropy change peak and RC values to fields that could not be experimentally reached. The obtained MCE values are listed in Table 8.2. Furthermore, Eqs. (8.7) and (8.9), together with the universal curves in Fig. 8.8 can be used to obtain the full ΔS_M shape at temperatures and fields out of the measured range.

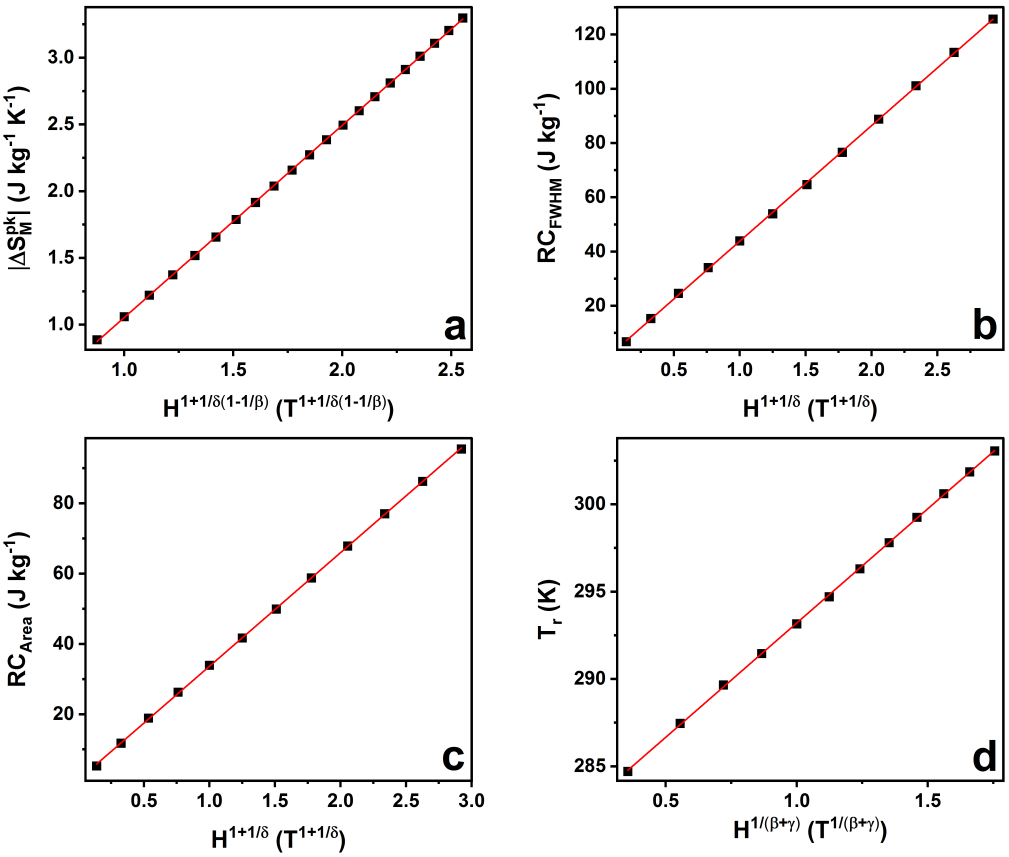


Figure 8.9: Scaling relations for: (a) $|\Delta S_M^{pk}|$, (b) RC_{FWHM}, (c) RC_{Area}, and (d) T_r. β, γ and δ are the ones in Table 8.1.

$\mu_0\Delta H$	$\lvert\Delta S_M^{pk}\rvert$ (J kg^{-1} K^{-1})	RC_{FWHM} (J kg^{-1})	RC_{Area} (J kg^{-1})
2 T	1.8	101	77
5 T	3.4[a]	307[a]	233[a]

[a] Extrapolated values using magnetocaloric scaling laws.

Table 8.2: Peak of the magnetic entropy change $|\Delta S_M^{pk}|$, RC_{FWHM}, and RC_{Area} at $\mu_0\Delta H = 2$ and 5 T.

8.4 Conclusions

We have used three diffraction techniques in order to study the temperature evolution of the crystal structure in $Y_{0.9}Pr_{0.1}Fe_2D_{3.5}$ *Laves phase* compound. We have concluded that this compound undergoes a first order structural order-disorder transition at $T_{\text{O-D}} \sim 343$ K, with a small thermal hysteresis. The deuteride evolves from a monoclinic structure at lower temperature to a pseudo-cubic crystal structure at higher temperature. The evolution of the monoclinic cell paramenters, with temperature, with a_M and c_M decreasing when temperature is increased until a minimum value at T_C, suggests the existence of a magnetostrictive effect (also spotted for the cubic phase) and the preferable orientation of the magnetic moments within the monoclinic *a-c* plane. The latter is supported by the critical behavior analysis which points to a 3D XY universality class.

We also found that, since the ferromagnetic ordering temperature ($T_C \sim 274$ K) is much lower than the O-D transition, both effects are not correlated, contrary to what was previously assumed for $YFe_2D_{3.5}$.

Finally, the magnetocaloric effect was obtained for the ferromagnetic transition and the critical exponents were used to check the scaling relations, which were later applied to extrapolate our data up to 5 T. The MCE also shows a small IMCE at $T_{\text{O-D}}$ related to an AFM peak.

9 | Conclusions and future work

"One never notices what has been done; one can only see what remains to be done."

– Marie Skłodowska Curie

A brief summary highlighting the main conclusions of this thesis is presented in this last section. A quick route through all the work done and the one to come, including a comparison of the magnetocaloric effect for all the families and materials we have worked with. Thus, the aim of this section is to put into perspective, in a quick single view, the previous experimental results and to explore the possible future paths to be taken.

Conclusions

Not few rare-earth based intermetallic materials and families have been studied in this work. It would be more precise to talk about several *"main goals"* for this thesis instead of a single *"main goal"*. The aim of combining thermal and magnetic techniques was not only focused on determining and finding the most promising materials for magnetic refrigeration (which is obviously important), but also on the understanding of the physics underlying the properties of those materials in order to set some light on what makes a compound a good candidate for technological applications. This is where the critical behavior theory plays a leading role.

Bearing this in mind, we have evaluated the magnetocaloric performance of our compounds, and discussed the critical behavior of their second order magnetic phase transitions. For the latter, magnetic and thermal techniques have been applied to obtain the critical exponents associated to different physical properties. These critical exponents and parameters (α, A^+/A^-, β, γ, δ) were then compared with the theorized universality classes giving us valuable information about the physics on the system. Furthermore, the critical exponents have been shown to be very useful in magnetocaloric scaling relations, allowing the extrapolation of the main magnetocaloric properties to temperatures and magnetic fields which may not be accessible for every experimental laboratory set-up. With this, the potential of the magnetocaloric scaling has been fully explored. Finally, the study of the magnetocaloric effect has also been proven to be a very useful technique in order to characterize the order of the magnetic transition through the construction of the *"master"* or *"universal"* curves and the temperature evolution of the n parameter.

One of our biggest interests during this work has been to explore the differences between intermetallic families, but also the effect caused by the substitution of the rare-earth (or any other element in the composition) on the thermal, magnetic, and magnetocaloric properties within the same intermetallic family. The conclusions for each family are briefly summarized in what follows.

◦ **RTX intermetallics:** The thermal diffusivity over a wide temperature range was obtained for R=Pr, Nd and Gd compounds. The resulting values of D around the transition regions are high compared to other values of magnetocaloric materials in literature, which makes these materials interesting from the point of view of their application. The critical behavior of the four Gd-based compounds was studied by means of calorimetric and magnetic techniques. All the results point to the 3D Heisenberg isotropic class as the one describing the interactions in the system; therefore, short-range order interactions are responsible for the magnetic ordering. Small deviations in the critical parameters with respect to the theoretical ones can be explained by the presence of small magnetocrystalline anisotropies arising from spin-orbit coupling. The magnetocaloric effect of the Nd- and Gd- based compounds was also studied. The latter present highly competitive magnetocaloric properties above 300 K, while the former have average magnetic entropy change values and low refrigerant capacities at ∼170-190 K. The magnetocaloric scaling relations were

satisfactorily fulfilled, and the construction of the universal curves for the different universality classes checked.

∘ **R_3CoNi intermetallics:** Four members of the R_3CoNi family (with R = Dy, Ho, Er, Tm) were synthesized for the first time and their crystal structure has been checked to agree with the rhombohedral Er_3Ni_2-type structure, as the previously reported Tb_3CoNi, which was also studied in this work. The magnetic ordering from a PM state towards a FM state takes place in the range 96-6 K, with decreasing temperature for increasing atomic number of R. Some of these samples were observed to contain further spin reorientations transitions at lower temperatures. The critical behavior of the spin ordering at higher temperature was studied. Specific heat and magnetic properties were used to this end. Tb_3CoNi compound agrees with the Mean Field model, while the critical exponents for Dy_3CoNi and Ho_3CoNi are closer to Chiral universality models, suggesting some kind of frustrated non-collinear ferromagnets. The magnetocaloric properties of this family turned out to be very promising for cryo-cooling applications in the gas liquefaction region.

∘ **R_3T intermetallics:** The thermal diffusivity for the three single crystals studied in this work (Dy_3Co, Tb_3Co and Tb_3Ni) was obtained and used, together with other thermal parameters, for the critical behavior analysis. All the PM-AFM transitions at zero applied field agree with the 3D Heisenberg class, with small deviations explained by the cystal field effects due to the occupation of non-equivalent positions by the rare-earth element. Different techniques were used to settle once and for all the weakly first order character of the lower temperature transition in Tb_3Co. Furthermore, a neutron diffraction analysis was performed for the previous sample. The complex magnetic structure of Tb_3Ni has been discussed and its magnetocaloric effect, as well as the one for Tb_3Co, obtained. Both materials show relevant magnetocaloric properties enhanced by their metamagnetic transitions, making them extremely interesting for magnetic refrigeration in gas liquefaction range. Tb_3Ni presents a great IMCE followed by a big DMCE, and a big magnetic anisotropy which results on a promising rotating magnetocaloric effect.

∘ **R_6TX_2 intermetallics:** Three *"sub-families"* of the parent R_6TX_2 family have been studied. What makes these compounds interesting is, on the one hand, the possibility to tune their transition temperature by playing with their stoichiometry, and, on the other hand, the wide plateau working region created by the existence of two consecutive magnetic transitions (except for Gd_6FeBi_2). The critical behavior of the PM-FM transition of these samples was studied by magnetic techniques, and in the case of (Gd, Tb)$_6$(Fe, Mn)Bi_2 also by thermal ones. The PM-FM transition in Ho_6(Fe, Mn)Bi_2 family is close to the Mean Field model, pointing to long-range order interactions. If the rare-earth element is substituted, this behavior changes. (Gd, Tb)$_6$(Fe, Mn)Bi_2 family shows a 3D Heisenberg behavior for Gd_6FeBi_2, while $Gd_3Tb_3FeBi_2$ agrees with the Mean Field class. Tb_6FeBi_2 and $Tb_6(Fe_{0.5}Mn_{0.5})Bi_2$ show an unconventional critical behavior. The latter is also observed on members of Dy_6(Fe, Mn)X_2

family, with the exception of Dy_6MnBi_2 and $Dy_6FeSbTe$ which are aligned with the Mean Field class. The table-like DMCE, caused by the superposition of the PM-FM transition and the lower temperature spin reorientation transition, can be tailored to work in many temperature regions, including room temperature, and is ideal for working on an Ericsson refrigeration cycle. An interesting IMCE is also present at low temperatures for some of the samples. Finally, the thermal diffusivity values in the working region of $Dy_6(Fe, Mn)X_2$ family show high enough values to be considered for application.

∘ **$Y_{0.9}Pr_{0.1}Fe_2D_{3.5}$ Laves phase intermetallic:** This compound has an order-disorder structural transition at 346 K and a FM ordering transition at T_C = 274 K. Three diffraction techniques, including neutron powder diffraction and X-Rays, have been used to study the crystal structure evolution with temperature, finding an evolution from a monoclinic structure to a pseudo-cubic one when temperature is increased. The critical behavior of the FM transition matches the 3D XY universality class, which agrees with neutron diffraction measurements. The magnetocaloric effect, which is close to room temperature, has been obtained and its scaling relations have been successfully tested.

The results for the magnetocaloric effect of all the studied compounds are presented in Fig. 9.1 for the shake of comparison. This figure is intended to be a visual summary of all the work done concerning the DMCE of our samples, where the behavior of the different presented intermetallic families can be seen at a glance. Fig. 9.1 represents three of the most important features in order to consider a material for its application. Firstly, the horizontal axis indicates temperature, and the bubbles are located at the temperature corresponding to their transitions, which, as we already know, is the temperature at which the magnetic entropy change shows a peak. In the case of R_6TX_2 family, both transitions (the PM-FM one at T_C and the spin reorientation one at T_m) are represented. Secondly, the position of the bubbles in the vertical axis represents the peak value of the negative magnetic entropy change: $-\Delta S_M^{pk}$. Lastly, the diameter of the bubbles is proportional to their full width half maximum refrigerant capacity: RC_{FWHM}. All of the previous parameters are given for $\mu_0\Delta H = 5$ T.

Fig. 9.1 clearly shows how this thesis has covered the study of materials with MCEs over a wide temperature range, from 0 to almost 400 K, with compounds all over that range, exploring all the regions of interest. At temperatures below 100 K both R_3CoNi and R_3T families show very promising magnetocaloric properties. In this region the spin reorientation transition at T_m of the R_6TX_2 family shows a lower $-\Delta S_M^{pk}$ value, though their high refrigerant capacities overcome this. In the intermediate temperature region (100-300 K) the MCE caused by the PM-FM transition in R_6TX_2 compounds dominates, showing the potential of this family for tuning their MCE by changing their stoichiometry. $Y_{0.9}Pr_{0.1}Fe_2D_{3.5}$ (RFe_2) compound is located close to room temperature (T_C = 274 K), and at temperatures higher than 300 K we find the Gd containing members of the RTX family (GdScSi, GdScGe, $GdSc(Si_{0.5}Ge_{0.5})$, $Gd(Sc_{0.5}Ti_{0.5})Ge$) and some members of the R_6TX_2 family: $Gd_3Tb_3FeBi_2$ (T_C =

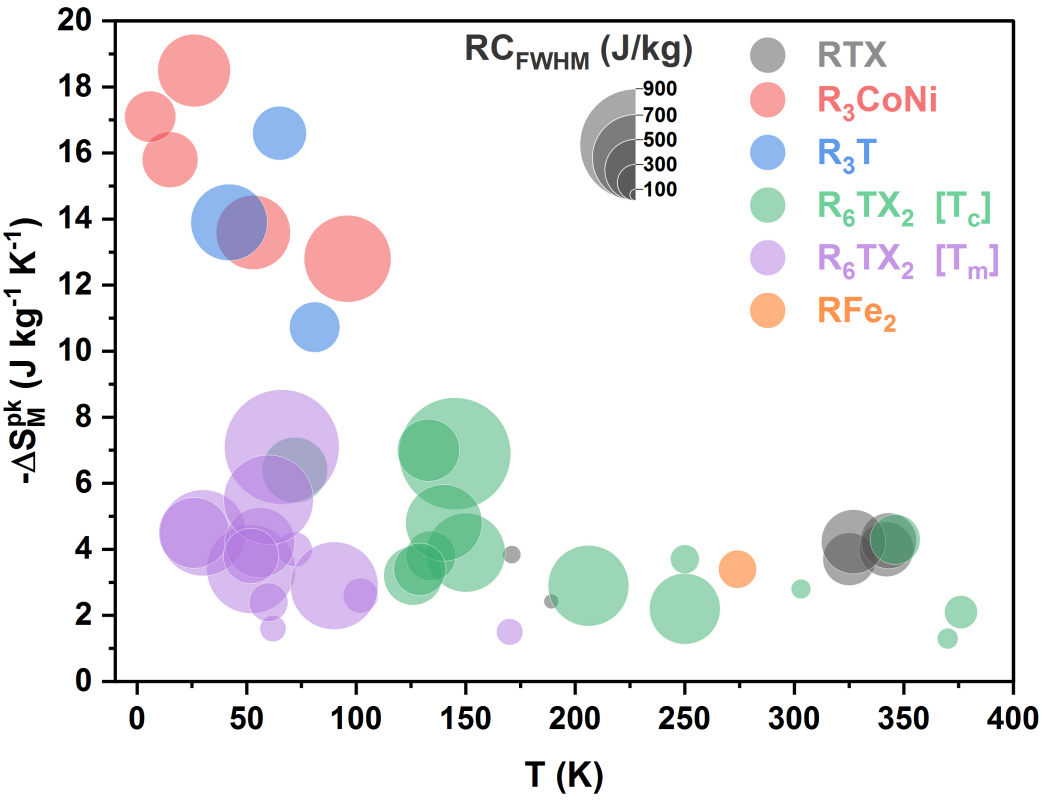


Figure 9.1: Comparison of the $-\Delta S_M^{pk}$ and the RC_{FWHM} with $\mu_0\Delta H = 5$ T for the intermetallic families studied on this thesis.

302 K), Gd_6FeBi_2 ($T_C = 348$ K), $Tb_6(Fe_{0.5}Mn_{0.5})Bi_2$ ($T_C = 376$ K), and Dy_6MnBi_2 ($T_C = 364$ K).

Future work

The work presented on this manuscript opens the door to several future research paths. As mentioned in Chapter 6, the magnetic properties of Tb_3Ni are very interesting and the magnetic anisotropy of the sample has aroused our interest on how this phenomena could be exploited to enhance the applicability of the compound. That is why we are currently working on a collaboration to explore the magnetocaloric behavior of Tb_3Ni at high fields (up to 50 T), where the adiabatic temperature change when a magnetic field is applied along the different crystallographic axes will be directly measured.

The potential of the new R_3CoNi family should also be further explored, specially the effect of combining different rare-earth elements on the same compound and the tuning of the critical temperature with R = Nd and Gd, which in the latter case is expected to be displaced to higher temperatures.

Laves phase compounds have been extensively studied for their diverse applications. In the particular case of RFe_2 materials, we have seen that it is very easy to modify their T_C by mixing different R elements. The hydrogenation of these compounds can be used to modify or enhance their structural, magnetic

and MCE properties. This is therefore a research field which requires attention in the near future.

A special mention is required for the ternary R_6TX_2 family, which has shown that materials with several spin reorientation transitions could be promising candidates for magnetic refrigeration due to the tableau region generated between those transitions, giving rise to big refrigerant capacities and relevant magnetic entropy change values over a wide temperature range. With the knowledge we have gained on this family the next step would be to look for compositions which are expected to show relevant MCE properties in the room temperature region, by appropriately playing with the stoichiometry. We have observed, for example, that the presence of Sb, instead of Bi, clearly enhances the magnetocaloric properties. Mn incredibly increases the Curie temperature, but it reduces the MCE with respect to Fe. Considering also how the substitution of Gd by Tb affects the properties and how Dy is the rare-earth which gives higher derivatives of the magnetization with respect to temperature, we are currently on the search of a relevant MCE around room temperature, exploring compounds specifically designed to this end. Furthermore, our research group is now focused on the study, via *ab-initio* calculations, of the hybridization processes in these compounds, which are still not well understood. Finally, the unconventional critical behavior found for several members of this family should be addressed by theoretical groups.

I would like to end by expressing my hope that with this manuscript I have been able to transmit the passion that I have put into this subject and how exciting it is.

Resumen

La refrigeración magnética ha emergido recientemente como una prometedora aliada tecnológica en la mitigación de los efectos del cambio climático. Esta tesis está dedicada al estudio de compuestos que podrían desempeñar un papel importante en la transición hacia una refrigeración más eficiente y respetuosa con el medio ambiente basada en materiales magnéticos.

Mi intención con este manuscrito, además de mostrar nuestro trabajo, es proporcionar al lector una guía sobre los antecedentes teóricos y las técnicas experimentales que pueden utilizarse para explorar los materiales magnetocalóricos y el comportamiento crítico de sus transiciones magnéticas. Con esta idea en mente, he dividido el manuscrito en dos partes principales. La primera está dedicada a la presentación del marco teórico general, que es válido para cualquier tipo de material magnético. La segunda parte está orientada a la aplicación de esta teoría a materiales específicos; los compuestos intermetálicos basados en tierras raras, en los que hemos centrado nuestro interés.

Nuestro trabajo se sustenta principalmente sobre cuatro pilares: las propiedades térmicas de los materiales, su naturaleza magnética, el efecto magnetocalórico que presentan y el comportamiento crítico de sus transiciones de fase. La caracterización y el estudio de las propiedades térmicas siempre ha sido de gran interés en muchas áreas científicas. Esto es así porque diferentes mecanismos (tanto a escala macroscópica como microscópica) dejan una huella en las propiedades térmicas. En la física del estado sólido, el transporte de calor está mediado principalmente por los fonones y los electrones (en el caso de los metales), y se ve afectado por el ordenamiento magnético y otros efectos. Para el estudio de estas propiedades hemos empleado la calorimetría fotopiroeléctrica *ac* (PPE por sus siglas en inglés). Esta técnica se denomina así porque se emplea un haz láser modulado (de ahí *foto* y *ac*) para generar un gradiente térmico en la muestra que posteriormente será convertido en una señal eléctrica por un detector *piroeléctrico*. La piroelectricidad es la capacidad de algunos materiales de cambiar su polarización espontánea cuando se aplica un gradiente de temperatura, o de cambiar su temperatura bajo una variación de su polarización.

La calorimetría fotopiroeléctrica *ac*, especialmente en su configuración trasera, es una técnica fototérmica ampliamente reconocida para la obtención de propiedades térmicas y, particularmente, para el estudio del comportamiento crítico delas transiciones de fase, el cual es uno de nuestros objetivos. Esta técnica presenta varias ventajas respecto a otras, como pueden ser su gran sensibilidad y resolución. Esto nos permiten realizar medidas muy precisas con variaciones de temperatura del orden de 10 mK/min y gradientes de tem-

peratura minúsculos que producen un ratio de señal-ruido muy bueno, asegurando el equilibrio térmico de la muestra durante toda la medida. La calorimetría PPE también nos permite extraer diversas propiedades térmicas simultáneamente. Mediante esta técnica podemos determinar directamente tanto la difusividad como la efusividad térmica, a partir de las cuales (utilizando relaciones termodinámicas) podemos obtener el calor específico y la conductividad térmica. El comportamiento crítico de estos parámetros térmicos, en la región próxima a las transiciones de fase, arrojará algo de luz sobre la estructura magnética y las interacciones de los materiales estudiados, permitiéndonos profundizar en la física subyacente del sistema.

Por su parte, el efecto magnetocalórico, MCE por sus siglas en inglés, es una propiedad intrínseca de todos los materiales magnéticos. Se define como un cambio adiabático (sin intercambio de calor) de la temperatura (ΔT_{ad}) cuando se aplica un campo magnético al material, es decir, el material se calienta o se enfría con la aplicación o retirada de un campo magnético externo. Alternativamente, también puede definirse como un cambio isotérmico (temperatura constante) de la entropía magnética (ΔS_M). Este efecto fue teorizado por primera vez en 1878 de la mano de Thomson, sin embargo, no fue descubierto experimentalmente hasta 1917, cuando Weiss y Piccard consiguieron medir un cambio de 0.7 K en el níquel tras la aplicación de un campo magnético de 1.5 T. La historia del efecto magnetocalórico ha vivido grandes hitos, pero fue en 1997 cuando, tras el descubrimiento del efecto magnetocalórico "gigante" y el desarrollo del primer modelo de refrigerador magnético a temperatura ambiente, el interés por este campo comenzó su ascenso exponencial.

Las aplicaciones del efecto magnetocalórico son muy diversas, van desde las nano-tecnologías mas punteras, pasando por la industria aero-espacial hasta el campo de la medicina. Sin embargo, su gran nicho de mercado se centra principalmente en su aplicación como refrigeradores magnéticos.

La teoría de las transiciones de fase y su comportamiento crítico conforman un enorme campo de investigación que permanece abierto en la actualidad y que, desde sus inicios, ha despertado el interés de científicos tanto teóricos como experimentales de todo el mundo. En particular, la hipótesis del escalado dentro del marco de la teoría de grupos de renormalización asegura que; el comportamiento crítico de las transiciones de fase de segundo orden en las proximidades de la temperatura crítica (T_C) se caracteriza por un conjunto de exponentes críticos asociados a diferentes propiedades térmicas y magnéticas, como pueden ser: el calor específico ($c_p(T) \sim A^{\pm}|t|^{-\alpha}$, con $t = (T - T_C)/T_C$), la magnetización espontanea ($M_S(T) \sim |t|^{\beta}$), el inverso de la susceptibilidad magnética inicial ($\chi_0^{-1}(T) \sim |t|^{\gamma}$), o la isoterma crítica ($M(H) \sim H^{1/\delta}$).

Lo interesante de los exponentes críticos es que toman valores diferentes para distintos modelos o clases de universalidad y, por lo tanto, la obtención de un conjunto de valores de esos exponentes críticos para un determinado material nos permite atribuir una clase de universalidad a una determinada transición de fase de segundo orden, lo que da una idea de la física subyacente en el sistema, así como del papel que pueden desempeñar otros mecanismos si los parámetros críticos obtenidos no coinciden exactamente con una de las clases (efecto de las interacciones espín-órbita, desorden, interacciones dipolares de

largo alcance, etc). Aparte de esto, ciertas propiedades magnetocalóricas obedecen leyes de escalado relacionadas con los exponentes críticos, permitiendo extrapolar los datos a valores de campo magnético y temperatura no accesibles experimentalmente.

Los resultados experimentales se centran en el caso particular de los compuestos intermetálicos basados en tierras raras. Nuestro interés en estos materiales proviene de su complejidad magnética, la cual provoca comportamientos no observados en otros materiales. El magnetismo de las tierras raras se rige por las interacciones de intercambio indirecto entre los orbitales *4f* internos, mediadas por la polarización de los electrones de conducción. El mecanismo preciso viene descrito por la interacción de intercambio de largo alcance Ruderman-Kittel-Kasuya-Yosida (RKKY). Sin entrar en más detalles, esto da lugar a complejas estructuras magnéticas helicoidales, cónicas y de onda longitudinal que se pueden observar en las tierras raras [1–3]. Cuando este peculiar comportamiento se mezcla con otros metales para formar compuestos intermetálicos, la complejidad del sistema aumenta y aparecen nuevos fenómenos magnéticos. Esto se ha explorado a lo largo de este trabajo a través del estudio de diferentes familias intermetálicas.

Esta tesis abarca cinco grandes familias de materiales intermetálicos, cada una de las cuales se recoge en un capítulo independiente en el que se presenta su interés, las técnicas experimentales, los análisis realizados y, obviamente, la correspondiente discusión sobre los resultados obtenidos. Aunque se han realizado estudios adicionales en algunos de los compuestos, todos los capítulos experimentales tendrán apartados específicos centrados en el comportamiento crítico de sus transiciones de fase magnéticas y en la evaluación de su efecto magnetocalórico, explorando el potencial de ambos análisis. Uno de nuestros objetivos a través de este estudio es observar el efecto que la sustitución de diferentes elementos (tierras raras especialmente, pero no exclusivamente) tiene sobre las propiedades de los compuestos, y más concretamente, cómo esto afecta al comportamiento crítico o cómo estas sustituciones pueden ser utilizadas para potenciar y afinar el efecto magnetocalórico dentro de una misma familia intermetálica. Teniendo esto en cuenta, hemos evaluado el comportamiento magnetocalórico de nuestros compuestos, y discutido el comportamiento crítico de sus transiciones de fase magnéticas de segundo orden. Para esto último, se han empleado técnicas magnéticas y térmicas con el objetivo de obtener los exponentes críticos asociados a diferentes propiedades físicas (α, β, γ, δ).

La familias intermetálicas estudiadas son: RTX, R_3CoNi, R_3T y R_6TX_2, siendo R una tierra rara, T un metal de transición y X un elemento del bloque *p*. Ademas se incluye parte del trabajo realizado durante una estancia de 3 meses en el *Institut de Chimie et des Matériaux Paris Est* en Thiais (Francia), donde, entre otras cosas, tuve la oportunidad de estudiar las propiedades del $Y_{0.9}Pr_{0.1}Fe_2D_{3.5}$, un compuesto intermetálico de la familia RFe_2 (fase de *Laves*). El trabajo realizado para cada familia se resume a continuación.

∘ **Intermetálicos RTX:** Se ha obtenido la difusividad térmica en un amplio rango de temperaturas para los compuestos con R = Pr, Nd y Gd. Los valores

resultantes de *D* alrededor de las regiones de transición son elevados en comparación con los valores de difusividad térmica de materiales magnetocalóricos que se pueden encontrar en la literatura, lo que hace que estos materiales sean interesantes desde el punto de vista de su aplicación. El comportamiento crítico de los cuatro compuestos basados en Gd se ha estudiado mediante técnicas calorimétricas y magnéticas. También se estudió el efecto magnetocalórico de los compuestos basados en Nd y Gd. Estos últimos presentan propiedades magnetocalóricas altamente competitivas por encima de 300 K, mientras que los primeros tienen valores medios de cambio de entropía magnética y modestas capacidades refrigerantes en el rango 170-190 K. Se han comprobado satisfactoriamente las relaciones de escalado magnetocalórico y se han construido las *"curvas maestras"* para las diferentes clases de universalidad a las que pertenecen estos materiales.

∘ **Intermetálicos R_3CoNi:** Se han sintetizado por primera vez cuatro miembros de la familia R_3CoNi (con R = Dy, Ho, Er, Tm) y se ha comprobado que su estructura cristalina concuerda con la estructura romboédrica de tipo Er_3Ni_2, al igual que la del Tb_3CoNi (previamente reportada), que también se ha estudiado en este trabajo. El ordenamiento magnético desde un estado PM hacia un estado FM tiene lugar en el rango 96-6 K, con la temperatura critica decreciendo con el aumento del número atómico de la tierra rara. Se ha observado que algunas de estas muestras contienen más transiciones de reorientación de espín a temperaturas más bajas. El comportamiento crítico de las transiciones magnéticas PM-FM también ha sido estudiado. Para ello se ha hecho uso del calor específico y de las propiedades magnéticas. Las propiedades magnetocalóricas de esta familia han resultado ser muy prometedoras para aplicaciones de crio-refrigeración en la región de licuefacción de gases.

∘ **Intermetálicos R_3T:** Los tres miembros de la familia R_3T que han sido estudiados (Dy_3Co, Tb_3Co y Tb_3Ni) se han crecido en forma de monocristales. El estudio del comportamiento critico se ha llevado a cabo mediante la difusividad térmica en el caso de Tb_3Co, y mediante el calor específico en el caso de Tb_3Ni, sin embargo, tanto la difusividad térmica, como el calor específico y la conductividad térmica han sido empleados en el caso de Dy_3Co. Se han utilizado diferentes técnicas para resolver de una vez por todas el carácter de la transición magnética de más baja temperatura del Tb_3Co, estableciéndose como débilmente de primer orden. Además, se ha realizado un análisis de difracción de neutrones para dicha muestra. También, se ha discutido la compleja estructura magnética del Tb_3Ni y se ha obtenido su efecto magnetocalórico, así como el del Tb_3Co. Ambos materiales muestran relevantes propiedades magnetocalóricas potenciadas por sus transiciones metamagnéticas, lo que los hace muy interesantes para la refrigeración magnética en el rango de la licuefacción de gases. El Tb_3Ni presenta un gran efecto magnetocalórico inverso seguido de un gran efecto directo, además, posee una gran anisotropía magnética que se traduce en un prometedor efecto magnetocalórico rotatorio.

◦ **Intermetálicos R_6TX_2:** Se han estudiado tres *"sub-familias"* (15 compuestos en total) de la gran familia R_6TX_2: Ho_6(Fe, Mn)Bi_2, (Gd, Tb)$_6$(Fe, Mn)Bi_2, y Dy_6(Fe, Mn)X_2. Lo que hace interesantes a estos compuestos es, por un lado, la posibilidad de modificar su temperatura de transición jugando con su estequiometría y, por otro lado, la amplia región de trabajo en forma de *plateau* creada por la existencia de dos transiciones magnéticas consecutivas (excepto en el caso de Gd_6FeBi_2). El comportamiento crítico de la transición PM-FM de estas muestras se ha estudiado mediante técnicas magnéticas, y en el caso de la familia (Gd, Tb)$_6$(Fe, Mn)Bi_2 también mediante técnicas térmicas. El efecto magnetocalórico directo de tipo tabla, causado por la superposición de la transición PM-FM y la transición de reorientación de espín a menor temperatura, puede adaptarse para trabajar en muchas regiones de temperatura, incluida la temperatura ambiente. En algunas de las muestras también se observa un interesante efecto magnetocalórico inverso a bajas temperaturas. Finalmente, los valores de difusividad térmica en la región de trabajo de la familia Dy_6(Fe, Mn)X_2 muestran valores lo suficientemente altos como para considerar su aplicación.

◦ **Intermetálico de fase de Laves $Y_{0.9}Pr_{0.1}Fe_2D_{3.5}$:** Este compuesto presenta una transición estructural de tipo orden-desorden a 346 K y una transición de ordenación FM a $T_C = 274$ K. Se han utilizado tres técnicas de difracción, incluyendo la difracción de neutrones y los rayos X, para estudiar la evolución de la estructura cristalina con la temperatura, encontrando una transición de una estructura monoclínica a una pseudocúbica al aumentar la temperatura. El comportamiento crítico de la transición magnética ha sido estudiado y se ha obtenido el efecto magnetocalórico, el cual se encuentra cercano a la temperatura ambiente. Finalmente se han comprobado con éxito las relaciones de escalado magnetocalóricas y se han construido las curvas de universalidad.

Publications

This thesis has resulted in the following scientific contributions.

Refereed contributions

1. **A. Herrero**, A. Oleaga, A. Salazar, A.F. Gubkin, N.V. Baranov, *Critical behavior of magnetic transitions in Dy_3Co single crystal*, J. Alloys Compd. 741 (2018) 1163-1168

2. **A. Herrero**, A. Oleaga, P. Manfrinetti, A. Provino, A. Salazar, *Critical behavior of the ferromagnetic transition in GdSc(Si,Ge) intermetallic compounds*, Intermetallics 101 (2018) 64-71

3. **A. Herrero**, A. Oleaga, A. Provino, P. Manfrinetti, A. Salazar, *Study of the magnetocaloric effect in intermetallics RTX (R = Nd, Gd; T = Sc, Ti; X = Si, Ge)*, Intermetallics 110 (2019) 106495

4. **A. Herrero**, A. Oleaga, A.F. Gubkin, M.D. Frontzek, A. Salazar, N.V. Baranov, *Comprehensive study of the magnetic phase transitions in Tb_3Co combining thermal, magnetic and neutron diffraction measurements*, Intermetallics 111 (2019) 106519

5. **A. Herrero**, A. Oleaga, A.F. Gubkin, A. Salazar, N.V. Baranov, *Peculiar magnetocaloric properties and critical behavior in antiferromagnetic Tb_3Ni with complex magnetic structure*, J. Alloys Compd. 808 (2019) 151720

6. **A. Herrero**, A. Oleaga, A. Salazar, A.V. Garshev, V.O. Yapaskurt, A.V. Morozkin, *Magnetocaloric properties, magnetic interactions and critical behavior in $Ho_6(Fe,Mn)Bi_2$ intermetallics*, J. Alloys Compd. 821 (2020) 153198

7. A. Oleaga, **A. Herrero**, A. Salazar, A.V. Garshev, V.O. Yapaskurt, A.V. Morozkin, *Magnetocaloric properties and unconventional critical behavior in $(Gd,Tb)_6(Fe,Mn)Bi_2$ intermetallics*, J. Alloys Compd. 843 (2020) 155937

8. **A. Herrero**, A. Oleaga, A. Provino, I.R. Aseguinolaza, A. Salazar, D. Peddis, P. Manfrinetti, *Crystallographic, magnetic and magnetocaloric properties in novel intermetallic materials R_3CoNi (R = Tb, Dy, Ho, Er, Tm, Lu)*, J. Alloys Compd. 865 (2021) 158948

9. V. Paul-Boncour, **A. Herrero**, V. Shtender, K. Provost, E. Elkaim, *Magnetic transitions with magnetocaloric effects near room temperature related*

to structural transitions in $Y_{0.9}Pr_{0.1}Fe_2D_{3.5}$ deuteride, J. Appl. Phys. 130 (2021) 113904

10. **A. Herrero**, A. Oleaga, I.R. Aseguinolaza, A. Garcia-Adeva, E. Apiñaniz, A.V. Garshev, V.O. Yapaskurt, A.V. Morozkin, *Tailoring the magnetocaloric, magnetic and thermal properties of Dy_6(Fe,Mn)X_2 intermetallics (X = Sb, Te, Bi)*, J. Alloys Compd. 890 (2022) 161849

Congress contributions

Oral communications:

1. A. Oleaga, **A. Herrero**, P. Manfrinetti, A. Provino, A. Salazar, *Thermal Diffusivity and Critical Behavior of RSc(Si, Ge) (R = rare earth) Intermetallic Compounds*, Twentieth Symposium on Thermophysical Properties, Boulder (Colorado), United States of America (2018)

2. **A. Herrero**, A. Oleaga, A. Salazar, A. Gubkin, N.V. Baranov, *Critical Behavior Study of the Magnetic Transitions in R_3Co (R = Rare Earth) by Means of Ac Photopyroelectric Calorimetry*, Twentieth Symposium on Thermophysical Properties, Boulder (Colorado), United States of America (2018)

3. **A. Herrero**, A. Oleaga, A. Salazar, A. Gubkin, N.V. Baranov, *ac photopyroelectric calorimetry applied to the study of critical behavior of magnetic transitions in R_3Co single crystals (R = rare earth)*, International School Of Quantum Electronics 62nd Course Progress in Photoacoustic & Photothermal Phenomena Focus on Biomedical, Nanoscale, NDE and Thermophysical Phenomena and Technologies, Erice (Sicily), Italy (2018)

4. **A. Herrero**, A. Oleaga, A. Salazar, A. Gubkin, N.V. Baranov, *Critical behavior of the antiferromagnetic transitions in intermetallics R_3T (R = Dy, Tb,T = Co, Ni)*, 2019 Joint MMM-Intermag, Washington DC, United States of America (2019)

5. **A. Herrero**, A. Herrero, A. Oleaga, P. Manfrinetti, A. Provino, A. Salazar, *Critical behavior and magnetocaloric effect in GdSc(Si,Ge) intermetallics*, 2019 Joint MMM-Intermag, Washington DC, United States of America (2019)

6. **A. Herrero**, A. Oleaga, P. Manfrinetti, A. Provino, A. Salazar, *ac photopyroelectric calorimetry applied to the study of the critical behavior of magnetic transitions in intermetallic materials*, 20-th International Conference on Photoacoustic and Photothermal Phenomena, Moscow, Russia (2019)

7. A. Oleaga, **A. Herrero**, A. Salazar, A.V. Garshev, A.V. Morozkin, V.O. Yapaskurt, *Tuning the magnetocaloric properties in (Gd,Tb)$_6$(Fe,Mn)Bi_2 intermetallics*, The 65th Annual Conference on Magnetism and Magnetic Materials, MMM (Virtual) (2020)

8. **A. Herrero**, A. Oleaga, I.R. Aseguinolaza, A. Salazar, A. Provino, P. Manfrinetti, *Structure, magnetocaloric properties and critical behavior in novel intermetallic materials R_3CoNi (R = Tb, Dy, Ho, Er, Tm, Lu)*, The 65th Annual Conference on Magnetism and Magnetic Materials, MMM (Virtual) (2020)

9. **A. Herrero**, A. Oleaga, A. Gubkin, A. Salazar, N.V. Baranov, *Direct and inverse magnetocaloric effects in antiferromagnetic Tb_3Ni*, The Joint European Magnetic Symposia, JEMS (Virtual) (2020)

10. **A. Herrero**, A. Oleaga, A. Salazar, A.V. Garshev, V.O. Yapaskurt, A.V. Morozkin, *Magnetocaloric properties and magnetic interactions in $Ho_6(Fe, Mn)Bi_2$ intermetallics*, The Joint European Magnetic Symposia, JEMS (Virtual) (2020)

11. **A. Herrero**, A. Oleaga, A. Salazar, A.V. Knotko, V.O. Yapaskurt, A.V. Morozkin, *Wide-range magnetocaloric properties of $(Gd, Tb)_6(Fe, Mn)Bi_2$*, THERMAG IX 2021: 9th IIR International Conference on Caloric Cooling and Applications of Caloric Materials, (Virtual) (2021)

Invited talks:

1. P. Manfrinetti, **A. Herrero**, A. Oleaga, I.R. Aseguinolaza, A. Salazar, C. Ritter, A. Provino, D. Peddis, *Structure, magnetic and magnetocaloric properties in new R_3CoNi intermetallics (R = Tb, Dy, Ho, Er, Tm)*, Muroran-IT Rare Earth Workshop (Virtual) (2020)

Bibliography

[1] J. Jensen, A.R. Mackintosh, *Rare Earth Magnetism: Structures and Excitations*, Clarendon Press, Oxford, 1991

[2] K.A. McEwen, *Chapter 6 Magnetic and transport properties of the rare earths*, Handbook on the Physics and Chemistry of Rare Earths 1 (1978) 411-488

[3] K.N.R. Taylor, *Intermetallic rare-earth compounds*, Adv. Phys. 20 (1971) 551-660

[4] D.P. Almond, P.M. Patel, *Photothermal Science and Techniques*, Chapman & Hall, London (1996)

[5] H.S. Carslaw, J.C. Jaeger, *Conduction of Heat in Solids*, Oxford University Press (1959)

[6] A. Salazar, *On thermal diffusivity*, Eur. J. Phys. 24 (2003) 351-358

[7] J.F. Nye, *Physical Properties of Crystals: Their Representation by Tensors and Matrices*, Claredon Press (1960)

[8] H.B.G. Casimir, *On Onsanger's Principle of Microscopic Reversibility*, Rev. Mod. Phys. 17 (1945) 343

[9] E. Marin, *The role of thermal properties in periodic time-varying phenomena*, Eur. J. Phys. 28 (2007) 429-445

[10] P.M. Morse, H. Feshbach, *Methods of theoretical physics*, McGraw-Hill, New York (1953)

[11] W.M. Rohscnow, J.P. Hartnett, *Handbook of Heat Transfer*, McGraw-Hill, New York (1973)

[12] A. Salazar, *Energy propagation of thermal waves*, Eur. J. Phys. 27 (2006) 1349-1355

[13] A. Mandelis, *Photothermal applications to the thermal analysis of solids*, J. Therm. Anal. 37 (1991) 1065-1101

[14] H. Vargas, L.C.M. Miranda, *Photoacoustic and related photothermal techniques*, Phys. Rep. 161 (1988) 43-101

[15] C. Glorieux, J. Thoen, G. Bednarz, M.A. White, D.J.W. Geldart, *Photoacoustic investigation of the temperature and magnetic-field dependence of the specific-heat capacity and thermal conductivity near the Curie point of gadolinium*, Phys. Rev. B 52 (1995) 12770-12778

[16] M. Marinelli, F. Mercuri, D.P. Belanger, *Specific heat, thermal diffusivity, and thermal conductivity of FeF_2 at the Néel temperature*, Phys. Rev. B 51 (1995) 8897-8903

[17] M. Marinelli, F. Mercuri, S. Foglietta, D.P. Belanger, *Effect of spin-system fluctuations on heat transport in close to the Néel temperature*, Phys. Rev. B 54 (1996) 4087-4092

[18] M. Massot, A. Oleaga, A. Salazar, D. Prabhakaran, M. Martin, P. Berthet, G. Dhalenne,*Critical behavior of CoO and NiO from specific heat, thermal conductivity, and thermal diffusivity measurements*, Phys. Rev. B 77 (2008) 134438

[19] A. Oleaga, A. Salazar, D. Prabhakaran, J.G. Cheng, J.S. Zhou, *Critical behavior of the paramagnetic to antiferromagnetic transition in orthorhombic and hexagonal phases of $RMnO_3$ (R=Sm, Tb, Dy, Ho, Er, Tm, Yb, Lu, Y)*, Phys. Rev. B 85 (2012) 184425

[20] A. Oleaga, V. Shvalya, A. Salazar, I. Stoika, Yu.M. Vysochanskii, *In search of a tricritical Lifshitz point in $Sn_2P_2(S_{1-x}Se_x)_6$ doped with Pb, Ge: A critical behavior study*, J. Alloys Compd. 694 (2017) 808-814

[21] A. Oleaga, V. Shvalya, V. Liubachko, G. Balakrishnan, L.D. Tung, A. Salazar, *Critical behavior study of the spin ordering transition in RVO3 (R = Ce, Pr, Nd, Sm, Gd, Er) by means of ac photopyroelectric calorimetry*, J. Alloys Compd. 703 (2017) 210-215

[22] A. Oleaga, A. Salazar, D. Skrzypek, *Critical behaviour of magnetic transitions in $KCoF_3$ and $KNiF_3$ perovskites*, J. Alloys Compd. 629 (2015) 178-183

[23] U. Zammit, S. Paoloni, F. Mercuri, M. Marinelli, F. Scudieri, *Self consistently calibrated photopyroelectric calorimeter for the high resolution simultaneous absolute measurement of the specific heat and of the thermal conductivity*, AIP Adv. 2 (2012) 012135
[24] U. Zammit, F. Mercuri, S. Paoloni, M. Marinelli, R. Pizzoferrato, *Simultaneous absolute measurements of the thermal diffusivity and the thermal effusivity in solids and liquids using photopyroelectric calorimetry*, J. Appl. Phys. 117 (2015) 105104
[25] M. Marinelli, U. Zammit, F. Mercuri, R. Pizzoferrato, *High-resolution simultaneous photothermal measurements of thermal parameters at a phase transition with the photopyroelectric technique*, J. Appl. Phys. 72 (1992) 1096
[26] S.B. Lang, *Pyroelectricity: From ancient curiosity to modern imaging tool*, Physics Today 58 (2005)
[27] U. Zammit, M. Marinelli, F. Mercuri, S. Paoloni, F. Scudieri, *Invited review article: Photopyroelectric calorimenter for the simultaneous thermal, optical, and structural characterization of samples over phase transitions*, Rev. Scient. Inst. 82 (2011) 121101
[28] M. Chirtoc, G. Mihilescu, *Theory of the photopyroelectric method for investigation of optical and thermal materials properties*, Phys. Rev. B 40 (1989) 9606
[29] A. Mandelis, M.M. Zver, *Theory of photopyroelectric spectroscopy of solids*, J. Appl. Phys. 57 (1985) 4421
[30] S. Delenclos, M. Chirtoc, A.H. Sahraoui, C. Kolinsky, J.M. Buisine, *Assessment of calibration procedures for accurate determination of thermal parameters of liquids and their temperature dependence using the photopyroelectric method*, Rev. Sci. Instrum. 73 (2002) 2773
[31] A. Salazar, *On the influence of the coupling fluid in photopyroelectric measurements*, Rev. Sci. Instrum. 74 (2003) 825
[32] A. Salazar, A. Oleaga, *Overcoming the influence of the coupling fluid in photopyroelectric measurements of solid samples*, Rev. Sci. Instrum. 83 (2012) 014903
[33] A. Salazar, A. Oleaga, *A New Method to Overcome the Underestimation of the Thermal Diffusivity of Solid Samples Induced by the Coupling Fluid in Photopyroelectric Measurements*, Int. J. Thermophys. 33 (2012) 1901-1907
[34] A. Salazar, A. Oleaga, *On the piezoelectric contribution to the photopyroelectric signal*, Rev. Sci. Instrum. 76 (2005) 034901
[35] J.R. Reitz, F.J. Milford, *Foundations of electromagnetic theory*, Addison-Wesley Publishing company, INC (1960)
[36] J.M.D. Coey, *Magnetism and Magnetic Materials*, Cambridge University Press (2009)
[37] A. Yoshimori, *A New Type of Antiferromagnetic Structure in the Rutile Type Crystal*, J. Phys. Soc. Jpn. 14 (1959) 807-821
[38] M. Uchida, Y. Onose, Y. Matsui, Y. Tokura, *Real-Space Observation of Helical Spin Order*, Science 311 (2006) 359-361
[39] H. Kawamura, *Critical properties of helical magnets and triangular antiferromagnets*, J. Appl. Phys. 63 (1988) 3086
[40] N.W. Ashcroft, N.D. Mermin, *Solid State Physics*, Cornell University (1976)
[41] M.A. Ruderman, C. Kittel, *Indirect Exchange Coupling of Nuclear Magnetic Moments by Conduction Electrons*, Phys. Rev. 96 (1954) 99
[42] T. Kasuya, *A Theory of Metallic Ferro- and Antiferromagnetism on Zener's Model*, Progr. Theor. Phys. 16 (1956) 45-57
[43] K. Yosida, *Magnetic Properties of Cu-Mn Alloys*, Phys. Rev. 106 (1957) 893
[44] V. Paul-Boncour, M. Guillot, O. Isnard, A. Hoser, *High field induced magnetic transitions in the $Y_{0.7}Er_{0.3}Fe_2D_{4.2}$ deuteride*, Phys. Rev. B 96 (2017) 104440
[45] M. Bałanda, *AC susceptibility studies of phase transitions and magnetic relaxation: conventional, molecular and low-dimensional magnets*, Acta Phys. Pol. 124 (2013) 964-976
[46] N.V. Baranov, N.V. Mushnikov, T. Goto, Y. Hosokoshi, K. Inoue, *Slow dynamics of the magnetization in the ordered state of molecule based magnets with one-dimensional chain structure*, J. Phys.: Condens. Matter 15 (2003) 8881-8897
[47] W. Jiang, X.Z. Zhou, G. Williams, Y. Mukovskii, K. Glazyrin, *Critical behavior and transport properties of single crustal $Pr_{1-x}Ca_xMnO_3$*, Phys. Rev. B 78 (2008) 144409
[48] W. Jiang, X.Z. Zhou, G. Williams, Y. Mukovskii, K. Glazyrin, *Griffiths phase and critical behavior in single-crystal $La_{0.7}Ba_{0.3}MnO_3$: Phase diagram for $La_{1-x}Ba_xMnO_3$ ($x \leqslant 0.33$)*, Phys. Rev. B 77 (2008) 064424

[49] W. Jiang, X.Z. Zhou, G. Williams, Y. Mukovskii, K. Glazyrin, *Magnetic ground state and two-dimensional behavior in pseudo-kagome layered system $Cu_3Bi(SeO_3)_2O_2Br$*, Phys. Rev. B 78 (2008) 144409

[50] W. Thomson, *II. On the thermoelastic, thermomagnetic, and pyroelectric properties of matter*, Lond. Edingurgh Dublin Philos. Mag. J. Sci. 5 (1878) 4-27

[51] A.M. Tishin, K.A. Gschneidner, V.K. Pecharsky, *Magnetocaloric effect and heat capacity in the phase-transition region*, Phys. Rev. B 59 (1999) 503-511

[52] V.K. Pecharsky, K.A. Gschneidner Jr., *Magnetocaloric effect and magnetic refrigeration*, J. Magn. Magn. Mater. 200 (1999) 44-56

[53] K.A. Gschneidner, V.K. Pecharsky, *Magnetic refrigeration materials (invited)*, J. Appl. Phys. 85 (1999) 5365-5368

[54] E. Warburg, *Magnetische Untersuchungen*, Ann. Phys. 249 (1881) 141-164

[55] P. Weiss, A. Piccard, *Sur un nouveau phénomène magnétocalorique*, Comptes Rendus (1918) 352-354

[56] P. Debye, *Einige Bemerkungen zur Magnetisierung bei tiefer Temperatur*, Ann. Phys. 81 (1926) 1154-1160

[57] W.F. Giauque, *A thermodynamic treatment of certain magnetic effects. a proposed method of producing temperatures considerably below 1° absolute*, J. Am. Chem. Soc. 49 (1927) 1864–1870

[58] W.F. Giauque, D. P. MacDougall, *Attainment of Temperatures Below 1° Absolute by Demagnetization of $Gd_2(SO_4)_3{\cdot}8H_2O$*, Phys. Rev. 43 (1933) 768

[59] G. V. Brown, *Magnetic heat pumping near room temperature*, J. Appl. Phys. 47 (1976) 3673

[60] V.K. Pecharsky, K.A. Gschneidner, *Giant magnetocaloric effect in $Gd_5(Si_2Ge_2)$*, Phys. Rev. Lett. 78 (1997) 4494-4497

[61] O. Tegus, E. Brück, K.H.J. Buschow, F.R. de Boer, *Transition-metal-based magnetic refrigerants for room-temperature applications*, Nature 415 (2002) 150-152

[62] Z.B. Guo, Y.W. Du, J.S. Zhu, H. Huang, W.P. Ding, D. Feng, *Large magnetic entropy change in perovskite-type manganese oxides*, Phys. Rev. Lett. 78 (1997) 1142-1145

[63] N. Raghu Ram, M. Prakash, U. Naresh, N. Suresh Kumar, T. Sofi Sarmash, T. Subbarao, R. Jeevan Kumar, G. Ranjith Kumar, K. Chandra Babu Naidu, *Review on Magnetocaloric Effect and Materials*, J Supercond. Nov. Magn. 31 (2018) 1971–1979

[64] M. Balli, S. Jandl, P. Fournier, A. Kedous-Lebouc, *Advanced materials for magnetic cooling: Fundamentals and practical aspects*, Appl. Phys. Rev. 4 (2017) 021305

[65] K.A. Gschneidner Jr., V.K. Pecharsky, A.O. Tsokol, *Recent developments in magnetocaloric materials*, Rep. Prog. Phys. 68 (2005) 1479-1539

[66] V. Franco, J.S. Blázquez, B. Ingale, A. Conde, *The magnetocaloric effect and magnetic refrigeration near room temperature: Materials and Models*, Annu. Rev. Mater. Res. 42 (2012) 305-342

[67] T. Krenke, E. Duman, M. Acet, E.F. Wassermann, X. Moya, L. Mañosa, A. Planes, *Inverse magnetocaloric effect in ferromagnetic Ni-Mn-Sn alloys*, Nat. Mater. 4 (2005) 450-454

[68] F. Hu, B. Shen, J. Sun, *Magnetic entropy change in $Ni_{51.5}Mn_{22.7}Ga_{25.8}$ alloy*, Appl. Phys. Lett. 76 (2000) 3460-3462

[69] O. Gutfleisch, M.A. Willard, E. Brück, C.H. Chen, S.G. Sankar, J.P. Liu, *Magnetic Materials and Devices for the 21st Century: Stronger, Lighter, and More Energy Efficient*, Adv. Mater. 23 (2011) 821-842

[70] V. Chaudhary, X. Chen, R.V. Ramanujan, *Iron and manganese based magnetocaloric materials for near room temperature thermal management*, Progress in Materials Science 100 (2019) 64-98

[71] A. Fujita, S. Fujieda, Y. Hasegawa, K. Fukamichi, *Intinerant-electron metamagnetic transition and large magnetocaloric effects in $La(Fe_xSi_{1-x})_{13}$ compounds and their hydrides*, Phys. Rev. B 67 (2003) 104416

[72] H. Wada, Y. Tanabe, *Giant magnetocaloric effect of $MnAs_{1-x}Sb_x$*, Appl. Phys. Lett. 79 (2001) 3302-3304

[73] F. Chen, J.L. Sanchez Llamazares, C.F. Sanchez-Valdes, F. Chen, Z. Li, Y.X. Tong, L. Li, *Large magnetic entropy change and refrigeration capacity around room temperature in quinary $Ni_{41}Co_{9-x}Fe_xMn_{40}Sn_{10}$ alloys (x = 2.0 and 2.5)*, J. Alloys Compd. 825 (2020) 154053

[74] B.G. Shen, J.R. Sun, F.X. Hu, H.W. Zhang, Z.H. Cheng, *Recent Progress in Exploring Magnetocaloric Materials*, Adv. Mater. 21 (2009) 4545-4564

[75] R. Gimaev, D. Kopeliovich, Y. Spichkin, A. Tishin, *Measurements of the magnetic and magnetothermal properties of heavy rare earths*, J. Magn. Magn. Mater. 459 (2018) 215-220

[76] S. Couillaud, E. Gaudin, V. Franco, A. Conde, R. Pöttgen, B. Heying, U.Ch Rodewald, B. Chevalier, *The magnetocaloric properties of GdScSi and GdScGe*, Intermetallics 19 (2011) 1573-1578

[77] S.K. Tripathy, K.G. Suresh, A.K. Nigam, *A comparative study of the magnetocaloric effect in Gd_3Co and Gd_3Ni*, J. Magn. Magn. Mater. 306 (2006) 24-29

[78] S. Gupta, K.G. Suresh, *Review on magnetic and related properties of RTX compounds*, J. Alloys Compd. 618 (2015) 562-606

[79] P. Kumar, N.K. Singh, A.K. Nayak, A. Haldar, K.G. Suresh, A.K. Nigam, *Large reversible magnetocaloric effect in Er_3Co compound*, J. Appl. Phys. 107 (2010) 09A932 (3 pp)

[80] J. Shen, J.L. Zhao, F.X. Hu, G.H. Rao, G.Y. Liu, J.F. Wu, Y.X. Li, J.R. Sun, B.G. Shen, *Magnetocaloric effect in antiferromagnetic Dy_3Co compound*, Appl. Phys. A 99 (2010) 853-858

[81] B. Li, J. Du, W.J. Ren, W.J. Hu, Q. Zhang, D. Li, Z.D. Zhang, *Large reversible magnetocaloric effect in Tb_3Co compound*, Appl. Phys. Lett. 92 (2008) 242504 (3 pp)

[82] Y. Zhang *Review of the structural, magnetic and magnetocaloric properties in ternary rare earth RE_2T_2X type intermetallic compounds*, J. Alloys Compd. 787 (2019) 1173-1186

[83] L. Li, M. Yan , *Recent progresses in exploring the rare earth based intermetallic compounds for cryogenic magnetic refrigeration*, J. Alloys Compd. 823 (2020) 153810

[84] L.W. Li, *Review of magnetic properties and magnetocaloric effect in the intermetallic compounds of rare earth with low boiling point metals*, Chin. Phys. B 25 (2016) 037502

[85] H. Zhang, Y.J. Sun, E. Niu, L.H. Yang, J. Shen, F.X. Hu, J.R. Sun, B.G. Shen, *Large magnetocaloric effects of RFeSi (R = Tb and Dy) compounds for magnetic refrigeration in nitrogen and natural gas liquefaction*, Appl. Phys. Lett. 103 (2013) 202412

[86] Niraj K. Singha, K.G. Suresha, A.K. Nigamb, S.K. Malikb, A.A. Coelhoc, S.Gama, *Itinerant electron metamagnetism and magnetocaloric effect in RCo_2-based Laves phase compounds*, J. Magn. Magn. Mater. 317 (2007) 68-79

[87] J.L. Sánchez Llamazares, P. Ibarra-Gaytán, C.F. Sánchez-Valdés, D. Ríos-Jara, P. Álvarez-Alonso, *Magnetocaloric effect in $ErNi_2$ melt-spun ribbons*, Journal of Rare Earths 38 (2020) 612-616

[88] Niraj K. Singha, K.G. Suresha, A.K. Nigam, *Itinerant electron metamagnetism and magnetocaloric effect in $Dy(Co,Si)_2$*, Solid State Comm. 127 (2003) 373-377

[89] H. Wada, Y. Tanabe, M. Shiga, H. Sugawara, H. Sato, *Magnetocaloric effects of Laves phase $Er(Co_{1-x}Ni_x)_2$ compounds*, J. Alloys Compd. 316 (2001) 245-249

[90] I. Tereshina, J. Cwik, E. Tereshina, G. Politova, G. Burkhanov, V. Chzhan, A. Ilyushin, M. Miller, A. Zaleski, K. Nenkov, L. Schultz, *Multifunctional Phenomena in Rare-Earth Intermetallic Compounds With a Laves Phase Structure: Giant Magnetostriction and Magnetocaloric Effect*, IEEE Trans. Magn. 50 (2014) 2504604

[91] V. Franco, J.S. Blázquez, J.J. Ipus, J.Y. Law, L.M. Moreno-Ramírez, A. Conde, *Magnetocaloric effect: from materials research to refrigeration devices*, Prog. Mater. Sci. 93 (2018) 112-232

[92] R. Gauß, G. Homm, O. Gutfleisch, *The Resource Basis of Magnetic Refrigeration*, Research and analysis 21 (2017) 1291-1300

[93] A.M. Tishin, Y.I. Spichkin, *The Magnetocaloric Effect and its Applications*, *Series in Condensed Matter Physics*, Institute of Physics Publishing, Bristol and Philadelphia (2003)

[94] A. Waske, M.E. Gruner, T. Gottschall, O. Gutfleisch, *Magnetocaloric materials for refrigeration near room temperature*, MRS Bulletin 43 (2018) 269-273

[95] O. Sari, M. Balli, *From conventional to magnetic refrigerator technology*, Int. J. Refrig. 37 (2014) 8-15

[96] A.M Tishin, Y.I. Spichkin, *Recent progress in magnetocaloric effect: Mechanisms and potential applications*, Int. J. Refrig. 37 (2014) 223-229

[97] J. Lyubina, *Magnetocaloric materials for energy efficient cooling*, J. Phys. D: Appl. Phys. 50 (2017) 053002

[98] T. Gotschall, K.P. Skokov, M. Fries, A. Taubel, I. Radulov, F. Scheibel, D. Benke, S. Riegg, O. Gutfleisch, *Making a cool choice: the materials library of magnetic refrigeration*, Adv. Energy Mater. 9 (2019) 1901322

[99] V.I. Zverev, A.M. Tishin, *Magnetocaloric effect: from theory to practice*, Physics Reports 489 (2010) 89–15

[100] E. Brück, *Developments in magnetocaloric refrigeration*, J. Phys. D: Appl. Phys. 38 (2005) R381-R391

[101] Z. Wei, A. Chak-Tong, D. You-Wei, *Review of magnetocaloric effect in perovskite-type oxides*, Chin. Phys. B 22 (2013) 057501

[102] N.A. de Oliveira, P.J. von Ranke, *Theoretical aspects of the magnetocaloric effect*, Physics Reports 489 (2010) 89–15

[103] S.C. Collins, F.J. Zimmerman, *Cyclic Adiabatic Demagnetization*, Phys. Rev. 90 (1953) 991

[104] C.V. Heer, C.B. Barnes, J.G. Daunt, *The Design and Operation of a Magnetic Refrigerator for Maintaining Temperatures below 1°K*, Rev. Sci. Instr. 25 (1954) 1088

[105] W.A. Steyert, *Stirling-cycle rotating magnetic refrigerators and heat engines for use near room temperature*, J. Appl. Phys. 49 (1978) 1216

[106] J.A. Barclay, W.A. Steyert, *Active magnetic regenerator*, U.S.Patent No. 4,332,135, June 1, 1982

[107] A. Greco, C. Aprea, A. Maiorino, C. Masselli, *A review of the state of the art of solid-state caloric cooling processes at room-temperature before 2019*, Int. J. Refrig. 106 (2019) 66-88

[108] H. Zhang, R. Gimaev, B. Kovalev, K. Kamilov, V. Zverev, *Review on the materials and devices for magnetic refrigeration in the temperature range of nitrogen and hydrogen liquefaction*, Phys. B Condens. Matter 558 (2019) 65-73

[109] A.M Tishin, Y.I. Spichkin, V.I. Zverev, P.W. Egolf, *A review and new perspectives for the magnetocaloric effect: New materials and local heating and cooling inside the human body*, Int. J. Refrig. 68 (2016) 177-186

[110] R.J. Joenk, *Adiabatic magnetization of antiferromagnets*, J. Appl. Phys. 34 (1963) 1097-1098

[111] P.J. von Ranke, V.K. Pecharsky, K.A. Gschneidner Jr., B.J. Korte, *Anomalous behavior of the magnetic entropy*, Phys. Rev. B 58 (1998) 14436-14441

[112] A. Kirste, M. von Ortenberg, A.A. Demidov, Z.A. Kazei, N.P. Kolmakova, V.V. Platonov, A.A. Sidorenko, O.M. Tatsenko, *Crossover in the Van Vleck paramagnet $TmPO_4$*, Physica B 336 (2003) 335-343

[113] Z.A. Kazei, V.V. Snegirev, J.-M. Broto, H. Rakoto, *Anomalous magnetocaloric effect in van vleck paramagnet $HoVO_4$ near energy level crossing*, JETP Lett. 87 (2008) 687-691

[114] P.J. von Ranke, N.A. de Oliveira, B.P Alho, E.J.R. Plaza, V.S.R. de Sousa, L. Caron, M.S. Reis, *Understanding the inverse magnetocaloric effect in antiferro- and ferrimagnetic arrangements*, J. Phys.: Condens. Matter 21 (2009) 056004

[115] T. Krenke, E. Duman, M. Acet, E.F. Wassermann, X. Moya, L. Mañosa, A. Planes, *Inverse magnetocaloric effect in ferromagnetic Ni-Mn-Sn alloys*, Nat. Mater. 4 (2005) 450-454

[116] A. Biswas, T. Samanta, S. Banerjee, I. Das, *Inverse magnetocaloric effect in polycrystalline $La_{0.125}Ca_{0.875}MnO_3$*, J. Phys. Condens. Matter 21 (2009) 506005

[117] L.V.B. Diop, O. Isnard, *Inverse and normal magnetocaloric effects in $LaFe_{12}B_6$*, J. Appl. Phys. 119 (2018) 213904

[118] J.Y. Law, V. Franco, A. Conde, S.J. Skinner, S.S. Pramana, *Modification of the order of the magnetic phase transition in cobaltites without changing their crystal space group*, J. Alloy. Comp. 777 (2019) 1080-1086

[119] K. Synoradzki, *Magnetocaloric effect in antiferromagnetic TmNiSn compound*, J. Magn. Magn. Mater. 482 (2019) 219-223

[120] C. Li, Y. Qiu, G.O. Barasa, S. Yuan, *Spin reorientation, normal and inverse magnetocaloric effects in heavy rare-earth iron garnets*, Ceramics International 46 (2020) 18758-18762

[121] V. Franco, A. Conde, J.M. Romero-Enrique, Y.I. Spichkin, V.I. Zverev, A.M. Tishin, *Field dependence of the adiabatic temperature change in second order phase transition materials: application to Gd*, J. Appl. Phys. 106 (2009) 103911

[122] J. Liu, T. Gottschall, K.P. Skokov, J.D. Moore, O. Gutfleisch, *Giant magnetocaloric effect driven by structural transitions*, Nat. Mater. 11 (2012) 620-626

[123] G. Green, J. Chafe, J. Stevens, J. Humphrey, *Gadolinium-terbium active regenerator*, Adv. Cryog. Eng. 35B (1990) 1165-1174

[124] H. Kato, K. Nara, M. Okaji, *Instrumentation for highly sensitive measurement of magnetocaloric effect: application to high T_C superconductors*, Cryogenics 31 (1991) 425-430

[125] W. Otowski, C. Glorieux, R. Hofman, J. Thoen, *New acoustic detection technique for a magnetocaloric effect*, Thermochim. Acta 218 (1993) 123-133

[126] B.R. Gopal, R. Chahine, M. Foeldeaki, T.K. Bose, *Noncontact thermoacoustic method to measure the magnetocaloric effect*, Rev. Sci. Instrum. 66 (1995) 232-238

[127] R.Z. Levitin, V.V. Snegirev, A.V. Kopylov, A.S. Lagutin, A. Gerber, *Magnetic method of magnetocaloric effect determination in high pulsed magnetic fields*, J. Magn. Magn. Mater. 170 (1997) 223-227

[128] B.R. Gopal, R. Chahine, T.K. Bose, *A sample translatory type insert for automated magnetocaloric effect measurements*, Rev. Sci. Instr. 68 (1997) 1818-1822

[129] S.Yu. Dan'kov, A.M. Tishin, V.K. Pecharsky, K.A. Gschneidner Jr., *Experimental device for studying the magnetocaloric effect in pulse magnetic fields*, Rev. Sci. Instrum. 68 (1997) 2432-2437

[130] K.A. Gschneidner, V.K. Pecharsky, *Magnetocaloric Materials*, Annu. Rev. Mater. Sci. 30 (2000) 387–429

[131] J.Y. Law, V. Franco, R.V. Ramanujan, *Direct magnetocaloric measurements of the Fe-B-Cr-X (X=La, ce) amorphous ribbons*, J. Appl. Phys. 110 (2011) 023907

[132] V.K. Pecharsky, K.A. Gschneidner, *Comparison of the Magnetocaloric Effect Derived from Heat Capacity, Direct, and Magnetization Measurements*, Adv. Cryog. Eng. 42 (1996) 423-430

[133] M. Földeàki, R. Chahine, T. K. Bose , *Magnetic measurements: A powerful tool in magnetic refrigerator design*, J. Appl. Phys. 77 (1995) 3528

[134] L.M. Moreno-Ramírez, J.S. Blázquez, J.Y. Law, V. Franco, A. Conde, *Optimal temperature range for determining magnetocaloric magnitudes from heat capacity*, J. Phys. D: Appl. Phys. 49 (2016) 495001

[135] Y. Hu, Y. Wang, Z- Li, X. Chi, Q. Lu, T. Hu, Y. Liu, A. Du, F. Shi, *Low-field magnetocaloric effect in single crystals controlled by magnetocrystalline anisotropy*, Appl. Phys. Lett. 113 (2018) 133902

[136] H. Neves-Bez, H. Yibole, A. Pathak, Y. Mudryk, V.K. Pecharsky, *Best practices in evaluation of the magnetocaloric effect from bulk magnetization measurements*, J. Magn. Magn. Mater. 458 (2018) 301-309

[137] L.M. Moreno-Ramírez, J.J. Ipus, V. Franco, J.S. Blázquez, A.Conde, *Analysis of magnetocaloric effect of ball milled amorphous alloys: Demagnetizing factor and Curie temperature distribution*, J. Alloy. Comp. 622 (2015) 606-609

[138] C. Romero-Muñiz, J.J. Ipus, J.S. Blázquez, V. Franco, A. Conde, *Influence of the demagnetizing factor on the magnetocaloric effect: Critical scaling and numerical simulations*, Appl. Phys. Lett. 104 (2014) 252405

[139] B. Schwarz, N. Mattern, J.D. Moore, K.P. Skokov, O. Gutfleisch, J. Eckert, *Influence of sample geometry on determination of magnetocaloric effect for $Gd_{60}Co_{30}Al_{10}$ glassy ribbons using direct and indirect methods*, J. Magn. Magn. Mater. 323 (2011) 1782-1786

[140] R. Caballero-Flores, V. Franco, A. Conde, L.F. Kiss, *Influence of the demagnetizing field on the determination of the magnetocaloric effect from magnetization curves*, J. Appl. Phys. 105 (2009) 07A919

[141] N.S. Bingham, H. Wang, F. Qin, H.X. Peng, J.F. Sun, V. Franco, H. Srikanth, M.H. Phan, *Excellent magnetocaloric properties of melt-extracted Gd-based amorphous microwires*, Appl. Phys. Lett. 101 (2012) 102407

[142] P. Álvarez-Alonso, P. Gorria, J. Sánchez-Marcos, J.L. Sánchez-Llamazares. J.A. Blanco, *The magnetocaloric effect in Er_2Fe_{17} near the magnetic phase transition*, J. Phys.: Condens. Matter 25 (2013) 496010

[143] A. de Campos, D.L. Rocco, A. Carvalho, G. Magnus, L. Caron, A.A. Coelho, S. Gama, L.M.D. Silva, F.C.G. Gandra, A.O.D. Santos, L.P. Cardoso, P.J. von Ranke, N.A. de Oliveira, *Ambient pressure colossal magnetocaloric effect tuned by composition in $Mn_{1-x}Fe_xAs$*, Nature Mater. 5 (2006) 802-804

[144] A. Giguère, M. Foldeaki, B. Ravi Gopal, R. Chahine, T. K. Bose, A. Frydman, J. A. Barclay, *Direct Measurement of the "Giant" Adiabatic Temperature Change in $Gd_5Si_2Ge_2$*, Phys. Rev. Lett. 83 (1999) 2262

[145] A.K. Pathak, I. Dubeko, S. Stadler, N. Ali, *The effect of partial substitution of In by Si on the phase transitions and respective magnetic entropy changes of $Ni_{50}Mn_{35}In_{15}$ Heusler alloy*, J. Phys. D: Appl. Phys. 41 (2008) 202004

[146] V.V. Khovaylo, K.P. Skokov, Y.S. Koshkid'ko, V.V. Koledov, V.G. Shavrov, V.D. Buchelnikov, S.V. Taskaev, H. Miki, T. Takagi, A.N. Vasiliev, *Adiabatic temperature change at first-order magnetic phase transitions: $Ni_{2.19}Mn_{0.81}Ga$ as a case study*, Phys. Rev. B 78 (2008) 060403

[147] A. Planes, L. Manosa, M. Acet, *Magnetocaloric effect and its relation to shape-memory properties in ferromagnetic Heusler alloys*, J. Phys.: Condens. Matter. 21 (2009) 233201

[148] H.W. Zhang, J. Shen, Q.Y. Dong, T.Y. Zhao, Y.X. Li, J.R. Sun, B.G. Shen, *The spike in the relation between entropy change and temperature in $LaFe_{11.83}Si_{1.17}$ compound*, J. Magn. Magn. Mater. 320 (2008) 1879-1883

[149] M. Balli, O. Sari, D. Fruchart, J. Forchelet, *Influence of the materials magnetic state on the accurate determination of the magnetocaloric effects*, EPJ Web of Conferences 29 (2012) 00005

[150] J.S. Amaral, V.S. Amaral, *On estimating the magnetocaloric effect from magnetization measurements*, J. Magn. Magn. Mater. 322 (2010) 1552-1557

[151] W. Cui, W. Liu, Z. Zhang, *The origin of the large overstimation of the magnetic entropy changes calculated directly by Maxwell relation*, Appl. Phys. Lett. 96 (2010) 222509

[152] G.J. Liu, J.R. Sun, J. Shen, B. gao, H.W. Zhang, F.X. Hu, B.G. Shen, *Determination of the entropy changes in the compounds with a first-order magnetic transition*, Appl. Phys. Lett. 90 (2007) 032507

[153] J.D. Zou, B.G. Shen, B. Gao, J. Shen, J.R. Sun, *The Magnetocaloric Effect of $LaFe_{11.6}Si_{1.4}$, $La_{0.8}Nd_{0.2}Fe_{11.5}Si_{1.5}$, and $Ni_{43}Mn_{46}Sn_{11}$ Compounds in the Vicinity of the First-Order Phase Transition*, Adv. Mater. 21 (2009) 693-696

[154] N.A. de Oliveira, P.J. von Ranke, *Magnetocaloric effect around a magnetic phase transition*, Phys. Rev. B 77 (2008) 214439

[155] M. Kataoka, *Ferromagnetic system with the first order transition and applicability of the Maxwell relation to its magnetocaloric effect*, J. Magn. Magn. Mater. 469 (2019) 494-503

[156] M. Balli, D. Fruchart, D. Gignoux, R. Zach, *The "colossal" magnetocaloric effect in $Mn_{1-x}Fe_xAs$: What are we really measuring?*, Appl. Phys. Lett. 95 (2009) 072509

[157] R. Caballero-Flores, N.S. Bingham, M.H. Phan, M.A. Torija, C. Leighton, V. Franco, A. Conde, T.L. Phan, S.C. Yu, H. Srikanth, *Magnetocaloric effect and critical behavior in $Pr_{0.5}Sr_{0.5}MnO_3$: an analysis of the validity of the Maxwell relation and the nature of the phase transitions*, J. Phys.: Condens. Matter 26 (2014) 286001

[158] F. Casanova, X. Batlle, A. Labarta, J. Marcos, L. Mañosa, A. Planes, *Entropy change and magnetocaloric effect in $Gd_5(Si_xGe_{1-x})_4$*, Phys. Rev. B 66 (2002) 100401(R)

[159] L. Caron, Z.Q. Ou, T.T. Nguyen, D.T. Cam Thanh, O. Tegus, E. Brück, *On the determination of the magnetic entropy change in materials with first-order transitions*, J. Magn. Magn. Mater. 321 (2009) 3559-3566

[160] V. Franco, *Determination of the magnetic entropy change from magnetic measurements: the importance of the measurement protocol*, http://www.lakeshore.com/products/Vibrating-Sample-Magnetometer/Pages/MCE.aspx (2014)

[161] V. Franco, J.Y. Law, A. Conde, V. Brabander, D.Y. Karpenkov, I. Radulov, K. Skokov, O. Gutfleisch, *Predicting the tricritical point composition of a series of LaFeSi magnetocaloric alloys via universal scaling*, J. Phys. D Appl. Phys. 50 (2017) 414004

[162] L. Tocado, E. Palacios, R. Burriel, *Entropy determinations and magnetocaloric parameters in systems with first-order transitions: Study of MnAs*, J. Appl. Phys. 105 (2009) 093918

[163] M.H. Phan, M.B. Morales, N.S. Bingham, H. Srikanth, *Phase coexistence and magnetocaloric effect in $La_{5/8-y}Pr_yCa_{3/8}MnO_3$ (y=0.275)*, Phys. Rev. B 81 (2010) 094413

[164] E.T. Dias, K.R. Priolkar, Ö. Çakir, M. Acet, A.K. Nigam, *Effect of composition on magnetocaloric properties of $Mn_3Ga_{(1-x)}Sn_xC$*, J. Appl. Phys. 117 (2015) 123901

[165] A. Biswas, N.S. Bingham, T.L. Phan, N.H. Dan, S.C. Yu, M.H. Phan, H. Srikanth, *Impacts of first-order phase transition and phase coexistence on the universal behavior of inverse magnetocaloric effect*, J. Appl. Phys. 115 (2014) 17A907

[166] M.K. Sharma, K. Mukherjee, *Magnetic and universal magnetocaloric behavior of rare-earth substituted* $DyFe_{0.5}Cr_{0.5}O_3$, J. Magn. Magn. Mater. 444 (2017) 178-183

[167] K. Das, P. Sen, *Magnetic and magnetocaloric properties of polycrystalline* $Pr_{0.55}(Ca_{0.75}Sr_{0.25})_{0.45}MnO_3$ *compound: Observation of large inverse magnetocaloric effect*, J. Magn. Magn. Mater. 485 (2019) 224-227

[168] L. Li, K. Nishimura, G. Usui, D. Huo, Z. Qian *Study of the magnetic properties and magnetocaloric effect in* RCo_2B_2 *(R=Tb, Dy and Ho) compounds*, Intermetallics 23 (2012) 101-105

[169] M.E. Wood, W.H. Potter, *General analysis of magnetic refrigeration and its optimization using a new concept: maximization of refrigerant capacity*, Cryogenics 25 (1985) 667-683

[170] L D. Griffith, Y. Mudryk, J. Slaughter, V.K. Pecharsky, *Material-based figure of merit for caloric materials*, J. Appl. Phys. 123 (2018) 034902

[171] J. Romero-Gómez, R. Ferreriro-Garcia, A. De Miguel-Catoira, M. Romero-Gomez, *Magnetocaloric effect: A review of the thermodynamic cycles in magnetic refrigeration*, Renewable and Sustainable Energy Reviews 17 (2013) 74-84

[172] O. Gutfleisch, T. Gottschall, M. Fries, D. Benke, I. Radulov, K.P. Skolov, H. Wende, M. Gruner, M. Acet, P. Entel, M. Farle, *Mastering hysteresis in magnetocaloric materials*, Phil. Trans. R. Soc. A 374 (2016) 20150308

[173] R. M'nassri, M.M. Nofal, P. de Rangoc, N. Chniba-Boudjada, *Magnetic entropy table-like shape and enhancement of refrigerant capacity in* $La_{1.4}Ca_{1.6}Mn_2O_7$–$La_{1.3}Eu_{0.1}Ca_{1.6}Mn_2O_7$ *composite*, RSC Adv. 9 (2019) 14916-14927

[174] C.H. Lambert, M.S. El Hadri, M. Hamedoun, A. Benyoussef, O. Mounkachi, S. Mangin, *Tunable magneto-caloric effect in* $Gd_{1-x}Tb_x$ *heterostructures thin film*, J. Magn. Magn. Mater. 443 (2017) 1-3

[175] A. Smaïli, R. Chahine, *Composite magnetic refrigerants for an Ericsson cycle: New method of selection using a numerical approach*, Advances in Cryogenic Engineering 42 (1996) 445-450

[176] L. Li, M. Kadonaga, D. Huo, Z. Qian, T. Namiki, K. Nishimura, *Low field giant magnetocaloric effect in RNiBC (R = Er and Gd) and enhanced refrigerant capacity in its composite materials*, Appl. Phys. Lett. 101 (2012) 122401

[177] P. Álvarez, J.L. Sánchez-Llamazares, P. Gorria, J.A. Blanco, *Enhanced refrigerant capacity and magnetic entropy flattening using a two-amorphous FeZrB(Cu) composite*, Appl. Phys. Lett. 99 (2011) 232501

[178] A.Chaturvedi, S. Stefanoski, M.H. Phan, G.S. Nolas, H. Srikanth, *Table-like magnetocaloric effect and enhanced refrigerant capacity in* $Eu_8Ga_{16}Ge_{30}$*-EuO composite materials*, Appl. Phys. Lett. 99 (2011) 162513

[179] A. Smaïli, R. Chahine, *Thermodynamic investigations of optimum active magnetic regenerators*, Cryogenics 38 (1998) 247-252

[180] S. Fujieda, Y. Hasegawa, A. Fujita, K. Fukamichi, *Thermal transport properties of magnetic refrigerants* $La(Fe_xSi_{1-x})_{13}$ *and their hydrides, and* $Gd_5Si_2Ge_2$ *and MnAs*, J. Appl. Phys. 95 (2004) 2429-2431

[181] D.J. Silva, B.D. Bordalo, J. Puga, A.M. Pereira, J. Ventura, J.C.R.E. Oliveira, J.P. Araújo, *Optimization of the physical properties of magnetocaloric materials for solid state magnetic refrigeration*, Applied Thermal Engineering 99 (2016) 514-517

[182] D.J. Silva, A. Davarpanah, J.S. Amaral, V.S. Amaral, *Temperature dependent thermal conductivity of magnetocaloric materials: Impact assessment on the performance of active magnetic regenerative refrigerators*, Int. J. Refrig. 106 (2019) 181-187

[183] K.K. Nielsen, K. Engelbrecht, *The influence of the solid thermal conductivity on active magnetic regenerators*, J. Phys. D: Appl. Phys. 45 (2012) 145001

[184] H.E. Stanley, *Introduction to Phase Transitions and Critical Phenomena*, Oxford University Press (1971)

[185] J.M. Yeomans, *Statistical Mechanics of Phase Transitions*, Oxford Science Publications (1992)

[186] I. Herbut, *A Modern Approach to Critical Phenomena*, Cambridge (2007)

[187] C. Domb, J.L. Lebowitz, *Phase Transitions and Critical Phenomena*, Academic Press. San Diego (1992)
[188] A. Smith, C.R.H. Bahl, R. Bjørk, K. Engelbrecht, K.K. Nielsen, N. Pryds, *Materials Challenges for High Performance Magnetocaloric Refrigeration Devices*, Adv. Energy Mater. 2 (2012) 1288–1318
[189] V.K. Pecharsky , K.A. Gschneidner Jr , Y. Mudryk , D. Paudyal, *Making the most of the magnetic and lattice entropy changes*, J. Magn. Magn. Mater. 321 (2009) 3541-3547
[190] S.N. Kaul, *Static critical phenomena in ferromagnets with quenched disorder*, J. Magn. Magn. Mater. 53 (1985) 5-53
[191] N. Goldenfeld, *Lectures on Phase Transitions and the Renormalization Group*, Westview Press (1992)
[192] L.D. Landau, *Theory of phase transformations. I*, Phys. Z. Sowjetunion 11 (1937) 26
[193] L.D. Landau, *Theory of phase transformations. II*, Phys. Z. Sowjetunion 11 (1937) 627
[194] L.D. Landau, E.M. Lifshitz, *Statistical Physics*, 3rd edition Amsterdam, Elsevier (1980)
[195] K.G. Wilson, *Renormalization Group and Critical Phenomena. I. Renormalization Group and the Kadanoff Scaling Picture*, Phys. Rev. B 4 (1971) 3174
[196] K.G. Wilson, *Renormalization Group and Critical Phenomena. II. Phase-Space Cell Analysis of Critical Behavior*, Phys. Rev. B 4 (1971) 3184
[197] K.G. Wilson, M.E. Fisher, *Critical Exponents in 3.99 Dimensions*, Phys. Rev. Lett. 28 (1972) 240
[198] R.B. Potts, *Some generalized order-disorder transformations*, Proc. Cambridge Philos. Soc. 48 (1952) 106-109
[199] F.Y. Wu, *The Potts model*, Rev. Mod. Phys. 54 (1982) 235
[200] H.E. Stanley, *Dependence of Critical Properties on Dimensionality of Spins*, Phys. Rev. Lett. 20 (1968) 589
[201] R. Guida, J. Zinn-Justin, *Critical exponents of the N-vector model*, J. Phys. A: Math Gen. 31 (1998) 8103-8121
[202] W. Lenz, *Beitrag zum Verständnis der magnetischen Erscheinungen in festen Körpern*, Phys. Zeitschrift 21 (1920) 613-615
[203] E. Ising, *Beitrag zur theorie des ferromagnetismus*, Z. Phys. 31 (1925) 253-258
[204] L. Osanger, *Crystal Statistics. I. A Two-Dimensional Model with an Order-Disorder Transition*, Phys. Rev. 65 (1944) 117
[205] A.B. Zamalodchikov, *Quantum Field Theory and Critical Phenomena*, Oxford University Press (1989)
[206] M. Hasenbusch, *Universal amplitude ratios in the three-dimensional Ising universality class*, Phys. Rev. B 82 (2010) 174434
[207] M. Campostrini, A. Pelissetto, P. Rossi, E. Vicari, *25th-order high-temperature expansion results for three-dimensional Ising-like systems on the simple-cubic lattice*, Phys. Rev. E 65 (2002) 066127
[208] M. Campostrini, M. Hasenbusch, A. Pelisseto, P. Rossi, E. Vicari, *Critical behavior of the three-dimensional XY universality class*, Phys. Rev. B 63 (2001) 214503
[209] M. Campostrini, M. Hasenbusch, A. Pelisseto, P. Rossi, E. Vicari, *Critical exponents and equation of state of the three-dimensional Heisenberg universality class*, Phys. Rev. B 65 (2002) 144520
[210] C. Hohenemser, N. Rosov, A. Kleinhammes, *Critical phenomena studied via nuclear techniques*, Hyperfine Interactions 49 (1989) 267-324
[211] H.E. Stanley, *Scaling, universality and renormalization: Three pillars of modern critical phenomena*, Rev. Mod. Phys. 71 (1999) 358-366
[212] A. Salazar, M. Massot A. Oleaga, A. Pawlak, W. Schranz, *Critical behaviour of the thermal properties of* $KMnF_3$, Phys. Rev. B 75 (2007) 224428
[213] W.P. Wolf, *The Ising Model and Real Magnetic Materials*, Braz. J. Phys. 30 (2000) 794-810
[214] G. Ahlers, *Critical phenomena at low temperature*, Rev. Mod. Phys. 52 (1980) 489
[215] A. Aharony, M.E. Fisher, *Nonlinear scaling fields and corrections to scaling near criticality*, Phys. Rev. B 27 (1983) 4394
[216] J. C. Le Guillou, J. Zinn-Justin, *Critical exponents from field theory*, Phys. Rev. B 21 (1980) 3976-3998

[217] A. Oleaga, V. Shvalya, A. Salazar, I. Stoika, Yu.M. Vysochanskii, *In search of a tricritical Lifshitz point in $Sn{-}2P_2(S_{1-x}Se_x)_6$ doped with Pb,Ge: A critical behavior study*, J. Alloys Compd. 694 (2017) 808-814

[218] V. Shvalya, A. Oleaga, A. Salazar, A. Kohutych, Yu. Vysochanskii, *Thermal diffusivity and 3D-XY critical behavior of ferroelectric semiconductors $(Pb_xSn_{1-x})_2P_2Se_6$*, J. Phys. Chem. Sol. 88 (2016) 78-84

[219] M. Marinelli, F. Mercuri, U. Zammit, R. Pizzoferrato, F. Scudieri, D. Dadarlat, *Photopyroelectric study of specific heat, thermal conductivity, and thermal diffusivity of Cr_2O_3 at the Néel transition*, Phys. Rev. B 49 (1994) 9523

[220] M. Marinelli, F. Mercuri, D.P. Belanger, *Specific heat, thermal diffusivity, and thermal conductivity of FeF2 at the Néel temperature*, Phys. Rev. B 51 (1995) 8897-8903

[221] M. Marinelli, F. Mercuri, S. Foglietta, D.P. Belanger, *Effect of spin-system fluctuations on heat transport in close to the Néel temperature*, Phys. Rev. B 54 (1996) 4087

[222] A. Pawlak, *Critical thermal diffusivity in anisotropic magnets*, Phys. Rev. B 68 (2003) 094416

[223] A. Oleaga, A. Salazar, YuM. Bunkov, *3D-XY critical behavior of $CsMnF_3$ from static and dynamic thermal properties*, J. Phys. Condens. Matter 26 (2014) 096001

[224] G. Ahlers, A. Kornblit, *Universality of the specific heat of Heisenberg magnets near the critical temperature*, Phys. Rev. B 12 (1975) 1938

[225] A. Oleaga, V. Liubachko, P. Manfrinetti, A. Provino, Yu Vysochanskii, A. Salazar, *Critical behavior study of NdScSi, NdScGe intermetallic Compounds*, J. Alloys Compd. 723 (2017) 559-566

[226] A. Oleaga, A. Salazar, M. Massot, A. Molak, M. Koralewski, *Thermal Diffusivity and Critical Behaviour of Uniaxial Ferroelectric $Pb_5Ge_3O_{11}$*, Ferroelectrics 369 (2008) 76-84

[227] A. Arrott, *Criterion for Ferromagnetism from Observations of Magnetic Isotherms*, Phys. Rev. 108 (1957) 01394

[228] A. Arrott, J.E. Noakes, *Approximate Equation of State For Nickel Near its Critical Temperature*, Phys. Rev. 19 (1967) 786

[229] S.K. Banerjee, *On a generalised approach to first and second order magnetic transitions*, Phys. lett. 12 (1964) 16

[230] M.E. Fisher, *The theory of equilibrium critical phenomena*, Rep. Prog. Phys. 30 (1967) 615-730

[231] J. Yang, Y.P. Lee, Y. Li, *Critical behavior of the electron-doped manganite $La_{0.9}Te_{0.1}MnO_3$*, Phys. Rev. B 76 (2007) 054442

[232] A.K. Pramanik, A. Banerjee, *Critical behavior at paramagnetic to ferromagnetic phase transition in $Pr_{0.5}Sr_{0.5}MnO_3$: A bulk magnetization study*, Phys. Rev. B 79 (2009) 214426

[233] J.S. Kouvel, M.E. Fisher, *Detailed magnetic behavior of Nickel near its Curie Point*, Phys. Rev. B 136 (1964) A1626-A1632

[234] H. Oesterreicher, F.T. Parker, *Magnetic cooling near Curie temperatures above 300 K*, J. Appl. Phys. 55 (1984) 4334-4338

[235] V. Franco, J.S. Blázquez, A.Conde, *Field dependence of the magnetocaloric effect in materials with a second order phase transition: A master curve for the magnetic entropy change*, Appl. Phys. Lett. 89 (2006) 222512

[236] V. Franco, A.Conde, *Scaling laws for the magnetocaloric effect in second order phase transitions: From physics to applications for the characterization of materials*, Int. J. Refrig. 33 (2010) 465-473

[237] C. Romero-Muñiz, R. Tamura, S. Tanaka, V. Franco, *Applicability of scaling behavior and power laws in the analysis of the magnetocaloric effect in second-order phase transition materials*, Phys. Rev. B 94 (2016) 134401

[238] A. Smith, K.K. Nielsen, C.R.H. Bahl, *Scaling and universality in magnetocaloric materials*, Phys. Rev. B 90 (2014) 104422

[239] P. Gębara, Á. Díaz-García, J. Yan Law, V. Franco, *Magnetocaloric response of binary Gd-Pd and ternary Gd-(Mn,Pd) alloys*, J. Magn. Magn. Mater. 500 (2020) 166175

[240] V. Franco, A.Conde, J.M. Romero-Enrique, J.S. Blázquez, *A universal curve for the magnetocaloric effect: an analysis based on scaling relations*, J. Phys.: Condens. Matter 20 (2008) 285207

[241] B. Mondal, S. Dan, S. Mondal, R.N. Bhowmik, R. Ranganathan, C. Mazumdar, *Identification and critical phenomenon studies of polymorphic phases in binary intermetallic compound $DyIr_3$*, Intermetallics 120 (2020) 106740

[242] C.M. Bonilla, F. Bartolomé, L.M. García, M. Parra-Borderías, J. Herrero-Albillos, V. Franco, *A new criterion to distinguish the order of the magnetic transitions by means of magnetic measurements*, J. Appl. Phys. 107 (2010) 09E131

[243] C.M. Bonilla, J. Herrero-Albillos, F. Bartolomé, L.M. García, M. Parra-Borderías, V. Franco, *Universal behavior for magnetic entropy change in magnetocaloric materials: An analysis on the nature of phase transitions*, Phys. Rev. B 81 (2010) 224424

[244] V. Franco, J.S. Blázquez, A. Conde, *Influence of Ge addition on the magnetocaloric effect of a Co-containing Nanoperm-type alloy*, J. appl. Phys. 103 (2008) 07B316

[245] Q.Y. Dong, H.W. Zhang, J.R. Sun, B.G. Shen, V. franco, *A phenomenological fitting curve for the magnetocaloric effect of materials with a second-order phase transition*, J. appl. Phys. 103 (2008) 116101

[246] V. franco, A. Conde, V. Provenzano, R.D. Shull, *Scaling analysis of the magnetocaloric effect in $Gd_5Si_2Ge_{1.9}X_{0.1}$ (X=Al, Cu, Ga, Mn, Fe, Co)*, J. Magn. Magn. Mater. 322 (2010) 218-223

[247] M. Sánchez-Pérez, L.M. Moreno-Ramírez, V. Franco, A.Conde, M. Marsilius, G. Herzer, *Influence of nanocrystallization on magnetic properties of Ni-based amorphous alloys: Determination of critical exponents in multiphase systems*, J. Alloys Compd. 686 (2016) 717-722

[248] V. franco, R. Caballero-Flores, A. Conde, Q.Y. Dong, H.W. Zhang, *The influence of a minority magnetic phase on the field dependence of the magnetocaloric effect*, J. Magn. Magn. Mater. 321 (2009) 1115-1120

[249] C. Romero-Muñiz, J.J. Ipus, J.S. Blázquez, V. franco, A. Conde, *Influence of the demagnetizing factor on the magnetocaloric effect: Critical scaling and numerical simulations*, Appl. Phys. Lett. 104 (2014) 252405

[250] K.R. Kumar, H.S. Nair, B.N. Sahu, S. Xhakaza, A.M. Strydom, *Large magnetocaloric effect and critical behaviour analysis in Gd_2Cu_2In*, EPL 122 (2018) 17003

[251] A. Biswas, S. Chandra, T. Samanta, M.H. Phan, I. Das, *The universal behavior of inverse magnetocaloric effect in antiferromagnetic materials*, J. Appl. Phys. 113 (2013) 17A902

[252] A. Biswas, T.L. Phan, N.H. Dan, P. Zhang, S.C. Yu, H. Srikanth, M.H. Phan, *The scaling and universality of conventional and inverse magnetocaloric effects in Heusler alloys*, Appl. Phys. Lett. 103 (2013) 162410

[253] A. Biswas, S. Chandra, T. Samanta, B.Ghosh, S. Datta, M.H. Phan, A.K. Raychaudhuri, I. Das, H. Srikanth, *Universality in the entropy change for inverse magnetocaloric effect*, Phys. Rev. B. 87 (2013) 134420

[254] S. Vadala, S. Asthana, *Magnetocaloric effect and critical field analysis in Eu substituted $La_{0.7-x}Eu_xSr_{0.3}MnO_3$ (x=0.0, 0.1, 0.2, 0.3) manganites*, J. Magn. Magn. Mater. 446 (2018) 68-79

[255] V. Franco, A. Conde, M.D. Kuz'min, J.M. Romero-Enrique, *The magnetocaloric effect in materials with a second order phase transition: Are T_C and T_{peak} necessarily coincident?*, J. Appl. Phys. 105 (2009) 07A917

[256] T.L. Phan, N.T. Dang, T.A. Ho, T.V. Manh, T.D. Thanh, C.U. Jung, B.W. Lee, A.D. Phan, S.C. Yu, *First-to-second-order magnetic-phase transformation in $La_{0.7}Ca_{0.3-x}Ba_xMnO_3$ exhibiting large magnetocaloric effect*, J. Alloys Compd. 657 (2016) 818-834

[257] H. Omrani, M. Mansouri, W. Cheikhrouhou Koubaa, M. Koubaa, A. Cheikhrouhou, *Critical behavior study near the paramagnetic to ferromagnetic phase transition temperature in $Pr_{0.6-x}Er_xCa_{0.1}Sr_{0.3}MnO_3$ (x ¼ 0, 0.02 and 0.06) manganites*, RSC Adv. 6 (2016) 78017

[258] J.Y. Law, V. Franco, L.M. Moreno-Ramírez, A. Conde, D.Y. Karpenkov, I. Radulov, K.P. Skokov, O. Gutfleisch, *A quantitative criterion for determining the order of magnetic phase transitions using the magnetocaloric effect*, Nat. Commun. 9 (2018) 2680

[259] L.M. Moreno-Ramírez, C. Romero-Muñiz, J.Y. Law, V. Franco, A. Conde, I. Radulov, F. Maccari, K.P. Skokov, O. Gutfleisch, *The role of Ni in modifying the order of the phase transition of $La(Fe,Ni,Si)_{13}$*, Acta Mater. 160 (2018) 137-146

[260] N.H. van Dijk, *Landau model evaluation of the magnetic entropy change in magnetocaloric materials*, J. Magn. Magn. Mater. 529 (2021) 167871

[261] L.M. Moreno-Ramírez, C. Romero-Muñiz, J.Y. Law, V. Franco, A. Conde, I. Radulov, I.A. Radulov, F. Maccari, K.P. Skokov, O. Gutfleisch, *Tunable first order transition in La(Fe,Cr,Si)$_{13}$ compounds: Retaining magnetocaloric response despite a magnetic moment reduction*, Acta Mater. 175 (2019) 406-414

[262] J.C. LeGuillou, J. Zinn-Justin, *Critical exponents from field theory*, Phys. Rev. B 221 (1980) 3976-3998

[263] C. Bervillier, *Estimate of a universal critical-amplitude ratio from its ϵ expansion up to ϵ^2*, Phys. Rev. B 34 (1986) 8141

[264] H. Kawamura, *Universality of phase transitions of frustrated antiferromagnets*, J. Phys.: Condens. Matter 10 (1998) 4707

[265] E.K. Riedel, F.J. Wegner, *Tricritical Exponents and Scaling Fields*, Phys. Rev. Lett. 29 (1972) 349-352

[266] Y. Liu, C. Petrovic, *Critical behavior of the quasi-two-dimensional weak itinerant ferromagnet trigonal chromium telluride $Cr_{0.62}Te$*, Phys. Rev. B 96 (2017) 134410

[267] A.T. Ogielski, *Dynamics of three-dimensional Ising spin glasses in thermal equilibrium*, Phys. Rev. B 32 (1985) 7384

[268] S. Singh, S.K. Dhar, C. Mitra, P. Paulose, P. Manfrinetti, A. Palenzona, *The nature of magnetism in CeScSi and CeScGe*, J. Phys. Condens. Matter 13 (2001) 3753-3766

[269] S.A. Nikitin, I.A. Ovtchenkova, YuV. Skourski, A.V. Morozkin, *Magnetic properties of ternary scandium rare earth silicides and germanides*, J. Alloys Compd. 345 (2002) 50-53

[270] S.N. Mishra, S.K. Dhar, *Magnetic interaction in NdScGe: A local investigation by perturbed angular correlation spectroscopy*, J. Phys. Condens. Matter 16 (2004) 635-640

[271] S. Singh, S.K. Dhar, P. Manfrinetti, A. Palenzona, D. Mazzone, *High magnetic transition temperatures in RScT (R=Pr, Nd and Sm; T=Si and Ge) compounds: multiple spin reorientations in PrScGe*, J. Magn. Magn. Mater. 269 (2004) 113-121

[272] J.M. Cadogan, D.H. Ryan, R. Gagnon, C.J. Voyer, *Magnetic structure of NdScGe*, J. Appl. Phys. 97 (2005) 10A916

[273] P. Manfrinetti, A.V. Morozkin, O. Isnard, P. Henry, A. Palenzona, *Magnetic structure of the CeScSi-type RScGe compounds (R = Pr, Nd, Tb)*, J. Alloys Compd. 450 (2008) 86-91

[274] F. Guillou, A.K. Pathak, T.A. Hackett, D. Paudyal, Y. Mudryk, V.K. Pecharsky, *Crystal, magnetic, calorimetric and electronic structure investigation of $GdScGe_{1-x}Sb_x$ compounds*, J. Phys. Condens. Matter 29 (2017) 485802

[275] A.V. Morozkin, L.M. Vitting, I.A. Sviridov, I.A. Tskhadadze, *CeScSi- and CeFeSi-type structures in compounds derived from GdTiGe*, J. Alloys Compd. 297 (2000) 168-175

[276] G. Skorek, J. Denyszczyk, J. Szade, B. Tyszka, *Electronic structure and magnetism of ferromagnetic GdTiSi and GdTiGe*, J. Phys. Condens. Matter 13 (2001) 6397-6409

[277] S.N. Mishra, *Magnetic interactions in equi-atomic rare-earth intermetallic alloys RScGe (R = Ce, Pr, Nd and Gd) studied by time differential perturbed angular correlation spectroscopy and ab initio calculations*, J. Phys. Condens. Matter 21 (2009) 115601

[278] P. Manfrinetti, M. Pani, A. Palenzona, S.K. Dhar, S. Singh, *Single crystal study of the high-Curie-temperature ferromagnet $Gd_{1.02}Sc_{0.98}Ge$ and of $Gd_{2.38}Sc_{2.62}Ge_3$*, J. Alloys Compd. 334 (2002) 9-13

[279] S.A. Nikitin, I.A. Tskhadadze, I.V. Telegina, A.V. Morozkin, YuD. Seropegin, *Magnetic properties of RTiGe compounds*, J. Magn. Magn. Mater. 182 (1998) 375-380

[280] K. Yvon, W. Jeitschko, E. Parthé, *LAZY PULVERIX, a computer program, for calculating X-ray and neutron diffraction powder patterns*, J. Appl. Crystallogr. 10 (1977) 73-74

[281] S.K. Dhar, P. Manfrinetti, A. Palenzona, M. Pani, *Structural and magnetic properties of the Mn_5Si_3-type $(Gd_{1-x}Sc_x)_5Ge_3$ compounds*, J. Alloys Compd. 347 (2002) 1-8

[282] A.O. Oliynyk, T.D. Sparks, M.W. Gaultois, L. Ghadbeigi A. Mar, *$Gd_{12}Co_{5.3}Bi$ and $Gd_{12}Co_5Bi$, Crystalline Doppelgänger with Low Thermal Conductivities*, Inorganic Chem. 55 (2016) 6625-6633

[283] A.K. Bashir, M.B.T. Tchokonté, A.M. Strydom, *Electrical and thermal transport properties of $RECu_4Au$ compounds, RE=Nd, Gd*, J. Magn. Magn Mater. 414 (2016) 69-73

[284] H. Misiorek, J. Stepién-Damma, W. Suski, E. Talik, B.Y. Kotur, V.M. Dmitriev, *Lattice parameters, magnetic susceptibility and thermal conductivity of $ScFe_4Al_8$ and YFe_4Al_8*, J. Alloys Compd. 363 (2004) 78–84

[285] A. Oleaga, A. Salazar, D. Prabhakaran, A.T. Boothroyd, *Critical behavior of $La_{1-x}Sr_xMnO_3$ ($0 \leq x \leq 0.35$) by thermal diffusivity measurements*, Phys. Rev. B 70 (2004) 184402

[286] A. Oleaga, A. Salazar, H. Kuwahara, *Thermal diffusivity and critical behavior of $Nd_{1-x}Sr_xMnO_3$ by thermal diffusivity measurements*, Physica B 378–380 (2006) 512-514

[287] A. Gamzatov, A.B. Batdalov, ShK. Khizriev, A.M. Aliev, L.N. Khanov, N.H. Yen, N.H. Dan, H. Zhou, S.-C. Yu, D.-H. Kim, *Phase transitions, thermal, electrical, and magnetocaloric properties of $Ni_{50}Mn_{37-x}Al_xSn_{13}$ (x = 2, 4) ribbon samples*, J. Alloys Compd. 842 (2020) 155783

[288] A.V. Morozkin, YuD. Seropegin, V.K. Portnoy, A.V. Leonov, I.A. Sviridov, *Crystallographic data of new ternary TiNiSi (Co_2Si)-type RMnGe (R=Sm, Gd, Dy-Tm) compounds*, J. Alloys Compd. 278 (1998) L1-L5

[289] C. Ritter, S.K. Dhar, R. Kulkarni, A. Provino, D. Paudyal, P. Manfrinetti, K.A. Gschneidner, *Electronically- and crystal-structure-driven magnetic structures and physical properties of RScSb (R = rare earth) compounds: a neutron diffraction, magnetization and heat capacity study*, J. Phys. Condens. Matter 26 (2014) 366001

[290] M. Colarieti-Tosti, T. Burkert, O. Eriksson, L. Nordström, M.S.S. Brooks, *Theory of the temperature dependence of the easy axis of magnetization in hcp Gd*, Phys. Rev. B 72 (2005) 094423

[291] A. Oleaga, A. Salazar, D. Prabhakaran, A.T. Boothroyd, *Critical behaviour of $RMnO_3$ (R = La, Pr, Nd) by thermal diffusivity and specific heat measurements*, J. Phys. Condens. Matter 17 (2005) 6729-6736

[292] J. Yang, Y.P. Lee, *Critical behavior in Ti-doped manganites $LaMn_{1-x}Ti_xO_3$ ($0.05 \leq x \leq 0.2$)*, Appl. Phys. Lett. 91 (2007) 142512

[293] N. Mtiraoui, J. Dhahri, M. Oumezine, *Critical behavior in Ag-doped managnites $La_{0.67}Pb_{0.33-x}Ag_xMnO_3$ (x = 0.1 and 0.15)*, J. Magn. Magn. Mater. 345 (2013) 118-124

[294] N. Ghosh, S. Röβler, U.K. Röβler, K. Nenkov, S. Elizabeth, H.L. Bhat, K. Dörr, K.H. Müller, *Heisenberg-like critical properties in ferromagnetic $Nd_{1-x}Pb_xMnO_3$ single crystals*, J. Phys. Condens. Matter 18 (2006) 557-567

[295] D.J. García, V. Vildosola, P.S. Cornaglia, *Magnetic couplings and magnetocaloric effect in the GdTX (T = Sc, Ti, Co, Fe; X = Si, Ge) compounds*, J. Phys. Condens. Matter 32 (2020) 285803

[296] E. Brück, *Handbook of Magnetic Materials*, K.H.J. Buschow (Ed.) vol. 17 Elsevier BV (2008) 235

[297] F. Canepa, M. Napoletano, S. Cirafici, *Magnetocaloric effect in the intermetallic compound Gd_7Pd_3*, Intermetallics 10 (2002) 731-734

[298] X.J. Niu, K.A. Geschneider Jr., A.O. Pecharsky, V.K. Pecharsky, *Crystallography, magnetic properties and magnetocaloric effect in $Gd_4(Bi_xSb_{1-x})_3$ alloys*, J. Magn. Magn. Mater. 234 (2001) 193-206

[299] Y.I. Spichkin, V.K. Pecharsky, K.A. Geschneider Jr., *Preparation, crystal structure, magnetic and magnetothermal properties of $(Gd_xR_{5-x})Si_4$, where R=Pr and Tb, alloys*, J. Appl. Phys. 89 (2001) 1738-1745

[300] A. Provino, V. Smetana, D. Paudyal, K.A. Gschneidner Jr, A.V. Mudring, V. K. Pecharsky, P. Manfrinetti, M. Putti, *Gd_3Ni_2 and $Gd_3Co_xNi_{2-x}$: magnetism and unexpected Co/Ni crystallographic ordering*, J. Mater. Chem. C 4 (2016) 6078-6089

[301] M. Hsini, M. Boutaleb, *Simulation of the magnetocaloric effect by means of theoretical models in Gd_3Ni_2 and Gd_3CoNi systems*, Eur. Phys. J. Plus (2020) 135:186

[302] C. Ritter, A. Provino, F. Fauth, S.K. Dhar, V.K. Pecharsky, P. Manfrinetti, *From Tb_3Ni_2 to Tb_3CoNi: The interplay between chemistry, structure, and magnetism*, Phys. Rev. Materials 3 (2019) 024406

[303] A.V. Morozkin, *Magnetic structures of Zr_6CoAs_2-type Ho_6FeSb_2, Ho_6CoBi_2, Ho_6FeBi_2, Ho_6MnBi_2*, J. Alloys Compd. 395 (2005) 7-16

[304] J. Zhang, Y.M. Kang, G. Shan. S. Bobev, *Structural analysis of Gd_6FeBi_2 from single crystal X-ray diffraction methods and electronic structure calculations*, Acta Crystallogr. C 75 (2019) 562-567

[305] A.V. Morozkin, R. Nirmala, S.K. Malik, *Magnetic structure of the Zr_6CoAs_2-type Er_6TX_2 compounds (T= Mn, Fe, Co and X=Sb, Bi)*, J. Alloys Compd. 394 (2005) 75-79

[306] N.V. Baranov, A.V. Proshkin, A.F. Gubkin, A. Cervellino, H. Michor, G. Hilscher, E.G. Gerasimov, G. Ehlers, M. Frontzek, A. Podlesnyak, *Enhanced survival of short-range magnetic correlations and frustrated interactions in R_3T intermetallics*, J. Magn. Magn. Mat. 324 (2012) 1907-1912

[307] J. Rodriguez-Carvajal, *Recent advances in magnetic structure determination by neutron powder diffraction*, Physica B 192 (1993) 55-69

[308] J.M. Moreau, D. Paccard, E. Parthé, *The monoclinic, CrB-related, crystal structure of Tb_3Ni_2, Dy_3Ni_2 and Ho_3Ni_2*, Acta Crystallogr. B 30 (1974) 2583-2586

[309] J.M. Moreau, D. Paccard, D. Gignoux, *The crystal structure of Er_3Ni_2*, Acta Crystallogr. B 30 (1974) 2122-2126

[310] P. Villars, J.L.C. Daams, *Atomic-environment classification of the chemical elements*, J. Alloys Compd. 197 (1993) 177-196

[311] F. Yuan, J. Du, B. Shen, *Controllable spin-glass behavior and large magnetocaloric effect in Gd-Ni-Al bulk metallic glasses*, Appl. Phys. Lett. 101 (2012) 032405

[312] N.K. Singh, P. Kumar, K.G. Suresh, A.K. Nigam, *Investigations on magnetic and magnetocaloric properties of the intermetallic compound TbAgAl*, J. Appl. Phys. 105 (2009) 023901

[313] J.L. Wang, C. Marquina, M.R. Ibarra, G.H. Wu, *Structure and magnetic properties of RNi_2Mn compounds(R=Tb, Dy, Ho, and Er)*, Phys. Rev. B 73 (2006) 094436

[314] H. Zhang, B.G. Shen, Z.Y. Xu, J. Shen, F.X. Hu, J.R. Sun, Y. Long, *Large reversible magnetocaloric effects in ErFeSi compound under low magnetic field change around liquid hydrogen temperature*, Appl. Phys. Lett. 102 (2013) 092401

[315] J.C. Debnath, J. Wang, *Magnetocaloric effect in $HoMn_2Si_2$ compound with multiple magnetic phase transitions*, Intermetallics 78 (2016) 50

[316] A. Murtaza, W. Zuo, J. Mi. Y. Li, A. Ghani, M. Yaseen, M.T. Khan, C. Hao, K. Li, Z. Dai, S. Yang, Y. Ren, *Magnetocaloric effect and critical exponent analysis around magnetic phase transition in $NdCo_2$ compound*, J. Phys. D: Appl. Phys. 53 (2020) 345003

[317] M.E. Fisher, S.K. Ma, B.G. Nickel, *Critical exponents for long-range order interactions*, Phys. Rev. Lett. 29 (1972) 917-920

[318] R. Li, P. Kumar, R. Mahendiran, *Critical behavior in polycrystalline $La_{0.7}Sr_{0.3}CoO_3$ from bulk magnetization study*, J. Alloys Compd. 659 (2016) 203-209

[319] Y. Yin, J.C. Han, Q. Yuan, L.S. Ling, B. Song, *Critical behavior in the antiperovskite Mn_3CuN at ferromagnetic to paramagnetic phase transition*, J. Magn. Magn. Mater. 346 (2013) 203-208

[320] Y. Jia, Y. Cheng, H. Wang, Z. Zhang, L. Li, *Magnetocaloric properties and critical behavior in double perovskite RE_2CrMnO_6 (RE= La, Pr, and Nd) compounds*, Ceramics International 46 (2020) 25043-25049

[321] H. Kawamura, *Renormalization-group analysis of chiral transitions*, Phys. Rev. B 38 (1988) 4916

[322] E.H Boubcheur, D. Loiso, H.T Diep, *Phase diagrams of XY antiferromagnetic stacked triangular lattices*, Phys. Rev. B 54 (1996) 4165

[323] M.L Plumer, A. Mailhot, *Tricritical behavior of the frustrated XY antiferromagnet*, Phys. Rev. B 50 (1994) 16113

[324] Y. Ajiro, H. Kikuchi, T. Nakashima, Y. Vnno, *Phase Transitions in the Frustrated ABX_3 Compounds*, Jpn. J. Appl. Phys. 26 (1987) 775-776

[325] T.E. Mason, M.F. Collins, B.D. Gaulin, *Experimental confirmation of the existence of a new universality class for stacked triangular lattices*, J. Phys. C: Solid State Phys. 20 (1987) L945

[326] D. Gaulin, M. Hagen, H.R. Child, *A critical scattering study of the helical antiferromagnets Ho and Dy*, J. Phys. Colloques 49 (1998) C8-327-328

[327] A.V. Morozkin, R. Nirmala, S.K. Malik, *Structural and magnetic properties of Fe_2P-type R_6TX_2 compounds (R=Zr, Dy, Ho, Er, T=Mn, Fe, Co, Cu, Ru, Rh, X=Sb, Bi, Te)*, Intermetallics 19 (2011) 1250-1264

[328] Y. Su, Y. Sui, J.-G. Cheng, J.-S. Zhou, X. Wang, Y. Wang, J.B. Goodenough, *Critical behavior of the ferromagnetic perovskites $RTiO_3$ (R = Dy, Ho, Er, Tm, Yb) by magnetocaloric measurements*, Phys. Rev. B 87 (2013) 195102

[329] L. Li, Y. Yuan, Y. Zhang, R. Pöttgen, S. Zhou, *Magnetic phase transitions and large magnetic entropy change with a wide temperature span in HoZn*, J. Alloys Compd. 643 (2015) 147-151

[330] X. Zheng, B. Shen, *The magnetic properties and magnetocaloric effects in binary R–T (R = Pr, Gd, Tb, Dy, Ho, Er, Tm; T = Ga, Ni, Co, Cu) intermetallic compounds*, Chin. Phys. B 26 (2017) 027501

[331] C.S. Garde, J. Ray, *Magnetic and supercundicting behaviour of R_3Ni (R = La, Pr, Gd, Tb, Ho and Er) systems*, J. Phys.: Condens. Matter 9 (1997) 7419-7434

[332] G.J. Primavesi, K.N.R. Taylor, *Magnetic transitions in the rare earth intermetallic compounds R_3Ni and R_3Co*, J. Phys. F: Metal Phys. 2 (1972) 761-770

[333] N.V. Tristan, S.A. Nikitin, T. Palewski, K. Skokov, *Comparative analysis of the magnetization processes of the Gd_3Ni and Gd_3Co single crystals*, J. Magn. Magn. Mat. 251 (2002) 148-154

[334] N.V. Baranov, A.V. Andreev, A.I. Kozlov, G.M. Kvashnin, H. Nakotte, H. Aruga Katori, T. Goto, *Magnetic phase transitions in Gd_3Co*, J. Alloys Compd. 202 (1993) 215-224

[335] N.V. Baranov, G. Hilscher, P.E. Markin, H. Michor, A.A. Yermakov, *Spin fluctuations induced by f–d exchange in R_3T compounds*, J. Magn. Magn Mater. 272–276 (2004) 637-638

[336] N.V. Tristan, S.A. Nikitin, T. Palewski, K. Nenkov, K. Skokov, *Specific heat of the Gd_3Co and Gd_3Ni compounds*, J. Magn. Magn Mater. 258 (2003) 583-585

[337] N.V. Tristan, K. Nenkov, T. Palewski, K.P. Skokov, S.A. Nikitin, *Specific heat of the R_3Co (R = heavy rare earth or Y) compounds*, Phys. Stat. Sol(A) 196 (2003) 325-328

[338] N.V. Baranov, A.V. Deryagin, A.I. Kozlov, YeV. Sinitsyn, *Field induced ferromagnetism and anomalies of the electrical resistivity in system $(Tb_{1-x}Y_x)_3Co$*, Phys. Met. Metall. 61 (1986) 97-106

[339] N.V. Baranov, A.F. Gubkin, A.P. Vokhmyanin, A.N. Pirogov, A. Podlesnyak, L. Keller, N.V. Mushnikov, M.I. Bartashevich, *High-field magnetization and magnetic structure of Tb_3Co*, J. Phys. Condens. Matter 19 (2007) 326213

[340] N.V. Baranov, A.N. Pirogov, A.E. Teplykh, *Magnetic state of Dy_3Co*, J. Alloys Compd. 226 (1995) 70-74

[341] N.V. Baranov, E. Bauer, R. Hauser, A. Galatanu, Y. Aoki, H. Sato, *Field-induced phase transitions and giant magnetoresistance in Dy_3Co single crystals*, Eur. Phys. J. B 16 (2000) 67-72

[342] P. Svoboda, H. Nakotte, A.M. Alsmadi, M. Doerr, *Magnetic phase diagram of Dy_3Co single crystal*, Acta Phys. Pol. B 34 (2003) 1449-1452

[343] N.V. Baranov, T. Goto, G. Hilscher, P.E. Markin, H. Michor, N.V. Mushnikov, J.-G. Park, A.A. Yermakov, *Irreversible field-induced magnetic phase transitions and properties of Ho_3Co*, J. Phys. Condens. Matter 17 (2005) 3445

[344] A.F. Gubkin, A. Podlesnyak, N.V. Baranov, *Single-crystal neutron diffraction study of the magnetic structure of Er_3Co*, Phys. Rev. B 82 (2010) 012403

[345] N.H. Duc, P.E. Brommer, K.H.J. Buschow (Ed.), *Chapter 3 Formation of 3d-moments and spin fluctuations in some rare-earth-cobalt compounds*, Handbook of Magnetic Materials, vol. 12, Elsevier Science B.V., Amsterdam (1999) 259-394 Chapter 3

[346] H. Kirchmayr, C.A. Poldy, K.A. Geschneidner Jr., L. Eyring (Eds.), *Chapter 14 Magnetic properties of intermetallic compounds of rare earth metals*, Handbook on Physics and Chemistry of Rare Earths, vol. 2, Amsterdam: North-Holland (1979) 55-230 Chapter 14

[347] A.F. Gubkin, L.S. Wu, S.E. Nikitin, A.V. Suslov, A. Podlesnyak, O. Prokhnenko, K. Prokes, F. Yokaichiya, L. Keller, N.V. Baranov, *Field-induced magnetic phase transitions and metastable states in Tb_3Ni*, Phys. Rev. B 97 (2018) 134425

[348] I.A. Campbell, *Indirect exchange for rare earths in metals*, J. Phys. F Met. Phys. 2 (1972) L47

[349] D. Gignoux, J.C. Gomez-Sal, D. Paccard, *Magnetic properties of a Tb_3Ni single crystal*, Solid State Comm. 44 (1982) 695-700

[350] G. Lorusso, O. Roubeau, M. Evangelisti, *Rotating Magnetocaloric Effect in an Anisotropic Molecular Dimer*, Angew. Chem. 128 (2016) 3421-3424

[351] M. Balli, B. Roberge, P. Fournier, S. Jandl, *Review of the Magnetocaloric Effect in $RMnO_3$ and RMn_2O_5 Multiferroic Crystals*, Crystals 7 (2017) 44

[352] Y. Hu, Q.B. Hu, C.C. Wang, Q.Q. Cao, W.L. Gao, D.H. Wang, Y.W. Du, *Large room-temperature rotating magnetocaloric effect in $NdCo_4Al$ polycrystalline alloy*, Solid State Comm. 250 (2017) 45-48

[353] J.L. Jin, X.Q. Zhang, G.K. Li, Z.H. Cheng, L. Zheng, Y. Lu, *Giant anisotropy of magnetocaloric effect in $TbMnO_3$ single crystals*, Phys. rev. B 83 (2011) 184431

[354] J.L. Jin, X.Q. Zhang, H. Ge, Z.H. Cheng, *Rotating field entropy change in hexagonal $TmMnO_3$ single crystal with anisotropic paramagnetic response*, Phys. rev. B 83 (2012) 214426

[355] M. Balli, B. Roberge, J. Vermette, S. Jandl, P. Fournier, M.M. Gospodinov, *Magnetocaloric properties of the hexagonal $HoMnO_3$ single crystal revisited*, Physica B 478 (2015) 77-83

[356] M. Balli, S. Mansouri, S. Jandl, P. Fournier, D.Z. Dimitrov, *Large rotating magnetocaloric effect in the orthorhombic $DyMnO_3$ single crystal*, Solid State Comm. 239 (2016) 9-13

[357] R. Huang, S. Cao, W. Ren, S. Zhan, B. Kang, J. Zhang, *Large rotating field entropy change in $ErFeO_3$ single crystal with angular distribution contribution*, Appl. Phys. Lett. 103 (2013) 162412

[358] Y.J. Ke, X.Q. Zhang, H. Ge, Y. Ma, Z.H. Cheng, *Low field induced giant anisotropic magnetocaloric effect in $DyFeO_3$ single crystal*, Chin. Phys. B 24 (2015) 037501

[359] M. Balli, S. Jandl, P. Fournier, M.M. Gospodinov, *Anisotropy-enhanced giant reversible rotating magnetocaloric effect in $HoMn_2O_5$ single crystals*, Appl. Phys. Lett. 104 (2014) 232402

[360] M. Balli, S. Jandl, P. Fournier, D.Z. Dimitrov, *Giant rotating magnetocaloric effect at low magnetic fields in multiferroic $TbMn_2O_5$ single crystals*, Appl. Phys. Lett. 108 (2016) 102401

[361] H. Zhang, Y.W. Li, E. Liu, Y.J. Ke, J.L. Jin, Y. Long, B.G. Shen, *Giant rotating magnetocaloric effect induced by highly texturing in polycrystalline DyNiSi compound*, Sci. Rep. 5 (2015) 11929

[362] X.Q. Zhang, Y.D. Wu, Y. Ma, Q.Y. Dong, Y.J. Ke, Z.H. Cheng, *Large rotating magnetocaloric effect in $ErAlO_3$ single crystal*, AIP Advances 7 (2017) 056418

[363] P.K. Das, A. Bhattacharyya, R. Kulkarni, S.K. Dhar, A. Thamizhavel, *Anisotropic magnetic properties and giant magnetocaloric effect of single-crystal PrSi*, Phys. Rev. B 89 (2014) 134418

[364] J.C.B. Monteiro, G.A. Lombardi, R.D. doe Reis, H.E. Freitas, L.P. Cardoso, A.M. Mansanares, F.G. Gandra, *Heat flux measurements of Tb_3M series (M=Co, Rh and Ru): specific heat and magnetocaloric properties*, Physica B 503 (2016) 64-69

[365] J.L. Sánchez-Llamazares, H. Flores-Zúñiga, P. Álvarez-Alonso, C.F. Sánchez-Valdés, G.A. Lara-Rodríguez, M.L. Fernández-Gubieda, *Magnetocaloric properties of rapidly solidified Dy_3Co alloy ribbons*, J. Appl. Phys. 117 (2015) 17A706

[366] A. Salazar, M. Massot, A. Oleaga, A. Pawlak, W. Schranz, *Critical behavior of the thermal properties of $KMnF_3$*, Phys. Rev. B 75 (2007) 224428

[367] A. Kowalczyk, M. Falkowski, *Thermal conductivity of $CeNiAl_4$ Kondo lattice*, Intermetallics 37 (2013) 65-68

[368] M. Wencka, M. Hahne, A. Kocjan, S. Vrtnik, P. Kozelj, D. Korze, Z. Jaglicic, M. Soric, P. Popcevic, J. Ivkov, A. Smontara, P. Gille, S. Jurga, P. Tomes, S. Paschen, A. Ormeci, M. Armbrüster, Yu Grin, J. Dolinsek, *Physical properties of the InPd intermetallic catalyst*, Intermetallics 55 (2014) 56-65

[369] N.V. Baranov, P.E. Markin, H. Nakotte, A. Lacerda, *Magnetic and transport properties of Tb_3Co studied on single crystals*, J. Magn. Magn. Mater. 177–181 (1998) 1133-1134

[370] D. Gignoux, R. Lemaire, J. Chassy, *Magnetic structures of the Tb_3Co compound*, Proceedings of the Int. Conf. on Magnetism ICM-73, 22-28 August 1973, vol 5, Nauka, Moscow (1974) 361-363

[371] A. Podlesnyak, G. Ehlers, H. Cao, M. Matsuda, M. Frontzek, O. Zaharko, V.A. Kazantsev, A.F. Gubkin, N.V. Baranov, *Temperature-driven phase transformation in Y_3Co: neutron scattering and first-principles studies*, Phys. Rev. B 88 (2013) 024117

[372] E. Talik, *Magnetic and transport properties of the R_3Ni system (R=Y, Gd, Tb, Dy, Ho, Er)*, Physica B: Condensed Matter 193 (1994) 213-220

[373] N.V. Tristan, K. Nenkov, K.P. Skokov, T. Palewski, *Specific heat and magnetic susceptibility of intermetallic compounds R_3Ni*, Physica B: Condensed Matter 344 (2004) 462-469

[374] A. Podlesnyak, A. Daoud-Aladine, O. Zaharko, P. Markin, N.V. Baranov, *Magnetic structures and magnetic phase transitions in Ho_3Co*, J. Magn. Magn. Mater. 272–276 (2004) 565-567

[375] M. Balli, D. Fruchart, D. Gignoux, R. Zach, *The colossal magnetocaloric effect in $Mn_{1-x}Fe_xAs$: what are we really measuring?*, Appl. Phys. Lett. 95 (2009) 072509

[376] J.D. Zou, B.G. Shen, B. Gao, J. Shen, J.R. Sun, *The magnetocaloric effect of $LaFe11.6Si_{1.4}$, $La_{0.8}Nd_{0.2}Fe_{11.5}Si_{1.5}$, and $Ni_{43}Mn_{46}Sn_{11}$ compounds in the vicinity of the first-order transition*, Adv. Mater. 21 (2009) 693-696

[377] W. Cui, W. Liu, Z. Zhang, *The origin of large overestimation of the magnetic entropy changes calculated directly by Maxwell relation*, Appl. Phys. Lett. 96 (2010) 222509

[378] P.J. von Ranke, N.A. de Oliveira, B.P. Alho, E.J.R. Plaza, V.S.R. de Sousa, L. Caron, M.S. Reis, *Understanding the inverse magnetocaloric effect in antiferro- and ferromagnetic arrangements*, J. Phys. Condens. Matter 21 (2009) 056004

[379] A.V. Morozkin, V.N. Nikiforov, B. Malaman, *Magnetic structure of the Zr_6CoAs_2-type Tb_6FeBi_2 compound*, J. Alloys Compd. 393 (2005) L6-L9

[380] A.V. Morozkin, YuMozharivskyj, V. Svitlyk, R. Nirmala, O. Isnard, P. Manfrinetti, A. Provino, C. Ritter, *Magnetic properties of Fe_2P-type R_6CoTe_2 compounds (R = Gd–Er)*, J. Solid State Chem. 183 (2010) 1314-1325

[381] A.V. Morozkin, Yu Mozharivskyj, V. Svitlyk, R. Nirmala, A.K. Nigam, *Magnetic properties of Fe_2P-type Tb_6FeTe_2, Tb_6CoTe_2, Tb_6NiTe_2 and Er_6FeTe_2 compounds*, J. Solid State Chem. 183 (2010) 3039-3051

[382] A.V. Morozkin, O. Isnard, P. Manfrinetti, A. Provino, C. Ritter, R. Nirmala, S.K. Malik, *The magnetic ordering in the Ho_6FeTe_2*, J. Alloys Compd. 498 (2010) 13-18

[383] F. Izumi, *The Rietveld Method*, R.A. Young (Ed.), Oxford University Press, Oxford (1993) Chap. 13

[384] S.A. Nikitin, A.S. Andreenko, A.M. Tishin, A.M. Arkharov, A.A. Zherdev, *Magnetocaloric effect in heavy rare earths*, Phys. Met. Metallogr. 60 (1985) 689-694

[385] G. Green, W. Patton, J. Stevens, *The magnetocaloric effects of some rare earth metals*, Adv. Cryog. Eng. 33 (1988) 777-783

[386] A.V. Morozkin, V.K. Genchel, A.V. Knotko, V.O. Yapaskurt, J. Yao, S. Quezado, S.K. Malik, *Structural and magnetic properties of Fe_2P-type R_6TTe_2 compounds (R=Tb, Dy, Ho, Er, T= Fe, Co, Ru): Magnetic properties and specific features of magnetic entropy change*, J. Solid State Chem. 258 (2018) 201-211

[387] A.V. Morozkin, Yu Mozharivskyj, V. Svitlyk, R. Nirmala, S.K. Malik, *New ternary Yb_5Sb_3-type $R_5T_{1-x}Sb$, Bi_{2-x} phases (R = Y, Dy, Ho, T = Co, Ru, Rh, Pd) and their magnetic properties*, Intermetallics 19 (2011) 302-306

[388] A.B. Harris, *Effect of random defects on the critical behaviour of Ising models*, J. Phys. C: Solid State Phys. 7 (1974) 1671-1692

[389] M. Fähnle, *Non-monotonic temperature dependence of the effective susceptibility exponent — a characteristic feature of many disordered spin systems*, J. Magn. Magn. Mater. 65 (1987) 1-6

[390] M. Haug, M. Fähnle, H. Kronmüller, F. Haberey, *The magnetic phase transition in ordered and disordered ferrimagnets*, J. Magn. Magn. Mater. 69 (1987) 163-170

[391] A. Perumal, V. Srinivas, *Quenched disorder and the critical behavior of a partially frustrated system*, Phys. Rev. Lett. 91 (2003) 137202

[392] F. Wang, J. Zhang, F. Yuan, Y. Cao, C. Gao, Y. Hao, J. Shen, J. Sun, B. Shen, *Magnetic properties and magnetocaloric effect in $Ho_{6-x}Er_xMnBi_2$ compounds*, J. Appl. Phys. 107 (2010) 09A918

[393] W. He, J. Zhang, L. Zeng, P. Qin, G. Cai, *Thermomagnetic properties near transitions of Tb_6FeX_2 (X = Sb, Bi)*, J. Alloys Compd. 443 (2007) 15-19

[394] J. Zhang, G. Shan, Z. Zheng, C.H. Shek, *Structure and magnetic behaviors of Gd_6FeBi_2 compound*, Intermetallics 68 (2016) 51-56

[395] A.V. Morozkin, *New Zr_6CoAs_2-type R_6FeBi_2 (R=Y, Lu, Gd-Dy, Er, Tm)*, J. Alloys Compd. 358 (2003) L9-L10

[396] L. Jia, M. Koehler, D. McCarthy, M.A. McGuire, V. Keepens, *Structural and magnetic properties of $Tb_6Fe_{1-x}Co_xBi_2$ ($0 \le x \le 0.375$) compounds*, J. Appl. Phys. 109 (2011) Article 07E331

[397] G. Cuia, H. Mab, K.W. Wongc, C.H. Shek, G. Shand, J. Zhange, *Understanding high ordering temperature in Gd_6FeBi_2 magnet: critical behavior, electronic structure and crystal-field analysis*, J. Magn. Magn Mater. 499 (2020) 166301

[398] J. Szade, M. Drzyzga, *Magnetism and electronic structure of Gd_5Bi_3 and Gd_4Bi_3*, J. Alloys Compd. 299 (2000) 72-78

[399] S. Legvold, E.P. Wohlfarth, *Rare Earth Metals and Alloys, Ferromagnetic Materials*, Edit, Amsterdam, North-Holland Publish. Comp. (1980) 183-295

[400] S.N. Kaul, S. Srinath, *Gadolinium: a helical antiferromagnet or a collinear ferromagnet*, Phys. Rev. B 62 (2000) 1114-1117

[401] G. Bednarz, D.J.W. Geldart, M.A. White, *Heat capacity of gadolinium near the Curie temperature*, Phys. Rev. B 47 (1993) 14247-14259

[402] D.A. Shishkin, A.S. Volegov, V.V. Obloblichev, K.N. Mikhalev, E.G. Gerasimov, P.B. Terentev, V.S. Gaviko, D.I. Gorbunov, N.V. Baranov, *Effect of Tb for Gd substitution ion magnetic and magnetocaloric properties of melt-spun* $(Gd_{1-x}Tb_x)_3Co$ *alloys*, Intermetallics 104 (2019) 1-7

[403] Y. Itoh, T. Mizoguchi, K. Yoshimura, *Novel critical exponent of magnetization curves near the ferromagnetic quantum phase transitions of* $Sr_{1-x}Ca_xRuO_3$ *(A=Ca,* $La_{0.5}Na_{0.5}$*, and La)*, J. Phys. Soc. Jpn. 77 (2008) 123702

[404] D. Fuchs, M. Wissinger, J. Schmalian, C.L. Huang, R. Fromknecht, R. Schneider, H.v. Löhneysen, *Critical scaling analysis of the itinerant ferromagnet* $Sr_{1-x}Ca_xRuO_3$, Phys. Rev. B 89 (2014) 174405

[405] N. Assoudi, M. Smari, I. Walha, E. Dhahri, S. Shevyrtalov, O. Dikaya, V. Rodionova, *Unconventional critical behavior near the phase transition temperature and magnetocaloric effect in* $La_{0.5}Ca_{0.4}Ag_{0.1}MnO_3$ *compound*, Chem. Phys. Lett. 706 (2018) 182-188

[406] M. Triki, E. Dhahri, E.K. Hlil, *Unconventional critical magnetic behaviour in the Griffiths ferromagnet* $La_{0.4}Ca_{0.6}MnO_{2.8}\square_{0.2}$ *oxide*, J. Solid State Chem. 201 (2013) 63-67

[407] T. Kida, A. Senda, S. Yoshii, M. Hagiwara, T. Takeuchi, T. Nakano, I. Terasaki, *Unconventional critical behaviour in the weak ferromagnet* $BaIrO_3$, Europhys. Lett. 84 (2008) 27004

[408] F. Kagawa, K. Miyagawa, K. Kanoda, *Unconventional critical behaviour in a quasi-two-dimensional organic conductor*, Nature 436 (2005) 534-537

[409] A. Omerzu, M. Tokumoto, B. Tadić, D. Mihailovic, *Critical Exponents at the ferromagnetic Transition in tetrakis(dimethylamino)ethylene-*C_{60} *(TDAE-*C_{60}*)*, Phys. Rev. Lett. 87 (2001) 177025

[410] A.V. Morozkin, *New* Zr_6CoAs_2*-type* R_6FeSb_2 *(R = Sc, Y, Lu, Dy, Ho, Tm) and* Ho_6FeBi_2 *compounds*, J. Alloys Compd. 353 (2003) L16-L18

[411] A.V. Morozkin, *New* Zr_6CoAs_2*-type* R_6MnSb_2 *and* R_6MnBi_2 *compounds (R=Y, Lu, Dy, Ho)*, J. Alloys Compd. 360 (2003) L1-L2

[412] A.V. Morozkin, Yu. Mozharivskyj, V. Svitlyk, R. Nirmala, A.K. Nigam, *Magnetic properties of* Fe_2P*-type* Tb_6FeTe_2, Tb_6CoTe_2, Tb_6NiTe_2 *and* Er_6FeTe_2 *compounds*, J. Solid State Chem. 183 (2010) 3039–3051

[413] Springer Materials The Landolt-Börnstein Database - Materials Science Data for 250000 Substances, http://www.springermaterials.com

[414] A.V. Morozkin, O. Isnard, P. Henry, P. Manfrinetti, R. Nirmala, S.K. Malik, *Magnetic structures of* Zr_6CoAs_2*-type* $Ho_{6-x}Er_xMnBi_2$ *solid solutions*, J. Alloys Compd. 450 (2008) 62-74

[415] M. Drzyzga, J. Szade, *Structure and magnetism of* R_5Bi_3 *(R = Tb, Dy, Ho, Er) and* Tb_4Bi_3, J. Alloys Compd. 321 (2001) 27-34

[416] I.P. Semitelou, P. Kotsanidis, J.K Yakinthos, E. Roudaut, *The sine-modulated magnetic structure of* Dy_5Sb_3, J. Magn. Magn. Mater. 116 (1992) 103-107

[417] J.Y. Law, A. Diaz-Garcia, L.M. Moreno-Ramirez, V. Franco, *Increased magnetocaloric response of FeMnNiGeSi high-entropy alloys*, Acta Materialia 212 (2021) 116931

[418] J.Y. Law, L.M. Moreno-Ramirez, A. Diaz-Garcia, A. Martin-Cid, S. Kobayashi, S. Kawaguchi, T. Nakamura, V. Franco, *MnFeNiGeSi high-entropy alloy with large magnetocaloric effect*, J. Alloys Compd. 855 (2021) 157424

[419] A.E. Clark, H.S. Belson, N. Tamagawa, *Huge magnetocrystalline anisotropy in cubic rare earth-*Fe_2 *compounds*, Phys. Lett. A 42 (1972) 160–162

[420] A.E. Clark, *Magnetostrictive* RFe_2 *intermetallic compounds*, In *Handbook on the Physics and Chemistry of Rare Earths*, Editors: K.A. Gschneidner Jr, L. Eyring, vol. 2. North-Holland Publishing Company (1979) 231

[421] V. Paul-Boncour, M. Guillot, G. Wiesinger, G. André, *Giant isotope effect on the itinerant-electron metamagnetism in* $YFe_2(H_yD_{1-y})_{4.2}$, Phys. Rev. B 72 (2005) 174430

[422] V. Paul-Boncour, M. Guillot, O. Isnard, B. Ouladdiaf, A. Hoser, T. Hansen, N. Stuesser, *Interplay between crystal and magnetic structures in $YFe_2(H_\alpha D_{1-\alpha})_{4.2}$ compounds studied by neutron diffraction*, J. Solid State Chem. 245 (2017) 98-109

[423] V. Paul-Boncour, A.J. Percheron-Guégan *The influence of hydrogen on the magnetic properties and electronic structures of intermetallic compounds: YFe_2–D_2 system as an example*, J. Alloys Compd. 237 (1999) 193-295

[424] K. Kanematsu, N. Ohkubo, K. Itoh, S. Ban, T. Miyajima, Y. Yamaguchi, *Magnetic and Crystallographic Properties of Deuterides YFe_2D_x*, J. Phys. Soc. Jpn. 65 (1996) 1072-1976

[425] K.H.J. Buschow, *Hydrogen absorption and its effect on the magnetic properties of rare-earth iron intermetallics*, Solid State Comm. 19 (1976) 421-423

[426] V. Paul-Boncour, M. Escorne, A. Mauger, M. Latroche, A. Percheron-Guégan, *Deuteride absorption and desorption effects on magnetic properties of YFe_2D_x*, J. Appl. Phys. 79 (1996) 4253

[427] M. Halder, S.M. Yusuf, M.D. Mukadam, K. Shashikala, *Magnetocaloric effect and critical behavior near the paramagnetic to ferrimagnetic phase transition temperature in $TbCo_{2-x}Fe_x$*, Phys. Rev. B 81 (2010) 174402

[428] A. Murtaza, W. Zuo, J. Mi, Y. Li, A. Ghani, M. Yaseen, M.T. Khan, C. Hao, K. Li, Z. Dai, S. Yang, Y. Ren, *Magnetocaloric effect and critical exponent analysis around magnetic phase transition in $NdCo_2$ compound*, J. Phys. D: Appl. Phys. 53 (2020) 345003

[429] M. Latroche, V. Paul-Boncour, A. Percheron-Guégan, F. Bourée-Vigneron, *Crystallographic Study of $YFe_2D_{3.5}$ by X-Ray and Neutron Powder Diffraction*, J. Solid State Chem. 133 (1997) 568-571